Synthesis and Functionalisation of Endohedral Nitrogen Fullerenes: Towards Quantum Devices



Shen Zhou

Linacre College

A thesis submitted for the Degree of Doctor of Philosophy

University of Oxford

Hilary Term 2017

Synthesis and Functionalisation of Endohedral Nitrogen Fullerenes: Towards Quantum Devices

Shen Zhou, Linacre College

Submitted for the Degree of Doctor of Philosophy

University of Oxford, Hilary Term 2017

Abstract

Endohedral nitrogen fullerenes (ENFs) have been proposed as building blocks for quantum information processing due to very long relaxation time for their incarcerated electron spins. However, fabricating quantum devices based on this exotic material is still limited by the low yield of ENFs synthesis and various difficulties in subsequent molecular engineering, including the chemical sensitivity of the molecules, assembling approaches of the molecular architecture, and control of spin-spin coupling between qubits. My contributions towards removing the aforementioned limitations by studying the synthesis and functionalisation of ENFs are presented herein. My aim has been to pave the way towards quantum devices based on ENFs.

Firstly, I enhanced the ENFs production yield by a factor of five. I accomplished this by optimizing the ion implantation apparatus and parameters during the synthesis of raw ENFs, in addition to adjusting the column and eluent during the purification of ENFs by high performance liquid chromatography (HPLC).

Secondly, I established (for the first time) a spin-compatible protocol for performing Bingel reactions on ENFs. Utilizing the developed method, I also demonstrated the feasibility of chemically modifying ENFs for different molecular requirements *via* synthesizing a series of ENF derivatives with rigid configuration, long molecular aspect ratio, and amphiphilic properties.

Subsequently, I covalently assembled ENFs at microscopic levels and axially aligned ENFs at macroscopic levels, respectively. At the microscopic scale, I synthesized ENF-containing dyads and dimers, and developed a method of coaxially dimerizing ENFs with rigid bridge molecules, which provides material foundation for multi-qubit manipulations with spin couplings. At the macroscopic scale, I achieved the best orientational alignment of ENFs reported to date by embedding elongated ENF derivatives within a liquid crystal, which is critical for ensemble qubit with anisotropic spin properties. Benefiting from the good alignment, a controllability of the ensemble spin anisotropy is demonstrated with zero-field splitting of ENF derivatives.

Finally, I studied the electron spin dipolar coupling in ENFs by measuring and comparing of the coupling strength at different conditions. I discovered that the electron spin dipolar coupling in N@C_{60}-CuPc dyads can be chemically tuned by altering the lengths of the spacing groups between the two spin centres, and be physically adjusted by changing the sample concentrations to aggregate the sample and suppress the Cu electron spin.

In summary, aiming for ENF-based quantum devices, I made progress in both the material production and the molecular engineering of ENFs.

Acknowledgements

This PhD project could not be done without many gifted and kind people's help and support.

First of all, I thank my supervisor Prof. Kyriakos Porfyrakis for his tuition of all the basis and techniques related to fullerene science, as well as the generous facility and chemical approval for many of my naïve ideas. I also thank my co-supervisor Prof. Andrew Briggs for the helpful discussions every term. My sincere thanks go to Dr. William Myers and Dr. Stuart Cornes, who respectively are my *de facto* tutors in cw-ESR spectroscopy and synthetic chemistry. I also acknowledge many other senior research colleges in my group, Dr. Panagiotis Dallas, Dr. Maria Lebedeva and Dr. Xin Qian, as their various background knowledge inspire many interesting results of this work. I will not forget to thank Miss. Christina Foldbjerg, our scientific technician, who made the busy lab proper-functioning in the past three years.

Among all my fellow students, I owe my thanks to Mr. Reuben Harding the most for his constant help throughout my study in Oxford and the interesting work on ENF-based atomic clock. I am grateful to Dr. Masanori Yamamoto for the experiment and discussion on CuPc. I appreciate all the other group members, Mr. Yi Han, Mr. Henry Borrill, Mr. Harry Macpherson, Mr. Gregory Rogers and Mr. Ilija Rasovic for our mutual support.

I thank Prof. Alberta Ferrarini and Dr. Guoquan Liu for the patient email replies to my questions on order parameter and electron spin coupling, respectively. I thank Prof. Haifeng Cheng, and National University of Defence Technology (NUDT) for the scholarship support covering all my tuition fees and living expenses.

Finally, I thank my family members for their understanding and support. Especially, I thank my wife Dr. Shanshan Wang. The gratitude is beyond words.

Contributions

Starting material:

Most starting materials were obtained commercially, except for follows:

- MPc–CHO was obtained from Mr. Masanori Yamamoto.
- NC_{59}–CHO was obtained from Dr. Nikos Tagmatarchis.
- β-cyclodextrin was obtained from Dr. Stuart Cornes.

Experiment:

- The HPLC experiment using hexane-toluene mixtures as the eluent (Figure 69) was done in the collaboration with Mr. Harry Macpherson.
- The NMR data for DEM-C_{60} (Figure 75) was obtained by Mr. Ilija Rasovic.
- The MALDI-MS data for DEM-C_{60} (Figure 75) and IND-C_{60} (Figure 86 right) were obtained by Mass Spectrometry Facility at Swansea University.
- The ^{1}H-NMR data for 5-Bz-5 dimer (Figure 113) were obtained by NMR service in Chemistry department, Oxford University.
- The synthesis (Figure 117) and characterization (Figure 119) of 6-OPE-6 were done in the collaboration with Dr. Stuart Cornes.
- The DFT calculation (Figure 136) and DLC experiment (Figure 140) of N@C_{60}–MPc dyads were performed by Masanori Yamamoto

I can confirm that all the other work included in this thesis was performed by me.

Shen Zhou

Oxford, 2017

List of Publications

Shen Zhou and Kyriakos Porfyrakis, Chapter 13 Preparation and Chemistry of N@C_{60}, *Endohedral Fullerenes: Electron Transfer and Spin*, Springer International Publishing AG, 2017, ISBN 978-3-319-47047-4 (Chapter 2 and 4)

Shen Zhou, Ilija Rasovic, G. Andrew D. Briggs and Kyriakos Porfyrakis, Synthesis of the first completely spin-compatible N@C_{60} cyclopropane derivatives by carefully tuning the DBU base catalyst, *Chem. Commun.*, **2015**, 51, 7096-7097 **Chosen as the issue cover** (Chapter 5)

Shen Zhou, Masanori Yamamoto, G. Andrew D. Briggs, Hiroshi Imahori, and Kyriakos Porfyrakis, Probing the Dipolar Coupling in a Heterospin Endohedral Fullerene−Phthalocyanine Dyad, *J.A.C.S.*, **2016**, 138, 1313-1319 (Chapter 6 and 8)

Shen Zhou, William K. Myer, G. Andrew D. Briggs, and Kyriakos Porfyrakis, Synthesis and alignment of endohedral fullerene derivatives towards a controllable fullerene qubits ensemble, *in preparation*. (Chapter 5, 6, and 7)

R. T. Harding, **S. Zhou**, J. Zhou, T. Lindvall, W. K. Myers, A. Ardavan, G. A. D. Briggs, K. Porfyrakis, E. A. Laird, The spin resonance clock transition of the endohedral fullerene ^{15}N@C_{60}, *Phy. Rev. Let.*, **2017**, accepted. (Chapter 4)

Stuart P. Cornes, **Shen Zhou** and Kyriakos Porfyrakis, Synthesis and EPR studies of the first water-soluble N@C_{60} derivative, *Chem. Commun.*, **2017**, submitted *(Chapter 5)*

Abbreviations

AFC	automatic frequency control
CNT	carbon nanotube
cw-ESR	continuous wave-electron spin resonance
DBU	1,8-Diazabicyclo(5.4.0)undec-7-ene
DCTB	*trans*-2-[3-(4-tert-butylphenyl)-2-methyl-2-propenylidene] malononitrile
DEER	double electron-electron resonance
DLS	dynamic light scattering
DMF	N,N-Dimethylformamide
EF	endohedral fullerene
EI	electron impact ionization
EMF	endohedral metallofullerene
ENF	endohedral nitrogen fullerene
ESI	electron spray ionization
FID	free induction decay
HFC	hyperfine coupling
HFCC	hyperfine coupling constant
HPLC	high performance liquid chromatography
HRTEM	high resolution transmission electron microscopy
I_h, D_{5h}, D_{6d}, T_d, D_2, C_2, C_{2v}, C_{3v}, *etc.*	point group symbols (Schoenflies notation)
IPR	isolated pentagon rule
MALDI	matrix-assisted laser desorption ionization
MBBA	4-methoxybenzylidene-4'-*n*-butylaniline

Mel	melamine
MS	mass spectrometry
NMP	N-methyl-2-pyrrolidone
NMR	nuclear magnetic resonance
NP problem	difficult problems which are not possible to solve within a polynomial time by any applicable algorithm
o-DCB	1,2-dichlorobenzene
P_1-*t*Bu	tert-butyliminotris(dimethylamino) phosphorene
PAA	4,4'-azoxyanisole
Pc	phthalocyanine
PL	photoluminescence
POM	polarizing optical microscope
ppm	parts per million
PTCDI	3,4,9,10-perylene tetracarboxylic diimide
QIP	quantum information processing
RF	radio frequency
RIDME	relaxation induced dipolar modulation
sc	supercritical
sccm	standard cubic centimetre per minute
STM	scanning tunnelling microscope
SWCNT	single-walled nanotubes
T_1	spin-lattice relaxation time
T_2	spin-spin relaxation time
TEM	transmission electron microscopy

TEMPO	2,2,6,6-Tetramethyl-1-piperidinyloxy
TLC	thin layer chromatography
TMS	tetramethylsilance
TPP	tetraphenylporphyrin
UV/Vis	ultraviolet-visible
XRD	X-ray diffraction
ZFS	zero-field splitting

Names of ENF derivatives

Compound abbreviation	Formula	Structure
DEM-N@C_{60}	N@$C_{67}H_{10}O_2$	Figure 73
IND-N@C_{60}	N@$C_{69}H_4O_2$	Figure 84
Iodo-QUI-N@C_{60}	N@$C_{69}H_6O_2NI$	Figure 84
IND-N@C_{70}	N@$C_{79}H_4O_2$	Figure 90
Bis-IND-N@C_{70}	N@$C_{88}H_8O_4$	Figure 90
β-CD-N@C_{60}	N@$C_{195}H_{232}O_{76}N_2$	Figure 93
N@C_{60}-1-CuPc	N@$C_{209}H_{193}O_{13}N_9Cu$	Figure 100
N@C_{60}-2-CuPc	N@$C_{215}H_{197}O_{14}N_9Cu$	Figure 100
N@C_{60}-1-ZnPc	N@$C_{209}H_{193}O_{13}N_9Zn$	Figure 100
PYR-N@C_{60}	N@$C_{76}H_{33}N$	Figure 104
PYR-N@C_{60} dimer*	N@$C_{160}H_{68}N_2O_2$	Figure 104
5-Bz-5 dimer*	N@$C_{132}O_4H_2$	Figure 112
6-NAPH-6 dimer*	N@$C_{136}O_4H_4$	Figure 115
6-OPE-6 dimer*	N@$C_{194}H_{64}O_4N_2$	Figure 120

* Half-filled dimer, only one of the fullerene moiety in the dimer contains an endohedral nitrogen atom.

Terms

empty-cage fullerene	Classical fullerenes without an endohedral chemical moiety
Fullerene soot (obtained from an ion implantation procedure)	The initial product collected from the deposition target, which contains soluble fullerenes and other insoluble by-products.
crude product (obtained from an ion implantation procedure)	Soluble part of the fullerene soot which contains the desired ENF and its corresponding empty-cage fullerene
spin-yield	The mole ratio between the ENF and the empty-cage fullerene in the crude product synthesized
column efficiency	The effectiveness of separation two species having similar retention time, quantified by number of theoretical plates
Recycling-mode HPLC	A method of enhancing the HPLC column efficiency, by resending the analyte back to the column multiple times, which enlarges the retention time difference without broaden the HPLC peaks too significantly
[6,6] bond	The carbon-carbon bond between two 6-membered rings on a fullerene cage
[5,6] bond	The carbon-carbon bond between a 5-membered ring and a 6-membered ring on a fullerene cage
addend	Functional groups added on the fullerene cage
molecular aspect ratio (of a fullerene molecule)	The ratio between the size of fullerene molecule in the long direction to that in the short direction
spin retention ratio (of an ENF reaction)	The parameter describing the ENF surviving ratio after a reaction, which is measured by dividing the double integral of the spin

	signal of the reaction mixture after the reaction by that before the reaction
spirocyclic-methano-fullerene	A type of novel methano-fullerenes synthesized in this work. The functional group attaches to the fullerene cage with a spirocyclic structure
half-filled ENF dimer	A fullerene dimer with one fullerene moiety being ENF, and one being empty-cage fullerene
double-filled ENF dimer	A fullerene dimer with both fullerene moieties being ENFs
microscopic assembly of ENFs	Gathering ENF molecules together in a microscopic scale
Macroscopic alignment of ENFs	Adjusting the orientations of the ENF molecules to the same direction for the molecular ensemble in macroscopic scale
HFC peaks (in a ENF derivative spectrum)	Main cw-ESR signal of ENF derivative, which is unchanged by the introduction of the ZFS
ZFS peaks (in a ENF derivative spectrum)	Small cw-ESR peaks on both sides of each of the HFC peak, which are caused by the ZFS

Contents

Chapter 1 Introduction 1
1.1 Project Aims 1
1.2 Scope of the thesis 4

Chapter 2 Literature review 5
2.1 Background: using ENF as a molecular qubit 5
2.1.1 Fullerenes and ENF 5
2.1.2 Quantum information processing and spin qubits 11
2.1.3 DiVincenzo criteria and ENF-based QIP 13
2.2 Synthesis and purification of ENFs 16
2.2.1 ENF synthesis 16
2.2.2 ENF purification 20
2.3 Fullerene chemistry and ENF derivatization 23
2.3.1 Pericyclic reaction 23
2.3.2 Nucleophilic addition 24
2.3.3 Previously reported ENF derivatives and their ZFS 28
2.4 Microscopic assembly of fullerenes for distance control between qubits 35
2.4.1 Fullerenes on substrates: assembly using 2D substrates 35
2.4.2 Fullerene peapod: assembly in single-walled nanotubes 38
2.4.3 Fullerene dimers: assembly with chemical bonds 39
2.5 Macroscopic alignment of fullerenes for orientational ordering of qubits 44
2.5.1 Fullerene alignment in the single crystal 44
2.5.2 Fullerene alignment in co-crystals 45
2.5.3 Fullerene alignment in liquid crystals 48
2.6 Dipolar coupling in EF-containing di-electron-spin systems 52
2.6.1 N@C_{60}–CuTPP dyad 52
2.6.2 FSc_3C_2@C_{80}–PNO radical 53
2.6.3 N@C_{60}–N@C_{60} dimer 54
2.7 Conclusions 57

Chapter 3 Methodology 59
3.1 Experimental Techniques 59
3.1.1 High performance liquid chromatography 59
3.1.2 Matrix-assisted laser desorption ionization mass spectrometry 61
3.1.3 X-band continuous wave electron spin resonance spectroscopy 63
3.1.4 Nuclear magnetic resonance spectroscopy 69
3.1.5 Ultraviolet-visible absorption spectroscopy 70
3.1.6 Photoluminescence spectroscopy 71
3.2 Preparation procedures for pristine ENFs 73

3.2.1 Synthesis of ENFs with ion implantation apparatus 73
3.2.2 Purification of ENFs with HPLC 74
3.3 Organic synthetic procedures 75
3.3.1 Synthesizing ENF derivatives using the spin-compatible Bingel reaction 75
3.3.2 Synthesizing N@C_{60}-containing dyads and dimers 78

Chapter 4 Optimizing the ENF production: Towards available and affordable qubits 83
4.1 Introduction 84
4.2 Optimizing the synthesis 86
4.2.1 Feedback control of fullerene deposition rates using LabVIEW 86
4.2.2 Parameter optimization for ion implantation using the DC25s ion source 88
4.2.3 Parameter optimization for implantation using the eH400 ion source 91
4.2.4 Suppressing the in-situ decomposition of ENF 95
4.3 Optimizing the HPLC purification procedure 98
4.3.1 Optimal column for the HPLC purification 98
4.3.2 Improving column capacity by automatic repeat injection/collection 102
4.3.3 Changing the analyte: cage size influence 103
4.3.4 Changing the mobile phase: eluent polarizability influence 105
4.3.5 Discussion on the retention time ratio for further improvements 106
4.4 Conclusions 109

Chapter 5 Functionalising ENFs with Bingel reactions: Towards chemically tuneable qubit
112
5.1 Introduction 113
5.2 Developing a spin-compatible Bingel reaction 115
5.2.1 Spin-Compatibility study of the Bingel reaction 115
5.2.2 Spin-destructive effect caused by excess of auxiliary base 119
5.3 Synthesis of spirocyclic-methano-ENFs for rigid and elongated molecular geometry 125
5.3.1 Spirocyclic-methano-N@C_{60} 125
5.3.2 Bis-spirocyclic-methano-N@C_{70} 132
5.4 Chemical functionalisation with β-cyclodextrin for amphiphilic ENFs 137
5.4.1 Preparation of β-CD-N@C_{60} 137
5.4.2 Electron spin signal of β-CD-N@C_{60} in different solvent 140
5.4.3 Radical detection with β-CD-N@C_{60} 143
5.5 Conclusion 146

Chapter 6 Synthesizing ENF-containing dyads and dimers: Towards covalently assembled qubits 148
6.1 Introduction 149
6.2 Synthesis and characterization of ENF containing hetero dyads 150
6.3 Dimerizing ENFs with amide bonds 154

6.3.1 Synthesis of PYR-N@C_{60} and PYR-N@C_{60} dimer 154
6.3.2 Characterization of PYR-N@C_{60} and PYR-N@C_{60} dimer 156
6.4 Dimerizing ENFs with rigid coaxial bridges 160
6.4.1 Dimer design 160
6.4.2 Synthesis and characterization of 5-Bz-5 dimer and 6-NAPH-6 dimer 163
6.4.3 Synthesis and characterization of 6-OPE-6 dimer 168
6.5 Conclusions 174

Chapter 7 Axially aligning ENFs in a liquid crystal: Towards orientationally ordered qubits 175
7.1 Introduction 176
7.2 Sample alignment and zero-field splitting 178
7.2.1 Aligning ENF derivatives in MBBA 178
7.2.2 Zero-field splitting and its containing orientation information 179
7.3 Extracting the alignment information 183
7.3.1 cw-ESR characterization of the aligned sample in the rigid limit 183
7.3.2 cw-ESR characterization of the aligned sample in the slow-motion 186
7.4 Controlling the strength zero-field splitting 190
7.5 Conclusions 193

Chapter 8 Probing dipolar coupling in ENF-containing dyads: Towards controllably coupled qubits 194
8.1 Introduction 195
8.2 Analysis of the electron spin properties of the hetero-spin dyad 197
8.2.1 Solution cw-ESR 197
8.2.2 Solid-state cw-ESR 200
8.3 Dipolar coupling strength study 205
8.3.1 Initial simulation for the spectra 205
8.3.2 Explaining the weak coupling strength 208
8.3.3 Simulation for the spectra taking aggregation into account 214
8.4 Concentration dependent cw-ESR 218
8.5 Conclusions 220

Chapter 9 Conclusions and Outlook 221
9.1 Conclusions 221
9.2 Future work 225

Appendix A. Supporting information 226

Appendix B. Programming codes 249

Appendix C. References 279

Chapter 1 Introduction

1.1 Project Aims

This work was motivated by the possibility of implementing of endohedral nitrogen fullerene (ENF)-based quantum devices. As one of the most interesting endohedral fullerene (EF), ENF has been proposed as a molecular qubit for quantum information processing (QIP) due to the long relaxation time of the incarcerated electron spins.[1–5] However, it has yet to be demonstrated that ENF-based qubits satisfy all of the DiVincenzo requirements, which are essential for implementing a universal quantum computer.[6] These include obtaining a scalable qubit system, performing two-qubit operations, and measuring individual qubits (red textboxes in Figure 1). These targets could be reached by exploiting the chemistry of ENFs with a plausible route map to consummate the material and to head towards an ENF-based QIP paradigm. As shown in blue textboxes in Figure 1, the three remaining DiVincenzo criteria can be achieved by the ENF microscopic assembly, the ENF spin coupling strength control, and the ENF alignment, respectively. The synthesis and chemical functionalisation of ENFs also need to be investigated due to their fundamental roles to the above studies.

Applying the route map to enhance the property of ENFs as build blocks towards quantum devices, I have set five corresponding aims for this thesis:

1. For the pristine ENFs, I studied the production of pristine ENFs and improved the extremely low yield of the material.

2. For the ENF chemical functionalisation, I developed a set of ENF-compatible chemical reactions to cope with the spin loss problem reported for ENF reactions.

3. For the microscopic assembly of ENFs, I synthesized ENF-containing dyads and dimers to pave the way towards multi-spin systems.

4. For the orientational alignment of ENFs, I prepared highly axially aligned ENF derivatives within a liquid crystal matrix and further demonstrated orientational control of the obtained spin ensembles.

5. For the spin coupling of ENFs, I investigated the spin coupling in ENFs and discovered approaches to tune the coupling strength physically and chemically.

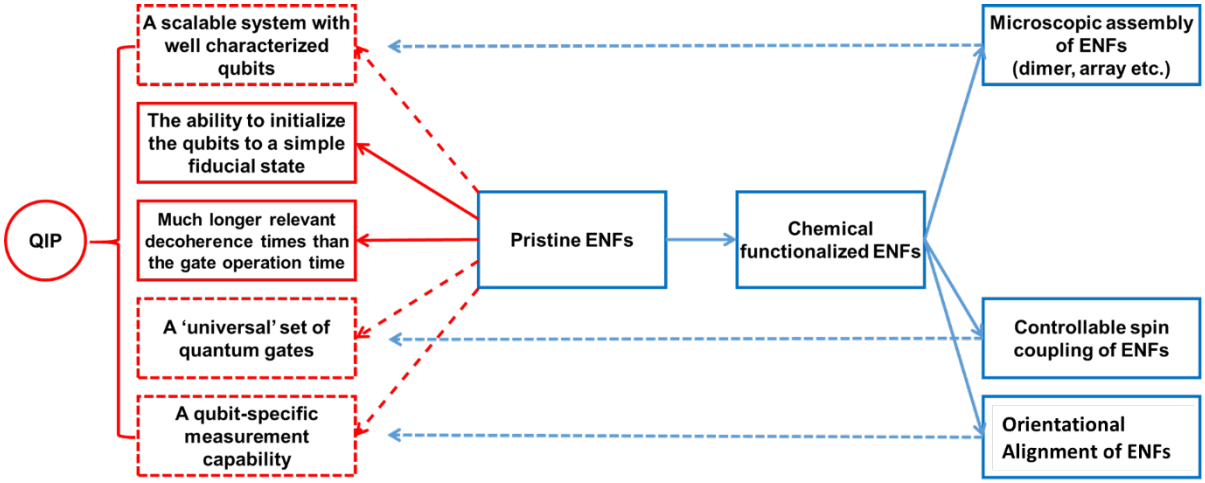


Figure 1 Incomplete satisfaction of pristine ENFs to DiVincenzo criteria (red boxes), and a viable route map to consummate the material of ENF and to head towards an ENF-based QIP using fullerene chemistry (Blue boxes).

Since the start of the work, the implementation of QIP has been progressed at an amazing pace. The universal quantum computer **IBM Q** and dedicated quantum computer **D-Wave** have been built. Beyond these achievements, remarkable progress has been made in other matter-based implementations of qubits, such as ion traps[7–9] superconducting circuits[10–12] and crystalline solids,[13,14] to such an extent that for the foreseeable future they are the leading candidates for building a quantum computer. Nevertheless, quantum technologies are here to stay, and, as they develop, opportunities may arise that can best be exploited using molecular-based spin systems. When that day comes, this work will have laid the foundation for

advanced chemical control of these materials. Meanwhile, the synthesis and chemical functionalisation studies on ENFs also provide feasible molecular engineering methodologies for the ENF system, which have already inspired and enabled new applications for this material, such as ENF-based molecular atomic clock, ENF-based sensitive radical indicator, *etc*.

1.2 Scope of the thesis

This thesis is composed of nine chapters, including the introduction, the literature review, the methodology, the results, and the conclusion. The introduction briefly depicts the aim and an investigation route of consummating ENF as a useful building block for quantum applications. The literature review explains the motivation for using ENFs as molecular qubits, and summarizes the reported synthesis and functionalisation studies on ENFs, which are relevant to the aforementioned investigation route, including the preparation, chemical reaction, assembly, alignment, and spin coupling researches on ENFs. The methodology part documents the experimental techniques and synthetic details involved in this work. The result chapters report my efforts and achievements towards the route. It consists of (1) an ENF production study, which leads to a five-time improvement on the productivity of ENFs by optimizing the efficiency of the synthesis and purification procedures; (2) an ENF chemical derivatization study, which opens up a diverse and reliable way to functionalise ENFs by developing the spin-compatible Bingel reaction; (3) an ENF dyad/dimer study, which demonstrates the synthesis of a series of ENF-containing dyads and dimers by applying the well-reported Prato reaction and my newly developed spin-compatible Bingel reaction; (4) an ENF axial alignment study, which establishes an approach to obtain and characterize the highly axially aligned ENF derivative arrays by selecting the ENF derivative and analysing the spin anisotropy, respectively; and (5) an ENF spin coupling study, which unfolds the insufficiently reported electron-electron dipole coupling studies on an EF-based system. The last chapter recaps my research with significant achievements for each sub-project. Potential future investigations on related topics are also discussed in the outlook section. In addition, this thesis also has three additional contents: The list of cited references, intermediate data supporting claims made in the results chapters, and relevant computer programmes are attached to the end of the thesis.

Chapter 2 Literature review

2.1 Background: using ENF as a molecular qubit

By briefly introducing ENF and QIP and reviewing the feasibility of using ENF as a qubit, this section explains the motivation of this thesis and my research aims, which have been highlighted in Chapter 1.

2.1.1 Fullerenes and ENF

In contrast to graphite and diamond, fullerenes are a type of carbon allotropes in molecular forms. Firstly reported by Kroto and Smalley *et al.*,[15] this group of hollow-ball-shaped molecules composed of carbon atoms with hexagons and pentagons caused a surge in carbon nanomaterial research. Even without considering other carbon nanomaterials, such as graphene[16] and carbon nanotubes,[16] the study of fullerenes alone consists of a large variety of interesting topics. For chemists and materials scientists, an intriguing aspect of fullerenes is their near-spherical structures, which results in a special symmetry. Commonly reported fullerenes are C_{60}-I_h, C_{70}-D_{5h}, C_{72}-D_{6d}, C_{76}-T_d, -D_2, and C_{84}-C_2, -C_{2v}, -C_{3v}, *etc*. (where the symbols following the chemical formula are the point groups representing the molecular symmetry),[17,18] but, mathematically, the fullerene family includes millions of homologues.[18]

Whilst C_{60}-I_h is the most experimentally abundant fullerene, it is also the smallest possible fullerene configuration that follows the “isolated pentagon rule” (IPR), which states that all

pentagons to be completely separated from each other by hexagons. The other potential isomers of C_{60} predicted by theories, which do not obey the IPR, were calculated to be at least $2\ \mathrm{eV}$ higher in energy than C_{60}-I_h, and therefore have not yet been experimentally discovered.[16] For clarity, symmetry notations are omitted in this thesis when the fullerene structure has no ambiguity, *e.g.* all C_{60} and C_{70} represent only the isomers C_{60}-I_h and C_{70}-D_{5h} that obey the IPR, respectively. IPR forbids the [5,5] type of bonds (carbon-carbon bond between two 5-membered rings) on a fullerene cage, and permits only [6,6] bonds ($1.355\ \text{Å}$ bond length in C_{60})[19] and [5,6] bonds ($1.467\ \text{Å}$ bond length in C_{60}).[19]

Despite the unique structure of a fullerene, the properties of this elementary substance are not sufficiently tuneable to satisfy various application requirements. Therefore, people moved one step forward to dope hetero elements inside carbon cages and obtain the endohedral fullerene (EF),[3,20–30] where “endohedral” is the combination of two Greek words (*ενδο* and *έδρα*) meaning “within the faces of a polyhedron”. Since then, fullerenes can be divided into two categories: the EFs and empty-cage fullerenes (classical fullerenes without an endohedral chemical moiety). EFs can be divided further into two categories, metallic and non-metallic, depending on the species that is incarcerated within the carbon cage (Table 1). The focus of this thesis, the endohedral nitrogen fullerene (ENF), belongs to the non-metallic category.

Table 1 Different EFs depending on the encapsulated species

Species	Metallic		Non-metallic	
	Metal ion(s)	Templated metallic cluster	Molecule/noble gases	Non-metallic atomic radical
Example	$Y@C_{82}$[31] $Sc_2@C_{66}$[32]	$Sc_3N@C_{80}$[33] $Sc_2C_2@C_{84}$[34]	$HF@C_{60}$[35] $He@C_{60}$[36,37]	ENFs[38] $P@C_{60}$[39]
Typical method of synthesis	Arc discharge[40]	Arc discharge[40]	Molecular surgary[35]	Ion implantation[38]

The majority of the published literature has focused on the metallic fullerenes, which are named endohedral metallofullerenes (EMFs). This is not only because their synthetic method

(arc discharge)[40] is similar to that of empty-cage fullerenes, but also because of the diverse species of metal (especially lanthanide) moieties and the cage sizes. The delicate combination of metal and carbon cage also offers an array of interesting structures, properties and performances,[21,26] which can hardly be achieved from neither a carbon cage on its own nor a metallic material. A detailed introduction to EMFs is beyond the scope of this work. However, it is worth mentioning that some mono-metallic EMFs, such as Y, Sc, and La@C_{82}, have been reported to show long electron spin relaxation times and may also have potential for QIP-related applications.[41]

The study of non-metallic EFs can be further divided into (1) fullerenes containing a stable molecule or a noble gas and (2) fullerenes containing a metastable radical. When a stable chemical moiety is enclosed inside of the carbon cage, the product can be regarded as two isolated molecules assembled in a core-shell manner. Both the mechanical rotation[35] and the chemical shift of the nuclear magnetic resonance (NMR) signal[36] of the encapsulated molecule is not significantly influenced by the cage outside. Due to the weak interactions between the two constituent parts, this type of EF is therefore a perfect platform for studying isolated atoms or molecules.[35,42]

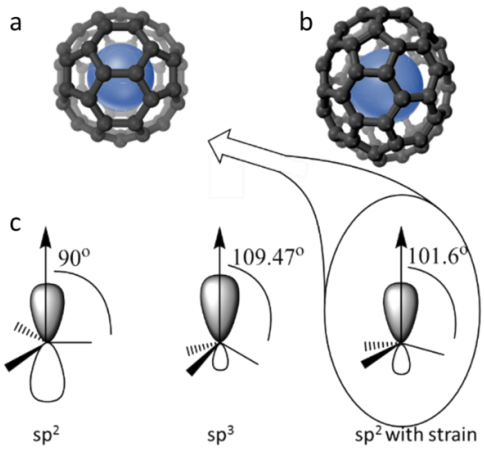


Figure 2 (a) Molecular models of N@C_{60} and (b) N@C_{70}. (c) Comparison of bond angles in ideally planar sp^2-hybridized carbon, ideally tetrahedral sp^3-hybridized carbon, and the distorted sp^2-hybridized carbon in C_{60}.

When a radical is enclosed inside of the carbon cage, interesting paramagnetic products such as ENFs will be obtained. Successfully synthesized ENFs include N@C_{60} and N@C_{70}

(Figure 2a, b). Regarding the structure of ENFs, both experimental[43,44] and theoretical[45,46] studies point out that this type of EF has no ionic bond or covalent bond between the cage and the nitrogen atom. The absence of the ionic interaction is due to the electron deficiency of both the fullerene and the nitrogen atom, which prohibits charge transfer between the core and shell. The reason for no covalent interactions lies in the extreme kinetic inertness of the inner surface of the carbon cage. Although all carbons on the cage are sp^2-hybridized, their bond angles are closer to those of an sp^3 carbon due to the non-planar geometry of the spherical cage surface (Figure 2c).[47] Therefore, the formation of an endohedral covalent bond is sterically hindered.

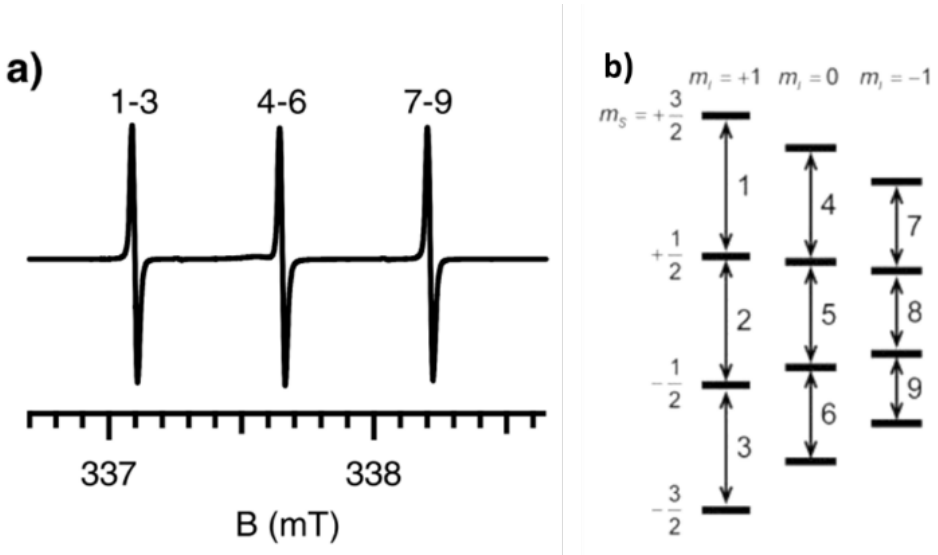


Figure 3 (a) cw-ESR spectrum of N@C_{60} diluted in C_{60} powder. (b) Energy diagram and allowed transitions of ^{14}N@C_{60} in high field limit. Figure reproduced from Harneit, W. *et al*.[5]

The absence of endohedral chemical bonding and the spherical structure of the cage make the paramagnetic systems of ENFs similar to an atomic nitrogen, which has three unpaired electrons in the degenerate $2p$ orbitals. ENFs' Hamiltonian can be written as:

$$\widehat{\mathcal{H}} = \frac{\mu_B}{\hbar}\boldsymbol{B}_0^T\boldsymbol{g}\hat{\boldsymbol{S}} + \hat{\boldsymbol{S}}^T\boldsymbol{A}\hat{\boldsymbol{I}}^{(N)} + \hat{\boldsymbol{S}}^T\boldsymbol{D}\hat{\boldsymbol{S}} \qquad \text{Eq.2.1}$$

where μ_B is the Bohr magneton, $\boldsymbol{B}_0$ is the external field, $\boldsymbol{g}$ is the *g*-tensor of the electron spin, $\boldsymbol{A}$ is the hyperfine coupling (HFC) tensor between the electron spin and nitrogen nucleus, and $\boldsymbol{D}$ represents the zero-field splitting (ZFS) tensor. The quadrupole coupling, the Zeeman energy of the nitrogen nucleus, and HFCs between the electron spin and ^{13}C nuclei on the

fullerene cage have been omitted here for their negligible impact. The *g*-tensor and the HFC tensor are isotropic, and the ZFS tensor equals zero. All these spin features result in a relatively simple X-band continuous wave- (cw-) electron spin resonance (ESR) spectrum for pristine ENFs, *e.g.* the spectrum of $^{14}N@C_{60}$ in Figure 3a showing the triplet pattern caused by the HFC of the ^{14}N nuclear spin ($I = 1$, Figure 3b).[5] This is conducive to displaying any change of the spin properties after a subtle variation on the chemical environment of the molecule. The application of this advantage will be demonstrated later by the cw-ESR spectroscopy studies of functionalised ENFs throughout this thesis.

The uniqueness of the cw-ENF spectrum not only lies in the simple pattern, but is also represented by the ultra-sharp resonance peaks. To resolve the linewidth of the peak, a high-resolution ESR measurement has been reported for $^{14}N@C_{60}$ (Figure 4), which zoomed in the small range of each of the triplet signals.[4] The linewidth was measured to be less than $0.3\ \mu T$, and more detailed spin features down to the 10^5 Hz scale, such as the pattern caused by the second-order hyperfine splitting of the nitrogen nuclear spin and the HFC of the ^{13}C nuclear spin, were also detected.[4,48]

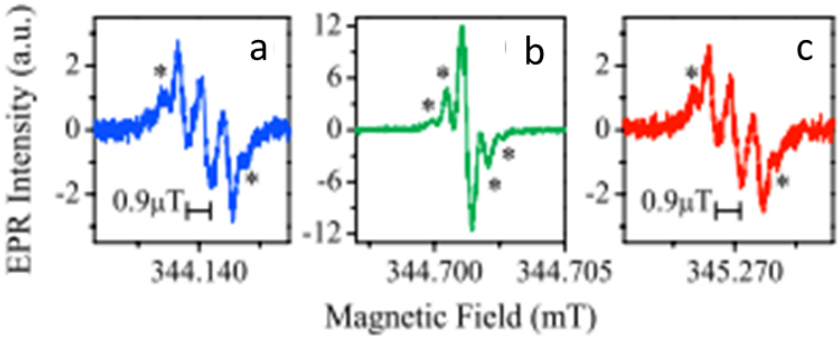


Figure 4 Zoom-in for each of the three HFC lines (a: $M_I = -1$, b: $M_I = 0$, and c: $M_I = +1$), showing the sharp linewidth and the second order hyperfine pattern. (Asterisks mark the line split by ^{13}C HFC interactions.) Figure reproduced from Morton, J. J. L. *et al*.[4]

The fundamental reason of the sharp spin signal of ENFs is the long election spin relaxation time.[49,50] The relaxation time consists of the spin-lattice relaxation time (T_1) and the spin-spin relaxation time (T_2), which respectively parameterize the decay of longitudinal and transverse magnetization when the electron spin is polarized along the X direction of the Bloch

sphere (Figure 5a). Spin-lattice relaxation involves interaction of the spin system with lattice vibrations (phonons), such as direct process, Raman process, Orbach process.[51] Spin-spin relaxation can be caused by a field inhomogeneity and/or a direct interaction between the spins without energy transfer to the lattice.[52] T_2 is always shorter than T_1 for a given spin system, hence it is often the decoherence time relevant for quantum technologies.[53] For $^{14}N@C_{60}$, $T_2 = 250\ \mu s$ was measured at $170\ K$ (Figure 5b), which is one of the longest spin-spin relaxation times for molecular radicals (surpassed only by $(d_{20}\text{-}Ph_4P)_2[V(C_8S_8)_3]$ in 2015).[54] The high structural symmetry of the whole molecule and a strong protection effect from the cage have been proposed as the main reasons for this behaviour.[55] Compared to other candidate qubits based on electron spins (Figure 6),[56–63] the long spin relaxation times of ENFs are in the desired range for electron spin based QIP.

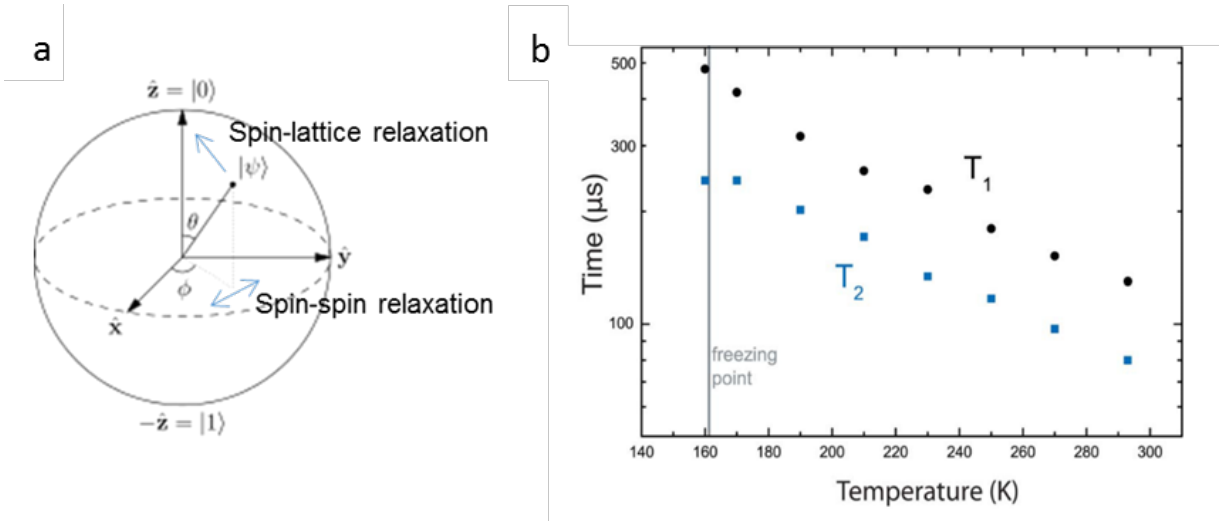


Figure 5 (a) spin-lattice relaxation and spin-spin relaxation. (b) Electron spin relaxation times (T_1 and T_2) of $N@C_{60}$ in CS_2, by measuring the $M_I = 0$ resonance (central signal in Figure 3a). Figure reproduced from Morton, J. J. L. *et al.*[49]

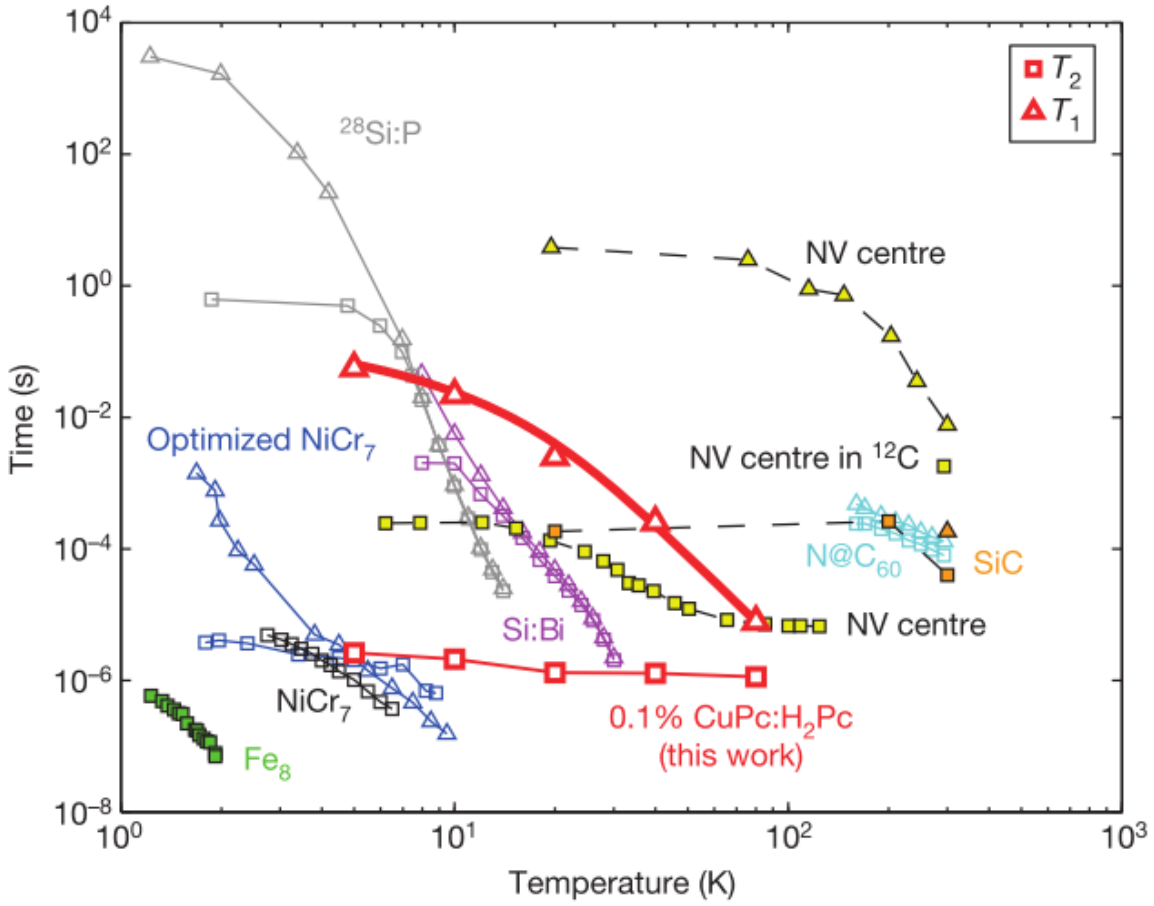


Figure 6 T_1 and T_2 versus temperature for different spin qubit candidates. It should be noted that the data in this comparison were not all collected at the same magnetic field, but represent the best available comparison from the literature: N@C_{60},[49] 0.1% CuPc:H_2Pc,[56] $NiCr_7$,[57] Fe_8,[57] optimized $NiCr_7$,[58] ^{28}Si:P,[59] Si:Bi,[60] nitrogen–vacancy (NV) center,[61] nitrogen–vacancy center in ^{12}C,[62] and defect in SiC.[63] Figure reproduced from Warner M. *et al*.[56]

2.1.2 Quantum information processing and spin qubits

While the modern electronics computing industry, founded upon the deterministic classical theory, has experienced an amazingly exponential growth for decades,[64] scientists have not limited their horizon just to the 0/1 binary world. Thus, a revolutionary way of computing, quantum information processing (QIP), has emerged.[6,56,65–68]

There are two practical facts that broaden researchers' attention from conventional computing to QIP. The first reason is to implement quantum algorithms which can effectively solve NP problems (difficult problems which are not possible to solve within a polynomial time by any applicable algorithm). Taking prime factorization as an example, it has been regarded

as an NP problem for conventional computers, and RSA public-key cryptography[69] relies on the difficulty of solving this problem. However, this cryptosystem can be cracked easily by the quantum Fourier transform algorithm (Shor's algorithm).[70] The other reason is the scale limitation of the computational components. Quantum interferences will affect electronic devices once their dimensions reach the atomic scale, in which case classical theories may no longer be applicable.[71] Therefore, quantum mechanics must be taken into consideration for the design of further smaller electronic devices. Utilizing the quantum effect to develop quantum computers rather than simply finding ways to solve the limitation of conventional computers could be a more feasible way for progress.

Different proposals have been put forward after the concept of quantum information processing emerged. In terms of using physical system of spins, the first inspirational achievement of factorizing 15 into 3 and 5 by Shor's algorithm was done using NMR quantum computing in 2001.[72] Using a similar approach, 143 was also successfully factorized in 2012.[73] However, before these experiments, the NMR approach had already been criticized because its failure of preparing pure initial states for the quantum computing to start with.[74] As the criticism addressed, the low flipping energy of nuclear spins, which is far below the thermal energy ($\mu_n g_I B_0 \ll kT$) makes nuclear spin qubits fluctuate constantly. Therefore, further progress of the NMR quantum computing experienced difficulty in initialisation. Researchers have tried to bypass the thermal energy problem through producing a pseudo-pure initial state[73] that can replace the non-achievable pure eigenstate as the effective qubit in a spin ensemble. Nevertheless, the effective qubit signal has an exponentially decay with respect to an increasing number of qubits in the system. Therefore, this solution is not scalable for quantum computing.

To directly tackle the low flipping energy problem, one may change the experimental conditions such as B_0 and T, or implement the experiment with other quantum mechanical systems having more pronounced energy splitting effects. For the first approach, a larger magnetic field B_0 and lower temperature T can promote the Zeeman splitting and diminish the

thermal energy, respectively. However, the generation of such a high magnetic field and low temperature to make nuclear spins reach pure states ($B_0{:}T > 10^3\ \mathrm{T/K}$) exceeds current technical capabilities. For the second approach, people turn to other quantum mechanical transitions. While the ion trapping[7–9] approach uses transitions between different atomic energy levels and superconducting circuit with Josephson junction[10–12] uses transitions between different circuit oscillation states, simply changing the resonance spin from nucleus to electron[13,14,75] can also effective address the problem due to the greater magnetic moment of the electron spin ($\mu_\mathrm{B} \approx 1836{\times}\mu_n$). Thus, an intriguing field of ESR-based QIP arises.

2.1.3 DiVincenzo criteria and ENF-based QIP

For physical systems to be used for universal quantum computation, a set of criteria developed by DiVincenzo are widely accepted:[6] "(1) a scalable system with well-characterized qubits; (2) the ability to initialize the qubits to a simple fiducial state; (3) long relevant decoherence times, which sufficiently exceed the gate operation time; (4) a 'universal' set of quantum gates; (5) a qubit-specific measurement capability." Among different electron spin candidates, the ENF-based qubit has advantages for the above criteria, but there are still unfulfilled requirements waiting for solutions. Both advantages and weaknesses for ENFs to fulfil each criterion are discussed as follows:

Criterion 1: To describe a qubit for QIP, a binary-state quantum system is required. In addition, such system needs to be scalable to a multi-qubit system with abilities such as quantum entanglement. ENFs fulfil this criterion partially. There are enough electron spin states in the electron spin of one molecule to represent two states of $|0\rangle$ and $|1\rangle$ as the electron spin qubit.[1] The $S = 3/2$ electron spin of ENFs could afford a qutrit or qudit for multilevel quantum computation.[76] The remaining question is how to scale-up the one-qubit molecule by assembling ENFs close to each other. Depending on the dimension of the assembling, proposed solutions ranges from ENF dimers/oligomers,[77–79] ENF-nanotube "peapod",[80–82] to ENF arrays on surfaces.[83–89] For all proposed solutions, it is important to have distance control

between ENFs.

Criterion 2: QIP requires the initial state of the qubit to be known and pure for the following gate operations. ENFs can fulfil this criterion, as the pure initial state can be prepared by the ground state of ENFs' electron spin. The thermal energy problem encountered in NMR can be tackled in ESR with its large Zeeman effect.[74] Based on the inequation of $\mu_B g_e B_0 > kT$, B_0: T should be greater than $0.74\ T/K$, which can be realized at a liquid helium temperature with the usage of a tesla-scale superconducting magnet.

Criterion 3: The information stored in the quantum states needs to be held for an enough long period of time so that desired quantum gate operations can be accomplished before the quantum state is irreversibly lost due to decoherence. As discussed in section 2.1.1, ENFs' electron spin can fulfil this criterion due to the sub-millisecond scale relaxation times (T_1 and T_2),[49] which is 10^3 times longer than the gate operation time in various proposals ($50\ \mathrm{ns}$ for CNOT gate[1], $10\ \mathrm{ns}$ for two-qubit π-phase gate).[90]

Criterion 4: To perform any quantum logic operations, only a basic set of quantum gates are required. The simplest "universal" set contains both single-qubit gates and a two-qubit gate. ENFs fulfil this criterion partially. Single-qubit gates with ENFs' electron spins were implemented using ESR pulses with a high fidelity.[49,91] In terms of the two-qubit gate, theoretical papers have proposed it by utilizing the electron spin dipolar coupling,[1,90] which has already been achieved for defect spins in diamond.[68] However, a similar mechanism is yet to be realized in the ENF-based system.

Criterion 5: To readout the qubit information, there are two key requirements: addressable and measurable. ENFs fulfil this criterion partially. By introducing a gradient magnetic field,[92,93] or using different nitrogen isotopes or cages,[1,94] the requirement of "addressable" can be met by allocating the ENF qubits with different addresses having various resonance frequencies. With the recently emerged single electron spin readout technology,[95] ENFs might also achieve the "measurable" requirement directly. Before implementing the readout approach of a single ENF spin, the qubit information can be acquired by a spin ensemble. However, this

necessitates an effective method to gather many identical copies of ENFs, and ensure they have the same direction for spin anisotropy. Thereby, the orientational alignment of ENFs is needed for the directional uniformity of the spin ensemble.

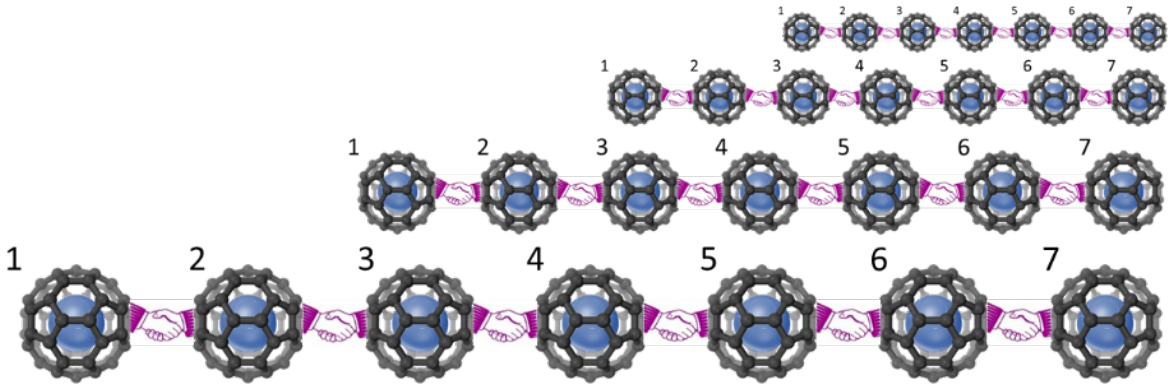


Figure 7 Schematic illustration of an ideal multi-scale molecular architecture of ENF for QIP application. At the microscopic scale, the ENFs need to be crosslinked in a controllable manner with quantum interaction between them to perform two-qubit gates and quantum algorithms. At the macroscopic scale, multiple axially aligned replications of the system is needed to form a spin ensemble for readout.

Overall, challenges in material science for ENFs to completely fulfil all DiVincenzo criteria are summarized as follows: (1) achieving a microscopic assembly of ENFs with a close and controllable distance between individual qubits, (2) controlling the spin coupling strength in ENFs, and (3) orientationally aligning ENFs to obtain the required directional uniformity of the spin ensemble (Figure 7). The aim of this thesis is to combat these three challenges and two more obstacles material wise, including the productivity of ENFs and the chemistry of ENFs. Once all five objects have been separately tackled, it would lead to an ENF system fulfilling all requirements for a universal quantum computer. Literature relevant to these five topics are reviewed below, in the sequence of (1) production of ENFs, (2) chemistry of ENFs, (3) assembly of ENFs, (4) alignment of ENFs' orientation, and (5) control of ENFs' spin coupling.

2.2 Synthesis and purification of ENFs

This work includes the preparation of pristine ENFs which is the cornerstone for the subsequent studies. With my effort on the optimization of the preparation of ENFs being discussed in Chapter 4, this section reviews the previously reported methods to synthesize and purify ENFs, and highlights the obstacles such as the low spin-yield (mole ratio of the ENF to the empty-cage fullerene in the crude product), and the poor separation between the ENF and the empty-cage fullerene using HPLC.

2.2.1 ENF synthesis

Table 2 Features of different methods utilized in ENFs synthesis

Method	Starting material	Soluble product in the fullerene soot	Spin yield
Commercial ion source implantation[96]	500 mg	100~150 mg	Up to 60 ppm
Glow discharge plasma implantation[97]	Lack of reports	10~50 mg	5~15 ppm
Radio frequency coupled plasma implantation[98]	200 mg	1~8 mg	20~8300 ppm

There are several techniques applied in the literature, which can be categorized into three methods listed in Table 2. Commercial ion source implantation[38] is the first method (Figure 8). The synthesis takes place in a vacuum chamber evacuated by a rotary pump coupled with a diffusion pump. An effusion cell is used to sublime C_{60} at 400~520 °C, which is gradually deposited on a water-cooled copper target to form a film. Meanwhile, nitrogen ions generated by a commercial ion source bombard the C_{60} film. The deposition target is aligned to have an angle of 45° with respect to the ion source so that both the fullerenes and nitrogen ions can efficiently reach the target (Figure 8). A thickness monitor, which records the fullerene

deposition rate, and a view port of the chamber are also installed for better observability of the synthesis procedure. The collected fullerene soot after the ion implantation is not entirely soluble (*c.a.* 40%).[96] The soluble fraction of the fullerene soot is the crude product that contains the desired ENF. While the initial spin-yield for the crude product was reported to be $1\sim100$ ppm,[38,97] a previous D.Phil. student in my group stabilized the productivity of the old experimental setup using this method at a sub-gram scale with a 60 ppm spin-yield.[96]

Compared to the other two methods discussed below, the main feature of using a commercial ion source is that the ion source is an independent sub-system. The limited coupling between the ion source to the remaining deposition system makes the experiment-scale apparatus easier to be up-graded to an industrial-scale apparatus, by changing the model of the ion source and the deposition chamber independently. However, this isolation also means the optimization has smaller parameter space to tune, hence optimal results from an experiment-scale apparatus may not be as good as the other methods.

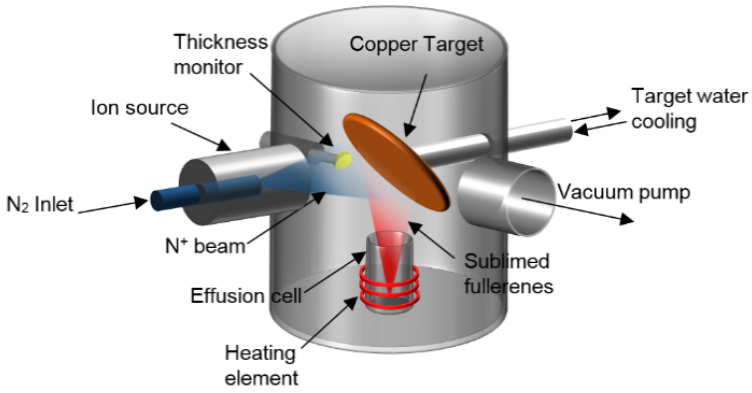


Figure 8 Experiment setup of nitrogen implantation apparatus using a commercial ion source (setup used on our lab)

The second method is “glow discharge” plasma implantation, which was designed for a lower cost apparatus and managed to synthesize N@C_{60} without a commercial ion source. As Figure 9 shows, the set-up is similar to a luminescence tube, except it uses nitrogen gas with fullerene rather than noble gas with phosphor. Simultaneous gas inlet and pumping are used to maintain the N_2 atmosphere at a pressure of 0.1 mbar, while C_{60} is vaporised by a tube furnace. The nitrogen plasma is formed by high voltage ionization of N_2, which subsequently

collides with C_{60} to form $N@C_{60}$, yielding a ratio between $N@C_{60}$ and C_{60} ranging from $5\ \mathrm{ppm}$ to $15\ \mathrm{ppm}$.[97,99]

Compared to the first method, cost-effective design has some unavoidable limitations. The dissociation process of N_2 under a relatively high gas pressure is less efficient, hence not only $N@C_{60}$ but also $N_2@C_{60}$ were found in the product. More importantly, the harsh reaction conditions, such as 650 °C oven temperature and 850 V electrode voltage, could decompose $N@C_{60}$, so that only the material condensed on the water-cooled electrode can survive. The poor spin-yield by this method highlights that the preservation of $N@C_{60}$ during the synthesis is an important issue when enhancing the productivity.

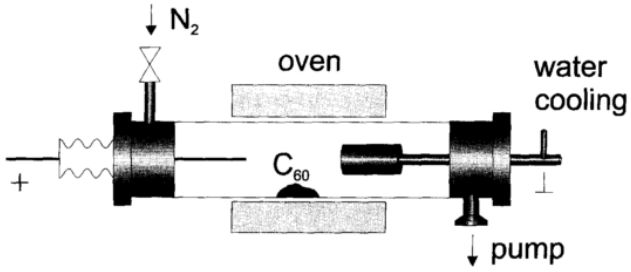


Figure 9 Schematic view of a glow discharge reactor. Figure reproduced from Pietzak, B. *et al*.[97]

The third method is radio frequency (RF) plasma implantation, which improves the second approach by replacing the glow discharge plasma with an RF capacitively coupled plasma system.[100,101] The nitrogen ions are created from nitrogen gas by a $13.56\ \mathrm{MHz}$ plasma generator, and are then implanted into C_{60} sublimated from an effusion cell (Figure 10). The introduction of RF, which triggers a Lorentz force on the charged particles and changes their trajectories to a coil shape, significantly improves the probability of collision between nitrogen ions and fullerene cages so that the spin-yield was reported to be better than an ordinary plasma method. Further benefiting from the tuneability of the system with adjustable parameters including the chamber pressure, grid voltage, beam energy and oven temperature, the ion radiation dosage and the fullerene sublimation rate can be well controlled. Therefore, the spin-yield was drastically improved from $200\ \mathrm{ppm}$ to $8300\ \mathrm{ppm}$.[98,102–104]

The main advantage of this method is the high spin-yield, which is presently two orders

of magnitude higher than the first method. This will effectively reduce the difficulty of the subsequent N@C_{60} purification procedure, which is reviewed in section 2.2.2. However, as the only literature reporting this result, it is worth noting that $8300\ \mathrm{ppm}$ was gained in an extremely dilute toluene solution with fullerene concentration ranging from $10^{-7}\ \mathrm{M}$ to $10^{-6}\ \mathrm{M}$, which might introduce uncertainty into the determination of the spin-yield. Despite the high ENF content in the crude product, the crude product only accounts for $1\%\sim5\%$ in the collected fullerene soot, and the rest of the fullerene soot are polymerized by-products which have to be discarded. Therefore, this method is more wasteful than the others. To achieve scalable ENF production using this method will require further optimization of the solubility of the resulting product. Another hidden drawback is the low fullerene deposition rate due to the relatively high pressure ($P_{\mathrm{N_2}} > 20\ \mathrm{Pa}$) involved in the process, which reduces the mean free path of the fullerene molecules to the millimetre scale. This disadvantage will be further exaggerated in a larger scale apparatus, which likely to have a longer distance between the oven and the deposition target. Overall, the scalability of this method is not as good as the others.

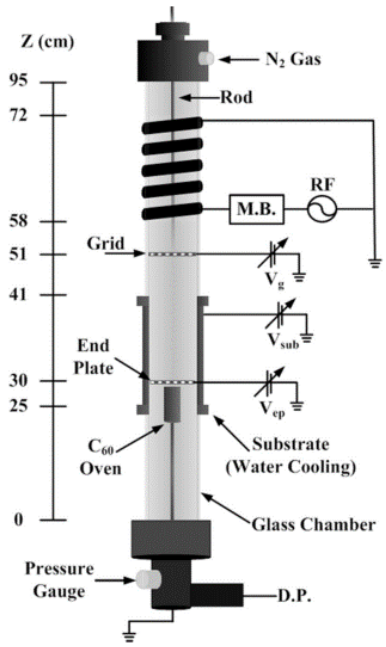


Figure 10 Schematic view of nitrogen implantation apparatus with RF plasma. Figure reproduced from Cho. S. C. *et al*.[98]

2.2.2 ENF purification

Since the synthesized crude product of ENFs always contains significant amounts of empty-cage fullerenes, enriching the spin-active species from the crude product is another important topic. Due to their almost identical chemical and physical properties (except for magnetism), no effective separation methods were reported other than high-performance liquid chromatography (HPLC). In contrast to ordinary chromatography practices utilizing polarity-induced affinity between the mobile and stationary phases, the current HPLC method for ENF purification is primarily based on the π-π interaction between the analyte and the stationary phase, where polarizability is the most relevant intermolecular force.[105–107] Either pure toluene[43,44,108,109] or a mixture of hexane/toluene[5,110,111] have typically been used as the main eluting solvents to effectively dissolve fullerenes. Different types of HPLC COSMOSIL columns from Nacalai tesque Inc. have been applied to the enrichment of N@C_{60}, such as PBB,[44,108] BuckyPrep[5,43,110,111,] and PYE.[44,109,111]

In addition to the limited content of N@C_{60} in the crude mixture, the retention time (t_R) ratio between N@C_{60} and C_{60} ($\alpha = {t_R}^{\mathrm{N@C_{60}}} : {t_R}^{\mathrm{C_{60}}}$) is also extremely low ($\alpha \approx 1.027$). These characteristics make HPLC incapable of separating them completely with a single process. Therefore, the purification was normally performed with repetitive manner. Each HPLC procedure only slightly enriched the N@C_{60}/C_{60} ratio. During the initial stages of the HPLC procedure, it was necessary to process large quantities of the mixture. As the enrichment proceeded, the sample volume shrunk exponentially, so later stages of the HPLC procedure worked on small quantities of samples.

Figure 11 and Figure 12 show the HPLC chart using PBB with toluene and BuckyPrep with hexane and toluene mixture, respectively. They were obtained separately in the initial stage[108] for enriching large amounts of low purity sample and in the final stage[5] for separating small amounts of extremely high-purity sample. At the low purity stage, external cw-ESR measurements were used to reconstruct the N@C_{60} peak which is not detectable using the

HPLC detector.[108] At the high purity stage, researchers managed to use the HPLC detector signal to directly indicate the N@C_{60} peak.[5] The initial stage had a worse separation result. Both the 1st cycle (Figure 11a, c) and 3rd cycle (Figure 11b, c) HPLC showed considerable peak overlapping, but the 8th cycle HPLC had negligible overlapping (Figure 12). The different preferences of the number of the recycling-mode in the initial and final stages were due to the sample quantity. The former one need to simultaneously tackled the problem of handling large amounts of material and achieving an adequate separation, whereas the latter one can focus only on a good separation by using some time-inefficient approaches. The worse separation in the initial stage is a compromise to the large sample amount. To improve the purification of ENFs, novel methods that simultaneously achieve the large sample capacity and reliable separation efficiency will be needed.

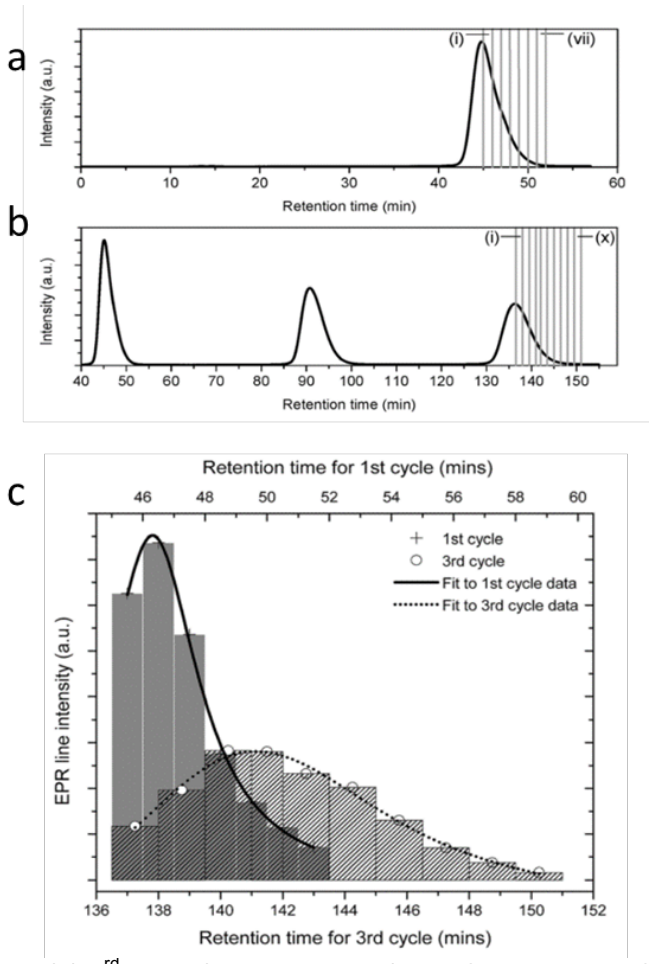


Figure 11 (a) 1st cycle and (b) 3rd cycle (recycling-mode) HPLC separation of the crude N@C_{60}/C_{60} mixture using a 15PBB 100×500 mm column with toluene eluting at the rate of $300\,\mathrm{ml/min}$. (c) Reconstructed elution peak of N@C_{60} using the intensities of the ESR signals of fractions at different retention times. Figure reproduced from Plant, S. R. *et al*.[108]

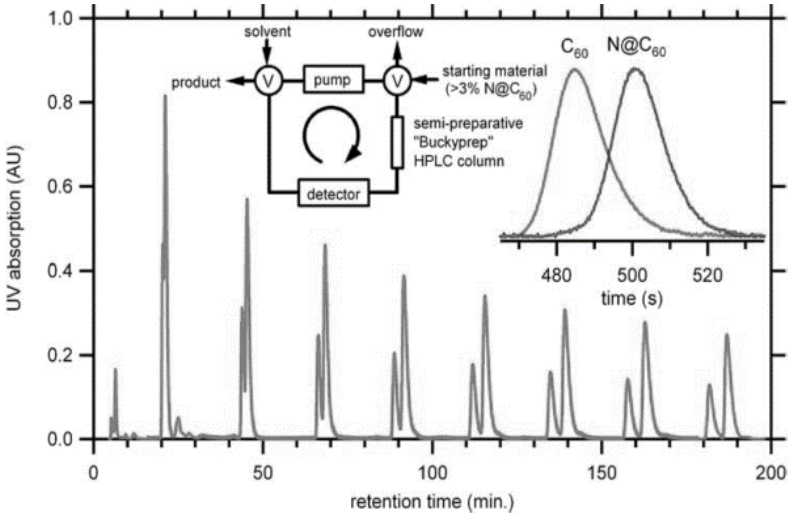


Figure 12 Recycling-mode HPLC chart (8th cycle) for $N@C_{60}/C_{60}$, using BuckyPrep with 4:1 toluene/hexane. (Inset) HPLC Setup in recycling-mode, and analytical HPLC trace of the pure substances using BuckyPrep with toluene. Figure reproduced from Harneit, W. *et al*.[5]

2.3 Fullerene chemistry and ENF derivatization

The chemical functionalisation of ENFs was the pathway to enhancing the performance of ENFs in this work. With my contributions to ENF derivatization being discussed in Chapter 5, this section reviews ENF-related chemistry, including general chemical functionalisation strategies for empty-cage fullerenes, previously-reported ENF derivatives, and the well-accepted characterization criteria to prove the successful synthesis of an ENF derivative.

2.3.1 Pericyclic reaction

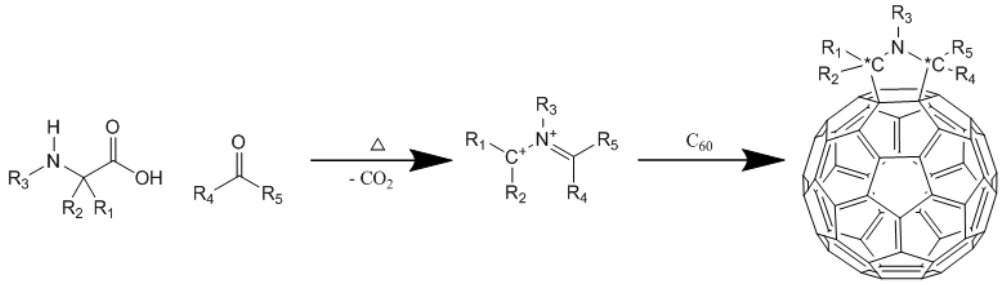


Figure 13 *In-situ* formation of an azomethine ylide, and its reaction with C_{60}

Reacting as a dienophile, C_{60} can perform different pericyclic reactions. The most reported pericyclic reaction of fullerene is the Prato reaction, a [3+2] cyclo-addition between a fullerene and a ylide to synthesize a fulleropyrrolidine.[112] The 1,3 dipole of ylide (a type of zwitterion having the positive and negative charge centres next to each other) is generated *in situ* from α-amino acid and aldehyde/ketone through a decarboxylation route (Figure 13). The advantage of using the Prato reaction lies in that functional groups/moieties (R_1 ~ R_5) can be introduced readily with different amino acids and aldehydes to make a vast range of ENF derivatives. However, it is worth noting that the products have two potential chiral centres in the pyrrolidine cycle. The regioselectivity of the Prato reaction is [6,6] bond addition (double bond addition between two hexagons), which was testified both experimentally and theoretically.[113] Apart from azomethine ylides, other 1,3 dipolars[114] may also react with C_{60}

following the similar concerted mechanism. Multi-functionalisation *via* the Prato reaction has not been frequently reported due to the poor regioselectivity. Nevertheless, large steric azomethine ylides can be used to introduce regioselectivity of the multi-addition externally.[115,116] In terms of the common properties of fulleropyrrolidines, the presence of the electron-deficient fullerene cage and the electron withdrawing effect reduce the basicity of the pyrrolidines (Figure 14a), as well as the tendency of the nitrogen to have a p-π conjugation.(Figure 14b).[117,118]

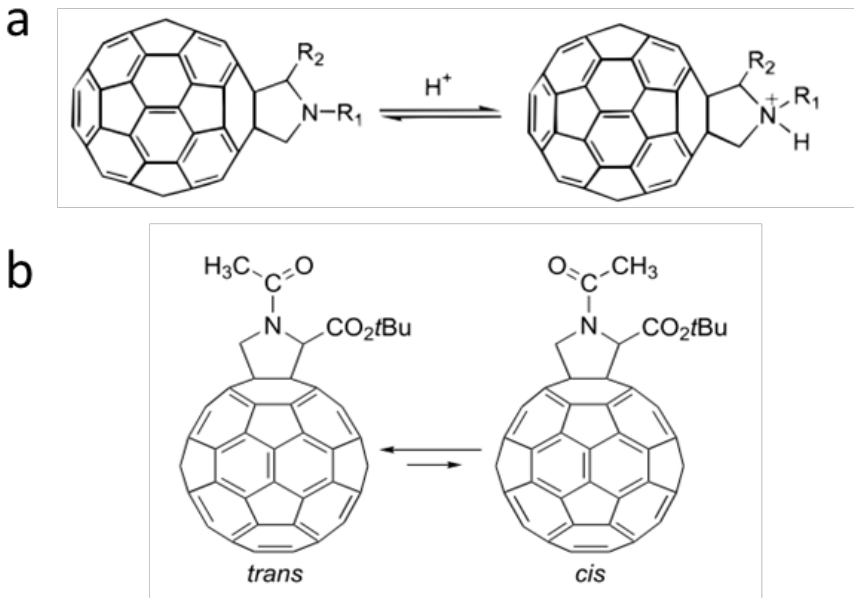


Figure 14 (a) Weakened basicity of the fulleropyrrolidines compared to the corresponding pyrrolidines.[117] (b) Weakened p-π conjugation compared to the corresponding pyrrolidines.[118]

The Diels-Alder [4+2] cyclo-addition is another well-reported pericyclic reaction for fullerenes. The dienophilic reactivity of C_{60} is comparable to those of the maleic anhydride and N-phenylmaleimide.[17] Nevertheless, the kinetics and the equilibrium of the reaction are more related to the properties of the dienes. As a highly reactive diene, o-quinodimethane was firstly introduced to perform a [6,6] bond addition,[119] and more dienes were successfully added to fullerene even at room temperature later.[120,121]

2.3.2 Nucleophilic addition

C_{60} is a good substrate for nucleophilic addition, due to its electron-deficient conjugated

system.[17] The most famous nucleophilic addition for fullerenes is the Bingel reaction.[122] The reaction uses bromomalonates or its analogues[17,123] to effectively react with C_{60} at room temperature with the help an auxiliary base (Figure 15a, c). The highly-basic auxiliary base effectively deprotonates the bromomalonates or their analogues to form carbanion nucleophiles. The use of nucleophilic auxiliary bases is not desirable, as it may cause competing reactions and by-products. Commonly, the non-nucleophilic base, 1,8-Diazabicyclo [5.4.0] undec-7-ene (DBU) (Figure 15b), is used for the Bingel reaction. There are two proposed mechanisms for the Bingel reactions depending on the number of the bromo-substitutions of the malonates (Figure 16a, b). Both mechanisms lead to the regioselectivity of the reaction being a [6,6] bond addition.[124]

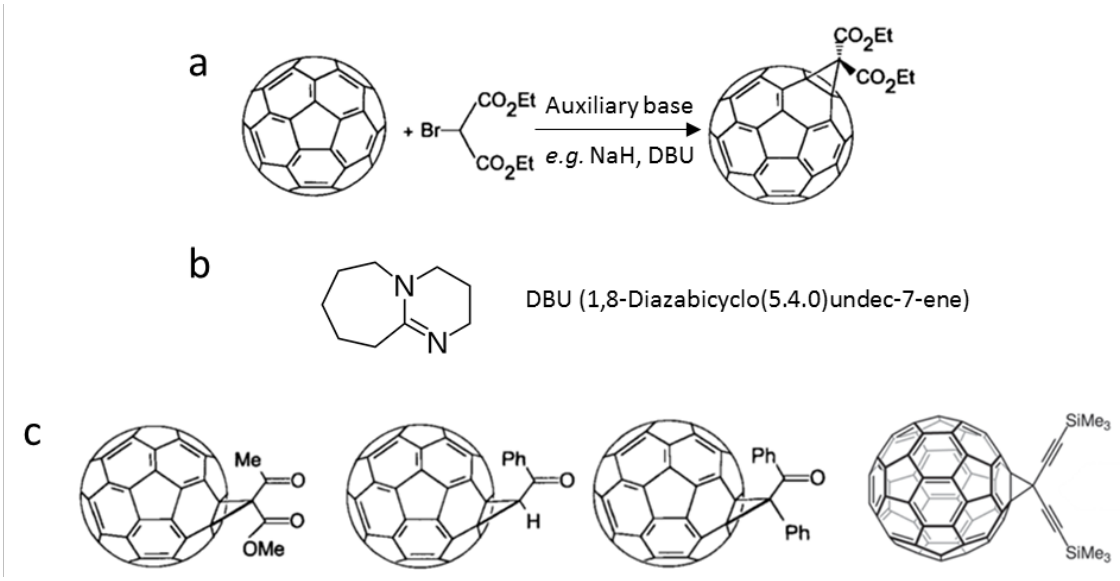


Figure 15 (a) Typical Bingel reaction. (b) Commonly used auxiliary base, DBU, due to its low nucleophilicity. (c) Other possible Bingel reaction products formed by altering the bromomalonates to its analogues.[122,123]

Considering the complexity of preparing brominated reagents in some cases, the modified Bingel reaction starting from pristine malonates was reported, in which the halogenated malonates form *in situ* in the presence of iodine[125–127] or CBr_4.[128] Chloromalonates, which are easier to synthesize but less reactive than bromomalonates,[129] were also studied and proved to be capable of performing a Bingel reaction with a longer reaction time.[130] In addition, the retro-Bingel reactions were investigated using cyclic

voltammetry.[131]

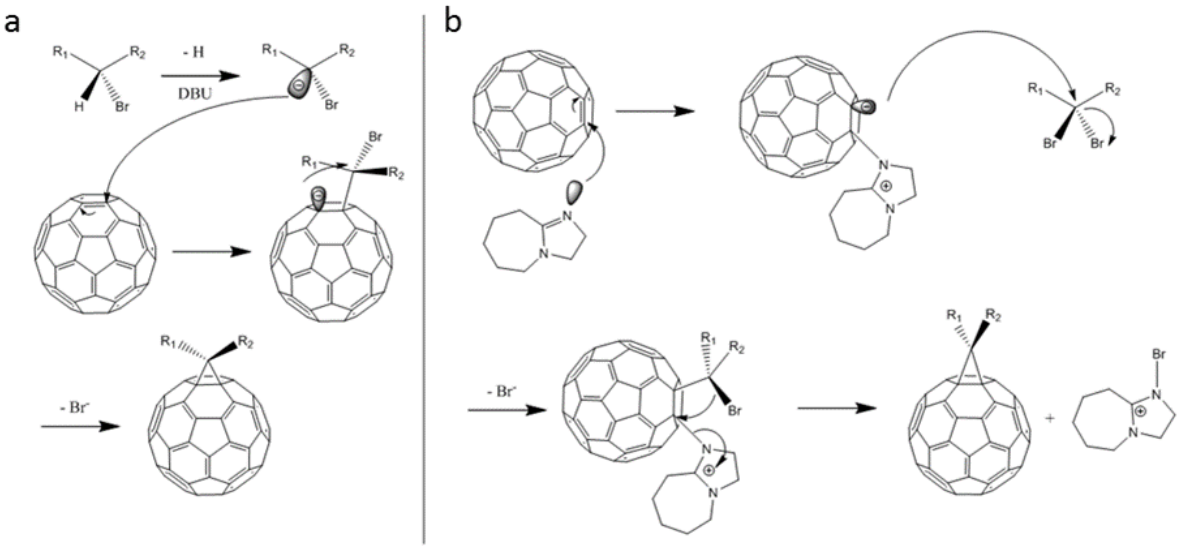


Figure 16 (a) Addition/elimination mechanism of Bingel reaction starting from the malonate.[225] (b) an alternative mechanism of Bingel reaction starting from the fullerene[226]

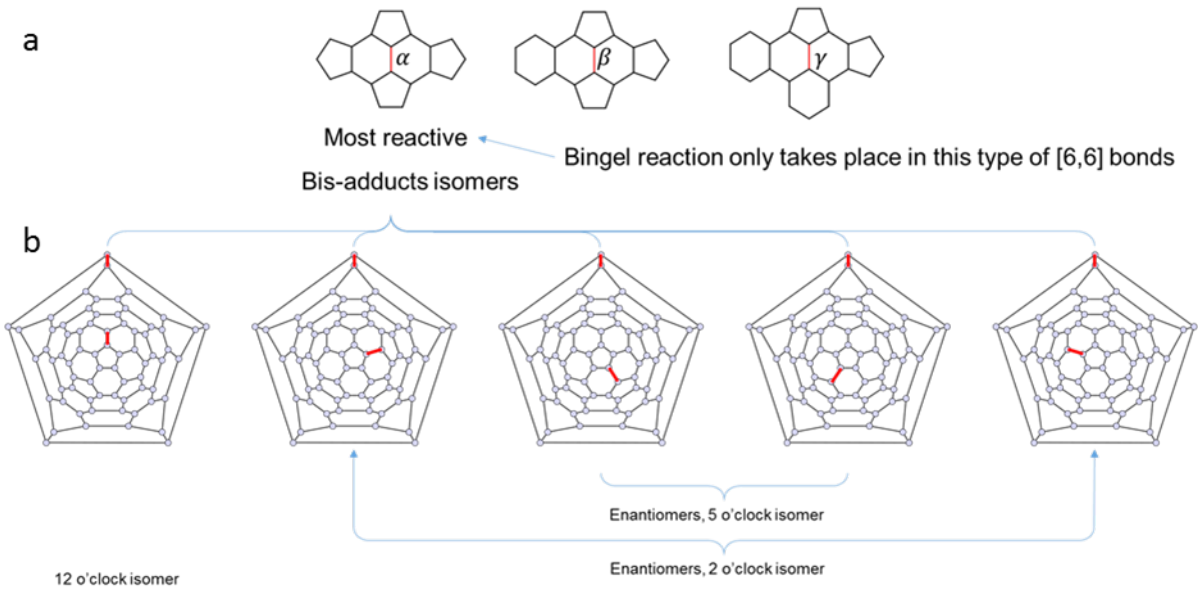


Figure 17 (a) Three types of [6,6] bonds on a C_{70} cage. (b) Schlegel diagram showing the two substitution positions of the possible clock isomer and enantiomers for Bis-functionalised C_{70}.

In terms of multi-addition, research revealed that hexa-adducts[132] could be regioselectively obtained through LUMO control.[133] Nevertheless, the geometric regioisomers formed by bis-additions to a C_{60} cage are not easy to control, and the reaction normally generates up to eight isomers, including *trans*-, *cis*- and equatorial products.[125] Better

regioselectivity of bis-additions was achieved by using tethered malonates[134] and replacing C_{60} with C_{70}.[135] While tethered malonates control the bis-product formation by steric conformation, the regioselectivity of bis-additions on a C_{70} cage originates from the different reactivity of the bonds. Due to its lower symmetry, there are three types of [6,6] bond on the cage. Only the α-type of bonds were reported to be sufficiently active[135] for a Bingel reaction to take place (Figure 17a). All of the ten α-type of bonds are evenly located at two poles of the rugby ball-shaped carbon cage. As bis-addition at the same pole would create a massive steric hindrance, there are only five structurally similar isomers that form (Figure 17b). These isomers are the 12-, 2- and 5-o'clock isomers, where the 2- and 5-o'clock isomers each have two pairs of enantiomers.

Apart from malonates, which can perform the Bingel reaction, organometallic compounds are also good nucleophilic reagents, and their reactions with C_{60} proceed quickly.[17,136,137] Although the mechanisms for organometallic addition are the same, the different reactivity of organometallic compounds changes the optimal reagents ratio. Taking $Me_3Si\text{-}C{\equiv}C\text{-}Li$ as an example, 4 equivalents of its solution were needed to reach a 45% yield,[136] whereas for the milder Grignard reagents, 5- to 27- fold excess was reported.[17] In terms of regioselectivity, fullerenes are different from other conjugated systems which usually prefer to form 1,4-adducts, which minimizes the product energy. The 1,2-organodihydrofullerenes were normally found to be more energetically favourable, as the 1,4-adducts suffer higher strain from the cage curvature.[138,139]

Primary and secondary aliphatic amines can easily react with C_{60}, owing to their high nucleophilicity. The reaction mixture will first turn green before forming a brown precipitate.[140] ESR spectroscopy demonstrates the presence of the amine/C_{60} di-radical in the green solution, while the sediment can be explained as zwitterions formed by the recombination of the di-radical. The reaction normally does not stop at a mono functionalisation stage, resulting in a complex mixtures of aminoadducts.[141]

2.3.3 Previously reported ENF derivatives and their ZFS

Due to the difficulty of obtaining pure ENFs, every reported ENF derivative was a mixture of an ENF derivative and the corresponding empty-cage fullerene derivative. Since conventional fullerene characterization techniques cannot directly detect the ENF derivative, studies reviewed in this section all conducted the structural characterizations on the empty-cage fullerene derivatives in the mixture, instead.

To prove the presence of the ENF derivatives in the product mixtures, researchers[142–148] further focused on the change of the cw-ESR signal of the reaction product. A small zero-field splitting (ZFS) effect was found to be a common spin feature of ENF derivatives compared to the pristine ENFs, and was normally used as the characteristic feature to prove the successful chemical functionalisation of ENFs.[142–148]

2.3.3.1 ENF derivatives synthesized by various reactions

Thanks to the abundant choice of aldehyde/ketone, the Prato reaction is the most widely reported chemical functionalisation method for N@C_{60}, despite that the reaction requires heating to around $110\,^{\circ}C$, which is undesirable given the low thermal stability of N@C_{60}.[149] Five different mono pyrrolidine derivatives of N@C_{60} listed in Figure 18 have been reported previously.[142–144] The synthesis conditions of these derivatives are directly adopted from the reaction conditions for a pristine fullerene. A quantitative study on the spin retention ratio (the intensity of the signal of ENF after a reaction divided by that before a reaction) for derivative C was reported to be *ca.* 73%, which means the reaction condition during a Prato reaction is to some extent compatible with the limited stability of N@C_{60}.

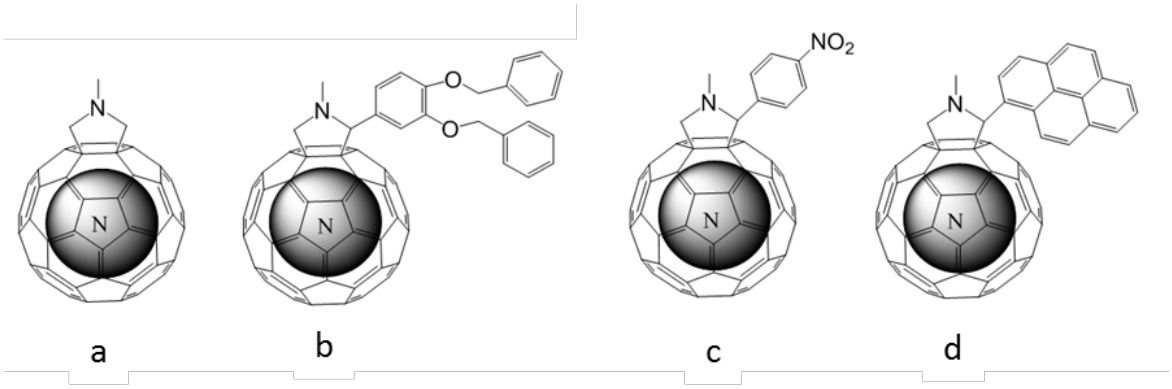


Figure 18 Four mono pyrrolidine derivatives of N@C_{60} reported in the literature (a),[142] (b),[142] (c),[143] and (d).[144]

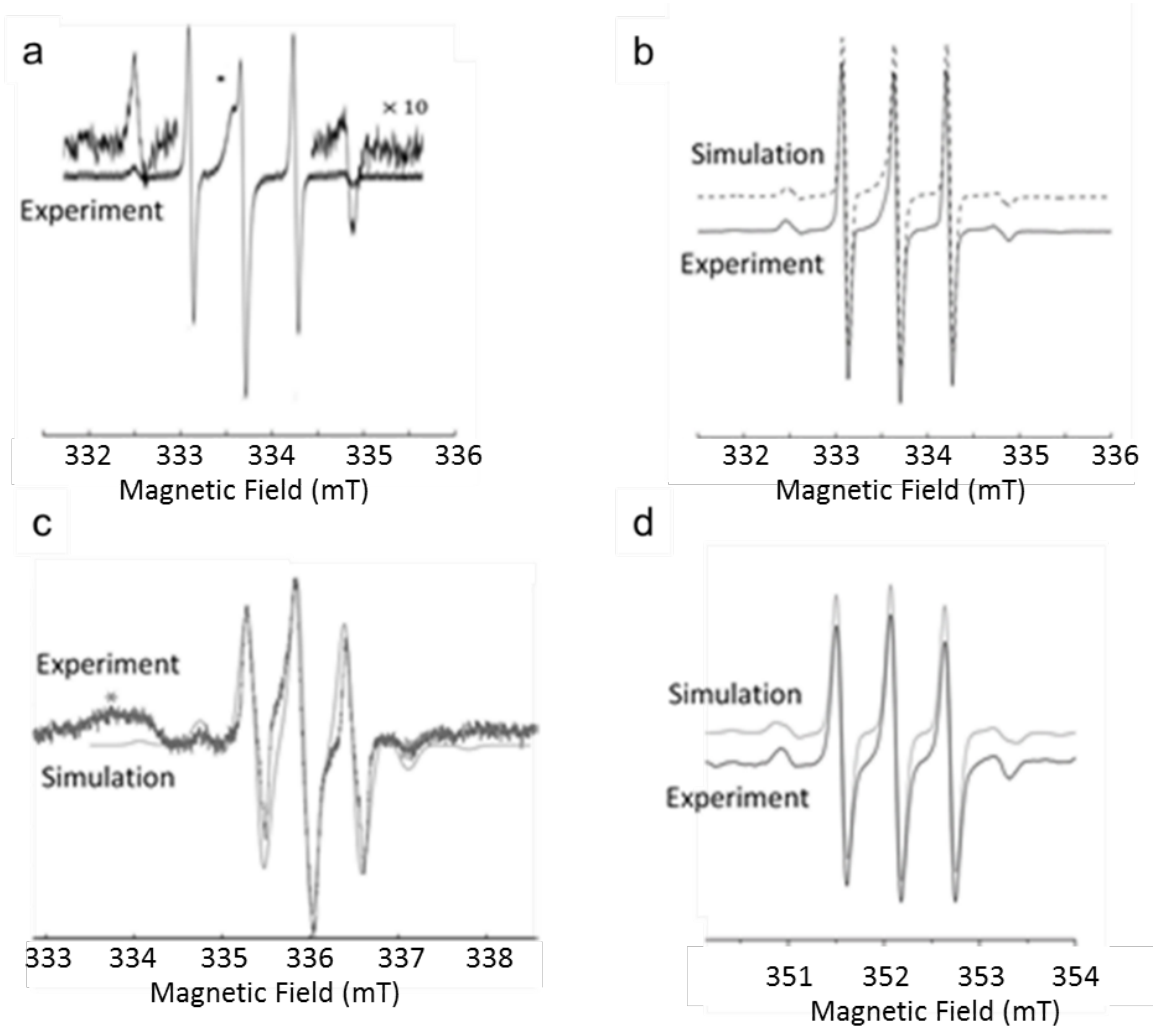


Figure 19 (a) cw-ESR spectra and simulation data for **A** ($g_{\mathrm{iso}} = 2.0028$, $A_{\mathrm{iso}}^{(\mathrm{N})} = 15.95\ \mathrm{MHz}$, $D = 16.4\ \mathrm{MHz}$, $E = 0.4\ \mathrm{MHz}$).[142] (b) cw-ESR spectra and simulation data for **B** ($g_{\mathrm{iso}} = 2.0031$, $A_{\mathrm{iso}}^{(\mathrm{N})} = 15.95\ \mathrm{MHz}$, $D = 17.2\ \mathrm{MHz}$, $E = 0.6\ \mathrm{MHz}$).[142] (c) cw-ESR spectra and simulation data for **C** (***g*** not reported, $A_{\mathrm{xx}}^{(\mathrm{N})} = A_{\mathrm{yy}}^{(\mathrm{N})} = 14.2\ \mathrm{MHz}$, $A_{\mathrm{zz}}^{(\mathrm{N})} = 18.5\ \mathrm{MHz}$, $D = 17.0\ \mathrm{MHz}$, $E = 0.8\ \mathrm{MHz}$).[143] (d) cw-ESR spectra and simulation data for **D** (***g*** not reported, $A_{\mathrm{xx}}^{(\mathrm{N})} = A_{\mathrm{yy}}^{(\mathrm{N})} = 16.44\ \mathrm{MHz}$, $A_{\mathrm{zz}}^{(\mathrm{N})} = 14.70\ \mathrm{MHz}$, $D = 16.75\ \mathrm{MHz}$, $E = 0.93\ \mathrm{MHz}$).[144] Figure reproduced from Franco, L. *et al.*[142] Zhang, J. *et al.*[143] and Liu, G *et al.*[144]

The cw-ESR signal of these derivatives (Figure 19) are relatively similar to each other, as the addends are all spin silent. The presence of the addends only disturbs the symmetry of the cage, which consequently lifts the degeneracy of different ESR transitions in the $S = 3/2$ spin system. Named as zero-field splitting (ZFS), this phenomenon leads to a set of side peaks in the cw-ESR spectrum which appear in almost all N@C_{60} functionalisation experiments. The next section will review and compare the ZFS in different N@C_{60} derivatives. Apart from the appearance of ZFS, it was found that the triplet HFC peaks became significantly unequal for derivative C. While the research initially assigned it to the anisotropy of HFC,[143] the significant increase of the middle peak might also be introduced by an unknown impurity formed during the chemical functionalisation reaction. A similar impurity signal overlapping the middle peak has also been reported in other different derivatives.[142,145,146] The spin multiplicity of the impurity signal has been determined by pulsed ESR nutation experiments to be $1/2$, which is different from that of N@C_{60}.[142]

Benefiting from the mild room temperature condition, the Bingel reaction was the first method of chemical functionalisation applied to N@C_{60}.[97,147,148] Demonstrated in Figure 20a, b, one early paper claimed that the incarcerated atom will not be influenced during the entire reaction. The cw-ESR signal of the Bingel reaction derivatives of N@C_{60} has also been studied. Similar to an ordinary Prato reaction derivative, functionalisation with a mono addend mainly causes a ZFS effect, while the *g*-factor and hyperfine coupling constant (HFCC) were found to be almost unchanged. In addition, the symmetric hexa-adduct shows negligible ZFS peaks.

Despite the success of applying Bingel reaction with N@C_{60} in the early days, a more recent report[150] revealed a drastic spin decay after applying a Bingel reaction shown in Figure 20c and d to N@C_{60} system.[150] The feasibility of using a Bingel reaction to functionalise ENFs is still controversial.

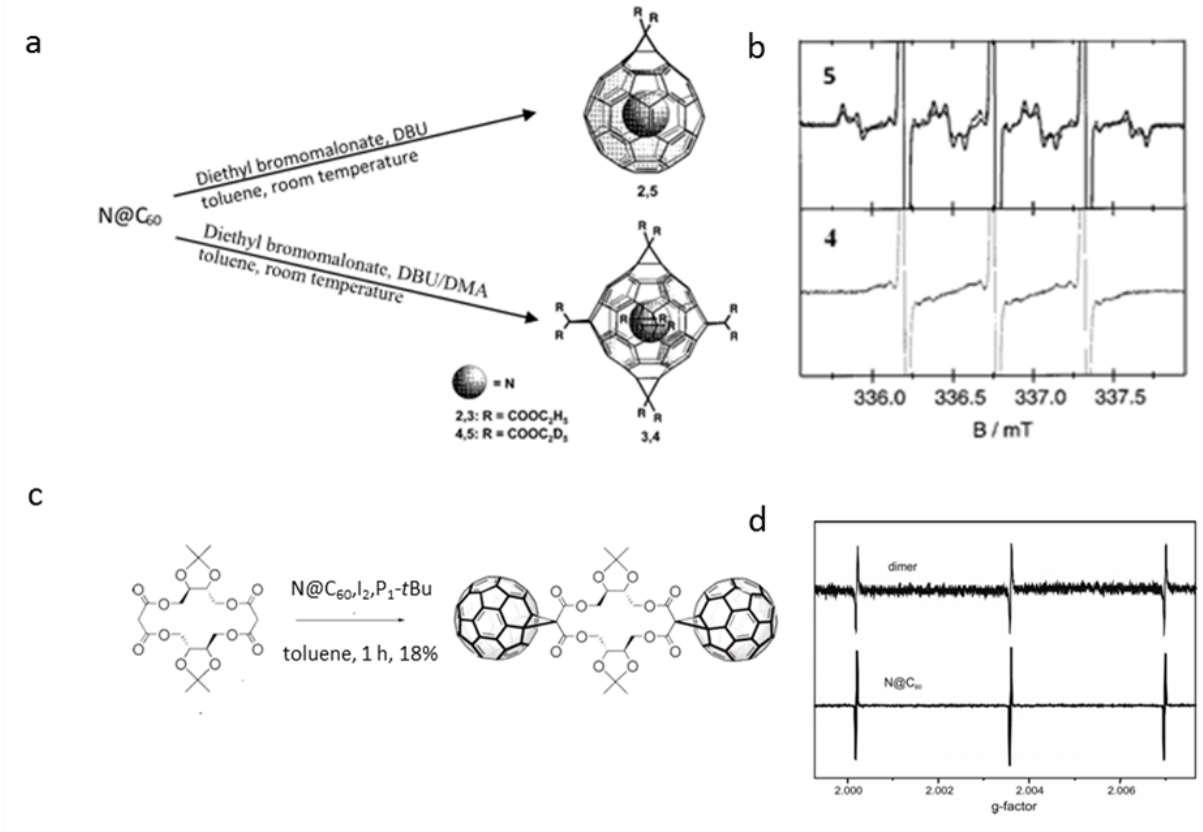


Figure 20 (a) Synthesis of mono- and hexa-adduct of N@C_{60} *via* the Bingel reaction. (b) cw-ESR signal of the corresponding two deuterated Bingel reaction derivatives of N@C_{60}.[147] (c) Synthesis of a N@C_{60} dimer *via* the Bingel reaction. (d) Significant signal decrease after a Bingel reaction.[150] Figure reproduced from Dietel, E. *et al.*[147] and Hörmann, F. *et al.*[150] DMA stands for 9,10-dimethylanthracene, and P_1-*t*Bu represents tert-butyliminotris(dimethylamino)phosphorane

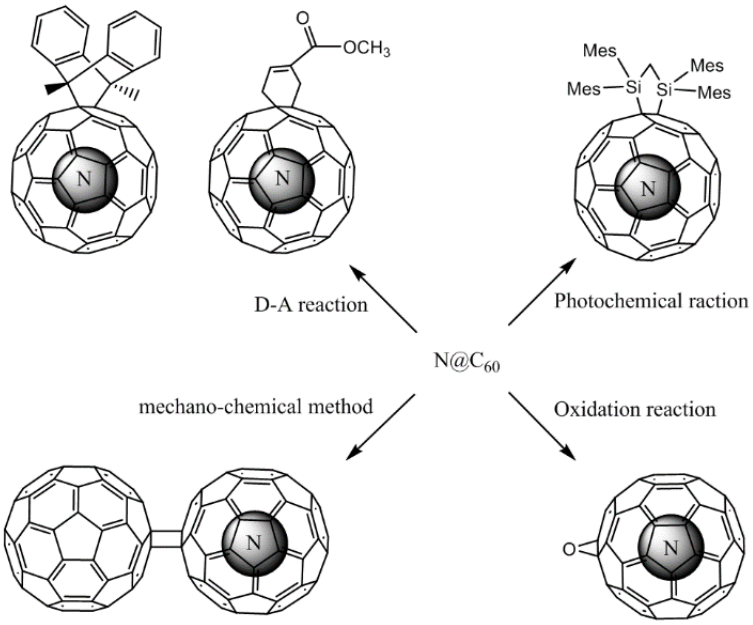


Figure 21 Other reactions that has been reported with N@C_{60}. Diels-Alde reaction products,[142] photochemical reaction product,[151] mechano-chemical dimerization product[145] and oxidant[146] of N@C_{60}

Apart from Prato and Bingel reactions, other N@C_{60}-related reactions are shown in Figure 21, but there are more obstacles needed to overcome for these chemical functionalisation methods to be useful. Two Diels-Alde reactions of N@C_{60} were also reported.[142] The reaction yield and the spin retention ratio were found to be suitable for the endohedral system. However, the drawback lies in the retro-reaction of a D-A reaction. It may cause decomposition of adducts, as well as undesired the tautomerization between different adduct isomers. In addition, compared with the Prato reaction, the less commercial availability of different dienes compared with azomethine ylide precursors leads to difficulties of preparing reagents for a desired molecular structure. A photochemical reaction has been utilized to link a disilirane with the N@C_{60},[151] but a sharp decrease of the spin signal was observed in the product. Apart from the lower photochemical reactivity of N@C_{60}, the decomposition of N@C_{60} may also contribute to the loss of the spin signal. Direct dimerization of N@C_{60} was performed,[145] which claimed that no spins were lost by utilizing a mechano-chemical method[152]. Nevertheless, the poor thermal stability[153] of C_{120} itself seriously limits the feasibility of synthesizing measurable amount of product. The N@C_{60} oxide have also been studied.[146] Although pure products were separated and characterized by HPLC and ESR spectroscopy, respectively, the N@C_{60} oxide were found to be thermally unstable. New spin signal will gradually replace the spin signal of N@C_{60} when heated at $100\,^{\circ}\mathrm{C}$. Dimerization and polymerization of N@C_{60}O at this temperature were proposed to be the reason of the instability, as the intermediate state of the dimerization and polymerization reactions might facilitate the decomposition.

2.3.3.2 Zero-field splitting: a characteristic feature for ENF derivatives

Characterized by cw-ESR techniques, the ZFS effect in N@C_{60} derivative is an important criterion to prove the successful functionalisation of the N@C_{60}, because other conventional technology such as mass spectrometry (MS), NMR spectroscopy, and ultraviolet–visible spectroscopy (UV/Vis) are not sufficiently sensitive. To measure ZFS, the sample must be in the solid-state, because the fast tumbling of the molecule in solution will average the traceless

$\boldsymbol{D}$ sensor to zero.

The strength of the ZFS is quantified by a traceless second-order tensor $\boldsymbol{D}$, which could be expressed as a diagonal matrix in its eigenframe with elements being $D_{xx} = -D/3 + E$, $D_{yy} = -D/3 - E$ and $D_{zz} = 2D/3$, where D and E are the ZFS parameters representing the axial and the non-axial component of the tensor. The magnitude of the ZFS is heavily affected by the symmetry of the molecule, as it is caused by angle-dependent factors including spin-spin dipolar coupling and spin-orbit coupling.[154] A non-distorted N@C_{60} has no ZFS, but less symmetrical molecules such as N@C_{60} derivatives and a N@C_{70} have detectable intrinsic ZFS effects. In addition to the ZFS introduced by chemical functionalisation, in some cases, matrix distortion of the molecular symmetry also introduces a measurable non-intrinsic ZFS effect.[155,156] Fortunately, the matrix distortion effect from common solvents for fullerenes, such as toluene or CS_2 were found to be negligible.[142] Hence, the intrinsic ZFS of a ENF derivative is normally measured in its frozen solution.

Table 3 Different simulated ZFS parameters reported in the literature

Derivative type	Ring size attached to the cage	[D, E]/MHz
Diels-Alde reaction product	6	$[16.2,0.4]$[142]
Prato reaction product	5	$[16.4, 0.4]$[142], $[17.2, 0.6]$[142], $[16.75, 0.93]$[144], ,$[16.1, 0.7]$[78], $[17.0, 0.8]$[143],
Dimerization product	4	$[14, 0.56]$[145]
Bingel reaction product	3	$[9.15, 0.45]$[147], $[8.6, 0.45]$[150]
Oxidization product	3	$[6.6, 0.5]$[146]

Table 3 lists different N@C_{60} derivatives and their intrinsic ZFS parameters. A positive relationship between the axial parameter D and the ring size of the addend could be found. Based on the literature, I performed a MM2 ForceField simulation to demonstrate that a larger ring size has a more pronounced influence on the cage symmetry in the axial direction (Figure 22). Therefore, more permanent distortions of the endohedral electronic distribution are

obtained with larger ring sizes. This explains the positive relationship between the magnitude of D and the size of the ring. No clear trend of the rhombic term of the ZFS could be extracted, but all reported ENF derivatives showed E smaller than $1\ \mathrm{MHz}$, which means the non-axial component of the ZFS effect is not significant.

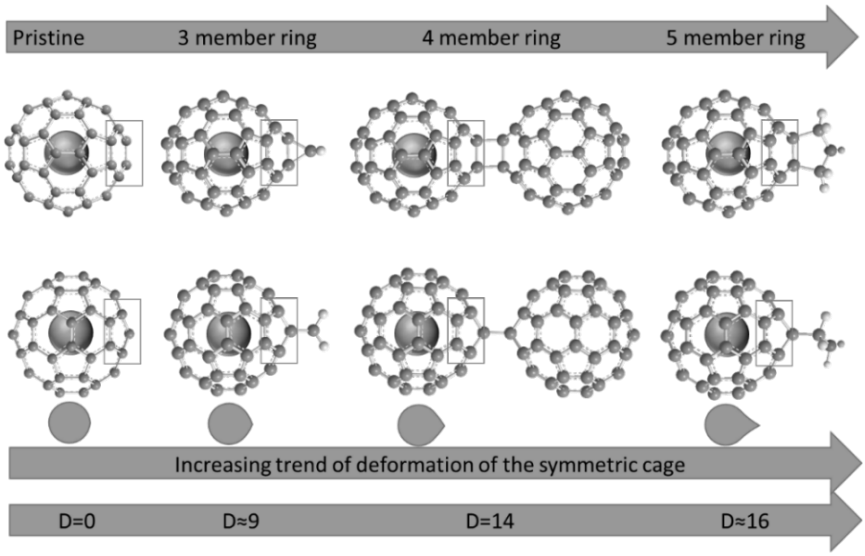


Figure 22 Relationship between the D value and the symmetry breaking effect caused by exohedral ring in different sizes adding on the cage.

ZFS was proposed to be a relaxation mechanism for N@C_{60} derivatives in solution.[143] Therefore, the chemical modification of the fullerene cage was commonly found to slightly reduce spin relaxation times ($T_{1,2}$) of the endohedral spin. However, such a decrease is minor compared to the impact caused by the presence of protons in the addends. Moreover, the ZFS and the resultant reduced relaxation times can also be mitigated by recovering the cage symmetry using the region-selective multi-functionalisation.

2.4 Microscopic assembly of fullerenes for distance control between qubits

Achieving a microscopic assembly of ENFs with a close and controllable distance between individual qubits is required for an ENF-based quantum device, because of DiVincenzo criterion 1 discussed in section 2.1.3. The assembly could be obtained by a two-dimensional array of ENFs adsorbed on a surface, a one-dimensional array of ENFs filling a nanotube, or a zero-dimensional array of ENFs linked covalently. While the higher dimensional arrays offer more scalable ENF architectures, the difficulty of preparing the arrays increases exponentially with the dimension. With my work focused on the covalent linkage approach discussed in Chapter 6, all three aforementioned methods reported for empty-cage fullerenes and EFs are reviewed and compared in this section.

2.4.1 Fullerenes on substrates: assembly using 2D substrates

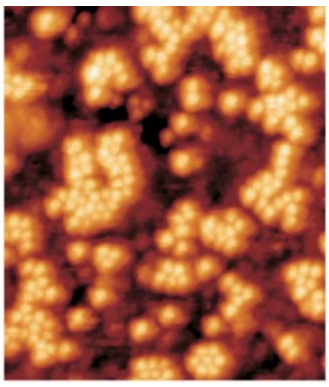


Figure 23 C_{70} islands deposited on the surface of $SrTiO_3$ (001). Figure reproduced from Deak, D. S. *et al.*[83]

2D arrays of empty-cage fullerenes and EMFs have been achieved by different methods. Due to the near-spherical molecular structure, directly aligning pristine fullerenes on an ordinary surface is difficult. The scanning tunnelling microscope (STM) image in Figure 23 illustrates a typical disordered island-like structure of fullerene molecules deposited on the (001) facet of a $SrTiO_3$ surface.[83] Therefore, introducing modifications to the fullerene cage or

the substrate is necessary to obtain an ordered structure.

The weak interaction between the fullerene and the substrate and the strong attraction between two fullerene molecules are the two main obstacles that prevent us from changing the island-like structure to a proper single layer of 2D array. Therefore, functionalised fullerenes with organic groups which can strongly interact with the substrate or effectively separate fullerene molecules have been reported as two ways to achieve the ordered structure. In the literature, absorbing a EMF derivative on the Au (111) surface through S-Au bonds (Figure 24)[84] is an example of the first approach, while assembling fullerene with long alkyl chains (Figure 25)[85] is an example of the second. According to the STM characterization, both approaches have achieved certain degrees of assembly for the 2D array of fullerene.

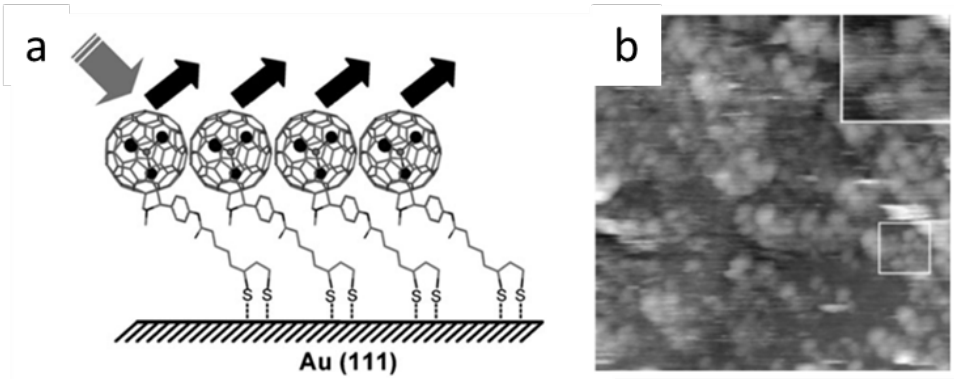


Figure 24 Self-assembled monolayer $Er_3N@C_{80}$ derivative on Au (111). (a) The molecular model of the $Er_3N@C_{80}$ derivatives and their interaction with Au (111) substrate. (b) STM image of the fullerene array. Figure reproduced from Gimenez-Lopez, M. del C.*et al.*[84]

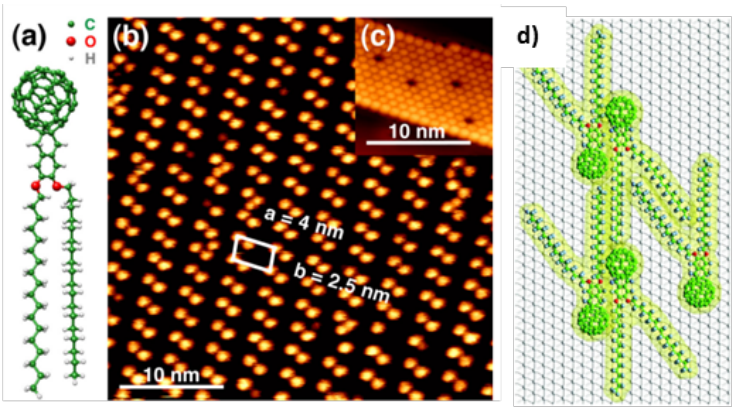


Figure 25 Self-assembled monolayer of C_{60} derivative on Ag (111). (a) The molecular model of the C_{60} derivative. (b) STM image of the fullerene array. (c) Comparison image of pristine C_{60} on Ag (111). (d) The proposed model of the geometries of the monolayer. Figure reproduced from Diaconescu, B.*et al.*[85]

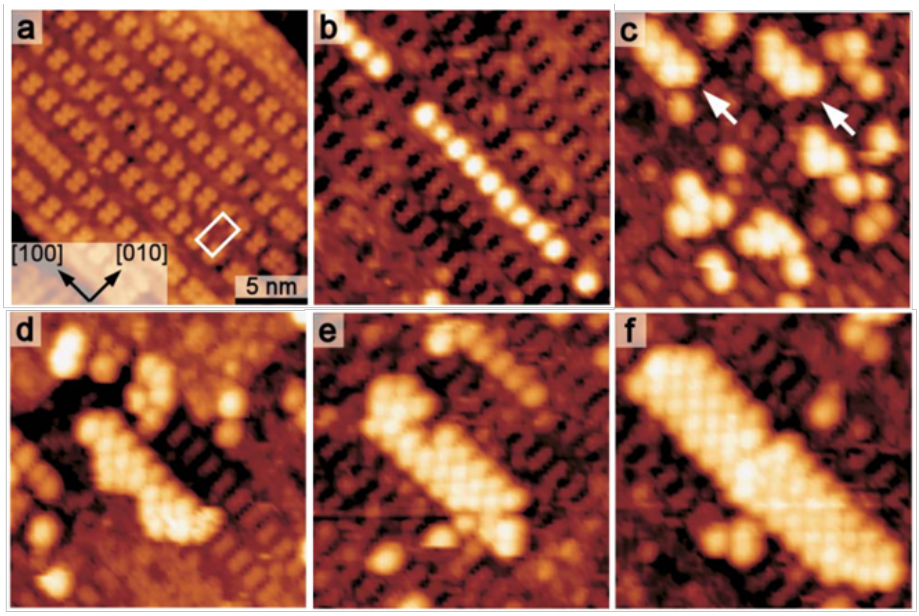


Figure 26 Epitaxial C_{70} islands on the nanostructured template. STM images of: (a) a naked surface of $SrTiO_3$ (001) made up of cross dot arrays with a (7×4) periodicity (white rectangle), (b) a one-molecule-wide chain of C_{70} molecules assembled on top of a row of cross dots, (c) several clusters of C_{70} including two-molecules-wide clusters (pointed out with arrows), (d) three-molecule-wide island of C_{70}, (e) four-molecule-wide island of C_{70}, (f) five-molecule-wide island of C_{70}. Figure reproduced from Deak, D. S. *et al.*[83]

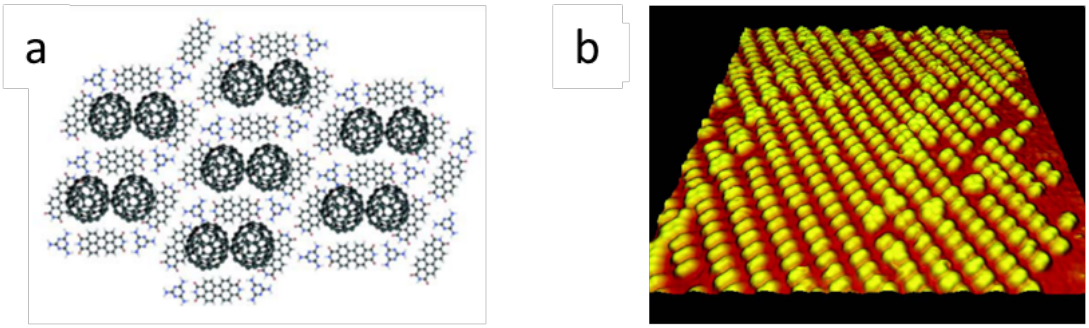


Figure 27 (a) Molecular model of the Mel/PTCDI template structure, with C_{70} pairs fitting in the template. (b) STM image of C_{70} array in the template. Figure reproduced from Silly, F. *et al.*[87]

Apart from chemically functionalising the fullerenes, changing the substrate to a template, and forcing the fullerenes to fit into the network in a similar way to placing eggs in an egg carton[86] has also been implemented. The template could either be physically patterned on a crystal surface[83,86] or chemically assembled by template molecules.[87–89] Figure 26 and Figure 27 illustrate STM image of aligning C_{70} molecules using a patterned $SrTiO_3$ substrate[83] and a Mel/PTCDI (melamine/ 3,4,9,10-perylene tetracarboxylic diimide) self-assembled network on the Au film,[87] respectively. The first method was capable of achieving fullerene arrays in

different sizes (1~5-molecule-wide). The MeI/PTCDI template obtained an ordered structure in a relatively larger range, and fullerene dimers were the elementary unit of the 2D array.

Although various fullerene assemblies have been achieved with empty-cage fullerenes and EMFs, I am not aware of any report on aligning ENFs using these methods. One concern of using surface self-assembling method to generate an ENF array is the high temperature used in the vapour deposition and annealing process, since heating above 500 K was proved to trigger an irreversible decomposition of N@C_{60}.[149] Therefore, I did not choose this assembly method for my work. Nevertheless, if approaches to improve the thermal stability of ENFs can be discovered, the 2D substrate assembly would be a promising option.

2.4.2 Fullerene peapod: assembly in single-walled nanotubes

A 1D array of empty-cage fullerenes can be achieved by encapsulating the molecules in single-walled nanotubes (SWCNT) (Figure 28). This assembling phenomenon was first detected by high resolution transmission electron microscopy (HRTEM) in 1998[80] after using a pulsed laser to synthesize nanotubes and C_{60}. A reproducible and controllable low temperature treatment to synthesize this type of peapod-like molecules was reported in 2004 using refluxing solvent[81] or supercritical (sc) fluids.[82]

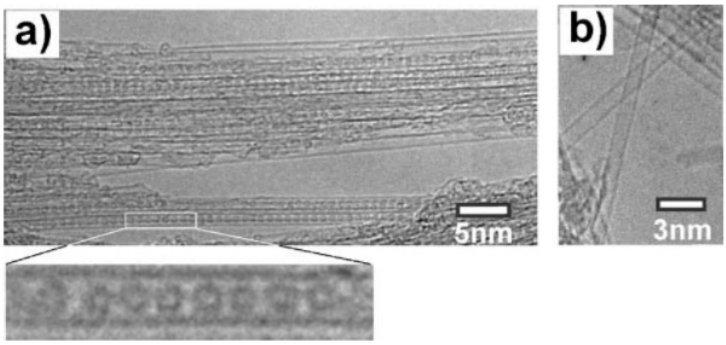


Figure 28 HRTEM micrographs of (a) SWCNTs of diameter $1.49\ \mathrm{nm}$ filled with C_{60} in sc CO_2 at room temperature. (b) SWNTs of diameter $1.36\ \mathrm{nm}$ remain empty under scCO_2 filling conditions. Figure reproduced from Khlobystov, A. N. *et al.*[82]

In contrast to the 2D substrate assembling, ENF arrays have been assembled successfully using nanotubes (Figure 29). While nanotube assembly could in theory lead to

perfect distance and orientation control of a one-dimensional ENF chain, three practical problems remain. Firstly, according to the cw-ESR spectrum given by peapods of ($N@C_{60}/C_{60}$) @SWCNT, more than half of the spin signal was lost during the refluxing solvent treatment.[81] Besides, some spin signal may not come from the peapod but is contributed from the $N@C_{60}$ molecules attached on the outside of the nanotube. Secondly, the electron spin properties of $N@C_{60}$ in the SWCNT, such as T_2 time, have been seriously impaired.[157] Thirdly, the spin signal of SWCNT itself[158] could suppress or interfere with the signal of ENFs. Therefore, I did not choose this assembly method for my work.

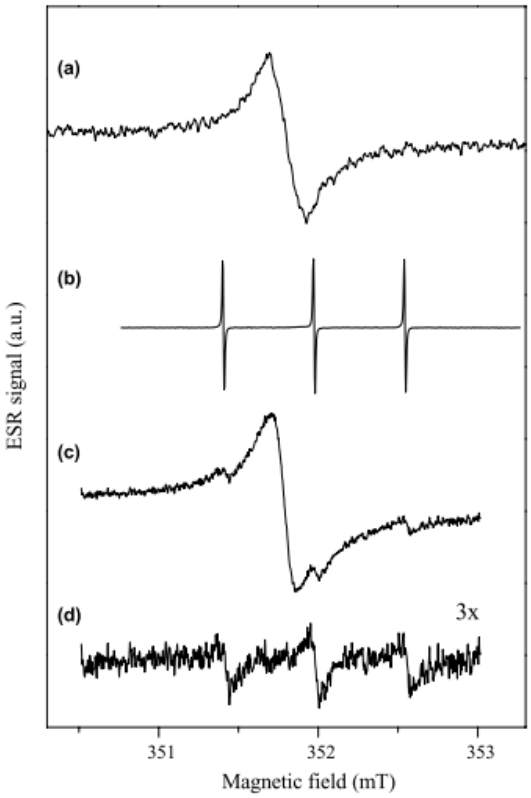


Figure 29 Room temperature cw-ESR spectrum of (a) pristine SWCNT, (b) crystalline $N@C_{60}/C_{60}$, (c) ($N@C_{60}/C_{60}$) @SWCNT and (d) the its triplet component. Figure reproduced from Simon, F. *et al.*[81]

2.4.3 Fullerene dimers: assembly with chemical bonds

Compared with the 2D and 1D assembly, the dimerization of ENFs has demonstrated the most successful microscopic controllability for the assembly so far. In addition, once

dimerization is achieved, a larger scale of ENF assembly, such as oligomer and polymer, could be applied.[159] This section first provides a brief overview of the general strategies for preparing empty-cage fullerene dimers, and then reviews previously reported ENF dimers.

The simplest fullerene dimer is a directly bonded dimer $(C_{60})_2$.[160] Bridged by a squared four-membered exohedral ring between two [6,6] bonds of two fullerenes, this type of dimer offers a rigid conformation that is ideal for the controllability of fullerene molecular assembly (Figure 30a). Unfortunately, the synthesis is hindered by the low yield and the generation of various by-products, such as $C_{120}O$ and $C_{120}O_2$[152]. In addition, a low thermal stability of the product, which decomposes at 175°C,[153] also limits the feasibility of applying this strategy to ENFs.[145]

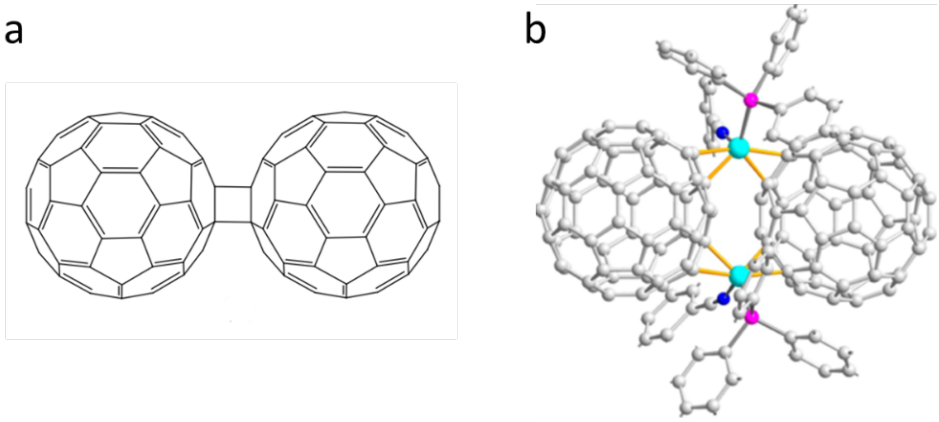


Figure 30 (a) Directly bonded dimer $(C_{60})_2$. (b) Metal bridged dimer $\{Co(Ph_3P)(C_6H_5CN)\}_2(\mu^2\text{-}\eta^2,\eta^2\text{-}C_{60})_2$, grey: carbon, blue: nitrogen, purple: phosphorus, and cyan: cobalt. Figure reproduced from Komatsu, K. *et al.*[160] Konarev, D. V. *et al.*[162]

Fullerene dimerization has also been achieved using metal bridges, where fullerenes act as ligands. Despite the bulky structure of fullerene and their innate electron deficiency, some metal centres such as Rh,[161] Ir,[161] and Co[162] were proved to form stable metal-fullerene coordinate bonds (*e.g.* Figure 30b). However, until now no metal bridged ENF dimer has been successfully prepared and reported.

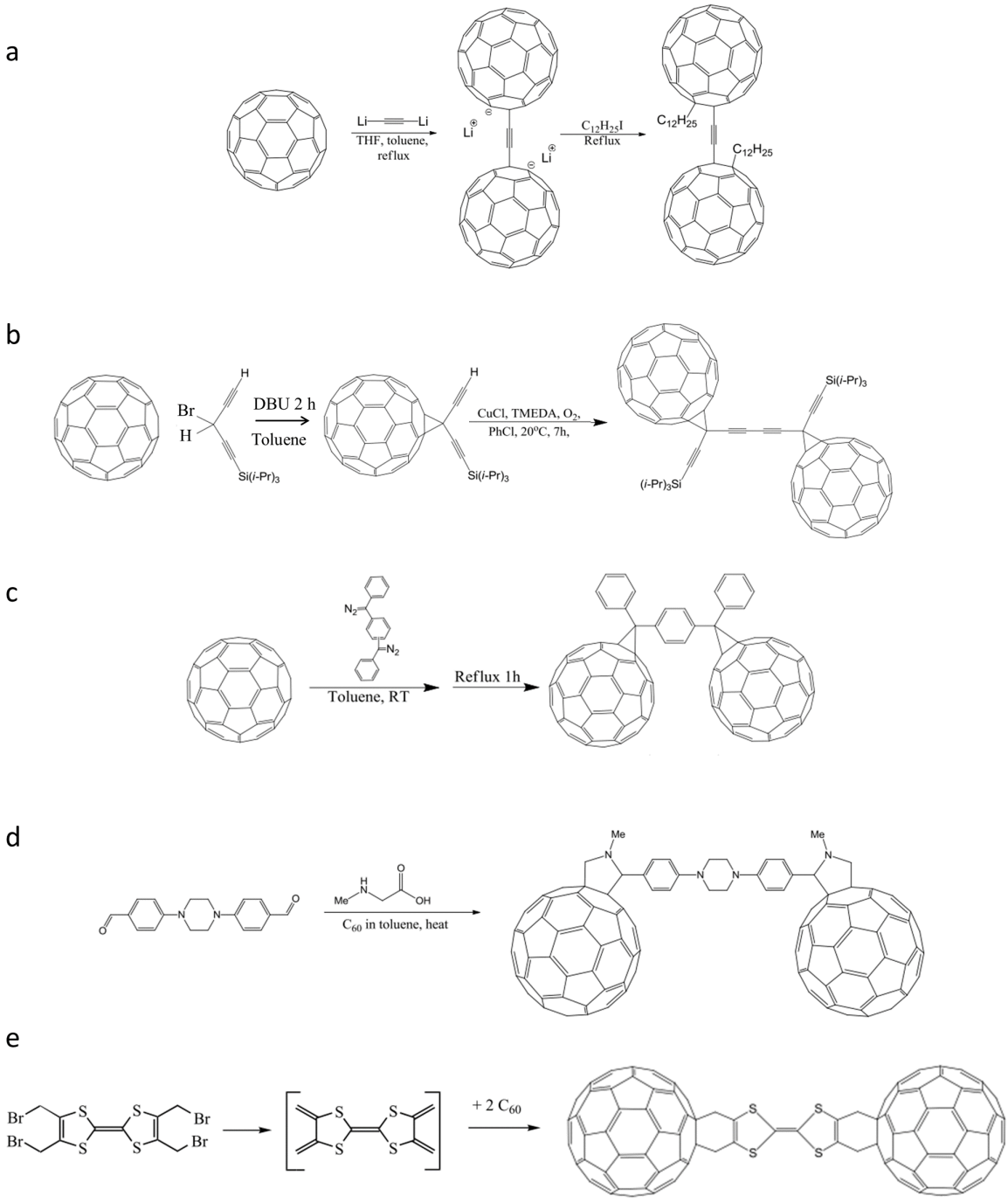


Figure 31 Synthesis of organic dumbbell dimers. (a) Nucleophilic addition with an organometallic compound.[163] (b) Nucleophilic addition with a malonate, and then Hay coupling.[163] (c) Radical addition with a diazo compound (the precursor of the carbene).[164] (d) [3+2] cyclo-additions with an aldehyde and an amino acid (the precursors for the ylide).[165] (e) [4+2] cyclo-additions with a bromo-methyl compound (the precursors for the diene).[166] Figure reproduced from Farrington, B. J.[96] Timmerman, P. *et al.*[163]and Liu, S.G. *et al.*[166]

The most well-reported fullerene dimers are organic dumbbell dimers, which utilize organic bridges to covalently link two fullerene moieties. This could be achieved through a

variety of fullerene chemical reactions, including nucleophilic additions with organometallic compounds (Figure 31a)[163] and malonates (Figure 31b),[163] radical addition with carbenes (Figure 31c),[164] and cyclo-additions with ylides (Figure 31d)[165] and dienes (Figure 31e).[166], A comprehensive review focusing on the preparation and properties of these organic dumbbell dimers was done by a previous member of my research group in his thesis.[96]

There are two points to estimate the reference value of these empty-cage dimerizations for preparing ENF dimers and assembling molecular qubits: (1) the feasibility of applying these synthetic schemes to the ENF systems, (2) the controllability of the dimer conformation including fullerene distance and bond angles.

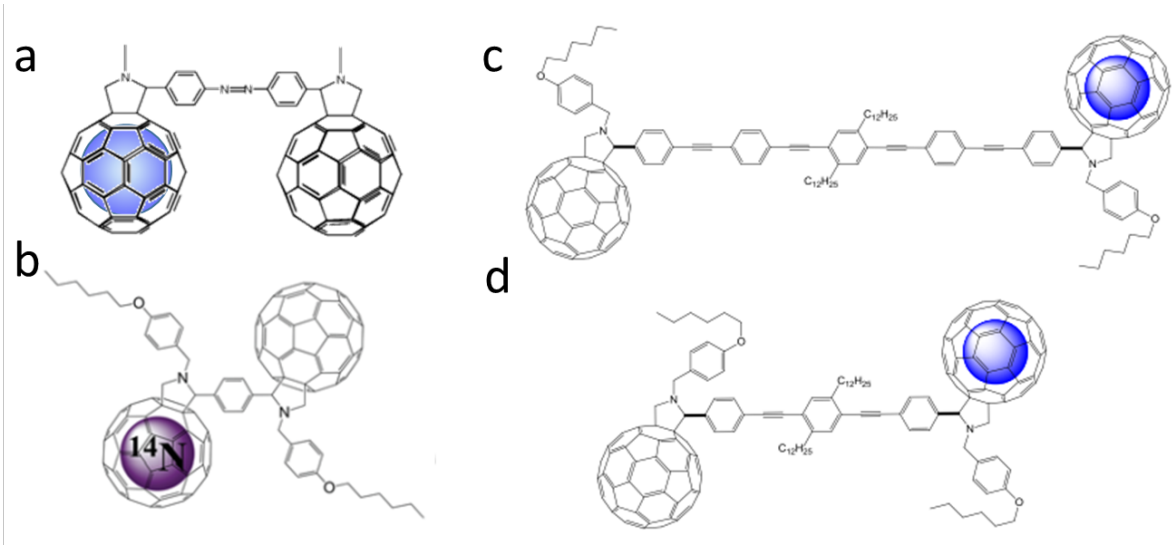


Figure 32 (a) ENF half-filled dimer with an azobenzene group.[78] (b) ENF half-filled dimer with a phenyl group.[77] (c) ENF half-filled dimer with a long oligo(p-phenyleneethynylene) group.[79] (d) ENF half-filled dimer with a short oligo(p-phenyleneethynylene) group.[79]

The first point depends on the viability of corresponding chemical reactions with ENFs. As reviewed in section 2.3, the protocol of the Prato reaction with ENFs is relatively developed. Thus, four ENF dimers have been synthesized using Prato reactions with the organic bridges being an azobenzene group (Figure 32a),[78] a phenyl group (Figure 32b),[77] and oligo(p-phenyleneethynylene) groups (Figure 32c, d),[79] respectively. Since obtaining pure ENFs is time-consuming and expensive, all these ENF dimer studies were using $N@C_{60}/C_{60}$ mixtures, and normally yielded a half-filled dimer (an ENF dimerized with an empty-cage). Nevertheless,

the double-filled dimer (two ENFs dimerized) can be formed using the same reaction condition by starting from pure ENFs.

The second point is the common limitation for these dimers lying in the α-position of the pyrrolidine. Although bonding through the α-position of the pyrrolidine leads to a facile synthesis route, it results in a decreased controllability on the molecular configuration, which conflicts with the second point. Taking the Prato dimer bridged by the phenyl group[77] as an example (Figure 33), the conformational isomers caused by the rotation of σ-bonds and enantiomers/meso isomers caused by chiral centres still need to be eliminated with an improved dimerization scheme. The difficulty of satisfying both points can be overcome by tuning the Prato ENF dimer design to improve its structural control, or by expanding the chemical functionalisation methods of ENFs to make more reaction schemes applicable to ENFs.

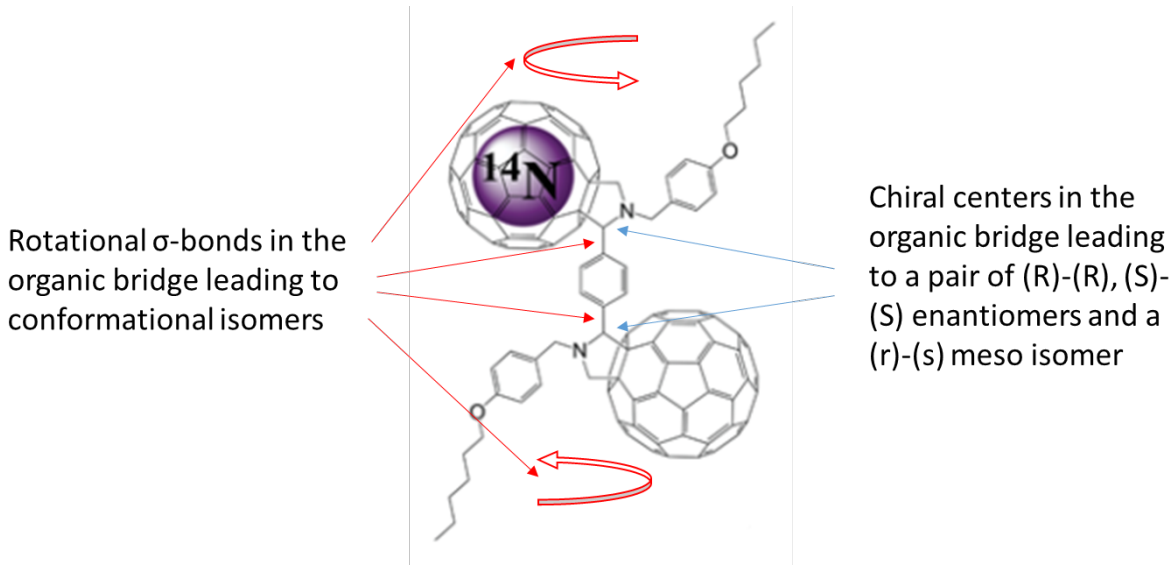


Figure 33 Rotational σ-bonds and chiral centres in the organic bridge of an ENF dimer synthesized by a Prato reaction,[77] and the potential conformational isomerism and optical isomerism of the dimer.

2.5 Macroscopic alignment of fullerenes for orientational ordering of qubits

Orientationally aligning ENFs to obtain directional uniformity of the spin ensemble is also required for an ENF-based quantum device, because of DiVincenzo criterion 5 (section 2.1.3). Due to the difficulty of crystallizing fullerenes, the alignments of empty-cage fullerene, EMFs and ENFs have been studied by embedding them in a crystal, a co-crystal, or a liquid crystal. With my work focusing on aligning ENFs in a liquid crystal discussed in Chapter 7, general alignment methods for fullerene are reviewed and compared in this section, many of which have demonstrated certain degrees of orientational ordering.

2.5.1 Fullerene alignment in the single crystal

While crystallization from solution usually yields a structure that include solvent molecules, sublimation in vacuum or inert gas atmosphere may lead to pure fullerene crystals (Figure 34).[167–169] Having the highest symmetry group of I_h amongst the fullerene family, C_{60} is not easy to align by crystallization, as the molecules are usually orientationally disordered.[170,171]

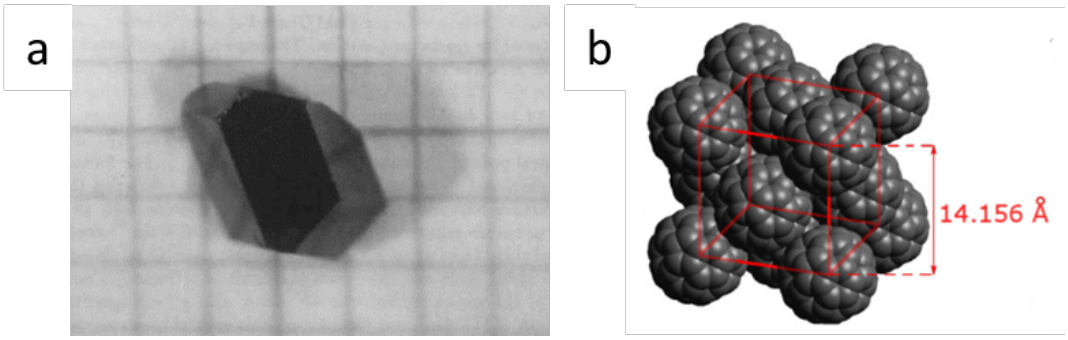


Figure 34 (a) Pure fullerene crystal in a millimetre scale at room temperature. (b) Face-centred cubic (FCC) unit cell of C_{60} crystal at room temperature, regarding the carbon cage as a sphere rather than an icosidodecahedron. Figure reproduced from Pichler, T. *et al.*[168] and Bussolotti, F. *et al.*[169]

Some studies pointed out that certain functional groups offering hydrogen bonding sites on the fullerene molecule are conducive to the orientation ordering and crystallization (Figure 35).[172] Nevertheless, the reported hexa-functionalisation occupies all chemically-reactive

bonds on the cage, and precludes introducing other functional groups and fullerene dimer linkage. Therefore, I did not choose crystallization as the ENF alignment method for my work.

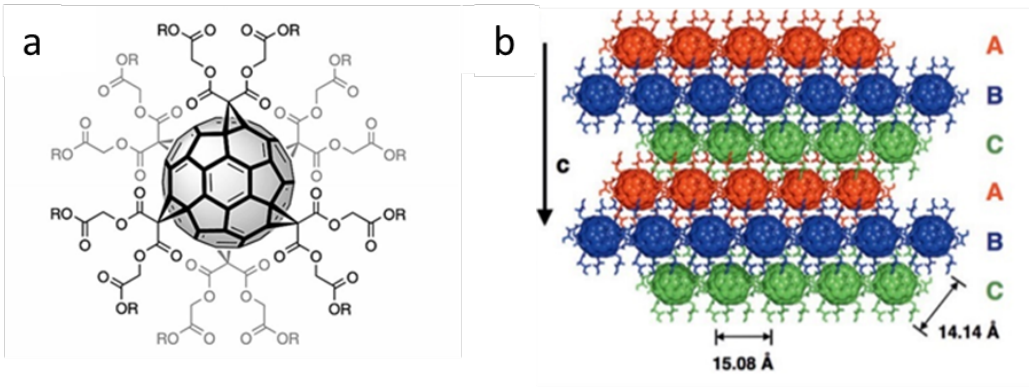


Figure 35 (a) Fullerene derivative synthesized for co-crystallizing them with MeOH and CH_2Cl_2. (b) 3D network of arranging fullerene derivatives formed by hydrogen bonding. Figure reproduced from Kraft, A. *et al.*[172]

2.5.2 Fullerene alignment in co-crystals

Since the single crystal of fullerene are difficult to obtain, crystalline fullerene samples are normally co-crystals with small molecules or macrocycle compounds, which are characterized by X-ray diffraction (XRD). Small molecules, such as ferrocene,[173] toluene,[174] iodine,[175] and cubane,[176] act as fillers to make up the gap between stacked carbon cages, which enhances the lattice energy, thus promoting crystallization. As shown in Figure 36, ferrocene[173] and toluene,[174] which can realize the π-π stack[177] with the cage, offer closely packed pristine fullerene molecules oriented in the same direction. Figure 37 demonstrates the other type of co-crystallization, where small molecules, like iodine[175] and cubane,[176] leave the fullerene cage free to rotate.[178–180] Macrocycle compounds, such as porphyrin, corrole, and their derivatives,[181,182] can form a well-ordered co-crystal through supramolecular assembly, which "holds" the fullerenes in their lattice position (Figure 38).[156] In contrast to small molecule co-crystallization, this type of co-crystal does not require a high degree of symmetry from the fullerenes, so fullerenes with ellipsoidal shapes (such as EMF) show good crystallographic results with this co-crystallization method.[25,33,181]

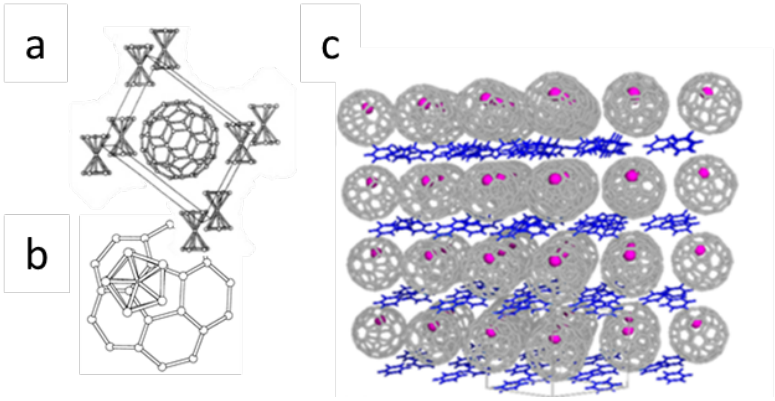


Figure 36 (a) Unit cell of the co-crystal of C_{60}(ferrocene)$_2$. (b) Detailed intermolecular structure of ferrocene and the pentagonal face of C_{60}. (c) The crystal structure of Y@C_{82}(toluene)$_2$. Figure reproduced from Crane, J. D. *et al.*[173] and Maki, S. *et al.*[174]

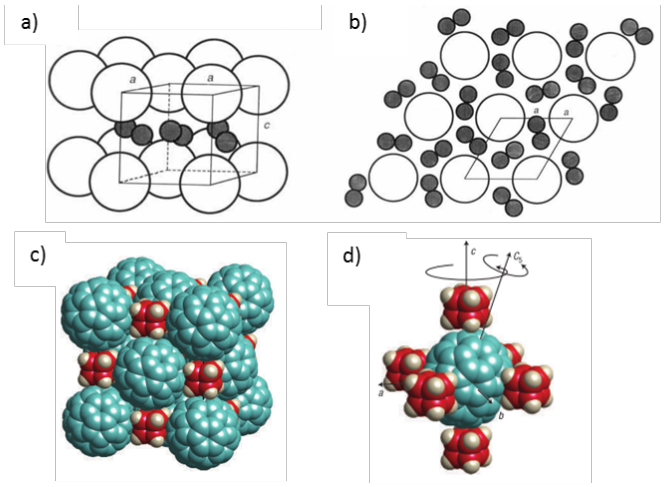


Figure 37 (a) Unit cell of $C_{60}(I_2)_2$. Large circles represent the skeletons of C_{60}, where small dumbbells are iodine molecules. (b) Plane projection of the structure of $C_{60}(I_2)_2$. (c) Unit cell of $C_{60}C_8H_8$. (d) Restricted motion of fullerene-cubane co-crystal. Figure reproduced from Zhu, Q. *et al.*[175] and Pekker, S. *et al.*[176]

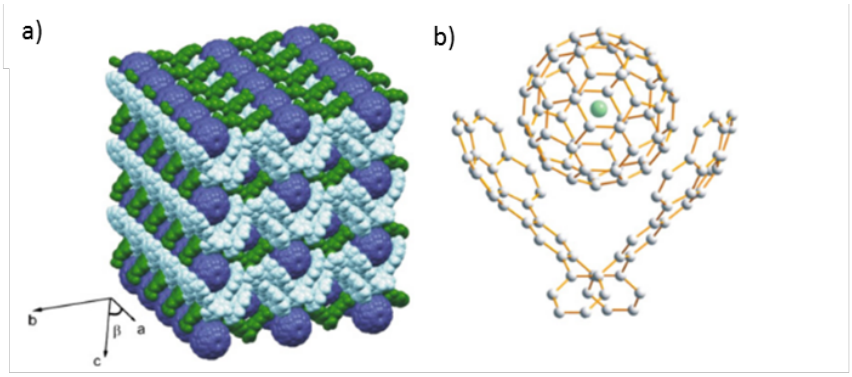


Figure 38 (a) Crystal structure of C_{60}@$C_{60}H_{28}$·2PhMe (green balls representing toluene molecules are disordered). (b)Highlight of fullerene held by buckycatcher: $C_{60}H_{28}$. Figure reproduced from Yang, J. *et al.*[156]

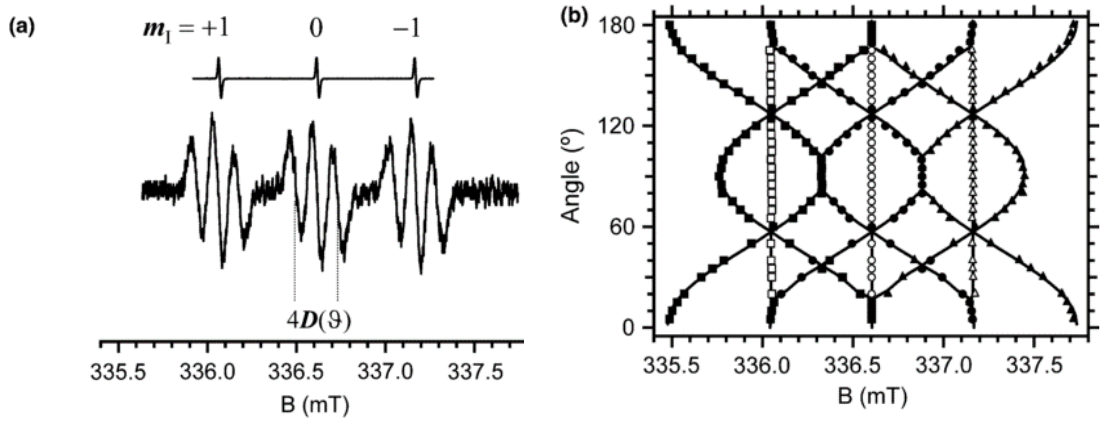


Figure 39 (a) Comparison of N@C_{60} cw-ESR spectra in the solid-state and in rhombohedral BrPOT crystalline matrix (oriented at 47°), (b) Angular dependence of the signal positions. Figure reproduced from Naydenov, B. *et al.*[155]

To apply the co-crystallization alignment study on ENFs, embedding N@C_{60} in a rhombohedral BrPOT crystalline matrix has been reported.[155] Figure 39 demonstrates the angle-dependent cw-ESR signal from the co-crystal. It is worth noting that the angle-dependent ZFS is caused by significant distortion of the cage during co-crystallization, rather than the intrinsic ZFS raised by the molecular structure. Therefore, this alignment method did not prove its capability of aligning the intrinsic molecular spin isotropy.

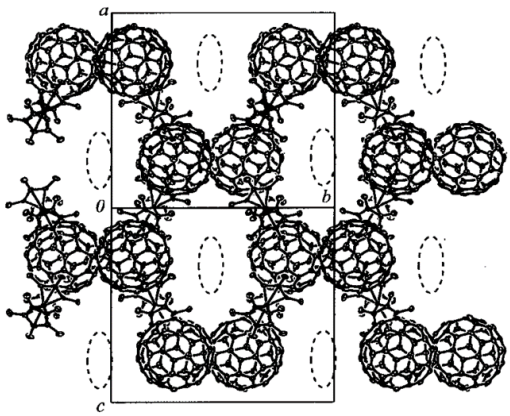


Figure 40 Crystal structure of fullerene dimer array formed by cooling $Cp_2Cr{\cdot}C_{60}(C_6H_4Cl_2)_2$ down to 100 K. Dimers are shown in their major orientation. $C_6H_4Cl_2$ molecules which are located in the dashed circles are omitted for clarity. Figure reproduced from Konarev, D. V.*et al.*[183]

Despite the perfectly ordered structure, there are two main drawbacks for using co-crystallization to align ENFs. Firstly, it does not have a good compatibility with scalable fullerene structures. Fullerene dimers, for example, can only be partly aligned (Figure 40).[183]

Secondly, too many hydrogen nuclear spins, which have a large gyromagnetic ratio, in the co-crystallization molecules that are closely packed with the spin centres, resulted in a degradation in the decoherence time of ENFs.[156] Therefore, I did not choose co-crystallization as the ENF alignment method for my work.

2.5.3 Fullerene alignment in liquid crystals

In contrast to the crystallization approaches which require lattice matching, embedding nanomaterials in a liquid crystal[184] is a more general method. Its effectiveness has been demonstrated with various materials, *e.g.* fullerene derivatives,[185] carbon nanotubes (CNT),[186] and gold nanoparticles (Figure 41).[187] The degree of the orientational ordering of guest molecules is normally parameterized by a second-order tensor called the Saupe matrix.[188] The axial component of the Saupe matrix is mathematically expressed as $O_{zz}(\theta_{zz}) = \frac{(3\cos^2\theta_{zz}-1)}{2}$, which represents the effectiveness of an axial alignment of the sample to a certain direction. The variable O_{zz}, which ranges from -0.5 to $+1$, is commonly referred to as the "order parameter". Depending on the tested materials, both the full Saupe matrix and the order parameter were characterized by various methods, such as transmission electron microscopy (TEM),[186] XRD,[186] and polarizing optical microscope (POM).[187] When the aligned species are electron spin-active, ESR spectroscopy is also a useful tool for extracting the alignment information.[189–191]

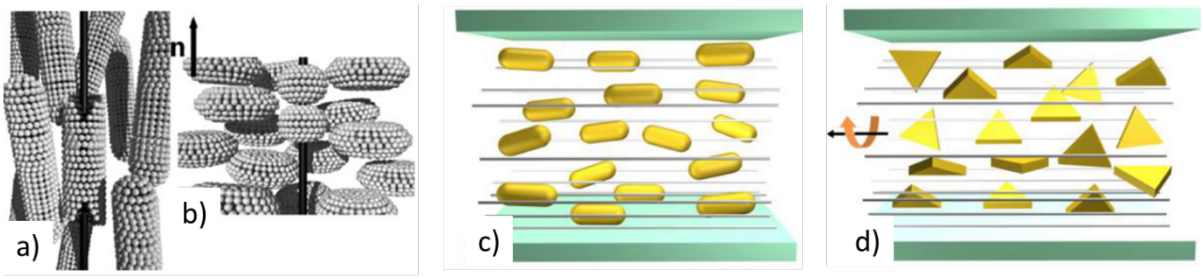


Figure 41 Schematic illustration of aligning different-shaped CNT (a, b)[186] and gold nanoparticles (c, d)[187] in the nematic phase of liquid crystals. Figure reproduced from Lagerwall, J. *et al.*[186] and Liu, Q. *et al.*[187]

Due to the extremely small amount of ENF in the corresponding aligned sample, only cw-ESR characterization has been successfully conducted to analyse the orientational ordering properties, with an order parameter $O_{zz} < 0.2$ achieved for both pristine N@C_{70} and N@C_{60} derivatives.

a

$$\bar{g}_{zz,ani} = O_{zz} \times g_{zz,ani}$$

$$\bar{A}_{zz,ani} = O_{zz} \times A_{zz,ani}$$

$$\bar{D}_{zz} = O_{zz} \times D_{zz}$$

b

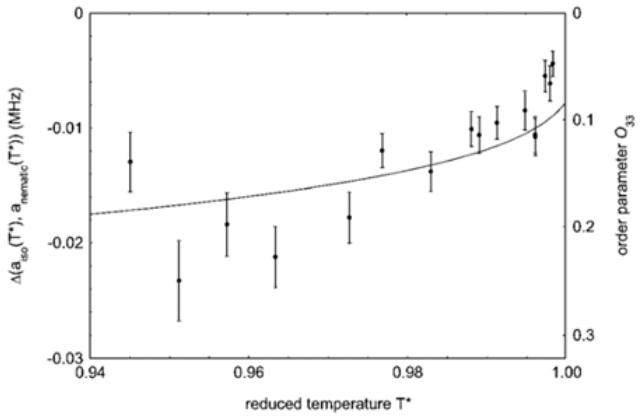


Figure 42 (a) Three ways of extracting O_{zz}: the spin anisotropy of the *g*-tensor, HFC tensor, and ZFS tensor. The "¯" symbol represents the effective value measured in the partially aligned sample, "$_{zz}$" symbol means the two directions parallel to the B_0 direction and the main axis of tensor frame, respectively, and "$_{ani}$" stands for anisotropic. (b) Temperature dependent order parameter extracted by the anisotropy of the HFC tensor. Figure reproduced from Jakes, P. *et al.*[192]

$O_{zz} = 0.18$ was reported for N@C_{70} aligned in 4-methoxybenzylidene-4'-*n*-butylaniline (MBBA) matrix at room temperature.[192,193] In the nematic phase, three ways to extract the order parameter were proposed (Figure 42a),[192,193] which are based on the measurement of the effective spin anisotropy of the g tensor ($\bar{g}_{zz,ani}$), of the HFC tensor ($\bar{A}_{zz,ani}$), and of the ZFS tensor ($\bar{D}_{zz}$), respectively. The ZFS tensor should be used to determine the order parameter, because it has the highest level of anisotropy and hence the best accuracy of the three methods. Researchers[192,193] attempted to measure the effective ZFS tensor $\bar{D}_{zz}$ as the anisotropy information to deduce the order parameter, but they failed to obtain the intrinsic D_{zz} from the solid-state spectrum of N@C_{70}. Therefore, they derived O_{zz} from $\bar{A}_{zz,ani}$ and $A_{zz,ani}$ (Figure 42b), under the hypothesis that the small value of $A_{zz,ani} = -94$ kHz measured at 80 K is still applicable to the room temperature experiment. However, it has been reported elsewhere that the HFCC of ENFs drifts with temperature.[194] Moreover, the low $A_{zz,ani}$ value causes the measured value as small as 0.3 μT, which is difficult to measure accurately. Thus,

both the hypothesis and the measurement accuracy of the experiment need to be improved.

In contrast to the alignment result for N@C_{70}, the order parameter for N@C_{60} derivatives was obtained more reliably,[195] as the larger ZFS tensor for N@C_{60} derivatives enables the measurement of D_{zz}. More importantly, comparative study was made possible by using different addends to functionalise ENFs. Applying the third equation in Figure 42a, order parameters for different N@C_{60} derivatives was determined ($O_{zz} = 0 \sim 0.24$, Figure 43). According to the alignment results of different derivatives, the authors concluded that the rigid structure of the addend plays an important role in giving a high order parameter for the ENF derivative.

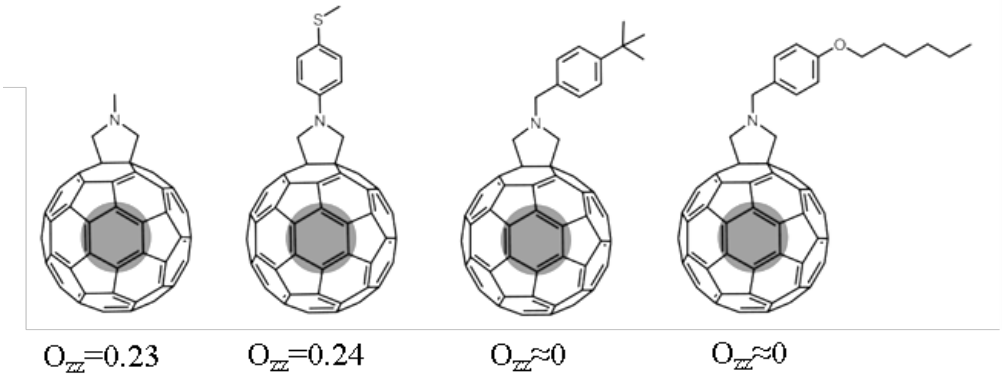


Figure 43 The molecular structure of the N@C_{60} derivatives, and their order parameter in MBBA Figure reproduced from Liu, G. *et al.*[195]

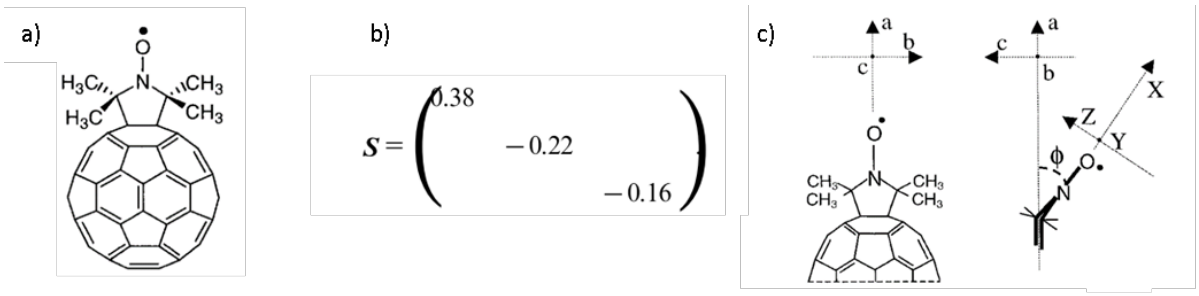


Figure 44 (a) Molecular structure of the spin labelled fullerene. (b) Saupe matrix of fullerene nitroxide in PAA. (c) Comparison between the molecular axes and spin label axes. Figure reproduced from Mazzoni, M. *et al.*[196]

A more comprehensive measurement of the ordered fullerenes in the liquid crystal was performed on spin-labelled empty-cages (Figure 44a).[196] The full Saupe matrix (Figure 44b) of fullerene nitroxide in 4,4'-azoxyanisole (PAA) was measured using cw-ESR . Since the

nitroxide spin label has a more significant HFC anisotropy than what ENFs have, the change of HFCC upon aligning the molecules can be measured precisely. Despite the better accuracy, the exohedral functionalised spin label introduces another error, as the experiment needs to predict the angle Φ between the spin label axe and the molecular axe (Figure 44c).

In addition to the nitroxide spin labelling approach, the transient spin signal from an excited triplet state of the carbon cage was studied using time-resolved ESR spectroscopy. Although the reported alignment result was even better ($O_{zz} = 0.52$ for a conventional methano-fullerene),[188] the universality of the stimulation of the transient spin could be a concern. Due to anisotropic illumination, certain molecules in any given orientation may be more likely to be stimulated, leading to an over-estimate of the order parameter.

2.6 Dipolar coupling in EF-containing di-electron-spin systems

A controllable dipolar coupling between ENF spins which is suitable to perform two-qubit gate operations is the remaining requirement towards an ENF-based quantum device, because of the DiVincenzo criterion 4 (section 2.1.3). Despite well-documented spin coupling studies on conventional radical molecular systems, such as 2,2,6,6-Tetramethylpiperidin-1-yl)oxyl (TEMPO),[197] the investigation on paramagnetic endohedral fullerenes is lacking. This section reviews electron dipolar coupling studies performed with endohedral fullerenes, on which my study in Chapter 8 was based.

2.6.1 N@C_{60}–CuTPP dyad

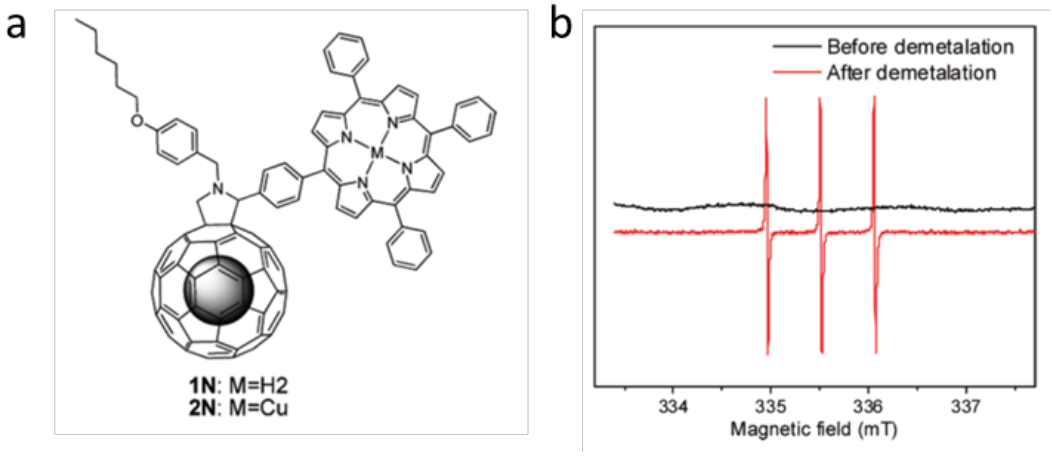


Figure 45 (a) N@C_{60}–MTPP dyads, where M = Cu or H_2. (b) Comparison of the ENF spin signal before and after converting the CuTPP to H_2TPP. Figure reproduced from Liu. G. *et al.*[198]

In 2012, a pair of ENF–porphyrin dyads was synthesized to study the spin coupling with ENFs in a qualitative manner (Figure 45).[198] In addition to the report on the successful synthesis of the first ENF-containing di-electron-spin systems, the authors also pointed out that the copper (II) tetraphenylporphyrin (TPP) can suppress the ESR signal of N@C_{60} through intramolecular dipolar coupling with a strength of 27.0 MHz.[198] By comparing nitrogen spin signal of CuTPP- and H2TPP-linked ENF dyads (Figure 45a, 1N and 2N), one observes a

dramatic intensity difference (Figure 45b). The authors attributed this phenomenon to the line width broadening and consequent decrease in the signal amplitude resulting from a dipolar coupling. While the result inspired a strategy of switching spin state between on and off, a more detailed study of the spin coupling is still needed. Considering the significant signal-suppressing effect in this reported dyad, a longer distance between two spin centres, and hence a smaller coupling strength, is necessary to confirm that the spin coupling is indeed a dipolar coupling.

2.6.2 $FSc_3C_2@C_{80}$–PNO radical

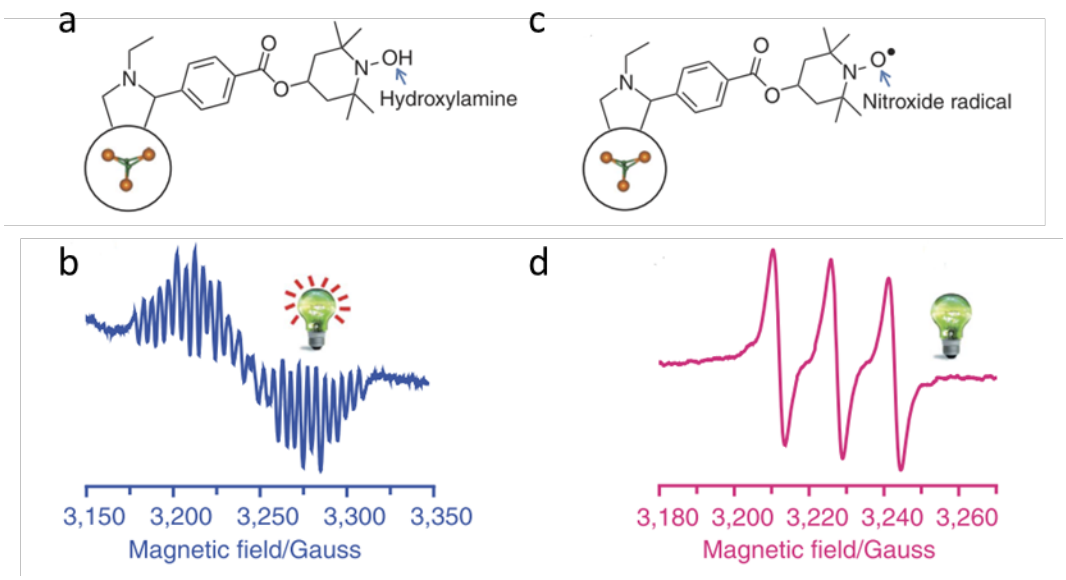


Figure 46 (a) Schematic illustration of $FSc_3C_2@C_{80}$-PNOH and (b) its cw-ESR spectrum. (c) Schematic illustration of $FSc_3C_2@C_{80}$-PNO radical and (d) its cw-ESR spectrum. The lamps show the 'on' and 'off' states of the $Sc_3C_2@C_{80}$ signals, respectively. Figure reproduced from Wu, B. *et al.*[199]

In 2015, similar qualitative spin coupling study with EF was performed with $Sc_3C_2@C_{80}$ (Figure 46, Figure 47).[199] Benefitting from the better availability of $Sc_3C_2@C_{80}$ than ENFs, this research not only demonstrated the same spin-on/spin-off experiment by changing the nitroxide group (Figure 46), but also studied the spin coupling phenomena with more variables: (1) chemically changing the distance between the nitroxide chemical moiety and the $Sc_3C_2@C_{80}$ moiety, and (2) physically tuning the temperature of the sample (Figure 47).

Consequently, incomplete spin signal suppression by the nitroxide radical was observed for the first time with the electron spins from a EF system.[199] However, one limitation of using $Sc_3C_2@C_{80}$ lies in its complicated spin anisotropy. The three Sc atoms are not equivalent to each other, once the EF is functionalised.[22] It resulted in a spin divergence,[22] which complicates a quantitative study of the endohedral fullerene moiety's cw-ESR spectra. If the poor availability of ENFs can be overcome, reproducing this cw-ESR experiment with ENFs would lead to more quantitative findings.

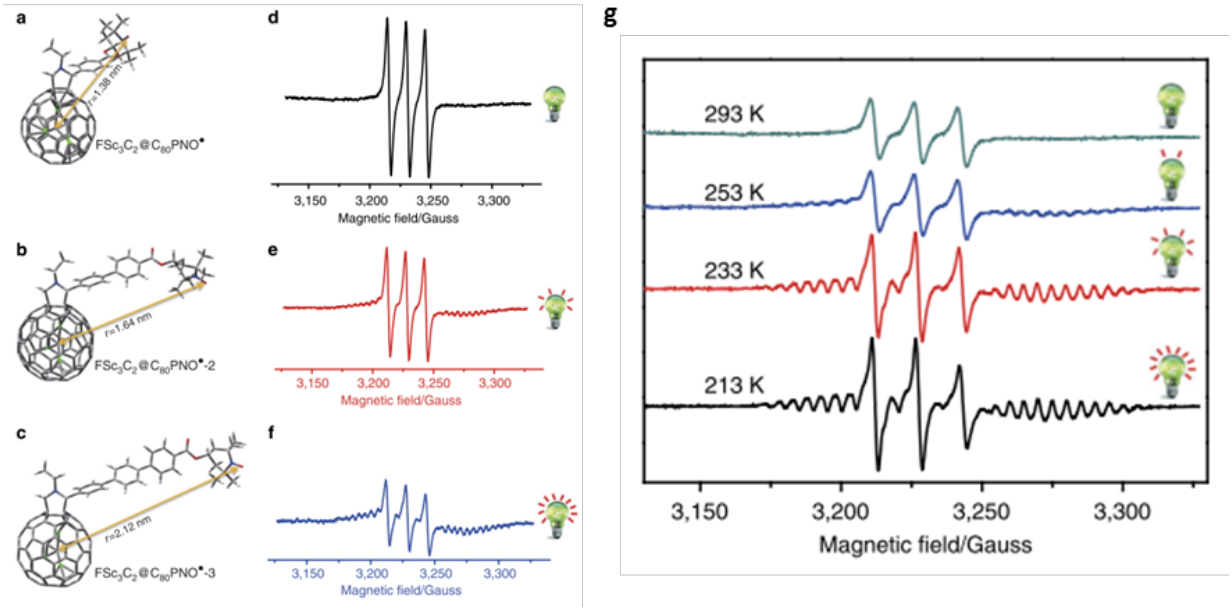


Figure 47 (a–c) Structures of the $FSc_3C_2@C_{80}PNO$ radical, $FSc_3C_2@C_{80}PNO$ radical-2 and $FSc_3C_2@C_{80}PNO$ radical-3, respectively. (d–f) cw-ESR spectra of $FSc_3C_2@C_{80}PNO$ radical, $FSc_3C_2@C_{80}PNO$ radical-2 and $FSc_3C_2@C_{80}PNO$ radical-3 at 293 K, respectively. (g) Comparison on cw-ESR spectra of the $FSc_3C_2@C_{80}PNO$ radical at variable temperatures in toluene solution. Figure reproduced from Wu, B. *et al.*[199]

2.6.3 $N@C_{60}$–$N@C_{60}$ dimer

Spin coupling between two covalently linked $N@C_{60}$ moieties was reported in 2012.[79,96] After the authors developed a five-minute one-pot method for the synthesis of a $N@C_{60}$ dimer, two different starting $N@C_{60}/C_{60}$ mixtures (1% and 50%) were used to link the dimer. When the 1% pure sample was used, the half-filled $N@C_{60}$ dimer (Figure 48a) was obtained (sample 1), whereas the 50% pure stating material led to both the half-filled (Figure 48a) and double-

filled (Figure 48b) N@C_{60} dimer (sample 2). The ratio of two species was estimated to be 49:19 based on statistics. To obtain a pure double-filled dimer signal, the authors subtracted the cw-ESR spectrum of sample 1 (Figure 48c, green) from that of sample 2 (Figure 48c, red). They further attributed the subtracted spectrum (Figure 48e green) to the cw-ESR signal caused by the double-filled N@C_{60} dimer, as its simulation contained an isotropically distributed dipolar coupling between the two N@C_{60} moieties with a strength of 2.67 MHz, which corresponds to a 2.7 nm separation of the two N@C_{60} centres.

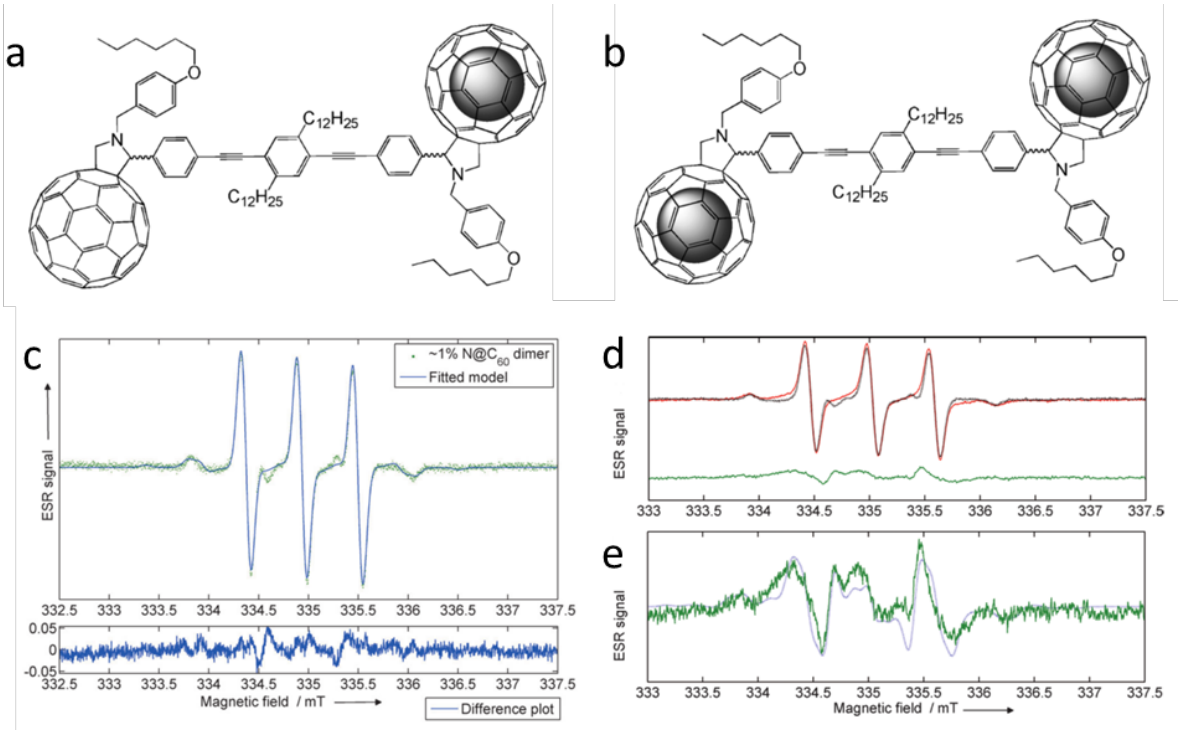


Figure 48 (a) Half-filled N@C_{60} dimer. (b) Double-filled N@C_{60} dimer. (c) Cw-ESR signal of the half-filled N@C_{60} dimer (green), the fitting (blue) and the residual error (below). (d) Cw-ESR signal of the sample containing only the half-filled N@C_{60} dimer (black), the sample containing both the half-filled N@C_{60} dimer and the double-filled N@C_{60} dimer (red), and the subtracted spectrum (green). (e) Fitting the subtracted spectrum (green) with the simulation (blue), which contains an isotropic distributed dipolar coupling between two N@C_{60} moieties of the dimer with a strength of 2.67 MHz. Figure reproduced from Farrington, B. J. *et al.*[79]

While the authors claimed that it is the first evidence of dipolar coupling between two covalently bonded N@C_{60} molecules, the potentially considerable error of the spectral subtraction is a concern for the research. Since cw-ESR spectroscopy detects signals from both the half-filled dimer and the double-filled dimer, spectral subtraction is necessary before a pure double-filled N@C_{60} dimer signal is obtained. However, applying double-filled N@C_{60}

dimer selective pulse-ESR experiments, such as double electron-electron resonance (DEER)[200] and relaxation induced dipolar modulation enhancement (RIDME),[201,202] might solve the problem without obtaining a pure sample. Alternatively, linking a low-purity $N@C_{60}/C_{60}$ mixture with a 100% pure hetero spin center would enable the cw-ESR study without requiring spectral subtraction.

2.7 Conclusions

This chapter explains the motivation of this thesis, which is using ENF as a molecular qubit. According to the demands of the DiVincenzo Criteria and the property of ENFs, the advantages of implementing QIP with ENFs are highlighted, and ENFs' limitations are also discussed, which includes (1) the low productivity, (2) the insufficiently understood chemistry, (3) the difficult spatial assembly, (4) the poor orientational alignment, and (5) the challenging spin coupling control. Aiming for the solution to each of the limitations, the current progress of ENF studies has been reviewed with both important achievements and unsolved problems summarized as below.

For the synthesis of ENFs, the spin-yield of the crude product remains at the ppm level in almost all reported literature. While the commercial ion source approach has showed the highest scalability, glow discharge and RF-coupled plasma implantation have been advantageous for achieving low cost and high spin-yield, respectively. The purification of ENFs from the low-purity crude product has been achieved using HPLC. Nevertheless, the separation is still partial, hence repetitive HPLC experiments have been generally utilized to gradually enrich the content of ENFs in the sample. This makes the procedure time-consuming, particularly for the initial passes, where simultaneously tackling the large quantity of the crude material and achieving the necessary precision is difficult.

Regarding ENF chemistry, despite the many reactions established for empty-cage fullerenes, few reactions have been systematically applied to the ENF system. While the Prato reaction shows the most successful chemical functionalisation results, the spin-compatibility of the Bingel reaction with ENF is still controversial. In terms of the characterization of ENF derivatives, it is conventional to use cw-ESR to measure the ZFS to determine whether or not the ENF has been successfully functionalised. Other characterization techniques, such as MS, NMR spectroscopy, and UV/Vis spectroscopy are also applied to study the structures of the empty-cage derivatives in the samples, as they can indirectly prove the addends attached to

ENFs.

For the microscopic assembly of ENFs, proposals of 2D surface adsorptions, 1D nanotube encapsulations, and covalent linkages have been put forward. Although higher dimensional assembly would lead to more scalable ENF molecular architectures, the covalent linkage is still the most feasible method to obtain a small-scale of ENF assembly, such as an ENF dimer. To enhance the conformation and spin distance controls of ENF dimers, novel dimerization schemes are realized, but there is still room for improvement.

For the orientational ordering of ENFs, general fullerene alignment properties in single crystals, co-crystals and liquid crystals are compared. While fullerenes are orientationally disordered in their single crystals, embedding them in both co-crystals and liquid crystals is capable of achieving certain degrees of orderings. The liquid crystal approach is believed to be a more compatible method, as it has less requirement on the lattice matching, compared to the co-crystallizations. To quantify the orientation distribution of spin-active fullerenes, a variety of order parameters, ranging from 0.2 to 0.5, determined by spin anisotropies, have been reported. The extraction of the spin anisotropies, such as the anisotropic HFC and the ZFS, is done by measuring the sample in the nematic phase or in the frozen phase.

For the dipolar coupling study with EFs, there are only a small number of pioneering researches, presumably due to the limited availability of spin-active EFs. Overall, current observations on dipolar coupling are consistent with conventional understandings obtained from ordinary radicals, but the detailed properties of the dipolar coupling in these EF systems has not been fully revealed. On the one hand, studies of the N@C_{60}–CuTPP dyad and the FSc_3C_2@C_{80}–PNO radical dyads are in a qualitative level, and only the extent of the signal suppressing caused by the dipolar coupling has been discussed. One the other hand, quantitative ESR study of the N@C_{60}–N@C_{60} dimer is of questionable reliability due to the spectra subtraction treatment, which is used to uncover the broad and weak dipolar coupling signal masked by the sharp and intense signal originating from the non-coupled ENF electron spins.

Chapter 3 Methodology

3.1 Experimental Techniques

3.1.1 High performance liquid chromatography

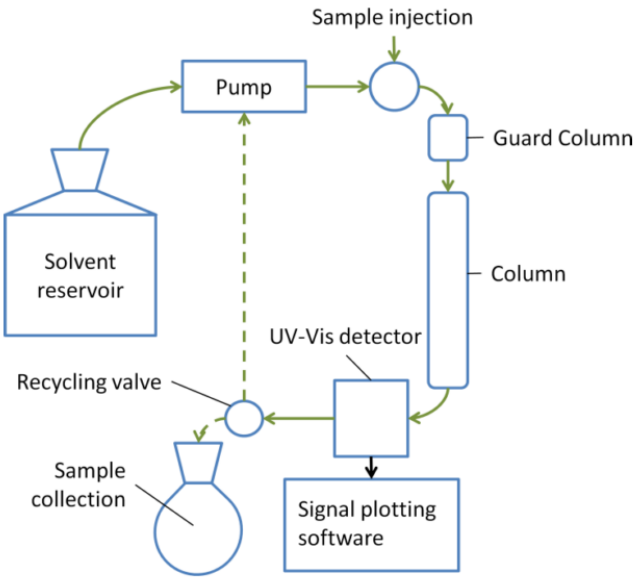


Figure 49 Schematic diagram of the preparative HPLC system. Figure reproduced from Farrington, B. J.[96]

Fullerenes are remarkable carbon materials with various unique properties. However, achieving a concentration suitable for further property and application investigations is not easy, as fullerenes coexist frequently with other irrelevant impurities. The most frequently used experimental technique during this work is a purification technique called high-performance liquid chromatography (HPLC), which is a powerful tool for separating soluble species based

on different interactions between various components in the sample mixture with the solid adsorbent material filled in the column. There are three preparative HPLC machines (JAI LC-250HS, JAI LC-9103 and JAI LC-908W) in our lab. In principle, they all follow the schematic diagram in Figure 49 and work as conventional liquid chromatography systems but with a higher pressure. The key component of the HPLC machines is the column. In my project, BuckyPrep-M, PYE and PBB manufactured by Nacalai tesque Inc. were applied (Figure 50), as silica functionalised with aromatic organic groups in those columns is ideal for the retention of fullerenes.

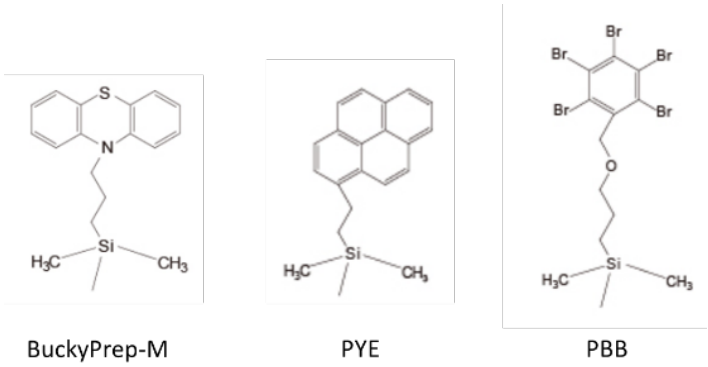


Figure 50 Functional groups of BuckyPrep-M, PYE and PBB manufactured by Nacalai tesque Inc.

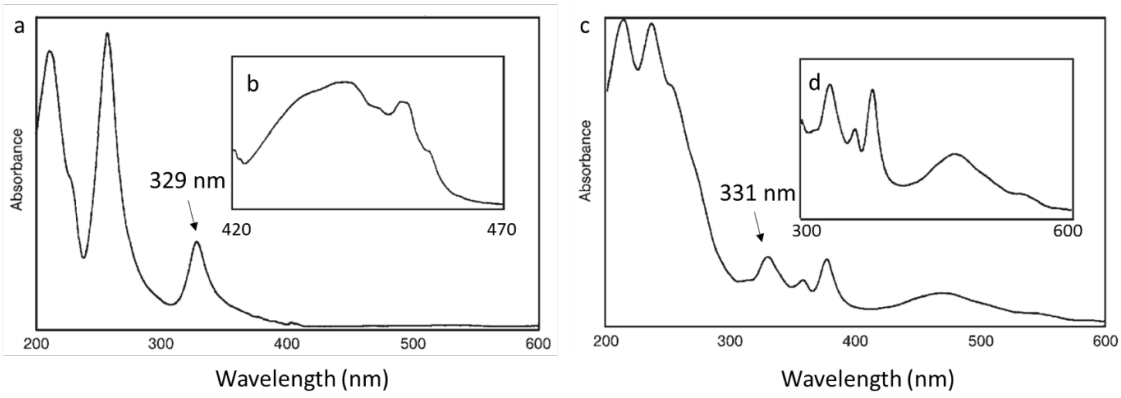


Figure 51 UV/Vis spectrum of C_{60} (a, b) and C_{70} (c, d) in *n*-hexane. Figure reproduced from Hirsch, A. *et al.*[17]

The HPLC signal is detected by a UV/Vis absorption sensor. This was set at a wavelength of $312\ \mathrm{nm}$, where fullerenes and their derivatives generally have a strong absorption, but the mobile phase has an insignificant one (*e.g.* the UV/Vis absorbance cut-off wavelength for toluene is $285\ \mathrm{nm}$). Taking C_{60} and C_{70} as two fullerene examples, near the detection

wavelength of $312\,\mathrm{nm}$, they have absorption peaks at $329\,\mathrm{nm}$ and $331\,\mathrm{nm}$, respectively (Figure 51).[17,203] The absorptions between 190 and $410\,\mathrm{nm}$ are due to allowed ${}^1T_{1u} - {}^1A_g$ transitions, and those between 410 and $620\,\mathrm{nm}$ are attributed to orbital forbidden singlet–singlet transitions.[204,205]

As the detailed operations and parameters will be specified in each HPLC result, an ordinary HPLC procedure is described as follows. The sample for HPLC separation is first dissolved in the same organic solvent that is used as the mobile phase. Unless otherwise noted, this solvent is toluene, because of its high fullerene solubility and relatively low boiling point. The dissolved sample is then loaded into the HPLC system manually *via* a syringe injection or automatically *via* a multi-injection port. If the sample is well-prepared with no precipitation, the pump will send the sample to the column; otherwise, the sample will be rejected, as the guard column gets blocked. After loading the sample, it will elute after a certain "retention time". Utilizing the retention time difference, different species of the sample can be collected separately. If species have very similar retention times, a recycling-mode of the HPLC will be used. Instead of collecting the elution fractions after they pass through the column once, the recycling valve is activated to resend them back to the column for further separation. Recycling elution of a sample in an ordinary column for N times is as effective as passing the sample through an N times longer column, so that better separation is obtained. Both the ordinary HPLC experiments and the recycling-mode HPLC experiments performed throughout this work were carried out at room temperature without the usage of a column oven.

3.1.2 Matrix-assisted laser desorption ionization mass spectrometry

Mass spectrometry (MS) is the most facile characterization technique for fullerenes (the very first fullerene was discovered by MS).[15] Generally, an MS spectrometer measures the mass-to-charge ratio of the charged sample particle or sample fragments, based on their different trajectories in response to Lorentz force applied by a magnetic field. Several specific

techniques are used to charge the sample particles, such as electron impact ionization (EI), electron spray ionization (ESI), and matrix-assisted laser desorption ionization (MALDI). The latter two techniques are considered as a type of “soft ionization” that causes little fragmentation of the sample and gives clear molecular ion peaks. Considering the molecular weight of fullerene species, MALDI, having a higher weight detection range, is the dominant method used for this work. Unless specified otherwise, all MALDI-MS experiments were performed with a Bruker Microflex.

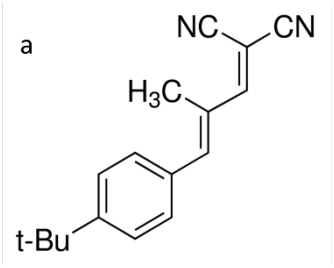


Figure 52 Molecular structure of the matrix used for the MALDI-MS experiments: (a) *trans*-2-[3-(4-tert-butylphenyl)-2-methyl-2-propenylidene] malononitrile (DCTB) and (b) dithranol.

To perform the MALDI-MS measurement, one drop of the solution sample was first mixed with one drop of the matrix/THF solution, which is $1\sim10\ \mathrm{mg/ml}$ dithranol or *trans*-2-[3-(4-tert-butylphenyl)-2-methyl-2-propenylidene] malononitrile (DCTB) in this work (Figure 52). The mixture was then drop-casted onto the sample board with a micropipette. For calibration purposes, a known sample of CsI_3 was also prepared in the same manner and drop-casted onto a separate position of the sample board. After loading the sample board, the instrument evacuated the detecting chamber down to a pressure of 2.5×10^{-6} torr. In terms of the detection method, reflection/linear and positive/negative modes are selectable. The reflection mode (ions will travel back and forth once) was always used due to a better mass resolution for fullerene sample. Both positive and negative ionization were used. When dithranol was used as the matrix, the chosen mode will be specified for each MALDI-MS result. In contrast, the DCTB matrix only works in negative ionization mode, as DCTB is neither a good electron acceptor nor a proton donor. Once the mode had been set, I turned on the laser to record the MS automatically. Depending on the noise level and the fragmentation condition, further tuning

of the laser power and number of laser shots was performed to obtain a high-quality spectrum. The measured MALDI-MS spectra were compared with the predicted molecular ion peaks simulated using an online programme from Scientific Instrument Services, Inc.[206]

When ENF derivatives were analysed using MALDI-MS, the corresponding molecular ion peaks are normally difficult to obtain, primarily due to primarily two reasons: (1) the low stability of ENFs under the laser ablation condition, and (2) the low mole ratio of ENFs to empty-cage fullerenes (*ca*. 0.1%). However, thanks to the great similarity in chemical reactivity of ENFs and empty-cage fullerenes, an indirect approach can still be applied to determine whether or not ENF derivatives have been formed. One can expect that, if a functional group is successfully bonded to empty-cage fullerenes, it should be capable of adding to ENFs in a similar mechanism. Therefore, the appearance of molecular ion peaks in MALDI-MS spectra corresponding to a certain type of functionalised empty-cage fullerenes can be regarded as evidence to support the successful generation of such kinds of functionalised ENFs. This treatment also follows the tradition of MS characterization of ENF derivatives, and no direct MS of ENF derivatives has been reported to data.[142–148,150] It is worth highlighting that, although this indirect way of assigning the MS of ENF derivatives was used throughout this work, there is one special derivative for which I managed to obtain molecular ion peaks with the endohedral nitrogen. A detailed discussion of this first observation is documented in section 6.2. Other than for this derivative, the direct evidence for the presence of the endohedral nitrogen in ENFs and their derivatives relies on the X-band cw-ESR characterization discussed below.

3.1.3 X-band continuous wave electron spin resonance spectroscopy

X-band (~9.5 GHz) cw-ESR spectroscopy was used as a powerful technique to characterize spin properties of ENF using Bruker EMX and Magnettech MiniScope MS200. The Bruker EMX at the CAESR facility of Oxford University has a high spin sensitivity and a good field stability for accurate measurements, while the Magnettech MiniScope MS200

located in our lab serves as a convenient tool for sample checking and repetitive measurements.

Generally, to measure the spin signal with X-band cw-ESR spectroscopy, the sample is located inside a microwave cavity and irradiated by a fixed-frequency microwave while sweeping the external magnetic field. Due to the Zeeman effect of the magnetic field, the electron spin angular momentum in the sample is aligned anti-parallel (ground state) or parallel (excited state) to the direction of the field. As Figure 53 shows, the energy difference between the split states requires a certain magnetic field to make the sample resonate with the given microwave frequency.

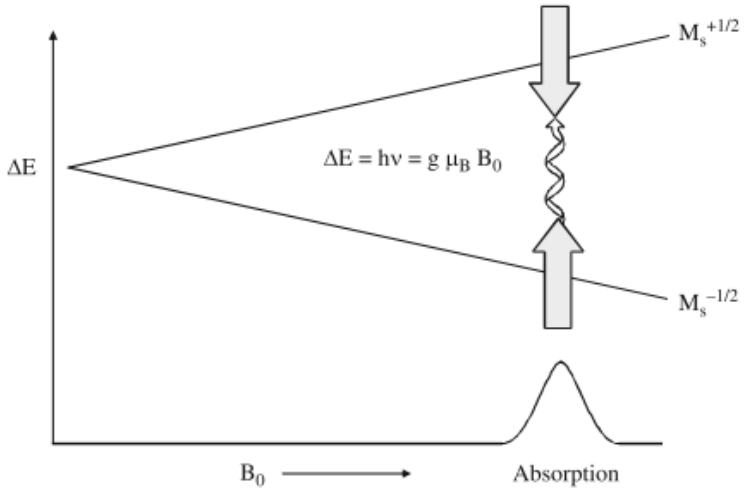


Figure 53 When the magnetic field is scanned, the energies of the two spin states of an unpaired electron diverge. At the magnetic field for which the energy difference between the two electron spin states is equal to hv for the spectrometer, there is absorption of energy by the spins, which is called resonance. Figure reproduced from Eaton, G. R. *et al.,*[207] where h is the Planck constant, v is the resonant frequency, g is the *g*-factor of the electron spin, μ_B is the Bohr magnetron and B_0 is the external field.

Practically, both ESR instruments measure the resonance of the spin *via* the reflection of microwave radiation from a resonant cavity. Figure 54a describes the correlation between the resonance of the sample and the microwave reflection from the cavity. The resonance condition of the sample in the cavity changes the magnetic susceptibility of the cavity (χ) from χ_1 to χ_2, thereby altering the impedance (Z) and the reflection coefficient (Γ) of the cavity. Automatic frequency control (AFC) is used to lock the frequency of the microwave (ν) to the

dip of Γ and compensate for effect of frequency drift on the amplitude of the reflected microwaves. Therefore, the microwave reflection power only depends on the resonance condition of the sample. When the cavity is initially critically coupled to the microwave source with the sample off-resonance, the resonance of the sample achieved by sweeping the magnetic field will lead to an increased reflection of the microwave, hence the spin signal can be detected (Figure 54b). However, the spin signal is normally mixed with noise, and is therefore difficult to resolve directly. To improve the signal-to-noise ratio, modulation of the external magnetic field is implemented. This leads to an oscillating reflection power. Measuring the amplitude of the oscillation, the slope of the reflection power vs. the field is obtained as the cw-ESR signal (Figure 54c),[207] whereas all noises apart from those which have the same frequency as the modulation frequency are effectively filtered. Due to this measuring scheme, the cw-ESR signal is normally in a derivative form.

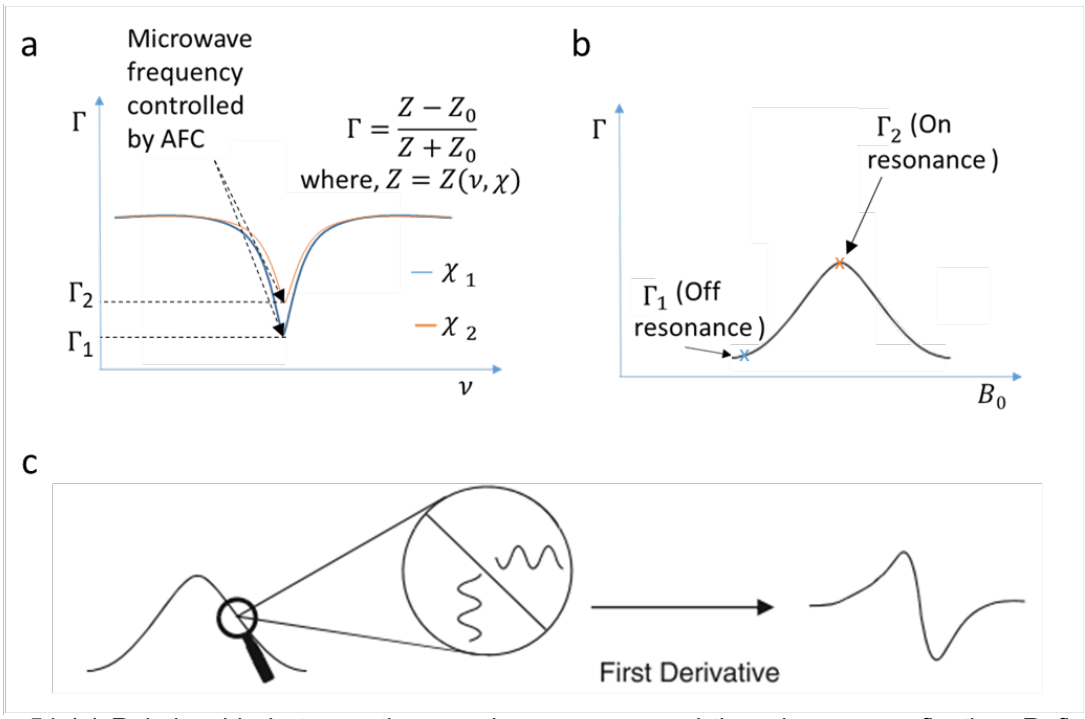


Figure 54 (a) Relationship between the sample resonance and the microwave reflection. Reflection coefficient Γ is related to the impedance of the cavity Z and the impedance of the source Z_0. The former impedance is the variable and changes with the frequency ν and the magnetic susceptibility χ of the cavity. The variation of ν is compensated by AFC, and the variation of χ is originated from the resonance of the sample. (b) Acquisition of the spin signal by sweeping the magnetic field. When the cavity is critically coupled to the microwave with the sample being off-resonance, a positive relationship between sample resonance and the microwave reflection will be achieved. Therefore, sweeping the field across the resonance range leads to a spin signal. (c) Picking up the spin signal in a derivative form by magnetic modulation. Panel c reproduced from Eaton, G. R. *et al.*[207]

In order to highlight how the spin signal is measured, the above simplification only includes the Zeeman effect. For spin-active fullerene samples, there is more than one resonant signal, because of energy splitting caused by ZFS, HFC, electron spin dipolar coupling, *etc*. The cause and interpretation of these signals will be documented in the relevant result chapter. Amongst different energy levels, the spin state pair that obeys the selection rules of $\Delta M_S = \pm 1$, $\Delta M_I = 0$ normally corresponds to a cw-ESR signal.

During the acquisition of cw-ESR spectra, I carefully chose a set of parameters to make the measurement record the true line shape and proportional signal intensity. To avoid line shape distortion, the modulation amplitude was selected to be considerably smaller than the linewidth, as the signal will otherwise contain an artificial lineshape caused by Gaussian convolution. To maintain the proportional relationship between the signal intensity and the spin number, the microwave power was also turned down to a low value to avoid the saturation of the spin. This is particularly important for EF samples, as they tend to have longer relaxation times[41,49,208] and hence are more likely to get saturated.[207] Since both a small modulation and a low microwave power are applied for the measurements, the signal-to-noise ratio was normally boosted by applying longer scan durations or multiple scan passes.

To interpret the solid-state cw-ESR spectra, I used EasySpin[209] to do the simulation with rigid limit approximations. The theoretical basis of the solid-state cw-ESR simulation with EasySpin is energy level modelling (see Figure 135 as an example). Through the simulation, all parameters in the spin Hamiltonian can be fitted. Detailed discussions of the fitted parameters and the relevant EasySpin scripts for each ENF derivatives are documented in the corresponding result chapters and appendix B, respectively. EasySpin also provides functions to simulate spectra in other dynamic regimes, including slow-motion regime, fast-motion regime, and isotropic limit, which have the theoretical basis of stochastic Liouville equation, Redfield theory, and Breit-Rabi formula respectively.[209] Unfortunately, those functions do not support spin systems with $S > 1/2$, hence EasySpin cannot be applied to simulate ENF spectra in those dynamic regimes.

In addition to applying the cw-ESR spectroscopy to resolve the signal pattern of the sample, I also used it quantitatively to do spin counting. Eq.3.1 shows the linear relationship between the spin number (n_S) and the double integral of the cw-ESR signal (DI):[207]

$$DI \propto \sqrt{P} \cdot B_m \cdot Q \cdot n_B \cdot S \cdot (S+1) n_S \qquad \text{Eq.3.1}$$

where P is the microwave power, B_m is the modulation amplitude, Q is the Quality factor of cavity, n_B is the Boltzmann factor for temperature dependence, and S is the total electron spin.

Since the spin number in the sample represents the ENF number, spin counting is useful to work out the spin-yield of an ENF synthesis, the spin enrichment of an ENF purification, and the spin retention ratio of an ENF chemical reaction. To avoid repetitively describing the mathematical treatment used to obtain the spin numbers given in the result chapters, an example of measuring of the spin number in a sample of $^{15}N@C_{60}/C_{60}$ mixture is demonstrated as follows.

Two cw-ESR spectra for $0.15\ \mathrm{ml}$ $^{15}N@C_{60}/C_{60}$ toluene solution and $0.15\ \mathrm{ml}$ TEMPO (2,2,6,6-Tetramethyl-1-piperidinyloxy) toluene solution were obtained under the same microwave power ($30\ \mathrm{dB}$) and room temperature, so that P and n_B were kept constant. Meanwhile, B_m and S are known based on the experimental settings and sample properties ($^{15}N@C_{60}/C_{60}$: $B_m = 200\ \mathrm{mG}$, $S = 3/2$; TEMPO: $B_m = 1000\ \mathrm{mG}$, $S = 1/2$). Finally, I assumed the quality factors for the cavity between these two experiments were the same, as both sample are dilute and mainly consist of toluene. Therefore, I obtained that $n_S^{(\mathrm{N@C_{60}/C_{60}})} = n_S^{(\mathrm{TEMPO})} \times DI^{(\mathrm{N@C_{60}/C_{60}})} \ / \ DI^{(\mathrm{TEMPO})}$. By double integrating the spin signal for each spectrum, DI for $^{15}N@C_{60}/C_{60}$ and TEMPO were determined to be 2.4147 and 2729.9, respectively (Figure 55). Therefore, the spin number in the $0.15\ \mathrm{ml}$ $^{15}N@C_{60}/C_{60}$ sample was worked out to be $1.818^{-11}\ \mathrm{mol}$. Considering that $0.15\ \mathrm{ml}$ of $0.92\ \mathrm{mg/ml}$ C_{60} sample contains $1.917^{-7}\ \mathrm{mol}$ of C_{60}, the spin content in the $^{15}N@C_{60}/C_{60}$ sample was calculated to be $948\ \mathrm{ppm}$.

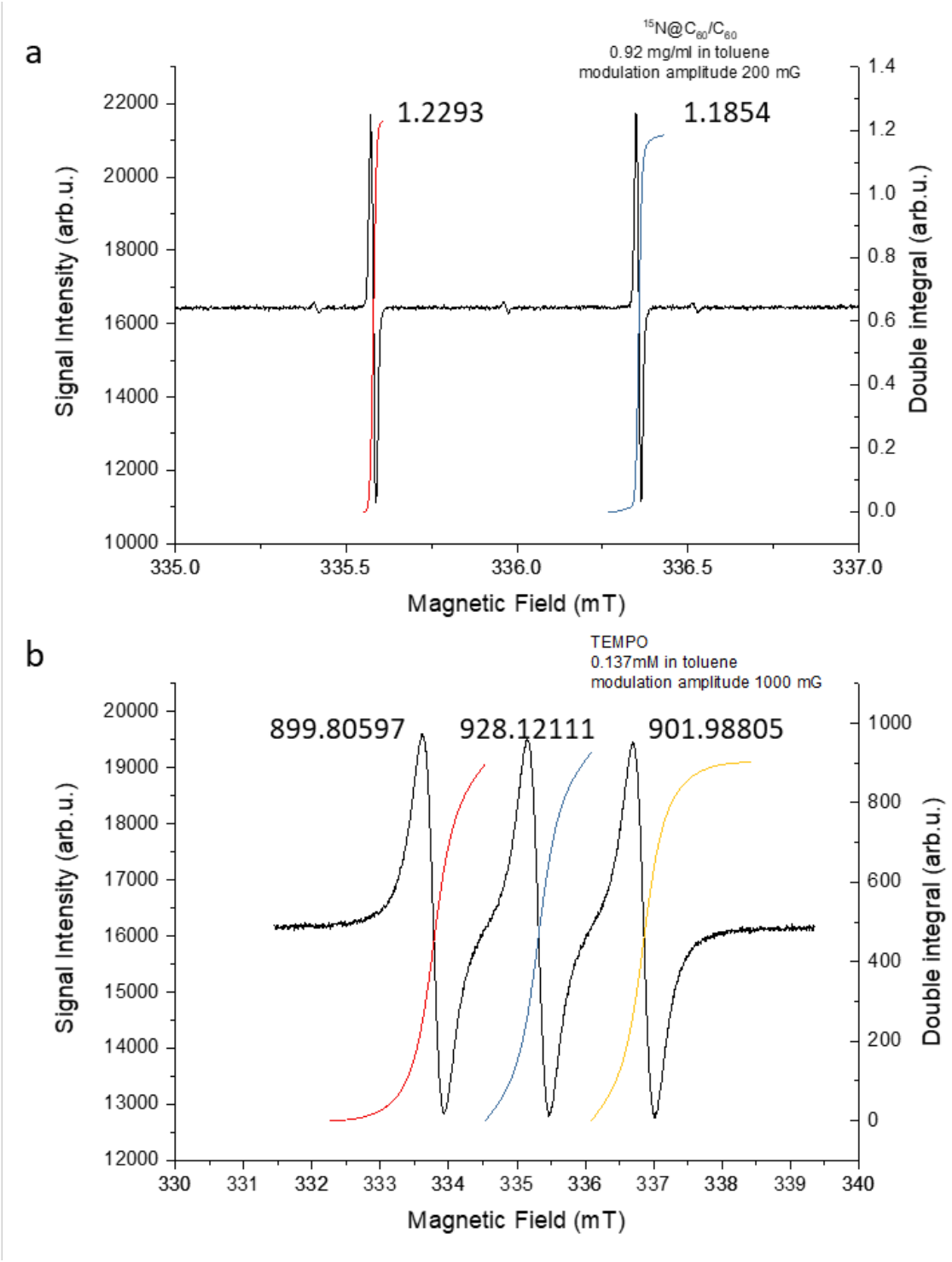


Figure 55 (a) cw-ESR (black) and the double integral (coloured) of an unknown $^{15}N@C_{60}/C_{60}$ sample (b) cw-ESR (black) and the double integral (coloured) of a known TEMPO sample. Data were acquired using a Magnettech MiniScope MS200 spectrometer. (a: 9.4324 GHz, 30.0 dB attenuation, room temperature, and 0.02 mT modulation amplitude; b: 94307 GHz, 30.0 dB attenuation, room temperature, and 0.10 mT modulation amplitude)

To guarantee the validity of the above treatment, it is important to make sure that (1) the spin signal is not saturated by the microwave power, and (2) those parameters assumed to

be constant, such as quality factors and ESR tube diameters, do not change between measurements. The first condition is not a problem for MiniScope MS200, which provides a small B_1 field during the measurement, due to the low power of its microwave source and the small quality factor of its cavity. The second condition was verified experimentally by measuring a known sample of N@C_{60} in five different ESR tubes with the same experimental settings (supporting information A). Based on the reproducibility of the result, I determined a *c.a.* 5% uncertainty level for the quantitative cw-ESR experiment using MiniScope MS200. This error bar is adopted in the later spin counting result, when MiniScope MS 200 was used as the cw-ESR instrument.

3.1.4 Nuclear magnetic resonance spectroscopy

As another spin resonance technique, the principle of NMR spectroscopy is similar to that of ESR spectroscopy, *i.e.* spins of nuclei in a magnetic field resonate with electromagnetic radiation. The relationship between the field and the radiation frequency for a certain nuclear spin can be expressed by the equation as below:

$$h\upsilon = \frac{\gamma h B_0}{2\pi} \qquad \text{Eq.3.2}$$

where h is the Planck constant, υ is the resonant frequency of the radiation, γ is the gyromagnetic ratio for the nuclear spin, and B_0 is the external field. Typically, NMR spectroscopy is performed using radio frequency pulses, and one normally acquires the NMR spectrum from the free induction decay (FID). For the purpose of having less dependence on the frequency of the spectrometer, NMR spectra always use chemical shift δ as the x axis:[210]

$$\delta = \frac{\nu - \nu_0}{\nu_0} \qquad \text{Eq.3.3}$$

where ν is the resonant frequency of the signal, and ν_0 is the resonant frequency of the reference sample, which is commonly tetramethylsilane (TMS). The unit of δ is taken as ppm.

The relation between δ and the structure has been established for a large range of organic groups, and is predictable by some software.

In my work, ^{1}H-NMR spectroscopy measured by Bruker AVIII 400 and AVII 500 spectrometer was used to characterize molecular structures. The sample for NMR measurements was firstly dried thoroughly to eliminate solvents and their protons, and then redissolved in deuterated solvents such as $CDCl_3$ or $C_6D_5CD_3$. When the solubility of the sample was not satisfactory, CS_2 was added to assist the dissolving. All measurements of ^{1}H-NMR were performed at room temperature. The assignment of NMR spectra was based on the NMR prediction function provided by ChemDraw software.[211]

3.1.5 Ultraviolet-visible absorption spectroscopy

This work uses ultraviolet-visible absorption spectroscopy (UV/Vis) measured using JASCO V-570. The causes of UV/Vis absorption are diverse, but, for non-metallic fullerenes, it normally originates from electronic transitions between molecular orbitals. For example, C_{60} strongly absorbs in the region below 400 nm (Figure 51a),[17,203] where absorption peaks are assigned to different electronic transitions related to the T_{1u} orbitals. While assigning the electronic absorption of fullerenes requires dedicated theoretical calculations,[204,205] which are beyond the scope of this project, UV/Vis spectroscopy characterization is mainly used to confirm the presence of a chemical moiety by comparing it with reference samples or reported results in the literature.

To record the absorption spectrum, the solution sample was loaded in a 1×1 cm cuvette located between the light source and the detector. Another cuvette with pure solvent was used as a reference to enable subtraction of the background signal caused by the solvent. By sweeping the wave length of the irradiating light source, wave length dependent absorption features were acquired for study.

Apart from being used for absorption spectrum acquisition, UV/Vis spectroscopy is also

a powerful tool to determine the sample concentration using the Beer-Lambert law, which is described as below:

$$A = -log_{10}\left(\frac{I}{I_0}\right) = \varepsilon \cdot l \cdot c \qquad \text{Eq.3.4}$$

where A is the absorbance, I_0 is the intensity of the light transmitted through the reference solvent, I is the intensity of light transmitted through the sample, ε is the molar extinction coefficient, l is the path length of the sample, and c is the concentration of the sample. The Beer-Lambert law only works for dilute solutions. After calibrating ε using a set of standard C_{60} samples (e.g. Figure 56), I can determine the concentration of an unknown C_{60} sample based on its absorbance.

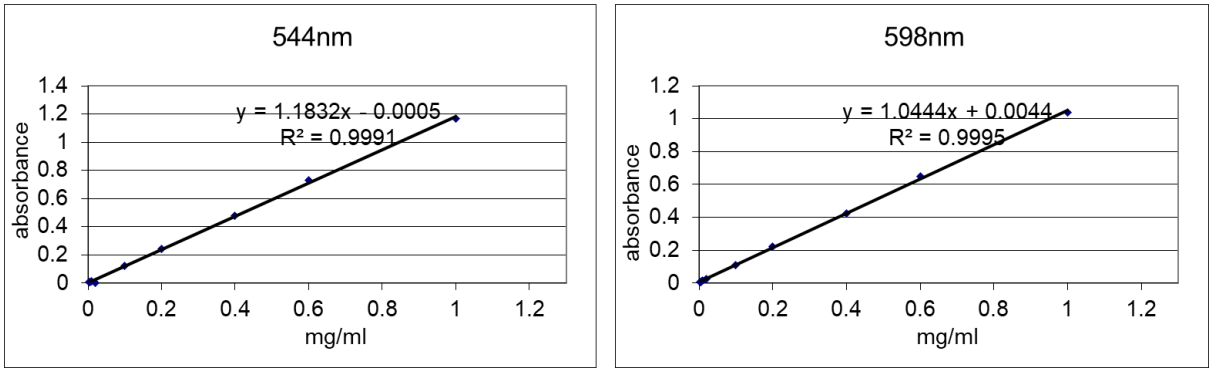


Figure 56 Calibrated relationship between C_{60} concentration and the sample absorbance in toluene.

3.1.6 Photoluminescence spectroscopy

This work uses photoluminescence spectroscopy (PL) (JASCO FP-6200) as a characterization technique for studying the luminescence behaviour of materials. The PL signal of a molecule is normally caused by transitions from photo-excited states to their ground states accompanied by photonic emissions. Instead of assigning PL peaks to different electronic transitions between fullerene orbitals, I used PL as an additional characterization technique to prove the presence of chemical moieties by comparing my samples' PL signals with those from reference samples or published literature.

The experimental operation of the PL measurement is similar to that of UV/Vis spectroscopy, which is also a combination of light radiation and detection. The sample is also prepared in a 1×1 cm cuvette, but the four walls of the PL cuvette are transparent, as the light path for the excitation and emission are orthogonal to each other. Because of the orthogonal arrangement, minimal transmission/scattering from the light source enters the PL detector, hence the emission signal is less interfered. To further differentiate transmission/scattering signals from PL signals of the sample, I constructed 2D-PL contour maps for the sample, which show the signal intensity as the function of the excitation wavelength (y axis) and the emission wavelength (x axis). In the 2D-PL contour map, signals caused by transmission or scattering (both Rayleigh and Raman scattering) can be easily identified due to the proportional relationship between the excitation and emission wavelengths, whereas PL signals from the sample remain unchanged no matter what excitation wavelength is applied. As an example, Figure 57 demonstrates 2D-PL spectra of C_{60} and C_{70} reported, previously.

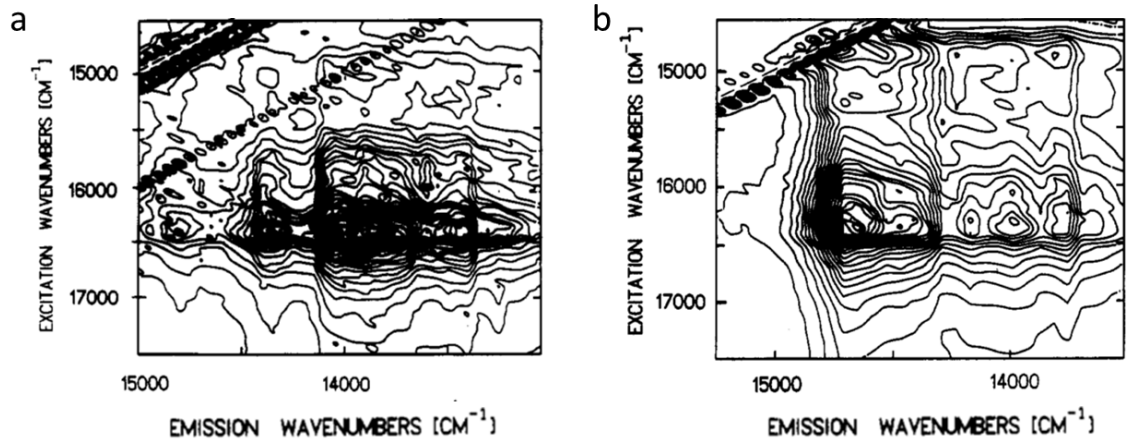


Figure 57 (a) 2D-PL spectrum of C_{60} in frozen benzene ($10^{-4}\,M$), showing multiple emission peaks around 710 nm. (b) 2D-PL spectrum of C_{70} in frozen benzene, showing twin emission peaks between $650\sim720$ nm. Figure reproduced from Palewska, K. *et al.*[235] Wavenumbers of 14000, 15000, 16000, and 17000 cm^{-1} can be converted to 714, 667, 625, 588 nm, respectively.

3.2 Preparation procedures for pristine ENFs

3.2.1 Synthesis of ENFs with ion implantation apparatus

After the optimizations discussed in Chapter 4, the generally used procedure for the preparation of ENFs is documented in this section.

Prior to starting an ion implantation procedure, I first checked the condition of the apparatus by confirming that (1) the tungsten filament of the ion source module was intact, (2) the lifetime of the quartz crystal used to monitor the deposition thickness was above 80% (measured by the Q-pod software), and (3) the pressure for the cooling water circulation system was $0.5 \sim 1\ \mathrm{bar}$. If the apparatus was not in the proper condition, I changed the filament, replaced the quartz crystal, or adjusted the water pressure, accordingly. I then loaded $0.5\ \mathrm{g}$ of C_{60} (or C_{70}) into the crucible, which was placed in the heating element. After adjusting the position of the heating element to the center of the vacuum chamber, I mounted the copper target with its orientation perpendicular to the ion radiation axis and sealed the vacuum chamber. With both the rotary pump and the turbo pump turned on, I left the system overnight to reach its vacuum limit. After that, the heating element was set to $200\ ^{\circ}\mathrm{C}$ for one hour to bake the C_{60} (or C_{70}) precursor thoroughly. Finally, I turned on the N_2 gas inlet and purged the vacuum system with a flow rate of $10\ \mathrm{sccm}$ (standard cubic centimetre per minute) for 1 minute.

The implantation procedure was automated with a LabVIEW programme shown in section 4.2.1. To obtain an optimal yield, I set the implantation parameters to be $5\ \mathrm{sccm}$ for the N_2 flow rate, $2.0\ \mathrm{Å}/s$ for the fullerene deposition rate, $200\ \mathrm{V}$ for the discharge voltage, $0.26\ \mathrm{A}$ for the emission current, and $0.13\ \mathrm{A}$ for the discharge current. After about 2 hours of implantation, the apparatus automatically stopped heating/subliming fullerene, because the LabVIEW programme sensed that the precursor went low. Subsequently, I manually shut down the rest components of the equipment one by one in the order of ion beam ($520\ ^{\circ}\mathrm{C}$), nitrogen flow ($400\ ^{\circ}\mathrm{C}$) and both vacuum pumps ($100\ ^{\circ}\mathrm{C}$).

To harvest the product, I scraped the deposited film from the copper target and dispersed the fullerene soot in toluene ($2\ \mathrm{mg/ml}$ for the synthesis of N@C_{60}, $1\ \mathrm{mg/ml}$ for the synthesis of N@C_{70}). After 30 minutes of sonication at room temperature, I used vacuum filtration to filter the insoluble by-product in the fullerene soot. The filtrate containing both the empty-cage fullerene and the ENF was characterized by quantitative UV/Vis and spin counting to determine the spin-yield, and was finally preserved in a labelled amber laboratory bottle, stored in a dark environment, prior to further purification.

3.2.2 Purification of ENFs with HPLC

I concentrated the ENF sample with a rotary evaporator (*ca.* $1.5\ \mathrm{mg/ml}$ for the purification of N@C_{60}/C_{60}, *ca.* $0.5\ \mathrm{mg/ml}$ for the purification of N@C_{70}/C_{70}, confirmed by UV/Vis spectroscopy). I then loaded the prepared sample into the HPLC system using an automatic repeat injection/collection method discussed in section 4.3.2. (A recalibration of the programmed retention time of the sample was applied, if the HPLC conditions, such as flow rate, pressure, or temperature, drastically changed.) Using a 5PBB column and toluene being the stationary phase and mobile phase, respectively, partial separation between the ENF and the empty-cage fullerenes was achieved. I discarded fraction 1, which was spin-depleted, and concentrated fraction 2, which was spin-enriched. The concentrated fraction 2 was then re-injected as a sample to continue the next HPLC pass. Depending on the experimental requirement for the spin signal, I repeated this procedure *ca.* 5 to 10 times to achieve 0.1% to 1% of N@C_{60} in C_{60} (or N@C_{70} in C_{70}).

3.3 Organic synthetic procedures

3.3.1 Synthesizing ENF derivatives using the spin-compatible Bingel reaction

The development of the spin-compatible Bingel reaction for ENFs is discussed in section 5.2. This section documents the detailed synthetic procedures of those Bingel reactions that I used in Chapter 5. These protocols were resembling to each other with small differences tuned to suit the change of the reagents and products.

3.3.1.1 DEM-N@C_{60}

1 mg of $^{14}N@C_{60}/C_{60}$ mixture (1.4 μmol, 0.14% spin content) was dissolved with 0.34 mg of diethyl bromomalonate (1.4 μmol, 92%, Sigma-Aldrich) in 2.5 ml of toluene (99.5%, Fisher Chemical), followed by an addition of 0.42 ml of 0.5‰ DBU toluene solution (1.4 μmol, 99.0%, Sigma-Aldrich), dropwise. The reaction mixture was stirred under an argon atmosphere in the dark at room temperature. After 1.5 hours of reaction, DEM-N@C_{60} was separated using HPLC (BuckyPrep-M, 16 ml/min, and toluene) and collected between 6.0~7.0 minutes (55% yield based on HPLC peak areas). **^{1}H NMR** (400 MHz, room temperature, Chloroform-*d*): δ = 4.60 (m, 4H; $COOCH_2$), 1.55 (t, 6H; CH_3). **MALDI-MS** (negative): *m/z*: 878.1, 879.1, and 880.1 $[M]^-$ ($C_{67}H_{10}O_4$, calc. 878.058, 879.061, 880.065, *etc.*).

3.3.1.2 IND-N@C_{60}

1 mg of $^{14}N@C_{60}/C_{60}$ mixture (1.4 μmol, 0.14% spin content) was dissolved with 0.32 mg of 2-bromo-1,3-indandione (1.4 μmol, 90.0%, Sigma-Aldrich) in 2.5 ml of toluene (99.5%, Fisher Chemical), followed by an addition of 0.42 ml of 0.5‰ DBU toluene solution (1.4 μmol, 99.0%, Sigma-Aldrich), dropwise. The reaction mixture was stirred under an argon atmosphere in the dark at room temperature. After 1.5 hours of reaction, IND-N@C_{60} was separated using HPLC (BuckyPrep-M, 16 ml/min, toluene, and 3 recycles) and collected between 24.1~26.1 minutes (55% yield based on HPLC peak areas). **^{1}H NMR** (400 MHz, room temperature, Chloroform-*d*): δ = 8.15, 7.96 (m, 4H; C_6H_4). **MALDI-MS** (negative): *m/z*: 864.0,

865.0, 866.0 and 867.0 $[M]^-$ ($C_{69}H_4O_2$, calc. 864.021, 865.024, 866.028, 867.031, *etc.*).

3.3.1.3 Iodo-QUI-N@C_{60}

1 mg of $^{14}N@C_{60}/C_{60}$ mixture (1.4 μmol, 0.1% spin content) was dissolved with 0.5 mg of 1-methyl-7-iodo-1H-Quinoline-2,4-dione (1.7 μmol, no analytical data on purity, FCH Group) and 0.4 mg of I_2 (1.6 μmol, 99.5%, Acros Organics) in 2.5 ml of 1:9 N,N-Dimethylformamide (DMF)/toluene solvent mixture (toluene: 99.5%, Fisher Chemical; DMF: anhydrous 99.8% Sigma-Aldrich), followed by an addition of 0.8 ml of 0.5‰ DBU toluene solution (2.8 μmol, 99.0% , Sigma-Aldrich), dropwise. The reaction mixture was stirred under an argon atmosphere in the dark at room temperature. After 1.5 hours of reaction, QUI-N@C_{60} was separated using HPLC (5PYE, 4 ml/min, toluene, and 3 recycles) and collected between 21.6~24.5 minutes (45% yield based on HPLC peak areas). **^{1}H NMR** (400 MHz, room temperature, Chloroform-*d*): $\delta = 7.98$, 7.76 (m, 3H; C_6H_3I), 3.81 (s, 3H; CH_3). **MALDI-MS** (negative): *m/z*: 1019.0, 1020.0, 1021.1 and 1022.2 $[M]^-$ ($C_{69}H_6O_2NI$, calc. 1018.944, 1019.948, 1020.951, 1021.954, *etc.*).

3.3.1.4 IND-N@C_{60} and Bis-IND-N@C_{70}

2.5 mg of $^{14}N@C_{70}/C_{70}$ mixture (3.0 μmol, 0.05% spin content) was dissolved with 0.7 mg of 2-bromo-1,3-indandione (3.1 μmol, 90.0%, Sigma-Aldrich) in 5 ml of toluene (99.5%, Fisher Chemical), followed by an addition of 0.9 ml of 0.5‰ DBU toluene solution (3.0 μmol, 99.0%, Sigma-Aldrich), dropwise. The reaction mixture was stirred under an argon atmosphere in the dark at room temperature. After 1.5 hours of reaction, IND-N@C_{70} was separated using HPLC (BuckyPrep-M, 16 ml/min, and toluene) and collected between 10.5~12.1 minutes (35% yield based on HPLC peak areas). **MALDI-MS** (negative): *m/z*: 984.0, 985.0, 986.0 and 987.0 $[M]^-$ ($C_{79}H_4O_2$, calc. 984.021, 985.025, 986.028, 987.031, *etc.*).

2.5 mg of $^{14}N@C_{70}/C_{70}$ mixture (3.0 μmol, 0.05% spin content) was dissolved with 2.7 mg of 2-bromo-1,3-indandione (12 μmol, 90.0%, Sigma-Aldrich) in 5 ml of toluene (99.5%, Fisher Chemical), followed by an addition of 3.6 ml of 0.5‰ DBU toluene solution (12 μmol, 99.0%,

Sigma-Aldrich), dropwise. The reaction mixture was stirred under an argon atmosphere in the dark at room temperature. After 1.5 hours of reaction, Bis-IND-N@C_{70} was separated using HPLC (BuckyPrep-M, 16 ml/min, and toluene) and collected between 13.1~17.9 minutes (85% yield based on HPLC peak areas). **^{1}H NMR** (400 MHz, room temperature, Chloroform-*d*): δ = 8.12, 7.94 (m, 4H; C_6H_3). **MALDI-MS** (negative): *m/z*: 1128.2, 1129.2, 1130.2, and 1131.2 $[M]^-$ ($C_{88}H_8O_4$, calc. 1128.042, 1129.046, 1130.049, 1131.052, *etc.*).

3.3.1.5 β-CD-N@C_{60}

4.9 mg of ^{14}N@C_{60}/C_{60} mixture (6.8 μmol, 0.2% spin content) was dissolved with 21.1 mg of β-cyclodextrin-malonate (6.8 μmol, acquired *via* collaboration) and 2.6 mg of I_2 (10.2 μmol, 99.5%, Acros Organics) in in 5 ml of toluene (99.5%, Fisher Chemical), followed by an addition of 4.1 ml of 0.5‰ DBU toluene solution (13.8 μmol, 99.0%, Sigma-Aldrich), dropwise. The reaction mixture was stirred under an argon atmosphere in the dark at room temperature. After an overnight reaction, β-CD-N@C_{60} was separated with preparative thin layer chromatography (TLC) using acetone/*n*-hexane mixture (1:1) as the mobile phase to obtain a brown solid (8.2 mg, 2.2 μmol, 32% yield). **^{1}H NMR** (400 MHz, room temperature, Chloroform-*d*): δ = 6.85 (t, ^3J(H,H) = 5.8 Hz, 2H; NH), 5.24~5.06 (m, 14H; CD 1-H), 4.77~4.63 (m, 4H; COOCH_2), 4.11~3.98 (m, 4H), 3.95~3.72 (m, 36H), 3.70~3.30 (m, 158H), 3.25~3.10 (m, 14H; CD 2-H). **^{13}C NMR** (126 MHz, room temperature, Chloroform-*d*): δ = 169.01, 163.53, 145.50, 145.41, 145.14, 145.11, 145.09, 144.87, 144.66, 144.03, 143.32, 143.26, 143.13, 142.32, 141.87, 141.16, 139.09, 99.36, 99.20, 99.05, 98.90, 98.85, 98.62, 82.38, 82.25, 82.23, 82.19, 82.08, 82.04, 81.97, 81.91, 81.85, 81.79, 81.60, 81.54, 80.52, 80.32, 80.16, 79.51, 71.68, 71.64, 71.54, 71.38, 71.35, 71.14, 71.08, 71.05, 70.99, 70.91, 69.93, 69.65, 69.33, 65.82, 61.70, 61.64, 61.59, 61.57, 61.55, 61.51, 59.41, 59.21, 59.19, 59.15, 59.10, 58.78, 58.76, 58.67, 58.59, 58.57, 58.54, 39.80, 31.89. **MALDI-MS** (negative): *m/z*: 3818.6 $[M - H]^-$ ($C_{195}H_{231}N_2O_{76}$ calc. 3818.434).

3.3.2 Synthesizing N@C_{60}-containing dyads and dimers

This section documents the detailed synthetic procedures to obtain N@C_{60}-containing dyads and dimers that I reported in Chapter 6.

3.3.2.1 N@C_{60}-1-CuPc

4.0 ml of ^{14}N@C_{60}/C_{60} mixture (*ca.* 1% spin content) toluene solution (0.5mg/ml) (2.8 μmol) was evaporated to dry. Then, it was mixed with 6.5 mg of CuPc-1-CHO (2.8 μmol, acquired *via* collaboration), and 0.3 mg of sarcosine (3 μmol, 98%, Sigma-Aldrich) in 1.5 ml of dry toluene (99.8%, Sigma-Aldrich). After simultaneous argon bubbling and sonication for 15 minutes, the reaction mixture was heated to 120 °C for 2 hours of refluxing and magnetic stirring, in the dark and N_2 atmosphere. N@C_{60}-1-CuPc and unreacted N@C_{60}/C_{60} was separated using HPLC (BuckyPrep-M, 16 ml/min, toluene) at retention time between 2.6~3.2 minute (22% yield based on HPLC peak areas). **MALDI-MS** (positive): *m/z*: 3099.3, 3100.3, 3101.3, 3102.3, 3103.3, and 3104.3 $[M]^+$ ($C_{209}H_{193}O_{13}N_9Cu$, calc. 3099.401, 3100.405, 3101.408, 3102.407, 3103.411, 3104.410, *etc.*).

3.3.2.2 N@C_{60}-2-CuPc

4.0 ml of ^{14}N@C_{60}/C_{60} mixture (*ca.* 1% spin content) toluene solution (0.5mg/ml) (2.8 μmol) was evaporated to dry. Then, it was mixed with 6.9 mg of CuPc-2-CHO (2.8 μmol, acquired *via* collaboration), and 0.3 mg of sarcosine (3 μmol, 98%, Sigma-Aldrich) in 1.5 ml of dry toluene (99.8%, Sigma-Aldrich). After simultaneous argon bubbling and sonication for 15 minutes, the reaction mixture was heated to 120 °C for 2 hours of refluxing and magnetic stirring, in the dark and N_2 atmosphere. N@C_{60}-1-ZnPc and unreacted N@C_{60}/C_{60} was separated using HPLC (BuckyPrep-M, 16 ml/min, toluene) at retention time between 2.6~3.2 minute (22% yield based on HPLC peak areas). **MALDI-MS** (positive): *m/z*: 3191.6, 3192.6, 3193.6, 3194.6, 3195.6, and 3196.6 $[M]^+$ ($C_{215}H_{197}O_{14}N_9Cu$, calc. 3191.428, 3192.431, 3193.434, 3194.434, 3195.437, 3196.440, *etc.*).

3.3.2.3 N@C_{60}-1-ZnPc

4.0 ml of $^{14}N@C_{60}/C_{60}$ mixture (*ca.* 1% spin content) toluene solution (0.5mg/ml) (2.8 μmol) was evaporated to dry. Then, it was mixed with 6.5 mg of ZnPc-1-CHO (2.8 μmol, acquired *via* collaboration), and 0.3 mg of sarcosine (3 μmol, 98%, Sigma-Aldrich) in 1.5 ml of dry toluene (99.8%, Sigma-Aldrich). After simultaneous argon bubbling and sonication for 15 minutes, the reaction mixture was heated to 120 °C for 2 hours of refluxing and magnetic stirring, in the dark and N_2 atmosphere. N@C_{60}-1-ZnPc and unreacted N@C_{60}/C_{60} was separated using HPLC (BuckyPrep-M, 16 ml/min, toluene/Hexane 99/1) at retention time between 2.6~3.2 minute (22% yield based on HPLC peak areas). **MALDI-MS** (positive): *m/z*: 3100.3, 3101.3, 3102.3, 3103.3, 3104.3, 3105.3, and 3106.3 $[M]^+$ ($C_{209}H_{193}O_{13}N_9Zn$, calc. 3100.401, 3101.404, 3102.408, 3103.416, 3104.405, 3105.404, 3106.403, *etc.*).

3.3.2.4 NC_{59}–N@C_{60}

6.0 ml of $^{14}N@C_{60}/C_{60}$ mixture (*ca.* 0.1% spin content) toluene solution (1.2 mg/ml) (10 μmol) was evaporated to dry. Then, it was mixed with 1.8 mg of NC_{59}-CHO (2.0 μmol, acquired *via* collaboration), and 2.7 mg of 2-aminohexadecanoic acid (10 μmol, 95%, Sigma-Aldrich) in 8 ml of dry toluene (99.8%, Sigma-Aldrich). After simultaneous argon bubbling and sonication for 15 minutes, the reaction mixture was heated to 120 °C for 12 hours of refluxing and magnetic stirring, in the dark. NC_{59}–N@C_{60} was separated with HPLC (BuckyPrep-M, 16 ml/min, toluene) at retention time between 12.7~14.8 minute (30% yield based on HPLC peak areas). **MALDI-MS** (negative): *m/z*: 1814.4, 1815.4, 1816.4, 1817.4, and 1818.4 $[M]^-$ ($C_{143}H_{38}O_2N_2$, calc. 1814.293 , 1815.297, 1816.300, 1817.303, 1818.307, *etc.*).

3.3.2.5 PYR-N@C_{60} dimer

6.0 ml of $^{14}N@C_{60}/C_{60}$ mixture (*ca.* 0.1% spin content) toluene solution (1.2 mg/ml) (10 μmol) was evaporated to dry. Then, it was mixed with 3.0 mg of polyformaldehyde $(CH_2O)_n$ ($100/n$ μmol, Sigma-Aldrich), and 5.4 mg of 2-aminohexadecanoic acid (20 μmol, 95%, Sigma-Aldrich) in 5 ml of dry toluene (99.8%, Sigma-Aldrich). After simultaneous argon bubbling and sonication for 15 minutes, the reaction mixture was heated to 120 °C for 20

minutes of refluxing and magnetic stirring, in the dark, N_2 atmosphere. PYR-N@C_{60} was separated with HPLC (BuckyPrep-M, $16\ \mathrm{ml/min}$, toluene) at retention time between $5.1\sim6.0$ minute (40% yield based on HPLC peak areas). **MALDI-MS** (negative): *m/z*: 959.6, 960.6, 961.7, and 962.7[M]$^-$ ($C_{76}H_{33}N$, calc. 959.261, 960.265, 961.268, 962.271, *etc.*).

About $20\ \mathrm{ml}$ of PYR-N@C_{60} ($2\ \mu\mathrm{mol}$ estimated by HPLC trace) toluene eluent was concentrated to $3\ \mathrm{ml}$ and then mixed with $0.4\ \mathrm{mg}$ of terephthaloyl dichloride ($2\ \mu\mathrm{mol}$, 99%, Sigma-Aldrich), directly. After the addition of $0.6\ \mathrm{ml}$ of $0.5‰$ DBU toluene solution ($2\ \mu\mathrm{mol}$, 99.0%, Sigma-Aldrich), the reaction mixture was kept in the dark with magnetic stirring for 12 hours. PYR-N@C_{60} dimer was separated with HPLC (BuckyPrep-M, $16\ \mathrm{ml/min}$, toluene) at retention time between $10.1\sim11.9$ minute (50% yield based on HPLC peak areas). **^{1}H NMR** ($400\ \mathrm{MHz}$, room temperature, Chloroform-*d*): $\delta = 7.98$ (m, 4H; C_6H_4), 4.04 (t, 1H; CHN), $2.76\sim3.08$ (m, 2H; CH_2N), 1.56 (m, 4H; CH_2CHN) 1.26 (m, 48H; CH_2), 0.88 (t, 6H; CH_3). **MALDI-MS** (negative): *m/z*: 2049.1, 2050.2, 2051.2, and 2052.2 [M]$^-$ ($C_{160}H_{68}N_2O_2$, calc. 2048.528, 2049.531, 2050.535, 2051.538, 2052.542, *etc.*).

3.3.2.6 5-Bz-5 dimer

$5.8\ \mathrm{mg}$ of ^{14}N@C_{60}/C_{60} mixture ($8\ \mu\mathrm{mol}$, 0.1% spin content) was dissolved with $0.9\ \mathrm{mg}$ of s-Indacene-1,3,5,7(2H,6H)-tetraone ($4\ \mu\mathrm{mol}$, no analytical data on purity, Sigma-Aldrich) and $2.0\ \mathrm{mg}$ of I_2 ($8\ \mu\mathrm{mol}$, 99.5% Acros Organics) in $10\ \mathrm{ml}$ of N-Methyl-2-pyrrolidone (NMP, 99%, Sigma-Aldrich), followed by addition of $4.8\ \mathrm{ml}$ of $0.5‰$ DBU/NMP solution ($16\ \mu\mathrm{mol}$, 99.0%, Sigma-Aldrich), dropwise. The reaction mixture was stirred at room temperature and isolated from light. After 1.5 hours of reaction, 5-Bz-5 dimer was obtained *via* reprecipitation by adding $15\ \mathrm{ml}$ of acetone (99.5%, Fisher Chemical) to the reaction mixture. The solid sample was then sonicated and filtered with excess of tetrahydrofuran (99.9%, inhibitor free, Sigma-Aldrich) and chloroform (99.8%, Fisher Chemical) to remove unreacted tetraone, base, and pristine fullerene. Finally, the sample ($1.0\ \mathrm{mg}$, $0.6\ \mu\mathrm{mol}$, 15% yield) was dissolved in 1,2-dichlorobenzene (*o*-DCB) (99%, Sigma-Aldrich) to preserve. **^{1}H NMR** ($500\ \mathrm{MHz}$, room temperature, Chloroform-*d*): $\delta = 8.22$ (m, 2H; C_6H_2). **MALDI-MS** (negative): *m/z*: 1650.3,

1651.3, 1652.3, 1653.3, and 1654.3 [M]$^-$ ($C_{132}O_4H_2$, calc. 1649.995, 1650.999, 1652.002, 1653.005, *etc.*).

3.3.2.7 6-NAPH-6 dimer

5.8 mg of $^{14}N@C_{60}/C_{60}$ mixture (8 μmol, 0.1% spin content) was dissolved with 1.1 mg of pyrene-1,3,6,8(2H,7H)-tetraone (4 μmol, no analytical data on purity, Sigma-Aldrich) and 2.0 mg of I_2 (8 μmol, 99.5%, Acros Organics) in 10 ml of N-Methyl-2-pyrrolidone (NMP, 99%, Sigma-Aldrich), followed by addition of 4.8 ml of 0.5‰ DBU/NMP solution (16 μmol, 99.0%, Sigma-Aldrich), dropwise. The reaction mixture was stirred at room temperature and isolated from light. After 1.5 hours of reaction, 6-NAPH-6 dimer was obtained *via* reprecipitation by adding 15 ml of acetone (99.5%, Fisher Chemical) to the reaction mixture. The solid sample was then sonicated and filtered with excess of tetrahydrofuran (99.9%, inhibitor free, Sigma-Aldrich) and chloroform (99.8%, Fisher Chemical) to remove unreacted tetraone, base, and pristine fullerene. Finally, the sample (1.5 mg, 0.9 μmol, 22% yield) was dissolved in *o*-DCB (99%, Sigma-Aldrich) to preserve. **MALDI-MS** (negative): *m/z*: 1700.3, 1701.3, 1702.3, 1703.3, and 1704.3[M]$^-$ ($C_{136}O_4H_4$, calc. 1700.011, 1701.014, 1702.018, 1703.021, 1704.024, *etc.*).

3.3.2.8 6-OPE-6 dimer

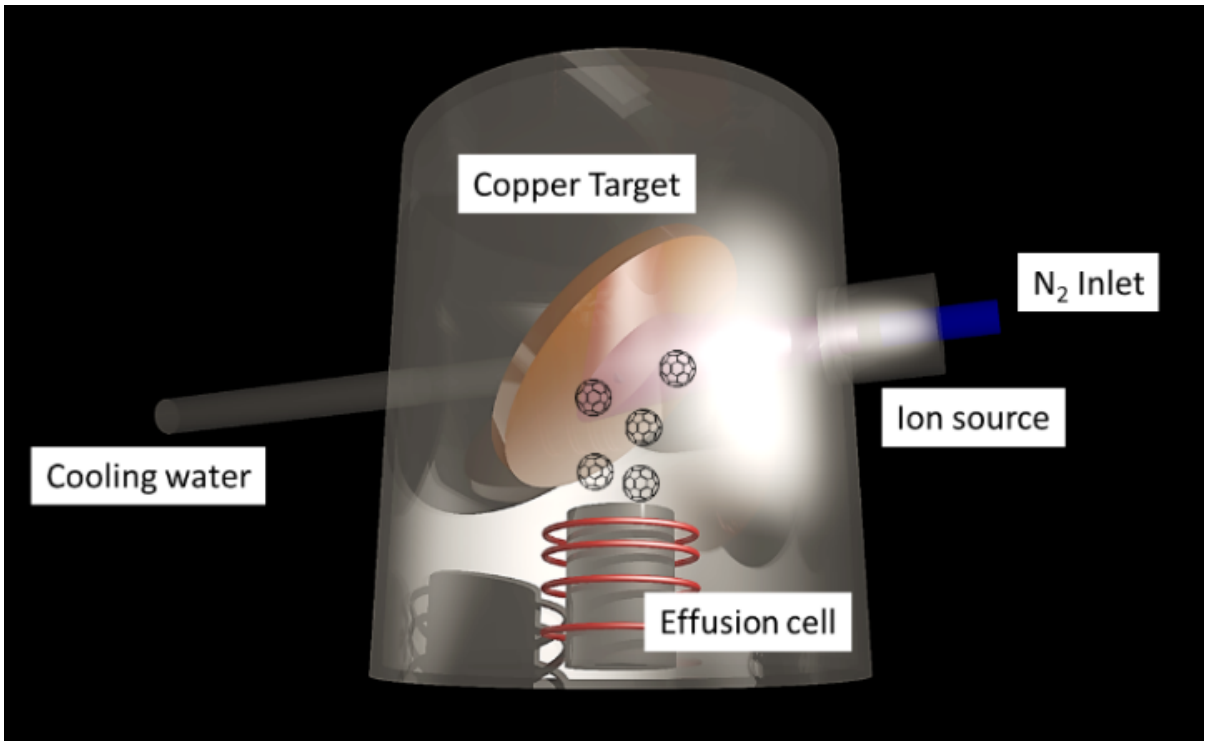
40.0 mg of 1,4-Didodecyl-2,5-diiodobenzene (60 μmol, no analytical data on purity, Sigma-Aldrich), 59 mg of TMS-acetylene (600 μmol, 98%, Sigma-Aldrich), 2.2 mg of $Pd(PPh_3)_2Cl_2$ (3 μmol, ≥ 99%, Sigma-Aldrich), and 1.2 mg of CuI (6 μmol, ≥ 99.5%, Sigma-Aldrich) were dissolved in 1:5 Et_3N (freshly distilled)/THF mixture, and reacted overnight. The reaction product was dried and then reacted with 82 mg K_2CO_3 (600 μmol, ≥ 99.99%, Sigma-Aldrich) in 4:3 THF/MeOH mixture for 2 hours. The organic phase was extracted from water and separated by preparative TLC to afford a yellow powder (1,4-didodecyl-2,5-diethynylbenzene, 16.6 mg, 36 μmol, 60% yield). **^{1}H NMR** (400 MHz, room temperature, CH_2D_2): $\delta = 7.19$ (m, 2H; C_6H_2, C_6H_3), 3.21 (s, 2H; CCH), 2.66 (m, 4H; CH_2) 1.57 (m, 4H; CH_2) 1.28 (m, 36H; CH_2), 0.88 (t, 6H; CH_3). 6.9 mg of the as-synthesized 1,4-didodecyl-2,5-

diethynylbenzene (15 μmol), 9 mg of 1-methyl-7-iodo-1H-Quinoline-2,4-dione (30 μmol, no analytical data on purity, FCH Group), 1.1 mg of $Pd(PPh_3)_2Cl_2$ (1.5 μmol, ≥ 99%, Sigma-Aldrich), and 0.6 mg of CuI (3 μmol, ≥ 99.5%, Sigma-Aldrich) were dissolved in 1:5 Et_3N/DMF mixture, and reacted overnight. The product (6-OPE-6) was separated by preparative TLC to afford a yellow powder (1.2 mg, 1.5 μmol, 10% yield). **^{1}H NMR** (400 MHz, room temperature, Chloroform-*d*): $\delta = 7.54, 7.02$ (m, 8H; C_6H_2, C_6H_3), 3.80 (s, 4H; $COCH_2CO$), 3.51 (s, 6H; NCH_3), 2.66 (m, 4H; CH_2) 1.57 (m, 4H; CH_2) 1.28 (m, 36H; CH_2), 0.88 (t, 6H; CH_3). **MALDI-MS** (negative): *m/z*: 808.6, and 809.6 $[M]^-$ ($C_{54}H_{68}N_2O_4$, calc. 808.518, 809.521, *etc.*).

1.2 mg of 6-OPE-6 (1.5 μmol) was dissolved with 2.5 mg of $^{15}N@C_{70}/C_{70}$ mixture (3.0 μmol, 0.1% spin content) and 0.8 mg of I_2 (3.1 μmol, 99.5%, Acros Organics) in 10 ml of 1:9 DMF/toluene solvent mixture (toluene: 99.5%, Fisher Chemical; DMF: anhydrous 99.8% Sigma-Aldrich), followed by addition of 1.9 ml of 0.5‰ DBU toluene solution (6.2 μmol, 99.0%, Sigma-Aldrich), dropwise. The reaction mixture was stirred under an argon atmosphere at room temperature and isolated from light. After 1.5 hours of reaction, 6-OPE-6 dimer was precipitate from the reaction mixture. The solid sample was then sonicated and filtered with an excess of toluene (99.5%, Fisher Chemical), chloroform (99.8%, Fisher Chemical), and methanol (99.9%, Fisher Chemical) to remove unreacted tetraone, base, and pristine fullerene. Finally, the sample (1.0 mg, 0.4 μmol, 26% yield) was dissolved in *o*-DCB (99%, Sigma-Aldrich) to preserve. **MALDI-MS** (positive): *m/z*: 2485.8, 2486.8, 2487.8, 2488.8, 2489.8, and 2490.8 $[M+H]^+$ ($C_{194}H_{65}O_4N_2$, calc. 2485.494, 2486.498, 2487.501, 2488.505, 2489.508, *etc.*).

Chapter 4 Optimizing the ENF production:

Towards available and affordable qubits



4.1 Introduction

ENF is an intriguing material due to its highly symmetric structure, the long decoherence times of its spin states, and its potential application to QIP. However, the material suffers from an ultra-low productivity and an inefficient purification method. Both limitations mean that the material struggles to meet the demand for multidisciplinary research, thus hindering further progress in the implementation of ENF-based QIP. Therefore, the focus of this chapter is on the optimization of the synthesis and purification procedure to improve throughput.

Firstly, based on the original commercial ion source implantation approach (reviewed in section 2.2.1), three aspects of the ENF synthesis were modified. As a first step, I improved the synthetic apparatus with a PID feedback control on the fullerene deposition rate (section 4.2.1). Then, I optimized the synthetic parameters to increase the yield of the spin-active product, based on the positive relationship discovered between the spin-yield and the nitrogen ion dosage (section 4.2.2 and section 4.2.3). After that, I resolved the *in-situ* ENF, which is potentially caused by the electron radiation, by putting the deposition target parallel to the ion source (section 4.2.4). During these optimizations, I also discovered that the formation of ENFs takes place in the vapour phase, which is different to previous understandings.

Secondly, I improved the HPLC purification of ENFs, which was reported to have difficulty in simultaneously achieving both a large sample capacity and a reliable separation efficiency (reviewed in section 2.2.2). By considering the column size, the recycling-mode, and the injecting method, I systematically optimized the original procedures (section 4.3.1 and section 4.3.2). I then studied the impact of the cage size and the mobile phase on the retention time ratio α between ENFs and empty-cage fullerenes (section 4.3.3 and section 4.3.4). It finally leads to an understanding of the retention mechanism of fullerenes, which is dominated by dispersion force (section 4.3.5).

Overall, this chapter reports an approximately five-time improvement on the productivity of ENFs compared with the original approach. Benefiting from the enhanced yield and

accelerated purification protocol, I managed to supply ENFs not only to the investigations in later chapters but also to my collaborators' research.

4.2 Optimizing the synthesis

4.2.1 Feedback control of fullerene deposition rates using LabVIEW

This section demonstrates the method and result of the improvement on the instrument. The ion implantation apparatus mainly consists of an effusion cell for fullerene deposition, an ion source for nitrogen bombardment, a deposition target on which the reaction takes place, and a pump system for the high vacuum generation. Since the latter three parts have already reached a relatively high level of stability, further improvements must come from optimizing the fullerene deposition rate, which depends upon several factors, including the heating temperature, the surface area of the precursor, the chamber pressure, *etc*.

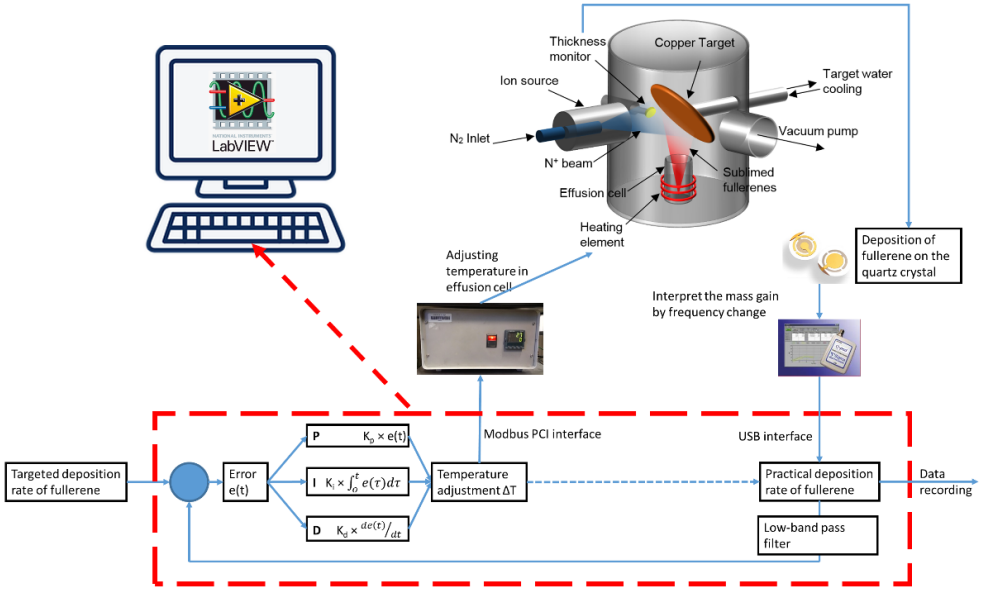


Figure 58 Schematic illustration of implementing the LabVIEW programme (programme A in appendix) for the fullerene deposition rate control.

Without building a comprehensive model to analyse the influence of all these factors, I controlled the fullerene deposition rate using a feed-back control programme implemented in LabVIEW virtual instrument software (Figure 58). As an independent module, the LabVIEW programme leaves the physical system unchanged, except for communicating with the

temperature controller and the thickness monitor *via* ModBus and USB interface, respectively. The core of the LabVIEW programme is a classic PID feedback control loop that adjusts the effusion cell temperature in response to changes in the deposition rate. Considering the large thermal capacity and sublimation enthalpy, the response of the system is slow enough to omit the derivative component of PID. For any desired deposition rate within the power range of the effusion cell, the optimal proportional gain and integral gain were determined by about three trial runs.

The red curve in Figure 59 shows an example of the deposition rate controlled by the LabVIEW programme, with the target rate set to $0.4\ \text{Å}/s$ and the proportional and integral gain set to 10 and 3, respectively. Compared to a manual step-wise heating, the LabVIEW programme significantly improves the tunablity and stability of the deposition rate, because both the huge overshot and the noise level of the deposition rate are tackled.

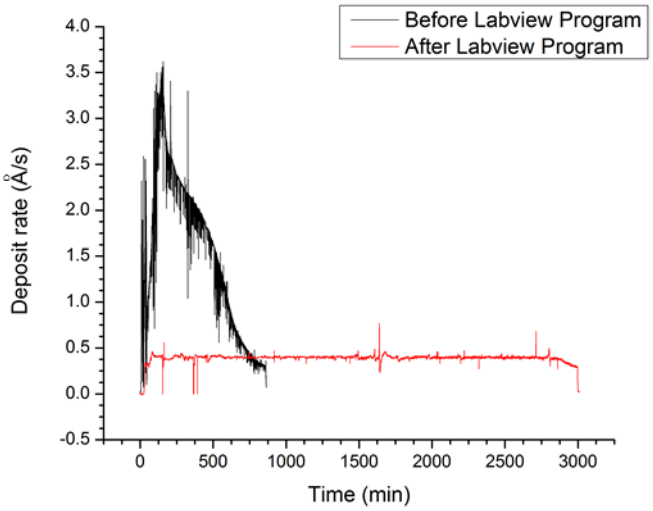


Figure 59 Controllability comparison of the C_{60} deposition rate between the recipe using the LabVIEW programme (red line) and that using manually step-wise heating (black line). Data were acquired using a thickness monitor (INFICON, Q-pod).

In addition to the deposition rate control, the LabVIEW programme also offers a better way of recording and displaying data with the customized user interface (Figure 60). Synthesis conditions, such as the temperature and the deposition rate, are simultaneously displayed and recorded. With the help of this user interface, an unattended synthesis procedure can be

achieved, which improves the time efficiency of the synthetic procedure.

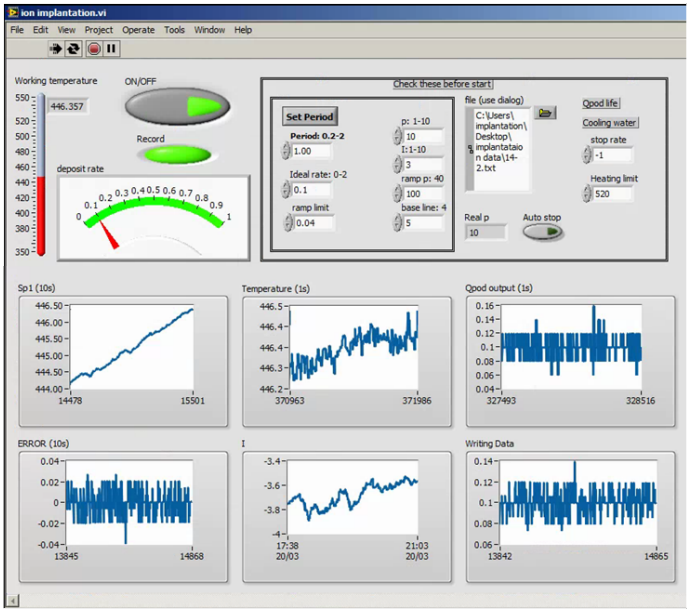


Figure 60 User interface of the LabVIEW programme during a typical synthesis procedure. The user interface enables adjustment on the deposition rate, the proportional gain, and the integral gain. It simultaneous displays and records the synthesis conditions, including the evaporation temperature and the deposition rate.

4.2.2 Parameter optimization for ion implantation using the DC25s ion source

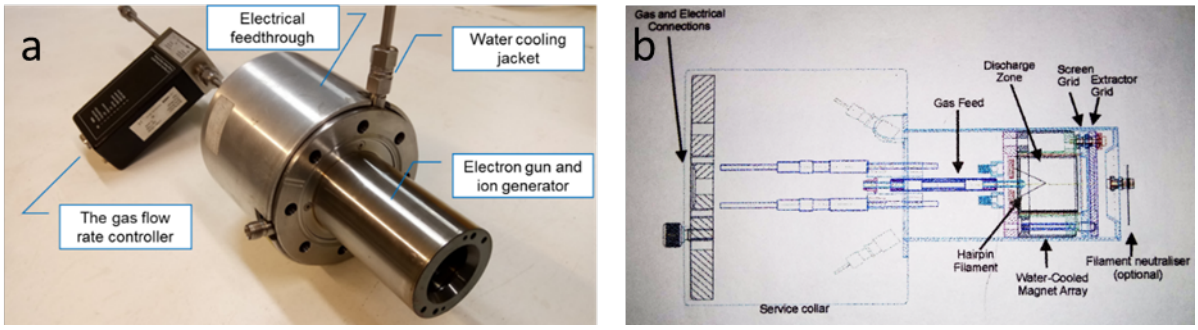


Figure 61 (a) Picture of the ion source of the DC25s manufactured by Oxford Applied Instruments. (b) Schematic drawing of the electron gun and ion generator parts (Acquired from the manufacturer, the optional filament neutralizer is not equipped in our setup).

After making the synthetic procedure automatic and more controllable, I started to optimize parameters of the synthetic procedure. This section focuses on the parameter optimization using the DC25s as the ion source. The DC25s (Figure 61) is the original commercial ion source used in our research group. It uses a tungsten electron gun to generate

electrons by cathode radiation, which subsequently collide with nitrogen gas molecules. Due to the applied axial magnetic field, electrons travel in a spiral path, which boosts the collision probability and the subsequent dissociation of nitrogen molecules to form N^+ and N_2^+ ions. The ions are accelerated by the charged grid to form an ion beam and are implanted into the carbon cage with a reaction of $\mathrm{N}^+ + \mathrm{C}_{60} \rightarrow \mathrm{N@C}_{60} + \cdots$. The progress of this reaction, which is conducted near/on a water-cooled target, is dependent on the condition of the two reactants. The deposition rate is the dominant factor related to the C_{60} reactant, while, in terms of the nitrogen ion beam, the relevant parameters are determined by the settings of the DC25s. In contrast to the large working range claimed by the manufacturer, I worked out the practical working range (Table 4), when it is mounted on our experimental setup. Among the six tuneable parameters, only the beam current and the beam energy can be adjusted independently because of the causal relationship between the electron emission/gas flow and the nitrogen ionization. Previous members of the research group have already optimized the beam energy, and found that 40 eV is the optimal beam energy,[96] in agreement with other literature.[110] Therefore, beam current is the only nitrogen ionization related parameter needed to be optimized.

Table 4 Practical working range for the DC25s mounted on experimental setup in Figure 8

Model	Electron emission related parameters			Nitrogen ionization related parameters		
	Cathode Current (A)	Extraction Voltage (V)	Emission Current (A)	Nitrogen flow rate (sccm)	Beam current (mA)	Beam energy (eV)
DC25s	$5\sim7$	$-400\sim0$	$0.12\sim0.28$	$0.15\sim0.50$	$0\sim1$	$0\sim200$

A control variable method was used to investigate how parameters of the beam current and the fullerene deposition rate affect the spin-yield ($N@C_{60}/C_{60}$ ratio) in crude product (the soluble fraction of the fullerene soot collected from the ion implantation procedure). The solubility of the fullerene soot (ratio of C_{60}/soot) was not an optimization target, because I always achieved ca. 40% soluble product, no matter what synthetic parameters were used. By carrying out a set of quantitative UV/Vis spectroscopy and ESR experiments, which

measure the amount of C_{60} and $N@C_{60}$, respectively, a set of spin-yields were determined (Table 5) and compared in Figure 62.

Table 5 Spin-yield of the product obtained by different synthetic parameters using the DC25s as the ion source. The spin-yield were calculated based on quantitative UV/Vis spectroscopy and cw-ESR spectroscopy, which acquire the $N@C_{60}$ amount and C_{60} amount, respectively. (The cw-ESR experiments are performed using a Magnettech MiniScope MS200 spectrometer, and the cw-ESR spectra documented in supporting information B.)

Batch	beam current (mA)	fullerene deposition rate (Å/s)	$N@C_{60}$ amount (mol/l)	C_{60} amount (mol/l))	Spin-yield ($N@C_{60}/C_{60}$ (ppm))
1	0.4	$0.2-0.4$	9.21×10^{-8}	1.57×10^{-3}	58.8
2	0.4	$0.2-0.4$	8.35×10^{-8}	1.41×10^{-3}	59.1
3	0.4	$0.2-0.4$	9.79×10^{-8}	1.75×10^{-3}	55.9
4	0.8	$0.2-0.4$	7.10×10^{-8}	1.77×10^{-3}	40.2
5	0.8	$0.2-0.4$	8.15×10^{-8}	1.98×10^{-3}	41.1
6	0.8	$0.2-0.4$	8.45×10^{-8}	2.09×10^{-3}	40.4
7	1.2	$0.2-0.4$	6.23×10^{-8}	2.21×10^{-3}	28.2
8	1.2	$0.2-0.4$	5.72×10^{-8}	1.95×10^{-3}	29.4
9	1.2	$0.2-0.4$	5.45×10^{-8}	1.96×10^{-3}	27.8
10	0.4	$0.6-0.8$	1.06×10^{-7}	1.49×10^{-3}	70.8
11	0.4	$0.6-0.8$	1.07×10^{-7}	1.59×10^{-3}	66.9
12	0.4	$0.6-0.8$	1.11×10^{-7}	1.63×10^{-3}	67.6
13	0.8	$0.6-0.8$	8.91×10^{-8}	1.83×10^{-3}	48.8
14	0.8	$0.6-0.8$	9.01×10^{-8}	1.66×10^{-3}	54.4
15	0.8	$0.6-0.8$	9.35×10^{-8}	1.81×10^{-3}	51.8
16	1.2	$0.6-0.8$	5.14×10^{-8}	1.34×10^{-3}	38.4
17	1.2	$0.6-0.8$	5.65×10^{-8}	1.52×10^{-3}	37.2
18	1.2	$0.6-0.8$	6.13×10^{-8}	1.63×10^{-3}	37.6
19	0.4	$0.9-1.1$	1.22×10^{-7}	1.54×10^{-3}	79.2
20	0.4	$0.9-1.1$	1.02×10^{-7}	1.27×10^{-3}	80.4
21	0.4	$0.9-1.1$	1.04×10^{-7}	1.31×10^{-3}	79.4
22	0.8	$0.9-1.1$	8.81×10^{-8}	1.35×10^{-3}	65.3
23	0.8	$0.9-1.1$	8.95×10^{-8}	1.32×10^{-3}	67.6
24	0.8	$0.9-1.1$	8.56×10^{-8}	1.34×10^{-3}	64.1
25	1.2	$0.9-1.1$	6.95×10^{-8}	1.41×10^{-3}	49.4
26	1.2	$0.9-1.1$	7.35×10^{-8}	1.52×10^{-3}	48.4
27	1.2	$0.9-1.1$	6.85×10^{-8}	1.34×10^{-3}	51.2

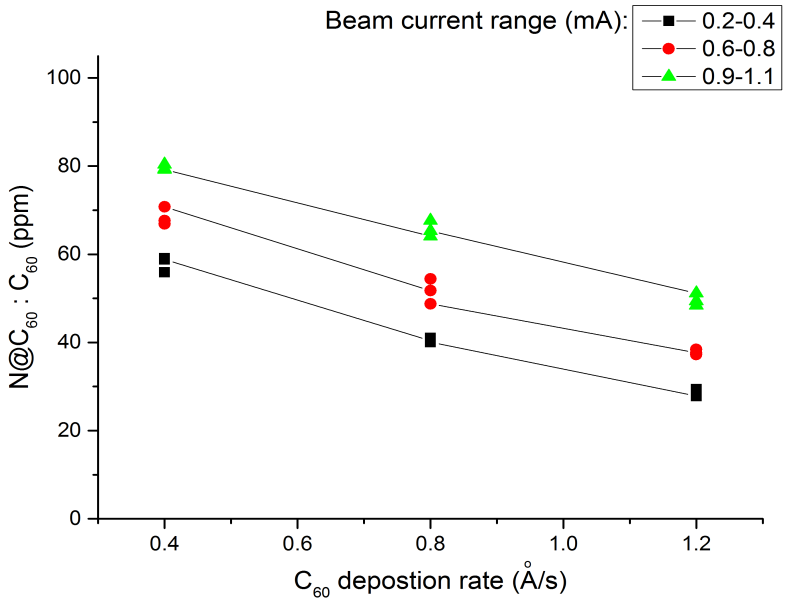


Figure 62 Spin-yield comparison of N@C_{60} with different parameters of beam current and fullerene deposition rate, using the DC25s as the ion source.

Both a high beam current and a low fullerene deposition rate can improve the spin-yield of the product, which means that a larger ion dosage per fullerene is favourable. Therefore, a low deposition rate of $0.4\ \text{Å/s}$ for C_{60} and a maximized beam current of $1.0\ \text{mA}$ for nitrogen ions were determined to be the optimal conditions to synthesize N@C_{60} with the DC25s ion source. The as-synthesized N@C_{60}/C_{60} mixture reached a purity of $80\ \text{ppm}$ and a production of $250\ \text{mg}$ per week. (Further decrease in the rate of deposition is not recommended as the DC25s cannot function continuously for a too long period of time. Besides, a too low deposition rate also slows down the synthesis procedure.)

4.2.3 Parameter optimization for implantation using the eH400 ion source

Since the maximum beam current of the DC25s restricted the optimization, a new ion source, the eH400 manufactured by Kaufman & Robinson, Inc., was bought to permit an increase in the beam current, and to enable a further parameter optimization. To match with the new ion source which demands large chamber space and nitrogen flow rate, the experimental setup was also upgraded from a one-chamber design to a two-chamber design

equipped with a turbo pump that was more powerful than the original diffusion pump (Figure 63a, b).

Similar to the DC25s, the eH400 ion source also uses a tungsten electron gun to generate electrons by the cathode radiation, but the process after the electron generation is different. Rather than using a grid to isolate the discharge zone and extracting only the positive ions as the output, the eH400 has an open discharge zone (Figure 63c). The absence of the screen grid plus the rear-positioned extraction electrode leaves the space between the filament and the target unobstructed, and therefore, significantly improves the likelihood of the positive ions reaching the target. The typical beam current provided by the eH400 is on the ampere scale, which is three orders of magnitude larger than that of the DC25s.

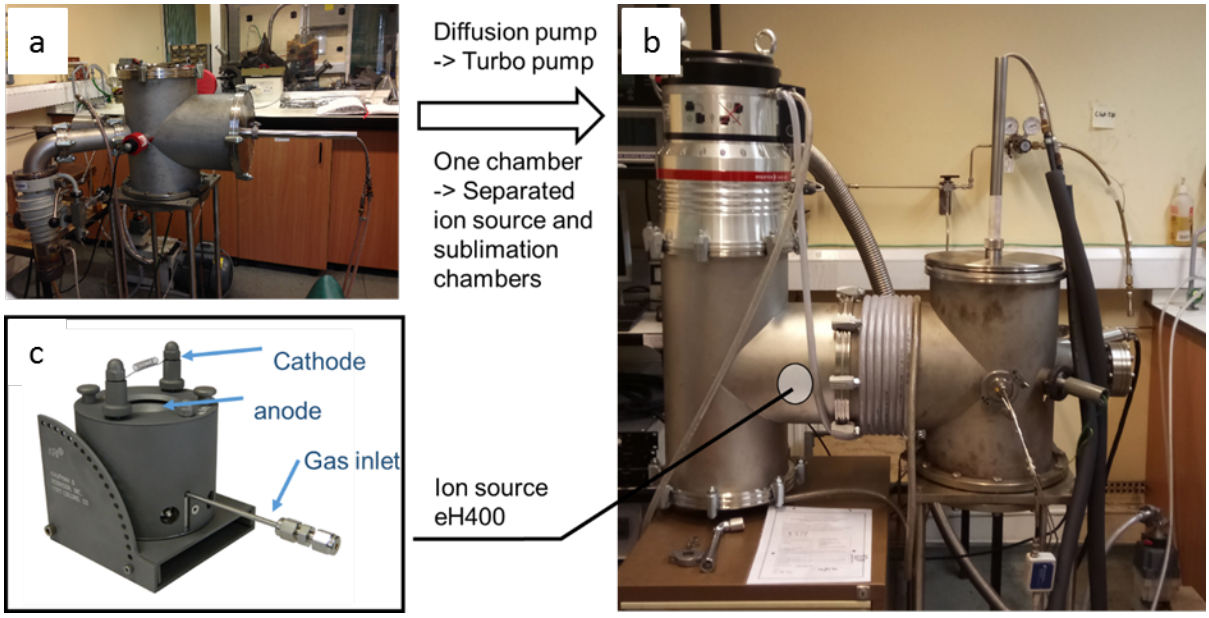


Figure 63 (a) Picture of the old setup. (b) Picture of the expanded setup with two chambers and a turbo pump to compatible with the eH400. (c) Picture of the eH400 ion source showing its design with no front grid and an open ionization zone.

Due to the larger beam current, the ion dosage per fullerene was sufficiently large to search for the optimal synthetic parameters, even with a maximized fullerene deposition rate. Therefore, the deposition rate of fullerene was always maximized ($2\ \text{Å}/\text{s}$) so as to accelerate the implantation procedure. This reduced the duration of one ion implantation procedure from several days to several hours.

Since there is no grid in front of the discharge zone, the beam current and beam energy are no longer readable from the control panel, which prevented me from conducting an experiment similar to the one presented in Figure 62. Instead, I varied the most beam-current-relevant parameter (nitrogen flow rate) and the most beam-energy-relevant parameter (extraction voltage) to find the optimal yield conditions. Table 6 shows the result for each synthetic procedure. The amount of the fullerene soot scraped from the deposition target was measured by an electronic balance, whereas the amount of C_{60} and $N@C_{60}$ amount were determined with a toluene solution using quantitative UV/Vis spectroscopy and cw-ESR spectroscopy, respectively. Figure 64 displays data showing how different extraction voltages and nitrogen flows affect the quality of the product by comparing the product solubility and spin-yield. The red bars indicate the $N@C_{60}/C_{60}$ ratio in the dissolved product and show that optimal spin-yield up to $250\ \mathrm{ppm}$ can be achieved with the extraction voltage and flow rate set to $200\sim250\ \mathrm{V}$ and $4.5\sim7\ \mathrm{sccm}$, respectively. Compared to the result of $80\ \mathrm{ppm}$ optimized in last section, applying a larger beam current further improves the yield. However, the improvement is not as good as the proportional enhancement. Compared to the DC25s which always induced approximately 60% fullerene polymerization, the polymerization problem became more severe. The solubility of the fullerene soot generally decreased, especially when a higher discharge voltage and/or a lower flow rate was used. The lower solubility of the product could be due to another drawback of the open discharge zone: unscreened electrons from the ion source could trigger fullerene polymerization.[212]

In order to balance the spin-yield and the product solubility, a discharge voltage of $200\ \mathrm{V}$ and a flow rate of $5\ \mathrm{sccm}$ were chosen as the optimal synthesis condition. Although the solubility of the fullerene soot was still lower than the DC25s method, the spin-yield was remarkably improved. More importantly, the ion implantation procedure was much faster using the eH400. Overall, the productivity of $N@C_{60}$ increased to *ca.* $200\ \mathrm{ppm}$ and $200\ \mathrm{mg}$ per week.

Table 6 Spin-yield and solubility of the product obtained by different synthetic parameters using the eH400 ion source. The spin-yield and solubility were calculated based on quantitative UV/Vis spectroscopy and cw-ESR spectroscopy, which acquire the $N@C_{60}$ amount and C_{60} amount, respectively. (The ESR experiments were performed using a Magnettech MiniScope MS200 spectrometer, and the ESR data for the crude product are documented in supporting information C.)

Extraction voltage (V)	Flow rate of Nitrogen (sccm)	Spin counting ($N@C_{60}$ amount (mol/l))	Solute quantity (C_{60} amount (mol/l))	Mass of the fullerene soot per 5 ml toluene (g)	Spin-yield ($N@C_{60}/C_{60}$ ratio (ppm))	Solute material percentage (C_{60}/soot ratio (‰))
250	7	5.24×10^{-7}	2.10×10^{-3}	0.24	250	31
200	4.5	4.87×10^{-7}	2.38×10^{-3}	0.12	205	69
200	5	4.43×10^{-7}	2.46×10^{-3}	0.33	180	53
250	5.5	1.85×10^{-7}	1.80×10^{-3}	0.21	103	31
175	5	1.76×10^{-7}	1.74×10^{-3}	0.07	101	89
150	6	1.19×10^{-7}	2.97×10^{-3}	0.11	40.1	93
150	7	7.5×10^{-8}	2.83×10^{-3}	0.10	27	101
80	10	2.1×10^{-8}	3.04×10^{-3}	0.05	6.9	214
100	13	9×10^{-9}	2.12×10^{-3}	0.02	4.2	348

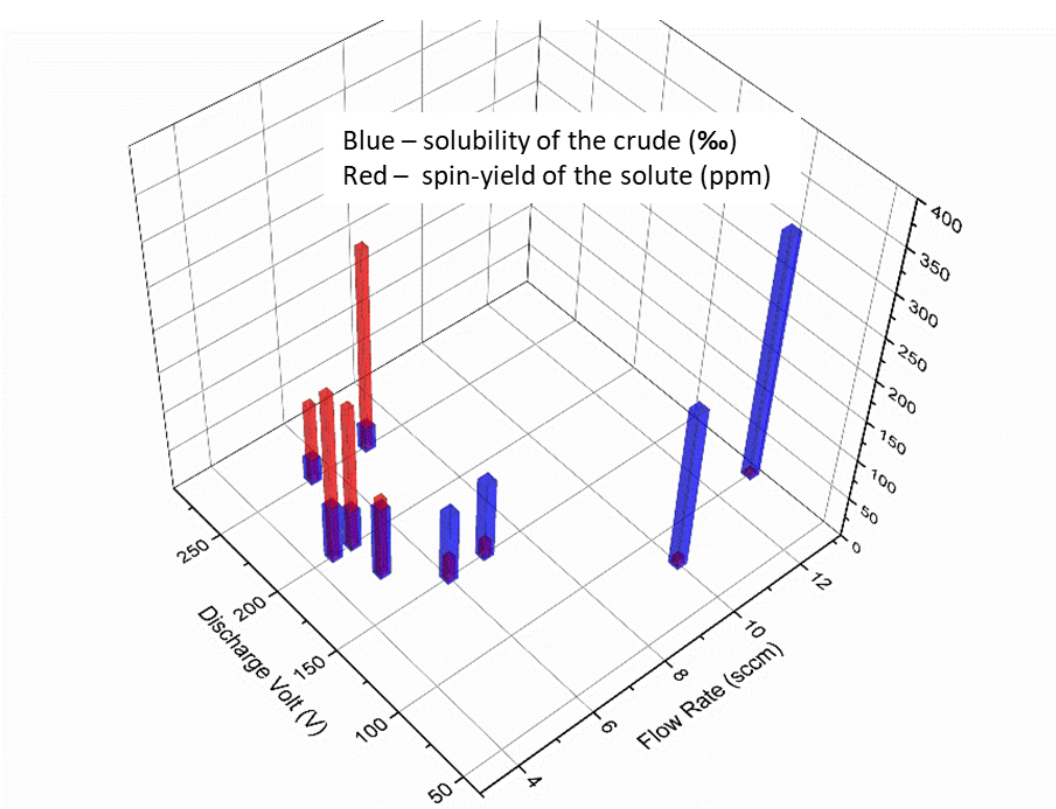


Figure 64 Product quality (solubility – blue, spin-yield – red) comparison under different synthetic parameters of discharge voltage and nitrogen flow rate, using the eH400 as the ion source.

4.2.4 Suppressing the *in-situ* decomposition of ENF

As is shown by the above parameter optimization studies, parameters that provide the highest spin-yield do not necessarily lead to an overall optimal synthesis result, since the synthesized ENF simultaneously undergoes decomposition procedures, such as polymerization. This section focuses on analysing the causes of the *in-situ* ENF decomposition, followed by developing feasible approaches to balance the competing ENF formation and decomposition reactions. This is crucial to scaling up the ENF synthesis from laboratory to industrial scale, as reducing the *in-situ* ENF decomposition could enable the implantation to run continually without frequent breakoffs to harvest the product.

Since electron radiation has been reported to induce fullerene polymerization,[212] the potential destructive influence from the cumulative electron radiation on the synthesized ENF needs to be tested. I investigated three ways to reduce the cumulative electron dosage. Firstly, I put a grounded conductive grid between the ion source and the deposition target to screen the electron dosage. Unfortunately, the grid screens both electron and the nitrogen ion, leading to zero yield of ENF. This ruled out my attempt to decrease the instantaneous electron dosage. Decreasing the time that the material is exposed to the electron radiation is an alternative way to limit the cumulative electron dosage. A scalable method would be to make a roll-to-roll deposition target (Figure 65a), which removes the synthesized ENF out of the beam after synthesis. Without introducing the scroll straight away, I performed a preliminary trial by covering the copper target with the aluminium foil to test the viability of replacing the copper target to a bendable deposition substrate. Unexpectedly, the product collected from the foil offers a low spin-yield with deteriorated polymerization. The poor yield on the aluminium foil could be because the foil is not directly well-grounded and water-cooled unlike the copper target. The low conductivity between the foil and the copper target needs to be tackled before the roll-to-roll scheme could be implemented. For the third way of decreasing the electron dosage, I changed the orientation of the target to make it parallel to the ion beam (Figure 65b). The reorientation of the target ensured the fullerene-ion and fullerene-electron collisions only

occurred in the vapour phase, before the fullerenes reached the target. The decrease of the spin-yield due to fewer nitrogen ions reaching the target was negligible, but the solubility of the product was improved from 10% to 30%. These results not only suggest that reducing the electron dosage can prevent the synthesized ENF from decomposing to fullerene polymers, but also indicate that the nitrogen ion implantation primarily takes place in the vapour phase rather than on the surface of the fullerene deposition. With the target parallel to the beam direction, the productivity was improved to *ca.* $500\ \mathrm{mg}$ of $200\ \mathrm{ppm}$ crude products per week.

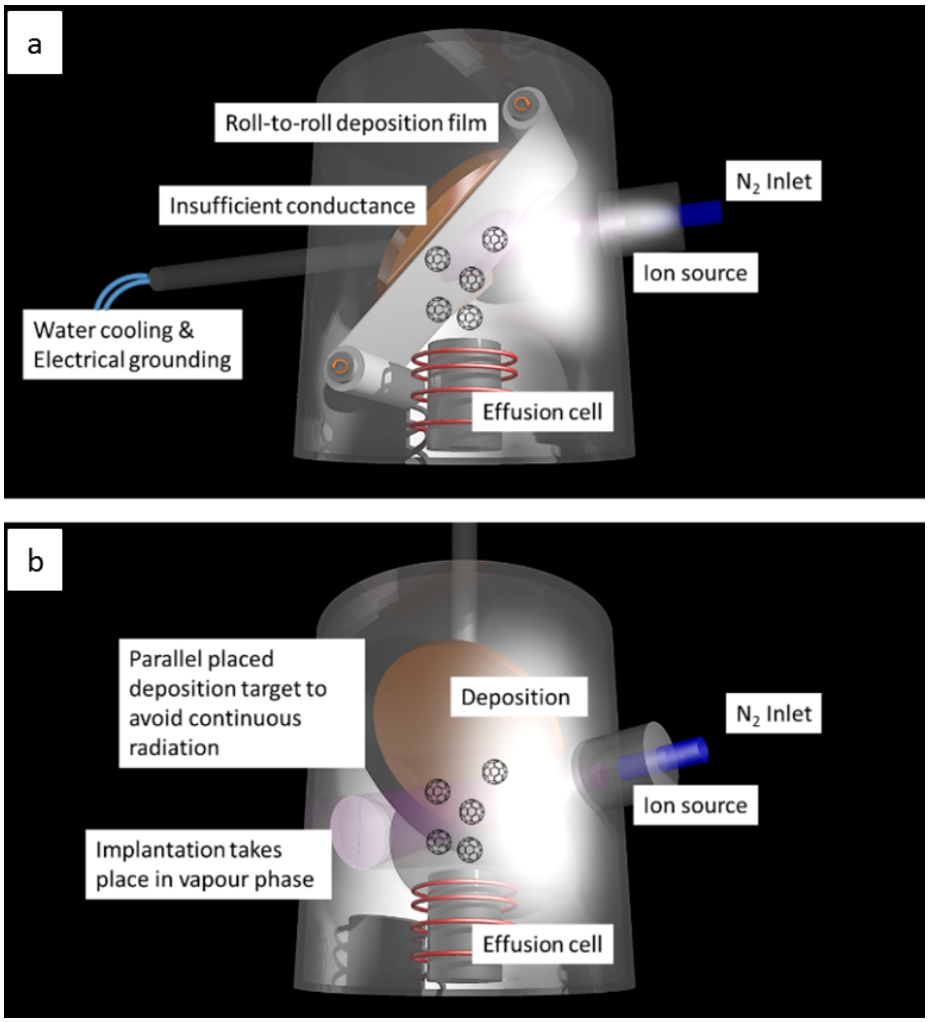


Figure 65 (a) Roll-to-roll design for preserving the product *in situ*. The conductance problem remains to be tackled. (b) Re-arrangement on the target orientation to avoid its directly facing to the ion source, which induces a continuous electron irradiation.

As temperatures higher than 500 K have been reported to decompose ENFs, as evidenced by a reduction in the spin signal,[149,213] product preservation against heat during the

synthesis of ENFs may also be needed. However, according to my experiments (supporting information D), the *in-situ* decomposition of ENF due to the thermal radiation from the effusion or the insufficient cooling was insignificant. Therefore, an improvement on the thermal condition of the synthetic procedure is unnecessary with our current apparatus.

4.3 Optimizing the HPLC purification procedure

4.3.1 Optimal column for the HPLC purification

As the column is an essential part of the HPLC system, choosing a suitable one is crucial for the optimization. Previous studies pointed out that a penta-bromobenzyl (PBB) functionalised column is better than a pyrene (PYE) functionalised column, because the bromine in the functional group can more effectively delay the retention time of N@C_{60} relative to that of C_{60}.[44] Based on this result, three preparative HPLC columns using PBB as the functional group, including a 15PBB 100×500 mm column (column **1**), a 5PBB 20×250 mm column (column **2**), and a 15PBB 20×250 mm column (column **3**), are compared in this section. The parameters in the column name represent the average particle size (μm), the column diameter and the column length, respectively. The retention time ratio between N@C_{60} and C_{60} was constant ($\alpha = 1.028$) between the different columns, since all columns have the same functional group. The measured retention time ratio is consistent with previous reports.[44] Therefore, a new set of criteria is required to evaluate the columns. The column capacity (the maximum sample volume processed by a column within a certain time) has been used as the criterion previously. As a result, column **1**, which has the largest physical dimension, was recommended as the best choice for ENF separation.[108] In addition to column capacity, I introduced the concept of column efficiency (the capability of a column to separate species having similar retention times)[214] as another criterion evaluating the performance of the columns. For a given material, such as C_{60}, the column efficiency can be parameterized as the number of theoretical plates $N = 5.545\ (t_R/\omega_{\mathrm{FWHM}})^2$, where, t_R is the retention time for C_{60}, and ω_{FWHM} is the full width at half maximum of the C_{60} peak. The larger the plate number is, the less overlap between the C_{60} and N@C_{60} peaks will be. Subsequently, I can divide the HPLC elution better into the spin-depleted and spin-enriched fractions. In addition to the subtype of the PBB columns, HPLC parameters, including the flow rate of the eluent, the

recycling time, and the injection volume have also been investigated together (Figure 66). Retention times and peak widths for each HPLC column and method were obtained from Figure 66, and listed in Table 7.

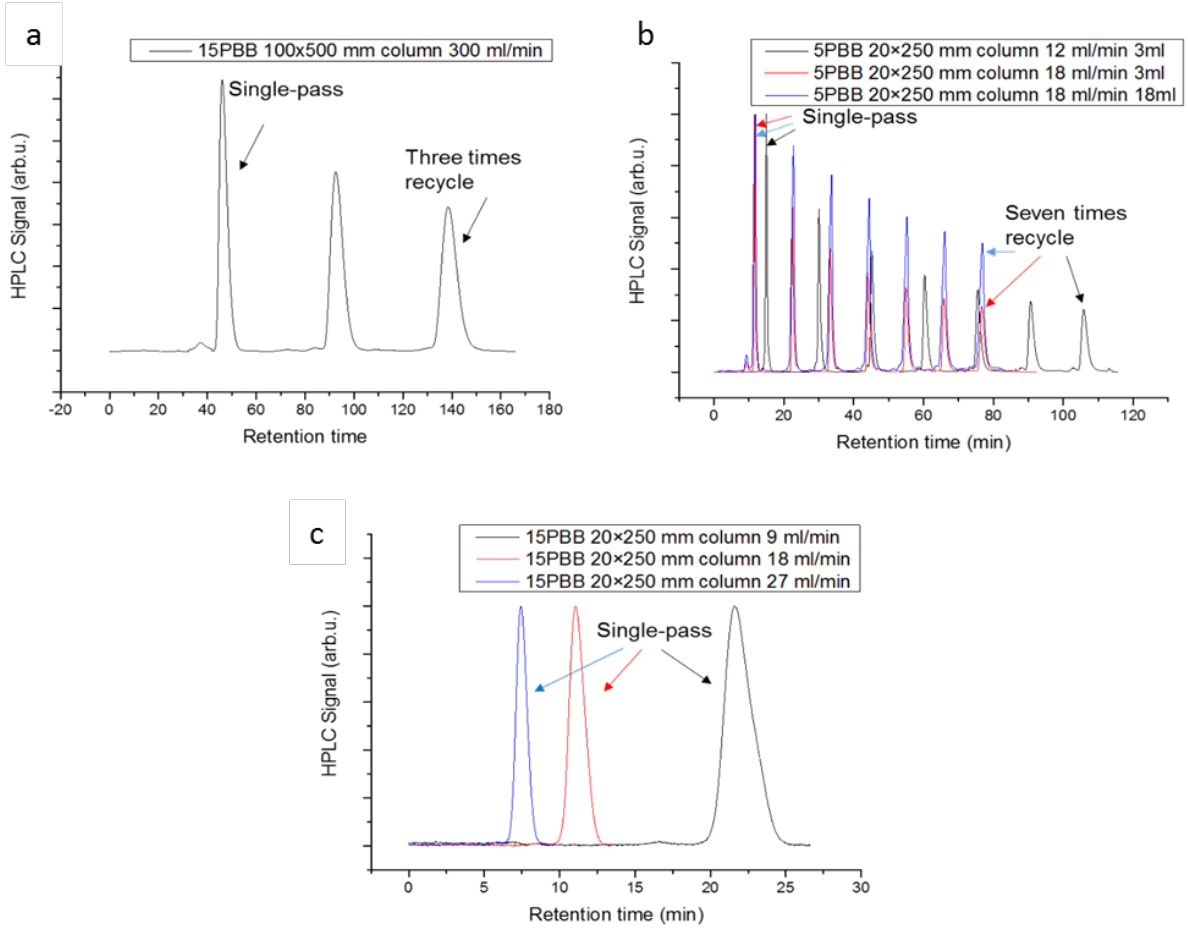


Figure 66 HPLC traces when different columns and different methods were used. (a) 15PBB 100×500 mm column, (b) 5PBB 20×250 mm column, and (c) 15PBB 20×250 mm column. The flow rate and recycling times are labelled by colours and arrows in the HPLC chart, respectively. All experiments used toluene as the mobile phase.

Based on the definition of the column capacity and efficiency, the calculated values are also compared in Table 7. In terms of the column capacity, the best result is achieved by column **1** with a single-pass, a flow rate of 300 ml/min and an injection volume of 150 ml. Due to a smaller column size, methods using column **2** and **3** generally show small capacities unless one deliberately overloads the sample. In terms of the column efficiency, column **2** generally shows the highest column efficiency, due to the smaller particle size of the silica. Besides, decreased solvent flow rate within a certain range only achieves a minor positive

influence on the theoretical plate number, which, in turn, results in a significant slowdown of HPLC elution, making such modification not worthwhile. Recycling-mode can also enhance the column efficiency. It can enhance the efficiency dramatically when the column is overloaded, but the enhancement becomes less significant with an increased number of HPLC recycles.

The optimal HPLC methods should have large values for both criteria. Therefore, the arithmetic product of the column efficiency and capacity, namely the score, for each HPLC column and method are compared in Table 7. I recommend the HPLC column and method with the highest score (20419) for ENF separation, which is 7-time recycling on column **2** with a flow rate of $18\ \mathrm{ml/min}$ and an injection volume of $18\ \mathrm{ml}$.

Table 7. Comparison of HPLC features, calculated column capacity, column efficiency, and method score when different column and method were used

Column	method	Features of HPLC curve		Column capacity	Column efficiency	Score
		Retention time t_R (min)	full width at half maximum ω_{FWHM} (min)	Injection volume / HPLC duration (ml/h)	theoretical plates $N = 5.545\,(\frac{t_R}{\omega_{FWHM}})^2$	Efficiency × capacity (10^4)
1	Single-pass, 300 ml/min flow, 150 ml injection	46.100	3.667	150	876	13.14
	Three times recycle, 300 ml/min flow, 150 ml injection	138.533	7.100	50	2111	10.555
2	Single-pass, 12 ml/min flow, 3 ml injection	14.993	0.450	6	6155	3.693
	Single-pass, 18 ml/min flow, 3 ml injection	11.617	0.352	9	6041	5.437
	Single-pass, 18 ml/min flow, 18 ml injection (overloading)	11.868	0.796	54	1233	6.658
	Three times recycle, 12 ml/min flow, 3 ml injection	45.218	0.957	3	12379	3.714
	Three times recycle, 18 ml/min flow, 3 ml injection	33.285	0.746	4.5	11039	4.968
	Three times recycle, 18 ml/min flow, 18 ml injection (overloading)	33.669	0.989	27	6426	17.350
	Seven times recycle, 12 ml/min flow, 3 ml injection	105.883	1.813	1.5	18913	2.837
	Seven times recycle, 18 ml/min flow, 3 ml injection	76.662	1.371	2	17338	3.468
	Seven times recycle, 18 ml/min flow, 18 ml injection (overloading)	76.890	1.388	12	17016	20.419
3	Single-pass, 9 ml/min flow, 3 ml injection	21.601	2.085	6	595	0.357
	Single-pass, 18 ml/min flow, 3 ml injection	11.046	1.166	12	498	0.598
	Single-pass, 27 ml/min flow, 3 ml injection	7.435	0.833	15	442	0.663

4.3.2 Improving column capacity by automatic repeat injection/collection

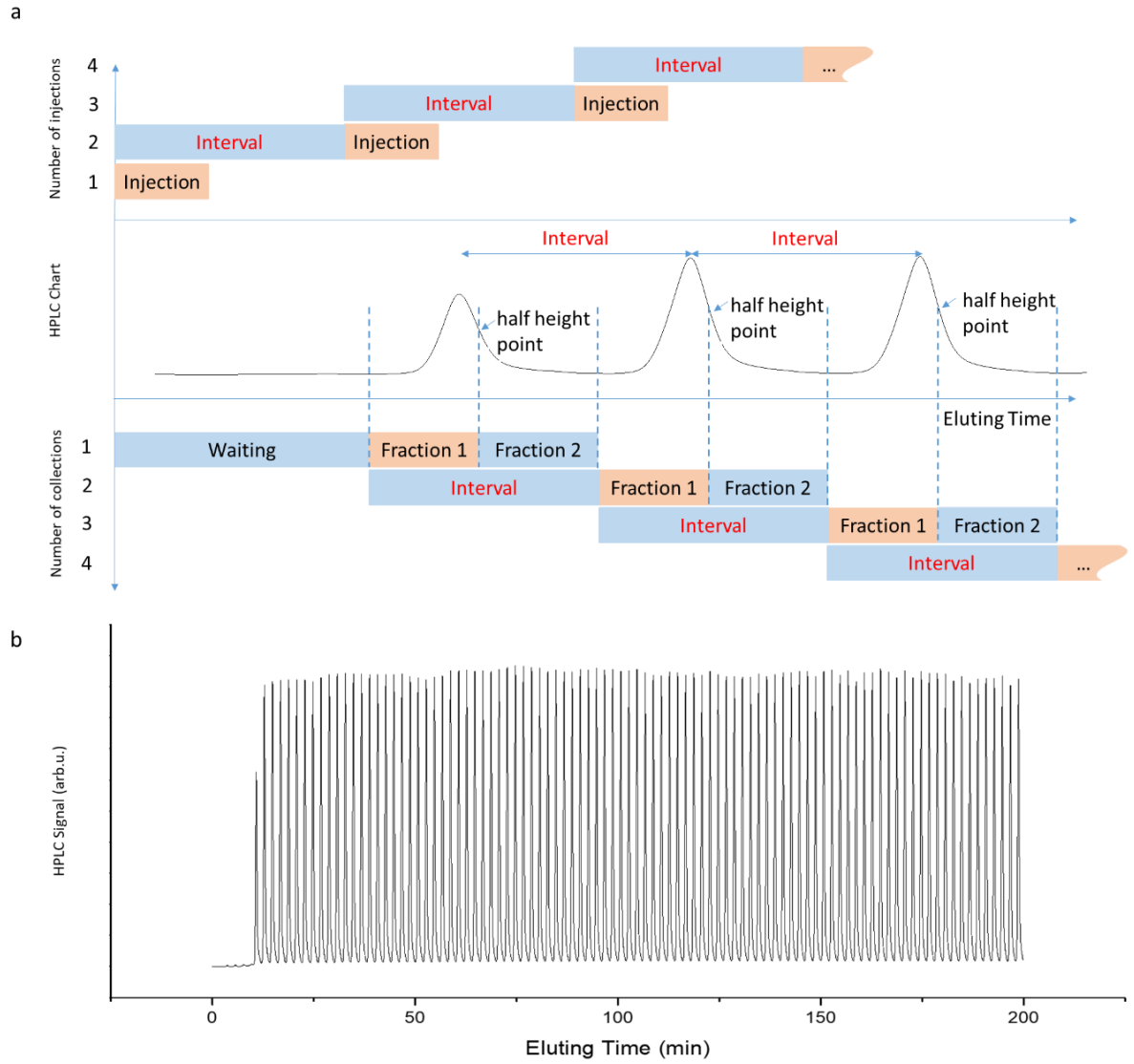


Figure 67. (a) Relationship among the repeat injection, the HPLC peaks of the injected samples, and the automatic collection programmed to repeatedly divide the eluted sample into two fractions, (b) The HPLC chart for 99 times repeat injection experiment HPLC chart (5PBB 20×250 mm column, toluene, 18 ml/min flow rate, and 2 minutes injection interval).

Apart from overloading column **2**, which showed best result of all HPLC methods compared in the last section, performing repeat injection (a HPLC method that continually injects the sample in a sequence before the last injected sample fully elutes) with column **2** is another way of improving the column capacity. However, it requires the HPLC operator to frequently change the collection flask for fraction collections. I therefore equipped the HPLC machine (JAI LC-908W) with a fraction collector, and programmed it to automatically collect the separated samples which were repeatedly injected.

As Figure 67a demonstrates, a serial of samples was automatically injected into the column with a certain interval time, which then eluted with the same interval time. Meanwhile, the programmed fraction collector repeatedly switches between two receivers for the spin-depleted fraction (Fraction 1) and the spin-enriched fraction (Fraction 2), respectively. The periodicity of the alternation was set as the interval time. The interval time needs to be longer than the duration of one peak elution to avoid the overlap of peaks between adjacent injections. With a flow rate of $18\ \mathrm{ml/min}$, this value was determined to be 2 minutes. Benefiting from the larger column efficiency of column **2**, the peak dividing point, i.e. the switching time between Fraction 1 and Fraction 2, was optimized to be the half-height point on the right-hand side. Compared with dividing the peak from the summit point when using column **1**, this peak dividing scheme filters out more empty-cage fullerenes per HPLC pass, thereby enriching the N@C_{60} content of Fraction 2 more rapidly.

As shown in Figure 67b, 99 injections of $3\ \mathrm{ml}$ samples ($297\ \mathrm{ml}$, in total) can be processed through column **2** by the single-pass mode within 3.5 hours. This method has a column capacity of $90\ \mathrm{ml/h}$ and the column efficiency of 6041. Overall, the score for this method is 54369, which is about 3 times higher the best result in Table 7. Practically, one can enrich the spin in $400\ \mathrm{mg}$ of material by the factor of 2 per day with a relatively automated method.

4.3.3 Changing the analyte: cage size influence

Although column and method optimization have been discussed, the enhancements are still limited by the low retention time ratio between the ENF and the empty-cage fullerene. It has been reported that separation of N@C_{70} is easier than N@C_{60}.[44,215] However, the retention time ratio for N@C_{70}/C_{70} was measured to be the same as that of N@C_{60}/C_{60} ($\alpha \approx 1.028$) in this literature.[44] The contradictory claims need to be verified, as a truly easier separation of N@C_{70} could lead to potential replacement of N@C_{60} with N@C_{70} for certain applications. Thus, I did a quantitative experiment to find out whether or not N@C_{70} has a larger retention time ratio to C_{70} in a PBB column.

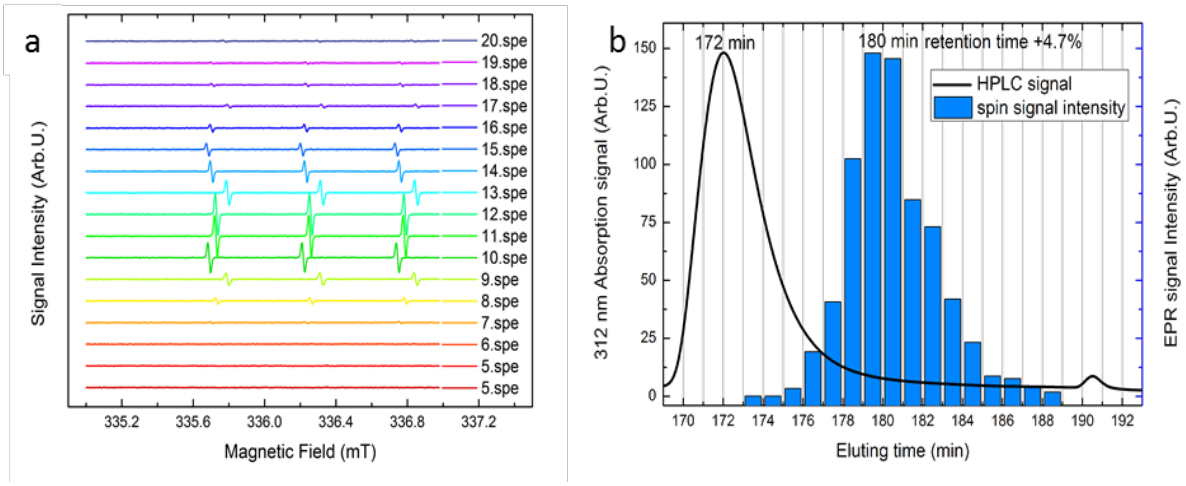


Figure 68 (a) cw-ESR signals for individual fractions everyone minute, from the 169 minutes to the 189 minutes, fraction 1-4 is omitted due to no signal. (experimental conditions: Magnettech MiniScope MS200, $30.0\ \mathrm{dB}$ attenuation, room temperature, and $0.02\ \mathrm{mT}$ modulation amplitude) (b) Comparison for HPLC trace for C_{70} and the reconstructed spin trace for N@C_{70} based on panel a. (5PBB $20\times250\ \mathrm{mm}$ column, toluene, and $18\ \mathrm{ml/min}$ flow rate).

0.1% N@C_{70} in C_{70} was synthesized and enriched by the same method as was used for N@C_{60}. and was then injected and recycled in a 5PBB column for nine loops. The relatively high purity of N@C_{70} improves the accuracy of the spin signal measurement, and the long HPLC time using the recycling-mode guarantees a low fractional error in time measurement for the fraction collection. When the ninth cycle starts to elute, the elution is collected in separated containers every single minute from 169 minutes to 189 minutes. I measured the spin intensity for each fraction (Figure 68a), the field offset for each sample is due to sample-to-sample microwave frequency variation. By studying the spin signal intensity, a reconstructed peak for spin species (which is invisible to HPLC detector) can be plotted with the HPLC curve (Figure 68b), and the retention time ratio α between N@C_{70} and C_{60} can be determined as $\alpha = 1.047 \pm 0.006$, which is noticeably larger than 1.028 reported for N@C_{60} in the same column and mobile phase. Applying the repeat injection method developed for N@C_{60} separation (section 4.3.2) to N@C_{70}, column efficiency and capacity were evaluated as 5480 and $30\ \mathrm{ml/h}$. Although both the column capacity and efficiency are decreased, the retention time ratio is a more predominant impact factor for separations. Therefore, I confirmed that purifying N@C_{70} is more efficient than N@C_{60}.

The larger retention time ratio obtained clarified that N@C_{70} is easier to separate. The larger retention time ratio for larger cage is reasonable as the larger cage moves more slowly through the column. By spending a longer time interacting with the stationary phase, the retention difference between ENFs and empty-cage fullerenes could be magnified.

4.3.4 Changing the mobile phase: eluent polarizability influence

Inspired by the delayed elution of N@C_{70}/C_{70} mixture and the resultant better separation between N@C_{70} and C_{70}, I tried to deliberately delay the retention time by another way. Since the retention time is the result of affinity competition between the stationary phase and the mobile phase, delaying retention time requires increasing the stationary phase affinity and decreasing the mobile phase affinity. While the optimum stationary phase, 5PBB, has already been determined,[44,108] the effect of changing the mobile phase from toluene to a solvent with a lower fullerene affinity was still an open question. Therefore, I used a $1:1$ *n*-hexane/toluene mixture to replace toluene as the mobile phase, with all the other parameters, *e.g.* flow rate, unchanged.

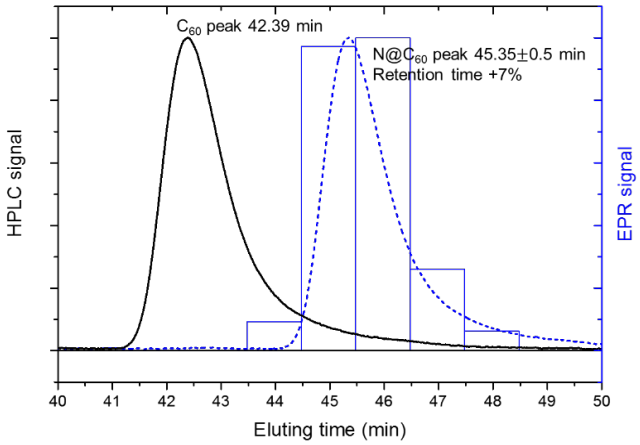


Figure 69 Comparison for HPLC trace for C_{60} and the reconstructed spin trace for N@C_{60} when $1:1$ *n*-hexane and toluene were used as the mobile phase. (5PBB 20×250 mm column and 18 ml/min flow rate) Data for N@C_{60} amounts were derived from spin-counting results by cw-ESR experiments, which were performed using a Magnettech MiniScope MS200 spectrometer by Mr. Harry Macpherson.

Similar to the analysis performed for N@C_{70} separation, the comparison of HPLC chart and ESR-reconstructed spin peak are shown in Figure 69. The retention time ratio α for

N@C_{60} and C_{60} was dramatically improved from the reported value[44] of 1.028 to 1.070 ± 0.012. Such delaying effect is more profound than changing C_{60} to C_{70}. The theoretical number of plates for the mixed solvent negligibly decreases from 6041 to 5929. One drawback of using *n*-hexane/toluene mixture is that it dissolves less fullerene, so the injection sample cannot be as concentrated as that for a pure toluene experiment. In addition, each HPLC peak takes longer to fully elute. Therefore, column capacity is low for this approach, and it is more suitable for the later stage of purification.

4.3.5 Discussion on the retention time ratio for further improvements

To understand the improvement to the retention time ratio α, (*i.e.* ${T_\mathrm{R}}^{(\mathrm{N@C_{60}})}/{T_\mathrm{R}}^{(\mathrm{C_{60}})}$), I built a qualitative model using a double Lennard-Jones potential (Figure 70). In this model, the analyte is constantly switching between the stationary and the mobile phases until it elutes. The retention time T_R is the sum of T_s and T_m, where T_s is the duration the analyte stays within the stationary phase, and T_m is the duration the analyte stays within the mobile phase, which is equal to the HPLC dead time T_0 (the time taken for the pure solvent to elute).

Namely,

$$T_\mathrm{R} = T_\mathrm{s} + T_\mathrm{m} = T_\mathrm{s}/T_\mathrm{m} \times T_0 + T_0 = (1 + T_\mathrm{s}/T_\mathrm{m}) \times T_0 \qquad \text{Eq.4.1}$$

Hence,

$$\alpha = {T_\mathrm{R}}^{(\mathrm{N@C_{60}})}/{T_\mathrm{R}}^{(\mathrm{C_{60}})} = \frac{1+{T_\mathrm{s}}^{(\mathrm{N@C_{60}})}/{T_\mathrm{m}}^{(\mathrm{N@C_{60}})}}{1+{T_\mathrm{s}}^{(\mathrm{C_{60}})}/{T_\mathrm{m}}^{(\mathrm{C_{60}})}} \approx \frac{{T_\mathrm{s}}^{(\mathrm{N@C_{60}})}/{T_\mathrm{m}}^{(\mathrm{N@C_{60}})}}{{T_\mathrm{s}}^{(\mathrm{C_{60}})}/{T_\mathrm{m}}^{(\mathrm{C_{60}})}} \qquad \text{Eq.4.2}$$

where, the approximation is achieved because both ${T_\mathrm{s}}^{(\mathrm{N@C_{60}})}/{T_\mathrm{m}}^{(\mathrm{N@C_{60}})}$ and ${T_\mathrm{s}}^{(\mathrm{C_{60}})}/{T_\mathrm{m}}^{(\mathrm{C_{60}})}$ are sufficiently larger than 1. Based on the potential model in Figure 70, where the ratio of $T_\mathrm{s}/T_\mathrm{m}$ is dependent on the difference between the Lennard-Jones potentials ($U_\mathrm{s} - U_\mathrm{m}$), I further obtained follows:

$$\alpha = \frac{e^{{U_\mathrm{s}}^{(\mathrm{N@C_{60}})} - {U_\mathrm{m}}^{(\mathrm{N@C_{60}})}}}{e^{{U_\mathrm{s}}^{(\mathrm{C_{60}})} - {U_\mathrm{m}}^{(\mathrm{C_{60}})}}} = e^{\Delta U_\mathrm{s} - \Delta U_\mathrm{m}} \qquad \text{Eq.4.3}$$

where, $\Delta U_\mathrm{s} = {U_\mathrm{s}}^{(\mathrm{N@C_{60}})} - {U_\mathrm{s}}^{(\mathrm{C_{60}})}$, and $\Delta U_\mathrm{m} = {U_\mathrm{m}}^{(\mathrm{N@C_{60}})} - {U_\mathrm{m}}^{(\mathrm{C_{60}})}$. Therefore, a larger ΔU_s

and a smaller ΔU_{m} is preferred for a large α. Due to the very low polarity of fullerenes, dispersion forces caused by polarizability will be the dominant factor when discussing the trends of ΔU_{s} and ΔU_{m} (Table 8). Because of the larger polarizability of N@C_{60} compared to C_{60}, its dipolar dispersion interaction with both the stationary and mobile phase are slightly larger ($\Delta U_{\mathrm{s}}, \Delta U_{\mathrm{m}} > 0$). As Figure 71 shows, a large dispersion force between the analytes and the stationary phase is preferred, as it increases ΔU_{s}, whereas a small dispersion force between the analytes and the mobile phase is also preferred, for it decreases ΔU_{m}. Therefore, the more polarizable PBB stationary phase showed better separation result than the less polarizable PYE stationary phase, and using less polarizable solvents such as *n*-hexane also improved the separation of N@C_{60}.

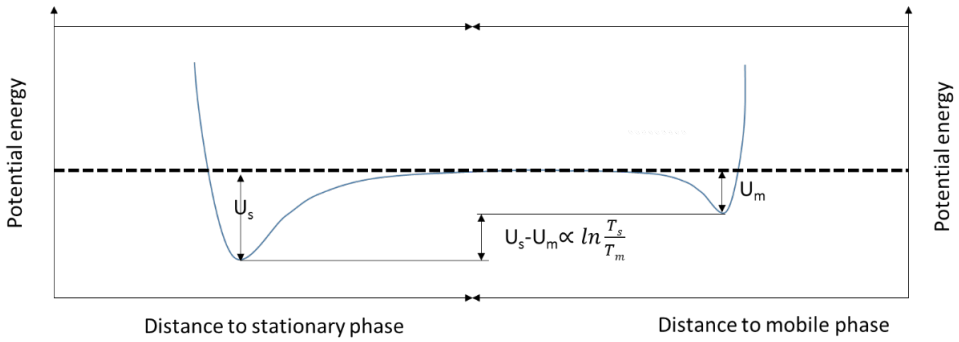


Figure 70 Illustration of the double Lennard-Jones potential model, describing the interaction competition between analyte/stationary phase and analyte/mobile phase, and governing the retention time of the analyte.

Based on the above analysis, if there is a solvent dissolving C_{60} and N@C_{60} by an intermolecular force other than the dispersion force, ΔU_{m} could become even lower. I recommend chloroform or dichloromethane, which are even less polarizable (8.53 and 6.48 $\mathrm{Å}^3$) than hexane, but have halogen bonding interactions to fullerene[216] which maintain the solubility.[217] As expected, preliminary experiment on using $4{:}\,1$ toluene/chloroform eluent has showed improved result to $1{:}\,1$ toluene/*n*-Hexane eluent, but more detailed analysis is still needed to quantitatively evaluate the improvement.

Table 8 Polarizabilities for analyte, stationary and mobile phase of HPLC. (Data labelled with * are calculated by website of "Chemicalize". According to the accuracy of predicting mono- and bis-bromo-benzene, the polarizability calculated for the stationary phase is estimable.)

Molecule	Bromo-benzene	1,2-dibromobenzene	Penta-bromo-benzene	Penta-bromo-benzyl silica
Polarizability ($Å^3$)	13.52[218]/13.09*	16.43[218]/16.18*	27.57*	41.79*
Molecule	C_{60}	$N@C_{60}$	Toluene	*n*-Hexane
Polarizability ($Å^3$)	82.7[219]	83.3[219]	12.4[218]	11.94[218]

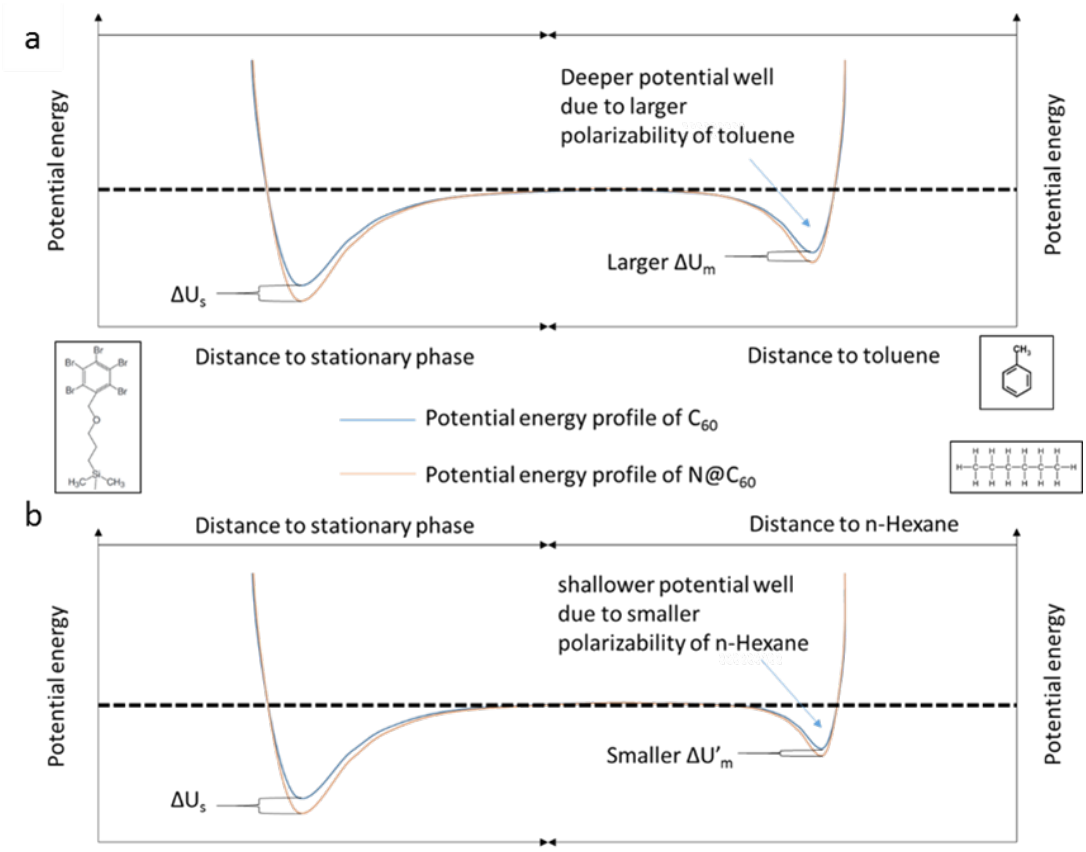


Figure 71 Comparisons of the double Lennard-Jones potential models for C_{60} (blue) and $N@C_{60}$ (orange) in PBB/toluene HPLC system (a) and in PBB/*n*-Hexane system (b).

4.4 Conclusions

This chapter focuses on optimization of the synthesis and purification of ENFs to improve the availability of the material. An overall five-fold productivity improvement has been accomplished by optimizing the ion implantation and the HPLC procedures. The synthesis was firstly improved by adding a LabVIEW programme for controllability and automatization. Optimized parameters and an upgraded ion source were also implemented for improved spin-yield of the product. The improvement is mainly achieved by enlarge the nitrogen ion dosage per fullerene molecule, due to its positive relationship with the spin-yield. Lastly, development on the *in-situ* product protection managed to enhance the productivity further by avoiding the continuous electron radiation, which decomposes the product. The improved productivity and efficiency resulting from different methods are summarized in Table 2 and Figure 72. The product quality characterized by the spin-yield of the crude product has been confirmed to be enhanced by $3\sim4$ times, together with a promotion on the time efficiency from 2 to 5, represented by the number of synthetic batches per week. In addition, increased labour efficiency was achieved by upgrading the synthetic model from manual to automatic operation. The raw material efficiency was first decreased due to the usage of the more powerful eH400 ion source, but, subsequently, I managed to partially mitigate the negative impact by *in-situ* product protection. Apart from the improved yield of ENF, I also observed that the formation of ENF is unaffected by whether or not the deposition target faces the ion source, which implies ENF synthesis occurs primarily in the vapour phase.

Table 9 Comparison of the synthesis method before and after each steps of optimization. * A spin-yield of *ca.* 40 ppm was achieved in my practice, possibly due to the degradation of the DC25s ion source.

Section	Method	Product quality	Time efficiency	Raw material efficiency	Labour efficiency
		Spin-yield (ppm)	Number of batches (500 mg) per week	Solubility of the fullerene soot (%)	Manual/auto

2.2.1	Original DC25s method[96]	Up to 60,[96]*	2	*ca.* 40%[96]	Manual
4.2.1	Above method + LabVIEW control	*ca.* 40	2	*ca.* 40%	Auto (If the DC25s is stable)
4.2.2	Above method + parameter optimization	*ca.* 80	1	*ca.* 40%	Auto (If the DC25s is stable)
4.2.3	Above method + eH400 new ion source	*ca.* 200	5	*ca.* 10%	Auto
4.2.4	Above method + *in-situ* product preservation	*ca.* 200	5	*ca.* 30%	Auto

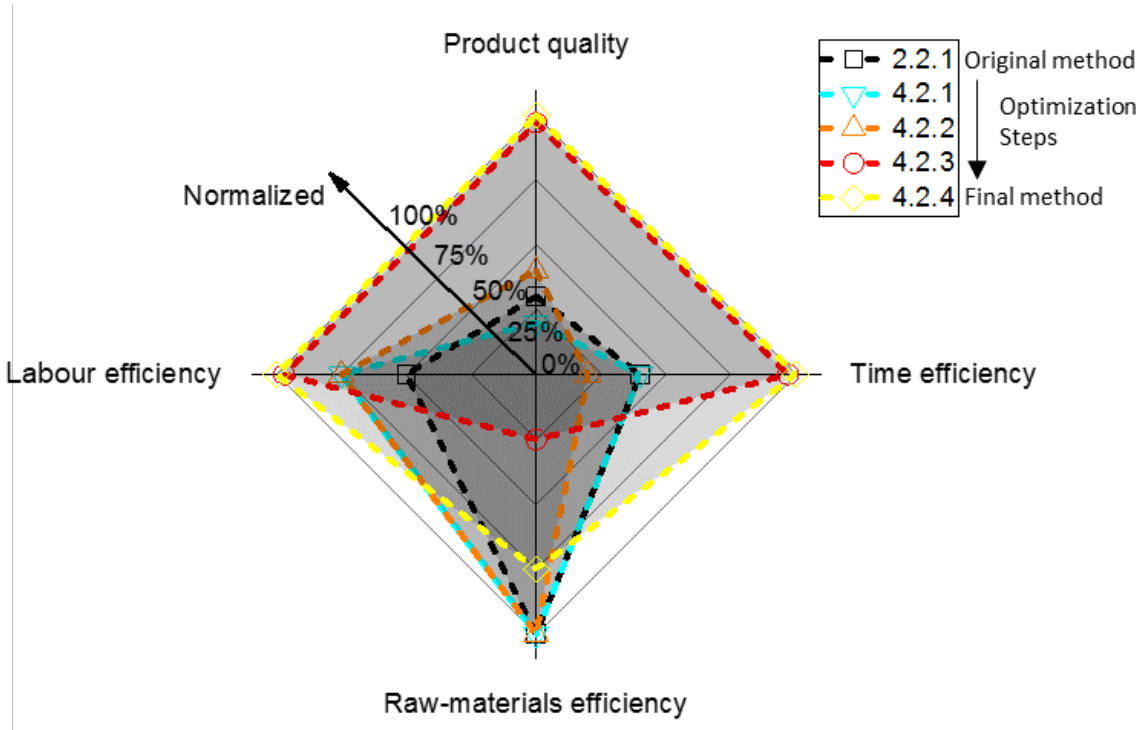


Figure 72 Radar chart for the comparison of the synthesis methods before and after each steps of optimization.

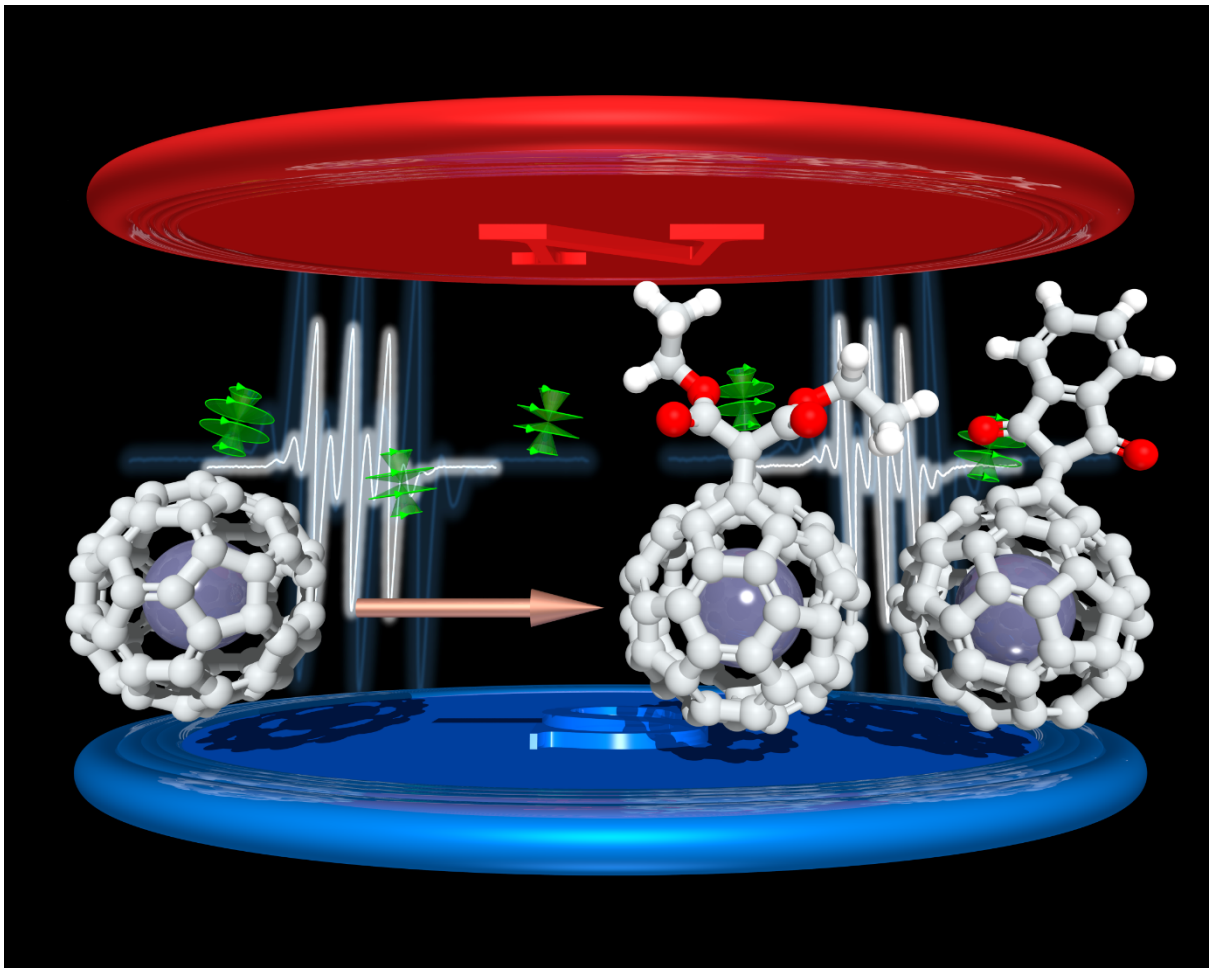
The result of the improvement on the purification is summarized in Table 10. For a given retention time ratio of 1.028, governed by the choice of the stationary and mobile phases (PBB and toluene), I estimated column efficiencies and capacities for different subtypes of PBB columns with variant HPLC methods. While overloading a 5PBB 20×250 mm column with a

7-time recycling and 18 ml/min flow rate showed an improved result compared to the old method recommended previously, I further enhanced the optimization by repeat injections, which increased the column capacity drastically. Meanwhile, I discussed ways to enlarge the small retention time ratio (α) between ENFs and empty-cage fullerenes. Better results were obtained either by using a larger carbon cage for the spin encapsulation or through applying a solvent with less fullerene affinity as the mobile phase, which leads to an increase of the retention time ratio α from 1.028 up to 1.047 and 1.070, respectively. As a qualitative explanation to the improved retention time ratio, a double Lennard-Jones potential model was developed to link the performance of HPLC separation to the dispersion forces caused by polarizability.

Table 10 Comparison of the purification methods

Section	method				evaluation		
	Column	Operation	Spin carrier	Mobile phase	Retention time ratio	Column efficiency	Capacity (ml/h)
2.2.2	15PBB 100× 500 mm	Normal	C_{60}	Toluene	1.028	876	150
4.3.1	5PBB 20× 250 mm	Overloading + 7-time recycling	C_{60}	Toluene	1.028	17016	12
4.3.2	5PBB 20× 250 mm	Repeat injection	C_{60}	Toluene	1.028	6041	90
4.3.3	5PBB 20× 250 mm	Repeat injection	C_{70}	Toluene	1.047	5480	30
4.3.4	5PBB 20× 250 mm	Repeat injection	C_{60}	Toluene/*n*-Hexane	1.070	5929	18

Chapter 5 Functionalising ENFs with Bingel reactions: Towards chemically tuneable qubit



5.1 Introduction

ENFs primarily rely on long spin relaxation time to be proposed as a qubit candidate, but some application competitors, such as ^{31}P spin doped in ^{28}Si and nitrogen-vacancy centres in diamond,[59,62] have even longer decoherence time (Figure 6). The reason why ENF is still of interest lies in its identity as a well-defined molecule. The carbon cage encapsulating the spin provides a vast range of possibilities for its chemical modification by a variety of exohedral functionalisation pathways, allowing researchers to alter its performance in a homogeneous and reproducible manner. Despite the fact that the chemical derivatization of ENFs is such a pivotal topic to fully exploit this exotic material, the literature is still rather unsystematic to date (reviewed in section 2.3). In order to fill the gap, this chapter focuses on developing the chemistry of ENFs using a spin-compatible Bingel reaction that I developed.

The Bingel reaction[122] was the first chemical reaction performed on $N@C_{60}$.[147,148] However, a more recent quantitative analysis of the Bingel addition to $N@C_{60}$, has shown a significant electron spin loss (up to 50%).[150,220] Before more sophisticated Bingel reactions are applied, it is worth studying the feasibility of using the Bingel reaction to functionalise ENFs and resolving the contradictory reports in the literature. As the first section of this chapter, I performed a typical Bingel reaction on $N@C_{60}$ without any spin loss by carefully controlling the reaction conditions (section 5.2.1). Moreover, I proposed a possible mechanism showing how the encapsulated nitrogen atom escapes from the fullerene cage during the reaction (section 5.2.2), which could explain the spin loss phenomenon observed in the previously reported result[150] and guide the synthesis of other $N@C_{60}$ derivatives.

My first example of applying the spin-compatible Bingel reaction is synthesizing spirocyclic-methano-ENFs. Fullerenes are difficult to align (reviewed in section 2.5), primarily due to their subspherical structure. Using the Bingel reaction to enlarge the molecular aspect ratio of ENF in a rigid way may resolve this structural disadvantage. As the second section of this chapter, I designed and synthesized five spirocyclic-methano-ENF derivatives, using

cyclo-1,3-dione type reagents to replace the commonly used malonates. With my study proving that cyclo-1,3-dione can effectively act as a malonate analogue for the Bingel reaction to take place on N@C_{60} (section 5.3.1) and N@C_{70} (section 5.3.2), the successful synthesis opened a better way of functionalising ENFs for a molecular rigidity and long aspect ratio. This type of fullerene derivatives will then show its advantages in the ENF alignment study reported in Chapter 7.

My second example of applying the spin-compatible Bingel reaction is to use it for β-cyclodextrin functionalisation of ENFs. Polar solvents are typically bad solvents for ENFs and their derivatives, which hinders their functionality and utility. Molecular surface modification of ENFs for water solubilisation could be a useful improvement, because it would make ENFs easier to handle chemically and more compatible with various application environments. Unfortunately, no water-soluble ENFs have been reported to date. Herein, by adapting a C_{60} water-soluble functionalisation method to ENFs, I report the first water-soluble ENF derivatives, and demonstrate a preliminary study on using the sharp spin signal of a water-soluble ENF to detect radicals.

5.2 Developing a spin-compatible Bingel reaction

5.2.1 Spin-Compatibility study of the Bingel reaction

To test the feasibility of the Bingel scheme for $N@C_{60}$ functionalisation, the simplest Bingel reaction (Figure 73) was performed on a spin-enriched $N@C_{60}/C_{60}$ mixture $(1:700)$ to synthesize **DEM-N@C_{60}** in a quantitative manner.

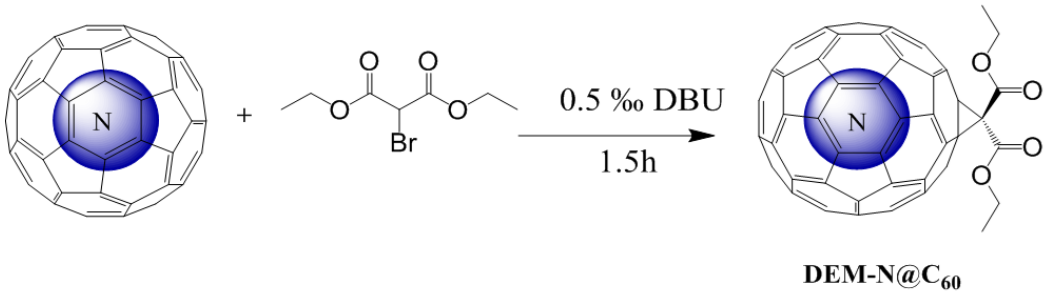


Figure 73 Reaction to synthesize **DEM-N@C_{60}**. Experimental method recorded in section 3.3.1.1.

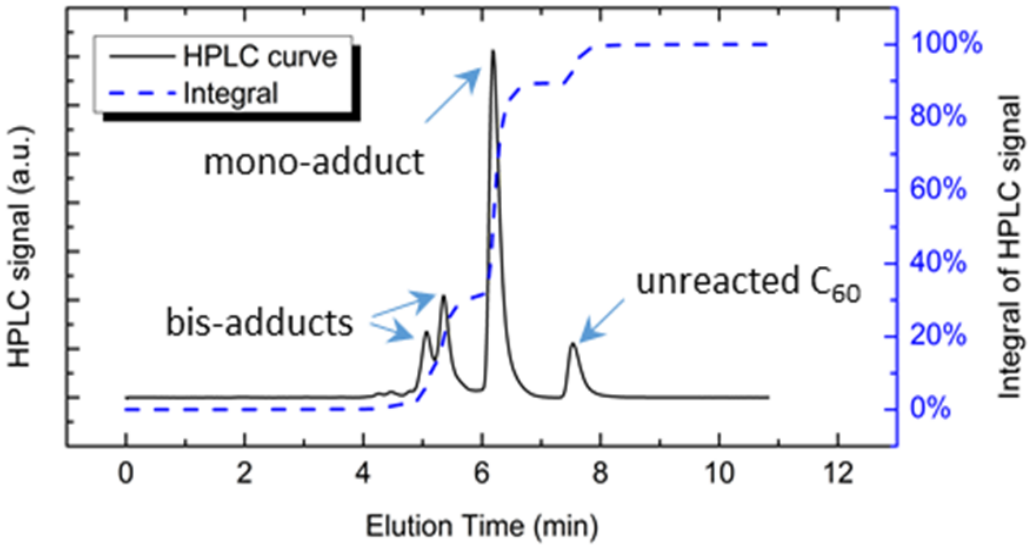


Figure 74 HPLC chart for the separation of the reaction mixture after a 1.5-hour reaction. (BuckyPrep-M 28×250 mm column, toluene, and 16 ml/min flow rate,)

0.34 mg $(1.4\ \mu mol)$ of diethyl bromomalonate was dissolved in 2.5 ml of toluene with 1 mg $(1.4\ \mu mol)$ of $N@C_{60}$, followed by an addition of 0.42 ml of $0.5‰$ DBU- toluene solution $(1.4\ \mu mol)$, dropwise. The mixture of reagents in stoichiometric ratio was stirred under an argon atmosphere at room temperature and isolated from light. After a 1.5-hour reaction, **DEM-**

N@C$_{60}$ was obtained with some by-products caused by multi-additions, which was subsequently separated by collecting the HPLC peak at 6.2 minutes (Figure 74). Assuming the same extinction coefficients for starting and resulting materials based on the same chromophore of fullerene, the integration of the HPLC absorption signal shows that the yield is approximately 55%.

The isolated mono-adduct (a mixture of **DEM-N@C$_{60}$** and **DEM-C$_{60}$**) was then characterized by MALDI-MS, UV/Vis spectroscopy and ^{1}H-NMR spectroscopy. Due to the low mole ratio between **DEM-N@C$_{60}$** and **DEM-C$_{60}$**, a direct structural characterization on **DEM-N@C$_{60}$** is not viable. Nevertheless, considering the similarity of the chemical reactivity of N@C$_{60}$ to C$_{60}$, a similar structure of **DEM-N@C$_{60}$** can be anticipated based on the characterization of **DEM-C$_{60}$**. As all reported N@C$_{60}$ derivatives were characterized in this way (reviewed in section 2.3.3), the rest of ENF derivatives synthesized in this work will keep use this assumption. The MALDI-MS (Figure 75a) was recorded in a negative ionization mode with DCTB being the matrix (m/z (M^-): 878.1, 879.1, and 880.1). Compared with the theoretical prediction (m/z: 878.058, 879.061, 880.065, *etc.*), the consistency of the mass/charge ratio and the isotope distribution of the molecular ion peaks proved the covalent linkage of the addend and the fullerene cage. The UV/Vis spectrum (Figure 75b) measured in toluene was similar to that of C$_{60}$ absorption,[17,203] with a broad range of overlapping absorption bands, because the fullerene moiety is the main chromophore of the product. The additional $430\ \mathrm{nm}$ absorption band compared to C$_{60}$ shows the evidence of a successful [6,6] bond addition,[221,222] because this $430\ \mathrm{nm}$ peak is absent in [5,6] fulleroid structures.[223,224] The ^{1}H-NMR spectrum (Figure 75c) measured in $CDCl_3$ confirms the two types of chemical environments for protons in the product, which give rise to a quartet signal at $\delta = 4.60$ and triplet signal at $\delta = 1.55$. The ratio of the peak integral for the quartet signal and triplet signal was measured to be $2:3$, matching the number ratio of protons in the targeted product. The remaining proton signals were triggered by the solvent residuals labelled in the spectrum.

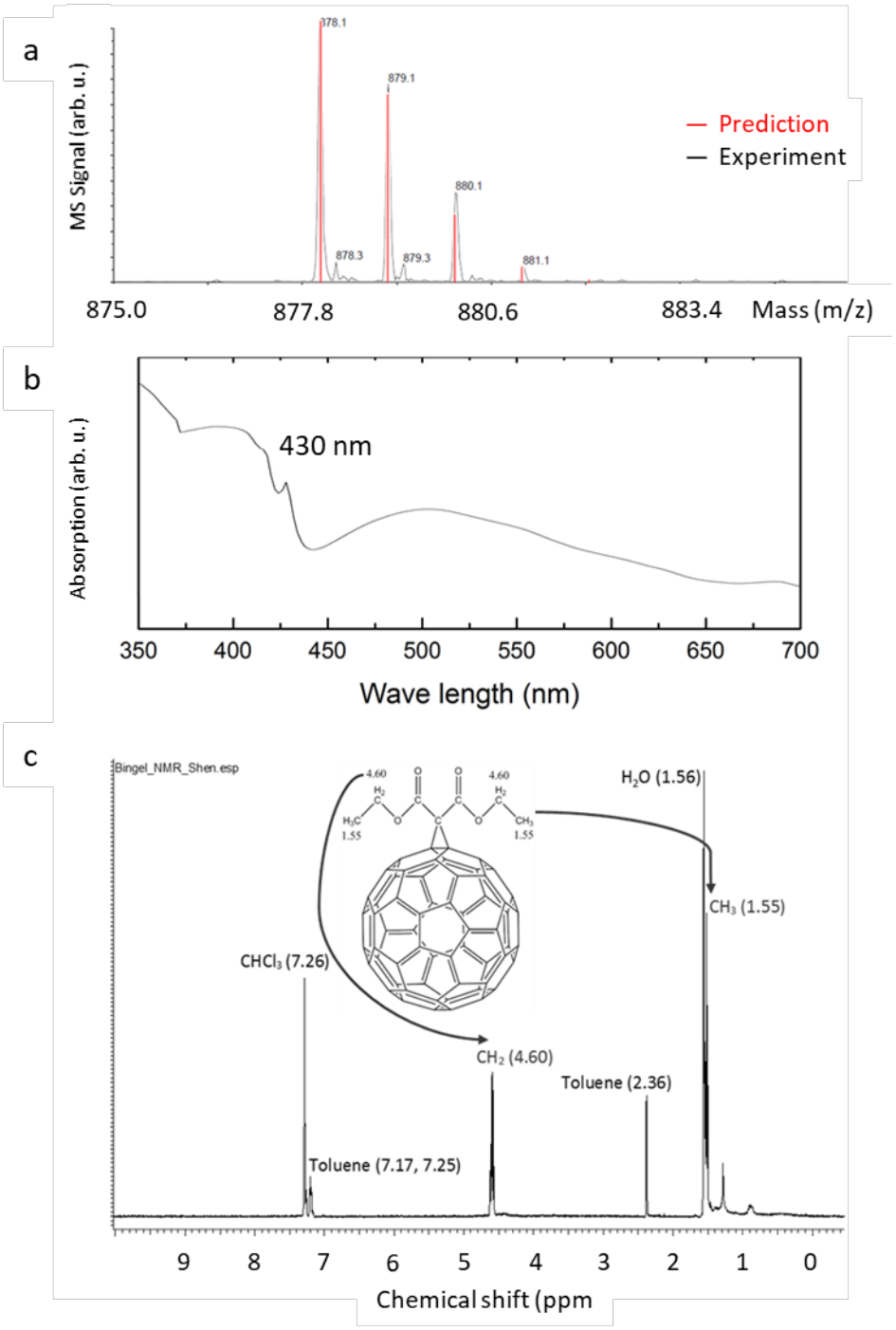


Figure 75 (a) MALDI-MS of DEM-N@C_{60} (DCTB matrix and negative mode), (b) UV/Vis spectrum of DEM-N@C_{60} (*c.a.* $0.4\ \mathrm{mg/ml}$ toluene solution), (c) ^{1}H-NMR spectrum of DEM-C_{60} ($400\ \mathrm{MHz}$, room temperature and $CDCl_3$ solution). The MALDI-MS was obtained by Mass Spectrometry Facility at Swansea University.

While the above methods characterize **DEM-C_{60}** in the product mixture, cw-ESR spectroscopy is the only sensitive way to confirm the formation of **DEM-N@C_{60}**. A solid-state cw-ESR spectrum was obtained by freezing the sample in a toluene matrix at $100\ \mathrm{K}$ (Figure 76). Compared to pristine N@C_{60}, the *g*-factor (2.00243) and HFCC ($A_{\mathrm{iso}}^{(\mathrm{N})} = 15.86\ \mathrm{MHz}$) were

found to be almost unchanged within the experimental error. Nevertheless, due to the functionalisation, each peak of the N@C_{60} triplet signal (Figure 3a) splits into three peaks, showing two small peaks separately located on both sides of the central spin signal. According to the previous study on ENF derivatives reviewed in section 2.3.3, the side peaks are attributed to the small ZFS caused by the symmetry breaking effect of the chemical functionalisation. The ZFS parameters of $D = 8.4\ \mathrm{MHz}$ and $E = 0.36\ \mathrm{MHz}$ were obtained by EasySpin simulation.[209] Such a small ZFS parameter are consistent with the Bingel reaction products seen in previous work.[147,148,150] Combined with the aforementioned structural characterization results for **DEM-C_{60}**, the presence of the small ZFS effect in the product proves the successful synthesis of **DEM-N@C_{60}**.

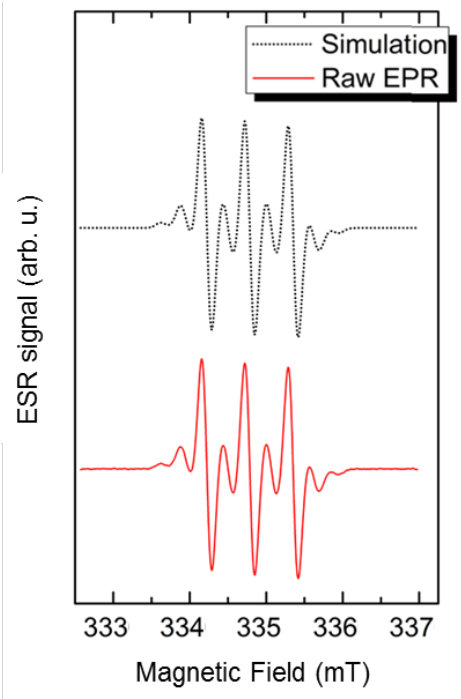


Figure 76 Solid-state cw-ESR spectrum of DEM-N@C_{60} in the frozen toluene and its best fit simulated by Easyspin[209] (programme B in appendix). Data for the solid-state cw-ESR experiment were acquired using a Bruker EMX spectrometer. ($9.3799\ \mathrm{GHz}$, $48.0\ \mathrm{dB}$ attenuation, $100\ \mathrm{K}$ temperature, and $0.08\ \mathrm{mT}$ modulation amplitude.)

An estimation of the spin-loss ratio during the reaction was then conducted. To do this the reaction was repeated under the same condition, and a series of $0.2\ \mathrm{ml}$ aliquots were taken from the reaction vessel to perform spin counting analysis at 0, 10, 20, 40 and 80 minutes after starting the reaction (Figure 77a). All aliquots were quickly measured, and then

immediately injected back into the reaction vessel to minimize the disturbance on the reaction proceeding. Since the reaction was performed at room temperature and protected under argon, the volumes of solution before and after the reaction were found to be unchanged. It means all measured samples were of equal concentration and, therefore, directly comparable. According to the spin number evolution (Figure 77b), a high percentage of the spin signal was retained (94%).

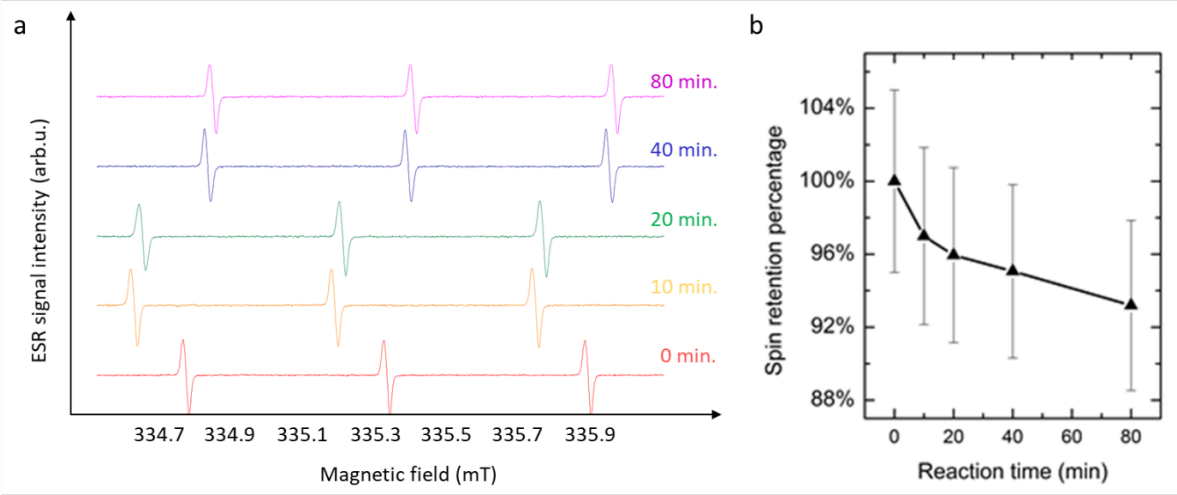


Figure 77 (a) cw-ESR data of the reaction mixture as different reaction times. (b) Evolution of the spin retention ratio during the reaction of synthesizing DEM-N@C_{60}, according to the double integral of signals presented in panel (a). Data for spin retention ratios were derived from spin-counting results by cw-ESR experiments, which were performed using a Magnettech MiniScope MS200 spectrometer. The signal shift in the magnetic field is due the slightly different microwave frequency used. The 5% error bar is based on error analysis of the Magnettech MiniScope MS200 (supporting information A)

5.2.2 Spin-destructive effect caused by excess of auxiliary base

To further understand the high spin retention ratio obtained and possible side-reactions causing the spin loss, I investigated the influence of the reaction conditions and found that the spin retention ratio is highly dependent on two parameters. One is the mole ratio between the base and malonate, and the other is the concentration of base added. This was confirmed by repeating the reaction with excess DBU and non-diluted DBU, respectively, followed by comparing their spin number evolutions (Figure 78). It shows that a much more significant spin-loss ratio (60%) occurs if a fourfold excess of DBU is added, whereas the spin-loss ratio observed under the stoichiometric condition is only 6%. It is also worth noting that the spin

number continued decreasing after the main reaction had finished. In terms of the influence of the DBU concentration on the spin retention ratio, applying pure DBU will lead to a rapid decrease in spin signal at the beginning of the reaction, resulting in a final spin-loss ratio of 18%, compared with the value of 6% achieved using dilute DBU. The extra spin loss due to usage of the concentrated base could be correlated with a local excess of DBU arising from a non-uniform mixture between different reagents at the initial stage of the reaction.

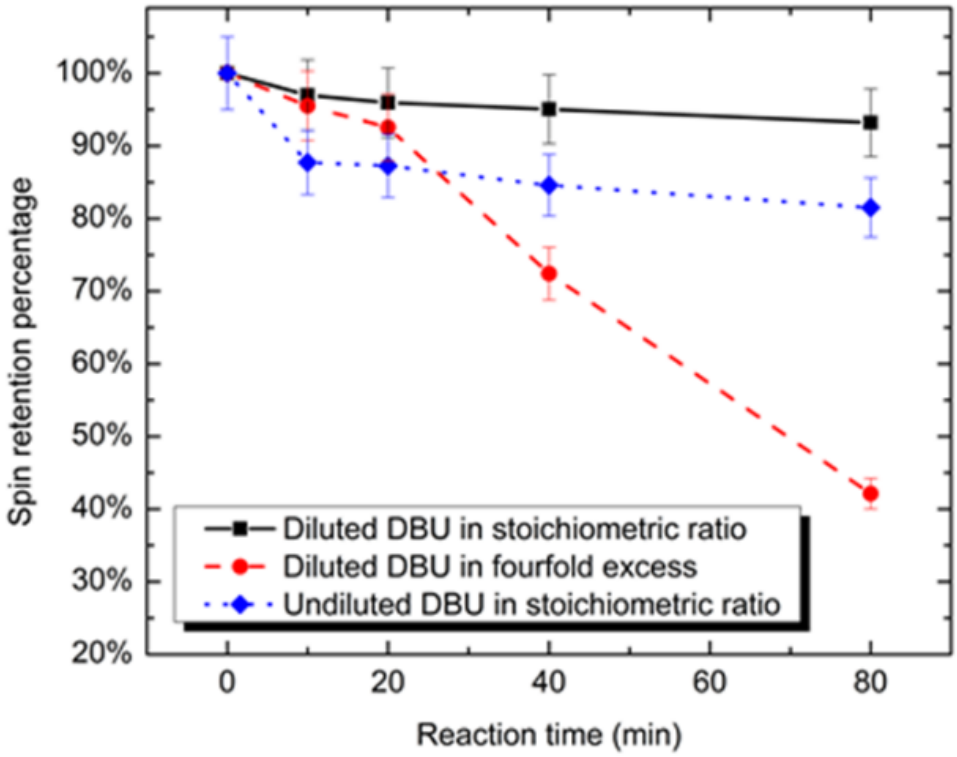


Figure 78 Different evolutions on the spin retention ratio when repeating the reaction using different amounts or concentrations of DBU. Data for spin retention ratios were derived from spin-counting results by cw-ESR experiments, which were performed using a Magnettech MiniScope MS200 spectrometer. (Quantitative UV/Vis and cw-ESR data documented in supporting information E). The 5% error bar is based on error analysis of the Magnettech MiniScope MS200 (supporting information A)

The above quantitative analysis suggests that a direct interaction between DBU and the ENF molecule or its derivatives is the fundamental cause of the spin loss. When the mole ratio is stoichiometric, the reaction will proceed smoothly with a typical Bingel reaction mechanism (Figure 79),[225] and all DBU is converted to its conjugate acid. However, if there is more DBU than halomalonate, the excess base can directly react with the fullerene or fullerene derivatives to form dissociated diradicals (Figure 80), which has been reported during a Bingel

reaction with an excessive amount of DBU,[226] as well as when reacting C_{60} with DBU directly.[140] Since the dissociated diradical experiences a long lifetime before finally combining to form a zwitterion and precipitating, there is sufficient time for $N@C_{60}$ decomposition to take place during the dissociated diradical stage.

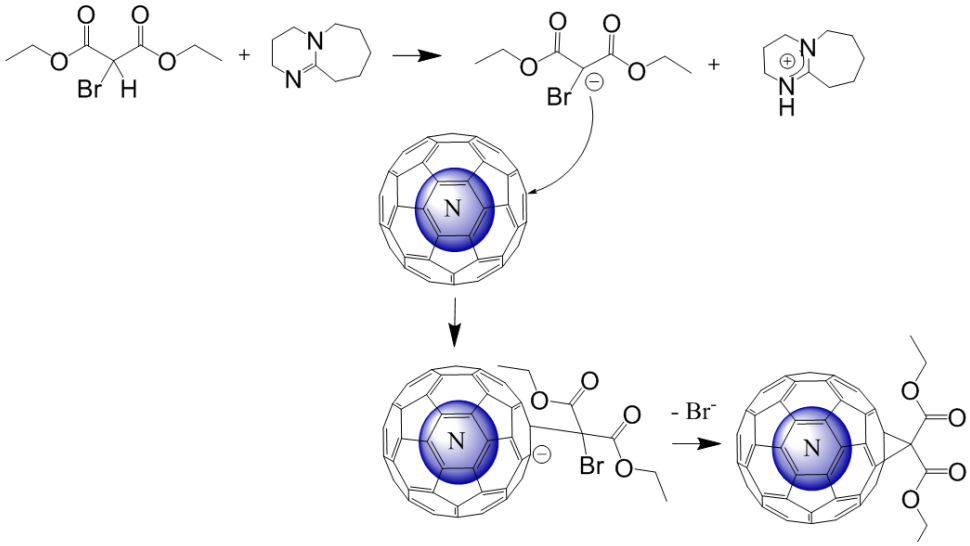


Figure 79 Reaction mechanism of Bingel reaction of $N@C_{60}$.

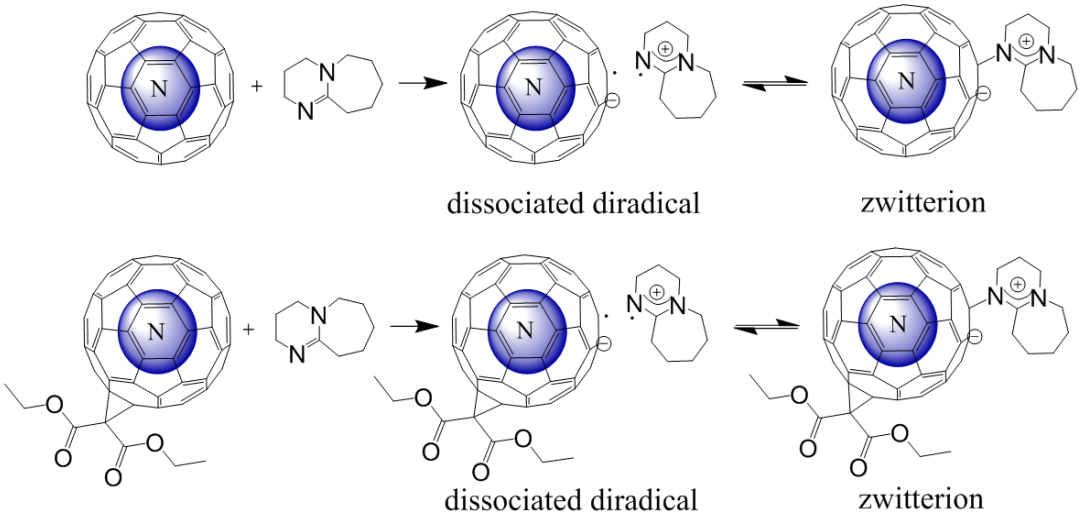


Figure 80 Direct interactions between DBU and $N@C_{60}$ or its derivative, which form a dissociated diradical and zwitterion.

Taking the decomposition of DBU^{+}–$N@C_{60}^{-}$ diradical as an example (Figure 81), this procedure is more likely to take place compared to that of pristine $N@C_{60}$. The possible reason can be summarized as follows. Firstly, the presence of the dangling bond on the C_{60}^{-} radical

may facilitate the N atom to approach the cage shell from the potential well located in the cage center.[110] Secondly, the closed-shell structure of the intermediate for $N@C_{60}^-$ decomposition is electronically more stable than that of pristine $N@C_{60}$. Besides, the smaller steric hindrance during the conformation inversion of the incarcerated[227] nitrogen atom further accelerates its decomposition. For the DBU^+–functionalised $N@C_{60}^-$ diradical, I propose that the spin loss mechanism is principally the same, because the functional group has a limited influence on the local structure of cage where the decomposition takes place.

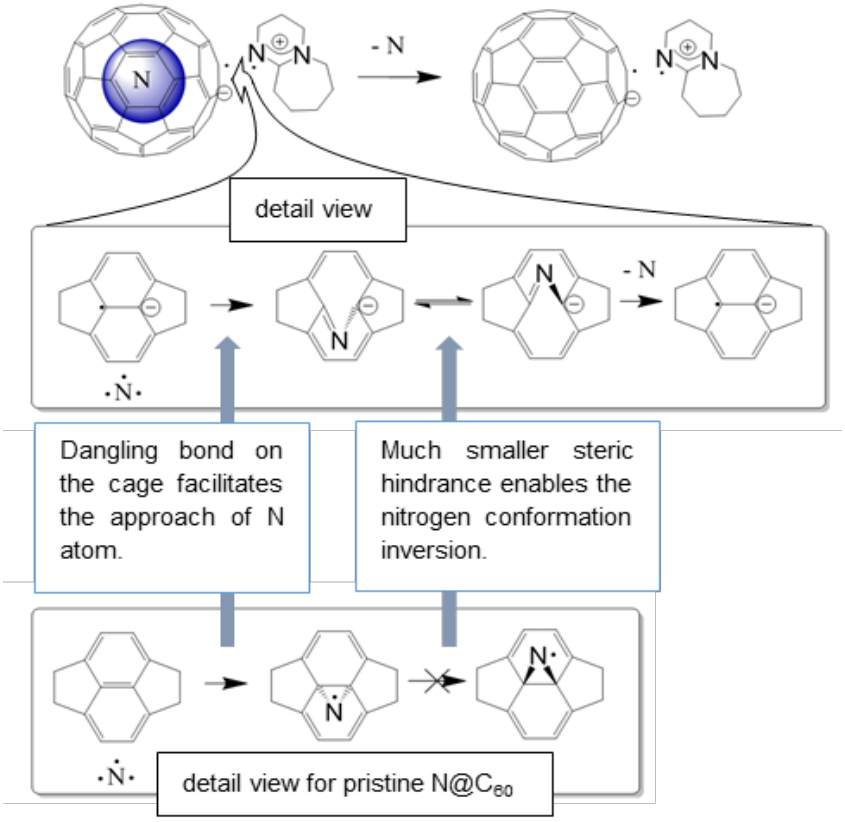


Figure 81 Decomposition pathway for $N@C_{60}^-$ in the zwitterion compared with that of pristine $N@C_{60}$.

I have qualitatively proven that the direct interaction between DBU and ENF is the fundamental cause of the spin loss (Figure 82). By a direct reaction between ENF and sufficient DBU for 1.5 hours, fullerene anions were formed, which show a broad spin signal. A noticeable signal in the $N@C_{60}$ signal range is displayed by the red spectra in Figure 82 (*g*-factor: 2.001, peak-to-peak linewidth (ΔH_{pp}) *ca.* 0.2 mT.) Another even broader spin signal was measured with a larger modulation amplitude and a stronger microwave power, both of which

are not suitable to measure ENFs, hence not compared here. (It has been controversial previously whether the origin of the $0.2\ \mathrm{mT}$ peak is the C_{60} mono-anion or not. While a considerable amount of literature directly assign the spin signal to C_{60}^- by mistake,[228] later research pointed out the signal of C_{60}^- has a linewidth as broad as $1.64\ \mathrm{mT}$[229] and a relaxation time $T_{1,2}$ as short as $1-10\ \mathrm{ns}$,[207] and the more noticeable sub-mT peak is an inevitable $C_{120}O^-$ by-product during the preparation of C_{60}^-.)[229,230] The typical spin signal of $N@C_{60}$ was completely suppressed by the fullerene anion signal. Since all reaction conditions were kept the same as for the previous Bingel reaction, the result suggests that DBU can directly interact with ENF and scavenge its spin signal. Moreover, after adding acid to neutralize the DBU, almost no spin signal was recovered (Figure 82). This means the endohedral system has irreversibly decomposed.

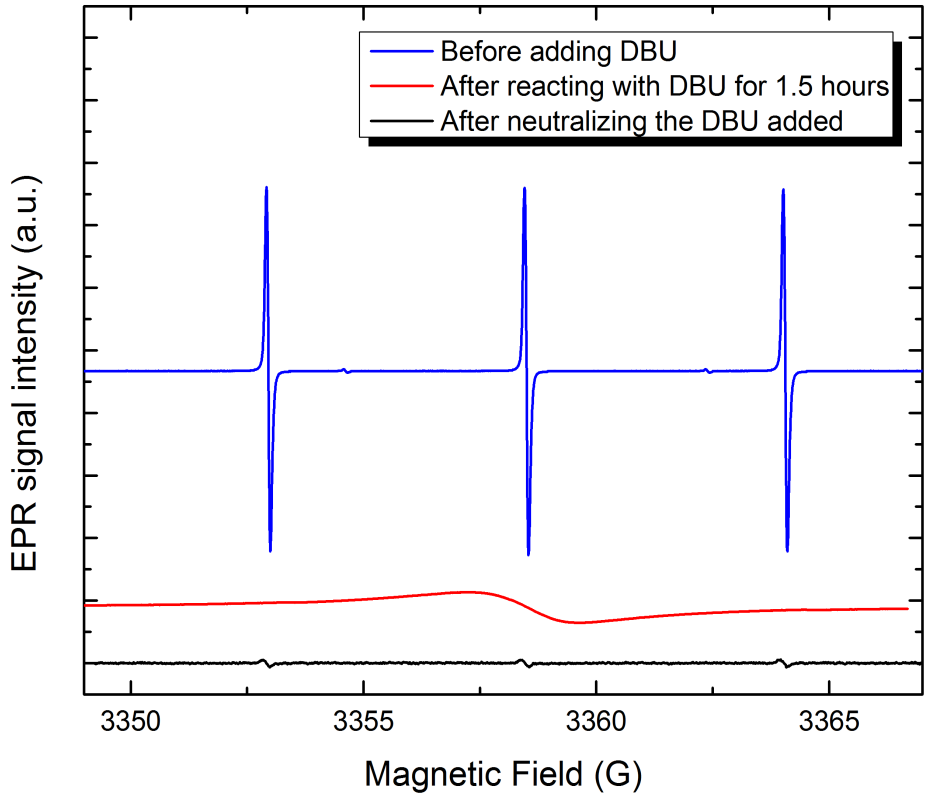


Figure 82 Significant influence of DBU on the spin signal of $N@C_{60}$, Data acquired using a Magnettech MiniScope MS200 spectrometer. (Experimental conditions: Blue: $9.4070\ \mathrm{GHz}$, $30.0\ \mathrm{dB}$ attenuation, room temperature, and $0.02\ \mathrm{mT}$ modulation amplitude. Red: $9.4325\ \mathrm{GHz}$, $30.0\ \mathrm{dB}$ attenuation, room temperature, and $0.20\ \mathrm{mT}$ modulation amplitude. Black: $9.4084\ \mathrm{GHz}$, $30.0\ \mathrm{dB}$ attenuation, room temperature, and $0.02\ \mathrm{mT}$ modulation amplitude.)

With the above analysis, the 50% spin loss[150] reported during the Bingel reaction reviewed in section 2.3.3 can now be explained. The halomalonate was synthesized *in situ* by adding iodine, malonate, and non-diluted tert-butyliminotris(dimethylamino)phosphorene (P_1-*t*Bu) which is stronger than DBU named. Therefore, the destructive interaction between the strong base and the ENF triggered the spin loss.

5.3 Synthesis of spirocyclic-methano-ENFs for rigid and elongated molecular geometry

5.3.1 Spirocyclic-methano-N@C_{60}

Ordinary Bingel reactions are performed using malonate esters. The free rotation of the σ-bond linking to the ester groups makes the addends flexible (Figure 83). Thus, the long molecular aspect ratio introduced by such malonates does not lead to rigid molecules, and reliable conformational control of the ENF derivatives could not be expected. If a Bingel reaction can be performed on with cyclo-1,3-dione type reagents, which act as analogues of the malonate due to the similar acidity of the α-hydrogen between two carbonyl groups, the rotation of the σ-bond will be limited (Figure 83). Moreover, the smaller the spirocycle is, the less flexible of the addend will be. The focus of this section is to introduce rigid addends to the ENF system by preparing spirocyclic-methano ENFs. The application of the rigid addend to co-axial dimerization and orientational alignment of ENFs will be discussed in Chapter 6 and Chapter 7, respectively.

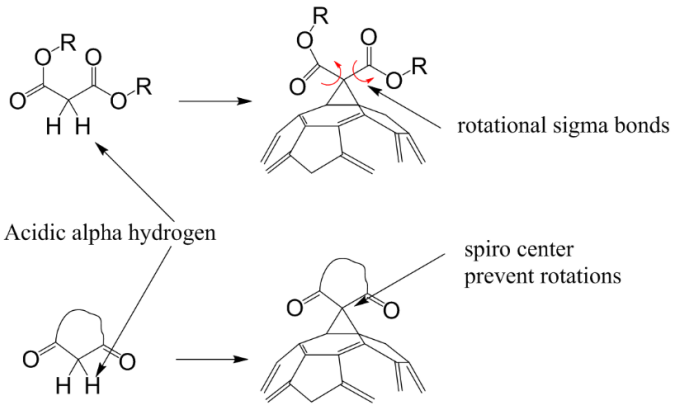


Figure 83 Comparison of using malonate and cyclo-1,3-dione to do the Bingel reaction

Before this work, only one cyclo-1,3-dione type reagent was used to perform a Bingel reaction on C_{60}, but it contained a flexible 26-membered ring, which has limited steric effect to prevent the rotation of the σ-bond.[231] In addition, a 1,3-indandione having the desired small cyclo-1,3-dione structure has been added onto C_{60} successfully with a diazo radical addition

reaction.[232] In comparison to the Bingel reaction, the diazo radical addition has not been reported for N@C_{60}. A higher reaction temperature, a longer reaction time, as well as a more sophisticated isomerization of [5,6] and [6,6] addition, makes the reported reaction difficult to apply to N@C_{60}.

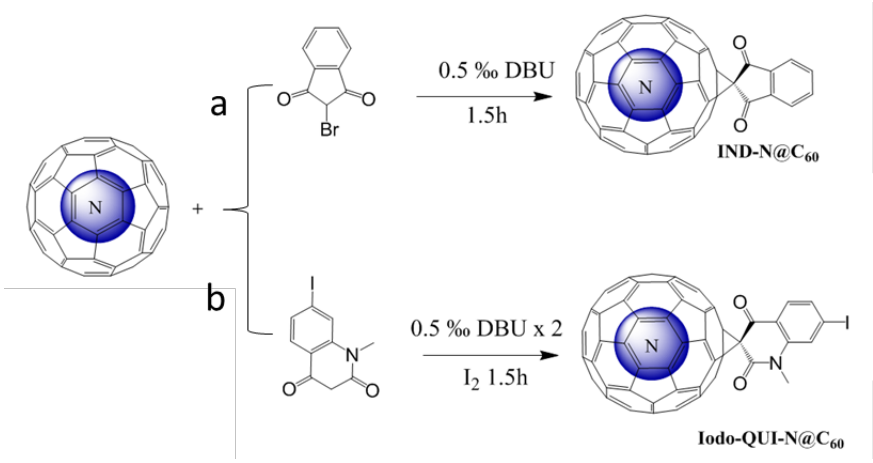


Figure 84 Reactions introducing spirocyclic-methano-addends to N@C_{60} for the functionality of the molecular rigidity and long aspect ratio, using the Bingel reactions with (a) a halogenated malonate analogue and (b) a non-halogenated malonate analogue (no halogen at position 3, the iodine at position 7 is inert for this reaction). Experimental methods recorded in section 3.3.1.2 and section 3.3.1.3, respectively.

Therefore, I investigated adding halogenated 1,3-indandione to N@C_{60} with a Bingel scheme, to obtain a the desired spirocyclic structure (Figure 84a). The spirocyclic-methano functionalisation was then further generalized with another reaction, which prepared the halogen substitution of the malonate analogue *in situ* (Figure 84b). A third spirocyclic-methano-N@C_{60} was also attempted. Due to a poor HPLC separation result, its NMR data still contained impurities. Therefore, the preliminary results of the third spirocyclic-methano-N@C_{60} (supporting information F) is not discussed in the main text.

The synthesis of **IND-N@C_{60}** started with a bromo substituted reagent (2-Bromo-1,3-indandione) and used the identical spin-compatible Bingel reaction conditions reported in section 5.2.1. With the synthetic procedure documented in section 3.3.1.2, $1\ \mathrm{mg}$ of N@C_{60}/C_{60} mixture, $0.32\ \mathrm{mg}$ of 2-bromo-1,3-indandione and $0.42\ \mathrm{ml}$ of $0.5‰$ DBU/toluene solution was reacted for 1.5 hours to prepare **IND-N@C_{60}**. According to the HPLC separation (Figure 85a), using the BuckyPrep-M column and toluene eluent, the yield was *ca.* 55%. The synthesis of

Iodo-QUI-N@C_{60} was achieved using the modified Bingel reaction scheme, which involves an addition of a halogenating agent to generate the halogenated malonate analogue *in situ*. The halogenation consumed one equivalent base to neutralize the halogen hydride. Following the spin-compatible criterion of avoiding direct interaction between DBU and fullerene, two-equivalent dilute DBU (0.8 ml of $0.5‰$ DBU/toluene solution) and one equivalent iodine (0.4 mg) were used to react with the ENF (1 mg of N@C_{60}/C_{60} mixture) and the malonate analogue (0.5 mg of 1-methyl-7-iodo-1H-Quinoline-2,4-dione). To thoroughly dissolve the malonate analogue with a slightly increased polarity, 10% DMF was added to the reaction solution. After a 1.5-hour reaction, the yield of **Iodo-QUI-N@C_{60}** was estimated to be 45%, based on the HPLC separation trace with a 5PYE column and toluene eluent (Figure 85b). In order to purify the mono-product, whose peak locates closely after that of the starting material in the HPLC chart, the purification was performed using three HPLC recycles, until a clear separation was obtained. Overall, both reactions successfully preserved electron spin, which further suggests that the spin-compatible Bingel conditions are also applicable to modified Bingel reactions where halogen substitution takes place *in situ*. The HPLC traces for the spirocyclic-methano ENFs were found to be non-conventional. In contrast to ordinary derivatives, which elute considerably faster than the pristine fullerene in HPLC (*e.g.* Figure 74), **IND-N@C_{60}** and **Iodo-QUI-N@C_{60}** both showed a certain extent of delay on the retention time. This could be caused by the spirocyclic structure and its resulting rigidity.

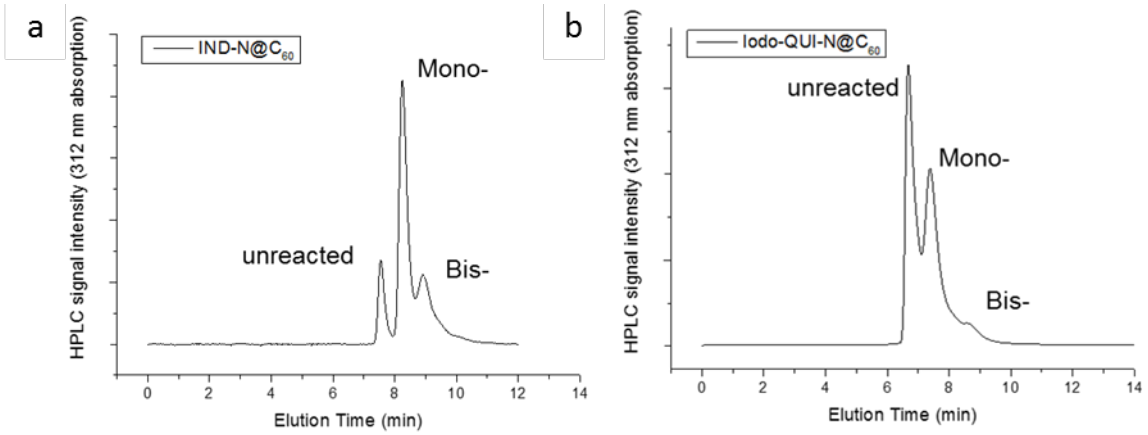


Figure 85 HPLC separation of (a) IND-N@C_{60} (BuckyPrep-M 28x250 mm column, toluene, and 16 ml/min flow rate), and (b) Iodo-N@C_{60} (5PYE 4.6x250 mm column, toluene, and 4 ml/min flow rate).

Both two types of isolated mono-adducts were then characterized by UV/Vis spectroscopy, MALDI-MS, and ^{1}H-NMR spectroscopy. For **IND-N@C$_{60}$**, the UV/Vis spectrum (Figure 86a) measured in toluene showed a strong resemblance to the absorption of **DEM-N@C$_{60}$**, because of the same [6,6] bond addition causing the $430\ \mathrm{nm}$ band[221,222] and fullerene moiety chromophore leading to the rest rich spectral patterns. The MALDI-MS (Figure 86b) was recorded in a negative ionization mode with DCTB being the matrix (m/z (M^-): 864.0, 865.0, 866.0 and 867.0), which is consistent with the theoretical prediction for the molecular ion peaks (m/z: 864.021, 865.024, 866.028, 867.031, *etc.*). The ^{1}H-NMR spectrum (Figure 86c) measured in $CDCl_3$ confirms two types of chemical environments for protons in the product, displaying two quartet signals at $\delta = 8.15$ and $\delta = 7.96$, respectively. The ratio of their integrals was measured to be $1:1$, agreeing with the ratio of proton numbers in the targeted product. The remaining proton signals were caused by the solvent residuals.

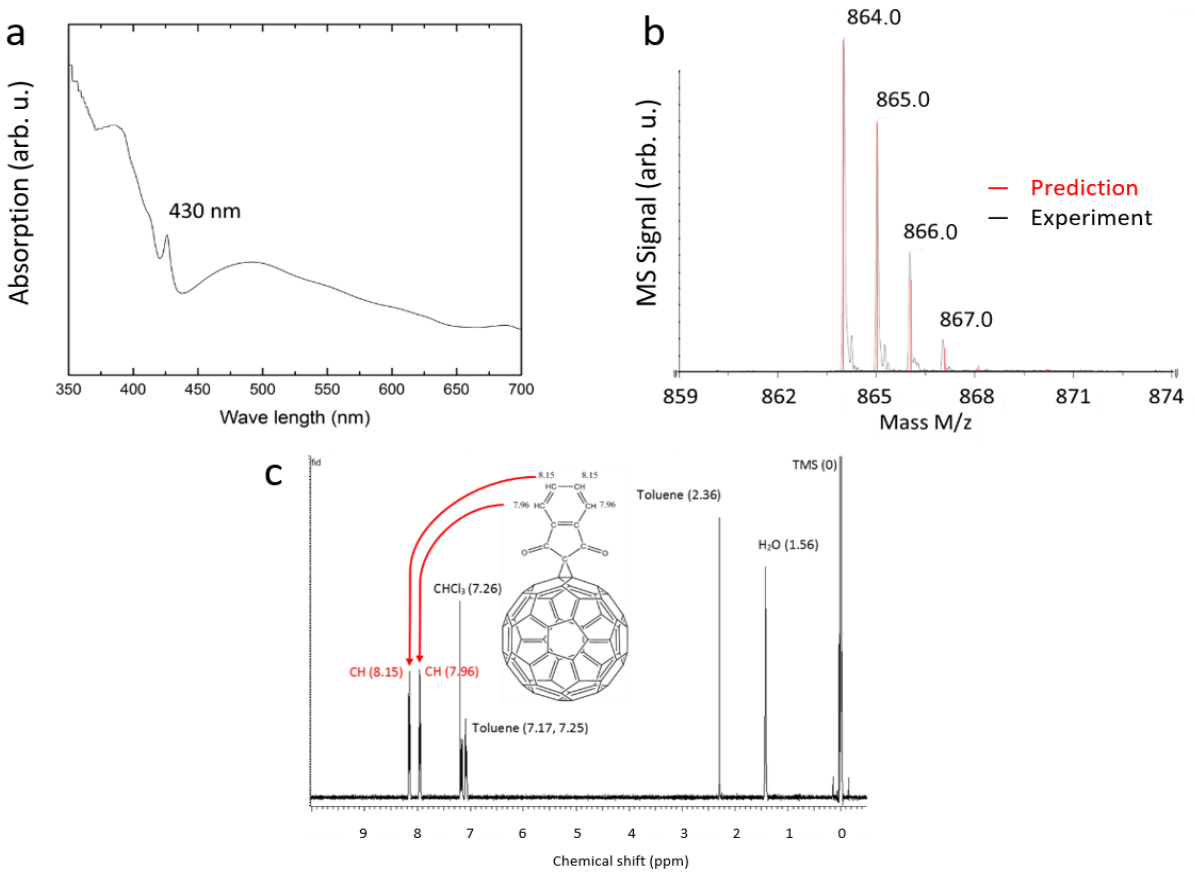


Figure 86 (a) UV/Vis spectrum of IND-N@C_{60} (*c.a.* $0.5\ \mathrm{mg/ml}$ toluene solution), (b) MALDI-MS of IND-N@C_{60} (DCTB matrix and negative mode), and (c) ^{1}H-NMR spectrum of IND-N@C_{60} ($400\ \mathrm{MHz}$, room temperature and $CDCl_3$ solution). The MALDI-MS was obtained by Mass Spectrometry Facility at Swansea University.

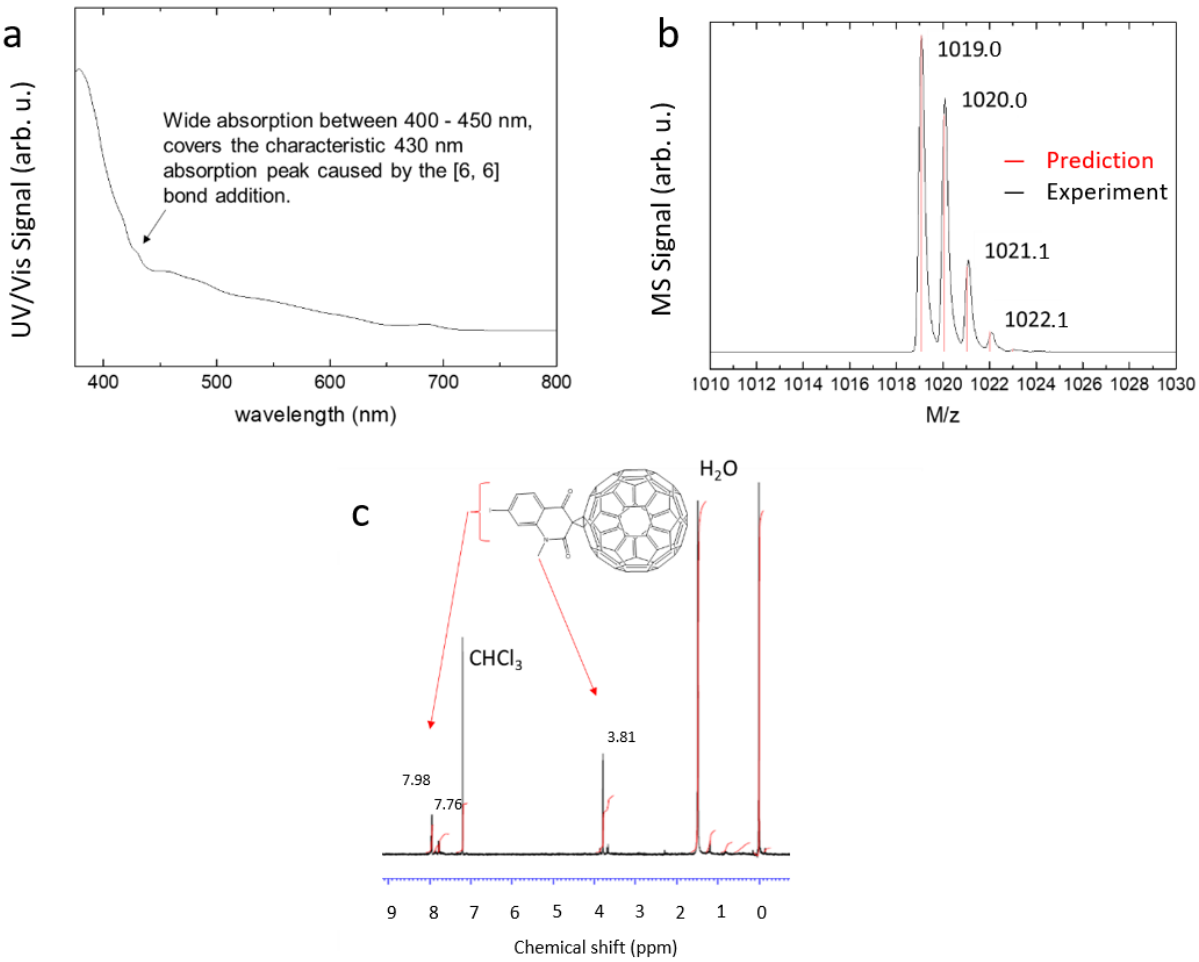


Figure 87 (a) UV/Vis spectrum of Iodo-QUI-N@C_{60} (*c.a.* $0.1\ \mathrm{mg/ml}$ toluene solution), (b) MALDI-MS of Iodo-QUI-N@C_{60} (DCTB matrix and negative mode), and (c) ^{1}H-NMR spectrum of Iodo-QUI-N@C_{60} ($400\ \mathrm{MHz}$, room temperature, and $CDCl_3$ solution).

For **Iodo-QUI-N@C_{60}**, a same set of characterization data was obtained. The UV/Vis spectrum (Figure 87a) measured in toluene showed a C_{60} absorption, but the valley between the wavelength of 400~450 nm was disappeared. This could be attributed to the absorption of the addend.[233] The [6,6] bond addition absorption band[221,222] was barely detectable as it was covered by the additional absorption of the addend between $400{\sim}450\ nm$. As the molecular ion peaks predicted (m/z: 1018.944, 1019.948, 1020.951, 1021.954, *etc.*), the MALDI-MS (Figure 87b) confirmed the product in a negative ionization mode with DCTB used as the matrix (m/z ($\mathrm{M^-}$): 1019.0, 1020.0, 1021.1 and 1022.2). The ^{1}H-NMR spectrum (Figure 87c) measured in $CDCl_3$ shows a triplet signal at $\delta = 3.81$ and a set of aromatic signals in the region of $\delta = 7.76{\sim}7.98$. Compared to 3 aliphatic protons and 3 aromatic protons in the desired

structure, the integrations of the peak intensity confirm the $1:1$ ratio between the aliphatic and aromatic protons. The remaining proton signals were caused by the solvent residuals labelled in the spectrum.

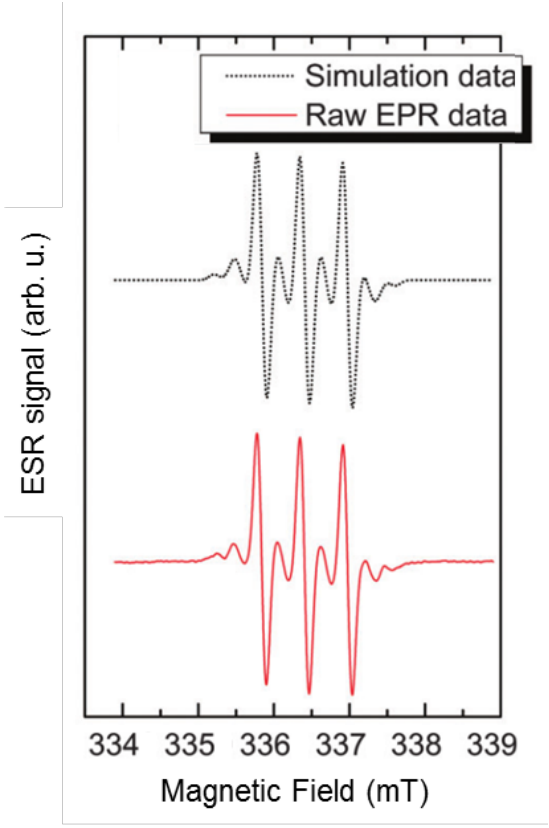


Figure 88 Solid-state cw-ESR spectrum of IND-N@C_{60} in the frozen toluene and its best fit simulated by Easyspin[209] (programme C in appendix). Data for the solid-state cw-ESR experiment were acquired using a Bruker EMX spectrometer. (Experimental conditions: $9.4280\ \mathrm{GHz}$, $48.0\ \mathrm{dB}$ attenuation, $100\ \mathrm{K}$ temperature, and $0.08\ \mathrm{mT}$ modulation amplitude).

After the structural characterization on the spirocyclic-methano C_{60} confirmed the desired molecular structure, solid-state cw-ESR spectroscopy and PL spectroscopy were performed on **IND-N@C_{60}** and **Iodo-QUI-N@C_{60}**, respectively. The solid-state cw-ESR signal of **IND-N@C_{60}** obtained at 100 K in a toluene matrix and its simulation (Figure 88) showed the expected *g*-factor (2.00243) and HFCC ($A_{\mathrm{iso}}^{(\mathrm{N})} = 15.86\ \mathrm{MHz}$). A set of ZFS peaks proved the successful chemical derivatization of the ENF. Compared with **DEM-N@C_{60}**, the similar value of the ZFS parameters of **IND-N@C_{60}** ($D = 8.9\ \mathrm{MHz}$ and $E = 0.57\ \mathrm{MHz}$), strengthens the correlation between the ZFS parameter and the size of the exohedral ring adding on the carbon cage, that I reviewed in section 2.3.3. On the other hand, the similarity of the ZFS

parameter imply that the chemical structure that is not directly bonded to the carbon cage, barely influences the ZFS of the nitrogen spin center. This is reasonable, because the electron spin of the endohedral nitrogen is 98% enclosed inside the cage, and has little interaction with the environment outside.[198,234] Therefore, the spin properties, including the ZFS of spirocyclic-methano ENFs, should have no fundamental difference with that of the conventional Bingel reaction products of ENFs in general.

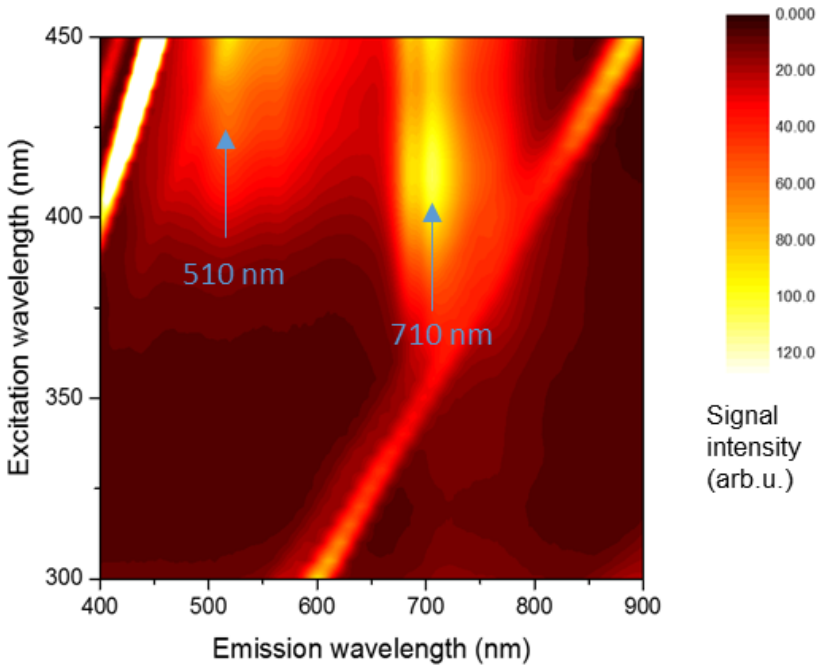


Figure 89 2D-PL contour map of Iodo-QUI-N@C_{60} (*c.a.* 0.1 mg/ml toluene solution). Diagonal signals are artefacts caused by light scattering during the measurements.

Fullerenes have interesting PL properties, hence how the spirocyclic-methano functionalisation affects the PL signal of fullerene was also explored. The 2D-PL contour mapping of **Iodo-QUI-N@C_{60}** is demonstrated in Figure 89, where the intensity of the excitation signal is represented by the colour. The detection of strong emission features (710 nm and 510 nm), which can be ascribed to the C_{60} moiety (*e.g.* Figure 57a),[235] means that the PL feature of the carbon cage is not dramatically varied. Although rigid molecules normally have strong fluorescence due to their conjugation structure, no distinct additional PL peaks were observed. (The diagonal excitation-dependent signals were not PL signals but originated from Rayleigh and Raman scattering.) The absence of the PL signal due to the

addend could come from a fluorescence-suppressing effect of the heavy halogen substituent, because the C–I bond can be cleaved easily, which would absorb the excitation energy through an internal conversion process.[27] Overall, the presence of the studied rigid addend does not affect the PL feature of the product compared to a pristine fullerene.

5.3.2 Bis-spirocyclic-methano-N@C_{70}

In addition to the rigid spirocyclic-methano-addends, the bis-addition with a *trans* regioselectivity will lead to derivatives having increased molecular aspect ratios.[236] As was reviewed in section 2.3.2, the geometric regioisomers formed by bis-addition to a C_{60} cage are not easy to control. Meanwhile, the isomerism is simpler on a C_{70} cage, as the number of potential isomers is less for the bis-addition of C_{70} (5 isomers) compared to that of the bis-addition of C_{60} (8 isomers). Moreover, the prevalent isomers all have the desired structure with two addends separately attached to two polar parts of the rugby-like carbon cage.[135] Hence, I performed the bis-addition on N@C_{70}, and studied the mixture of the 5 regioisomers as a whole.

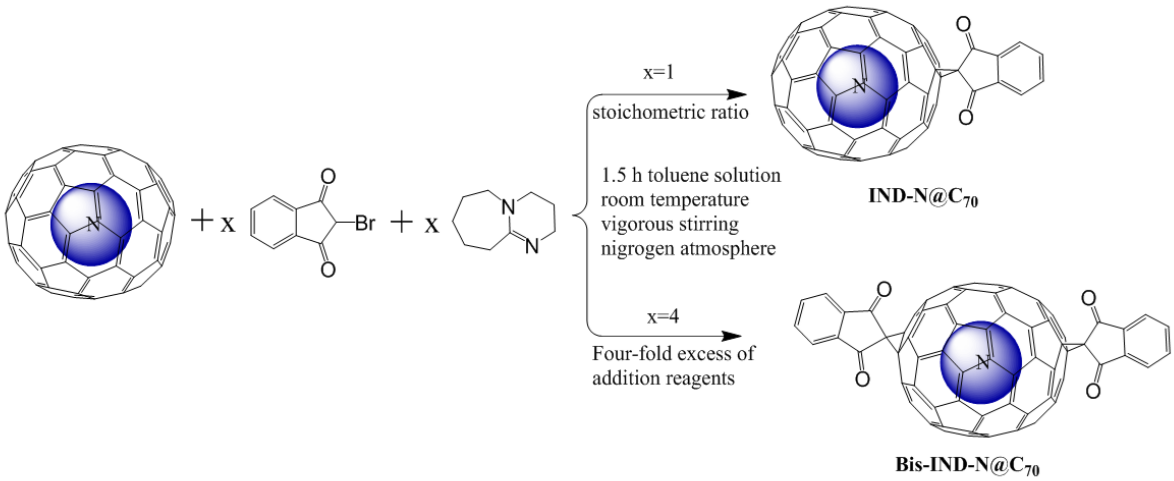


Figure 90 Reaction schemes for synthesis of IND-N@C_{70} and Bis-IND-N@C_{70}. Experimental methods recorded in section 3.3.1.4.

Figure 90 shows the reaction scheme to functionalise N@C_{70} with 2-Bromo-1,3-indandione. Different stoichiometric ratios of the starting materials were utilized to synthesize mono- and bis-products: **IND-N@C_{60}** was prepared by using 2.5 mg of ^{14}N@C_{70}/C_{70}, 0.7 mg of

2-bromo-1,3-indandione and $0.9\ \mathrm{ml}$ of $0.5‰$ DBU/toluene solution; **Bis-IND-N@C$_{60}$** was prepared by using $2.5\ \mathrm{mg}$ of N@C$_{70}$/C$_{70}$, $2.7\ \mathrm{mg}$ of 2-bromo-1,3-indandione and $3.6\ \mathrm{ml}$ of $0.5‰$ DBU/toluene solution. Detailed experimental procedures for the synthesis of **IND-N@C$_{60}$** and **Bis-IND-N@C$_{60}$** are recorded in section 3.3.1.4. By comparing the spin signal of the reaction mixture before and after the 90-minute reactions, 90% of the spins were maintained. Therefore, these two reactions confirm that the spin-compatible method reported for the mono-addition of N@C$_{60}$ in section 5.2.1 also works for N@C$_{70}$ and bis-functionalisation, respectively.

Since the focus of this section is bis-functionalisation, a full set of characterization techniques were performed on **Bis-IND-N@C$_{70}$**, including HPLC, MALDI-MS, UV/Vis spectroscopy, PL spectroscopy, ^{1}H-NMR spectroscopy, and solid-state cw-ESR spectroscopy (Figure 91). According to the HPLC trace of the reaction mixture (Figure 91a) using the BuckyPrep-M column and toluene eluent, a *ca.* 85% yield was obtained for the reaction. The product of **Bis-IND-N@C$_{70}$** eluted at 15 minutes. The high yield was benefited from the high conversion ratio of the starting material of the N@C$_{70}$/C$_{70}$ mixture, which was barely resolved at 9.5 minutes. However, there were still a small HPLC signal from the by-products eluting later than **Bis-IND-N@C$_{70}$**. The by-products with a retention time between $18\sim25$ minutes were studied by MALDI-MS. A qualitative estimation based on the intensity of the MS peaks showed that the by-products were mainly oxidized **Bis-IND-N@C$_{70}$**. Under the condition of excessive nucleophile, the deficient formation of higher addition by-products (tris- and tetrakis-adducts) is unexpected. This can be attributed to the reactivity of C$_{70}$.[135] In addition to the product separation and yield estimation, the HPLC experiment also confirmed the unique delaying feature on the retention time for spirocyclic methano fullerenes compared to parent fullerenes. The MALDI-MS (Figure 91b) for the purified product was recorded in negative ionization mode using DCTB as the matrix: m/z 1128.2, 1129.2, 1130.2, and 1131.2 (M^{-}). Compared with the theoretical prediction: m/z 1128.042, 1129.046, 1130.049, 1131.052, *etc.*, the consistency of the mass/charge ratio and the isotope distribution of the molecular ion

peaks between the experimental and predicted data proves the covalent linkage of the addend and the fullerene cage. Figure 91c shows the absorption spectrum of **Bis-IND-N@C_{70}**, which is remarkably similar to that of the pristine C_{70}[203] with all bands blue-shifted slightly. This could be the result of an enlarged HOMO-LUMO bandgap after introducing addends. The twin peaks in the PL spectrum (Figure 91d, $650\sim720\ \mathrm{nm}$) display a typical C_{70} 2D-PL spectrum (*e.g.* Figure 57b) under a wide range of excitation,[235] which adds extra evidence for the presence of C_{70} moiety in the product. Meanwhile, the insignificant PL signal contributed by the spirocyclic-methano addends is consistent with the observation on **Iodo-QUI-N@C_{60}** shown in Figure 89. The ^{1}H-NMR spectrum (Figure 91e) measured in $CDCl_3$ showed two sets of quartet signals for aromatic protons with $\delta = 8.12$ and $\delta = 7.94$, respectively, which are close to what was observed for **IND-N@C_{60}** in the former section (Figure 86c). The ratio of the peak integrals is measured to be $1:1$. The remaining proton signals were caused by the solvent residuals labeled in the spectrum. The solid-state cw-ESR spectroscopy of **Bis-IND-N@C_{70}** (Figure 91f) was obtained by freezing the toluene solution of the sample at $100\ \mathrm{K}$. Compared to pristine N@C_{70}, the *g*-factor (2.0013) and HFCC ($A_{\mathrm{iso}}^{(\mathrm{N})} = 14.65\ \mathrm{MHz}$) were found to be almost unchanged within the experimental error. However, the axial component of the ZFS parameters of this N@C_{70} derivative obtained by simulation ($D = 5.0\ \mathrm{MHz}$ and $E = 0.64\ \mathrm{MHz}$) is noticeably smaller than that of the N@C_{60} derivatives. This could originate from the structural difference between N@C_{60} and N@C_{70}. The increased cage size of C_{70} makes addends remote from the center of endohedral electron spin, thereby, generating a small ZFS effect after being chemical functionalised. As far as I know, **Bis-IND-N@C_{70}** is the only N@C_{70} derivative to date. Therefore, it is not possible to determine a trend of how chemical functional groups affect the size of the ZFS parameters in a N@C_{70} system. Nevertheless, it can be verified that **Bis-IND-N@C_{70}** has the highest ZFS compared to its corresponding mono-addition product and pristine N@C_{70}. The latter two compounds showed significantly overlapped ZFS peaks in their solid-state cw-ESR spectra, which are not reliable to use simulation to evaluate the ZFS parameters.

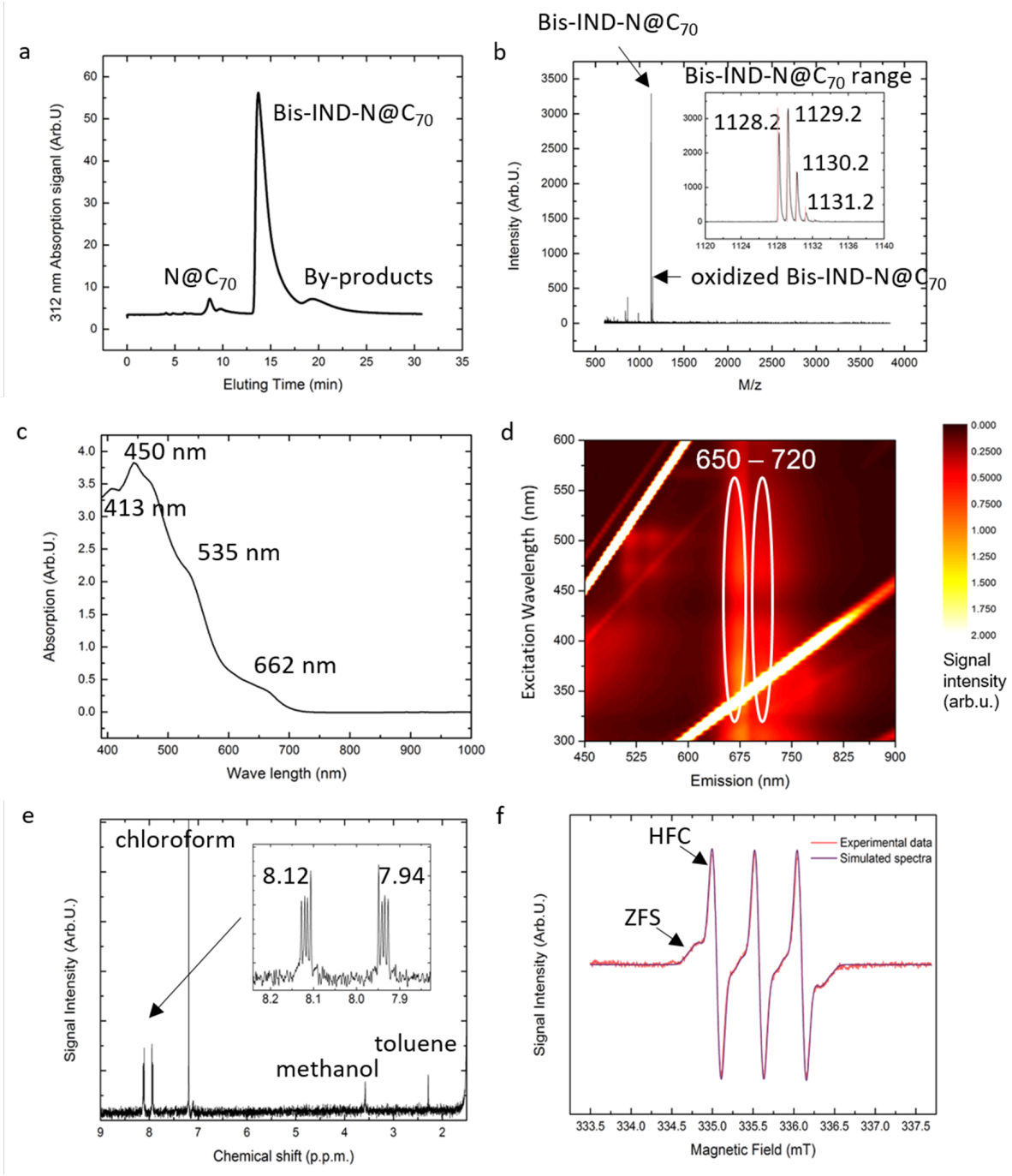


Figure 91 Characterizations for Bis-IND-N@C_{70}: (a) HPLC chart (BuckyPrep-M $28\text{x}250\ \text{mm}$ column, toluene, and $16\ \text{ml/min}$ flow rate), (b) MALDI-MS (DCTB matrix and negative mode) (predicted spectrum shown in red in the inner panal), (c) UV/Vis spectrum (*c.a.* $0.2\ \text{mg/ml}$ toluene solution), (d) 2D-PL spectrum (*c.a.* $0.2\ \text{mg/ml}$ toluene solution), (e) ^{1}H-NMR spectrum ($400\ \text{MHz}$, room temperature, and $CDCl_3$ solution), and (f) solid-state cw-ESR spectrum. (Bruker EMX with experimental conditions: $9.4045\ \text{GHz}$, $53.0\ \text{dB}$ attenuation, $100\ \text{K}$ temperature, and $0.10\ \text{mT}$ modulation amplitude). The cw-ESR spectrum was simulated by Easyspin[209] (programme D in appendix).

Finally, I theoretically estimated the molecular aspect ratio of the synthesized spirocyclic-methano-ENFs by MM2 ForceField simulation (Figure 92, atomic nitrogen omitted for simplicity). While **IND-N@C_{60}**, and **Iodo-QUI-N@C_{60}** improve the molecular aspect ratio of

N@C_{60} from $1:1$ to nearly $2:1$, all potential **Bis-IND-N@C_{70}** isomers have a ratio larger than $3:1$. Further tests with the molecular dynamics function in Chem3D using a heating speed of 2.5 and a target temperature of $600\ \mathrm{K}$ showed the rigidity of all products, as the molecular aspect ratios of these molecules do not vary by more than 10%.

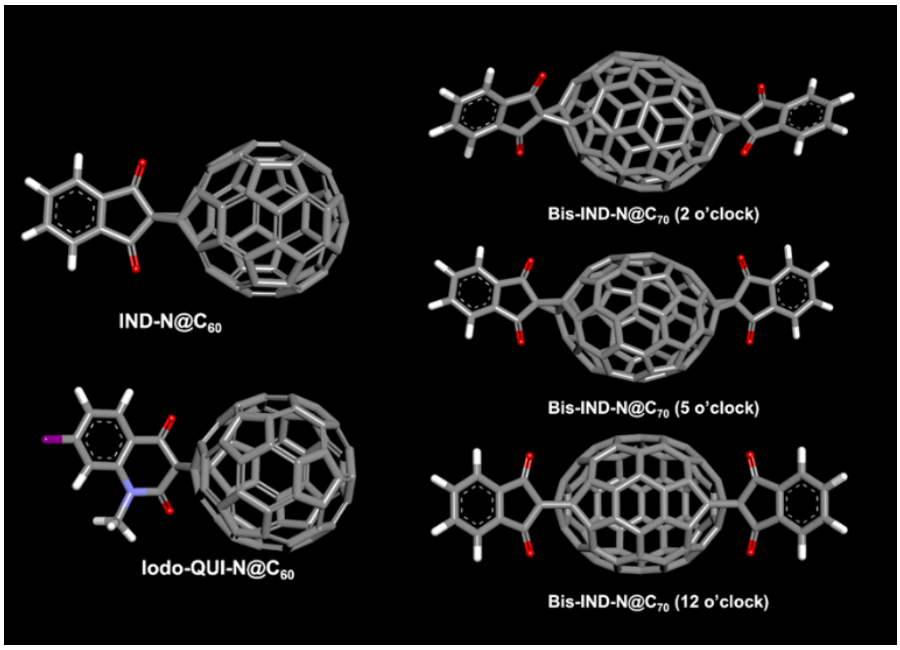


Figure 92 Molecular optimal configuration according to MM2 force filed relaxed by Chem3D and visualized by Discovery Studio.

5.4 Chemical functionalisation with β-cyclodextrin for amphiphilic ENFs

5.4.1 Preparation of β-CD-N@C_{60}

Using Bingel reactions, β-cyclodextrin-C_{60} derivatives have been reported in the literature to make C_{60} soluble in a wide range of polar solvents.[237,238] In contrast to the surface modification with groups directly added on the fullerene cage (e.g. fullerenol by multi-hydroxylation of fullerene),[239] which has problems with regioselectivity[240] and spin-compatibility, the mono-addition of the Bingel reaction is a more promising approach to make ENFs amphiphilic. Therefore, β-cyclodextrin functionalisation of ENF was targeted here. In addition to the amphiphilicity introduced, the synthesis also acts as the second example to demonstrate the validity of the spin-compatible Bingel reaction condition reported in section 5.2. This is a collaborative work between myself and Dr. Stuart Cornes from my group, who synthesized the malonate-containing β-cyclodextrin (β-CD).

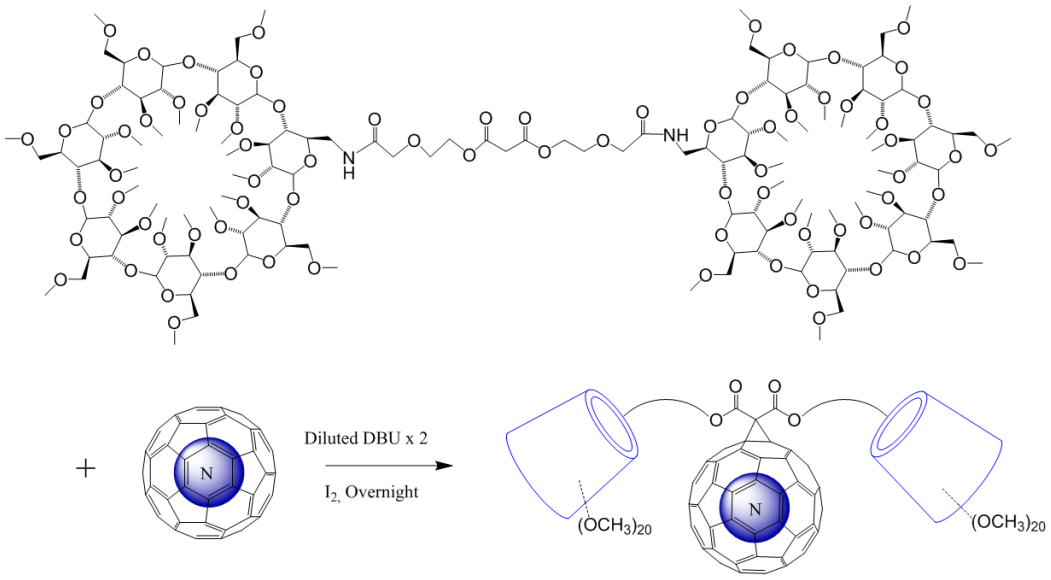


Figure 93 Bingel reaction synthesizing β-cyclodextrin–N@C_{60} from β-CD provided by Dr. Stuart Cornes. Experimental method recorded in section 3.3.1.5.

As Figure 93 shows, mono-functionalisation using a Bingel reaction was utilized to integrate N@C_{60} with β-CD. The novel malonate was designed to introduce 40 methoxy

groups, which modify the molecular surface. Compared to ordinary β-CD terminated with hydroxyl groups, the methylation makes the molecular surface compatible with not only water but also polar organic solvents. Due to the difficulty of selectively substituting the β-CD with one halogen, the reaction adopted a modified Bingel reaction scheme, which has been tested for spin-compatibility *via* the synthesis of **Iodo-QUI-N@C_{60}**.

Starting with $4.9\ \mathrm{mg}$ of N@C_{60}/C_{60} mixture (0.2%), $21.1\ \mathrm{mg}$ of β-CD, $2.6\ \mathrm{mg}$ of I_2 and $4.1\ \mathrm{ml}$ of $0.5‰$ DBU/toluene solution in the mole ratio of $1:1:1:2$, **β-CD-N@C_{60}** was synthesized by an overnight reaction performed in toluene at room temperature (detailed experimental methods recorded in (section 3.3.1.5). The product failed to elute from HPLC with both Buckyprep-M and PYE columns. Therefore, the separation was performed using thin layer chromatography (TLC) using an acetone/cyclo-hexane mixture $(1:1)$ as the mobile phase (Figure 94a). The major coloured band in the TLC was the desired **β-CD-N@C_{60}**. As expected, the product showed good solubility in polar solvents, such as deionized water and acetone (*ca.* $200\ \mathrm{mg/ml}$) (Figure 94b, c).

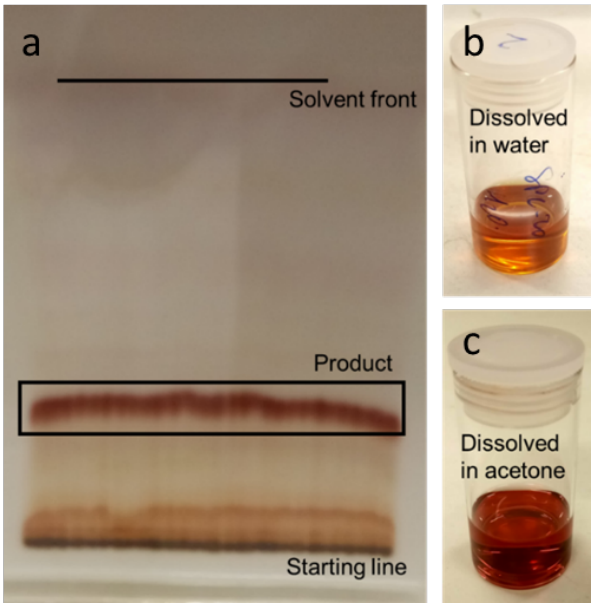


Figure 94 (a) Preparative TLC separation of β-CD-N@C_{60} from the reaction mixture. Purified β-CD-N@C_{60} was dissolved in deionized water (b) and in acetone (c) with the concentration of *ca.* $200\ \mathrm{mg/ml}$.

The successful synthetic procedure was verified by ^{1}H-NMR spectroscopy and MALDI-MS. The ^{1}H-NMR spectrum (Figure 95b) for the product was similar to that obtained from the

starting material of β-CD, except for the triplet signal with a chemical shift of $\delta = 4.89$, which is marked by asterisk. The only different NMR signal was assigned to the four hydrogen atoms that are located closest to the fullerene cage. The left-shifting trend proved the successful linkage between the β-CD and the electron-withdrawing fullerene moiety. In contrast to other ENF derivatives reported in this work, the MALDI-MS signals for β-CD-C_{60} molecular ion peaks (Figure 95c) were considerably broader, and the predicted isotropic distribution (3818, 3819, 3820, 3821, 3822, 3823, 3824, 3825, *etc.*) could not be resolved. In order to assign the peak, I excluded the possibility that the broader MS signal is a fragmentation peak from a bis-addition product, based on the absence of a molecular ion peak for the bis-addition product in the 6000~8000 Da range. Therefore, despite the broadness, the MALDI-MS signal with the expected molecular mass of 3818.5 Da can support the formation of the targeted product.

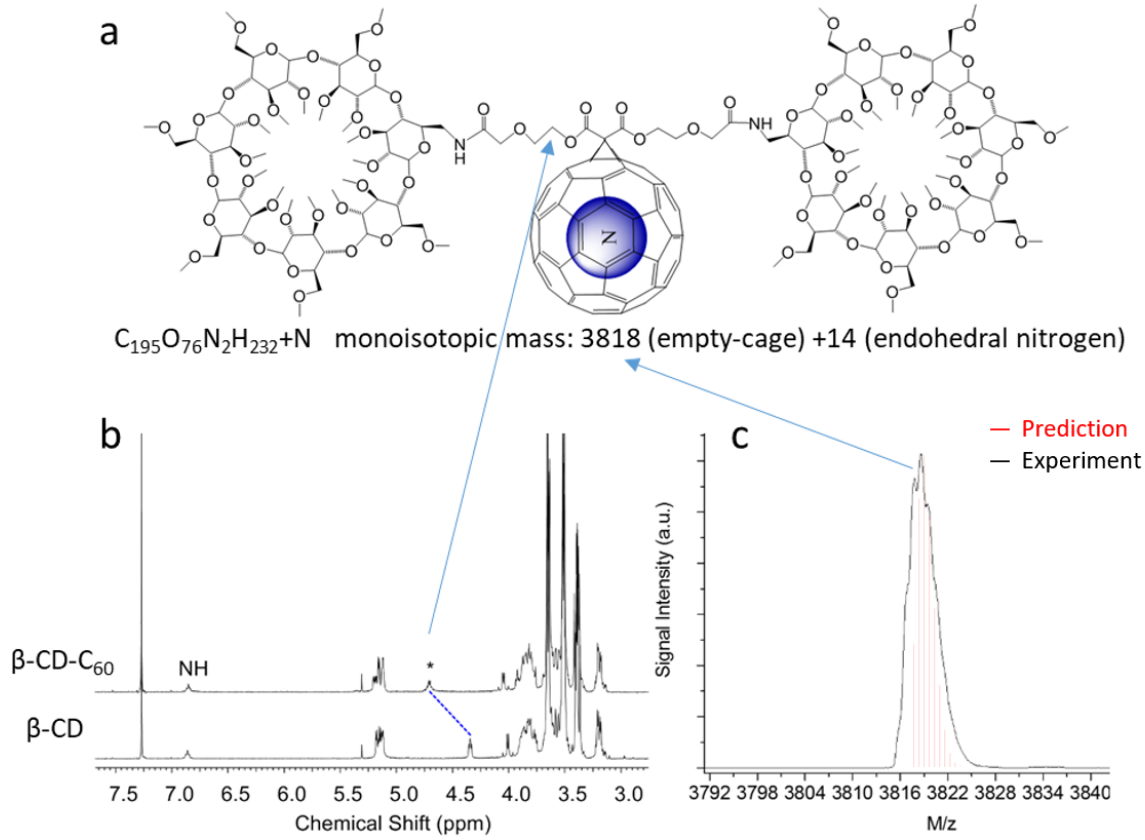


Figure 95 (a) Structure diagram of β-CD-N@C_{60}. (b) ^{1}H-NMR spectrum of β-CD and β-CD-N@C_{60} (400 MHz, room temperature, and $CDCl_3$ solution, obtained by Dr. Stuart Cornes), (c) MALDI-MS of β-CD-N@C_{60} (dithranol matrix and negative mode).

5.4.2 Electron spin signal of β-CD-N@C_{60} in different solvent

To further confirm the formation of β-CD-N@C_{60}, solid-state cw-ESR spectrum of the product was collected in both frozen toluene and water (containing ~10% glycerol) matrix at 100 K (Figure 96a red). Since the presence of the characteristic ZFS peaks for functionalised N@C_{60}, the formation of β-CD-N@C_{60} was proved. According to the EasySpin[209] simulations for both samples (Figure 96a black), primary parameters, including the isotropic *g*-factor (2.00263), zero-field parameters ($D = 8.7\ \mathrm{MHz}$, $E = 0.57\ \mathrm{MHz}$) and isotropic HFCC ($A_{\mathrm{iso}}^{(\mathrm{N})} = 15.77\ \mathrm{MHz}$), do not vary within experimental errors. The negligible influence of the solvent on the spin signal in the solid-state is due to a nearly perfect protection of the endohedral spin by the fullerene cage. The only simulation difference between these two spectra is the ratio between the contribution to linewidth from Gaussian and Lorentzian broadening for each sample, which is $[0.1121\ 0.0093]\ \mathrm{mT}$ for the toluene sample and $[0.0913\ 0.0241]\ \mathrm{mT}$ for the water sample. A slightly more Lorentzian lineshape was obtained for the sample dissolved in water. To further investigate the linewidth difference between two samples, I recorded the room temperature cw-ESR spectra as well. The water sample at room temperature degraded the quality factor (Q-factor) of the cavity, and made the cw-ESR instrument difficult to tune. To tackle this difficulty, a Q-band tube having a much smaller size than an X-band tube was used to load the sample (Figure 96b), which consequently decreased the volume of water and its influence on the tuning procedure. Because the small sample decreased the signal-to-noise ratio of the spectra recorded, multiple scans were utilized to compensate for the weak signal problem. Demonstrated in Figure 96c, the linewidth difference was more obvious in the solution cw-ESR spectra. Using a peak-fitting with the Lorentz lineshape, the peak-to-peak linewidth for **β-CD-N@C_{60}** in water ($\Delta H_{\mathrm{pp}} = 0.014\ \mathrm{mT}$) was measured, which is twice as broad as that in toluene ($\Delta H_{\mathrm{pp}} = 0.007\ \mathrm{mT}$). (Due to the different microwave frequencies used for two measurements, I converted the X axis of the spectrum from the magnetic field to the effective *g*-factor to offset the frequency shift, and highlight the comparability between the water sample and the toluene sample.)

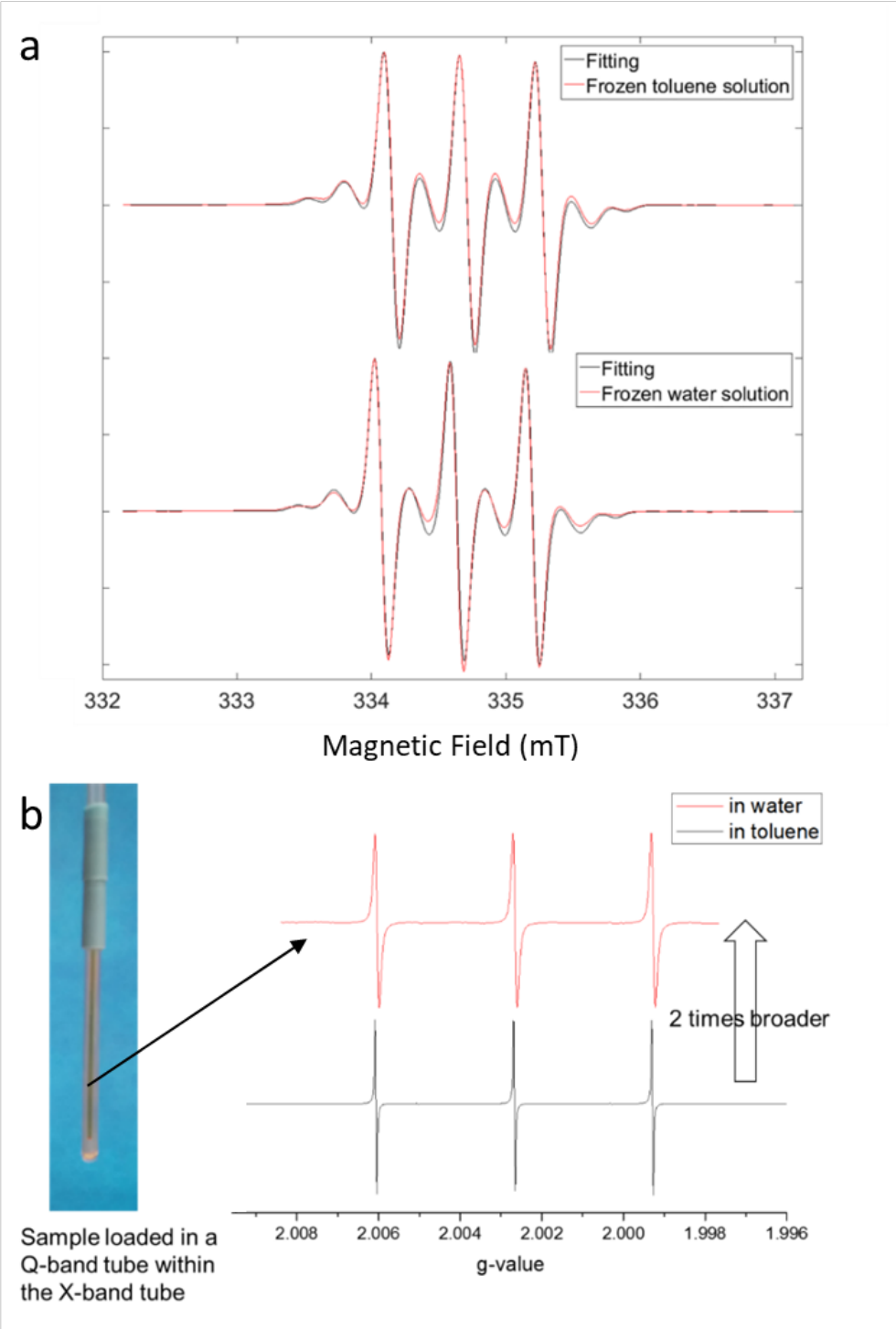


Figure 96 (a) Comparison between the solid-state cw-ESR spectra for β-CD-N@C_{60} in the frozen toluene and that in water, respectively. Data were acquired using a Bruker EMX spectrometer. (Experimental conditions: the toluene sample: $9.3818\ \mathrm{GHz}$, $53.0\ \mathrm{dB}$ attenuation, $100\ \mathrm{K}$ temperature, and $0.08\ \mathrm{mT}$ modulation amplitude. the water sample: $9.3797\ \mathrm{GHz}$, $53.0\ \mathrm{dB}$ attenuation, $100\ \mathrm{K}$ temperature, and $0.08\ \mathrm{mT}$ modulation amplitude). Simulation were conducted by EasySpin[209] (programme E in appendix). (b) Sample of the water solution of β-CD-N@C_{60} loaded inside a Q-band ESR tube. (c) Comparison between the solution cw-ESR for β-CD-N@C_{60} in toluene and that in water. Data were acquired using a Bruker EMX spectrometer. (Experimental conditions: the toluene sample: $9.3809\ \mathrm{GHz}$, $53.0\ \mathrm{dB}$ attenuation, room temperature, and $0.002\ \mathrm{mT}$ modulation amplitude; the water sample: $9.3814\ \mathrm{GHz}$, $40.0\ \mathrm{dB}$ attenuation, room temperature, and $0.007\ \mathrm{mT}$ modulation amplitude).

The broader linewidth for **β-CD-N@C_{60}** in water could be attributed to various reasons, including power broadening, the relaxation effect due to the solvent protons, and aggregation of sample in water. The first reason is discounted because of the sharp linewidth of **β-CD-N@C_{60}** in an acetone solution (discussed later in Figure 98). If the water experiment was power broadened, the acetone experiment would have been power broadened more significantly, as it was measured in a similar Q-band tube with a higher microwave power and a larger cavity Q-factor. The second reason is excluded by reproducing the experiment with deuterated water as the solvent, which led to the same broadening effect. The third reason, which attributes the linewidth broadening to the molecule aggregation, was supported by a dynamic light scattering (DLS) experiment. The sample of **β-CD-N@C_{60}** dissolved in water had a considerably larger diameter compared with that in acetone (Figure 97). The result suggests that although an ENF was successfully dissolved in water for the first time, the molecules dispersed in the aqueous solution as micelles. To eliminate micelle formation and the consequential broader linewidth of **β-CD-N@C_{60}** in water, further tuning of the functionalisation is needed.

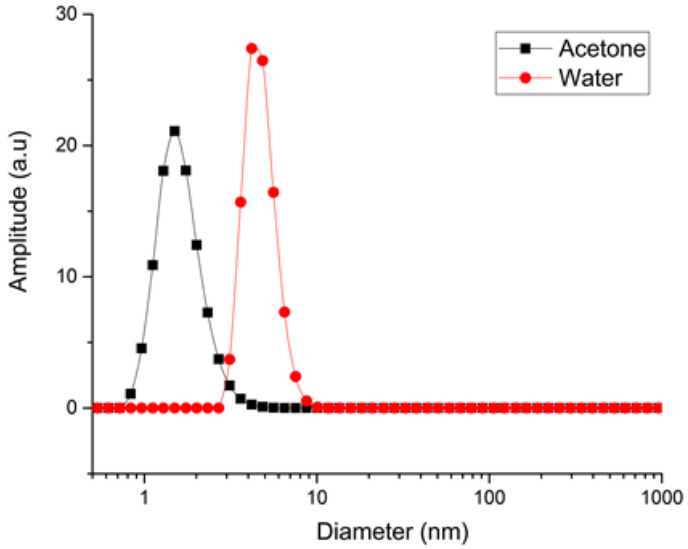
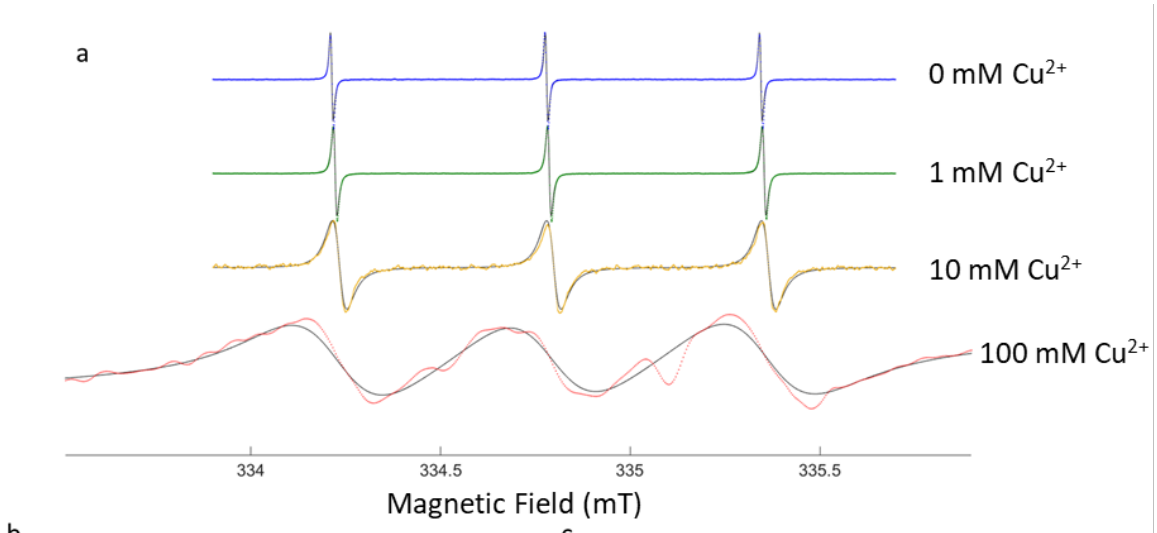


Figure 97 Comparison of the particle size distribution for **β-CD-N@C_{60}** in acetone and water. (Obtained by dynamic light scattering experiment performed with a Malvern Zetasizer Nano ZS instrument using a $0.25\ \mathrm{mM}$ sample concentration and with the refractive index set to 2.2.)

5.4.3 Radical detection with β-CD-N@C_{60}

Benefiting from the polar solvent compatibility of ENFs, potential applications using ENFs in those solvent systems may arise. For example, using the sharp spin signal of ENFs to detect other radicals in bio-enviroments would be an interesting topic. Unfortunately, as a result of the potential aggregation and the micelle formation, physically mixing **β-CD-N@C_{60}** with copper ions (simulating the radicals) in water failed to demonstrate a radical concentration dependent cw-ESR signal of **β-CD-N@C_{60}** (supporting information G). This means, even though the product is dissolved in water, the micelle prohibits the intermolecular interaction between **β-CD-N@C_{60}** and other dissolved components.



b

[Cu(II)] (mM)	LW_{pp} (mT)	ΔLW_{pp} (mT)
0	0.006829	0
1	0.009191	0.002363
10	0.037787	0.030958
100	0.265757	0.258928

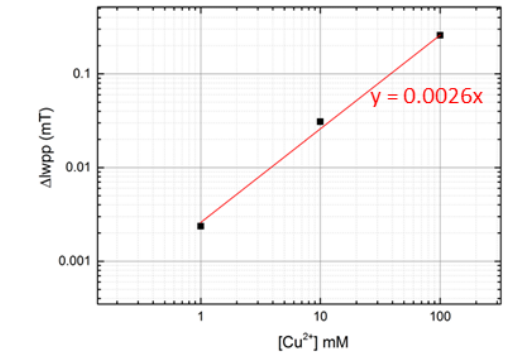


Figure 98 (a) cw-ESR signal comparison of β-CD-N@C_{60} dissolved in acetone with different amounts of Cu^{2+}. Data were acquired using a Bruker EMX spectrometer. (Experimental conditions: Blue: 9.3845 GHz , 36.0 dB attenuation, room temperature, and 0.006 mT modulation amplitude. Green: 9.3843 GHz , 33.0 dB attenuation, room temperature, and 0.006 mT modulation amplitude. Yellow: 9.3850 GHz , 33.0 dB attenuation, room temperature, and 0.006 mT modulation amplitude. red: 9.3848 GHz, 33.0 dB attenuation, room temperature, and 0.04 mT modulation amplitude.) All spectra were fitted with Lorentz peaks. (b) Simulated peak-to-peak linewidth for the spin signal of β-CD-N@C_{60}, depending on Cu^{2+} concentration. (c) Broadening effect of the ENF spin signal depending on Cu^{2+} concentration.

While chemical ways to mitigate the formation of the micelle are still under investigation, I studied the copper concentration dependent cw-ESR signal of **β-CD-N@C$_{60}$** in acetone for the proof of concept (Figure 98a coloured). Despite a similar dependency having been reported in toluene solution,[198,241] this is the first demonstration of its kind in a polar solvent. By fitting with a set of Lorentzian derivative peaks (Figure 98a black), the peak-to-peak linewidths of each set of spin signals were determined and compared in Figure 98b. The magnitude of the broadening effect was plotted against the concentration of Cu^{2+} (Figure 98c), showing a linear relationship. The dependency was consequently estimated to be $0.0026\ \mathrm{mT/mM}$ in the millimolar concentration range.

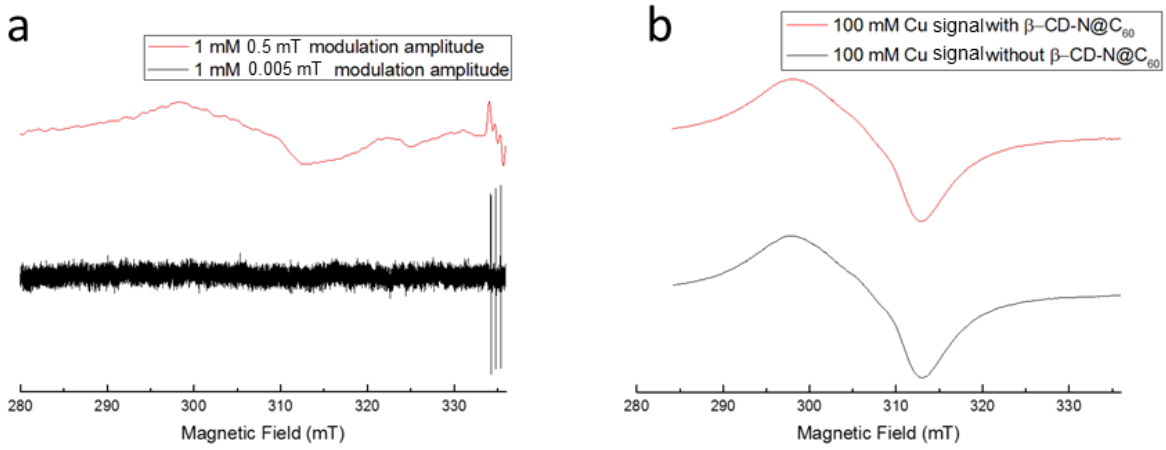


Figure 99 (a) Spectra comparison showing that a large modulation amplitude is needed to directly measure the Cu^{2+} spin in a low concentration. Data were acquired from Bruker EMX (Experimental conditions: Red: $9.3847\ \mathrm{GHz}$, $25.0\ \mathrm{dB}$ attenuation, room temperature, and $0.5\ \mathrm{mT}$ modulation amplitude; Blue: $9.3847\ \mathrm{GHz}$, $25.0\ \mathrm{dB}$ attenuation, room temperature, and $0.005\ \mathrm{mT}$ modulation amplitude). (b) Spectra comparison showing that the presence of β-CD-N@C_{60} has non-detectable influence on the Cu^{2+} spin. Data were acquired from Bruker EMX (Experimental conditions: Red: $9.3848\ \mathrm{GHz}$, $25.0\ \mathrm{dB}$ attenuation, room temperature, and $0.2\ \mathrm{mT}$ modulation amplitude; Blue: $9.3843\ \mathrm{GHz}$, $25.0\ \mathrm{dB}$ attenuation, room temperature, and $0.2\ \mathrm{mT}$ modulation amplitude).

Two preliminary experiments were performed to highlight the potential advantages of using ENF as a radical sensor. To demonstrate the good sensitivity of **β-CD-N@C$_{60}$** as a radical sensor, Figure 99a (black) shows that the spin signal of Cu^{2+} in $1\ \mathrm{mM}$ concentration was not directly observable when a low modulation amplitude was applied, but the ENF spin signal containing the information regarding the concentration of Cu^{2+} was resolved in the same spectrum. Although a larger modulation amplitude can be used to resolve the Cu^{2+} spin signal

(Figure 99a red), it would be difficult to choose the optimal modulation amplitude for an unknown sample, especially when it contains multiple species that need to be measured with different optimal modulation amplitudes. To prove that the interference imposed by the potential radical sensor of **β-CD-N@C_{60}** on the analyte is small, Figure 99b compares the Cu^{2+} spin signal with and without the ENF sample. Since only 0.1% of the fullerene derivative used in this research contains the spin, the dosage of the actual spin probe was on the nanomolar scale. Therefore, the influence on the analyte is insignificant.

5.5 Conclusion

This chapter starts with a study of the reaction condition necessary to achieve a spin-compatible Bingel reaction with N@C_{60} (**DEM-N@C_{60}**). I discovered that, if a stoichiometric quantity of diluted DBU is used for the reaction, the endohedral electron spin will be minimally affected (94% spin retention ratio). Such spin-compatibility is substantially greater than that of the well-reported Prato reactions with N@C_{60}, which have a spin retention ratio of only $73\%\sim79\%$.[79,143] With the reproducibility of the spin-compatible reaction conditions confirmed by the synthesis of **IND-N@C_{60}**, I further demonstrated its generalizability with *in-situ* Bingel reactions (by synthesizing **Iodo-QUI-N@C_{60}** and **β-CD-N@C_{60}**), N@C_{70} Bingel reactions (by synthesizing **IND-N@C_{70}**), and bis-addition Bingel reactions (by synthesizing **Bis-IND-N@C_{70}**).

In addition to confirming spin-compatibility, another goal of the novel ENF derivatives synthesized in this chapter was to introduce new molecular features, such as the molecular rigidity, long aspect ratio, or amphiphilicity. Those molecular features will be applied for subsequent molecular engineering of ENFs in the later chapters. Firstly, by using cyclo-1,3-dione type reagents which effectively act as malonate analogues, elongated ENF derivatives (**IND-N@C_{60}**, **Iodo-QUI-N@C_{60}**, **IND-N@C_{70}**, and **Bis-IND-N@C_{70}**) were successfully synthesized. Due to the larger molecular aspect ratios of these ENF derivatives provided by rigid co-axial addends, the spirocyclic-methano functionalisation study establishes the foundation for research into co-axial ENF dimerization based on the synthetic method (Chapter 6), as well as an investigation into the axial alignment of ENF utilizing the functionalised products (Chapter 7). Secondly, I demonstrated the synthesis of the first water-soluble ENF derivative (**β-CD-N@C_{60}**). Benefiting from the amphiphilic functional group of β-CD attached on the fullerene cage, sharp electron spin signals from ENF were obtained in both water (0.014 mT) and toluene (0.007 mT) at room temperature. The successful solvation of N@C_{60} in both a polar and a non-polar system improves the solvent compatibility of ENFs which permits its use as a building block for quantum information processing. In addition,

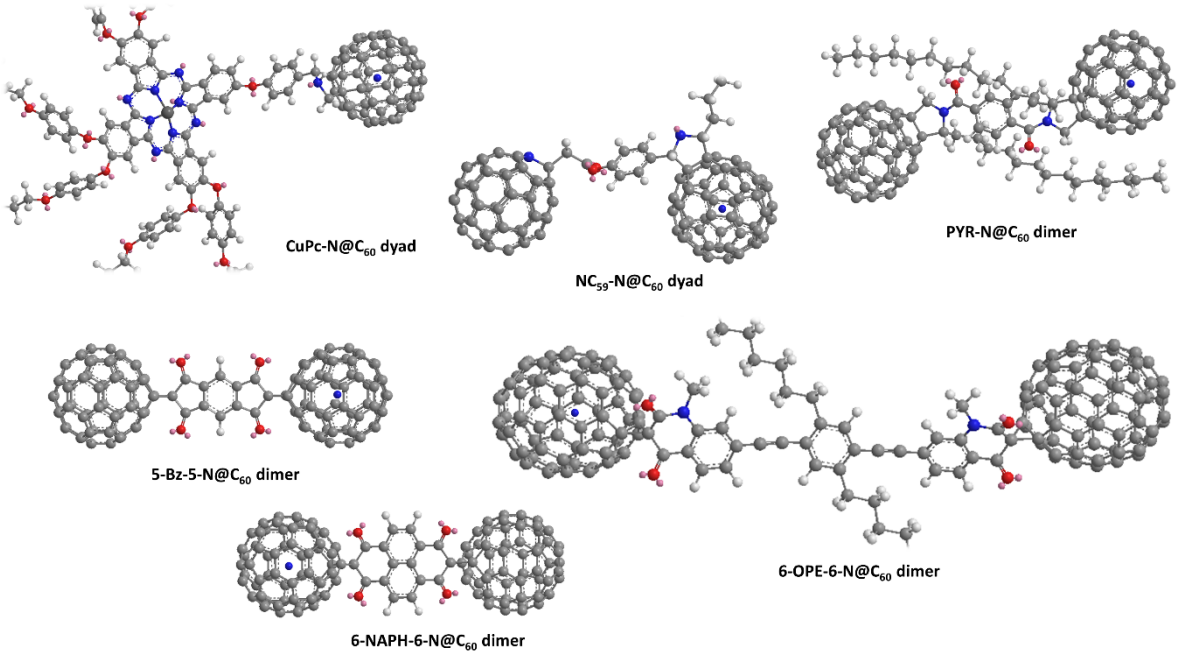
preliminary experimental results on the [Cu^{2+}] concentration dependent cw-ESR signals were obtained in a polar solvent system, which inspired a potential application of **β-CD-N@C_{60}** in detecting radicals.

All newly reported N@C_{60} derivatives achieved by this chapter shows relatively low magnitude of the ZFS effect. Combining other derivatives obtained in other chapters, it is relevant to summarize the tendency of their ZFS parameters here (Table 11), which echoes literature observations reviewed in section 2.3.3. My observations on N@C_{60} derivatives are consistent with a positive relationship between the axial parameter D and the ring size of the addend. The magnitude of the rhombic term E is less than $1\mathrm{MHz}$ for all derivatives tested. Both parameters proved that the discussion of ZFS trends, which I developed in section 5.2, is still applicable for N@C_{60} derivatives. Besides, ZFS parameters of a N@C_{70} derivative has been obtained for the first time. Due to the change of the fullerene cage, its values of the ZFS parameters are not consistent with those measured for N@C_{60}. In particular, its axial term D is considerably smaller than that which is obtained from N@C_{60} derivatives.

Table 11 Summarization of all ENF derivatives obtained throughout this work. (a) parameters were extracted from a ESR spectra that still contain a small spin contamination. (b) parameter was negligible.

ENF derivative	ENF type	Ring size attached to the cage	D/MHz	E/MHz
DEM-N@C_{60}	N@C_{60}	3	8.4	0.36
IND-N@C_{60}	N@C_{60}	3	8.9	0.57
β-CD-N@C_{60}	N@C_{60}	3	8.7	0.57
5-Bz-5 dimer	N@C_{60}	3	$10.0^{(a)}$	$0.5^{(a)}$
N@C_{60}-ZnPc	N@C_{60}	5	14.2	$0^{(b)}$
PYR-N@C_{60}	N@C_{60}	5	13.6	0.69
PYR-N@C_{60} dimer	N@C_{60}	5	14.7	0.61
Bis-IND-N@C_{70}	N@C_{70}	3 (two addends)	5.0	0.64

Chapter 6 Synthesizing ENF-containing dyads and dimers: Towards covalently assembled qubits



6.1 Introduction

ENF microscopic assembly is required for an ENF-based quantum device. As I reviewed in section 2.5, this could be obtained in various dimensions with different molecular engineering technologies. While the 2D[83–89] and 1D[81,82] arrays of ENFs still suffer from certain difficulties, such as low spin-compatibilities[149] and undesired spin-active impurities,[158] this chapter focuses on the covalent linkage approach to chemically assembling ENFs with a hetero moiety or with another ENF molecule to form ENF dyads and ENF dimers, respectively.

Firstly, I used one-pot Prato reactions to synthesize dyads constructed by N@C_{60} and phthalocyanine (Pc)hetero moiety. N@C_{60}-ZnPc dyad was prepared as a reference sample, and two distinct N@C_{60}-CuPc dyads with different distances between the two chemical moieties were synthesized. The successful preparation of these dyads provides a set of di-electron spin systems to study spin coupling in Chapter 8.

Secondly, I continued the half-filled ENF dimer investigation with the Prato reaction. My aim is to provide a Prato scheme of dimerization, leading to a more sterically controllable ENF dimers. This was achieved by dimerizing at the nitrogen position of the pyrrolidine, which is not a chiral active center. This differs from the α-position substitution of the pyrrolidine that was commonly used in previous literature.

Lastly, I utilized the spin-compatible Bingel reaction developed in Chapter 5 to link half-filled ENF dimers. This novel synthesis method not only completely excludes the chirality of the dimer by avoiding the pyrrolidine, but also maintains the coaxial relationship between the molecular axis and the spin center axis by co-axial spirocyclic-methano functionalisation. Moreover, the fully sp^2-conjugated bridge provides the rigidity necessary for future dipolar coupling studies, which require spatial and conformational control of the two fullerene moieties.

6.2 Synthesis and characterization of ENF containing hetero dyads

Three different N@C_{60}–phthalocyanine dyads (**N@C_{60}-1-CuPc**, **N@C_{60}-2-CuPc** and **N@C_{60}-1-ZnPc**, Figure 100) were synthesized by reacting spin-enriched N@C_{60}/C_{60} mixture ($2\ \mathrm{mg}$, *ca.* 1% spin content) with sarcosine ($0.3\ \mathrm{mg}$) and the corresponding phthalocyanine aldehyde ($6.5\ \mathrm{mg}$~$6.9\ \mathrm{mg}$). The phthalocyanine aldehydes were obtained via collaboration with Masanori Yamamoto, who was supervised by Professor Hiroshi Imahori in Kyoto University. The assembly of ENF and phthalocyanine was achieved *via* the α-substituted pyrrolidine addends, which has been demonstrated successfully with other functional groups in literature.[142–144] Detailed synthetic procedures are documented in section 3.3.2.1, 3.3.2.3, and 3.3.2.2.

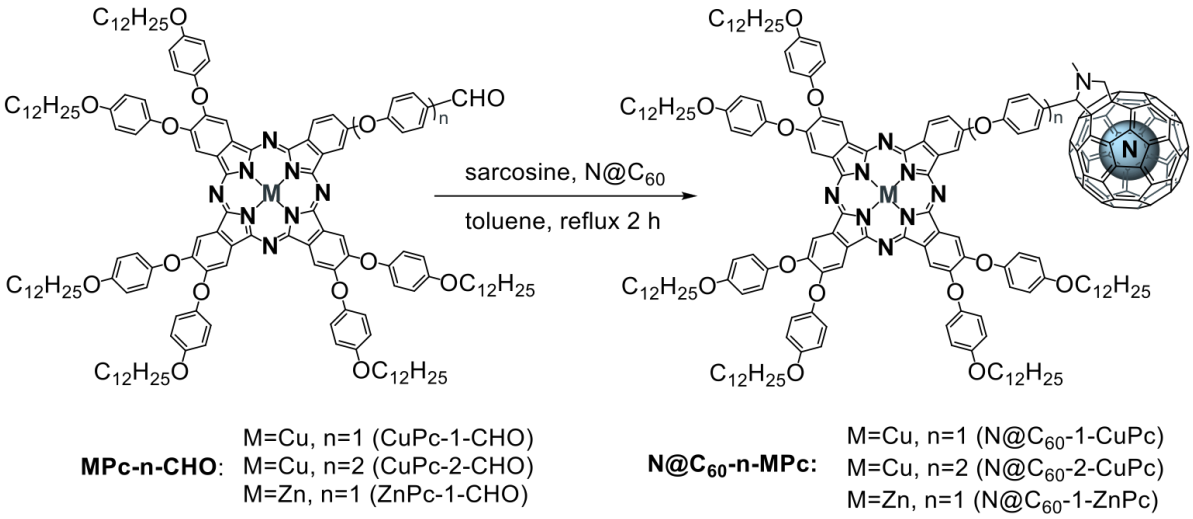


Figure 100 Synthesis of N@C_{60}–n-MPc dyads. **M** represents the copper or zinc ion, and **n** stands for the number of the phenoxy groups in the bridging unit. Experimental methods recorded in section 3.3.2.1, 3.3.2.2, and 3.3.2.3. MPc–CHO were offered by Mr. Masanori Yamamoto and Prof. Hiroshi Imahori, Kyoto University, Japan.

In order to effectively protect the ENF against heat and maintain its spin content, I performed all reactions in mild conditions with a compromise on the conversion ratio. The reagents in stoichiometric ratio dissolved in toluene were refluxed for two hours in the dark. The product dyads were then isolated from the reaction mixture by HPLC through the BuckyPrep-M column and toluene eluent (separation of the two potential enantiomers were

not attempted). Figure 101a shows a representative HPLC trace for the separation of **N@C$_{60}$-1-CuPc**. Although the yield of the product was relatively low (*ca.* 22% based on the integrated area percentage of the product peak to the whole HPLC curve), the unreacted reagents were collected and reused for a second reaction batch, which improved the overall conversion ratio to higher than 40%.

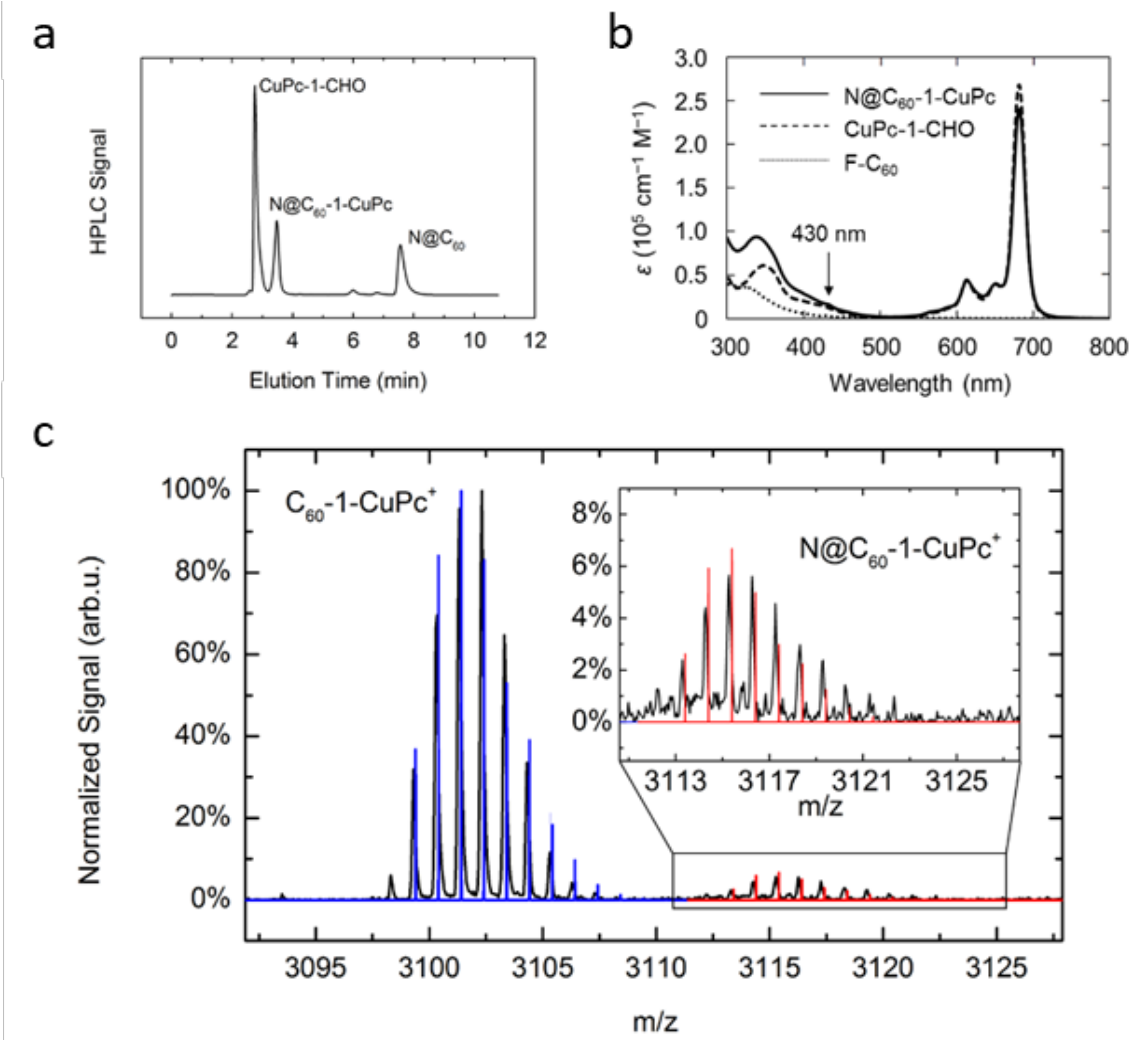


Figure 101 (a) HPLC curve for the separation of N@C_{60}-1-CuPc (BuckyPrep-M 28x250 mm column, toluene, 16 ml/min flow rate), (b) UV/Vis spectrum for the toluene solution of N@C_{60}-1-CuPc (solid line), which is similar to the superposition of UV/Vis spectra from phthalocyanine aldehydes (dashed line) and functionalised fullerene reference (dotted line). (c) MALDI-MS of N@C_{60}-1-CuPc in dithranol matrix at positive mode with the theoretical predictions. The dominant peaks are from the empty-cage fullerene dyad (blue lines), but the weak MS peaks representing the ENF dyad (red lines) are also detectable.

The successful formation of the products is demonstrated by UV/Vis spectroscopy and MALDI-MS. As depicted in Figure 101b, the spectrum for the toluene solution of **N@C$_{60}$-1-CuPc** (solid line) is a superposition of the absorption features of the phthalocyanine aldehyde

(dashed line) and a functionalised fullerene reference (dotted line), which suggests the existence of both the phthalocyanine and fullerene moieties in the product molecule. In addition, the characteristic absorption band at 430 nm, indicating the 1,2-substituted structure of the fullerene, was also observed in the spectrum.[221,222] The MALDI-MS characterization for **N@C_{60}-1-CuPc** is shown in Figure 101c. The molecular ion peaks for the empty-cage fullerene dyad (*m/z*: 3099.3, 3100.3, 3101.3, 3102.3, 3103.3, and 3104.3) are consist with the theoretical prediction data in blue (*m/z*: 3099.401, 3100.405, 3101.408, 3102.407, 3103.411, 3104.410, *etc.*). In addition, the weak MS peaks representing the ENF dyad (*m/z*: 3113.3, 3114.3, 3115.3, 3116.3, 3117.3, and 3118.3) were detectable and agree with the theoretical predictions in red (*m/z*: 3113.404, 3114.408, 3115.411, 3116.411, 3117.414, 3118.413, *etc.*), presumably due to a relatively high concentration of spins and the better ionization property of phthalocyanine. To the best of my knowledge, this is the first direct MS observation of ENF derivatives.

Similar characterization data, which show the absorption features of the combination of the functionalised fullerene and phthalocyanine moieties by UV/Vis spectrum were also obtained for **N@C_{60}-2-CuPc** and **N@C_{60}-1-ZnPc** (Figure 102a). The molecular ion peaks of the empty cage fullerene dyads for **N@C_{60}-2-CuPc** (3191.6, 3192.6, 3193.6, 3194.6, 3195.6, and 3196.6) and **N@C_{60}-1-ZnPc** (3100.3, 3101.3, 3102.3, 3103.3, 3104.3, 3105.3, and 3106.3) were also obtained by MALDI-MS, which are consistent with the theoretical predications (Figure 102b). In addition, the NMR characterization of **C_{60}-1-ZnPc** has been published by my collaborators elsewhere.[274]

This section demonstrates the successful synthesis and structural characterization of N@C_{60}–MPc dyads, with the corresponding cw-ESR studies discussed in Chapter 8. In addition to the ENF–Pc dyads, I also synthesized a ENF–aza-fullerene dyad, for which a preliminary study is documented in Supporting Information H.

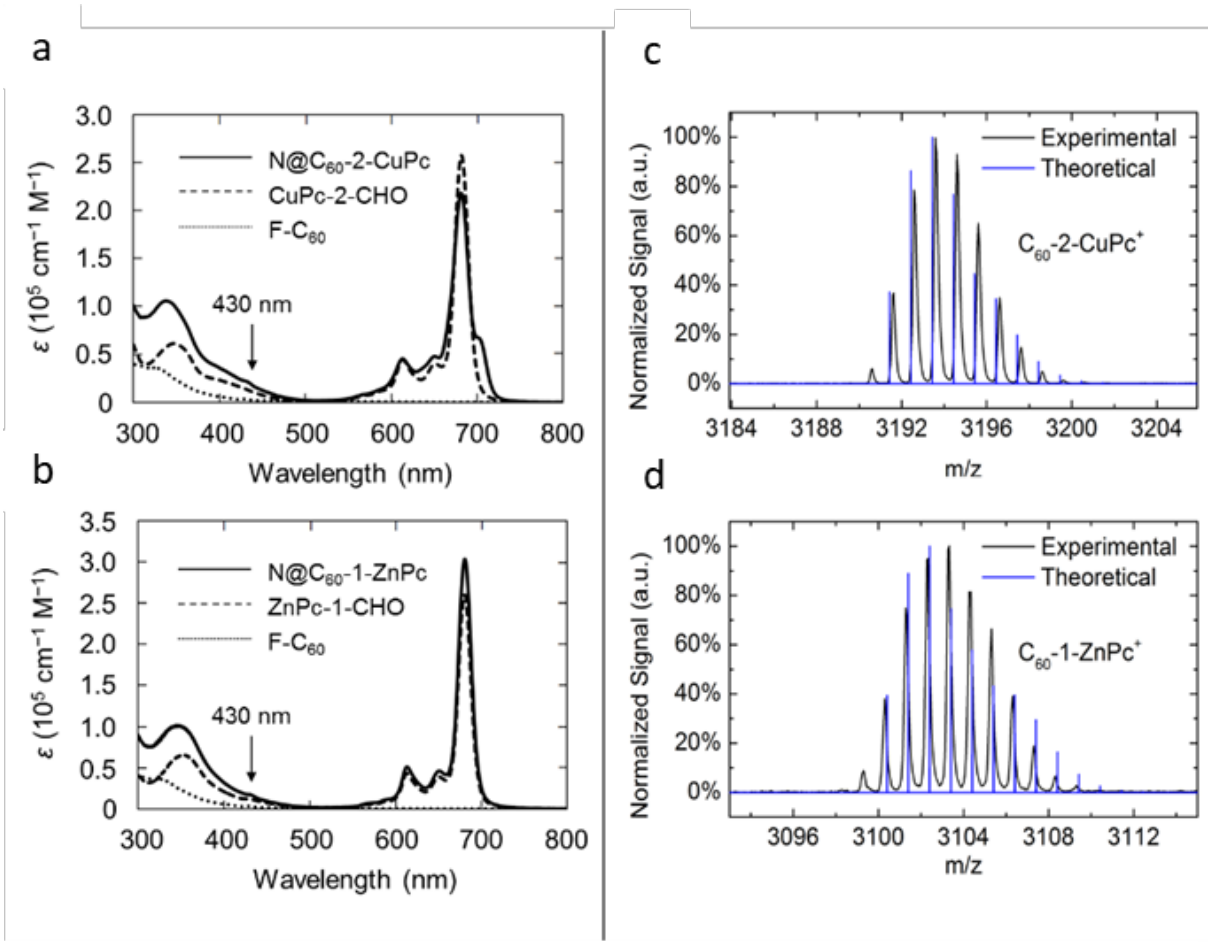


Figure 102 (a) UV/Vis absorption spectra for the dyad of N@C_{60}-2-CuPc (solid line), its corresponding phthalocyanine aldehyde of CuPc-2-CHO (dashed line), and the functionalised fullerene reference of F-C_{60} (dotted line). (b) UV/Vis absorption spectra for the dyad of N@C_{60}-1-ZnPc (solid line), its corresponding phthalocyanine aldehyde of ZnPc-1-CHO (dashed line), and the functionalised fullerene reference of F-C_{60} (dotted line). (c) MALDI-MS obtained for the dyad of N@C_{60}-2-CuPc in dithranol matrix at positive mode (black), and its theoretical predictions (blue). (d) MALDI-MS obtained for the dyad of N@C_{60}-1-ZnPc in dithranol matrix at positive mode (black), and its theoretical predictions (blue).

6.3 Dimerizing ENFs with amide bonds

6.3.1 Synthesis of PYR-N@C_{60} and PYR-N@C_{60} dimer

In addition to the dyads synthesized in the last section, all ENF dimers reported to date (reviewed in section 2.4) were also dimerized at the α-position of the pyrrolidine by Prato reactions.[77–79] Despite a good commercial availability of the aldehyde reagents for these types of ENF covalent assembly schemes, they lead to less distance controllability due to potential diastereomers (Figure 33 in section 2.4). Without moving away from the Prato reaction completely, dimerizing ENFs with amide bonds to the nitrogen-position of the pyrrolidine can avoid introducing new chiral centres to the ENF dimer. Unfortunately, the attempt failed to directly introduce an acyl group by substituting the amine group in the corresponding amino acid precursor. The chemical reactivity of the amino acid to form ylide decreases due to the presence of the electron-withdrawing acyl group, thus preventing the Prato reaction from happening.[242] To avoid this reactivity problem, a step-wise approach was proposed (Figure 103).

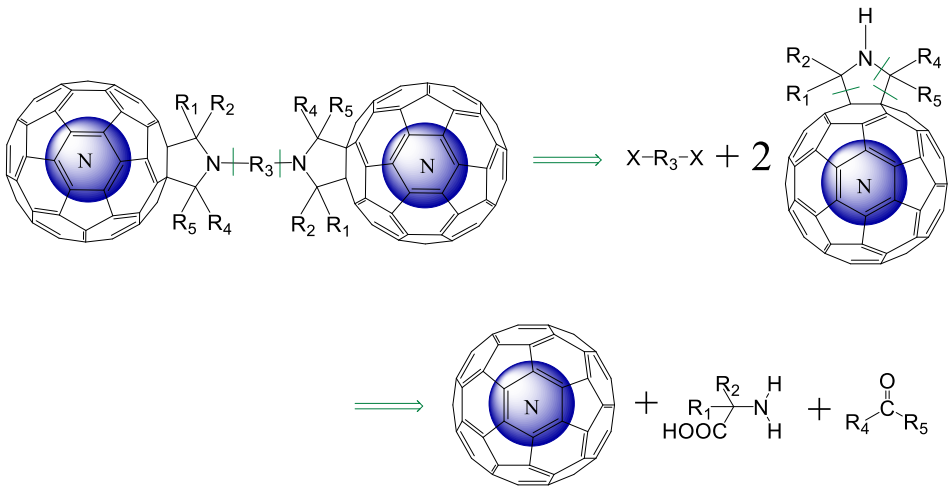


Figure 103 Retrosynthetic analysis of ENF dimerization *via* the nitrogen positon of the pyrrolidine. The X linked to R_3 could be a halogen element, which can lead to a condensation reaction with amine.

Dimerizing ENFs with amide bonds is demonstrated with the two-step reaction shown in Figure 104. The first step is a typical Prato scheme for the purpose of introducing a secondary amine group. As the high temperatures required by the Prato reaction were proven to cause

electron spin loss,[79,149] I optimized the reaction conditions to minimize the duration of the heating procedure. Therefore, I used 2-aminohexadecanoic acid because it was found to be more reactive than glycine due to its better solubility in toluene. A number of potential side reactions may occur during the formation of the secondary amine group,[112] including the dimerization of the ylides formed[243] or amine addition to C_{60}.[244] However, these were not observed due to the steric hindrance provided by the long tetradecyl chain next to the amine group. The drawback of using 2-aminohexadecanoic acid, which has a chirality, is that the product would maintain its chiral center. Fortunately, such steric isomerism is not as problematic as that introduced by α-position dimerizing, because the chiral center introduced by 2-aminohexadecanoic acid is not the joint point of the fullerene dimer and can, in principally, be avoided by choosing chirality-free amino acid in the future.

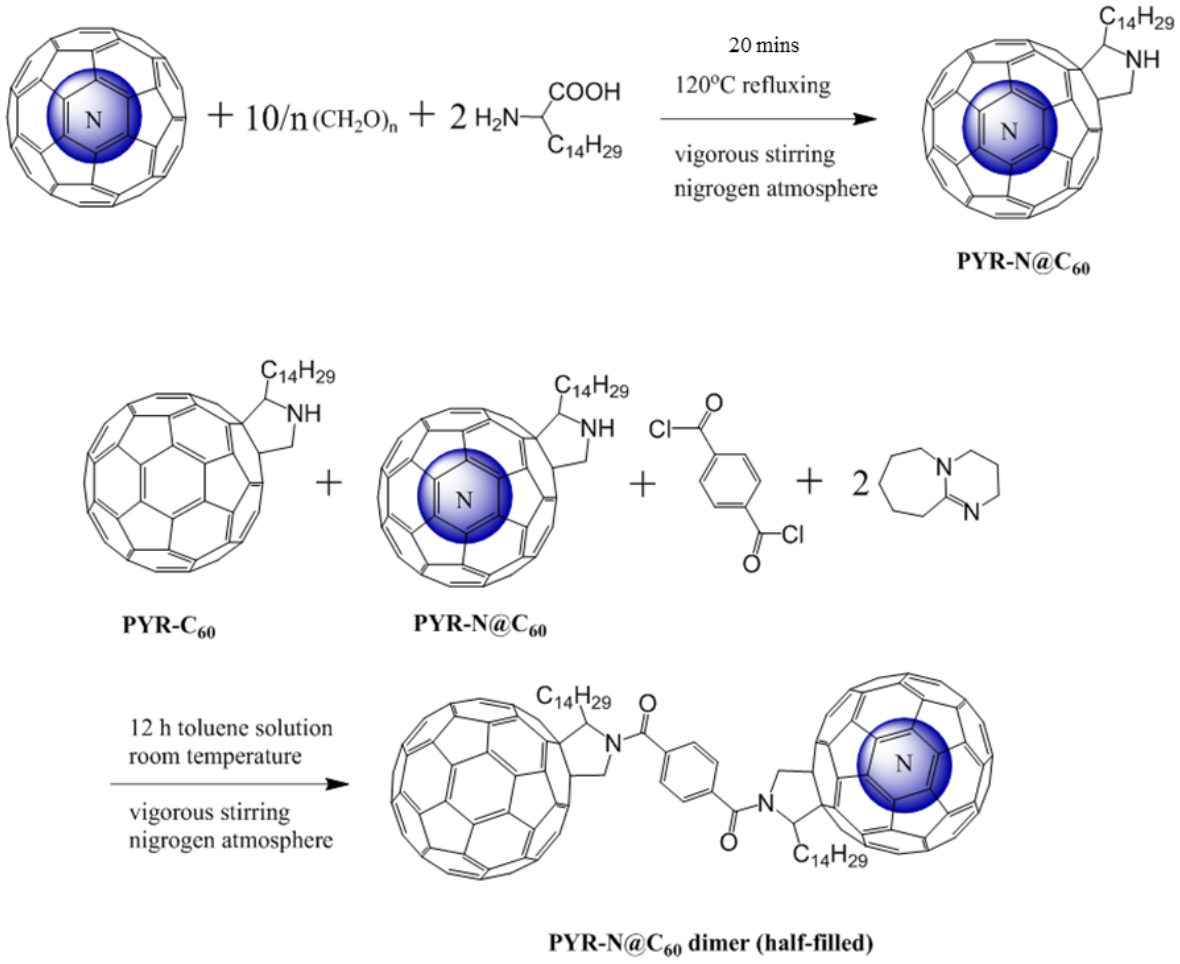


Figure 104 Two-step dimerization reaction linking N@C_{60} with a C_{60} by amide coupling. Experimental methods recorded in section 3.3.2.5.

Aiming for a fast fullerene conversion rate, adding a two-fold and a ten-fold excess of the amino acid ($5.4\ \mathrm{mg}$) and aldehyde ($3.0\ \mathrm{mg}$) to the ENF ($7.2\ \mathrm{mg}\ 0.1\%$ spin content), respectively, showed the potential for acceleration without causing side reactions. In contrast, a two-hour pre-heating of the amino acid and the aldehyde for ylide formation showed no reaction acceleration. As a result of the reaction condition optimization, I achieved a fullerene conversion ratio of 40% within twenty minutes of reaction time, according to the area of the HPLC peaks obtained by the subsequent separation procedure (Figure 105a). In the second step, **PYR-N@C$_{60}$** ($1.9\ \mathrm{mg}$) is dimerized *via* forming two amide bonds with terephthaloyl dichloride ($0.4\ \mathrm{mg}$) in a stoichiometric ratio. Due to the mild conditions in which the amidation was performed, no spin loss was noticed after a 12-hour reaction. The as-produced **PYR-N@C$_{60}$ dimer** was then purified by HPLC. Assuming that a dimer absorbs twice as much as a monomer does in the HPLC chart, the dimerization offered a 50% yield (Figure 105b). Detailed synthetic procedures for PYR-N@C$_{60}$ dimer is documented in section 3.3.2.5.

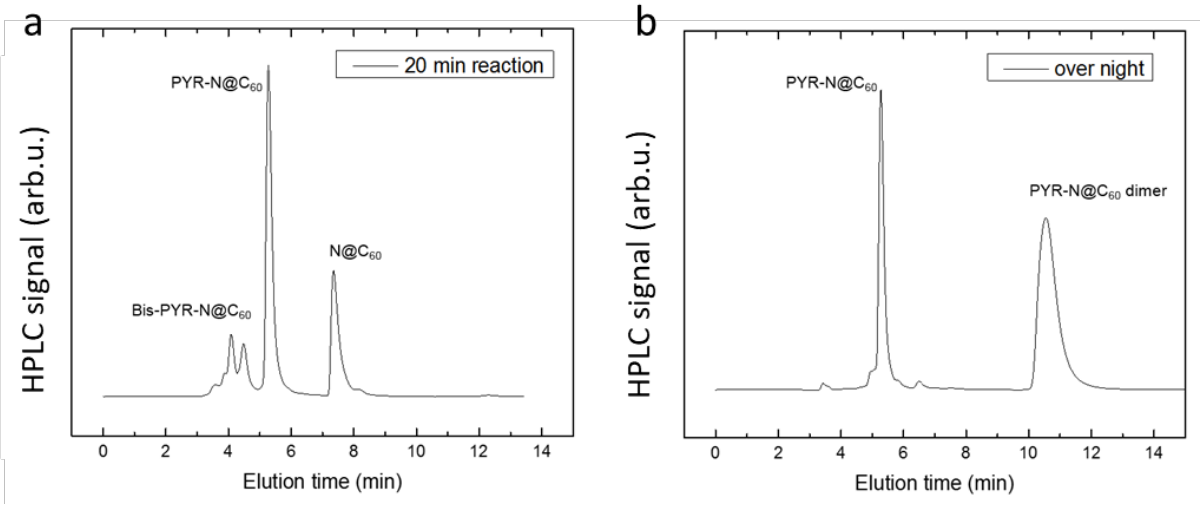


Figure 105 HPLC charts of reaction mixture to synthesize PYR-N@C$_{60}$ (a) and PYR-N@C$_{60}$ dimer (b), respectively (BuckyPrep-M $28\mathrm{x}250\ \mathrm{mm}$ column, toluene, and $16\ \mathrm{ml/min}$ flow rate).

6.3.2 Characterization of PYR-N@C$_{60}$ and PYR-N@C$_{60}$ dimer

The synthesis of the intermediate product of **PYR-N@C$_{60}$** was confirmed by MALDI-MS (Figure 106a) and UV/Vis spectroscopy (Figure 106b). The MALDI-MS of the sample in a

negative mode using DCTB as the matrix shows only one set of signals corresponding to **PYR-C_{60}**. The MS signal (m/z (M^-): 959.6, 960.6, 961.7, and 962.7) agrees with the prediction (959.261, 960.265, 961.268, 962.271, *etc.*). The UV/Vis spectrum of the sample dissolved in toluene shows a typical fullerene absorption feature plus an additional 430 nm absorption band, indicating a [6,6] addition due to the Prato reaction.

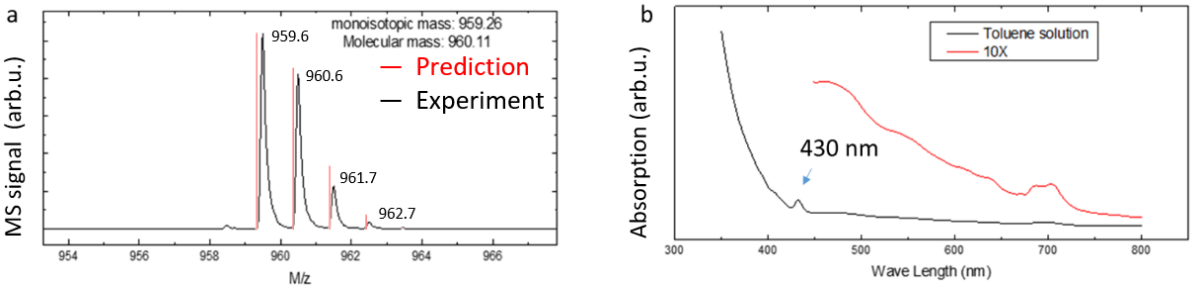


Figure 106 (a) MALDI-MS (DCTB matrix and negative mode) and (b) UV/Vis spectrum (*c.a.* 1 mg/ml toluene solution) measured for the PYR-N@C_{60} sample.

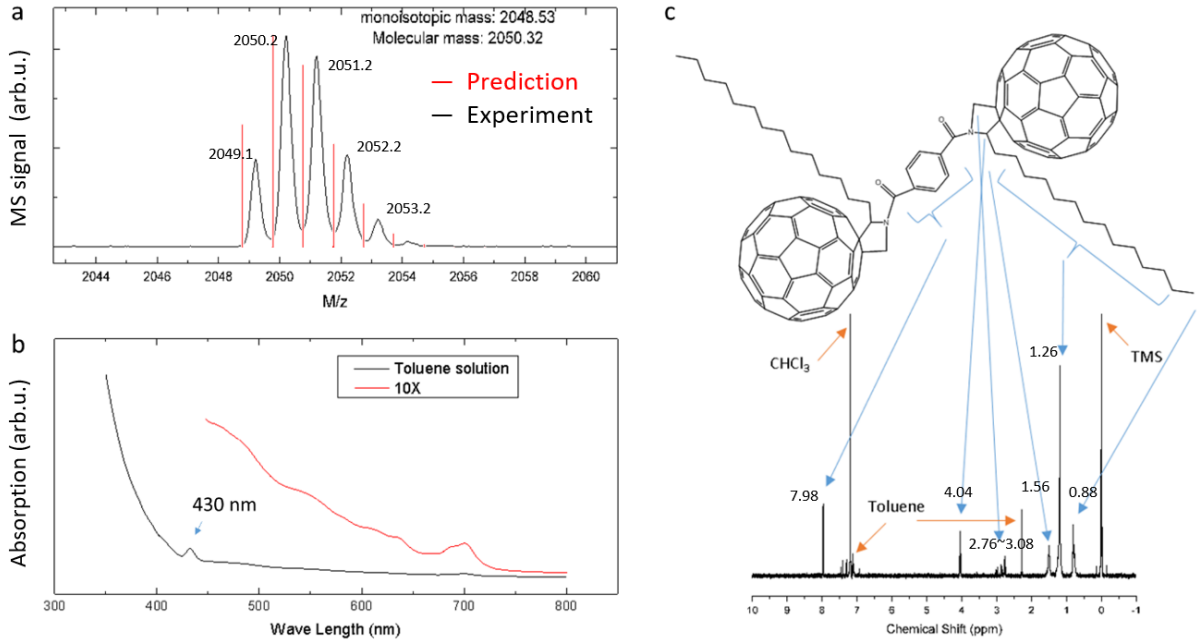


Figure 107 (a) MALDI-MS (DCTB matrix and negative mode), (b) UV/Vis spectrum (*c.a.* 1 mg/ml toluene solution), and (c) ^{1}H-NMR spectrum (400 MHz, room temperature, and $CDCl_3$ solution) measured for the PYR-N@C_{60} dimer sample.

Similar characterization results of MALDI-MS (Figure 107a) and UV/Vis spectroscopy (Figure 107b) were also acquired from **PYR-N@C_{60} dimer**. The obtained MS signal (m/z(M^-) 2049.1, 2050.2, 2051.2, and 2052.2) matches the predicted spectrum (2048.528, 2049.531,

2050.535, 2051.538, 2052.542, *etc.*), and the UV/Vis spectrum of **PYR-N@C$_{60}$ dimer** shows a great similarity to that of **PYR-N@C$_{60}$** due to the identical chromophore in both molecules. The ^{1}H-NMR spectrum for the **PYR-N@C$_{60}$ dimer** sample dissolved in $CDCl_3$ is shown in Figure 107c. Alkyl protons ($\delta = 0.88, 1.26, 1.56$), pyrrolidine protons ($\delta = 2.76\sim3.08, 4.04$), and aromatic protons ($\delta = 7.98$) were assigned. The rest of the proton signals were caused by toluene and chloroform residue.

In addition to the above characterization techniques, which only probe the molecular structure of the empty cage fullerene derivatives in the product, solution and solid-state ESR spectroscopy were used to confirm the formation of the ENF derivatives (Figure 108). The cw-ESR spectra of both compounds, collected in toluene solution, do not significantly change compared to pristine N@C$_{60}$, due to their identical *g*-factor (2.00243) and HFCC ($A_{\mathrm{iso}}^{(\mathrm{N})} = 15.86\ \mathrm{MHz}$). However, the signal for the dimer shows a more noticeable linewidth broadening ($\Delta H_{\mathrm{pp}} = 0.021\ \mathrm{mT}$) compared to that of the monomer ($\Delta H_{\mathrm{pp}} = 0.025\ \mathrm{mT}$). This trend is consistent with the observation for the NC$_{59}$–N@C$_{60}$ dyad (supporting information H) and literature,[78,143] which can be explained by a reduction of the tumbling rate caused by the large molecular dimension. There are two obstacles to quantitatively interpreting the tumbling rate for this cw-ESR measurement: (1) Although the linewidth is dependent on the tumbling rate, experimental conditions, such as the homogeneity and the modulation of the magnetic field, also have an influence. For the ultra-sharp spin signal of ENF derivatives in solution, the latter two factors are not negligible. (2) the EasySpin simulation is not applicable, as this software does not support any spin system with S>1/2 unless the simulation is performed using a rigid limit assumption with zero tumbling rate. Therefore, in order to quantitatively determine the tumbling rate, more experiment or simulation is still needed. Measuring the T_1 and T_2 decays of ENF derivatives in carbon disulphide has been reported to provide its tumbling rate.[78,143] One can deduce the tumbling rate based on the fluctuating rate of the ZFS term. Since the fluctuating ZFS term leads to the main relaxation mechanism of an ENF derivative,[49] the tumbling rate can be determined by fitting the T_1 and T_2 decay curve.[78,143]

The solid-state cw-ESR spectra were taken by freezing the toluene solution using liquid nitrogen in a finger Dewar. The pyrrolidine addends on both products impose symmetry breaking effects on carbon cages and lead to a ZFS term for the $S = 3/2$ electron spin. Therefore, additional side peaks were observed. By simulating the solid-state spectra with EasySpin,[209] **PYR-N@C$_{60}$** and **PYR-N@C$_{60}$ dimer** were found to have similar ZFS parameters ($D = 13.6\ \mathrm{MHz}$, $E = 0.69\ \mathrm{MHz}$ and $D = 14.7\ \mathrm{MHz}$, $E = 0.61\ \mathrm{MHz}$, respectively), identical isotropic *g*-factor ($g_{\mathrm{iso}} = 2.00243$) and HFCC ($A_{\mathrm{iso}}^{(N)} = 15.86\ \mathrm{MHz}$), which agree with previous ENF derivatives functionalised by Prato reactions (section 2.3.3). This similarity between the monomer and the dimer suggests that the amide bond, the phenyl group, and the second fullerene moiety are too far away from the encapsulated spin center to dramatically affect it.

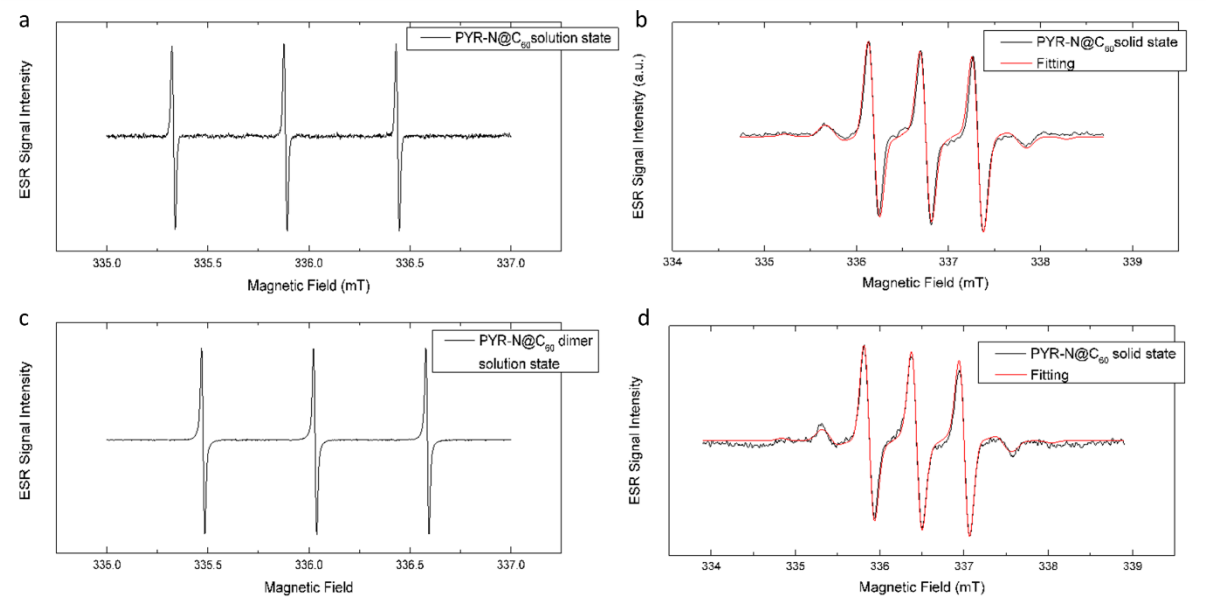


Figure 108 Comparison of the cw-ESR spectra. (a) Solution cw-ESR of PYR-N@C$_{60}$. (b) Solid-state cw-ESR and simulation of PYR-N@C$_{60}$. (c) Solution cw-ESR of PYR-N@C$_{60}$ dimer. (d) Solid-state cw-ESR and simulation of PYR-N@C$_{60}$ dimer. Data were acquired using a Magnettech MiniScope MS200 spectrometer. (Experimental conditions: a: $9.4078\ \mathrm{GHz}$, $30.0\ \mathrm{dB}$ attenuation, room temperature, and $0.02\ \mathrm{mT}$ modulation amplitude; b: $9.4353\ \mathrm{GHz}$, $30.0\ \mathrm{dB}$ attenuation, $77\ \mathrm{K}$, and $0.08\ \mathrm{mT}$ modulation amplitude; c: $9.4204\ \mathrm{GHz}$, $30.0\ \mathrm{dB}$ attenuation; room temperature, and $0.02\ \mathrm{mT}$ modulation amplitude; d: $9.4273\ \mathrm{GHz}$, $30.0\ \mathrm{dB}$ attenuation, $77\mathrm{K}$, and $0.08\ \mathrm{mT}$ modulation amplitude). The cw-ESR spectra were simulated by EasySpin[209] (programme F in appendix).

6.4 Dimerizing ENFs with rigid coaxial bridges

6.4.1 Dimer design

Although the **PYR-N@C_{60} dimer** synthesized in last section has less conformational complexity than the Prato dimers reported in the literature,[77–79] the rotation of some σ-bonds in the bridge and the slightly bent conformation of the pyrrolidine cycle still impair conformational control of the molecule. Direct evidence for this comes from the axial alignment results discussed in Chapter 7, which show that **PYR-N@C_{60} dimer** was more difficult to align than the spirocyclic-methano-ENF derivatives. Thereby, three spirocyclic-methano type ENF dimers, **5-Bz-5 dimer**, **6-NAPH-6 dimer**, and **6-OPE-6 dimer** shown in Figure 109, with rigid coaxial bridges were proposed to further improve the ENF dimer design. According to MM2 ForceField simulation, the distance between the two spin centres in the double-filled dimers are approximately constant. (*ca.* 1.3 nm for the short dimers and 3.0 nm for the long dimer).

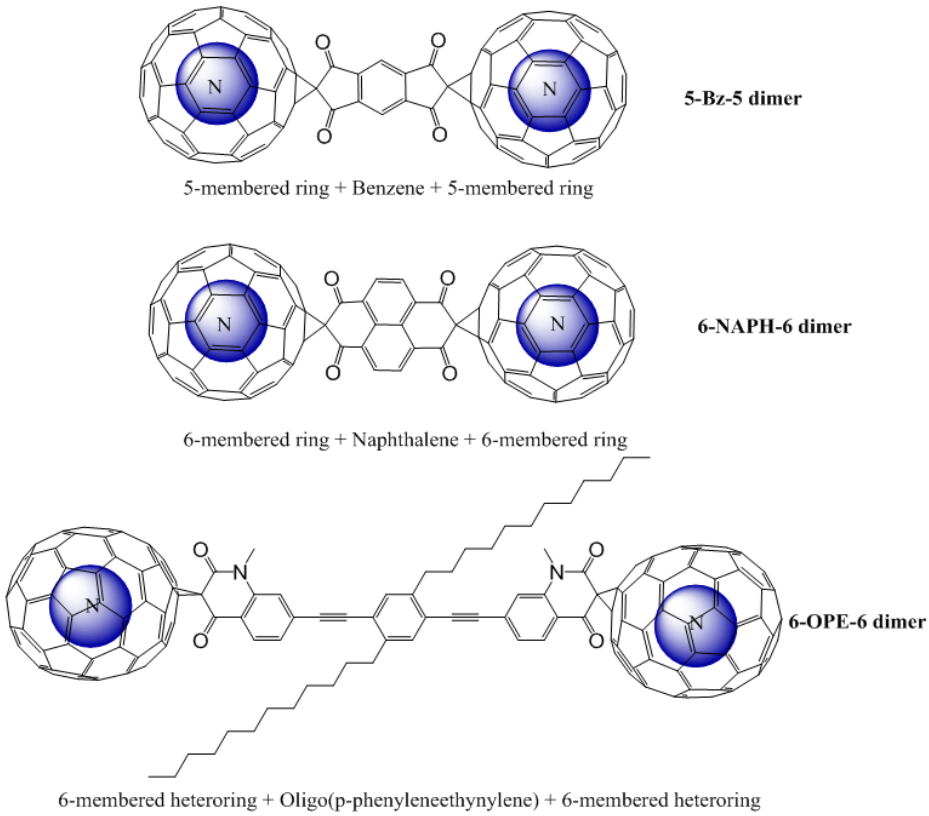


Figure 109 Designed coaxial dimers providing differently fixed special separations. Each dimer is briefly named after the components in the bridge group.

These ENF dimers synthesized by the Bingel reaction will not only solve the chiral isomerism problem but may also show good alignment due to the spirocyclic-methano-addends. Moreover, the main aim of dimeric assembling of ENFs is providing controllable electron spin dipolar coupling, which is not only affected by the spin-spin separation but also related to the spin-spin orientation with the respect to the external field. Compared to Dimer-3Bz for example,[79,96] the co-axial relationship between the bridge axis and the spin-spin coupling axis (Figure 110) will result in a narrow distribution of dipolar coupling strengths.

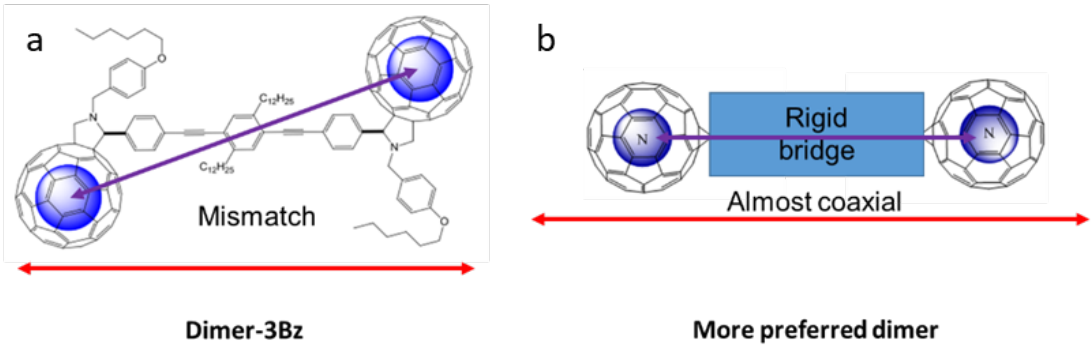


Figure 110 Coaxial issue between dipolar coupling axis (purple) and molecule axis (red) in a previously reported dimer (a),[79,96] compared to a more preferred dimer (b).

Synthesizing a double-filled dimer requires pure ENF as the starting material, which is unnecessarily time-consuming to obtain at this stage of the dimerization study. While the experiments below all work on half-filled dimers with only one spin center, I predicted spectra for double-filled dimers. Based on the different distances of the designed dimers, I simulated the cw-ESR spectral both in the powder (Figure 111a) and aligned form (Figure 111b) using the spin Hamiltonian as follows:

$$\widehat{\mathcal{H}} = \widehat{\mathcal{H}}^{(\mathrm{N@C_{60}},1)} + \widehat{\mathcal{H}}^{(\mathrm{N@C_{60}},2)} + \widehat{\mathcal{H}}^{(\mathrm{dip.})} = \left(\frac{\mu_\mathrm{B}}{\hbar}\boldsymbol{B}_0^T\boldsymbol{g}^{(1)}\widehat{\boldsymbol{S}}^{(1)} + \widehat{\boldsymbol{S}}^{(1)^T}\boldsymbol{D}^{(1)}\widehat{\boldsymbol{S}}^{(1)} + \widehat{\boldsymbol{S}}^{(1)^T}\boldsymbol{A}^{(1,\mathrm{N})}\widehat{\boldsymbol{I}}^{(1)}\right) + \left(\frac{\mu_\mathrm{B}}{\hbar}\boldsymbol{B}_0^T\boldsymbol{g}^{(2)}\widehat{\boldsymbol{S}}^{(2)} + \widehat{\boldsymbol{S}}^{(2)^T}\boldsymbol{D}^{(2)}\widehat{\boldsymbol{S}}^{(2)} + \widehat{\boldsymbol{S}}^{(2)^T}\boldsymbol{A}^{(2,\mathrm{N})}\widehat{\boldsymbol{I}}^{(2)}\right) + \left(\widehat{\boldsymbol{S}}^{(1)^T}\boldsymbol{J}_{\mathrm{dip.}}{}^{(1,2)}\widehat{\boldsymbol{S}}^{(2)}\right) \quad \text{Eq.6.1}$$

Where the *g*-tensors, $\boldsymbol{g}^{(1)}$ and $\boldsymbol{g}^{(2)}$, were simulated with the isotropic value of 2.00243, the HFC tensors, $\boldsymbol{A}^{(1,\mathrm{N})}$ and $\boldsymbol{A}^{(2,\mathrm{N})}$ were simulated with the isotropic value of $15.86\ \mathrm{MHz}$, the ZFS tensors, $\boldsymbol{D}^{(1)}$ and $\boldsymbol{D}^{(2)}$, caused by the addition of the bridge were simulated with the axial term $D = 8.0\ \mathrm{MHz}$ and rhombic term $E = 0.5\ \mathrm{MHz}$, and the dipolar coupling tensor, $\boldsymbol{J}_{\mathrm{dip.}}{}^{(1,2)}$, was

simulated with a coupling strength of $23.6\ \mathrm{MHz}$ for the short dimer, $1.92\ \mathrm{MHz}$ for the long dimer, and $0\ \mathrm{MHz}$ for the monomer.

The cw-ESR signal of the short dimer will be significantly affected and weakened by the intramolecular electron spin dipolar coupling between the two ENF moieties in both powder and aligned sample, and the original triplet pattern is completely changed. For the long dimer, the weaker coupling will lead to detectable cw-ESR features in powder and perfectly aligned samples. Based on the predicted cw-ESR spectra for the dimers in the powder form, the longer dimer can assign its electron spin dipolar coupling better due to its more intense spin signal. Nevertheless, as long as the samples are aligned, both types of dimers will give clear spin signals that prove the spin coupling.

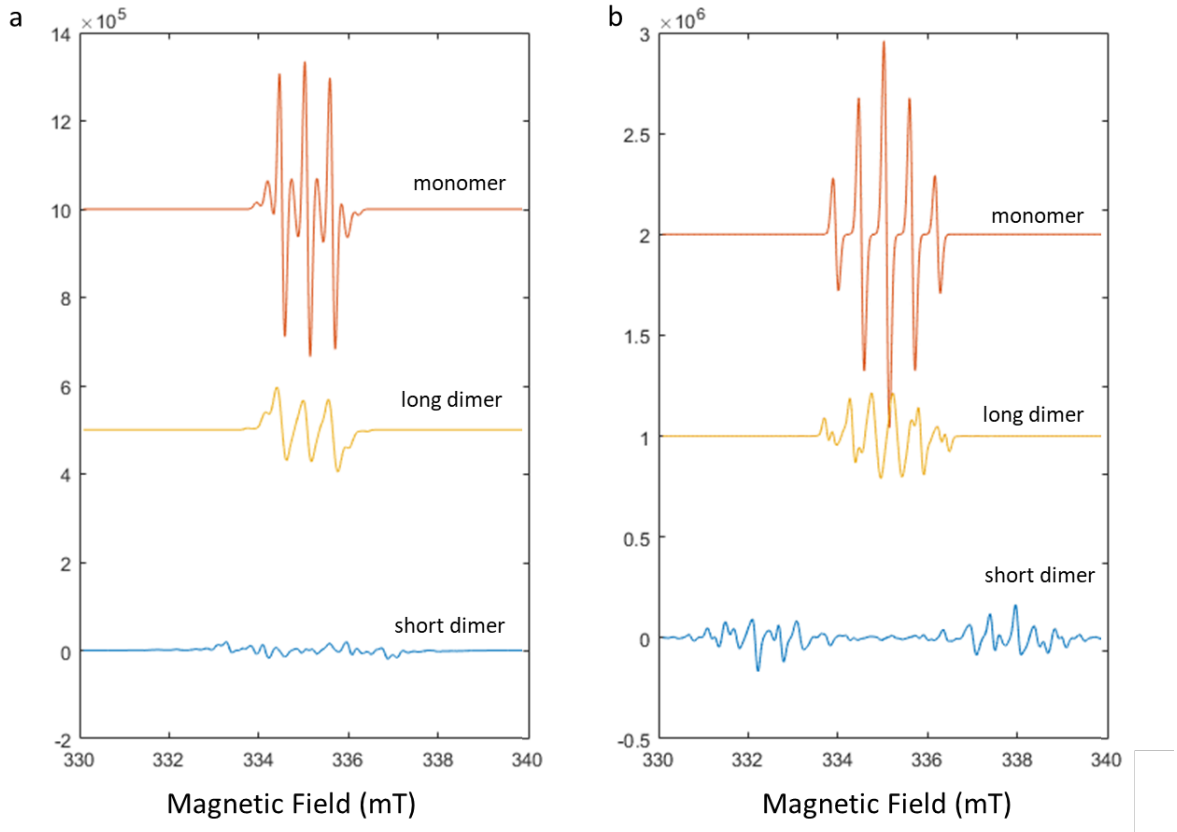


Figure 111 Simulated spectra of monomer, long and short dimers in powder form (a) and perfectly aligned form (b), which demonstrate deferent electron spin dipolar couplings (EasySpin,[209] programme G in appendix).

6.4.2 Synthesis and characterization of 5-Bz-5 dimer and 6-NAPH-6 dimer

According to the formation of IND-N@C_{60} reported in section 5.3.1, starting from N@C_{60} ($5.8\ \mathrm{mg}$, 0.1% spin content) and s-Indacene-1,3,5,7(2H,6H)-tetraone (Janus dione) ($0.9\ \mathrm{mg}$, mole ratio $2:1$), **5-Bz-5 dimer** (half-filled) should be readily formed via a one-pot Bingel addition reaction. However, the tetraone has such a poor solubility in toluene that even adding DMF up to 30% failed to solubilize the reagent. Further increasing the content of DMF in the solvent leads to poor C_{60} solubility. To overcome the conflict of dissolving the non-polar C_{60} and the polar tetraone together, I found that 50% DMF plus 50% CS_2 can keep both reagents in the solution. However, the reaction proceeded rather slowly, presumably due to the low mass transfer rate in the mixed solvent system.

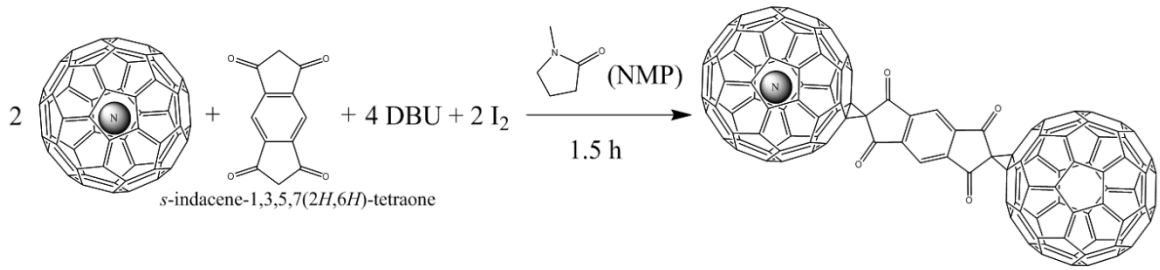


Figure 112 Synthesis of 5-Bz-5 dimer with Bingel reaction in NMP. Experimental method recorded in section 3.3.2.6.

Since N-Methyl-2-pyrrolidone (NMP) is the only good polar solvent reported for C_{60},[217] I tried to perform the Bingel reaction for N@C_{60} in NMP (Figure 112). In addition to tackling the solubility problem, the reaction rate in NMP was also faster than other Bingel reactions in toluene, because polar solvents accelerate nucleophilic additions. Using the aforementioned reagents and $4.8\ \mathrm{ml}$ of $0.5‰$ DBU/NMP solution and $2\ \mathrm{mg}$ of I_2 as the auxiliary base and halogenating agent, the bis-fullerene addition on the tetraone was completed in 1.5 hours. No mono-fullerene addition product remained, according to MALDI-MS analysis of the reaction mixture. However, there was still pristine fullerene in the reaction mixture, which needed to be purified. When an aliquot of the reaction mixture was injected to the BuckyPrep-M column with toluene eluent, no HPLC peak for the product was observed within one hour of elution. The fact that **5-Bz-5 dimer** does not elute is consistent with the increased retention time trend for

spirocyclic-methano-fullerenes on BuckyPrep-M column observed in section 5.3.

To separate the unreacted starting material, reprecipitation and solvent washing were applied. To avoid high temperature rotary evaporation, I firstly precipitated the mixture out from NMP (boiling point $203\,°C$) by adding an equivalent volume of acetone. Observable precipitations took half an hour to appear, so I left the precipitation for one day to crash out thoroughly. I then thoroughly washed the precipitated mixture with tetrahydrofuran (THF) and chloroform. Those solvents respectively dissolve the unreacted tetraone/base, and pristine fullerene. Finally, 1,2-dichlorobenzene (*o*-DCB) was added to dissolve **5-Bz-5 dimer**. The synthetic procedure of **5-Bz-5 dimer** is summarised in section 3.3.2.6.

The **5-Bz-5 dimer** *o*-DCB solution sample was first characterized by MALDI-MS, UV/Vis spectroscopy, PL spectroscopy, and ^{1}H-NMR spectroscopy. Since there was no HPLC data to prove the purity of the sample, a full-ranged MALDI-MS was conducted (Figure 113a). The MS confirms that the purification protocol worked fine, as the main peaks correspond to the **5-Bz-5 dimer** (Figure 113a, insert). The main peaks located at $m/z\,(\mathrm{M}^-)$: 1650.3, 1651.3, 1652.3, 1653.3, and 1654.3, matching with the theoretical prediction (1649.995, 1650.999, 1652.002, 1653.005, *etc.*). The trace amount of C_{60} peaks in the large range MS is not a purity concern, because it is also unavoidable in the HPLC purified compound. It might originate from fragmentation of the C_{60} derivatives or the *in-situ* generation of C_{60} by laser ablation. The UV/Vis spectrum (Figure 113b) contains the typical absorption band for [6,6] bond addition at $430\,\mathrm{nm}$ range. While this additional band proves the formation of the fullerene derivative, it also suggests that using NMP as the solvent for the Bingel reaction does not change the regio-selectivity of the [6,6] bond addition. Shown in Figure 113c, the PL signal of the **5-Bz-5 dimer** is very strong, especially in the region around $400\,\mathrm{nm}$, which can be assigned to the PL signal from the bridge moiety. A typical C_{60} signal (*e.g.* Figure 57a)[235] at $710\,\mathrm{nm}$ in the 2D-PL contour map (Figure 113c) are also shown. The strong PL signal indicates the lack of vibration mode caused by the high molecular symmetry. The $400\,\mathrm{nm}$ emission excited by $600\,\mathrm{nm}$ excitation plotted at the top-left corner of the contour map is likely an instrumental artefact, as a more

precise two-photon excitation test[245] does not confirm this non-linear optical property. The ^{1}H-NMR spectrum of the dimer ($\delta = 8.22$) was very weak due to its low proton content and poor solubility. I zoomed in the spectrum to highlight its weak signal in Figure 113d. The low hydrogen content of the dimer is benificial for maintaining the long spin relaxation of the endohedral electron spin, since ^{1}H has one of the highest nuclear gyromagnetic ratios among all elements/isotopes, and can cause electron spin relaxation *via* HFC.

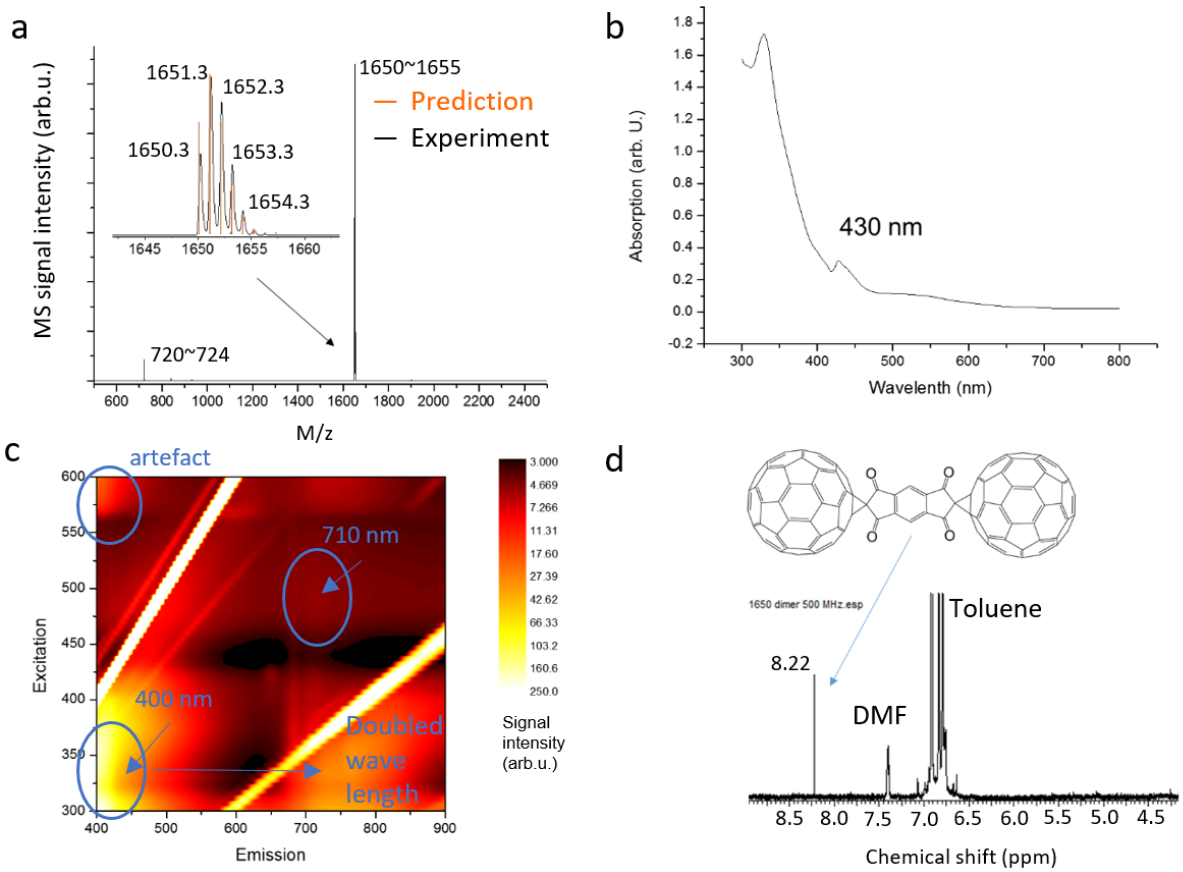


Figure 113 (a) MALDI-MS of 5-Bz-5 dimer (DCTB matrix and negative mode), (b) UV/Vis spectrum of 5-Bz-5 dimer (*c.a.* $0.1\ \mathrm{mg/ml}$ *o*-DCB solution), (c) 2D-PL contour map of 5-Bz-5 dimer (*c.a.* $0.1\ \mathrm{mg/ml}$ *o*-DCB solution), and (d) ^{1}H-NMR spectrum of 5-Bz-5 dimer ($500\ \mathrm{MHz}$, room temperature, and CS_2 solution with one drop of deuterated toluene)

Solid-state cw-ESR spectroscopy on **5-Bz-5 dimer** was also performed. The spectrum (Figure 114) was likely to be contaminated compared to other ENF derivatives reported in this work. It seems that there is an impurity signal overlapped on the signal of **5-Bz-5 dimer**. As mentioned in section 2.3.3, similar impurity signal obtained and proved previously pulsed ESR nutation experiments confirming $S = 1/2$. The impurity quantity was comparable to the ENF

quantity, which is only 0.1% compared to C_{60}. Therefore, it is a rather small impurity in the whole sample but sufficiently significant to affect cw-ESR experiments. I ruled out the possibility of cross-contamination, because repeating the synthesis and purification cannot eliminate the impurity. In spite of the large impurity signal, the low-filed side of the spectrum is not affected. Since ENF derivatives generally have symmetrical cw-ESR spectra with isotropic *g*-factor (2.00243) and HFCC ($A_{\mathrm{iso}}^{(N)} = 15.86\ \mathrm{MHz}$), it is reasonable to assume **5-Bz-5 dimer** maintain this trend, and only fit the left half of the spectra. The simulation suggests ZFS parameters of $D = 10.0\ \mathrm{MHz}$ and $E = 0.5\ \mathrm{MHz}$. In comparison to both Bingel reaction products of $N@C_{60}$ reviewed in section 2.3.3 and synthesized in Chapter 5, the ZFS parameters are in the conventional range. To verify the assignment, a clean solid-state cw-ESR spectrum is still needed.

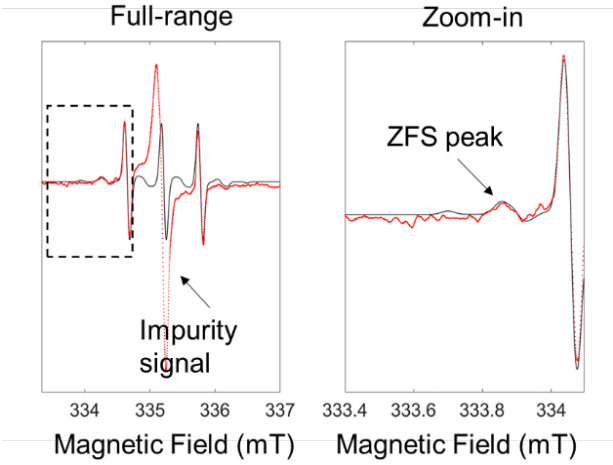


Figure 114 Solid-state cw-ESR of 5-Bz-5 dimer, and the simulation spectrum for the ZFS determination by Easyspin[209] (programme H in appendix). Data were acquired using a Magnettech MiniScope MS200 spectrometer. (Experimental conditions: $9.3960\ \mathrm{GHz}$, $30.0\ \mathrm{dB}$ attenuation, $77\ \mathrm{K}$, and $0.08\ \mathrm{mT}$ modulation amplitude).

The synthesis of **6-NAPH-6 dimer** (Figure 115) followed the same route of **5-Bz-5 dimer** with $N@C_{60}$ $(5.8\ \mathrm{mg},\ 0.1\%$ spin content), pyrene-1,3,6,8(2H,7H)-tetraone $(1.1\ \mathrm{mg})$, I_2 $(2.0\ \mathrm{mg})$, and $4.8\ \mathrm{ml}$ of $0.5‰$ DBU/NMP solution being the starting materials. After the synthesis and purification, which is described in section 3.3.2.7, the product was characterized by MALDI-MS, UV/Vis spectroscopy and solid-state cw-ESR spectroscopy. MALDI-MS (Figure 116a) proves the expected molecular weight of **6-NAPH-6 dimer** (m/z predicted: 1700.011,

1701.014, 1702.018, 1703.021, 1704.024, *etc.*, m/z experimental: 1700.3, 1701.3, 1702.3, 1703.3, and 1704.3). The UV/Vis spectrum (Figure 116b) showed more significant scattering component than conventional N@C_{60} derivatives reported in this work. The background in an exponential function shape masked the absorption in 430 nm. This could be attributed to the poor solubility of **6-NAPH-6 dimer**, which results in aggregation of the dimer in *o*-DCB during the measurement. The solid-state cw-ESR spectrum (Figure 116c) has a similar impurity issue, but ZFS peaks identifying the ENF derivatization were still observable.

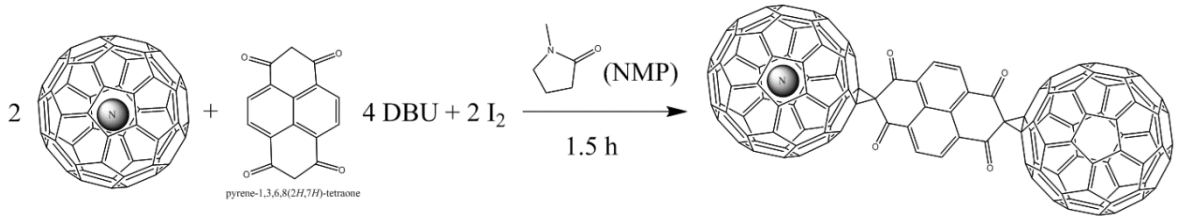


Figure 115 Synthesis of 6-NAPH-6 dimer with Bingel reaction in NMP. Experimental method recorded in section 3.3.2.7.

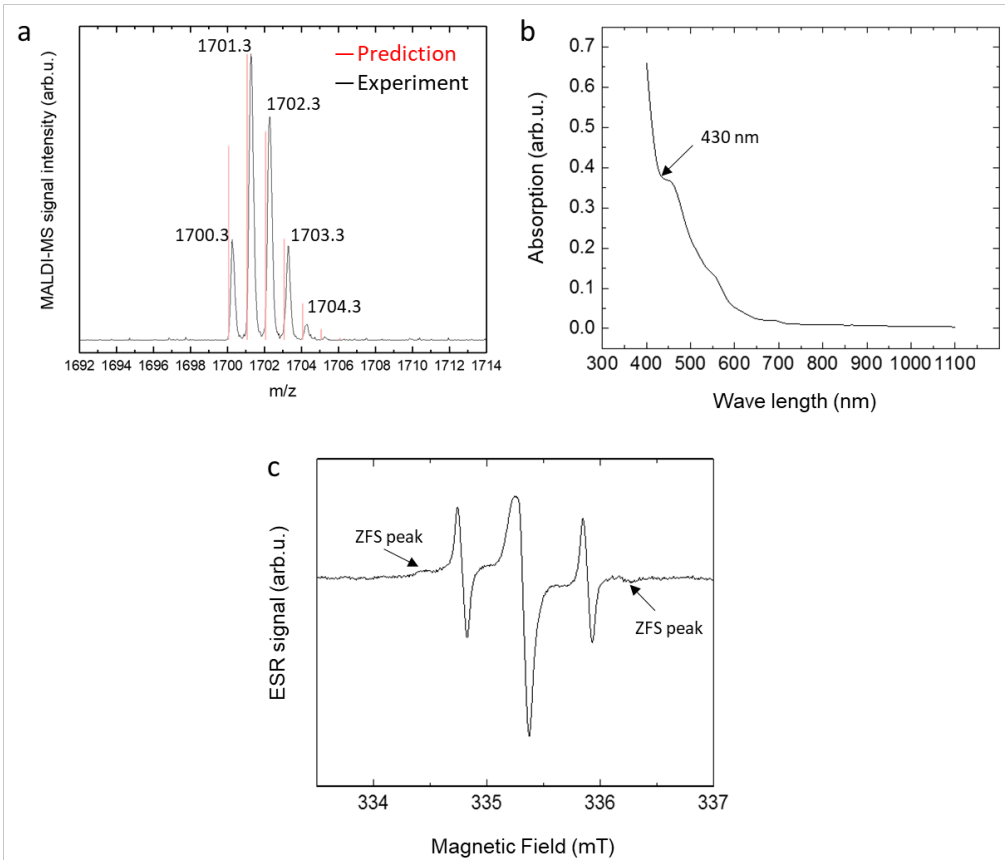


Figure 116 (a) MALDI-MS of 6-NAPH-6 dimer (DCTB matrix and negative mode), (b) UV/Vis spectrum of 6-NAPH-6 dimer (*c.a.* 0.1 mg/ml *o*-DCB solution), and (c) solid-state cw-ESR spectrum of 6-NAPH-6 dimer (Magnettech MiniScope MS200, 9.3953 GHz, 30.0 dB attenuation, 77 K, and 0.08 mT modulation amplitude.)

6.4.3 Synthesis and characterization of 6-OPE-6 dimer

In order to synthesize the **6-OPE-6 dimer**, the bridge of **6-OPE-6** was prepared first *via* a collaboration with Dr. Stuart Cornes in my group. As Figure 117 shows, there are two potential ways of synthesizing the bridge, which start by introducing the trimethylsilyl-acetylene (TMS-acetylene) to the side moiety (**Iodo-QUI**) and to the central moiety (**10-Bromo-Bz** or **12-Iodo-Bz**), respectively.

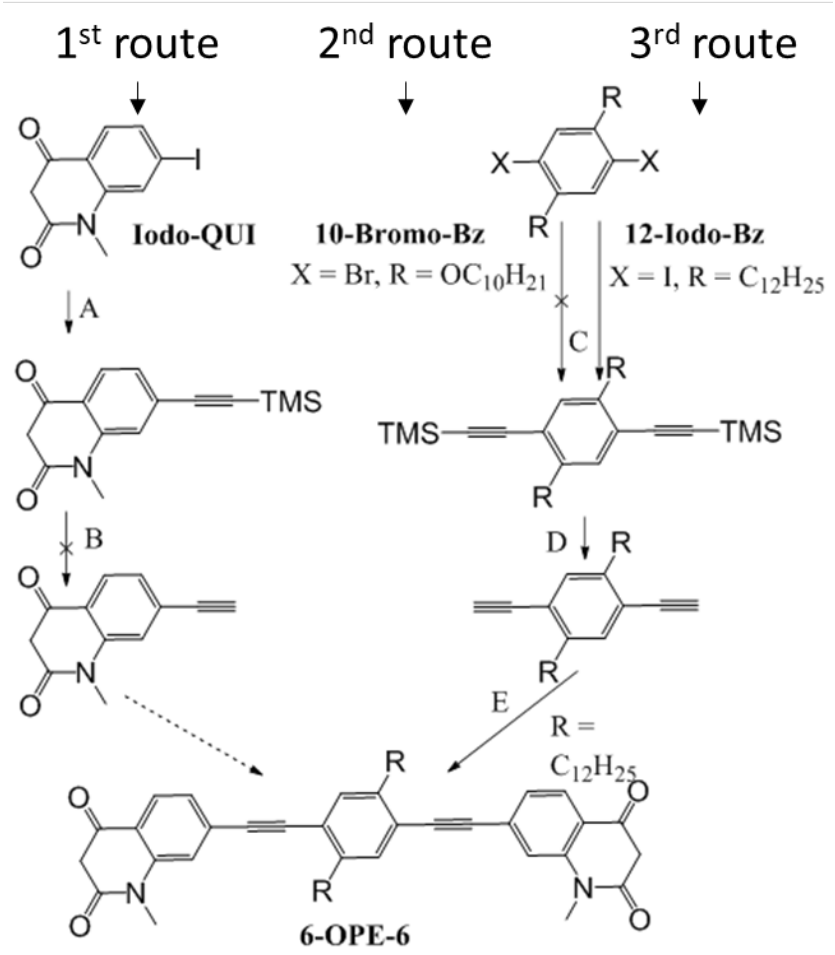


Figure 117 Potential synthesis routes to prepare 6-OPE-6, starting from Iodo-QUI, 10-Bromo-Bz and 12-Iodo-Bz. The reaction conditions are A: 2-fold TMS-acetylene, 5% $Pd(PPh_3)_2Cl_2$, 10% CuI in 1:5 Et_3N/THF mixture, overnight. B: 10-fold K_2CO_3 in 4:3 THF/MeOH mixture, 2 hours. C: 10-fold TMS-acetylene, 5% $Pd(PPh_3)_2Cl_2$, 10% CuI in 1:5 Et_3N/THF mixture, overnight. D:10-fold K_2CO_3 in 4:3 THF/MeOH mixture, 2 hours. E: 2-fold Iodo-QUI, 5% $Pd(PPh_3)_2Cl_2$, 10% CuI in 1:5 Et_3N/DMF mixture, overnight.

The first route was successful for the Sonogashira coupling (Figure 117, step A), despite the low solubility of **Iodo-QUI** in the reaction mixture. This is evidenced by the NMR spectrum of the coupling product (supporting information I). However, the product failed to perform the

sequential TMS deprotection under basic conditions (Figure 117, step B), due to the acidic nature of the α-hydrogen of the 1,3-dione. Thus, this synthesis route was abandoned.

Two types of central moieties are commercially available, but starting from **10-Bromo-Bz** (the second route), bis-addition *via* the Sonogashira coupling suffers a low yield after an overnight reaction with ten-fold of TMS-acetylene (Figure 117, step C). It was difficult to remove the by-product of mono-addition by column chromatography, as confirmed by a purity test with NMR (supporting information I). Replacing the bromine substituted reagent by more the reactive iodine substituted one, **12-Iodo-Bz**, both the low yield and by-product problem were tackled in the same reaction conditions. The corresponding bis-addition product (Figure 118a) and TMS-deprotected product (Figure 118b) were confirmed by ^{1}H-NMR spectroscopy.

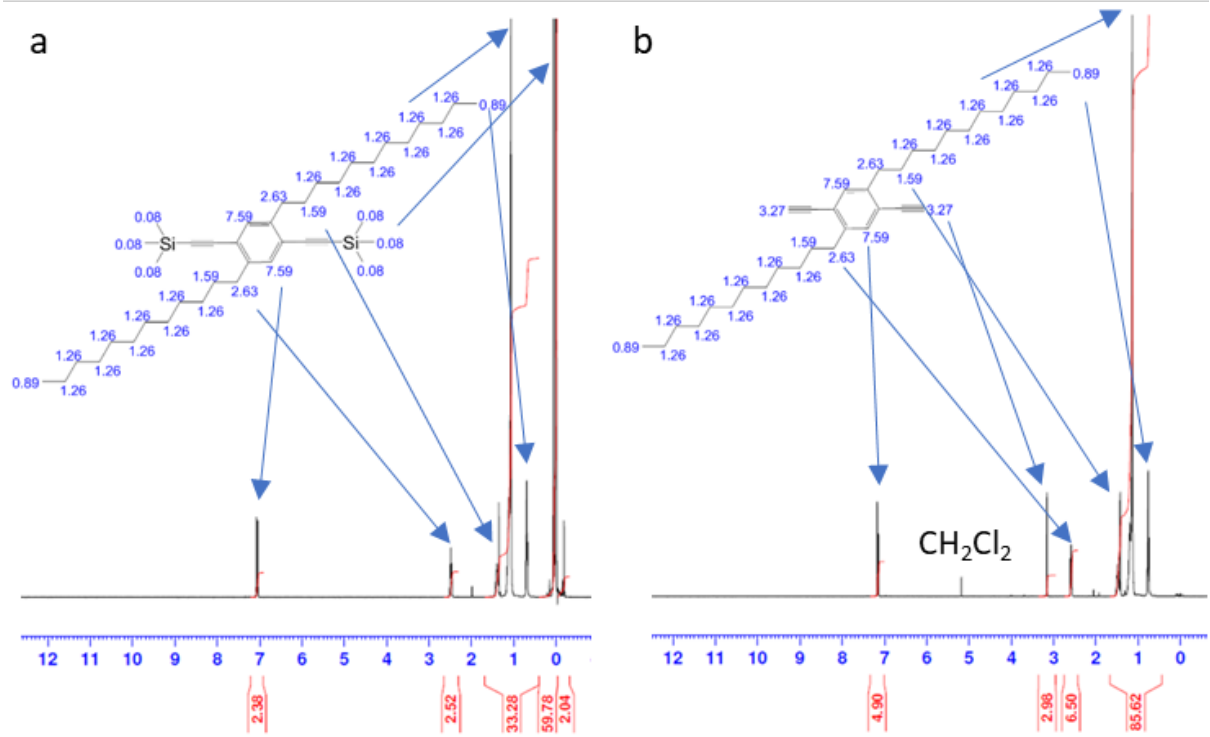


Figure 118 ^{1}H-NMR spectra confirming the formation of bis-addition of Sonogashira coupling between 12-Iodo-Bz and TMS-acetylene (a), and the corresponding deprotected product (b). (400 MHz and $CDCl_3$ solution).

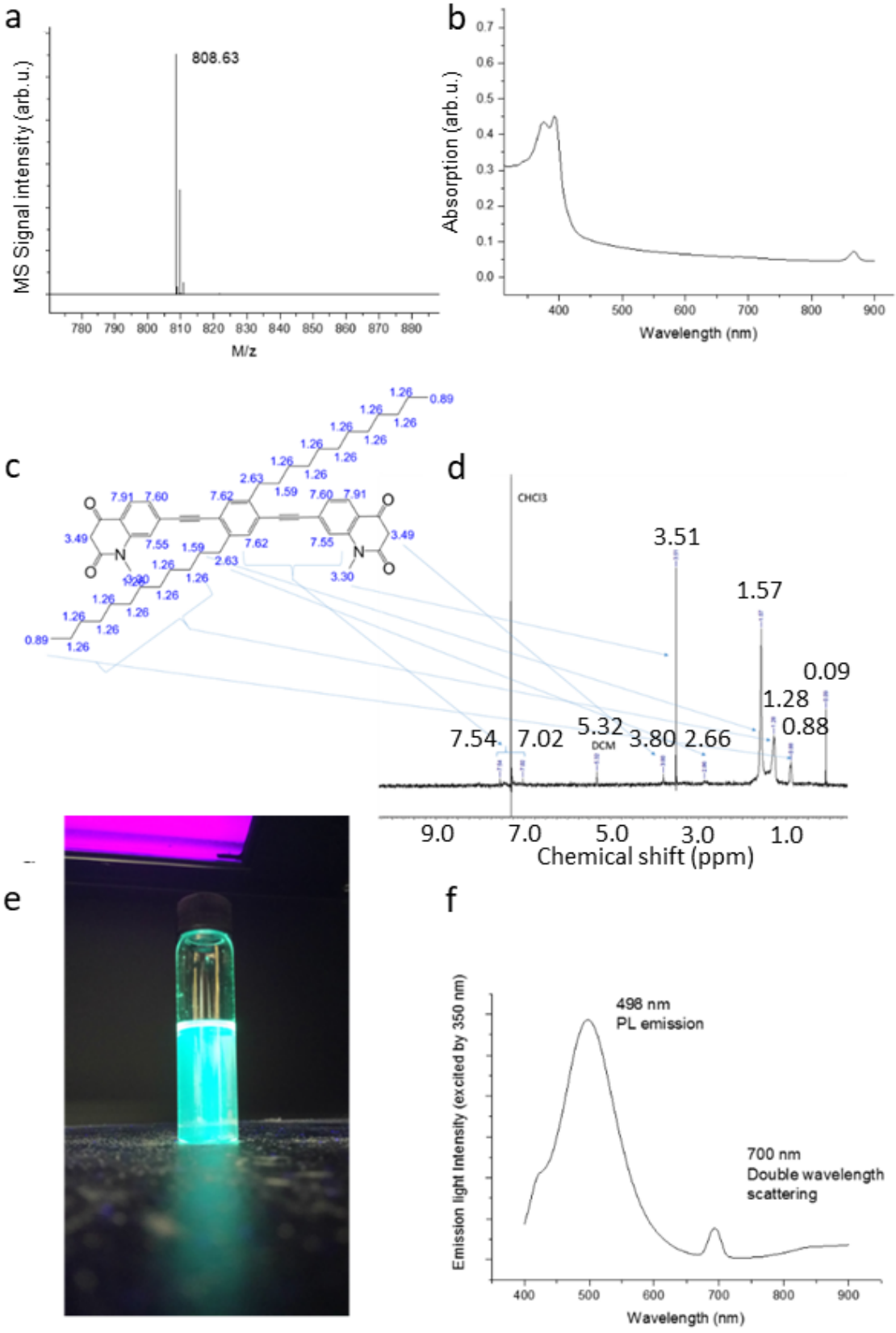


Figure 119 (a) MALDI-MS of 6-OPE-6 (DCTB matrix and negative mode), (b) UV/Vis spectrum of 6-OPE-6 (*c.a.* 0.05 mg/ml toluene solution), (c) Molecular structure and predicted chemical shift of 6-OPE-6, (d) ^{1}H-NMR spectrum of 6-OPE-6 (400 MHz and $CDCl_3$ solution), (e) Picture showing the strong PL of 6-OPE-6, and (f) PL spectrum of 6-OPE-6 (*c.a.* 0.05 mg/ml toluene solution).

I performed another Sonogashira coupling reaction on the deprotected product to link to **Iodo-QUI** and form **6-OPE-6**. Considering the solubility of **Iodo-QUI**, DMF was used to replace THF. Even so, the bis-addition product **6-OPE-6** remained low after an overnight reaction (< 10%). **6-OPE-6** was carefully purified *via* a preparative TLC to isolate starting material and mono-addition by-products. The molecular structure and optical properties of **6-OPE-6** after the purification were confirmed by MALDI-MS (Figure 119a), UV/Vis spectroscopy(Figure 119b), ^{1}H-NMR spectroscopy(Figure 119c, d), and PL spectroscopy(Figure 119f). It is worth noting that the product glows under a UV lamp with a cyan colour; even at μM concentration, this is observable by the naked eye. (Figure 119e).

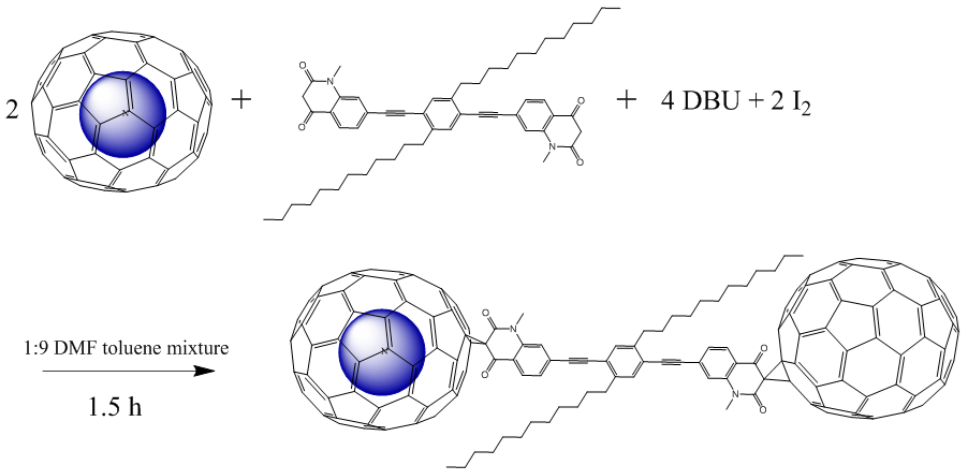


Figure 120 Synthesis of 6-OPE-6 dimer with Bingel reaction. Experimental method recorded in section 3.3.2.8.

With **6-OPE-6** bridge already obtained, the diversity of the Bingel reaction in dimer formation was demonstrated by using $^{15}N@C_{70}$ as the ENF for the synthesis of **6-OPE-6 dimer** (Figure 120). Benefiting from the alkyl chain, the **6-OPE-6** bridge was soluble in 1:9 DMF toluene mixture, thus, no NMP reaction was needed. After 1.5 hours of reaction with $^{15}N@C_{70}/C_{70}$ mixture (2.5 mg), **6-OPE-6** (1.2 mg), I_2 (0.8 mg), and DBU (1.9 ml, 0.5‰ diluted in toluene), precipitants were found in the reaction mixture. After filtration, only C_{70} was obtained in the solution phase, according to a MALDI-MS experiment. The precipitation containing the product was purified by rinsing with different solvents, as HPLC is not applicable to insoluble samples. I washed the precipitation with toluene, chloroform, and methanol in

sequence to dissolve absorbed reagents. After that, the precipitation was dissolved in 1,2-Dichlorobenzene and confirmed as **6-OPE-6 dimer** using UV/Vis spectroscopy, PL spectroscopy, MALDI-MS, and solid-state cw-ESR spectroscopy.

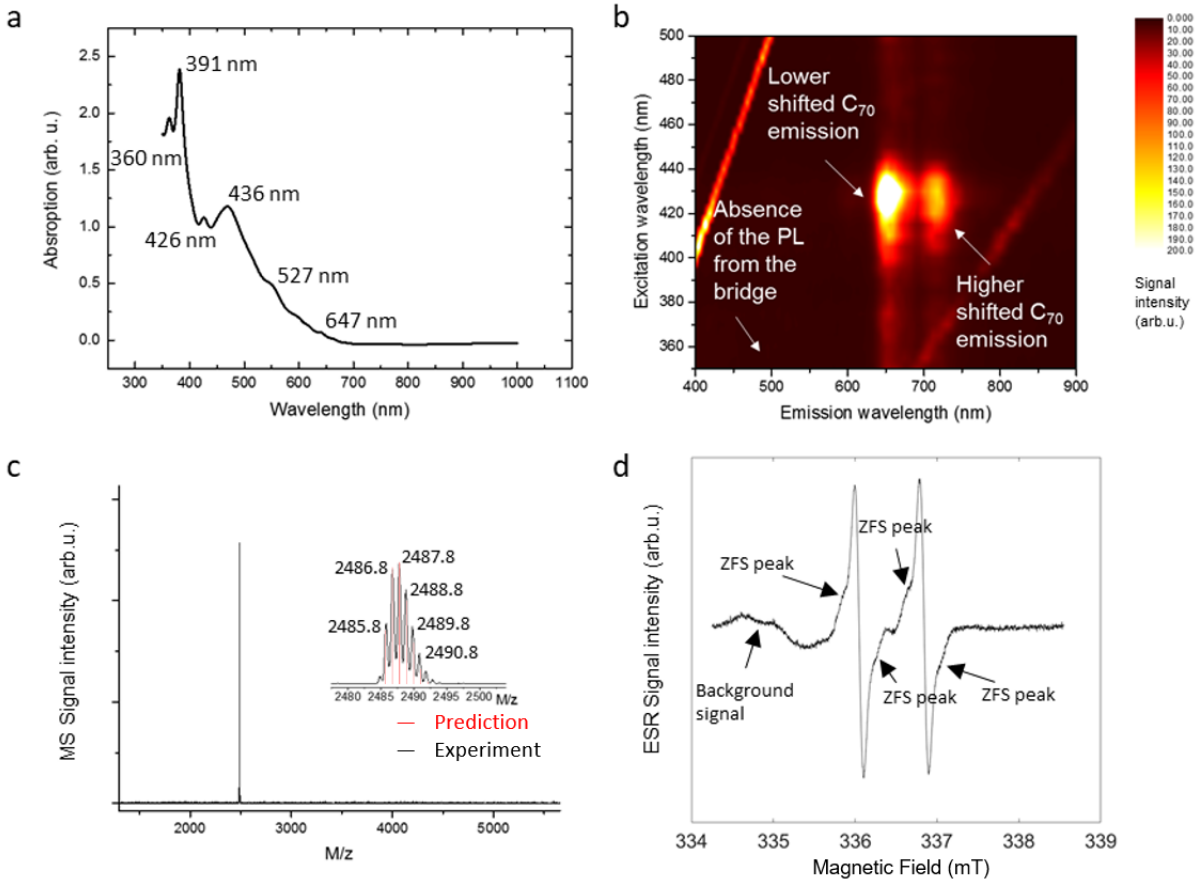


Figure 121 (a) UV/Vis spectrum of 6-OPE-6 dimer (*c.a.* 0.2 mg/ml *o*-DCB solution), (b) 2D-PL contour map of 6-OPE-6 dimer (*c.a.* 0.2 mg/ml *o*-DCB solution), (c) MALDI-MS of 6-OPE-6 dimer (DCTB matrix and negative mode), and (d) solid-state cw-ESR of 6-OPE-6 dimer (Magnettech MiniScope MS200, 9.4289 GHz, 30.0 dB attenuation, 77 K, and 0.08 mT modulation amplitude).

The optical absorption (Figure 121a) maintains the features of C_{70}, with all peaks blue shifted locating at 360, 391, 436, 527, and 647 nm. The blue shifting effect is more pronounced than what was observed for **Bis-IND-N@C$_{70}$** in section 5.3.2. In addition, an absorption peak was obtained at 426 nm presumably due to the presence of the bridge moiety in the dimer. The 2D-PL contour map (Figure 121b) contains slightly shifted C_{70} emissions between 635~745 nm, compared to the twin emission peaks between 650~720 nm, which are shown in Figure 57b and Figure 91d for pristine C_{70}[235] and **Bis-IND-C$_{70}$**, respectively. The signal intensity is enhanced for excitation wavelengths close to 426 nm, which is believed to

be the absorption band of the bridge moiety. In contrast, the strong PL signal of the bridge molecule at $498\,\mathrm{nm}$ was completely quenched after the chemical linkage between the fullerene and the bridge. The MALDI-MS (Figure 121c) recorded in a positive ionization mode with dithranol as the matrix showing that $m/z(\mathrm{M}+\mathrm{H}^{+})$: 2485.8, 2486.8, 2487.8, 2488.8, 2489.8, and 2490.8. Compared with the theoretical prediction (m/z 2485.494, 2486.498, 2487.501, 2488.505, 2489.508, *etc.*), the consistency of the mass/charge ratio and the isotope distribution of the molecular ion peaks between experimental and predicted data proves the covalent linkage of two fullerene cages by the bridge. The solid-state cw-ESR spectrum (Figure 121d) shows two set of HFC peaks caused by ^{15}N ($I = 1/2$) and ZFS peaks due to the symmetry degradation of the cage after the addition. Since N@C_{70} derivatives have smaller ZFS effect than N@C_{60} (reported in 5.3.2), and spectral fitting of the heavily overlapped ZFS peak need good resolution of the lineshape. Therefore, better quality of the solid-state cw-ESR spectrum than Figure 121d is still needed to perform a conclusive simulation.

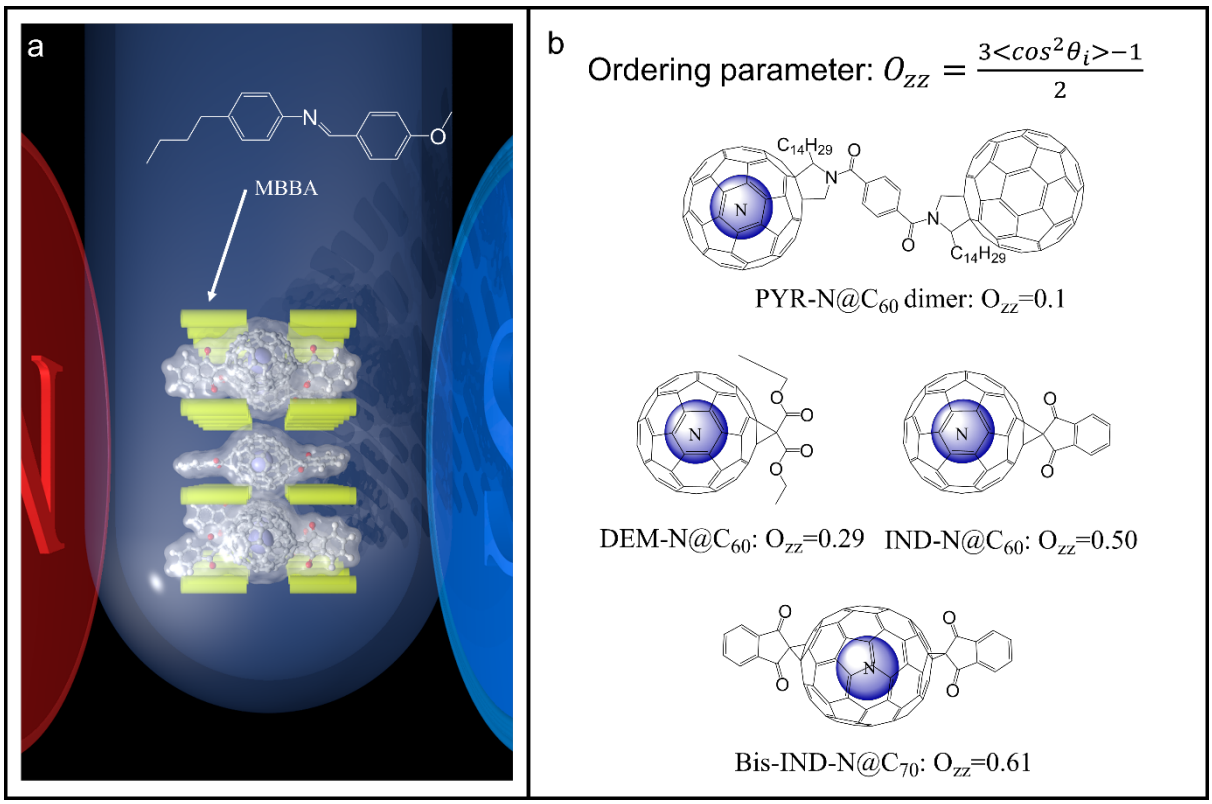
6.5 Conclusions

This chapter focuses on the covalent linkage approach to chemically assembling ENFs to form dyads and dimers. For the dyad preparation, I have synthesized three different ENF−phthalocyanine dyads, which were characterized by UV/Vis spectroscopy and high-resolution MALDI-TOF mass spectrometry. Benefiting from the ionization property of the phthalocyanine, the direct mass spectrum of an ENF derivative was obtained for the first time. The successful linkage of two spin active chemical moieties enables a spin dipolar coupling study later in Chapter 8.

For the dimer preparation, both novel Prato and Bingel schemes are applied. The successful synthesis of the **PYR-N@C_{60} dimer** using the Prato reaction demonstrates that dimerization *via*. N-substitution of the pyrrolidine-attached ENFs are feasible. This new approach can effectively avoid chirality of the spacer group caused by α-substitution of the pyrrolidine, which is prevalently utilized in the literature. The **PYR-N@C_{60} dimer** will be applied to the alignment study in Chapter 7.

The Bingel dimerization schemes is implemented by the synthesis of three ENF dimers (**5-Bz-5-**, **6-NAPH-6-**, and **6-OPE-6 dimer**) with rigid bridge and coaxial conformation. The reactions are made possible by innovatively performing the Bingel reaction in NMP, as this solvent can dissolve both polar reagents and the non-polar fullerenes. Successful characterization using UV/Vis spectroscopy, PL spectroscopy, MALDI-TOF mass spectrometry, and cw-ESR spectroscopy of the products have been conducted to verify their formation. These dimers have the desired conformation control necessary for implementation of ENF assembly. Limited by the difficulty of the product purification, the trace impurity signal displayed in the cw-ESR spectra still needs to be characterized and overcome.

Chapter 7 Axially aligning ENFs in a liquid crystal: Towards orientationally ordered qubits



7.1 Introduction

Using ENFs as a molecular qubit will require directly reading, writing, and adjusting the quantum information embedded within them. For the purpose of obtaining sufficiently strong signals, researchers may process the quantum information in an ensemble way, which reads and manipulates Avogadro-scale numbers of spins as a whole.[72,73] A completely identical spin ensemble is difficult to realize, but still, the more similar the copies of spins are, the less error in QIP will be involved. The orientation uniformity (coherence) of ENF molecules in the ensemble is required to utilize anisotropic spin properties, such as a dipolar coupling between two spin centres and a ZFS within one spin center. Unfortunately, aligning fullerenes axially is not easy.[170,171] As reviewed in section 2.5, different alignment methods for fullerenes, including co-crystallization[155,156] and the liquid crystal alignment,[184,188,192,193,195,196,246,247] have emerged to tackle this problem. While the co-crystallization normally requires thermal treatment or lattice matching of the molecules, the liquid crystal method offers better compatibility with the thermally-sensitive molecules and can be extended to large-scale alignment of molecules.

The orientational uniformity of the sample can be quantified by the order parameter (O_{zz}), which is expressed as follows:

$$O_{zz} = \frac{3\overline{\cos^2\theta}-1}{2} \qquad \text{Eq.7.1}$$

where θ is the molecular angle between the molecule direction and the alignment direction, and the bar symbol represents for the average over all molecules. (E.g. if molecules in a sample has an angular distribution of $p(\theta)$, $\overline{\cos^2\theta} = \int_0^\pi \cos^2\theta \times p(\theta) \times \sin(\theta)\mathrm{d}\theta \,/\, \int_0^\pi p(\theta) \times \sin(\theta)\mathrm{d}\theta$.) Unfortunately, with the order parameter O_{zz} reported in the range of $0\sim0.2$,[192,193,195] previous ENF alignment in liquid crystals was still far from the desired orientation uniformity. Herein, based on novel ENF derivatives reported in Chapter 5 and Chapter 6, I report a set of effective liquid crystal alignment results. A higher order parameter up to 0.61 was measured, which improves upon the best alignment result for ENFs reported previously.

This chapter begins with the liquid crystal alignment method (section 7.2.1) and an explanation of how to characterize the orientation using the ZFS (section 7.2.2). Then ZFS is measured at low temperature (section 7.3.1) and room temperature (section 7.3.2), with order parameters for four different ENF derivatives extracted accordingly. Finally, the controllability of the ZFS anisotropy with a well-aligned ENF derivative assembly is investigated (section 7.4).

7.2 Sample alignment and zero-field splitting

7.2.1 Aligning ENF derivatives in MBBA

To study the alignment of ENF derivatives, four types of representative ENF derivatives (**PYR-N@C_{60} dimer**, **DEM-N@C_{60}**, **IND-N@C_{60}** and **Bis-IND-N@C_{70}**) synthesized in section 5.2, 5.3, and 6.3 were investigated in this chapter. Meanwhile, MBBA (N-(4-Methoxybenzylidene)-4-butylaniline) was selected as the liquid crystal due to its nematic phase at room temperature ($20\sim47\ ^{\circ}\mathrm{C}$).[248] Aiming for an axial alignment of the **PYR-N@C_{60} dimer**, approximately $0.1\ \mathrm{mg}$ of the **PYR-N@C_{60} dimer** was firstly dried completely on a Schlenk line and then dispersed in a slightly-warmed MBBA matrix in its isotropic phase. Sonication at $40\ ^{\circ}\mathrm{C}$ was applied to further mix the host and guest molecules homogeneously in an $\text{ø}\ 4\ \mathrm{mm}$ cylindrical ESR tube. The sample embedded in the liquid crystal was exposed to a magnetic field ($\boldsymbol{B}_0$) around $350\ \mathrm{mT}$ at room temperature to axially align the nematic phase parallel to the $\boldsymbol{B}_0$ field. After 1 minute, an axial alignment for the **PYR-N@C_{60} dimer** was achieved. The other three ENF derivatives were also aligned in the same way.

During the alignment procedure, mutual interactions between the host and guest molecules would be expected. Firstly, the guest ENF derivative may affect the host matrix by their magnetism, but the dipolar field originating from the endohedral electron spin was calculated to be lower than $2\ \mathrm{mT}$ at a $1\ \mathrm{nm}$ distance. This is considerably weaker than the external field and causes no consequence. Secondly, the influence of the host matrix on the guest fullerene is more critical. The axially aligned MBBA molecule forces the embedded fullerene to further align through the van der Waals interaction. The validity of this alignment method was confirmed by successfully reproducing the literature of the cw-ESR spectrum for an aligned N@C_{70} sample (supporting information J).

While the alignment of the sample is supported by the visible anisotropy from specimen's transparency in different directions, a quantitative interpretation of the alignment remains challenging. This is because ENFs, as scarce and precious materials, are typically available

on the nanomolar scale. Common orientation measurements, such as UV/Vis spectroscopy, PL spectroscopy, X-ray diffraction, polarized Raman spectroscopy, have not been reported to detect their presence successfully. Measuring the alignment of the more abundant analogue of the empty-cage fullerene instead might enable us to infer the alignment of the ENF, but the magnetic property difference between the paramagnetic ENF molecules and the diamagnetic empty-cage fullerene molecules may vary their alignment behaviour and cause deviations. Therefore, the best way to directly measure the alignment of an ENF sample in a liquid crystal is to extract the orientational information from its cw-ESR spectrum. Since both the *g*-tensor and the HFC tensor for ENFs and their derivatives were found to be almost isotropic.[142,144,147] I used the ZFS tensor, which is anisotropic, as a good indicator to characterize the sample alignment.

7.2.2 Zero-field splitting and its containing orientation information

The spin Hamiltonian and energy levels of the $S = 3/2$ spin system of an ENF derivative are illustrated in Figure 122a. The non-zero ZFS lifts the degeneracy of the transitions plotted in blue (M_S: $3/2 \longrightarrow 1/2$) red (M_S: $1/2 \longrightarrow -1/2$) and green (M_S: $-1/2 \longrightarrow -3/2$) in the energy diagram. Due to the ZFS, the transitions plotted in blue and green experience a negative and a positive energy shift ΔE_{ZFS}, respectively, and the red transitions remain unchanged. For clarity, I named the peaks corresponding to the blue and green transitions as “the ZFS peaks”, and referred to the peaks corresponding to the red transitions as “the HFC peaks”. Figure 122b is a simulated crystalline cw-ESR spectrum that shows the representative spectral features. Six ZFS peaks appear by the side of the three HFC peaks, and the energy difference between the ZFS peak and the corresponding adjacent HFC peak is ΔE_{ZFS}. This splitting energy is anisotropic and is normally quantified by the traceless ZFS tensor, which can be expressed as a diagonal matrix in the tensor frame (Figure 122c). Therefore, the splitting energy depends on four independent variables:

$$\Delta E_{\mathrm{ZFS}} = \Delta E_{\mathrm{ZFS}}(D, E, \theta', \varphi') \qquad \text{Eq.7.2}$$

where D is the axial term of ZFS, E is the rhombic term of ZFS, the tensor angles, θ' and φ', are the polar angle and the azimuthal angle of the external magnetic field (Z axis of the laboratory frame) with respect to the tensor frame, respectively. When the external magnetic field is parallel to the Z axis of the tensor frame, Eq. 7.2 is maximized and equals twice the axial term D. Otherwise, its value is related to the new $D_{33}{}'$ term after Euler transforming the ZFS tensor from the tensor frame to the laboratory frame. Taking **Bis-IND-N@C$_{70}$** as an example, which has $D = 5\ \mathrm{MHz}$ and $E = 0.64\ \mathrm{MHz}$, as reported in section 5.3.2, Figure 122d depicts the 3D polar contour mapping of the $\Delta E_{\mathrm{ZFS}}(\theta', \varphi')$ value, which depends on the field direction with respect to the tensor frame.

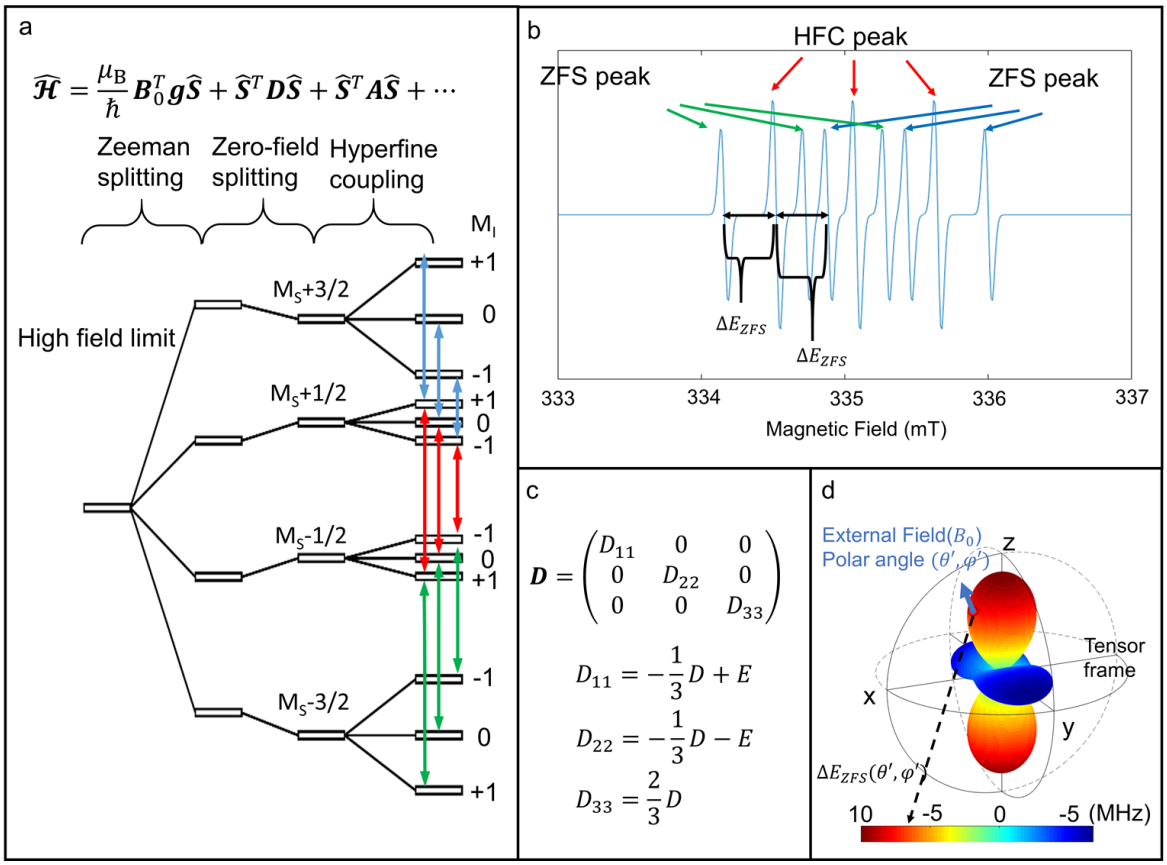


Figure 122 (a) Spin Hamiltonian and energy levels of the $S = 3/2$ spin system in ENF derivatives. (b) Simulated crystalline cw-ESR spectrum. Six ZFS peaks are labelled by green and blue arrows, representing the green and blue transitions in panel a. Three HFC peaks are labelled by red arrows, representing the red transitions in panel a. The energy differences between ZFS peaks and the corresponding adjacent HFC peaks are ΔE_{ZFS}. For clarity, only two of them are representatively marked by black brackets. (c) ZFS tensor in the tensor frame. (d) 3D polar contour mapping of $\Delta E_{\mathrm{ZFS}}(\theta', \varphi')$ for Bis-IND-N@C$_{70}$ ($D = 5.0\ \mathrm{MHz}$, $E = 0.64\ \mathrm{MHz}$) (programme I in appendix).

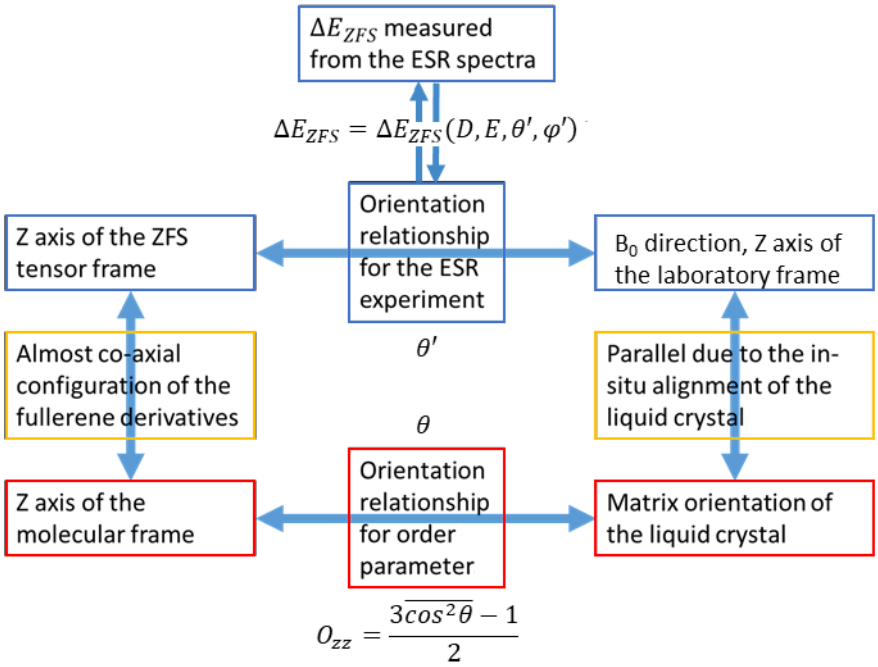


Figure 123 Flow chart demonstrating the relationships between different frames involved in the alignment experiment. Blue boxes: the tensor angle θ' between the ZFS tensor frame and the laboratory frame determines the ZFS energy (ΔE_{ZFS}), thus θ' can be reversely solved by ΔE_{ZFS} fitting. Yellow boxes: the co-axial relationships correlate the ZFS tensor frame and the laboratory frame to the molecular frame and the liquid crystal frame, respectively. Red boxes: the molecular angle θ between the molecular frame and the liquid crystal frame determines the order parameter O_{zz}, which is the alignment result of the ENF derivatives.

One can work out the orientation relationship (θ', φ') between the tensor frame and the laboratory frame by measuring the value of ΔE_{ZFS} (blue boxes in Figure 123) from the contour map. Under the axial alignment experimental condition, the azimuthal angle φ' can be regarded as evenly distributed. Therefore, a relationship between ΔE_{ZFS} and the tensor θ' can be obtained. If the tensor frame and the laboratory frame are parallel to the molecular orientation frames of the ENF and the liquid crystal, respectively (yellow boxes in Figure 123), the tensor angle θ' obtained from ΔE_{ZFS} can represent the molecular angle θ between the ENF direction and the liquid crystal direction. Therefore, the order parameter of an ENF sample embedded in the liquid crystal (red boxes in Figure 123) can be indirectly characterized using the value of ΔE_{ZFS}. To achieve the aforementioned parallel relationships (yellow boxes in Figure 123), both the ENF derivatives and the alignment method were selectively designed in this work. Firstly, the ENF derivatives must have a co-axial conformation to ensure the tensor frame and the molecular orientation frame are parallel to one another (Figure 124). This

is achieved by the novel ENF derivatization schemes in section 5.3 and 6.3. Secondly, the parallel relationship between the field direction and the liquid crystal direction was achieved by *in-situ* alignment of the liquid crystal with the magnetic field of the ESR spectrometer.[248] Unless the orientation of the sample is deliberately tilted after the alignment procedure, which I will discuss later in section 7.4, the prevalent direction of MBBA is parallel to the field direction. The distribution of the orientation of MBBA molecules is the remaining concern, because ENF molecules are aligned parallel to individual MBBA molecule. MBBA has been reported to have an order parameter of $O_{zz} \approx 0.7$, [249,250] when it is at room temperature, and this value further improves to 0.92,[249] when the sample is in a supercooled smectic phase.[251] Both order parameters are sufficiently large for the alignment of ENFs. Therefore, it is reasonable to assume the parallel relationship between the field direction and the liquid crystal direction. Overall, the tensor angle θ' obtained from ΔE_{ZFS} can represent the molecular angle θ.

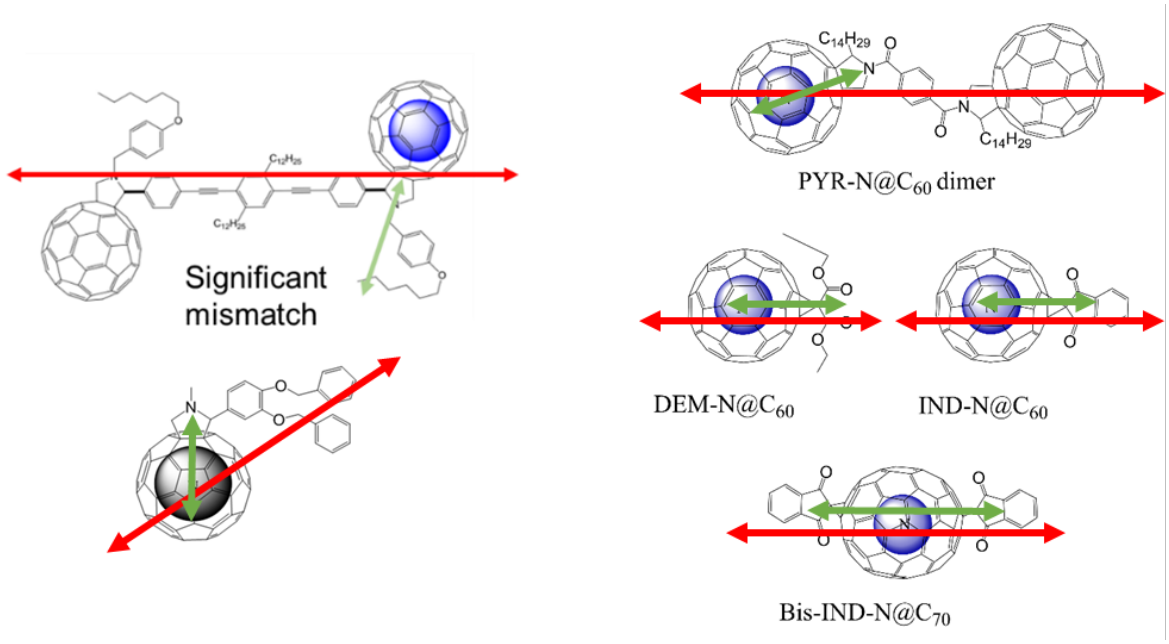


Figure 124 Decease of the intersection angle between the molecular orientation frame (red arrows) and the ZFS tensor frame (green arrows), which is determined by the addend group direction. Compared to α-substituted fulleropyrrolidines,[79,142] derivatives studied in this work have better co-axial conformations.

7.3 Extracting the alignment information

7.3.1 cw-ESR characterization of the aligned sample in the rigid limit

One can use either solid-state or slow motion cw-ESR to measure ΔE_{ZFS} and hence deduce the degree of alignment. Herein, I study the alignment in the rigid-limit regime by freezing the liquid crystal at low temperature in its supercooled smectic phase. A room temperature experiment in the nematic phase of MBBA with a corresponding study on the alignment in a slow-motion regime will be discussed in section 7.3.2.

After using the liquid crystal alignment method to achieve axial alignments of the ENF derivatives (section 7.2.1), I rapidly froze the aligned samples with liquid nitrogen to lock the alignment, and recorded their cw-ESR spectra at $100\ \mathrm{K}$ by inserting the samples into a pre-cooled cryostat. I also tried slowly cooling a sample, but it disturbed the alignment and led to a powder-like ESR spectrum. This is probably due to the impact of the matrix phase transition and solute segregation during the slow cooling procedure.

Given that **Bis-IND-N@C$_{70}$** has the best alignment of all tested derivatives, a complete cw-ESR study and orientation distribution analysis are depicted with this compound first (A brief report for cw-ESR spectra and alignment results for the other derivatives will follow the analysis.). Figure 125a compares cw-ESR spectra of the aligned and the unaligned (powder) **Bis-IND-N@C$_{70}$** sample at $100\ \mathrm{K}$. The three HFC peaks remain unchanged, because they are not related to the ZFS. The ZFS peaks, however, show different patterns in two spectra. Those in the aligned sample are relatively more remote from their adjacent HFC peaks. The axially aligned sample has more molecules orientated closely along the field direction. As section 7.2.2 analysed, it induces most values of ΔE_{ZFS} distributed close to the maximum value, $2D$, where D is the axial term of ZFS ($\mathrm{Z}^{\parallel}$). The orientations of the powder sample have a uniform spherical distribution. Therefore, the powder spectrum has most values of ΔE_{ZFS} distributed near the minimum value ($-D \pm 3E$) obtained in the perpendicular direction ($\mathrm{Z}^{\perp}$).

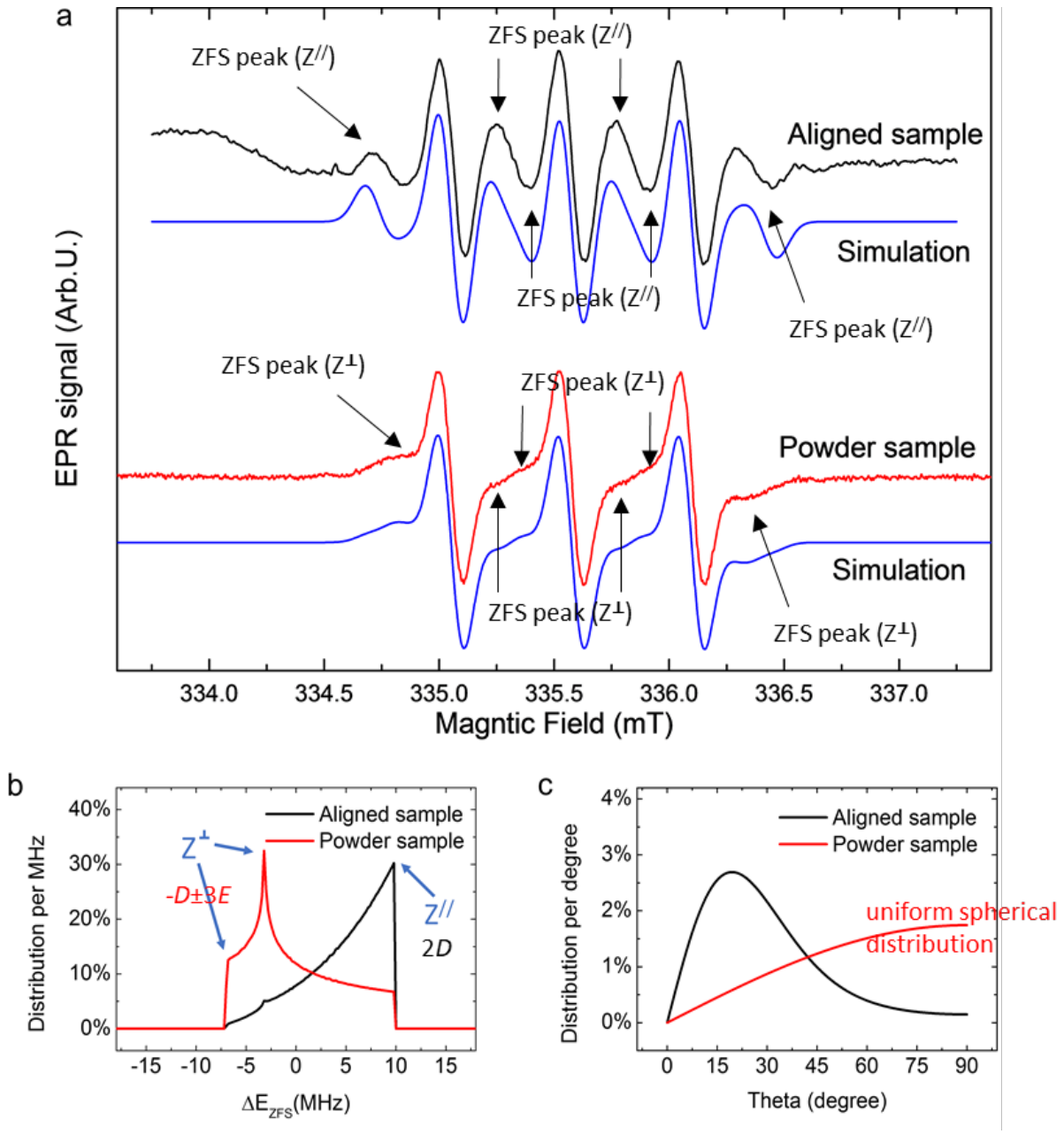


Figure 125 Comparison between an aligned Bis-IND-N@C_{70} sample and a powder one on cw-ESR spectra (a), distributions $p(\Delta E_{\mathrm{ZFS}})$ of the spitting energy of ZFS (ΔE_{ZFS}), (b), and distributions $p(\theta)$ of the molecule direction (θ) (c). The powder data is discussed in Figure 91. The aligned data were acquired from Bruker EMX. (Experimental conditions: $9.4017\ \mathrm{GHz}$, $48.0\ \mathrm{dB}$ attenuation, $100\ \mathrm{K}$, and $0.10\ \mathrm{mT}$ modulation amplitude) The aligned data were simulated by EasySpin[209] (programme J in appendix).

To further explain the difference between the aligned spectrum and the powder spectrum, I performed spectral simulation (Figure 125a) based on modelling the distribution of ΔE_{ZFS}, $p(\Delta E_{\mathrm{ZFS}})$ (Figure 125b). Utilizing the indirect correlation between ΔE_{ZFS} and the molecule direction θ discussed in section 7.2.2, the distribution $p(\theta)$ of the **Bis-IND-N@C_{70}** molecule (Figure 125c) is the key to simulating. Assuming θ follows a Boltzmann distribution, $p(\theta)$ can

be expressed as follows:

$$p(\theta) = \exp\left(\frac{-U(\theta)}{k_{\mathrm{B}}T}\right) / \int \exp\left(\frac{-U(\theta)}{k_{\mathrm{B}}T}\right) d\theta \qquad \text{Eq.7.3}$$

where θ is the molecular angle with respect to the field; $p(\theta)$ is the distribution density of θ; T is the temperature; k_{B} is the Boltzmann constant, and $U(\theta)$ is the axially-simplified ordering potential. Assuming the molecule can be treated as a rigid rotor, $U(\theta)$ can be expressed:

$$U(\theta) = k_{\boldsymbol{B}} T C_{20} d^2_{0,0} = k_{\boldsymbol{B}} T C_{20} \frac{3cos^2\theta - 1}{2} \qquad \text{Eq.7.4}$$

where $d^2_{0,0}$ is from the Wigner *d*-matrix, and C_{20} is the axial ordering potential coefficient.

Using the relationship between C_{20} and the molecule distribution ($p(\theta)$), a least-squares fitting to the cw-ESR spectrum with C_{20} being the variable were then performed (programme J in appendix). Assuming the same spin Hamiltonian parameters for the aligned and powder spectra simulation, I worked out that the axial ordering potential coefficient are 3.0 and 0 for the aligned sample and the powder sample, respectively. By substituting $C_{20} = 3.0$ into Eq. 7.4, 7.3, and 7.1, sequentially, $O_{zz} = 0.61$ was obtained for **Bis-IND-N@C$_{70}$**, which, as far as I know, is higher than any value reported previously for alignment using liquid crystals.[192,193,195]

By applying the same analysis to other derivatives, I determined order parameters **PYR-N@C$_{60}$ dimer**: $O_{zz} \approx 0.1$, **DEM-N@C$_{60}$**: $O_{zz} = 0.29$ and **IND-N@C$_{60}$**: $O_{zz} = 0.50$ (Figure 126). It was found that rigidity and aspect ratio of the molecule are the two main factors that determine the quality of alignment. Rigid derivatives, including both **IND-N@C$_{60}$** and **Bis-IND-N@C$_{70}$**, showed relatively high degrees of alignment, whereas **PYR-N@C$_{60}$ dimer** and **DEM-N@C$_{60}$** exhibited poor alignment results, whether they have a long molecular aspect ratio or not. This observation agrees well with a previous report.[195] However, once sufficient rigidity has been achieved, the molecular aspect ratio begins to play a significant role. This is supported by the fact that the alignment result for **Bis-IND-N@C$_{70}$** surpasses that of **IND-N@C$_{60}$,** where both molecules possess rigid conformations but the former has a longer molecular aspect ratio than the latter.

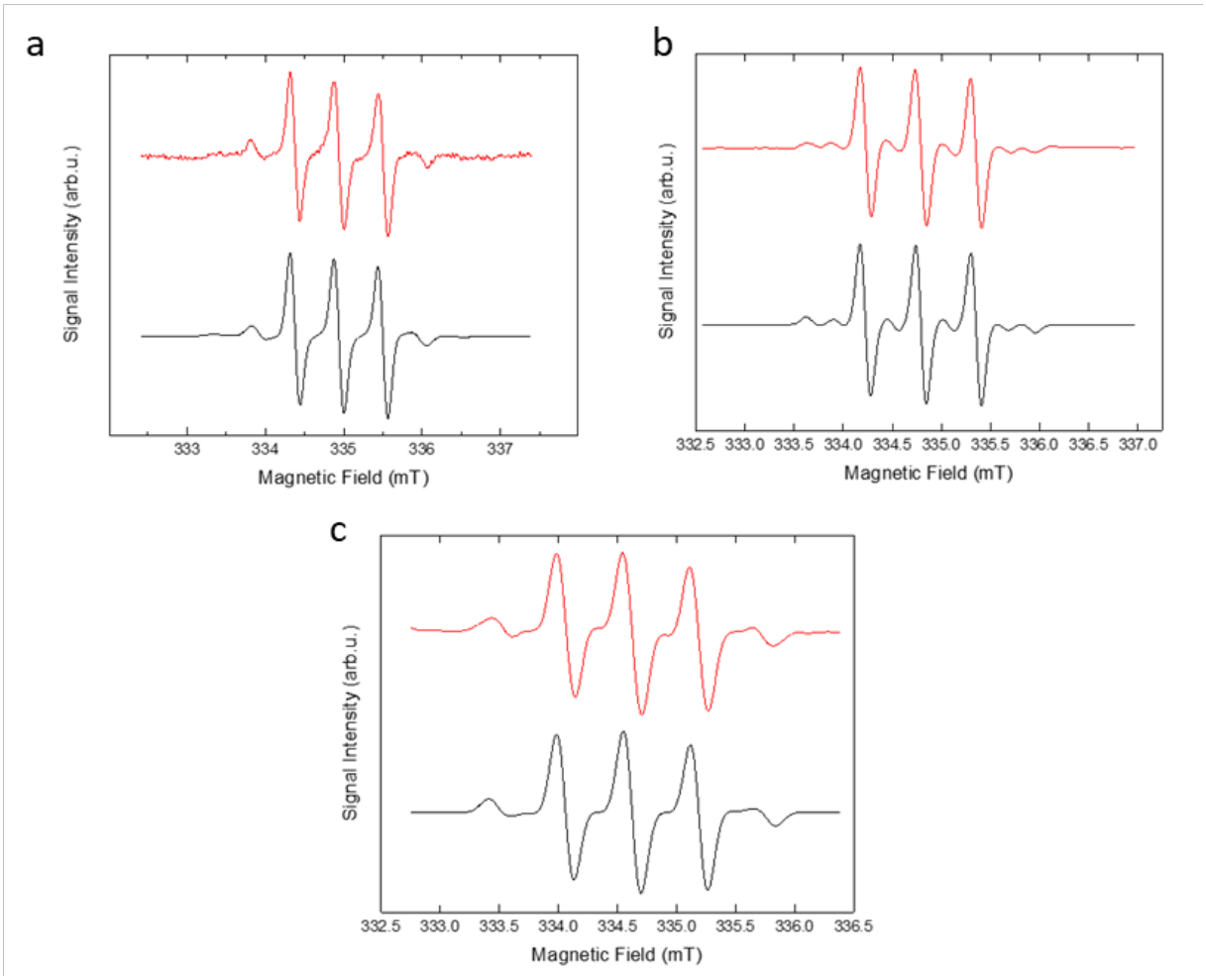


Figure 126 (a) cw-ESR spectra for aligned PYR-N@C_{60} dimer (red) and the simulation based on the order parameter of $O_{zz} = 0.1$ (black). (b) cw-ESR spectra for aligned DEM-N@C_{60} (red) and the simulation based on the order parameter of $O_{zz} = 0.29$ (black). (c) cw-ESR spectra for aligned IND-N@C_{60} (red) and the simulation based on the order parameter of $O_{zz} = 0.50$ (black). The experimental data were acquired from Bruker EMX. (Experimental conditions: PYR-N@C_{60} dimer: 9.3871 GHz, 48.0 dB attenuation, 100 K, and 0.10 mT modulation amplitude. DEM-N@C_{60}: 9.3800 GHz, 58.0 dB attenuation, 100 K and 0.10 mT modulation amplitude. IND-N@C_{60}: 9.3794 GHz, 48.0 dB attenuation, 100 K and 0.10 mT modulation amplitude.) Data for aligned samples were simulated by EasySpin[209] with the same method reported in Figure 125.

7.3.2 cw-ESR characterization of the aligned sample in the slow-motion

At room temperature, the cw-ESR experiment is in the slow-motion regime. The widely-distributed values of ΔE_{ZFS} discussed in the last section are time-averaged. Therefore, the room temperature cw-ESR spectrum shows sharp ZFS peaks, and the energy shift of the ZFS peak with respect to the adjacent HFC peak is $\pm\overline{\Delta E_{\mathrm{ZFS}}}$, where the bar symbol denotes average over time. Instead of simulating the distribution of ΔE_{ZFS}, the order parameter can be directly

extracted from the splitting energy ($\overline{\Delta E_{\mathrm{ZFS}}}$), because:

$$\overline{\Delta E_{\mathrm{ZFS}}} = 2 \cdot \frac{3}{2} \overline{D_{zz}} = 2D\overline{P_2(\theta)} = 2DO_{zz} \qquad \text{Eq.7.5}$$

where the first equality is based upon the definition of the ZFS (Figure 122b), the second equality is derived from the time-average of the second Legendre polynomial,[192] and the final equality is based on the definition of the order parameter (Eq.7.1).

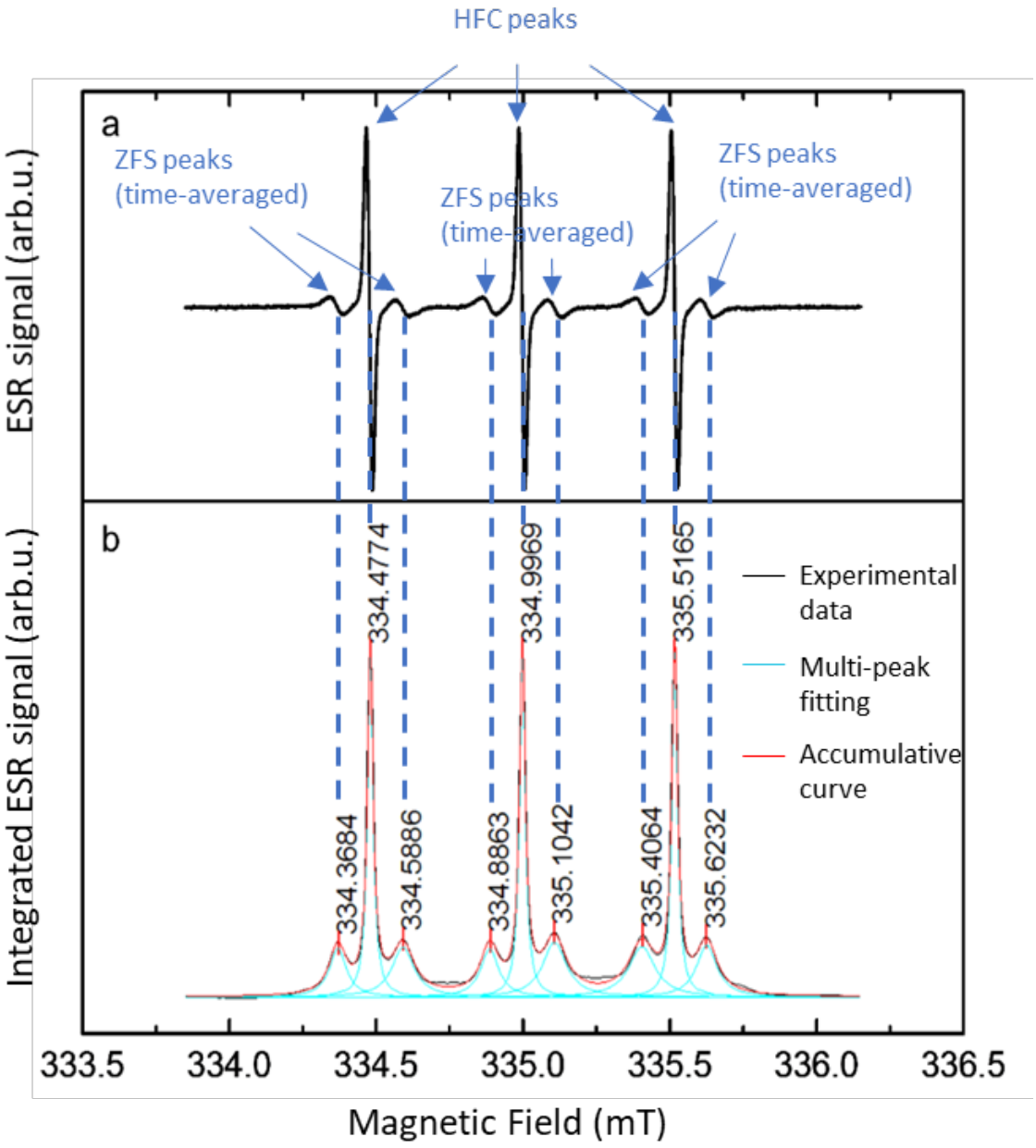


Figure 127 (a) cw-ESR spectrum of Bis-IND-N@C_{70} in MBBA at room temperature. (b) Measuring $\overline{\Delta E_{\mathrm{ZFS}}}$ by fitting the integrated signal with nine Lorentzian peaks. Data were acquired using a Magnettech MiniScope MS200 spectrometer. (Experimental conditions: $9.3883\ \mathrm{GHz}$, $20.0\ \mathrm{dB}$ attenuation, room temperature, and $0.04\ \mathrm{mT}$ modulation amplitude.)

I continue to use **Bis-IND-N@C$_{70}$** as an example to derive the alignment information. The room temperature cw-ESR spectrum of **Bis-IND-N@C$_{60}$** aligned in MBBA is shown in Figure 127a. The six less intense peaks are the ZFS peaks separated from the HFC peaks by the value of $\overline{\Delta E_{\mathrm{ZFS}}}$. To assign the position of each ZFS peaks, I first integrated the cw-ESR signal, and then fitted the integrated spectrum using six small peaks and three large ones (Figure 127b). The ratio between the area of a ZFS peak and a HFC peak is fitted to $3:4$, which matches the theoretical transition probability ratio. Measuring the distance between the ZFS peaks and the HFC peaks, I worked out that $\overline{\Delta E_{\mathrm{ZFS}}}$ for **Bis-IND-N@C$_{70}$** equals $3.1\ \mathrm{MHz}$. The order parameter was subsequently deduced to be 0.31 by applying Eq.7.5 while using the intrinsic ZFS value $D = 5.0\ \mathrm{MHz}$ obtained in section 5.3.

Applying the same analysis to the spectra of the other ENF derivatives (Figure 128), I obtained alignment results for **DEM-N@C$_{60}$** ($O_{zz} = \overline{\Delta E_{\mathrm{ZFS}}}/2D = 3.5\ \mathrm{MHz}/(2{\times}8.4\ \mathrm{MHz}) = 0.21$) and **IND-N@C$_{60}$** ($O_{zz} = \overline{\Delta E_{\mathrm{ZFS}}}/2D = 4.6\ \mathrm{MHz}/(2{\times}8.9\ \mathrm{MHz}) = 0.26$). Unfortunately, no obvious ZFS peaks could be detected in **PYR-N@C$_{60}$ dimer** sample, which means its order parameter is too small to cause a measurably large $\overline{\Delta E_{\mathrm{ZFS}}}$. By assuming that the ZFS peaks are located within the linewidth of the HFC peaks, the $\overline{\Delta E_{\mathrm{ZFS}}}$ for the **PYR-N@C$_{60}$ dimer** must be less than $1.1\ \mathrm{MHz}$, and hence the order parameter of this derivative is estimated to be less than 0.04.

Overall, in comparison to the low temperature cw-ESR characterization, the room temperature characterization provides worse axial alignment results. This is likely due to tumbling of the molecules in the non-rigid nematic phase and a wider Boltzmann distribution caused by a higher temperature. Nevertheless, the order parameter of **Bis-IND-C$_{70}$** still managed to show an improvement, compared to other ENF derivatives, including **PYR-N@C$_{60}$ dimer**, **DEM-N@C$_{60}$**, and **IND-N@C$_{60}$** reported in this work, as well as N@C$_{70}$ and[192] N-substituted-fullero[6,6]pyrrolidines[195] reported previously. Such a result further reinforces the hypothesis that high molecular rigidity and a high aspect ratio are critical to achieving a high degree of axial alignment with a spin ensemble formed from ENF-derivative molecules.

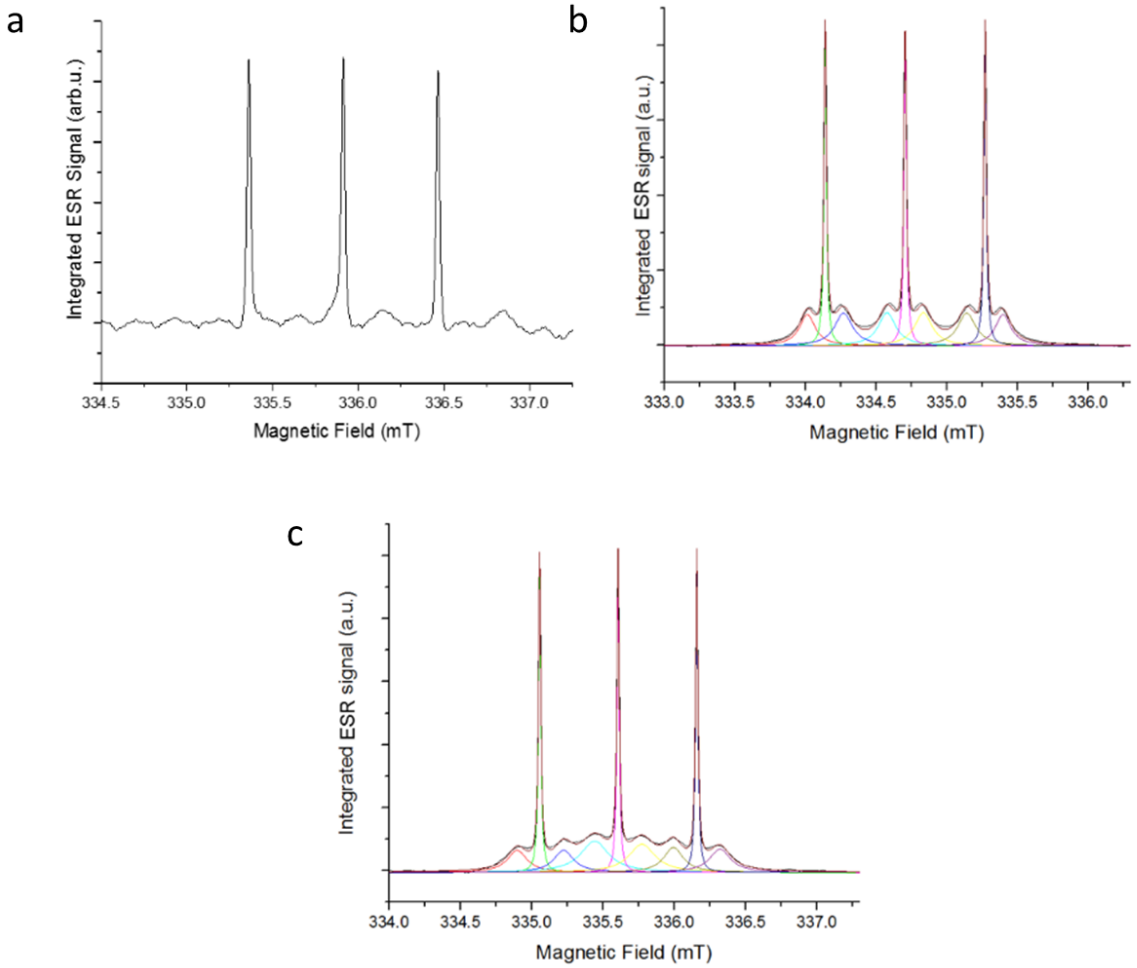


Figure 128 Measuring $\overline{\Delta E_{\mathrm{ZFS}}}$ with PYR-N@C_{60} dimer (a), DEM-N@C_{60} (b), and IND-N@C_{60} (c). The PYR-N@C_{60} dimer failed to show clear ZFS peaks for the multi-peak fitting. Data were acquired using a Magnettech MiniScope MS200 spectrometer. (Experimental conditions: PYR-N@C_{60} dimer: $9.3883\ \mathrm{GHz}$, $20.0\ \mathrm{dB}$ attenuation, room temperature, and $0.04\ \mathrm{mT}$ modulation amplitude. DEM-N@C_{60}: $9.3796\ \mathrm{GHz}$, $20.0\ \mathrm{dB}$ attenuation, room temperature, and $0.04\ \mathrm{mT}$ modulation amplitude. IND-N@C_{60}: $9.4056\ \mathrm{GHz}$, $20.0\ \mathrm{dB}$ attenuation, room temperature, and $0.04\ \mathrm{mT}$ modulation amplitude.)

7.4 Controlling the strength zero-field splitting

The advantage of using the rigid limit cw-ESR experiment is not only limited to a better alignment result. It also provides orientation controllability of the spin ensemble. With the well-aligned samples, **IND-N@C$_{60}$** and **Bis-IND-N@C$_{70}$**, obtained using the frozen liquid crystal method, I performed a series of angle-dependent cw-ESR tests to demonstrate the controllability of the anisotropic ZFS effect.

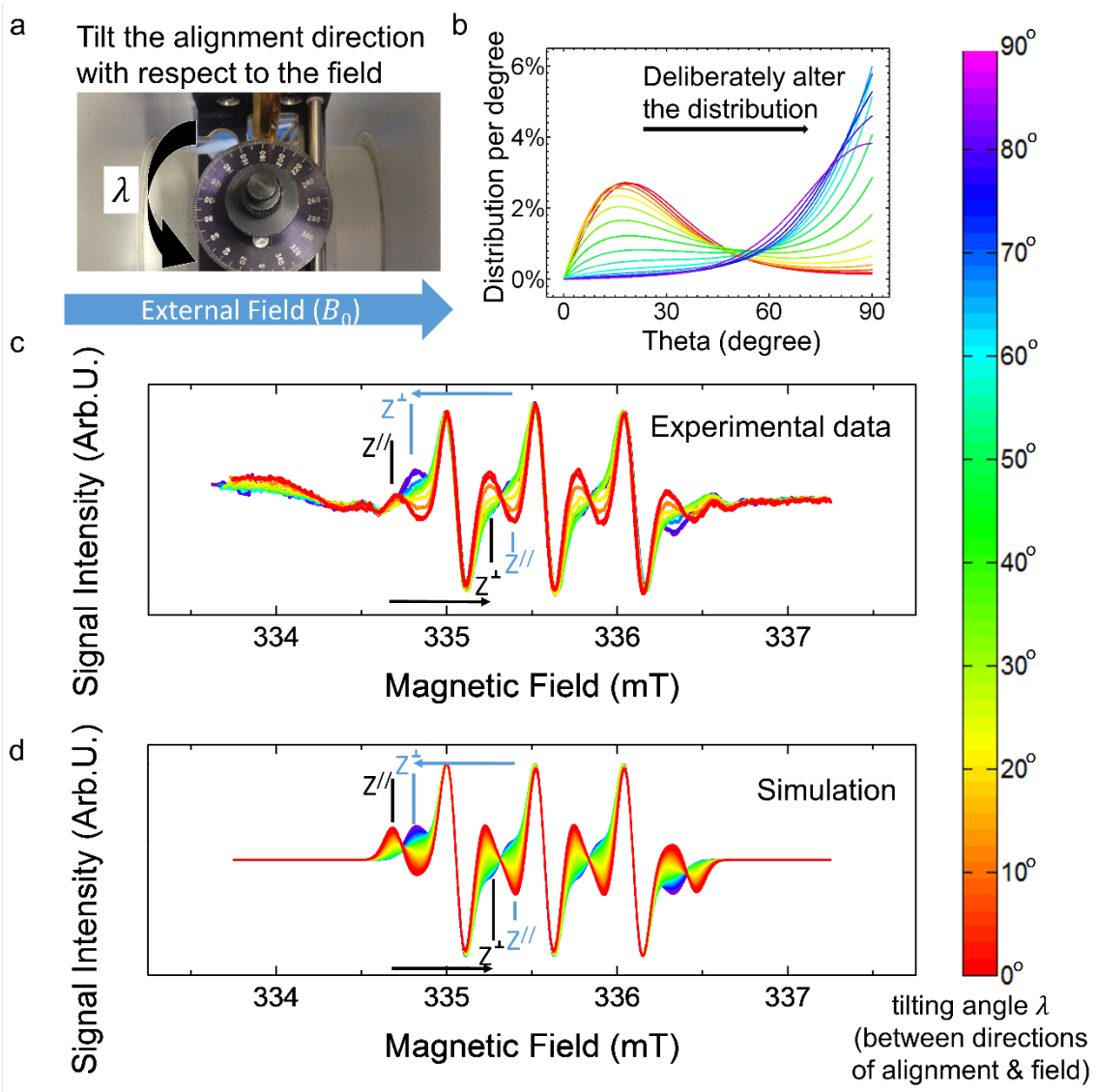


Figure 129 (a) Experimental setup of tilting the alignment direction of the frozen sample with respect to the external magnetic field *in situ*. (b) Calculated distributions of the ZFS tensor Z axes with respect to the field after a tilting angle λ applied. (c) cw-ESR spectra with various the tilting angles. (d) Simulated angle-dependent cw-ESR spectra. The aligned data were acquired from Bruker EMX. (Experimental conditions: $9.4017\ \mathrm{GHz}$, $48.0\ \mathrm{dB}$ attenuation, $100\ \mathrm{K}$, and $0.10\ \mathrm{mT}$ modulation amplitude) Simulation was performed using EasySpin[209] (programme K in appendix).

Figure 129 demonstrates continuous strength control of the anisotropic ZFS effect in **Bis-IND-N@C$_{70}$**. By rotating the frozen sample inside the magnetic field at $100\ \mathrm{K}$ (Figure 129a) from $0°$ to $90°$, the direction relationship between the liquid crystal and the external field can be manipulated. Therefore, the parallel relationship (Figure 123) between the liquid crystal direction and the magnetic field direction is changed. I recalculated the relationship between the tensor angle θ' (angle between the ZFS tensor Z axis and the magnetic field direction) and molecular angle θ (between the ENF direction and the liquid crystal direction) as follows:

$$\theta' = \arccos\left(\cos(\theta)\cos(\lambda) - \sin(\theta)\cos(\pi - \varphi)\sin(\lambda)\right) \qquad \text{Eq.7.6}$$

where λ is the tilting angle of the sample respect to the magnetic field, and φ is the azimuthal angle of ENF direction with respect to the liquid crystal frame. Since MBBA is a uniaxial liquid crystal, φ is evenly distributed in the liquid crystal frame ($p(\varphi) = 0.278\%$ per degree). The distribution of $p(\theta)$ in the liquid crystal frame, which is only depends on C_{20} has been discuss in Eq.7.3 and 7.4. Applying those distributions to Eq.7.6, I calculated how the distribution of the tensor angle θ' in the laboratory frame depended on tilting angle λ, and present a serials of distribution profiles in Figure 129b. As expected, by changing the distribution of the tensor angle θ' with different tilting angles, the splitting ΔE_{ZFS} could be experimentally controlled in a continuous manner (Figure 129c). To verify the observation, I used the distribution of the tensor angle θ' to simulate a set of angle-dependent spectra with EasySpin[209] (Figure 129d). The agreement between Figure 129c and d confirms that the order parameter assigned to the sample is accurate, and orientational control of the ZFS anisotropy is feasible in practice by a macroscopic rotation. During the rotation, the resonant fields of all six ZFS transitions gradually shift from one side to the other side of the adjacent HFC peaks (depicted by arrows in Figure 129c, d). The shift of peak positions corresponds to the molecule changing from the parallel direction ($Z^{\parallel}$) to the perpendicular directions ($Z^{\perp}$) with respect to the external magnetic field, where the maximum ($2D$) and minimum values ($-D \pm 3E$) of ΔE_{ZFS} were reached,

respectively. At the magic angle of $\lambda = 54.7^{o}$ ($\frac{3\cos^2 54.7^{o}-1}{2} = 0$), the ZFS peaks overlap with the HFC peaks, and ΔE_{ZFS} is effectively zero.

Similarly, an angle-dependent ZFS for axially aligned **IND-N@C$_{60}$** could also be measured. The experiment with a tilt angle of $0°$ has the most separated ZFS peaks, which is caused by the parallel alignment preference of the ENF-derivative molecules (Figure 130a). The experiment with a tilt angle of $90°$ can be interpreted with molecules from perpendicular orientations (Figure 130c). The experiment with a tilt angle of $54.7°$ (magic angle) shows a spectrum with both parallel and perpendicular transitions partially suppressed (Figure 130b). This is because the molecule tilted by $54.7°$ with respect to the magnetic field has $\Delta E_{\mathrm{ZFS}} = 0$, and the corresponding ZFS peaks overlap with the HFC peaks. The residual ZFS peaks that are still visible in Figure 130b can be explained by imperfect alignment of the molecules. Considerable numbers of molecules in the sample were not exactly aligned to the magic angle.

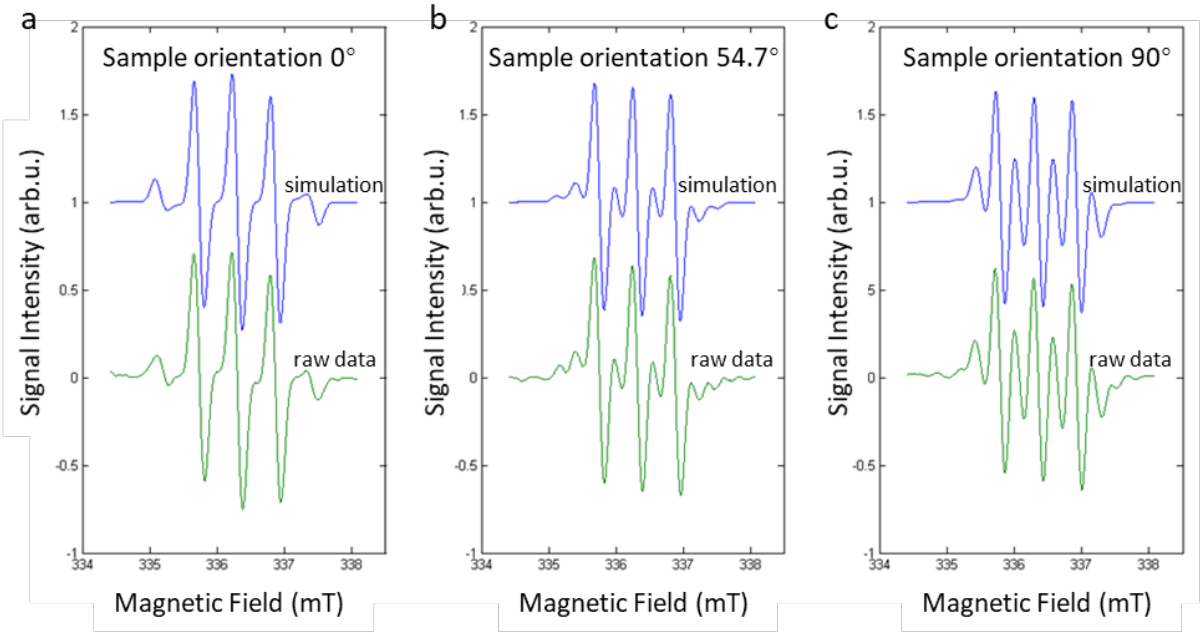


Figure 130 Angle-dependent cw-ESR signal for IND-N@C$_{60}$ obtained at angle 0^{o}, 54.7^{o} and 90^{o}, respectively. The aligned data were acquired from Bruker EMX. (Experimental conditions: 9.3794 GHz, 48.0 dB attenuation, 100 K and 0.10 mT modulation amplitude) The aligned data were simulated by EasySpin[209] with the same method reported in Figure 129d.

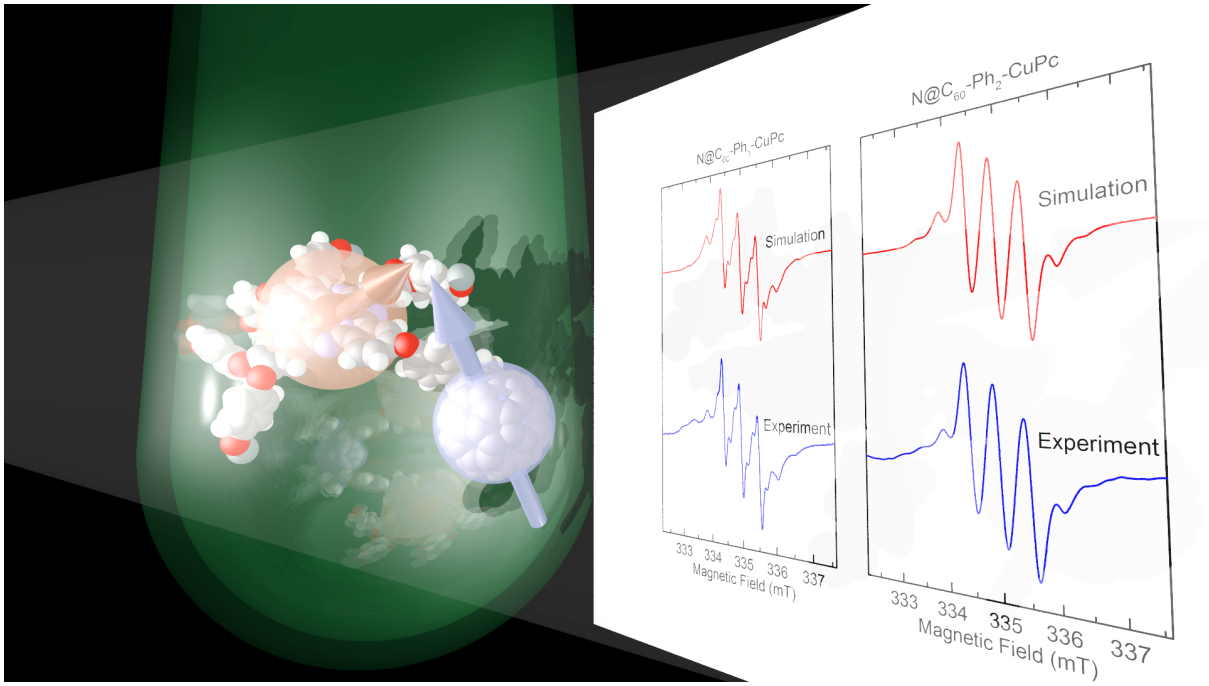
7.5 Conclusions

This chapter analyses the orientation of ENF derivatives using information derived from the ZFS. Alignment results were obtained for four ENF derivatives in both frozen and non-frozen states of a liquid crystal. I found that the lower temperature experiment generally showed better results. This is presumably because the rotation and vibration of fullerene derivatives, which deviate aligned molecules from the energetically favourable orientation, are less significant at a lower temperature.

For the aligned molecules, the results show that a high-rigidity molecule is the primary factor for a good alignment. Once this criterion has been achieved, the aspect ratio of the molecule starts to play a dominant role. Therefore, the best alignment result, with an order parameter as high as 0.61, was obtained with **Bis-IND-N@C_{70}**. With the improved order parameter, an enhanced orientation coherence of ENF spin ensembles was made possible.

With the aligned samples, I demonstrated control over the strength of the intrinsic ZFS of the ENF derivative by macroscopic rotation of the sample. A clear angle-dependent ZFS pattern was achieved. In contrast to the previous study, where the ZFS was caused by the cage distortion imposed by the matrix lattice,[155] the angle dependence of **Bis-IND-N@C_{70}** and **IND-N@C_{60}** are due to the intrinsic ZFS triggered by chemical functionalisation. Such controllability can be directly implemented for other angle-dependent intramolecular spin features, such as dipolar coupling with a di-electron-spin system.

Chapter 8 Probing dipolar coupling in ENF-containing dyads: Towards controllably coupled qubits



8.1 Introduction

In principle, once the microscopic assembly (Chapter 6) and macroscopic alignment (Chapter 7) of ENFs are realized, QIP could be implemented by manipulations of the spin dipolar coupling.[252,253] Various spin dipolar coupling phenomena are well understood, both theoretically and experimentally, in other physical systems.[254–258] Previous electron spin dipolar coupling studies on EF-containing di-electron-spin systems, including N@C_{60}–CuTPP dyad,[198] FSc_3C_2@C_{80}–PNO radical[199] and N@C_{60}–N@C_{60} dimer,[79] are reviewed in section 2.6. Unfortunately, detailed properties of the dipolar coupling in these EF systems were not fully revealed for various reasons. For the N@C_{60}–CuTPP dyad, the spin signal from the fullerene molecule was completely suppressed by the CuTPP moiety because of a strong interaction between the spins. For the FSc_3C_2@C_{80}–PNO radical, the complicated HFC interaction from the three non-equivalent Sc ($I_{Sc} = 7/2$) atoms made the spectra difficult to interpret, and obscured any effect of dipolar coupling. Studies of dipolar coupling in the N@C_{60}–N@C_{60} dimer have been limited by the purity of N@C_{60}. The broad and weak dipolar coupling signal was masked by the sharp and intense signal originating from the half-filled dimer that was also present.

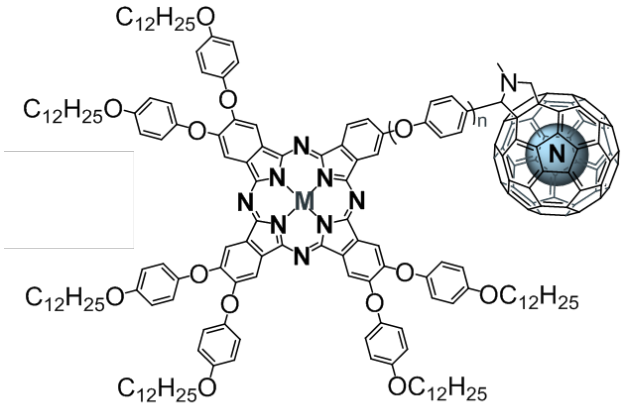


Figure 131 Molecular structure of the ENF–phthalocyanine dyads

As the synthetic detail discussed in section 6.2, a series of hetero-spin systems based on ENF–phthalocyanine dyads (**N@C_{60}-MPc**) were designed and obtained (Figure 131). Three main improvements to the molecular design enable us to overcome the limitations listed above: (1) the long spacer groups between spin centres avoid the complete suppression phenomenon; (2) the use of N@C_{60}, which has sharper spin signals than Sc_3C_2@C_{80}, as the probing spin to simplify spectral interpretation; (3) the hetero-spins resonating at different magnetic fields due different *g*-factors solve the overlap problem without having to use 100% pure N@C_{60}. In addition to these improvements, since CuPc has also been suggested as a promising spin qubit candidate,[56,259] a combination of two different spin-qubits offers extra possibilities for future investigation.

With these novel molecules, I achieved the first comprehensive characterization of the dipolar coupling effect in ENF-containing di-electron-spin systems. By comparing the spectral features of dyads with different spin distances, I showed that changing the spacer group enables tuning of the dipolar coupling strength. Utilizing the aggregation and the resultant Cu electron spin suppressing, I further demonstrated that the concentration of the sample can also be used to influence the coupling strength in a controllable manner.

8.2 Analysis of the electron spin properties of the hetero-spin dyad

8.2.1 Solution cw-ESR

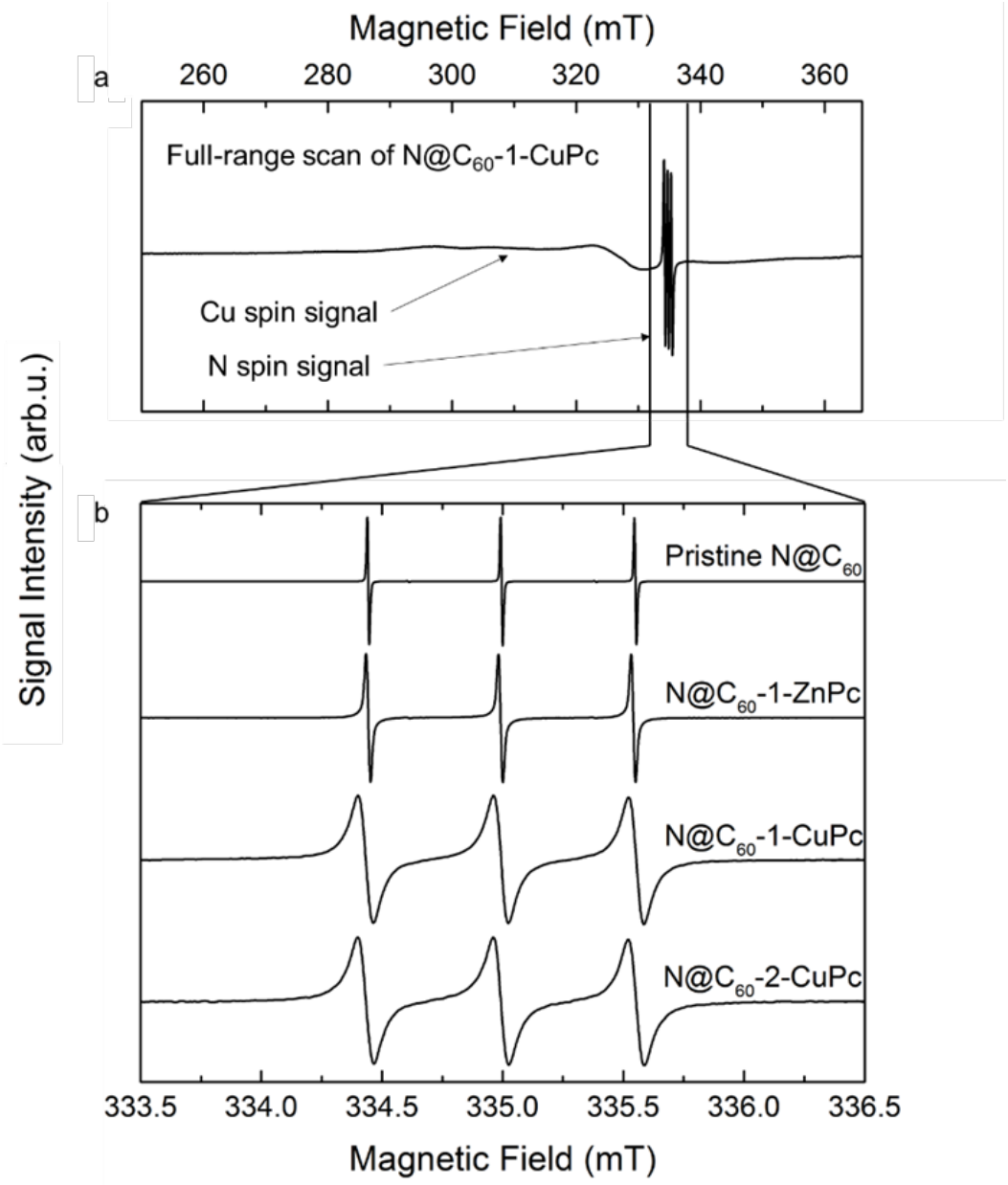


Figure 132 (a) Solution cw-ESR spectrum of N@C_{60}-1-CuPc (full-range), highlighting the fact that the spin signals of Cu and N do not overlap. (b) Solution cw-ESR spectra comparison between pristine N@C_{60}, N@C_{60}-1-ZnPc, N@C_{60}-1-CuPc and N@C_{60}-2-CuPc, which focus on the nitrogen spin region. Data were acquired from Bruker EMX (Experimental conditions: the pristine N@C_{60} sample: Bruker EMX, $9.3882\ \mathrm{GHz}$, $48.0\ \mathrm{dB}$ attenuation, room temperature, $10^{-5}\ \mathrm{M}$ in toluene, and $0.002\ \mathrm{mT}$ modulation amplitude; N@C_{60}-1-ZnPc: Bruker EMX, $9.3831\ \mathrm{GHz}$, $48.0\ \mathrm{dB}$ attenuation, room temperature, $10^{-5}\ \mathrm{M}$ in toluene, and $0.01\ \mathrm{mT}$ modulation amplitude; N@C_{60}-1-CuPc: Bruker EMX, $9.3815\ \mathrm{GHz}$, $48.0\ \mathrm{dB}$ attenuation, room temperature, $10^{-5}\ \mathrm{M}$ in toluene, and $0.03\ \mathrm{mT}$ modulation amplitude; N@C_{60}-2-CuPc: Bruker EMX, $9.3825\ \mathrm{GHz}$, $48.0\ \mathrm{dB}$ attenuation, room temperature, $10^{-5}\ \mathrm{M}$ in toluene, and $0.03\ \mathrm{mT}$ modulation amplitude.)

I first used cw-ESR spectroscopy to study the spin properties of the **N@C$_{60}$-MPc** dyads at room temperature. Among the three dyads, **N@C$_{60}$-1-CuPc** and **N@C$_{60}$-2-CuPc** are di-electron-spin systems, while **N@C$_{60}$-1-ZnPc** contains just one electron spin center. N@C$_{60}$ and CuPc, which contain the $^4S_{3/2}$ state of the endohedral nitrogen atom and the $3d^9$ electron configuration of the central Cu^{2+} ion, respectively, are spin active, whereas ZnPc is spin-silent. Compared with **N@C$_{60}$-1-ZnPc**, the spin signals from the di-electron-spin systems are more complicated. Fortunately, as the full-range spectrum of **N@C$_{60}$-1-CuPc** shows (Figure 132a), the signals from the copper spin and the endohedral nitrogen spin do not overlap, which enables us to interpret them separately. Due to the low concentration of N@C$_{60}$ in the N@C$_{60}$/C$_{60}$ mixture (*ca.* $1:100$), only 1% of CuPc moieties are covalently linked with N@C$_{60}$, whereas 99% of them are coupled with empty-cage fullerenes in the dyad sample. Therefore, studying the electron spin of N@C$_{60}$ moiety has a higher relevance to the spin-spin interaction. In addition, the nitrogen spin also displays a better sensitivity to dipolar coupling due to its sharp signal, compared to the copper spin. With the spin signal of CuPc-CHO discussed in supporting information K, in this section I mainly focus on the electron spin of N@C$_{60}$ moiety.

The zoomed-in solution cw-ESR spectra of the nitrogen spin region (Figure 132b) were studied first. For pristine N@C$_{60}$, **N@C$_{60}$-1-ZnPc**, **N@C$_{60}$-1-CuPc** and **N@C$_{60}$-2-CuPc** dissolved in toluene (10^{-5} M), I obtained the same triplet patterns, which are attributed to the HFC between the nitrogen electron spin ($S = 3/2$) and the nitrogen nuclear spin ($I = 1$). The absence of any extra spectral splitting in the dyad spectra leads to two conclusions: (1) the molecules tumble rapidly in their respective toluene solutions, so that all anisotropic interactions with a traceless tensor, such as the potential ZFS peaks and electron spin dipolar coupling features, are averaged-out; (2) there is no discernible electron spin-spin exchange coupling in either of the dyads ($J_{\mathrm{iso}} \ll 1.7$ MHz based on the linewidth). The second result is different from other diradical molecular systems,[255,260,261] with similar spin separations, that show an exchange coupling splitting in their solution spectra. This can be attributed to the near-perfect protection of the fullerene cage that precludes electronic wavefunction overlap.[198]

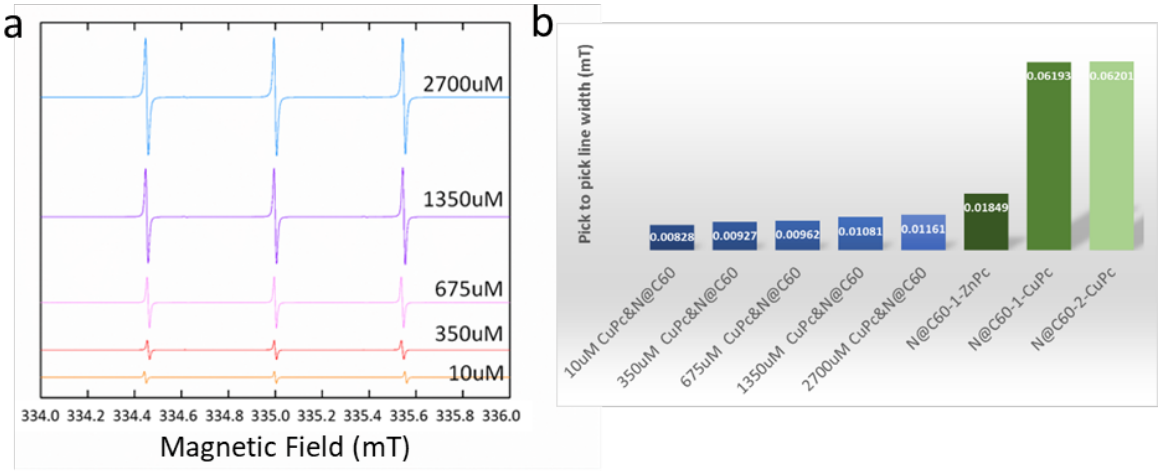


Figure 133 (a) Solution cw-ESR signal (nitrogen spin region) for different concentrations of a CuPc/N@C_{60} mixture $(1{:}1)$ sample in toluene solution. (b) Linewidth comparison between the mixture and the N@C_{60}-n-CuPc dyads. (Experimental conditions: Magnettech MiniScope MS200, 30.0 dB attenuation, room temperature, and 0.005 mT modulation amplitude).

In contrast to the similarity of the spectral splitting patterns, the linewidths, which are inversely proportional to spin relaxation time, varies, provide us with a qualitative approach to compare the relaxation time of the electron spin for each compound. The averaged peak-to-peak linewidth (ΔH_{pp}) for pristine N@C_{60} is measured to be less than 3 μT, representing an ultra-long relaxation time, consistent with previous reports.[49] The averaged ΔH_{pp} of **N@C_{60}-1-ZnPc** is slightly broadened, due to the degradation of the high molecular symmetry,[55] the relatively lower tumbling rate,[143] and dipolar coupling to protons in the Pc moiety,[50] but it is still as sharp as 18 μT. However, the electron spin signals of the di-electron-spin molecules, **N@C_{60}-1-CuPc** and **N@C_{60}-2-CuPc**, are substantially broader, with the averaged ΔH_{pp} increasing to 60 μT and 63 μT, respectively. Considering that physically mixing N@C_{60} with CuPc does not lead to such a significant broadening effect, even at very high concentrations (Figure 133), the broadened linewidths of 60 μT and 63 μT are attributed to the chemical linkage of the two spin centres, which decreases the relaxation time of the endohedral spin considerably due to strong intramolecular electron spin interaction. Since the electron spin exchange coupling has been ruled out in the splitting pattern analysis, the electron spin dipolar coupling has to be the major intermolecular spin interaction mechanism.

8.2.2 Solid-state cw-ESR

Having established the existence of dipolar coupling, I proceeded to measure the solid-state cw-ESR spectra, which allow me to extract more information on the electron spin dipolar coupling strength. Benefiting from the well-controlled reaction conditions, all solid-state spectra of pristine N@C_{60}, **N@C_{60}-1-ZnPc**, **N@C_{60}-1-CuPc** and **N@C_{60}-2-CuPc** have excellent signal-to-noise ratios, and are free of the $S = 1/2$ impurity commonly reported in powder spectra of functionalised N@C_{60}.[142,145]The nitrogen spin regions of these spectra are compared in Figure 134. The solid-state cw-ESR spectrum of pristine N@C_{60} only shows three HFC peaks, which exist in all spectra (indicated by blue arrows). In comparison, **N@C_{60}-1-ZnPc**, which has a lower molecular symmetry, shows characteristic weak and broad ZFS side peaks (marked by red arrows). The ZFS of **N@C_{60}-1-ZnPc** is studied in Figure 135. The simulation (Figure 135b, red trace) of N@C_{60}-1-ZnPc dyad's spin signal was done using EasySpin[209] with the simplified spin Hamiltonian:

$$\widehat{\mathcal{H}} = \left(\frac{\mu_B}{\hbar}\boldsymbol{B}_0^T\boldsymbol{g}^{(N)}\widehat{\boldsymbol{S}}^{(N)} + \widehat{\boldsymbol{S}}^{(N)^T}\boldsymbol{D}^{(N)}\widehat{\boldsymbol{S}}^{(N)} + \widehat{\boldsymbol{S}}^{(N)^T}\boldsymbol{A}^{(N,N)}\widehat{\boldsymbol{I}}^{(N)}\right) \quad \text{Eq.8.1}$$

where μ_B is the Bohr magneton, $\boldsymbol{B}_0$ is the external field, $\boldsymbol{g}^{(N)}$ is the *g*-tensor of the electron spin, $\boldsymbol{D}^{(N)}$ is the zero-field splitting tensor and $\boldsymbol{A}^{(N,N)}$ is the HFC tensor. The small nuclear Zeeman effect and quadrupole interaction were ignored. Using this spin Hamiltonian, the energy level diagrams for differently oriented molecules can be calculated. Figure 135a displays the energy levels for a molecule whose main axis is perpendicular to the magnetic field (the most populated orientation for a powder sample), as well as the allowed transitions between these energy levels. The correspondence between the transitions and the signals is indicated by red arrows. By fitting the simulation to the solid-state cw-ESR spectrum, the axial ZFS parameter D was determined to be $14.2\ \mathrm{MHz}$, and parameter E was negligible, both of which are typical for N@C_{60} pyrrolidine derivatives. The evenly sized HFC peaks as well as the simulated isotropic HFCC, ($A_{iso}^{(N,N)} = 15.4\ \mathrm{MHz}$) confirm that the HFC remains isotropic.

This provides further experimental evidence about the influence of functionalisation of pyrrolidine addends on the HFC to the contradictory reports in the literature mentioned in section 2.3.3.[142,143]

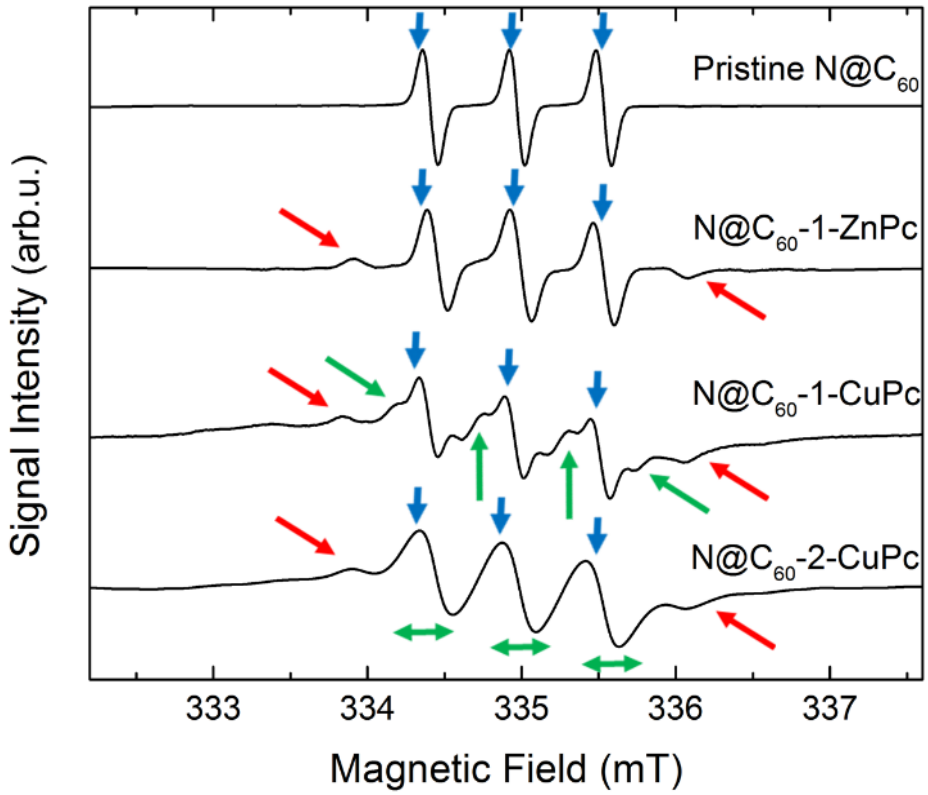


Figure 134 Solid-state cw-ESR spectra (nitrogen spin region) for pristine N@C_{60}, N@C_{60}-1-ZnPc, N@C_{60}-1-CuPc and N@C_{60}-2-CuPc, respectively. The peaks of HFC and ZFS are labelled with blue and red arrows, respectively. The dipolar coupling features, such as fine shoulder peaks and line-broadening, are marked with green arrows. (Experimental conditions: the pristine N@C_{60} sample: Bruker EMX, $9.3874\ \mathrm{GHz}$, $48.0\ \mathrm{dB}$ attenuation, $100\ \mathrm{K}$, $10^{-5}\ \mathrm{M}$ in toluene, and $0.05\ \mathrm{mT}$ modulation amplitude; the N@C_{60}-1-ZnPc sample: Bruker EMX, $9.3890\ \mathrm{GHz}$, $48.0\ \mathrm{dB}$ attenuation, $100\ \mathrm{K}$, $10^{-5}\ \mathrm{M}$ in toluene, and $0.05\ \mathrm{mT}$ modulation amplitude; the N@C_{60}-1-CuPc sample: Bruker EMX, $9.3860\mathrm{GHz}$, $48.0\ \mathrm{dB}$ attenuation, $100\ \mathrm{K}$, $10^{-5}\ \mathrm{M}$ in toluene, and $0.05\ \mathrm{mT}$ modulation amplitude; the N@C_{60}-2-CuPc sample: Bruker EMX, $9.3860\ \mathrm{GHz}$, $48.0\ \mathrm{dB}$ attenuation, $100\ \mathrm{K}$, $10^{-5}\ \mathrm{M}$ in toluene, and $0.05\ \mathrm{mT}$ modulation amplitude.)

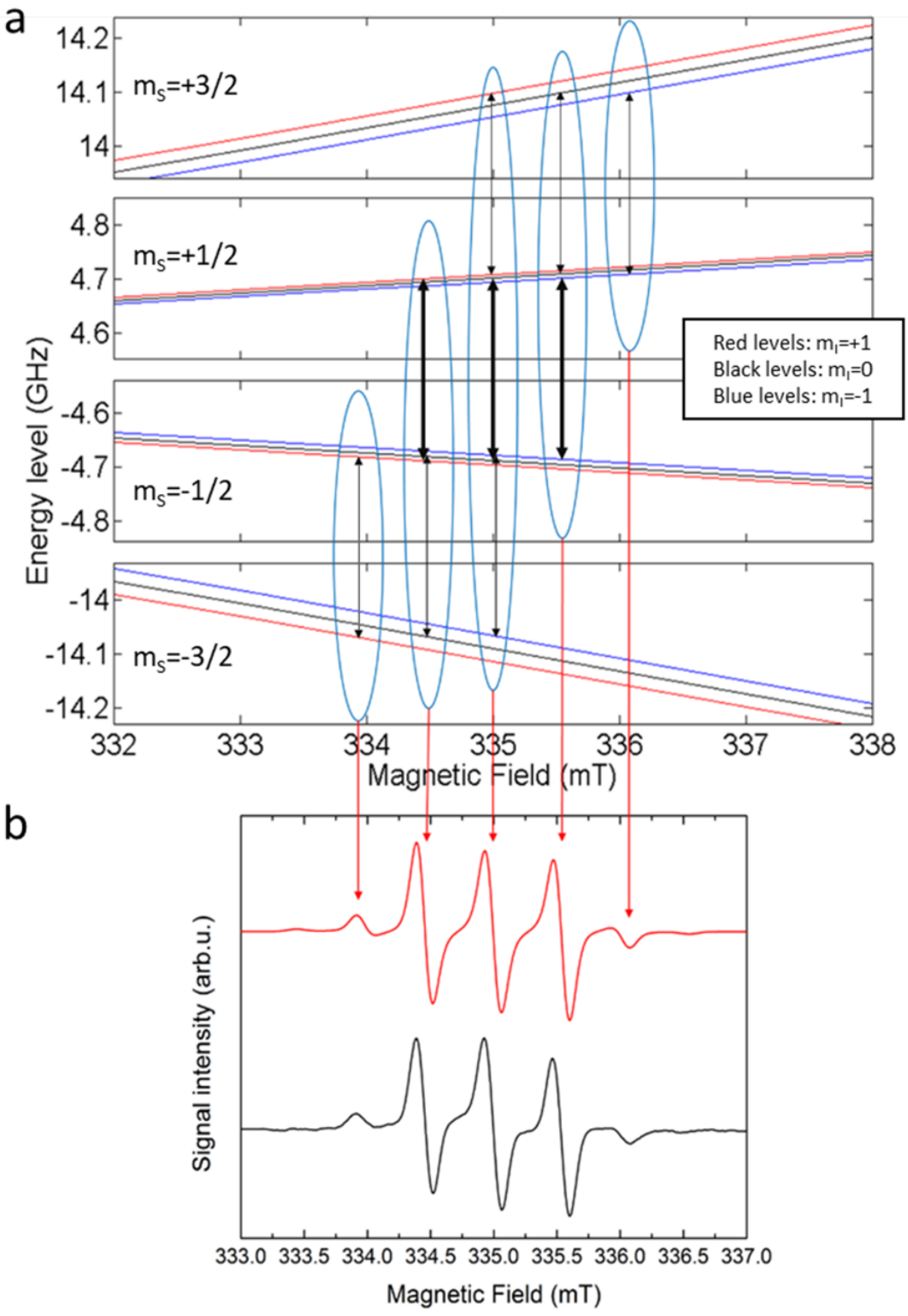


Figure 135 (a) Energy levels of N@C_{60}-1-ZnPc and the allowed transitions. The different widths of the black arrows qualitatively represent different transition probabilities. (b) Simulated spectrum (red) and experimental data (black) for frozen N@C_{60}-1-ZnPc toluene solution. The experimental data is reproduced from Figure 134. Simulation was performed using EasySpin[209] (programme L in appendix). The relationship between the transitions and the signals is indicated by red arrows.

The spectra of **N@C_{60}-1-CuPc** and **N@C_{60}-2-CuPc** in the nitrogen spin region are different from that of **N@C_{60}-1-ZnPc** (see fine features marked by green arrows in Figure 134), even though all these three molecules should have similar ZFS and HFC features due to the nearly-identical structure and electron configuration in the fullerene moiety. I ascribed both of the additional fine features to the variant electron spin dipolar coupling effects, which have been proved to be the major intramolecular spin interaction by the above solution cw-ESR study. However, the fine features of the dipolar coupling in the two spectra still vary. The spectrum of **N@C_{60}-1-CuPc** has more obvious splitting with shoulder peaks emerging next to the HFC peaks, whereas the spectrum of **N@C_{60}-2-CuPc** shows broadened HFC peaks only. I attribute such splitting variation as follows: The extent of the splitting is proportional to the coupling strength,[262] and the dipolar coupling strength is reciprocally proportional to the cube of the spin-spin distance Figure 136a. According to the calculated spin density distributions and preferential configurations for the dyads (Figure 136b and c, performed by Masanori Yamamoto), theoretical estimation suggests that the separations between the spin centres are 16.65 Å (**N@C_{60}-1-CuPc**) and 20.96 Å (**N@C_{60}-2-CuPc**). Subsequently, I further determined that the coupling strength for **N@C_{60}-1-CuPc** (11.2 MHz) is twice as much as for **N@C_{60}-2-CuPc** (5.6 MHz), which explains the splitting variation in their spectra. To the best of my knowledge, this is the first comparison between the solid-state spectra of two variably distanced ENF-containing di-electron-spin systems. In addition, I have demonstrated experimentally chemical tunability of the dipolar coupling strength between the potential spin qubits N@C_{60} and CuPc by changing the length of the bridging unit between them.

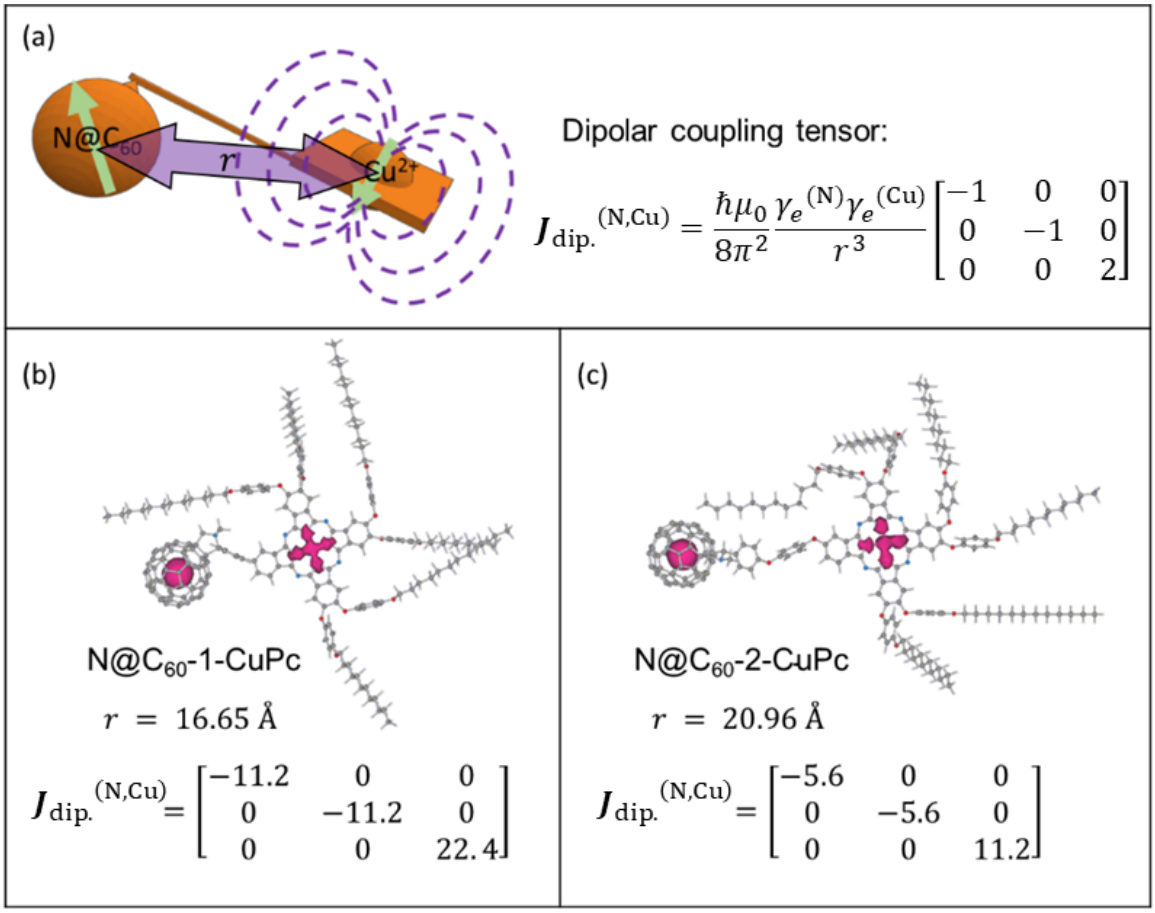


Figure 136 (a) Illustration and equation of the electron spin dipolar coupling depending on spin separation. (b, c) The spin density distributions of the di-electron-spin systems in their corresponding preferential configurations (contour levels are 1×10^{-3} e/au), on the basis of which the electron spin distances and dipolar coupling strength were calculated.

8.3 Dipolar coupling strength study

8.3.1 Initial simulation for the spectra

Despite a successful qualitative interpretation of the dipolar splitting, a quantitative one remains far more challenging. The initial simulation model is based on the spin Hamiltonian for the di-electron-spin systems of the dyads:

$$\begin{aligned}\widehat{\mathcal{H}} &= \widehat{\mathcal{H}}^{(\mathrm{N@C_{60}})} + \widehat{\mathcal{H}}^{(\mathrm{CuPc})} + \widehat{\mathcal{H}}^{(\mathrm{dip.})} \\ &= \left(\frac{\mu_B}{\hbar}\boldsymbol{B}_0^T\boldsymbol{g}^{(\mathrm{N})}\widehat{\boldsymbol{S}}^{(\mathrm{N})} + \widehat{\boldsymbol{S}}^{(\mathrm{N})^T}\boldsymbol{D}^{(\mathrm{N})}\widehat{\boldsymbol{S}}^{(\mathrm{N})} + \widehat{\boldsymbol{S}}^{(\mathrm{N})^T}\boldsymbol{A}^{(\mathrm{N,N})}\widehat{\boldsymbol{I}}^{(\mathrm{N})}\right) \\ &+ \left(\frac{\mu_B}{\hbar}\boldsymbol{B}_0^T\boldsymbol{g}^{(\mathrm{Cu})}\widehat{\boldsymbol{S}}^{(\mathrm{Cu})} + \widehat{\boldsymbol{S}}^{(\mathrm{Cu})^T}\boldsymbol{A}^{(\mathrm{Cu,Cu})}\widehat{\boldsymbol{I}}^{(\mathrm{Cu})} + \sum_{i=1}^{4}\widehat{\boldsymbol{S}}^{(\mathrm{Cu})^T}\boldsymbol{A}^{(\mathrm{Cu,ligand\ N}\ i)}\widehat{\boldsymbol{I}}^{(\mathrm{ligand\ N}\ i)}\right) \\ &+ \left(\widehat{\boldsymbol{S}}^{(\mathrm{N})^T}\boldsymbol{J}_{\mathrm{dip.}}{}^{(\mathrm{N,Cu})}\widehat{\boldsymbol{S}}^{(\mathrm{Cu})}\right)\end{aligned} \qquad \text{Eq.8.2}$$

where all notations are explained in Table 12.

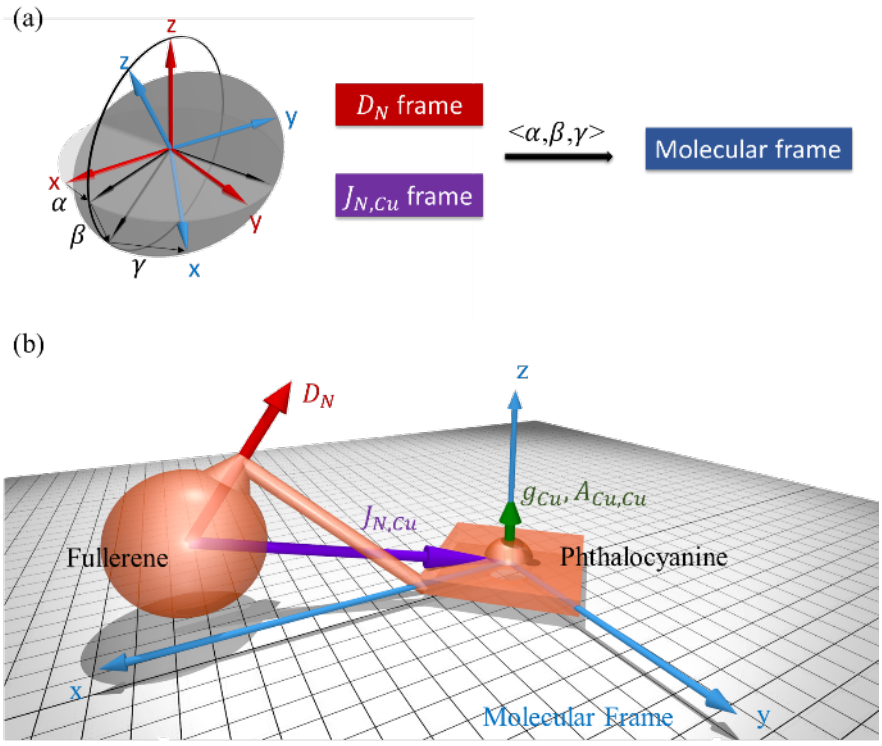


Figure 137 . (a) The definition of the Euler angle converting the tensor frames to the molecular frame. (b) Skeleton model showing the various orientations of different tensor frames and the chosen molecular frame. The molecular frame (blue arrows) is chosen to be parallel to the tensor frame of the *g* tensor and HFC tensor of phthalocyanine (green arrow), while the Z direction of the ZFS tensor (red arrow) and dipolar coupling tensor (purple arrow) need to be rotated to the molecular frame with the Euler angles listed in Table 12

Table 12 Parameters in the spin Hamiltonian for N@C_{60}-1-CuPc and N@C_{60}-2-CuPc

Parameter	Definition	Parameter value in the tensor frame	Euler angle
$\boldsymbol{g}^{(\mathrm{N})}$	*g*-tensor of N@C_{60} electron spin	$\begin{bmatrix} 2.0024 & 0 & 0 \\ 0 & 2.0024 & 0 \\ 0 & 0 & 2.0024 \end{bmatrix}$	Isotropic in both dyads
$\boldsymbol{D}^{(\mathrm{N})}$	zero-field splitting tensor of the N@C_{60} electron spin	$\begin{bmatrix} -7.1 & 0 & 0 \\ 0 & -7.1 & 0 \\ 0 & 0 & 14.2 \end{bmatrix}$ MHz	N@C_{60}-1-CuPc: $< 0°, 83°, 38° >$ N@C_{60}-2-CuPc: $< 0°, 21°, 74° >$
$\boldsymbol{A}^{(\mathrm{N,N})}$	hyperfine coupling tensor between the N@C_{60} electron spin and its nuclear spin	$\begin{bmatrix} 15.4 & 0 & 0 \\ 0 & 15.4 & 0 \\ 0 & 0 & 15.4 \end{bmatrix}$ MHz	Isotropic in both dyads
$\boldsymbol{g}^{(\mathrm{Cu})}$	*g*-tensor of the Cu^{2+} electron spin	$\begin{bmatrix} 2.04 & 0 & 0 \\ 0 & 2.04 & 0 \\ 0 & 0 & 2.16 \end{bmatrix}$	Defined to be $< 0, 0, 0 >$ in both dyads
$\boldsymbol{A}^{(\mathrm{Cu,Cu})}$	hyperfine coupling tensor between the Cu^{2+} electron spin and its nuclear spin	$\begin{bmatrix} -86 & 0 & 0 \\ 0 & -86 & 0 \\ 0 & 0 & -643 \end{bmatrix}$ MHz	Defined to be $< 0, 0, 0 >$ in both dyads
$\boldsymbol{A}^{(\mathrm{Cu,ligand\ N}\ i)}$	hyperfine coupling tensor between the Cu^{2+} electron spin and the nuclear spin from the i^{th} nitrogen ligand spin	$\begin{bmatrix} 50 & 0 & 0 \\ 0 & 50 & 0 \\ 0 & 0 & 50 \end{bmatrix}$ MHz	Isotropic approximation in both dyads
$\boldsymbol{J}_{\mathrm{dip.}}{}^{(\mathrm{N,Cu})}$	electron spin dipolar coupling tensor between the endohedral nitrogen electron spin and the Cu^{2+} electron spin	N@C_{60}-1-CuPc: $\begin{bmatrix} -11.2 & 0 & 0 \\ 0 & -11.2 & 0 \\ 0 & 0 & 22.4 \end{bmatrix}$ MHz N@C_{60}-2-CuPc: $\begin{bmatrix} -5.6 & 0 & 0 \\ 0 & -5.6 & 0 \\ 0 & 0 & 11.2 \end{bmatrix}$ MHz	N@C_{60}-1-CuPc: $< 0°, 70°, 0° >$ N@C_{60}-2-CuPc: $< 0°, 73°, 0° >$

The spin Hamiltonian (Eq.8.2) contains three groups of terms, including endohedral nitrogen spin terms, copper phthalocyanine spin terms and a dipolar coupling term. The negligible HFC between widely-separated nuclei and the electron spins, insignificant nuclear quadrupole interactions and undetected spin-spin exchange coupling are omitted for simplicity.

Individual parameter values in each term were then worked out. For N@C_{60} spin terms, I obtained the parameters by studying the mono-spin sample **N@C_{60}-1-ZnPc**. Likewise, the CuPc-related parameters were adapted from the result of a CuPc sample reported previously,[263] except for the anisotropy of the HFC between the copper electron spin to the nuclear spins of the isoindole nitrogen ligands. This parameter was neglected due to its insignificant influence on the electron spins, thus, not deserving to simulate and fit it simultaneously. More importantly, coping with the anisotropy of $\boldsymbol{A}^{(\mathrm{Cu,ligand\ N}\ i)}$ will cost a great calculation capability, because the four isoindole ligands having different orientations would introduce four anisotropic tensors and their corresponding Euler angles to the simulation. For the last term in Eq.8.2, the dipolar coupling strengths for each dyad were calculated theoretically. The results are given in Figure 136b, c. Apart from obtaining the tensor value, I rotated tensor frames of $\boldsymbol{D}^{(\mathrm{N})}$ and $\boldsymbol{J}^{(\mathrm{N,Cu})}$ to a common molecular frame (Figure 137). The molecular frame is defined based on the *g*-tensor frame of CuPc, and I chose the projection of the line joining the two spin centres in the $X-Y$ plane to be the X axis. The Euler angles rotating the ZFS and dipolar coupling frames to the molecular frame were determined based on the molecular configurations predicted by the quantum chemical calculation using Gaussian 03 software. Other isotropic tensors were directly transformed into the molecular frame without any rotation. For both dyads, Table 12 summarizes the parameter values in the tensor frames, and the Euler angles converting individual tensor frames to the molecular frame.

Based on the spin Hamiltonian and the parameters obtained in Table 12, I fitted the experimental data (Figure 138). Surprisingly, the simulated dipolar coupling is much stronger than the experimental data. The apparent dipolar coupling strengths in the experimental data are *ca.* 30% weaker than the theoretical predictions of $11.2\ \mathrm{MHz}$ and $5.6\ \mathrm{MHz}$ for the two dyads. The reasons for the less prominent dipolar coupling features will be discussed in the following section.

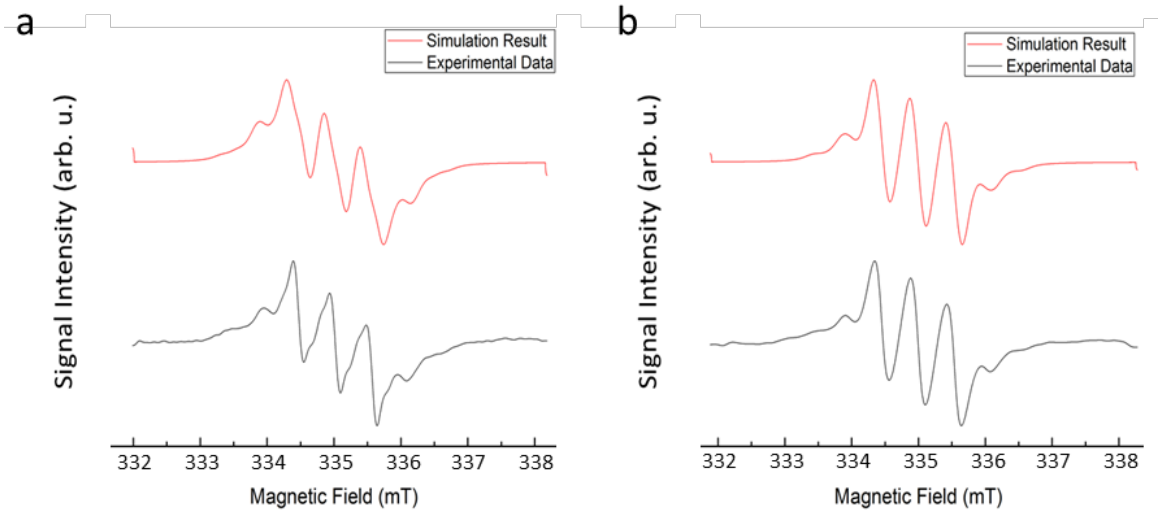


Figure 138 Comparison between experimental and simulated cw-ESR spectra for N@C_{60}-1-CuPc (a) and N@C_{60}-2-CuPc (b). The experimental spectra show a 30% weaker dipolar coupling splitting than the simulated result. Experimental data reproduced from Figure 134.

8.3.2 Explaining the weak coupling strength

One hypothesis is the presence of alternative conformations, such as thermal vibrations of the preferential conformation or the co-existence of different conformers. If these enlarge spin separations in both dyads, lower coupling strengths would be expected. However, when I decreased the measurement temperature to 77 K, the unchanged cw-ESR spectra of each dyad suggests that thermally-induced vibrations do not play a crucial role in spectral deviations. In addition, according to the dynamic MM2 simulation, the dyad molecules vibrate insignificantly due to the relatively rigid molecular structure. Moreover, the vibration decreases the distance between the two dyad moieties, rather than stretching the distance to decrease the coupling strength. Therefore, the simulation's failure to predict the weak coupling cannot be fully explained by alternative conformations.

Another potential explanation could be the magnetic shielding effect of the fullerene cage, because the ring-current effect of the π-conjugated electrons on the fullerene cage may be capable of partially shielding the dipolar magnetic field experienced by the endohedral spin. However, based on the shielding effect reported previously (6 ppm for ^{3}He@C_{60} vs. free ^{3}He,[36] and 19 ppm for N@C_{70} vs. N@C_{60}),[148] the shielding effect of the fullerene cage should be

negligible compared to the observed effect.

With the above reasons excluded, the last potential explanation is that the aggregation of the phthalocyanine moiety in the form of stacking.[264,265] This could indirectly decrease the apparent dipolar coupling strength, because CuPc aggregation in the α-phase can lead to the formation of an anti-parallelly aligned electron spin array, which cancel out the dipolar field from the CuPc moiety.[259,266,267] Figure 139 illustrates the dyad molecules in the non-aggregated and aggregated cases. In the non-aggregated case, the standard dipolar coupling can take place. When the CuPc moieties aggregate, the dipolar field of the copper spin experienced by the nitrogen spin can be significantly suppressed, as the anti-parallel alignment of the copper spins can cancel out the field. Therefore, a weaker apparent dipolar coupling strength can be expected. The evidences for the aggregation and the spin suppressing are demonstrated as follows.

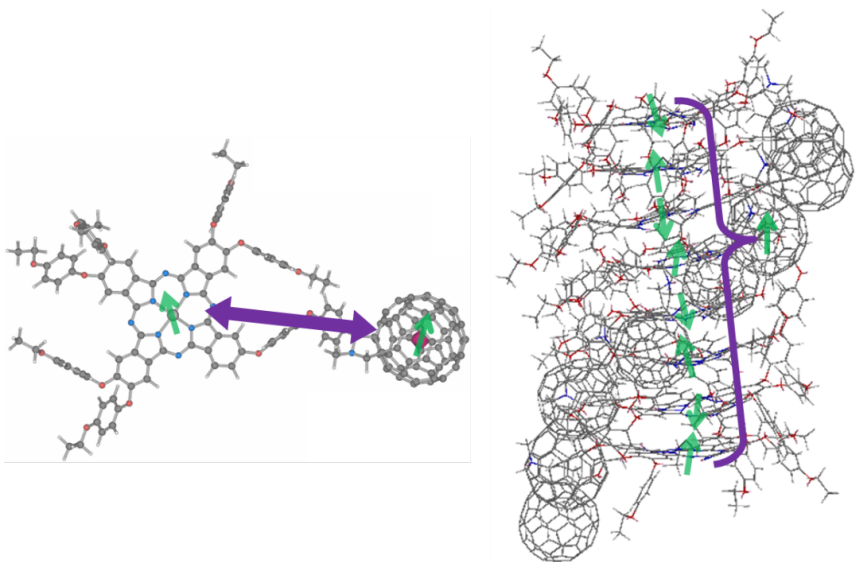


Figure 139 Different dipolar coupling strength experienced by the nitrogen spin in the non-aggregated and aggregated cases. Only one nitrogen spin is expected in the aggregated cluster, due to the 1% ENF content in the reagent.

The aggregation phenomena were confirmed by a room temperature dynamic light scattering (DLS) experiment shown in Figure 140. **N@C$_{60}$-1-CuPc** showed various particle size distribution with the solution concentration ranging from 10^{-7} to 10^{-3} M. Starting from the molecular dimension of 2.1 nm, the average size of the particle grows with increasing concentrations, which means the molecules aggregate to different extents. Since the distance

between two aggregated CuPc layers was reported to be *ca.* $0.4\ \mathrm{nm}$,[268] the average aggregation size could be up to 10 molecules at high concentrations. Nevertheless, even concentrations as high as to $10^{-3}\ \mathrm{M}$, there are still some monomeric particles according to the broad distribution of the bar chart shown in Figure 140. Such a conclusion is also applicable to the solid-state sample, as I froze it into a glass phase rapidly, thus leaving the aggregation clusters insufficient time and energy to change the particle size. Also, the aggregation effect of **N@C$_{60}$-2-CuPc** is principally similar to the result obtained from **N@C$_{60}$-1-CuPc**. Therefore, I confirmed that there are partial aggregation effects in the sample for the solid-state measurements.

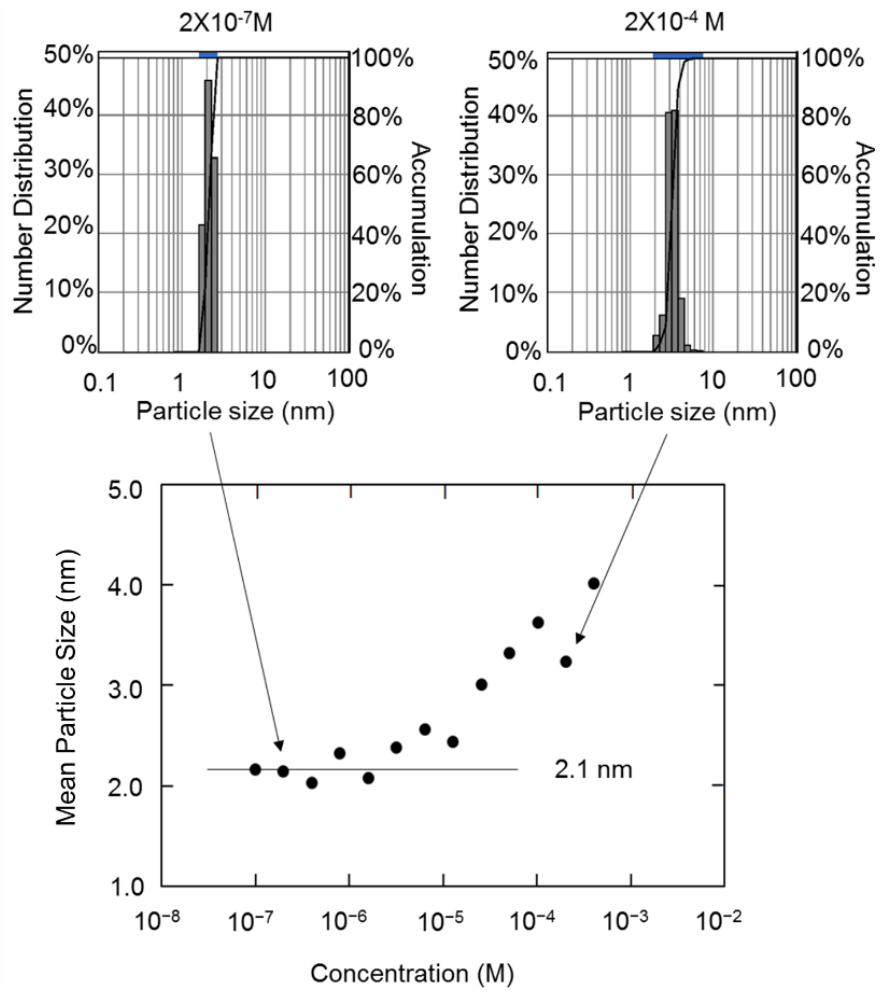


Figure 140 Aggregation behaviour of N@C$_{60}$-1-CuPc in various concentrations in toluene solution according to the dynamic light scattering experiment measured at room temperature. The distributions of particle sizes of two points representing the low and high concentration are selectively demonstrated, showing that partial aggregation occurs over the entire concentration range measured.

Moreover, a cw-ESR study on the intensity of the CuPc electron spin signal suggested a significant spin suppressing phenomenon, which could attribute to a possible antiferromagnetic ordering in the molecular aggregation. Since the antiferromagnetic behaviour of CuPc reported previously[259,266,267] depends strongly on the distance between adjacent CuPc spin centers,[267] one can study the signal suppressing phenomenon of the Cu^{2+} electron spin by intentionally separating stacked CuPc moieties apart. Diluting the sample was first attempted, but the slightly enhanced intensity of the CuPc signal at lower concentration was not strong enough for signal assignment (supporting information L). Adding an excess of **ZnPc-1-CHO**, which has a similar phthalocyanine structure, was chosen to achieve the separation, as ZnPc can form an aggregated array together with CuPc. As illustrated in Figure 141, before adding **ZnPc-1-CHO**, I could barely obtain a heavily distorted and suppressed Cu^{2+} spectrum, whereas after the mixing a spin pattern appears. Since ZnPc-1-CHO is spin silent and cannot give rise to any new cw-ESR signals, I assigned the arising spin signal to the Cu^{2+} spin, based on the spectra simulation and a spectrum from a reference sample of $CuPc^{t}$ (copper(II) 2,9,16,23-tetra-tert-butyl-29H,31H-phthalocyanine). More discussion of the CuPc spin signal based on the starting material of CuPc-1-CHO is documented in supporting information K. The arising of the Cu^{2+} electron spin signal confirms that the stacking of CuPc leads to spin suppressing. In addition to the dilution experiment, I also found that the suppressing of the Cu^{2+} spin signal at $100\ \mathrm{K}$ is much significant than that of the room temperature one. This suppressing phenomenon could be explained by the formation of antiferromagnetic array, which has been reported in other CuPc studies.[259,266,267] Overall, the phenomena of Cu^{2+} electron spin suppressing was demonstrated in the aggregated CuPc moieties, hence, the resultant weakening of the dipolar field strength of the CuPc moiety must be considered. I will discuss the dipolar field strength in the next section and use it to modify the spectral simulation of the dyads.

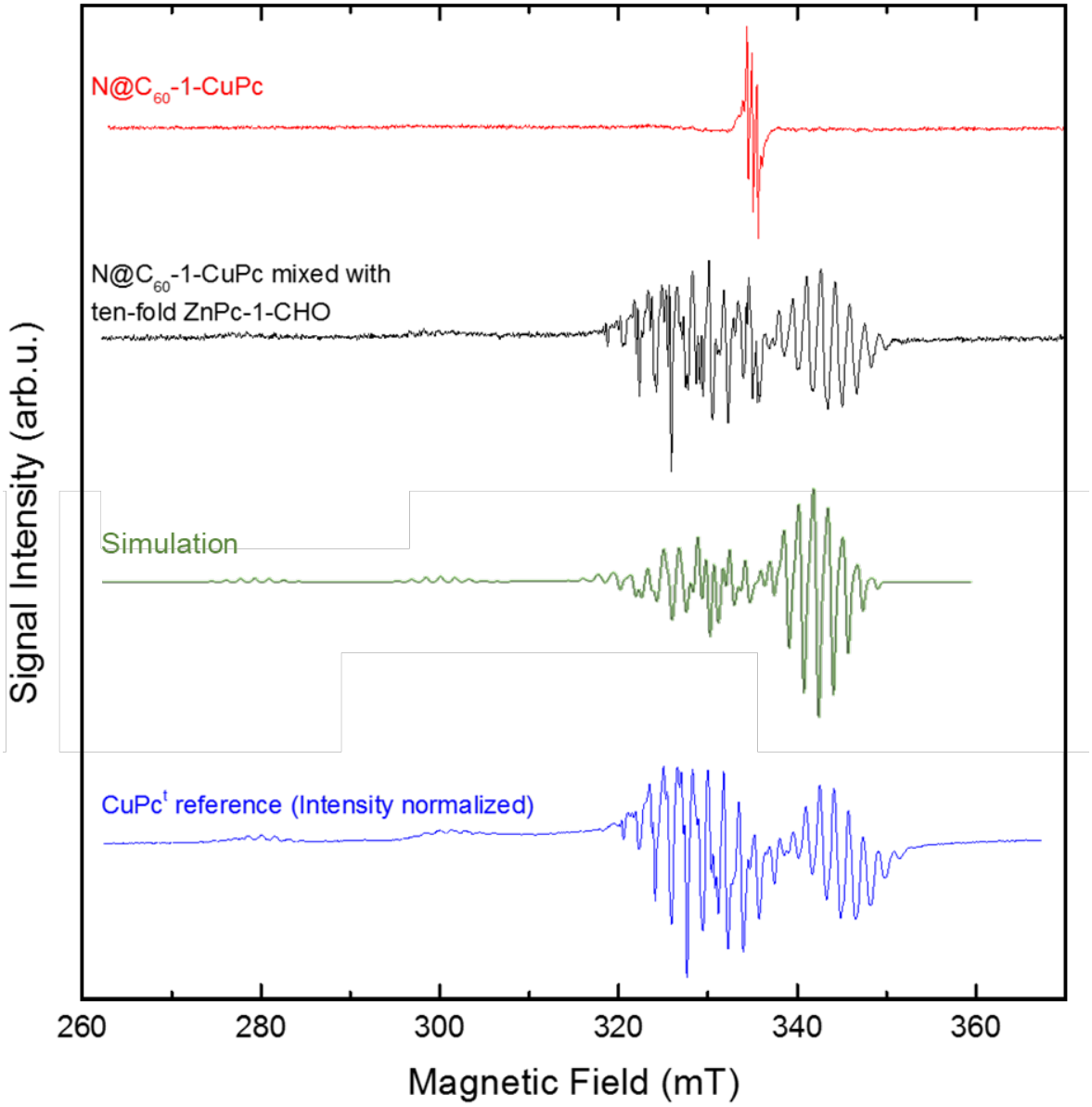


Figure 141 Comparison of solid-state cw-ESR spectra (full-ranged). Red, black, green, and blue curves represent spectra measured from the sample of 10^{-5} M N@C_{60}-1-CuPc in toluene, the sample of 10^{-5} M N@C_{60}-1-CuPc plus 10^{-4} M ZnPc-1-CHO in toluene, a CuPc spin simulation, and a reference CuPc^{t} sample in toluene, respectively. After adding ZnPc-1-CHO, the "release" of the Cu spin, which is supported by the simulation and reference spectrum, proves the electron spin suppressing phenomenon in the aggregated CuPc moieties. The red spectrum was measured with Bruker EMX, 9.3860GHz, 48.0 dB attenuation, 100 K, 10^{-5} M in toluene, and 0.05 mT modulation amplitude. The black spectrum was measured with Bruker EMX, 9.3845 GHz, 28.0 dB attenuation, 100 K, and 0.10 mT modulation amplitude. The green spectrum was simulated by EasySpin,[209] with parameters as follows: $g_{\perp} = 2.0405$, $g_{\parallel} = 2.1625$, $A_{\perp}^{(\mathrm{Cu})} = -86$ MHz, $A_{\parallel}^{(\mathrm{Cu})} = -643$ MHz, $A_{\mathrm{iso}}^{(\mathrm{ligand\ N})} = 50$ MHz, and the $\Delta H_{pp} = 0.5$ mT (programme M in appendix), which match with the reference well.[263] The blue spectrum was measured using a Magnettech MiniScope MS200 spectrometer, 9.4412 GHz, 25.0 dB attenuation, 77 K, and 0.05 mT modulation amplitude.

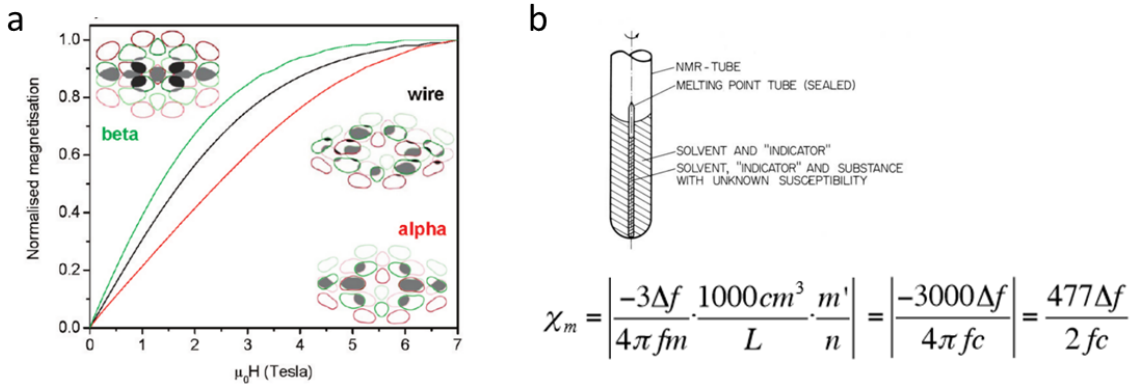


Figure 142 (a) Measuring the antiferromagnetism with SQUID. The magnetization is a function of field at 2 K for alpha (antiferromagnetic), beta (paramagnetic), and wire samples of CuPc (weak antiferromagnetic). The curves were normalized at 7 T; actual moments at those fields are close to 1 μB for beta sample, 0.8 μB for alpha sample, and intermediate between these values for wire sample. Figure reproduced from Wang, H. *et al.*[259] (b) Measuring the antiferromagnetism with Evans method. The antiferromagnetism is proved by the molar susceptibility, which is measured by the NMR signal shift $\Delta f/f$ and the sample concentration. Figure reproduced from Löliger, J *et al.*[271] and Johnson, A. R.[272]

Based on the relationship between the signal intensity and the number of spins,[207] the dramatic intensity change of a cw-ESR spectrum suggested a potential antiferromagnetism of the CuPc moiety. To verify this interesting phenomenon, there are other methods that can directly study the antiferromagnetic coupling. The first method is to measure the sample using the superconducting quantum interference device (SQUID) magnetometry.[259,269] Taking an antiferromagnetic study on another CuPc sample as an example (Figure 142a), magnetization was measured as a function of magnetic field strength ($\mu_0 H = 0\sim7$ T, where μ_0 is the magnetic permeability of free space). Qualitatively, the antiferromagnetic α-CuPc sample showed a less bent curve compared to that of the paramagnetic β-CuPc sample. The CuPc wire sample, which the authors proved was a 1D quantum antiferromagnet, showed an intermediate magnetization feature between the former two.[259] By fitting the magnetization curve with Brillouin functions, the number of spins in the molecule can be determined to prove the antiferromagnetism quantitatively.[269] The second way is the Evans method, which measures the molar susceptibility (χ_m) with NMR spectroscopy.[270,271] Figure 142b shows the sample for the Evans method. The sample is loaded in the inner tube, and both tubes contain a solvent system consisting of a solvent plus a certain percentage of an inert "indicator"

compound. Due to the susceptibility of the sample loaded in the inner tube, the NMR signals measured for the “indicator” have different chemical shifts in the two tubes. The measurement utilizes the shift to determine the molar susceptibility of the paramagnetic substances. The equation describing the relationship between the shift of the NMR signal and the molar susceptibility, if the experiment is performed with a coaxial magnetic field, is shown in Figure 142b.[272,272] Both approaches introduced above open up new avenues to investigate the antiferromagnetic interactions in materials, and are well worth implementing in future research.

8.3.3 Simulation for the spectra taking aggregation into account

In order to amend the direct simulation model, which is limited to an intramolecular level, and to quantitatively interpret the low coupling strength, the aggregation and Cu^{2+} electron spin suppressing have to be taken into consideration. However, the suppressing depends on the size of the aggregation, so it is difficult to individually analyse the varying extent of aggregation in the sample. Noticing that the strength of the dipolar field tends to zero as the size of the aggregated cluster grows, a complete suppression approximation, which assumes the net magnetic moment from the CuPc arrays in all aggregated cases is negligible, can simplify the complicated weakening effect. This leaves only two extreme cases to simulate: the non-aggregated case, with the predicted dipolar coupling strength, and the aggregated case, which has a completely suppressed dipolar coupling.

I combined the complete suppression approximation with the spin Hamiltonian model explained in section 8.3.1, and did the simulations by fitting ratio between the non-aggregated case to the aggregated case. As shown in Figure 143, the simulated spectra composed of 75% of non-aggregated case plus 25% of aggregated case and 73% of non-aggregated case plus 27% of aggregated case fit well the experimental spectra for **N@C_{60}-1-CuPc** and **N@C_{60}-2-CuPc**, respectively.

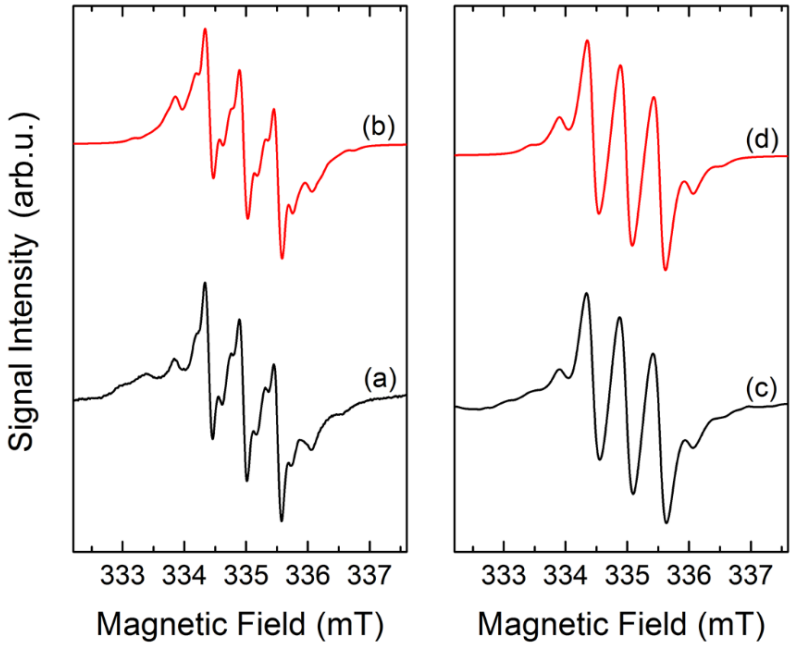
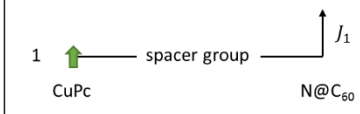
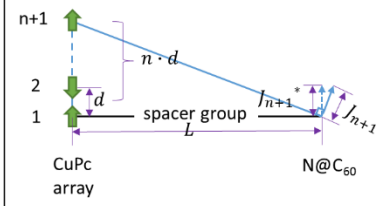
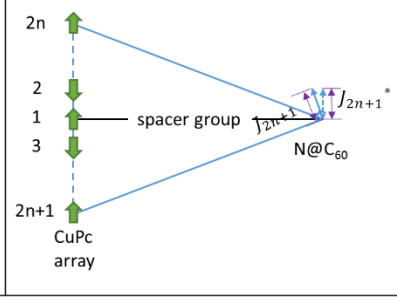


Figure 143 Solid-state cw-ESR spectra for N@C_{60}-1-CuPc (a) and N@C_{60}-2-CuPc (c), and their corresponding simulation results (b) and (d). Simulations were done by EasySpin[209] (programme N in appendix). Experimental data reproduced from Figure 134.

Depending on the validity of the complete suppression approximation, some aggregated cases may still have considerable residual dipolar coupling in the cw-ESR spectra. As a result, the simulated ratio between the aggregated case and the non-aggregated case may be under estimated. To exclude this concern, I validate that the complete suppression approximation holds in most aggregation cases by enumerating the residual dipolar coupling strength. The residual dipolar field of the suppressed Cu electron spin experienced by the N@C_{60} spin is affected by three conditions, which are the position of the ENF in the aggregated cluster, the distance ratio of Cu-Cu to Cu-N (d/L), and the size of the CuPc array. For the first condition, the edge and central position are the two extreme scenarios. If the complete suppression approximation is applicable to these, it will be applicable to other possible positions. Thus, only these two positions need to be discussed. For the second condition, the ratio can be calculated. Since the Cu-Cu distance has been reported to be about 0.4 nm,[268] and the DFT calculation results suggest that the Cu^{2+} to N@C_{60} distance varies between 1.665 or 2.096 nm depending on the bridge groups, I tested different distance ratios ranging from $1/3$ to $1/7$ to

cover all experimental situations and potential variations. For the third condition, a small aggregated cluster is more likely to have large residual dipolar coupling. Therefore, I calculated the dipolar coupling strength in aggregated cases with size smaller than 11 CuPc units. Table 13 shows the calculated dipolar coupling strength as a function of the distance ratio (d/L) and the cluster size with two N@C_{60} positions. Substituting the distance ratio (from $1/3$ to $1/7$) and cluster size (from 1 to 11) to the formula, Figure 144 enumerates the residual dipolar coupling strengths. Most aggregated clusters have a residual coupling strength less than 60% of that observed for the non-aggregated case. Such a weak coupling strength cannot be resolved in the cw-ESR spectrum due to the signal linewidth. Therefore, it is valid to neglect the dipolar coupling for in this case, and the simulation in Figure 143 is reliable.

Table 13 Calculated coupling strength in the non-aggregated case, the aggregated case with the ENF on the edge and the aggregated case with the ENF in the center. The square bracket represents the rounding down operation in the formula.

Non-aggregated case		The coupling strength	J_1
Aggregated case with the endohedral fullerene dyads on the edge		The component of the coupling strength from the No. n+1 CuPc	$J_{n+1}^* = J_{n+1} \times \frac{L}{\sqrt{(n\cdot d)^2+L^2}}$ $= J_1 \cdot \frac{(-1)^n \cdot L^3}{((n\cdot d)^2+L^2)^{3/2}} \times \frac{L}{\sqrt{(nd)^2+L^2}}$ $= J_1 \cdot \frac{(-1)^n}{((n\cdot\frac{d}{L})^2+1)^2}$
		The overall coupling strength from all CuPcs	$\sum_{i=1}^{n+1} J_i^* = J_1 \cdot \sum_{i=0}^{n} \frac{(-1)^i}{((i\cdot\frac{d}{L})^2+1)^2}$
Aggregated case with the endohedral fullerene dyads in the center		The component of the coupling strength from the No. 2n+1 / No. 2n CuPc	$J_{2n+1}^* = J_{2n}^* = J_1 \cdot \frac{(-1)^n}{((n\cdot\frac{d}{L})^2+1)^2}$
		The overall coupling strength from all CuPcs	$\sum_{i=1}^{2n+1} J_i^* = J_1 \cdot (\sum_{i=1}^{2n+1} \frac{(-1)^{[i/2]}}{\left(\left([i/2]\cdot\frac{d}{L}\right)^2+1\right)^2})$

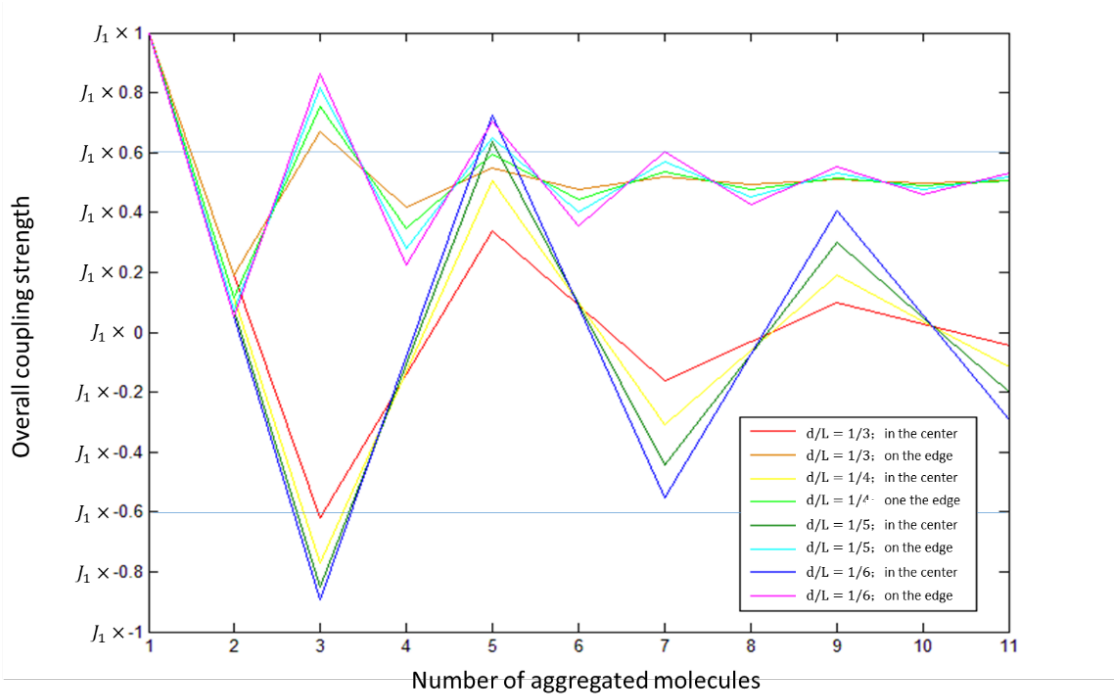


Figure 144 Relative overall coupling strengths when the sample has different size of aggregation and different N@C_{60} locations in the cluster. two to eleven aggregated molecules and two extreme postions of N@C_{60} in the cluster are enumerated, proving the coupling strengths in the aggregated cases are generally considerably weaker ($< 60\%$) then that in the non-aggregated case.

Apart from using cw-ESR, another method for measuring the dipolar coupling strength in these dyads is relaxation-induced dipolar modulation enhancement (RIDME).[201,202] Compared to other pulse-ESR experiment schemes, such as double electron-electron resonance (DEER),[200] RIDME is not limited by the requirement that the bandwidth of the microwave source should span the resonant frequencies of both N@C_{60} and CuPc electron spins. It is also more sensitive to detect the weak spin signal of the 0.1% N@C_{60}. More importantly, N@C_{60}–CuPc dyads are the perfect molecular system on which to perform a RIDME measurement due to the distinct T_1 times of N@C_{60} ($> 10^{-4}$ s measured in CS_2 at room temperature)[49] and CuPc ($< 10^{-5}$ s measured in 0.1% CuPc:H_2Pc at 80 K).[56] The modulation of the N@C_{60} spin echo caused by spontaneous spin-flips of the Cu spin due to relaxation of the CuPc spin enables quantitative analysis of the spin-spin interaction.[202] As I learnt this approach at the end of the project, I did not manage to apply it, but performing a RIDME experiment with the dyads would be an interesting future investigation.

8.4 Concentration dependent cw-ESR

The spectral simulation based on the complete suppression approximation proposed in the above section is effectively a two-component simulation. While the two components have been explained by aggregated and non-aggregated case, they might also be explained by other two cases superimposed, e.g. two different conformers, which I excluded in the beginning of section 8.3.2. In order to confirm the influence of aggregation on the apparent dipolar coupling strength further, I measured and fitted additional cw-ESR spectra for different concentrations of **N@C_{60}-1-CuPc**. All concentration dependent spectra (Figure 145a) were taken with a small microwave power $P = 3.170\ \mu W$, for which signal intensity was proportional to the square root of microwave power. Therefore, the observed spectral variation is caused by the increasing aggregation of progressively concentrated samples, rather than power saturation. It shows that the dipolar coupling features became increasingly significant for the dilute and less aggregated samples, which confirms the suppressing effect of aggregation on the apparent dipolar coupling strength. The trend in aggregation percentage derived from simulations of cw-ESR data (Figure 145b) is consistent with the trend derived from dynamic light scattering data (Figure 140) and previously reported results.[273] Hence the complete suppression approximation is also validated. On the other hand, other two-component simulations, such as two different conformers superimposed, are unlikely to have such a dramatic concentration dependence.

The concentration dependence opens up a new way of tuning the dipolar coupling strength in this dyad system. I can turn on the dipolar coupling by diluting the sample, and turn off it by concentrating the sample. Compared with tuning the dipolar coupling chemically by adjusting the size of the spacer group, changing concentration does not require any change in the molecular structure. Since the aggregation effect changes gradually with the concentration, the variation on the sample concentration cannot enable us to turn on and off the dipolar coupling in a real device. However, if one could adjust the dyad molecules to make

the aggregation effect strongly dependent on any external stimuli, such as pH, temperature or electric potential, control of the dipolar coupling could be realized at the device level. This is a first step in this direction.

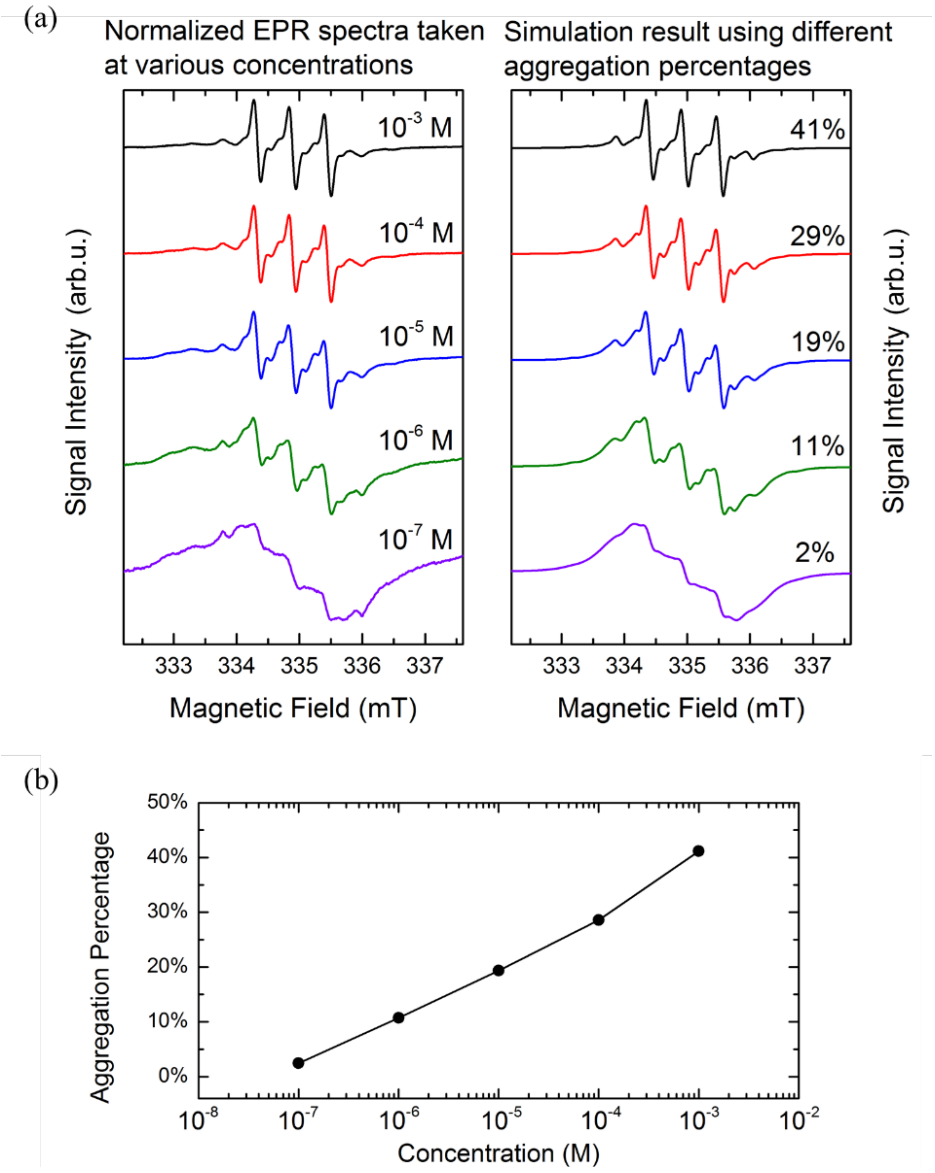


Figure 145 (a) Solid-state cw-ESR spectra for N@C_{60}-1-CuPc in frozen toluene solution (100 K) taken at various concentrations, and their corresponding simulation results with different aggregation percentages. (b) Concentration dependence of the aggregation percentage for the sample of N@C_{60}-1-CuPc in frozen toluene solution based on the simulation results. Simulations were done by EasySpin[209] (programme O in appendix).

8.5 Conclusions

In summary, comprehensive cw-ESR studies of **N@C_{60}-1-ZnPc**, **N@C_{60}-1-CuPc**, and **N@C_{60}-2-CuPc** dyads were presented in this chapter. In my analysis of solution and solid-state cw-ESR data, I compared the spectral differences in dyads with differing spin-spin distance, thereby demonstrating that chemical adjustment of the spacer group is sufficient to change the dipolar coupling strength. With the additional discussion of the aggregation, I managed to quantitatively interpret the experimental result with a simulation model, and discovered a new way of tuning the dipolar coupling strength, which utilizes the suppressing of Cu electron spin by aggregation to turn down the dipolar coupling, respectively.

Chapter 9 Conclusions and Outlook

9.1 Conclusions

Due to their long coherence times, endohedral nitrogen fullerenes (ENFs) have been proposed as a molecular system to embody qubits for quantum information processing (QIP). Even though it is a feasible and advantageous proposal, there are still significant obstacles before a fullerene-based QIP architecture to fulfil all the criteria raised by DiVincenzo. The scalable multi-qubit system, the implementation of a two-qubit gate, and the spin qubit readout approach are the main challenges. Solutions to those problems could be found in different disciplines, but from a materials science perspective, providing a multi-scale molecular architecture of ENFs might meet the unfulfilled requirements of the DiVincenzo criteria. At the macroscopic scale, ENFs would need to be replicated up to a readable amount, and each copy needs to be identical or sufficiently similar in the way it responds to quantum information operations. At the microscopic scale, ENFs would need to be assembled in a controllable and scalable way and offer tunable spin interactions for two-qubit gates and quantum algorithms.

To improve this material's suitability as a building block for quantum devices, I have selected improvement on the ENFs' productivity, better understanding of the ENF chemistry necessary for molecular engineering, covalent assembly reactions of ENFs, orientational alignment of ENFs, and spin-spin coupling studies in an ENF-containing bi-spin system as the aims of this project. My contributions to these topics are illustrated in Figure 146 and are summarized as follows.

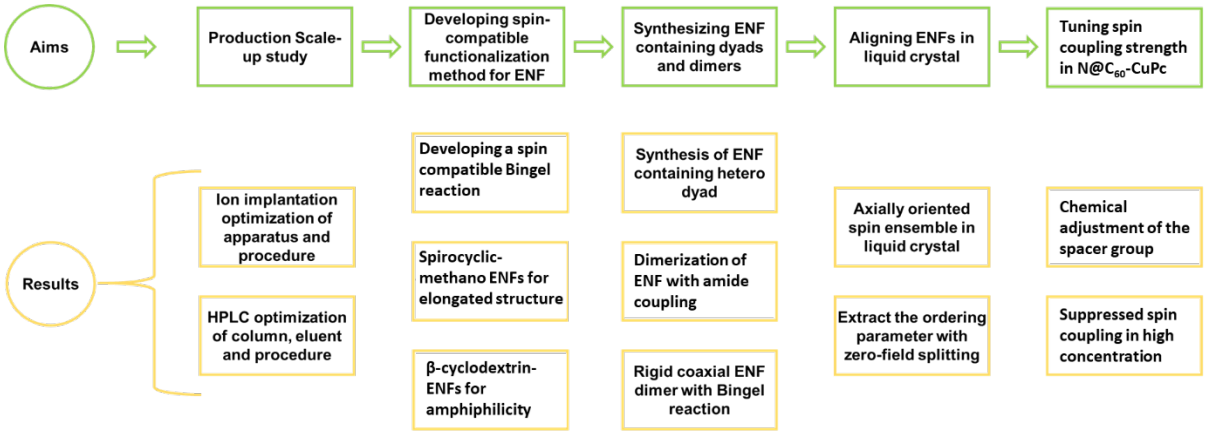


Figure 146 Aims set for the thesis (green boxes) and results achieved by the thesis (yellow boxes).

Before the QIP application-oriented study, optimization of the synthesis and purification of ENFs were targeted to improve the availability of the material, as the extremely low productivity hinders all applications of ENFs. An overall five-fold improvement was accomplished by optimizing the ion implantation and the high-performance liquid chromatography (HPLC) procedures described in Chapter 4. A better ion implantation apparatus with optimal parameters was built during this project. Compared to the previous synthetic approach, a set of improvements, including a LabVIEW automation programme and *in-situ* product preservation, have been applied, and increased spin content in the crude product can be obtained with good time, raw materials, and labour efficiencies. Meanwhile, based on the current choice of stationary and mobile phase for HPLC, I established a better purification protocol by incorporating a fine particle-size 5PBB column with a repeat injection programme. This simultaneously provides a high column efficiency and a large column capacity. I also performed a more innovative HPLC experiment with the preliminary results showing that a bigger fullerene cage size and lower solvent polarizability could further improve the separation of the empty-cage fullerenes from the ENFs.

As well-defined molecules, ENFs are suitable for chemical reactions and allow researchers to alter materials' performance in a homogeneous and reproducible manner. A series of ENF derivatizations were studied in Chapter 5 to further develop the field of ENF chemistry. A spin-compatible reaction condition was established for the controversial Bingel

reaction, followed by an in-depth study on the interaction between the ENFs and the base, which explains the potential spin loss and discovers an approach to avoid it. Based on the developed reaction condition for the Bingel reaction, spirocyclic-methano-ENFs were synthesized, which opens a general way to functionalise ENF molecules to improve their rigidity and the aspect ratio. Moreover, β-CD modified N@C_{60} was prepared, showing a structurally controllable method of making ENFs amphiphilic.

In addition to the knowledge of both the production and the chemistry of ENFs, molecular engineering of this material is further demonstrated in Chapter 6 and Chapter 7. At the microscopic scale, I covalently linked an ENF to a phthalocyanine and another fullerene with various organic bridges, to synthesize ENF containing dyads and dimers, respectively. By applying the well-reported Prato reaction to ENFs, using both one-pot and multi-step methods, I demonstrate multiple ways of linking ENFs to other interesting chemical moieties. Based on the spin-compatible Bingel reaction I developed, I innovatively designed and synthesized three ENF dimers with rigid bridges and near-coaxial conformations. Although only half-filled dimers were achieved, double-filled dimers could be obtained using my approach if pure ENF were available in larger quantities. Such dimers pave the way towards scalable microscopic assembly of ENFs for a multiple qubit system. At the macroscopic scale, I demonstrated alignment results of four different ENF derivatives in both frozen and non-frozen liquid crystals. Benefiting from the high molecular rigidity and the long aspect ratio of Bis-IND-N@C_{70}, I achieved, for the first time, an order parameter as high as 0.61. With the aligned samples, the ENF spin ensemble has a good orientation coherence between individual molecules, and anisotropic spin properties, such as zero-field splitting, can be controlled by sample rotation at a macroscopic scale.

Lastly, in order to advance the knowledge of spin coupling which will be used in the implementation of two qubit gates, Chapter 8 studies the electron spin dipolar coupling in ENFs. In a comprehensive cw-ESR investigation of three ENF–phthalocyanine dyads, I compared the spectral differences in two dyads with variant spin-spin distances, which proves

that chemical adjustment of the spacer group is capable of changing the dipolar coupling strength. In my discussion of the aggregation and the resultant electron suppressing phenomenon of the CuPc moiety, I managed to quantitatively interpret the experimental result using a theoretical model I developed, and discovered a new way of tuning the dipolar coupling strength by means of the solution concentration.

9.2 Future work

Apart from the results summarized above, there are more interesting findings that need additional time and effort to fully discover. For the production of ENFs, I recommend further research into the optimal eluent mixture for HPLC purification. The study could continue with chloroform or dichloromethane, which have even lower polarizabilities than hexane but higher fullerene solubility. For the ENF chemistry, regioselective multi-functionalisation would be a useful tool for improving the performance of the material. Symmetric addition can mitigate the cage distortion resulting from mono-functionalisation, and the additional organic groups may further tackle the solubility problem of the rigid derivatives. For multi-scale assembly of ENFs, aligning coaxial ENF dimers (especially the **6-OPE-6 dimer**) in liquid crystals will push the research one step closer to the ideal molecular architecture for ENF-based QIP. Given the relationship between the molecular structure and the alignment result, coaxial ENF dimers might have an even better order parameter than **Bis-IND-N@C_{70}**. For the spin coupling study, applying pulse-ESR techniques, such as DEER and RIDME, to the dyad system reported in this work would lead to more conclusive spin coupling results. Alternatively, synthesizing double-filled versions of a coaxial ENF dimer may provide a directly observable spin dipolar coupling. If one can further combine the double-filled dimer with the liquid crystal alignment method, control of spin dipolar coupling and spin entanglement could be implemented. This would be a truly remarkable achievement in the journey that others before me started and I have continued.

Appendix A. Supporting information

A. Error analysis of using a Magnettech MiniScope MS200 spectrometer to measure the quantity of N@C_{60}

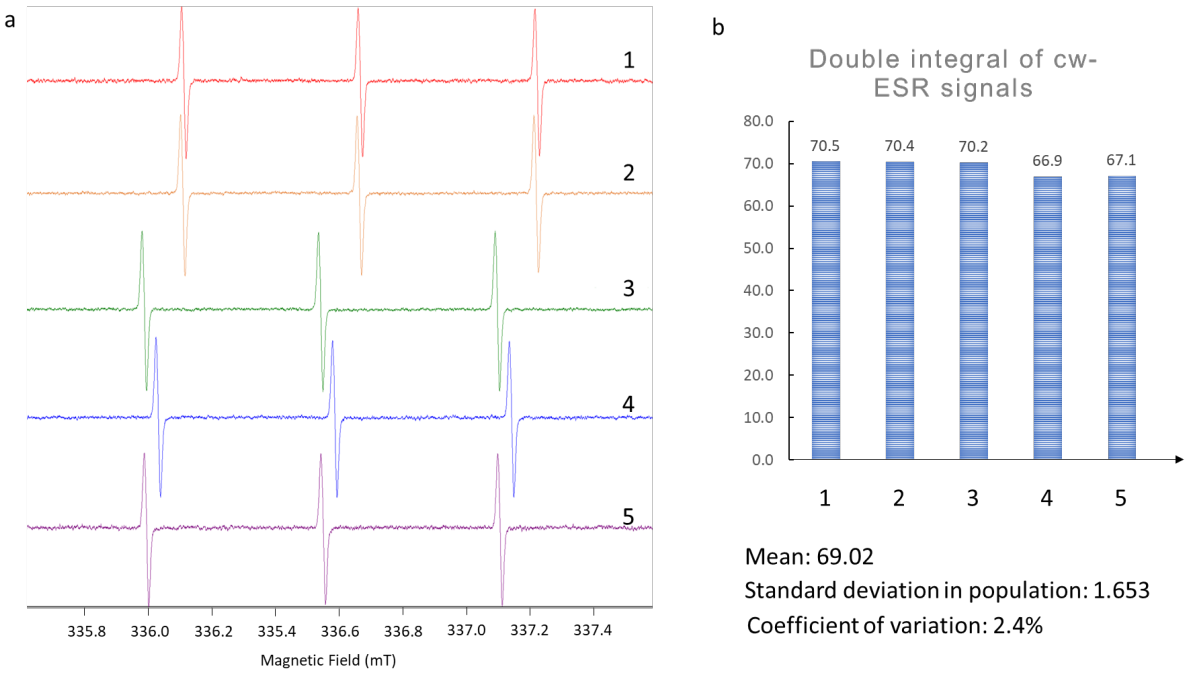


Figure 147 (a) Parallel ESR result for the same ENF/toluene sample prepared in different tubes. (b) calculation of the coefficient of variation of the double integral of ESR signals.

Measuring the same toluene solution sample of N@C_{60}/C_{60} mixture within different tubes five times gave out a set of parallel experimental data (Figure 147a). The peak shift in the magnetic field was caused by drifted in the microwave frequency between experiments. The reproducibility of the double integral of the cw-ESR signal gives the accuracy of using a

Magnettech MiniScope MS 200 spectrometer to determine spin numbers. As calculated (Figure 147b), a coefficient of variation of 2.4% was obtained. This means that the reproducibility of ENF measurements made using the MiniScope MS200 is relatively acceptable. The error could be caused by variation of the ESR tubes and slight variations in the Q-value of the resonant cavity.

B. Spin counting results for the yields comparison when the DS25s was used as the ion source

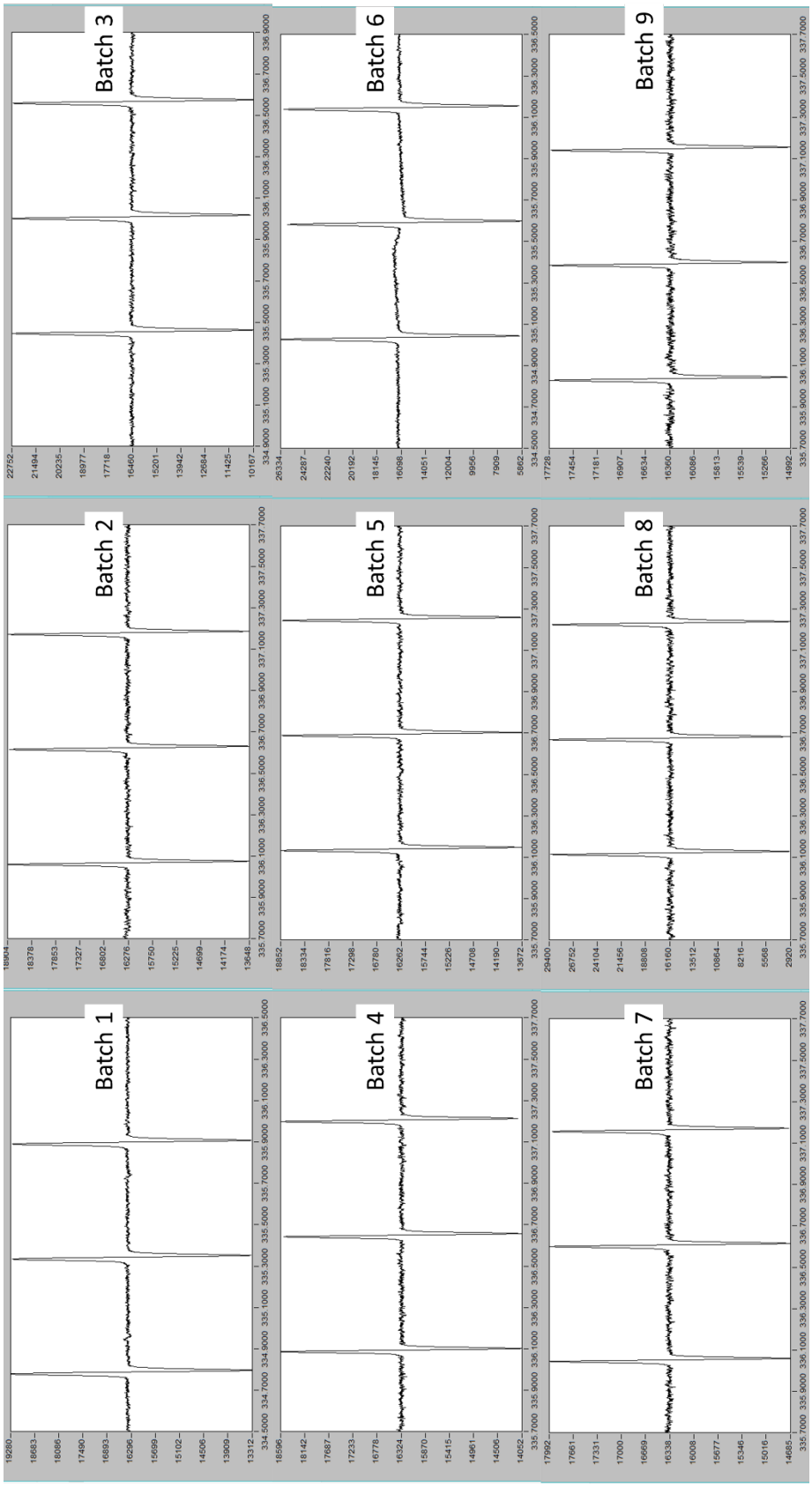


Figure 148 Comparison of cw-ESR spectra with different signal intensities of the crude products obtained from different batches of ion implantation experiments using the DC25s as the ion source. The x axis for all spectra are the magnetic field (mT).

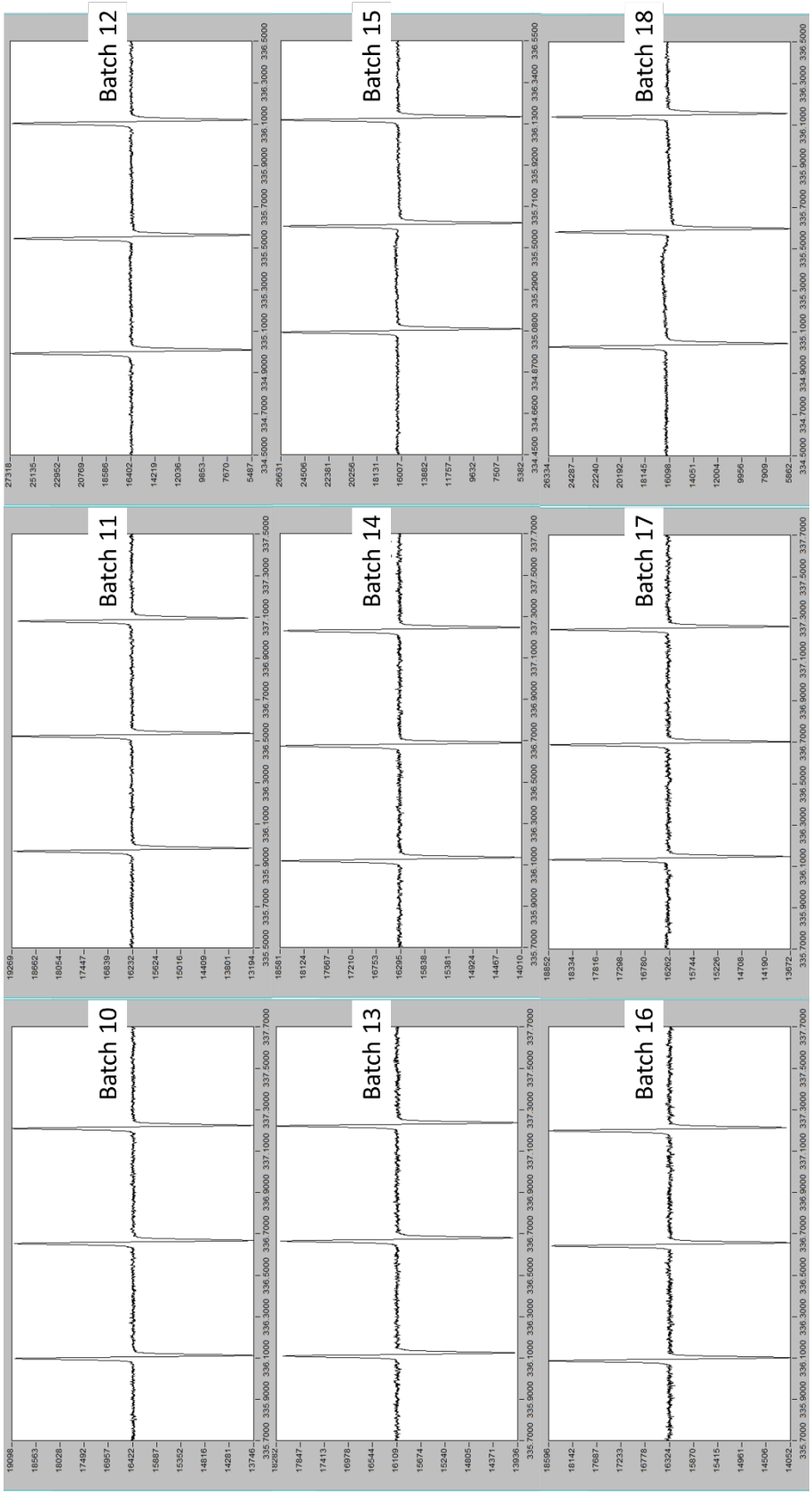


Figure 149 Comparison of cw-ESR spectra with different signal intensities of the crude products obtained from different batches of ion implantation experiments using the DC25s as the ion source. The x axis for all spectra are the magnetic field (mT).

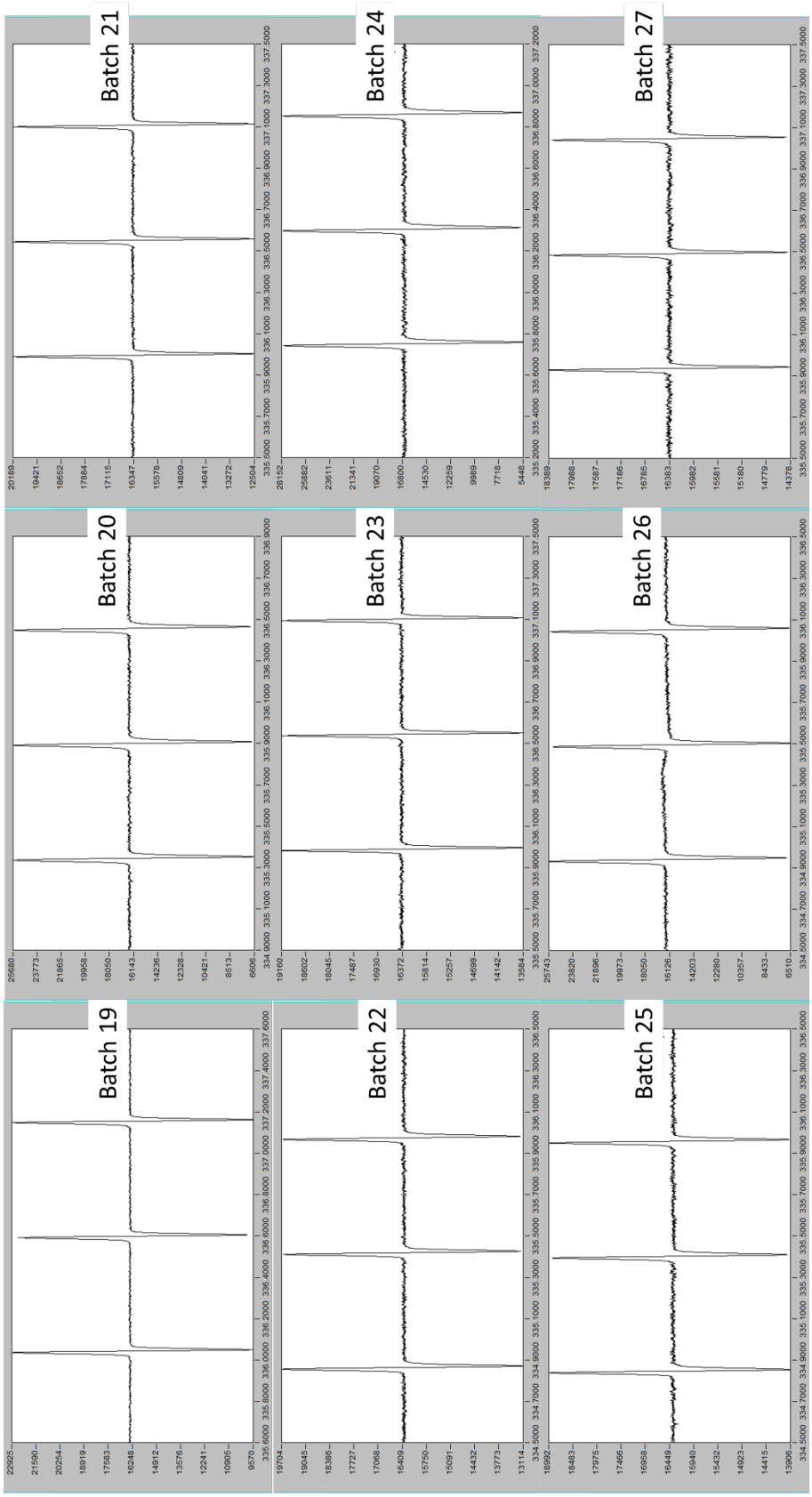


Figure 150 Comparison of cw-ESR spectra with different signal intensities of the crude products obtained from different batches of ion implantation experiments using the DC25s as the ion source. The x axis for all spectra are the magnetic field (mT).

C. Spin counting results for the yields comparison when the eH400 was used as the ion source

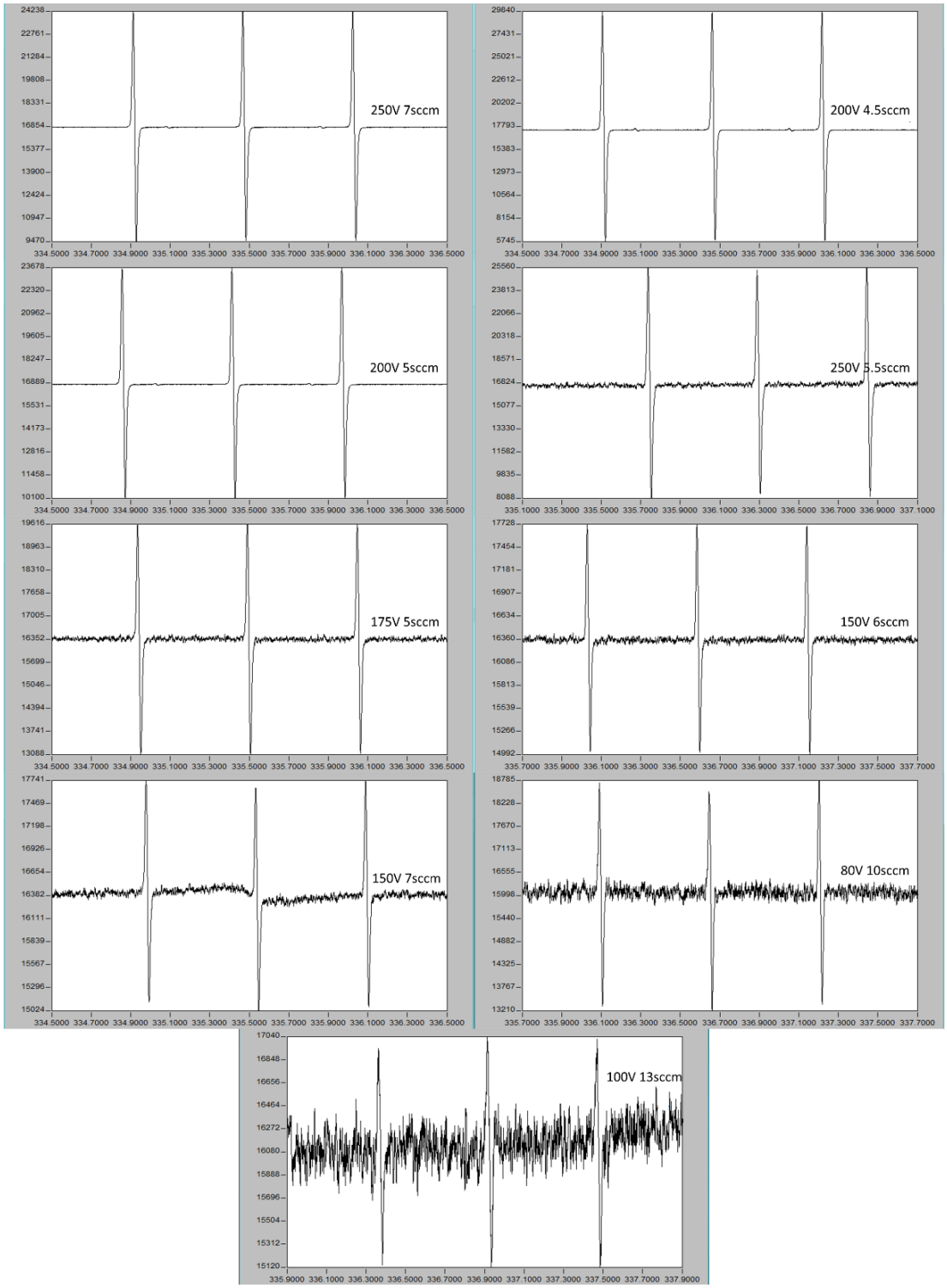


Figure 151 Comparison of cw-ESR spectra with different signal intensities of the crude products obtained from different batches of ion implantation experiments using the eH400 as the ion source. The x axis for all spectra are the magnetic field (mT).

D. Insignificant heat-induced decomposition during the synthesis of $N@C_{60}$

To understand the significance of the heat-induced ENF decomposition during the synthesis procedure, the impact of both the upper limit temperature of the effusion cell (the main heat source) and the deposition position of the material relative to the effusion cell on the spin-yield has been investigated (Figure 152a). For the temperature limit study, the comparable result in Figure 152b suggests that a high upper-limit temperature of the effusion cell does not trigger extra product decomposition. The second trial was to vary the position of the material collected by dividing the deposition target into three regions having different distances to the effusion cell (Figure 152c). Once again, variations between different samples were not prominent (Figure 152d). Apart from study on influence of the thermal radiation, the investigation on the cooling efficiency was also conducted by changing the circular cryogen for the deposition target from 17 °C water to 0 °C ethylene glycol/water mixture. However, no improvement of the product yield was observed.

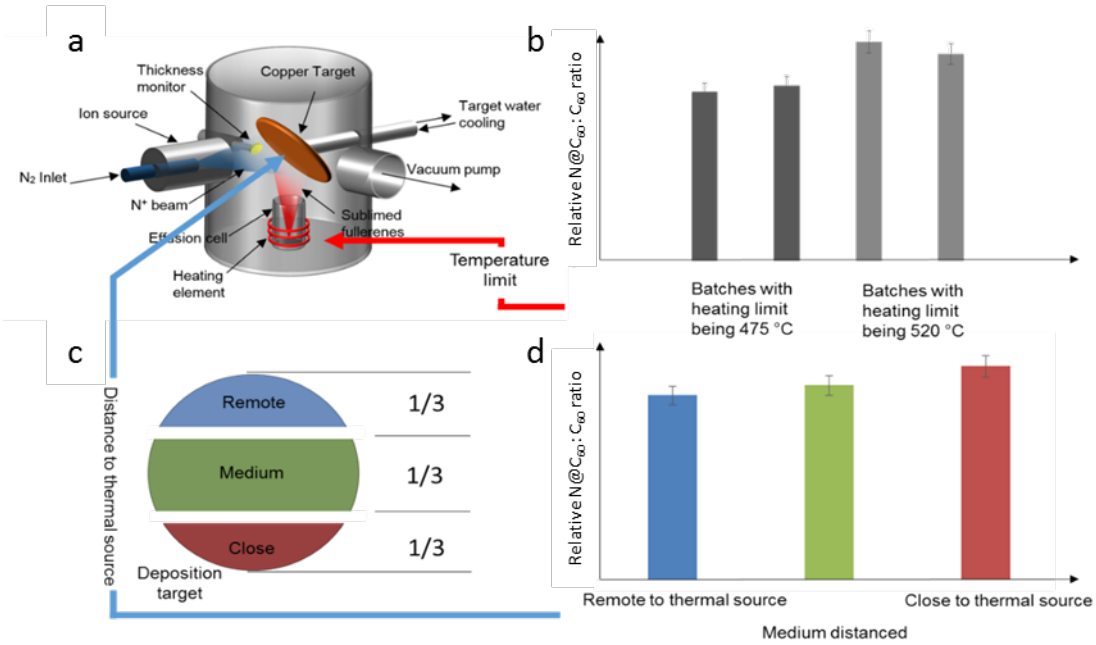


Figure 152 Study on the temperature influence on the product quality. (a) Experimental setup. (b) Yield comparison between different temperature upper limits of the effusion cell. (c) Products deposited on three different parts of the target based on their distance from the effusion cell, labelled in blue, green, and red, respectively. (d) Comparison on the yield of products deposited at three corresponding location in panel c.

E. cw-ESR signal intensity evaluation during the synthesis of DEM-N@C_{60} under non-spin-compatible conditions

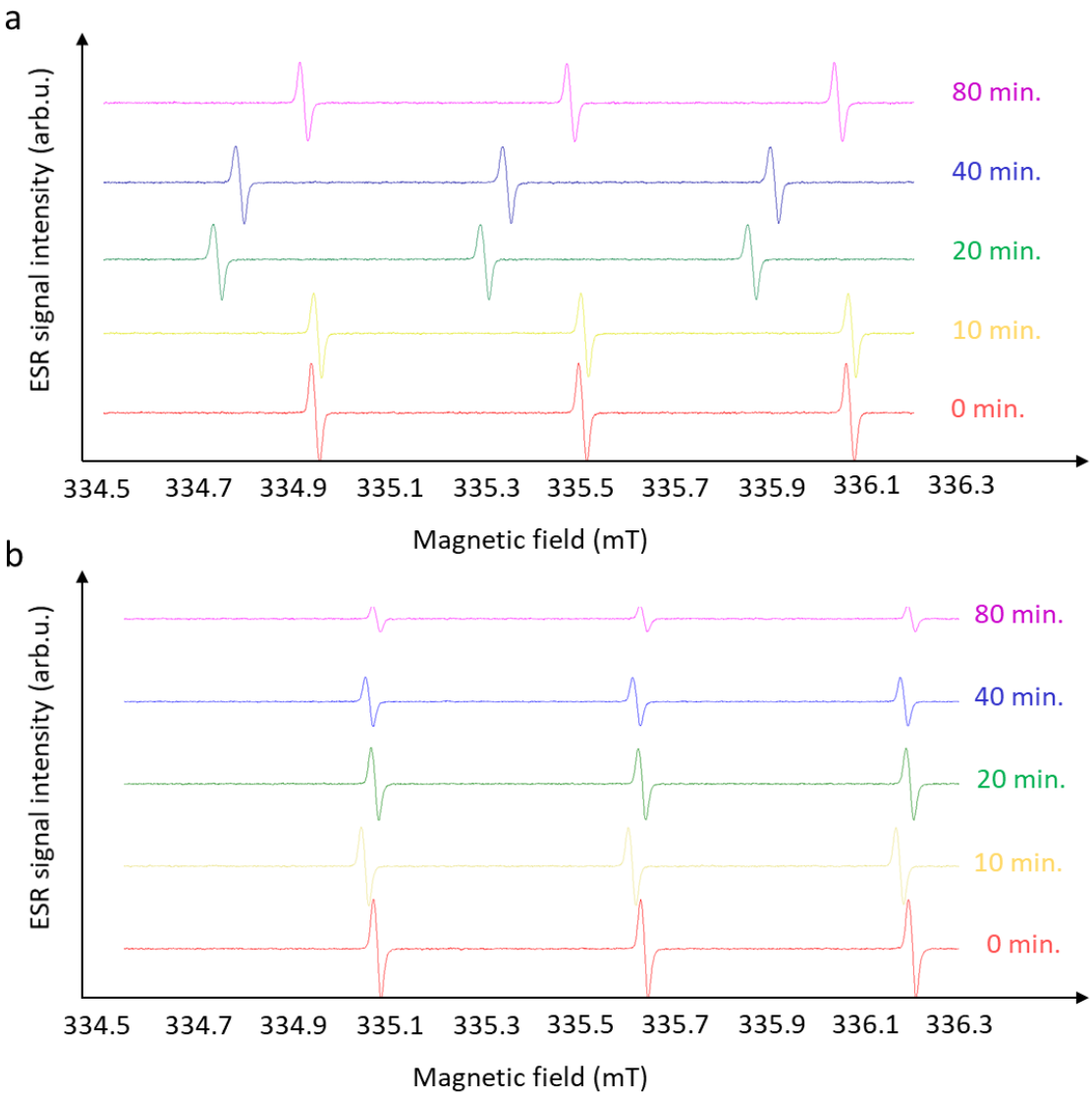


Figure 153 (a) cw-ESR spectra recorded at different reaction times during the Bingel reaction with undiluted DBU. (b) cw-ESR spectra recorded at different reaction times during the Bingel reaction with 4-fold excess of diluted DBU. The signal shift in the magnetic field is due the slightly different microwave frequency used. The comparison of the double integrations which represent the number of spins is discussed in the main text (Figure 78).

F. Preliminary results for the synthesis and characterization study of the third Spirocyclic-methano-N@C_{60}, QUI-N@C_{60}

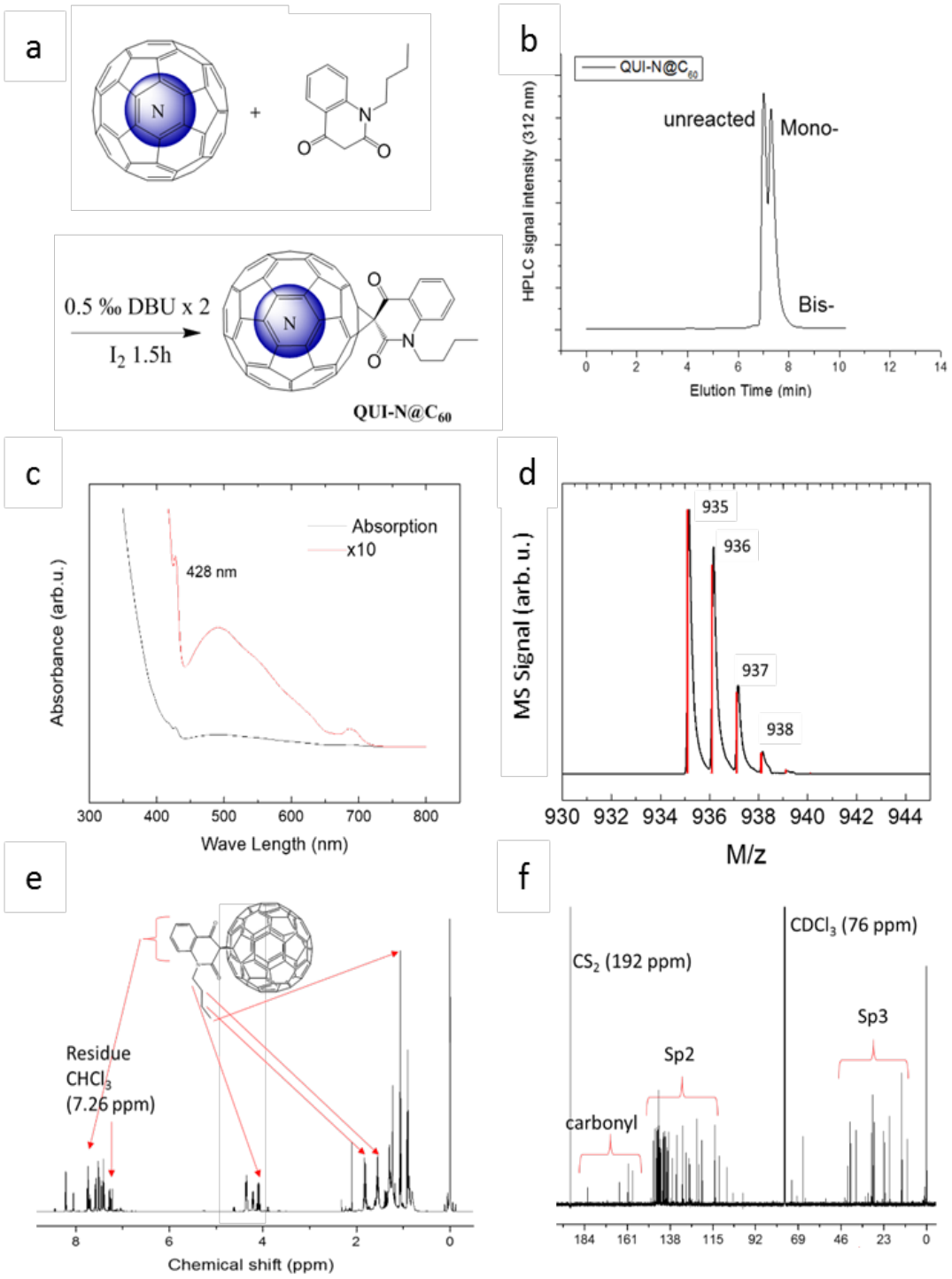


Figure 154 (a) Reaction scheme of the synthesis of QUI-N@C_{60}, (b) HPLC trace for the separation of QUI-N@C_{60} to the starting material and by-products (5PYE, toluene, $4\ \mathrm{ml/min}$), (c) UV/Vis spectrum of QUI-N@C_{60} (*ca.* $0.5\ \mathrm{mg/ml}$ toluene solution), (d) MALDI-MS of QUI-N@C_{60} (DCTB matrix and negative mode), (e) ^{1}H-NMR spectrum of QUI-N@C_{60} ($500\ \mathrm{MHz}$, room temperature, and $CDCl_3$ solution), and (f) ^{13}C-NMR spectrum of QUI-N@C_{60} ($500\ \mathrm{MHz}$, room temperature, $CDCl_3$ solution, and proton decoupled mode)

The synthesis of QUI-N@C_{60} was implemented using the spin-compatible Bingel reaction reported in section 5.2, and the halogenation of the malonate analogue was performed *in situ* by adding iodine (Figure 154a). $1\ \mathrm{mg}$ of $^{14}N@C_{60}/C_{60}$ mixture ($1.4\ \mu\mathrm{mol}$, 0.1% spin content) was dissolved with $0.3\ \mathrm{mg}$ of 1-Butyl-1H-Quinoline-2,4-dione ($1.4\ \mu\mathrm{mol}$, no analytical data on purity, Sigma-Aldrich) and $0.4\ \mathrm{mg}$ of I_2 ($1.6\ \mu\mathrm{mol}$, 99.5%, Acros Organics) in $2.5\ \mathrm{ml}$ of toluene (99.5%, Fisher Chemical), followed by an addition of $0.8\ \mathrm{ml}$ of $0.5‰$ DBU toluene solution ($2.8\ \mu\mathrm{mol}$, 99.0%, Sigma-Aldrich), dropwise. The reaction mixture was stirred under an argon atmosphere in the dark at room temperature for 1.5 hours. The HPLC separation for the product was not very successful, because (1) no retention time difference was obtained when Buckyprep-M was used as the column (not demonstrated here), (2) small retention time difference was obtained when 5-PYE was used as the column (Figure 154b). To perform the separation, I recycled the mixture for 5 times with the 5-PYE column, which is the maximum recycling time, as more recycles would lead to an overlap between HPLC peaks from adjacent cycles. The reaction yield based on the HPLC peak area was estimated to be 40%. The UV/Vis spectrum of the separated product in toluene (Figure 154c) showed features typical of a fullerene derivative, but in the region below $450\ \mathrm{nm}$, the signal increases exponentially. Similar features were obtained when a fullerene sample is not well dispersed in the solution and caused light scatterings. To further confirm the reason of the higher absorption below $450\ \mathrm{nm}$, remeasuring the sample in a much lower concentration would rule out the potential light scattering artefacts. The MALDI-MS (Figure 154d black) was performed with the matrix of DCTB in a negative ionization mode. The molecular ion peaks (m/z 935.0, 936.0, 937.0, and 938.0) matched the theoretical predications (Figure 154d red, m/z: 935.095, 936.098, 937.101, 938.105, *etc.*). The ^{1}H-NMR and ^{13}C-NMR spectrum contains the proton and carbon signal with the expected chemical shifts (assigned in Figure 154e, f). However, other NMR signals was obtained as well. This might due to the insufficient HPLC separation, aggregation of the product, or unexpected conformational isomers of the product. To improve the quality of the NMR result, these potential problems need to be tackled in the future.

G. Insensitive spin signal of β-CD-N@C_{60} to the concentration of Cu^{2+} in water

Water soluble **β-CD-N@C_{60}** sample is mixed with different amount of $CuSO_4$ in water to investigate the influence of Cu^{2+} on the ENF spin signal. Surprisingly, for up to $0.5\ \mathrm{M}$ $CuSO_4$ dissolved in the **ENF** sample, no significant linewidth broadening effect was observable (Figure 155). Simulating the ESR signals with Lorentzian derivative peaks, the linewidth variation between the sample tested were smaller than $1\ \mu\mathrm{T}$. Therefore, I conclude the spin signal of **β-CD-N@C_{60}** is insensitive to Cu^{2+} ions in water.

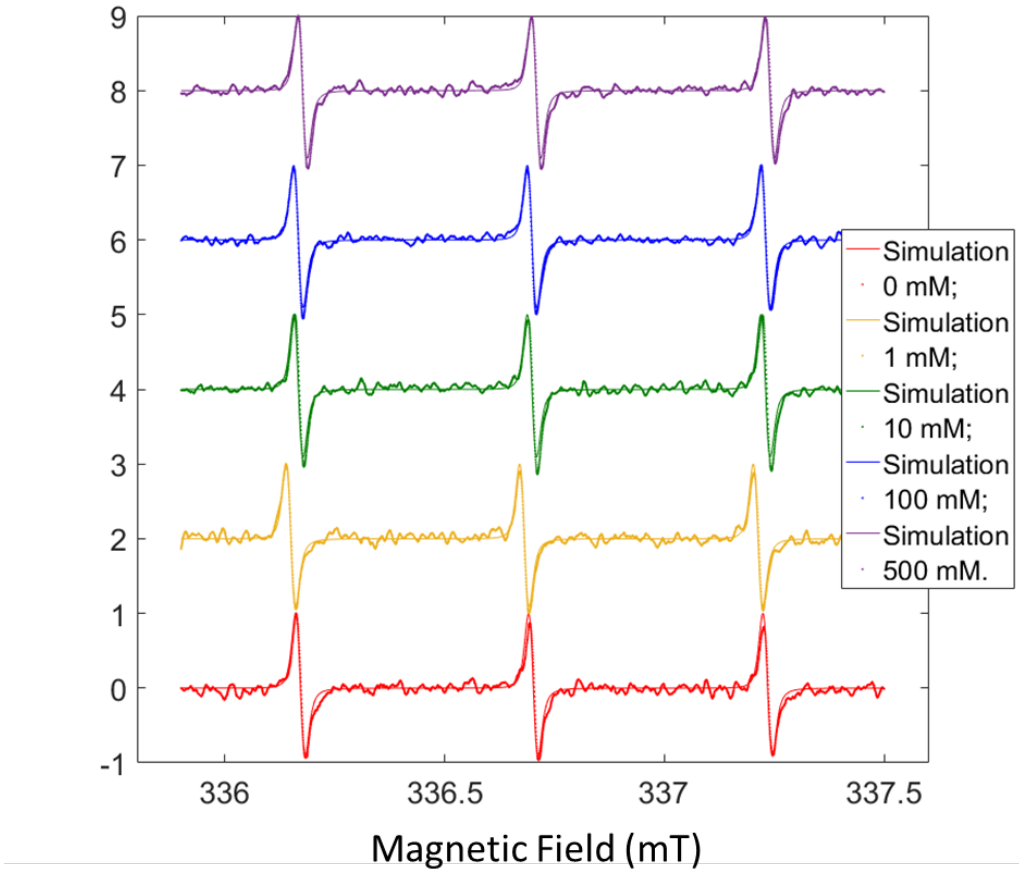


Figure 155 Invariant linewidth of β-CD-N@C_{60} to the concentration of Cu^{2+} in water. Experimental conditions adopted from the water experiment demonstrated in Figure 96b.

H. Preliminary study on NC_{59}–$N@C_{60}$ dyad

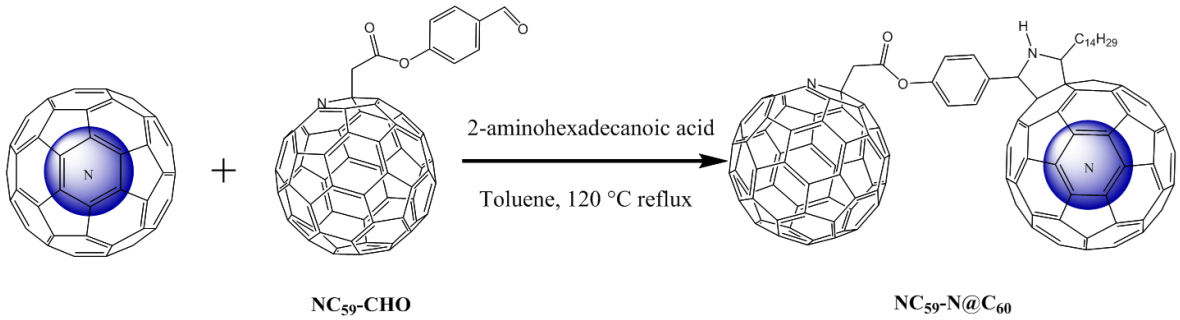


Figure 156 Reaction scheme for functionalising $N@C_{60}$ with an aza-fullerene moiety to form NC_{59}–$N@C_{60}$. Experimental method recorded in section 3.3.2.4. NC_{59}–CHO offered by Dr. Nikos Tagmatarchis, Theoretical and Physical Chemistry Institute, Greece

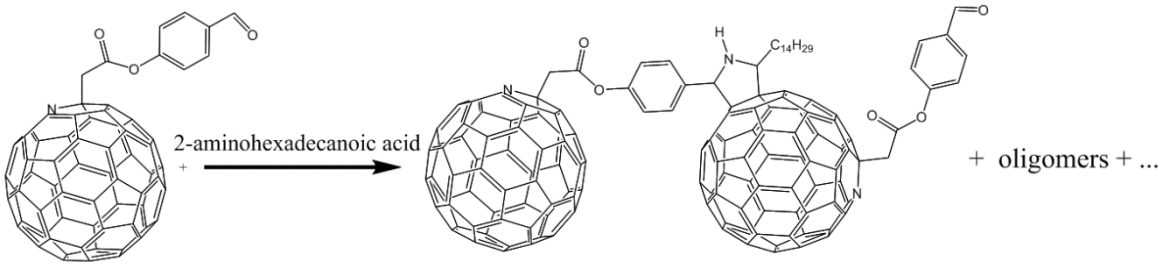


Figure 157 Possible side reactions during the linkage of NC_{59} and $N@C_{60}$

To prepare **NC_{59}–$N@C_{60}$**, a Prato reaction was performed using NC_{59}-CHO, $N@C_{60}$ (0.1% in C_{60}) and 2-aminohexadecanoic acid (Figure 156). Due to the concern of side reaction of the formations of a aza-fullerene dimer and oligomers (Figure 157), a five-fold excess of $N@C_{60}$ and 2-aminohexadecanoic acid was added to statistically suppress the Prato reaction on the aza-fullerene moiety.

After a 12-hour reaction at 120°C in the dark, **NC_{59}–$N@C_{60}$** was synthesized, followed by a HPLC purification (Figure 158). The HPLC signal area ratio between the product and **NC_{59}–CHO** is approximately 7:8. If the extinction coefficient of the product is assumed to be twice that of **NC_{59}–CHO** (two fullerenes in the product molecule), the conversion ratio of **NC_{59}–CHO** would be 30% for an overnight reaction. This is slightly lower than typical Prato reactions, and is probably caused by slow reaction kinetics due to the aldehyde linking a bulky aza-fullerene. There are no obvious side-products in HPLC trace.

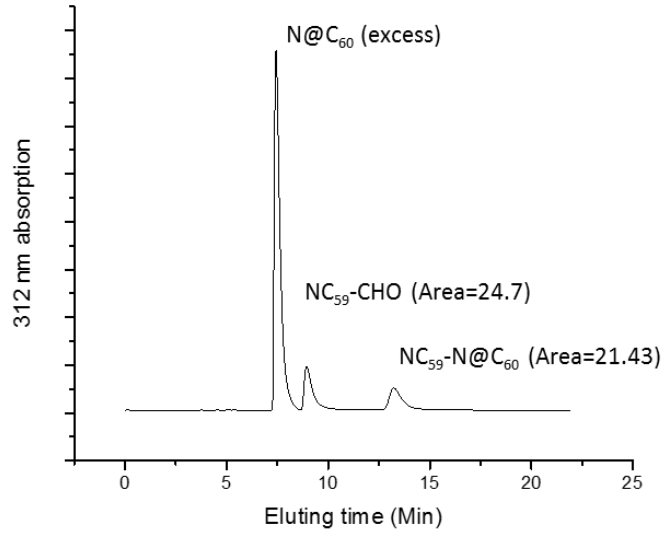


Figure 158 HPLC charts for the separation of the reaction mixture after 12 hours. (16 ml/min flow rate, BuckyPrep-M 28x250 mm column)

After separating the **NC_{59}–N@C_{60}** by collecting the HPLC peak at 13.3 minutes, MALDI-MS, UV/Vis spectroscopy, PL spectroscopy and cw-ESR spectroscopy were performed to confirm the formation of the product (Figure 159). MALDI-MS (1814.4, 1815.4, 1816.4, 1817.4, and 1818.4) showed a good agreement with the molecular weight prediction (). Due to the 0.1% concentration of the EF and the fragmentation during the ionization, the mass contribution from the endohedral nitrogen is not expected. Reversely, not clear MS peaks for the reaction mixture could be confirmed for the potential aza-fullerene dimer or oligomers, which validates the effectiveness of using an excess of N@C_{60}. The optical properties of the product in UV/Vis spectrum and PL spectrum confirm the presence of both N@C_{60}, and NC_{59} moieties. Both spectra were superpostions of the spectra of the parent N@C_{60} and **NC_{59}–CHO** molecules. An additional feature in the absorption spectra at 430 nm is the characteristic absorption band caused by [6,6] addition to a C_{60} cage. This absorption band shows that the reaction proceded as a standard Prato reaction. The PL spectrum was deconvoluted with two Gaussian peaks at 711 and 812 nm (Figure 160). The cw-ESR signal of the N@C_{60} moiety in solution is not dramatically changed after the functionalisation including the *g*-factor and HFCC. No electron spin interaction with the aza-fullerene is expected, as the aza-fullerene had already lost its electron spin when the aldehyde group was introduced. The signal of the

N@C_{60} moiety is slightly broadened ($\Delta H_{\mathrm{pp}} = 0.027\ \mathrm{mT}$), compared to that of a pristine N@C_{60}. The broadening indicates the successful linkage of the ENF and aza-fullerene. Unfortunately, the solid-state cw-ESR characterization of this compound was not very successful, because of the low signal-to-noise ratio caused by the dilute sample. To calculate angle-dependent electron spin parameters, such as the ZFS tensor, from a solid-state cw-ESR spectrum, the dyad must be resynthesized again using higher-purity N@C_{60} as the starting material.

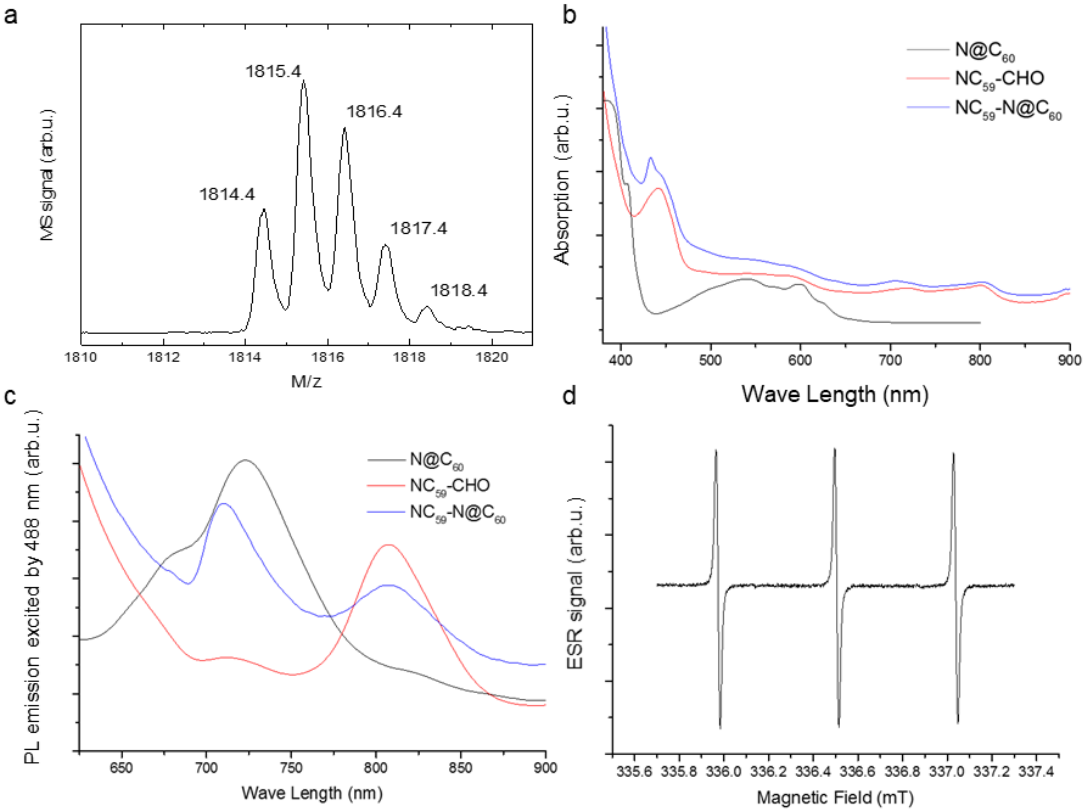


Figure 159 (a) MALDI-MS of NC_{59}–N@C_{60} (dithranol matrix, negative mode). (b) UV/Vis spectra and (c) PL spectra comparisons among N@C_{60}, NC_{59}–CHO and NC_{59}–N@C_{60}, showing the spectroscopic superposition relationship between reagents and product (*ca.* $0.1\ \mathrm{mg/ml}$ toluene solution for all samples). (d) cw-ESR spectrum of NC_{59}–N@C_{60} (Magnettech MiniScope MS200, $9.4021\ \mathrm{GHz}$, $30.0\ \mathrm{dB}$ attenuation, room temperature, and $0.02\ \mathrm{mT}$ modulation amplitude).

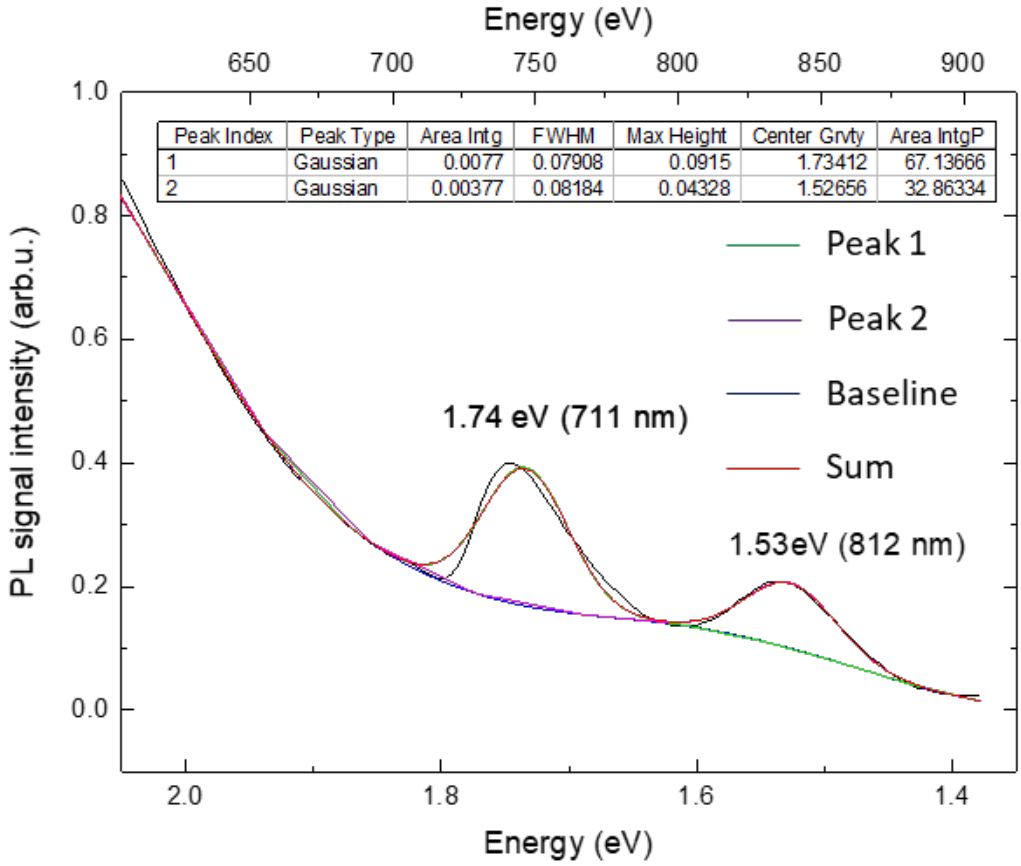


Figure 160 Multi-peak fitting for the PL spectrum of NC_{59}-N@C_{60} dyad, showing the emission peaks at 711 and 812 nm. The X-axis is converted to energy to perform the fitting. The background is determined by asymmetric least squares smoothing function in the software of OriginPro 2017.

I. Alternative synthetic route to obtain 6-OPE-6 dimer

For the first synthetic route (Figure 117), the NMR evidence of the successful Sonogashira coupling between **Iodo-QUI** and TMS-acetylene was shown in Figure 161. The ^{1}H-NMR spectrum recorded for the product has signals assigned to three Keto–enol tautomers. However, the product failed to demonstrate an effective deprotection of the TMS group later. Therefore, this route to obtain **6-OPE-6 dimer** was abandoned.

For the second route, **10-Bromo-Bz**, is not reactive enough to achieve a bis-addition. It was difficult to remove the mono-addition product by column chromatography, as confirmed by purity testing with NMR (Figure 162). After a preparative TCL separation, the ^{1}H-NMR spectrum of the purified bis-addition product (red spectrum) still contain considerable aromatic proton signals that can be assigned to the mono-addition product.

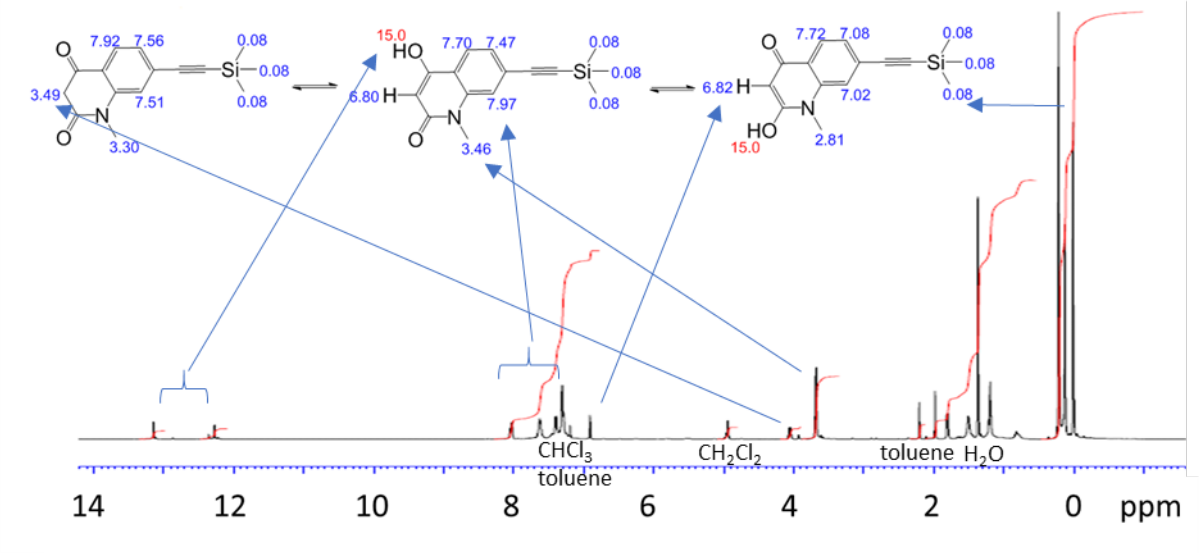


Figure 161 ^{1}H-NMR spectrum of reaction product formed by the Sonogashira coupling between Iodo-QUI and TMS-acetylene (400 MHz and $CDCl_3$).

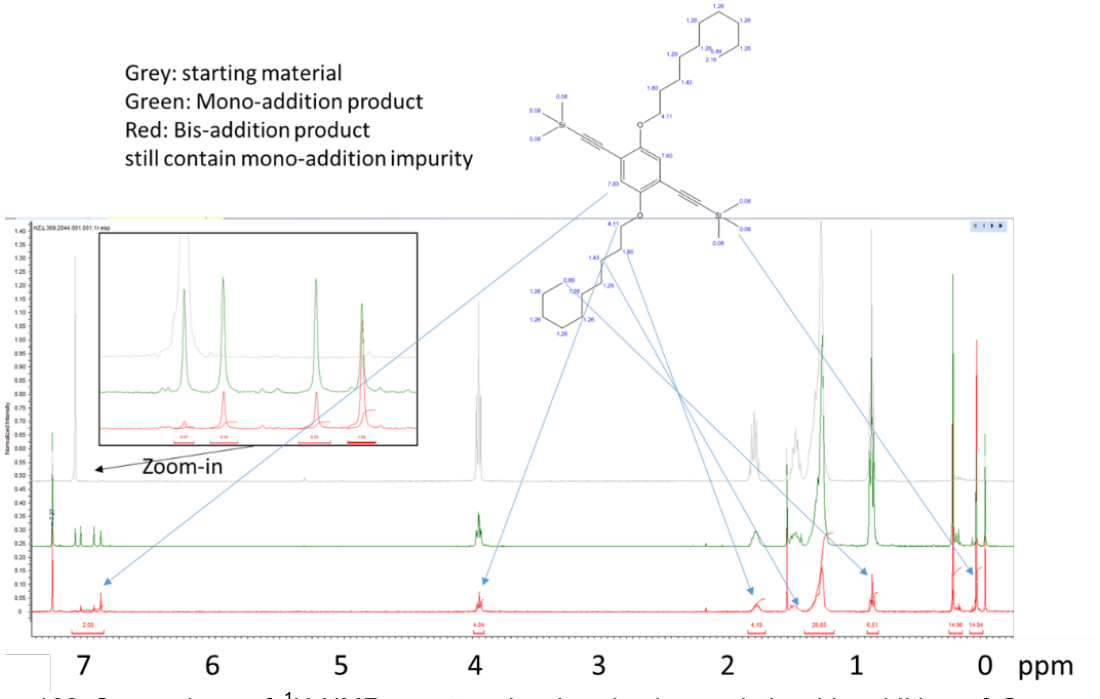


Figure 162 Comparison of ^{1}H-NMR spectra showing the incompletion bis-addition of Sonogashira coupling between 10-Bromo-Bz and TMS-acetylene (400 MHz and $CDCl_3$ solution).

J. Reprocessing the N@C_{70} alignment in MBBA reported in the literature

Since the liquid crystal alignement method has been applied to ENFs previously (reviewed in section 2.5.3),[192,195] I briefly reproduced the N@C_{70} room temperature cw-ESR experiment (Figure 163). The comparable result ($D_{\mathrm{eff}} = 0.40\ \mathrm{MHz}$) obtained confirms that my operation and the sequential studies in Chapter 7 are consistent with previous ones.

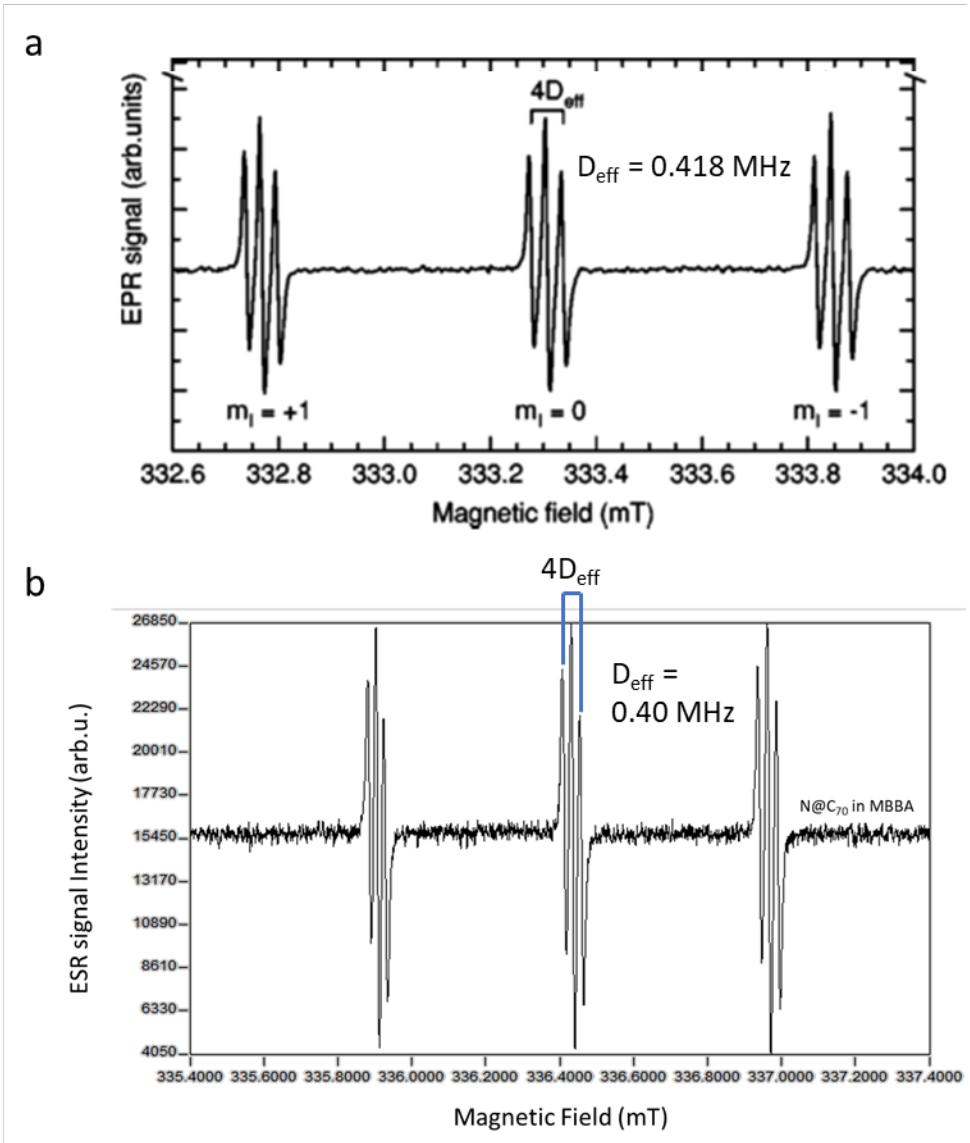


Figure 163 (a) cw-ESR of an aligned N@C_{70} sample in MBBA reported in the literature.[192] (b) Reproducing the alignment experiment for N@C_{70} reported. Data were acquired using a Magnettech MiniScope MS200 spectrometer. (Experimental conditions: $9.4286\ \mathrm{GHz}$, $30.0\ \mathrm{dB}$ attenuation, room temperature, and $0.01\ \mathrm{mT}$ modulation amplitude.)

K. Electron spin signal of CuPc-CHO in toluene

As Figure 164a demonstrated, the X-band cw-ESR spectrum of CuPcCHO is not clear in toluene with a concentration of 10^{-4} M at 100 K. Compared to $CuPc^t$ (copper(II) 2,9,16,23-tetra-tert-butyl-29H,31H-phthalocyanine) that is reported in the literature (Figure 165a),[263] I could not assign this noisy spectrum to the copper spin. The reason for the weakness of this signal could be the aggregation of CuPcCHO, as this molecule was originally synthesized for discotic liquid crystals, and its aggregation nature has been discussed elsewhere.[274] In order to resolve the Cu^{2+} spin signal, separation of the aggregated CuPcCHO molecules in toluene is needed. I mixed a ten-fold excess of ZnPcCHO powder into the CuPcCHO solution. With the mixture toluene solution of 10^{-4} M CuPcCHO and 10^{-3} M ZnPcCHO, the probability of having CuPcCHO molecules stacking on each other is one-tenth that of CuPcCHO molecules stacking on ZnPcCHO molecules. Therefore, effective separation between adjacent CuPcCHO can be expected. I then recorded the 100 K X-band cw-ESR spectrum again. This time, a rich spectrum appeared (Figure 164b). The spectrum contains the signal features that was previously reported for $CuPc^t$ both in toluene and in H_2Pc matrixes (Figure 165c).[263] The failure of the simulated singlet spin signal at $g = 2.00$ region for the H_2Pc matrix one also appeared in my observation (stronger intensity when larger ZnPc to CuPc ratio is used). Previous reports assign it to a spin signal introduced by the mixing of H_2Pc and CuPc.[263,275–277] Because measuring the ZnPcCHO on its own fails to show an intense spin signal (Figure 164c), I suggest that this singlet radical signal in Figure 164b could also be attributed to the mixing of ZnPc and CuPc.

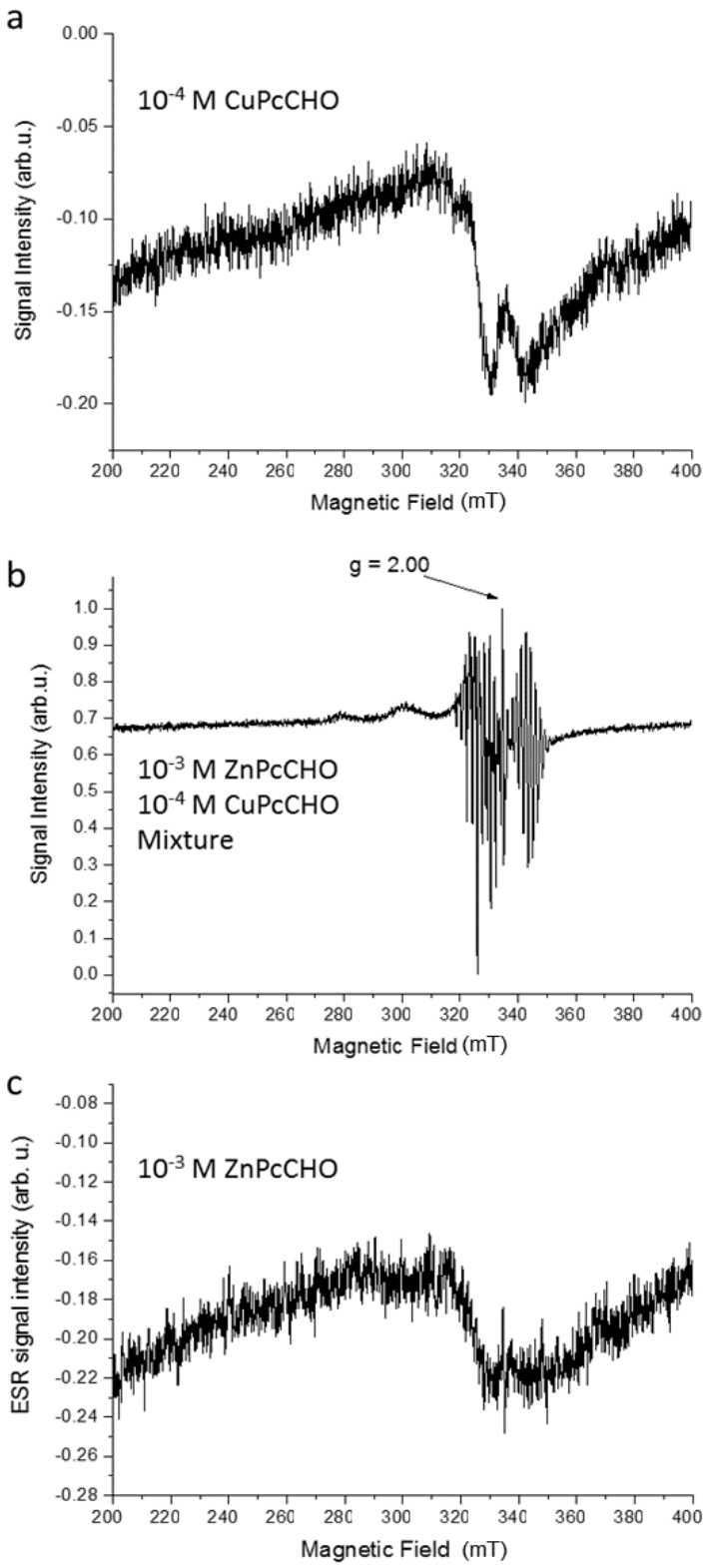


Figure 164 (a) 10^{-4} M CuPcCHO in the frozen toluene at 100 K. (b) Mixture of 10^{-4} M CuPcCHO and 10^{-3} M ZnPcCHO in toluene at 100 K. (c) 10^{-3} M ZnPcCHO in toluene at 100 K. The cw-ESR were acquired from Bruker EMX. (a. 9.3823 GHz, 15.0 dB attenuation, and 0.20 mT modulation amplitude. b. 9.3835 GHz, 15.0 dB attenuation, and 0.10 mT modulation amplitude. c. 9.3835 GHz , 20.0 dB attenuation, and 0.10 mT modulation amplitude.)

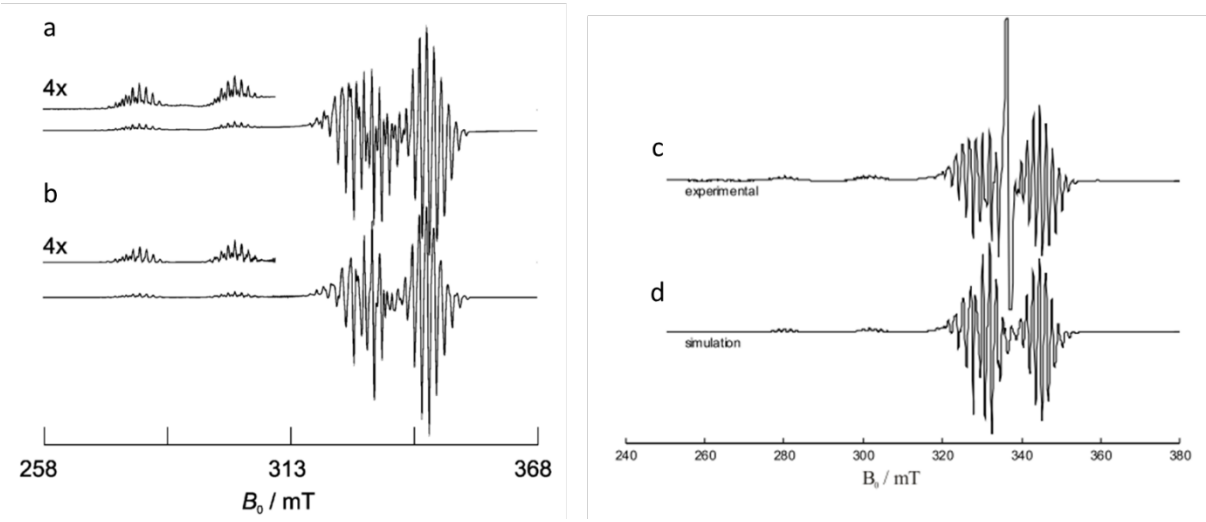


Figure 165 X-band cw-ESR spectra for tert-butyl substituted CuPc[t]. (a) 10^{-3} M toluene solution, (b) simulation for a, (c) 1:100 diluted in solid H_2Pc, and (d) simulation for c. Figure reproduced from Finazzo, C. *et al*.[263]

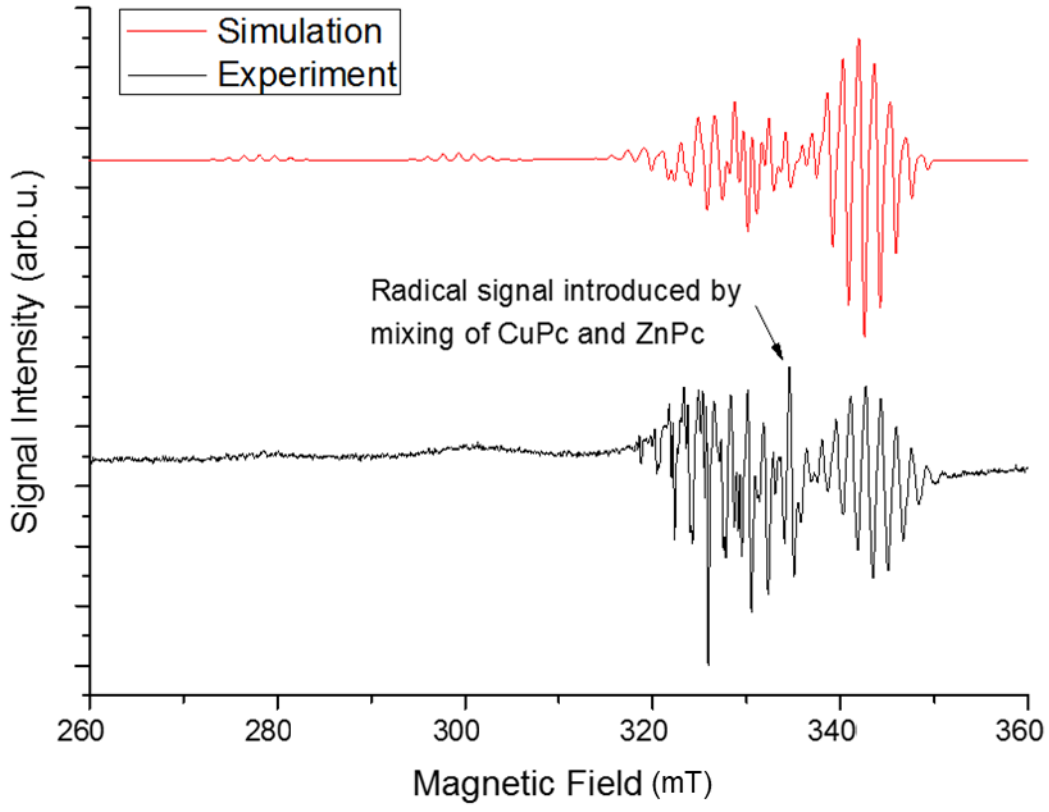


Figure 166 Simulation for the mixture of 10^{-4} M CuPcCHO and 10^{-3} M ZnPcCHO in toluene at 100 K (Figure 164b). Simulation was performed using EasySpin.[209] (Simulation parameters: $g_{\perp} = 2.0405$, $g_{\parallel} = 2.1625$, $A_{\perp}^{(\mathrm{Cu})} = -86$ MHz, $A_{\parallel}^{(\mathrm{Cu})} = -643$ MHz, $A_{\mathrm{iso}}^{(\mathrm{ligand\ N})} = 50$ MHz, and the $\Delta H_{pp} = 0.5$ mT)[263]

The comparison between Figure 164b and the literature[56,263,275–278] proves that the CuPcCHO starting material has a typical electron spin feature of a Cu^{2+} nitrogen complex. I then used EasySpin[209] to simulate the spectrum of the CuPcCHO/ZnPcCHO sample with parameters reported for $CuPc^{t}$ (Figure 166). Limited by the calculation power of a desktop computer, both copper isotopes were assumed to have the same HFC tensor, and the four HFCs between isoindole nitrogen nuclei and the copper electron spin were treated as isotropic. The first simplification is acceptable because the nuclear spins of both ^{63}Cu and ^{65}Cu are $3/2$. For the second simplification, considering the comparatively much smaller anisotropy of the reported HFCs tensor of the isoindole nitrogen ligands $(\mathrm{diag}\,(56.4, 44.8, 45.7))$[263] than that of the *g*-tensor and HFC tensor of the Cu^{2+}, such simplification will not fundamentally change the pattern of the spin signal. Comparing the simulation and the experiment, two resonances are obtained in the lower field ($260\sim310\ \mathrm{mT}$), so the spin signal corresponding to the $g^{\parallel}$ value there is not as clear as the simulation. This could be due to the influence of the molecular stacking in $g^{\parallel}$ direction. The spin signal corresponding to the $g^{\perp}$ value region is in principle fitted, apart from the $g = 2.00$ radical spin signal introduced by the usage of ZnPcCHO. The imperfect HFC features in $320\sim330\ \mathrm{mT}$ region could be caused by the isotropic simplification of the HFC tensor of the isoindole nitrogen ligands, and the slightly different HFC tensors of ^{63}Cu and ^{65}Cu.

Overall, I proved that, except for the higher tendency to aggregation, the CuPcCHO used in this chapter can be regarded as a typical CuPc.

L. Dilution effect on cw-ESR of N@C_{60}-1-CuPc in the Cu^{2+} range

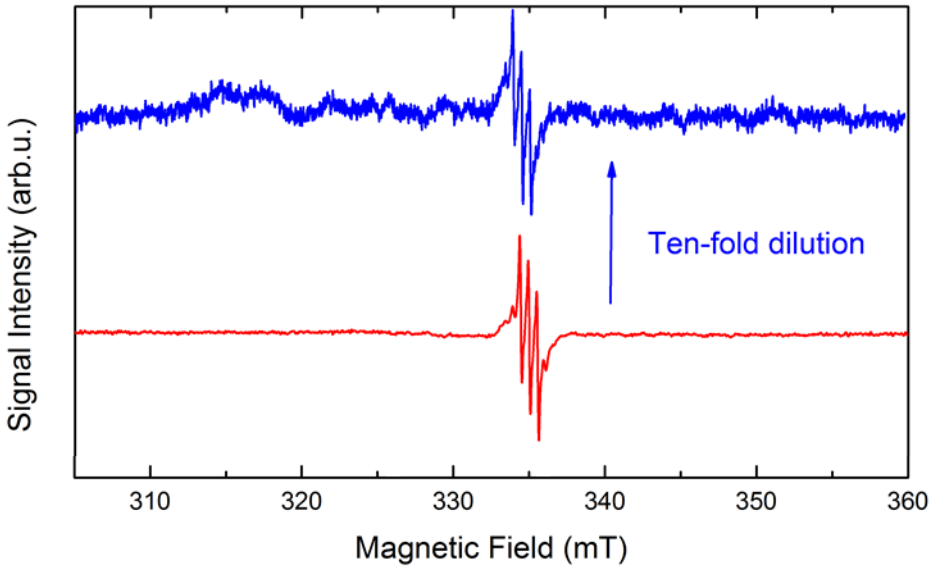
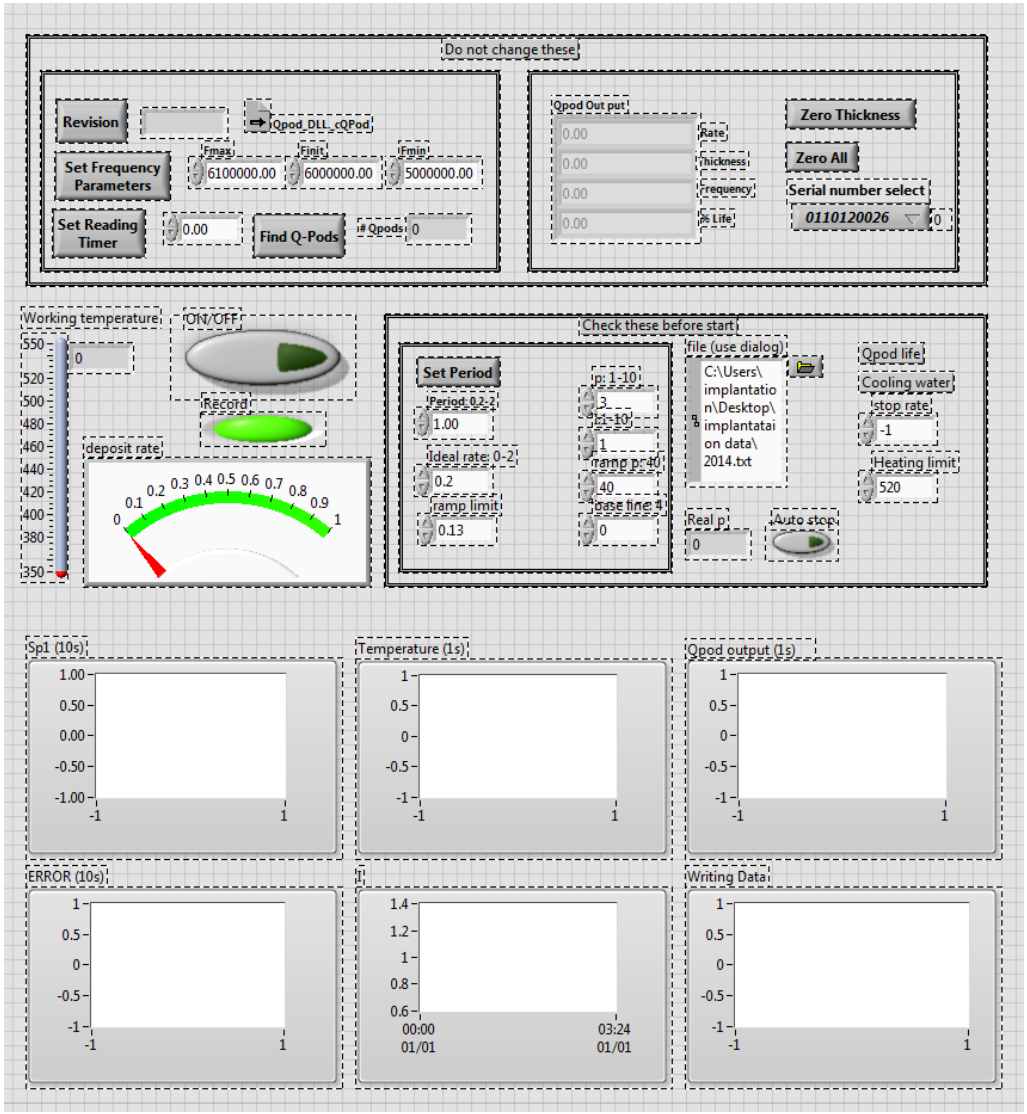


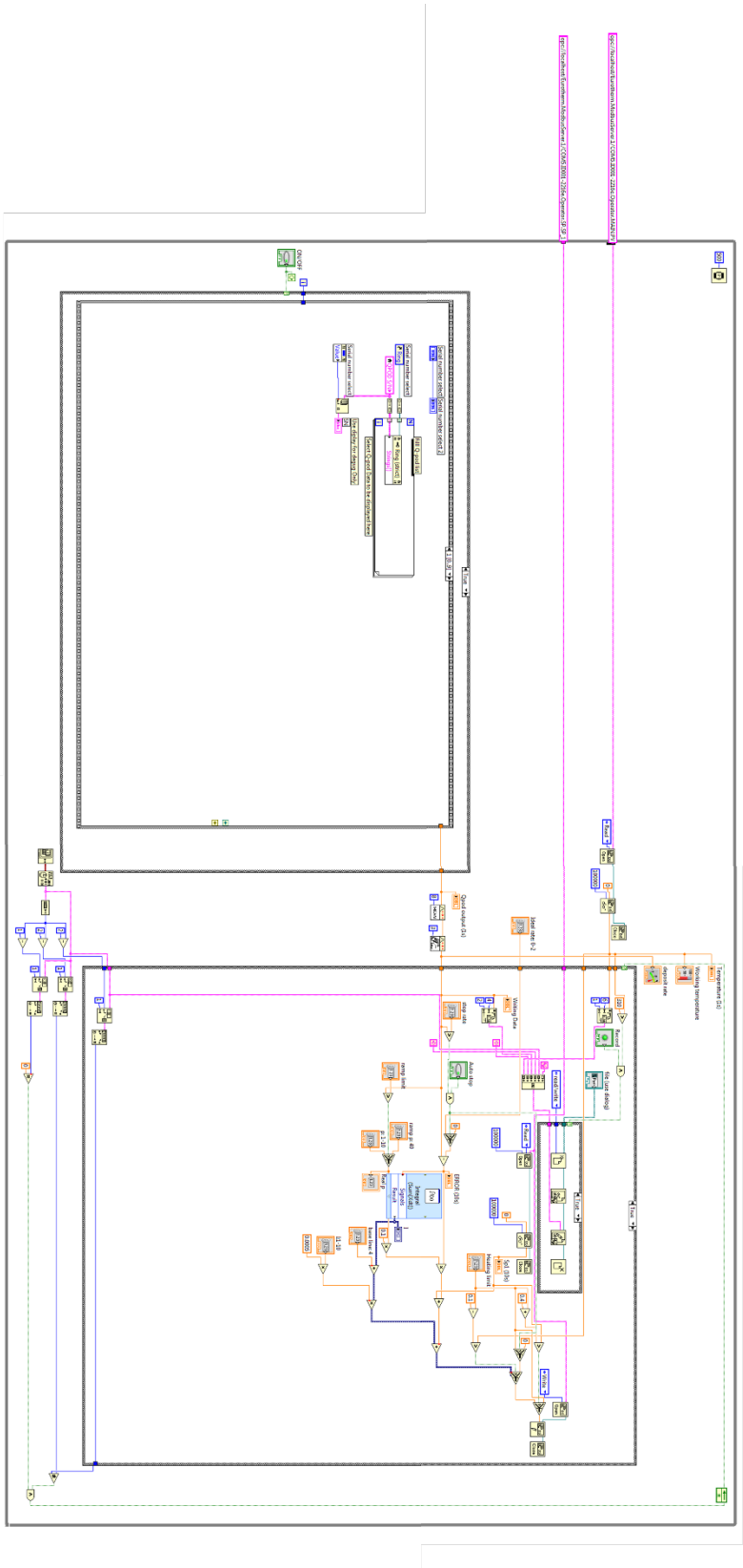
Figure 167 Comparison of the full-range cw-ESR spectra of N@C_{60}-1-CuPc with the concentration of 10^{-5} M (red) and 10^{-6} M (blue).

Since the aggregation effect is weaker at lower sample concentrations, a release of the Cu^{2+} should be expected upon diluting the dyad sample. As depicted in Figure 167, the full-range ESR signal of the 10^{-6} M sample showed an uneven baseline compared to that of the 10^{-5} M one. Unfortunately, assigning the Cu^{2+} signal is not possible due to its weak signal intensity.

Appendix B. Programming codes

A. LabVIEW scripts





B. EasySpin scripts for the cw-ESR simulation shown in Figure 76

```
clear, clc;
[B,spc]=textread('DEM-N@C60.txt','%f %f','headerlines',0);
%this loads the spectrum with file named here
B=B/10; %G to mT
%Initialization
Sys1.g = 2.00243; %g factor; isotropic
Sys1.S = 3/2; %Spin quantum number
Sys1.Nucs = 'N'; %nucleus
Sys1.A = 15.86; %hyperfine coupling constant; isotropic; Unit: MHz
Sys1.D = [8.4 0.36]; %zero field splitting parameter; axial; Unit: MHz
Sys1.lwpp = [0.11 0.03]; %positive peak to negative peak distance; Unit: mT
Exp.mwFreq = 9.379945; %Unit: GHz
Exp.Range = [min(B) max(B)]; %Unit: mT
%parameter searching range
Vary1.g=0.0005; %these ranges are changeable according to the fitting result
Vary1.A = 2;
Vary1.D = [2 1];
Vary1.lwpp = [0.04 0.03];
%Fitting
SimOpt.Method = 'perturb' % this is the method used for simulation
FitOpt.Method = 'simplex int'; %this is the method used for fitting
esfit('pepper',spc,Sys1,Vary1,Exp,SimOpt,FitOpt); %this opens an optimization window
%select “target” “data as is”
%wait for fitting
%Use the best parameter as the initial values and repeat the optimization.
%%plot
[x,y]=pepper(Sys1,Exp);
ratio= (max(spc)-min(spc))/(max(y)-min(y));
offset=0;
plot(x,y*ratio+offset,B,spc);
```

C. EasySpin scripts for the cw-ESR simulation shown in Figure 88

```
clear, clc;
[B,spc]=textread('IND-N@C60.txt','%f %f','headerlines',0);
%this loads the spectrum with file named here
B=B/10; %G to mT
%Initialization
Sys1.g = 2.00243; %g factor; isotropic
Sys1.S = 3/2; %Spin quantum number
Sys1.Nucs = 'N'; %nucleus
Sys1.A = 15.86; %hyperfine coupling constant; isotropic; Unit: MHz
Sys1.D = [8.9 0.57]; %zero field splitting parameter; axial; Unit: MHz
Sys1.lwpp = [0.11 0.03]; %positive peak to negative peak distance; Unit: mT
Exp.mwFreq = 9.428045; %Unit: GHz
Exp.Range = [min(B) max(B)]; %Unit: mT
%parameter searching range
Vary1.g=0.0005; %these ranges are changeable according to the fitting result
Vary1.A = 2;
Vary1.D = [2 1];
Vary1.lwpp = [0.04 0.03];
%Fitting
SimOpt.Method = 'perturb' % this is the method used for simulation
FitOpt.Method = 'simplex int'; %this is the method used for fitting
esfit('pepper',spc,Sys1,Vary1,Exp,SimOpt,FitOpt); %this opens an optimization window
%select “target” “data as is”
%wait for fitting
%Use the best parameter as the initial values and repeat the optimization.
%%plot
[x,y]=pepper(Sys1,Exp);
ratio=(max(spc)-min(spc))/(max(y)-min(y));
offset=0;
plot(x,y*ratio+offset,B,spc);
```

D. EasySpin scripts for the cw-ESR simulation shown in Figure 91

```
clear, clc, clf;
%powder fitting
[B,spc]=textread('Bis-IND-N@C70.txt','%f %f','headerlines',2);
B=B/10; %G to mT
Sys.g = 2.0013;
Sys.S = 3/2;
Sys.Nucs = '14N';
Sys.A = 14.65;
Sys.D= [5.0 0.64];
Sys.lwpp = 0.1;
Exp.mwFreq = 9.404493;
Exp.ModAmp=0.1;
Exp.Range = [333.4996 337.6885];
Vary.A = 0.1;
Vary.g = 0.001;
Vary.D = [5 1];
Vary.lwpp = 0.08;
SimOpt.Method = 'matrix'
FitOpt.Method = 'simplex int';
esfit('pepper',spc,Sys,Vary,Exp,SimOpt,FitOpt);
[B0,spc0] = pepper(Sys,Exp);
spc=(spc-mean(spc))/7.5;
plot(B0,spc0,B,spc);
```

E. EasySpin scripts for the cw-ESR simulation shown in Figure 96

```
%frozen toluene
clear, clc, clf;
[B,spc]=textread('watersoluable_toluene_frozen.txt','%f %f','headerlines',0);
B=B/10; %G to mT
Sys.g = 2.00263;
Sys.S = 3/2;
Sys.Nucs = '14N';
Sys.A = 15.77;
Sys.D= [8.72 0.57];
Sys.lwpp = [0.1121 0.0093];
Exp.mwFreq = 9.381845;
Exp.Range = [332.15 337.15];
Exp.mwPhase = 6*pi/180;
Vary.g = 0.0001;
Vary.D = [0.1 0.1];
Vary.A = 0.1;
Vary.lwpp = [0.1 0.008];
SimOpt.Method = 'matrix'
FitOpt.Method = 'simplex int';
esfit('pepper',spc,Sys,Vary,Exp,SimOpt,FitOpt);
[B0,spc0] = pepper(Sys,Exp);
spc0=spc0/max(spc0);
spc=(spc-spc(1))/max(spc-spc(1));
plot(B0,spc0,B,spc);

%%frozen water
clear, clc, clf;
[B,spc]=textread('purewater_frozen.txt','%f %f','headerlines',0);
B=B/10;
Sys.g = 2.00263;
Sys.S = 3/2;
Sys.Nucs = '14N';
Sys.A = 15.77;
Sys.D= [8.72 0.57];
Sys.lwpp = [0.0913 0.0241];
Exp.mwFreq = 9.379719;
Exp.Range = [332.15  337.15];
Vary.g = 0.0001;
Vary.D = [0.1 0.1];
Vary.A = 0.1;
Vary.lwpp = [0.1 0.008];
SimOpt.Method = 'matrix'
FitOpt.Method = 'simplex int';
esfit('pepper',spc,Sys,Vary,Exp,SimOpt,FitOpt);

[B0,spc0] = pepper(Sys,Exp);
spc0=spc0/max(spc0);
spc=(spc-spc(1))/max(spc-spc(1));
plot(B0,spc0,B,spc);
```

F. EasySpin scripts for the cw-ESR simulation shown in Figure 108

```
clear, clc;
[B,spc]=textread('PYR-N@C60.txt','%f %f','headerlines',0);
%this loads the spectrum with file named here
%Initialization
Sys1.g = 2.00243; %g factor; isotropic
Sys1.S = 3/2; %Spin quantum number
Sys1.Nucs = 'N'; %nucleus
Sys1.A = 15.86; %hyperfine coupling constant; isotropic; Unit: MHz
Sys1.D = [13.6 0.7]; %zero field splitting parameter; axial; Unit: MHz
Sys1.lwpp = [0.11 0.03]; %positive peak to negative peak distance; Unit: mT
Exp.mwFreq = 9.4353; %Unit: GHz
Exp.Range = [min(B) max(B)]; %Unit: mT
%parameter searching range
Vary1.g=0.0005; %these ranges are changeable according to the fitting result
Vary1.A = 2;
Vary1.D = [2 1];
Vary1.lwpp = [0.04 0.03];
%Fitting
SimOpt.Method = 'perturb' % this is the method used for simulation
FitOpt.Method = 'simplex int'; %this is the method used for fitting
esfit('pepper',spc,Sys1,Vary1,Exp,SimOpt,FitOpt); %this opens an optimization window
%select “target” “data as is”
%wait for fitting
%Use the best parameter as the initial values and repeat the optimization.
%%plot
[x,y]=pepper(Sys1,Exp);
ratio= (max(spc)-min(spc))/(max(y)-min(y));
offset=0;
plot(x,y*ratio+offset,B,spc);



%%


clear, clc;


[B,spc]=textread('PYR-N@C60-dimer.txt','%f %f','headerlines',0);
%this loads the spectrum with file named here
%Initialization
Sys1.g = 2.00243; %g factor; isotropic
Sys1.S = 3/2; %Spin quantum number
Sys1.Nucs = 'N'; %nucleus
Sys1.A = 15.86; %hyperfine coupling constant; isotropic; Unit: MHz
Sys1.D = [14.7 0.6]; %zero field splitting parameter; axial; Unit: MHz
Sys1.lwpp = [0.11 0.03]; %positive peak to negative peak distance; Unit: mT
Exp.mwFreq = 9.4273; %Unit: GHz
Exp.Range = [min(B) max(B)]; %Unit: mT
%parameter searching range
Vary1.g=0.0005; %these ranges are changeable according to the fitting result
Vary1.A = 2;
```

```
Vary1.D = [2 1];
Vary1.lwpp = [0.04 0.03];
%Fitting
SimOpt.Method = 'perturb' % this is the method used for simulation
FitOpt.Method = 'simplex int'; %this is the method used for fitting
esfit('pepper',spc,Sys1,Vary1,Exp,SimOpt,FitOpt); %this opens an optimization window
%select “target” “data as is”
%wait for fitting
%Use the best parameter as the initial values and repeat the optimization.
%%plot
[x,y]=pepper(Sys1,Exp);
ratio= (max(spc)-min(spc))/(max(y)-min(y));
offset=0;
plot(x,y*ratio+offset,B,spc);
```

G. EasySpin scripts for the cw-ESR simulation shown in Figure 111

```
clear, clc, clf;
zp0=3;
m=0;
Sys.S=[3/2 3/2];
Jiso=0;
Sys.g=[2.00243; 2.00243];
Sys.Nucs='14N, 14N';
Sys.A=[15.86,0;0,15.86];
Sys.D=[8, 0.5; 8, 0.5];
Sys.lwpp=0.121;
Jdip=23.6;%through space dipolar coupling estimated by http://easyspin.org/documentation/tools.html
Exp=struct('mwFreq',9.392534,'CenterSweep',[335.0862,10]);
%Exp.Ordering = @(ph,th) exp(zp0*(3*(cos(th)*cos(m)-sin(th).*cos(pi-ph)*sin(m)).^2-1)/2);
%Exp.CrystalOrientation = [0, 0 ,0];
Sys.ee=Jiso+Jdip*[1 1 -2];
[x,y]=pepper(Sys,Exp);
plot(x,y);
hold on
Sys.S=[3/2 3/2];
Jiso=0;
Sys.g=[2.00243; 2.00243];
Sys.Nucs='14N,14N';
Sys.A=[15.86,0;0,15.86];
Sys.D=[8, 0.5; 8, 0.5];
Sys.lwpp=0.121;
Jdip=0;%through space dipolar coupling estimated by http://easyspin.org/documentation/tools.html
Exp=struct('mwFreq',9.392534,'CenterSweep',[335.0862,10]);
%Exp.Ordering = @(ph,th) exp(zp0*(3*(cos(th)*cos(m)-sin(th).*cos(pi-ph)*sin(m)).^2-1)/2);
%Exp.CrystalOrientation = [0, 0 ,0];
Sys.ee=Jiso+Jdip*[1 1 -2];
[x,y]=pepper(Sys,Exp);
plot(x,y);
hold on
Sys.S=[3/2 3/2];
Jiso=0;
Sys.g=[2.00243; 2.00243];
Sys.Nucs='14N,14N';
Sys.A=[15.86,0;0,15.86];
Sys.D=[8, 0.5; 8, 0.5];
Sys.lwpp=0.121;
Jdip=1.92;%through space dipolar coupling estimated by http://easyspin.org/documentation/tools.html
Exp=struct('mwFreq',9.392534,'CenterSweep',[335.0862,10]);
%Exp.Ordering = @(ph,th) exp(zp0*(3*(cos(th)*cos(m)-sin(th).*cos(pi-ph)*sin(m)).^2-1)/2);
%Exp.CrystalOrientation = [0, 0 ,0];
Sys.ee=Jiso+Jdip*[1 1 -2];
[x,y]=pepper(Sys,Exp);
plot(x,y);


%%


clear, clc, clf;
zp0=3;
m=0;
```

```
Sys.S=[3/2 3/2];
Jiso=0;
Sys.g=[2.00243; 2.00243];
Sys.Nucs='14N, 14N';
Sys.A=[15.86,0;0,15.86];
Sys.D=[8, 0.5; 8, 0.5];
Sys.lwpp=0.121;
Jdip=23.6;%through space dipolar coupling estimated by http://easyspin.org/documentation/tools.html
Exp=struct('mwFreq',9.392534,'CenterSweep',[335.0862,10]);
%Exp.Ordering = @(ph,th) exp(zp0*(3*(cos(th)*cos(m)-sin(th).*cos(pi-ph)*sin(m)).^2-1)/2);
Exp.CrystalOrientation = [0, 0 ,0];
Sys.ee=Jiso+Jdip*[1 1 -2];
[x,y]=pepper(Sys,Exp);
plot(x,y);
hold on
Sys.S=[3/2 3/2];
Jiso=0;
Sys.g=[2.00243; 2.00243];
Sys.Nucs='14N,14N';
Sys.A=[15.86,0;0,15.86];
Sys.D=[8, 0.5; 8, 0.5];
Sys.lwpp=0.121;
Jdip=0;%through space dipolar coupling estimated by http://easyspin.org/documentation/tools.html
Exp=struct('mwFreq',9.392534,'CenterSweep',[335.0862,10]);
%Exp.Ordering = @(ph,th) exp(zp0*(3*(cos(th)*cos(m)-sin(th).*cos(pi-ph)*sin(m)).^2-1)/2);
Exp.CrystalOrientation = [0, 0 ,0];
Sys.ee=Jiso+Jdip*[1 1 -2];
[x,y]=pepper(Sys,Exp);
plot(x,y);
hold on
Sys.S=[3/2 3/2];
Jiso=0;
Sys.g=[2.00243; 2.00243];
Sys.Nucs='14N,14N';
Sys.A=[15.86,0;0,15.86];
Sys.D=[8, 0.5; 8, 0.5];
Sys.lwpp=0.121;
Jdip=1.92;%through space dipolar coupling estimated by http://easyspin.org/documentation/tools.html
Exp=struct('mwFreq',9.392534,'CenterSweep',[335.0862,10]);
%Exp.Ordering = @(ph,th) exp(zp0*(3*(cos(th)*cos(m)-sin(th).*cos(pi-ph)*sin(m)).^2-1)/2);
Exp.CrystalOrientation = [0, 0 ,0];
Sys.ee=Jiso+Jdip*[1 1 -2];
[x,y]=pepper(Sys,Exp);
plot(x,y);
```

H. EasySpin scripts for the cw-ESR simulation shown in Figure 114

```
clear, clc;
[B,spc]=textread('5-bz-5dimer.txt','%f %f','headerlines',0;
spc=spc-mean(spc);
accept=100000000000000;
for k =1:21
    D0=9.0+(k-1)/10;
for j = 1:11
    E0= (j-1)/10;
Sys1.g = 2.00243;
Sys1.S = 3/2;
Sys1.Nucs = 'N';
Sys1.A = 15.86;
Sys1.D = [D0 E0]; %fitting variable
Sys1.lwpp = [0.11 0.03];
Exp.nPoints = 4095;
Exp.mwFreq = 9.3960;
Exp.Range = [min(B) max(B)];
[x,y]=pepper(Sys1,Exp);
for i=1:4095; %fitting range
    if (B(i)>334.9)
        spc(i)=0;
    end
    if (x(i)>334.9)
        y(i)=0;
    end
end

ratio= (max(spc)-min(spc))/(max(y)-min(y));

error=spc'-y;
accept0=sum(error.*error);
if (accept0 < accept)
   accept=accept0;
   D=D0; %optimal D
   E=E0; %optimal E
end
end
end
```

I. Matlab scripts for simulation shown in Figure 122

```
clear;
clf;
D=5;
E=0.6;
Ddiag=[-D/3+E -D/3-E 2*D/3];
k=300;
for i=1:k
   for j=1:k
      temp=[-j/k*pi -i/k*2*pi 0];
      R=erot(temp);
      Ddiag2=R*diag(Ddiag)*R.';
      r(i,j)=3*Ddiag2(3,3);
      x(i,j)=r(i,j)*sin(i/k*2*pi)*cos(j/k*pi);
      y(i,j)=r(i,j)*sin(i/k*2*pi)*sin(j/k*pi);
      z(i,j)=r(i,j)*cos(i/k*2*pi);
   end
end
t = 0:pi/50:pi;
st = sin(t)*12;
ct = cos(t)*12;
t=0*t;
t0 = pi:pi/50:2*pi;
st0 = sin(t0)*12;
ct0 = cos(t0)*12;
t0=0*t0;
t2= -12:0.01:12;
t3=t2*0;
surface(x,y,z,r,'EdgeColor','flat')
hold on
plot3(0*t,st,ct, 'black')
plot3(ct,st,0*t, 'black')
plot3(st,0*t,ct, 'black')
plot3(0*t0,st0,ct0,'--', 'color', [0.3 0.3 0.3])
plot3(ct0,st0,0*t0,'--', 'color', [0.3 0.3 0.3])
plot3(st0,0*t0,ct0,'--', 'color', [0.3 0.3 0.3])
plot3(t3,t3,t2,'black')
plot3(t3,t2,t3,'black')
plot3(t2,t3,t3,'black')
xlim([-12,12]);
ylim([-12,12]);
zlim([-12,12]);
hold off;
```

J. EasySpin scripts for the cw-ESR simulation shown in Figure 125

```
%figure a

%aligned sample

%searching for the optimal C20
clear, clc, clf;
m=0*pi/180;%sample direction Z with the respect to the external field (both the molecular Z axis, and the ZFS tensor Z axis)
accept = 1000000000;%initializing the accepting threshhold
for i = 0:50;%searching for optimal C20 to fit the spectrum
    C20=0.1*i;
    Sys.g = 2.0023;%fitted from powder spectra
    Sys.S = 3/2;
    Sys.Nucs = '14N';
    Sys.A = 14.65;%fitted from powder spectra
    Sys.lwpp = 0.1047;%fitted from powder spectra, this value is tested by manual variation, the optimal result is not affected in the reasonable range of 0.9-0.11;
        Sys.D=[5 0.64]
    Exp.nPoints=4095;
    Exp.ModAmp=0.08;
    Exp.Range =  [333.7509  337.2500];
    Exp.mwFreq = 9.401713;
        Exp.Temperature = 100;
    Exp.Ordering = @(ph,th) exp(C20*(3*(cos(th)*cos(m)-sin(th).*cos(pi-ph)*sin(m)).^2-1)/2)+exp(C20*(3*(cos(th)*cos(m)-sin(th).*cos(ph)*sin(m)).^2-1)/2);%Partially axially aligned sample with the energy profile obeying the distribution model discussed in this work
    [B0,spc0]=pepper(Sys,Exp);
    [spc0]=[spc0]/max(spc0);
%compare the simulation and the raw data
    [B,spc]=textread('N@C70 bis ind 100 in MBBA 0.txt','%f %f','headerlines',2);
    B=B/10;
    spc=(spc-mean(spc))/(max(spc)-mean(spc));
    error=spc'-spc0;
    accept0=sum(error.*error);
    %find the best C20
    if (accept0 < accept)
        accept=accept0;
        C=C20;
    end
end

%%
%fit the spectra with the optimal C20
C20=C;%use the best C20 to simulate the raw data and plot it
    Sys.g = 2.0023;%fitted from powder spectra
    Sys.S = 3/2;
    Sys.Nucs = '14N';
    Sys.A = 14.65;%fitted from powder spectra
    Sys.lwpp = 0.1047;%fitted from powder spectra
        Sys.D=[5 0.64]
    Exp.nPoints=4095;
    Exp.ModAmp=0.08;
```

```
   Exp.Range =  [333.7509  337.2500];
   Exp.mwFreq = 9.4044;
      Exp.Temperature = 100;
   Exp.Ordering = @(ph,th) exp(C20*(3*(cos(th)*cos(m)-sin(th).*cos(pi-ph)*sin(m)).^2-
1)/2)+exp(C20*(3*(cos(th)*cos(m)-sin(th).*cos(ph)*sin(m)).^2-1)/2);%Partially axially aligned
sample with the energy profile obeying the distribution model discussed in this work
   [B0,spc0]=pepper(Sys,Exp);
   [spc0]=[spc0]/max(spc0);
%compare the simulation and the raw data
   [B,spc]=textread('N@C70 bis ind 100 in MBBA 0.txt','%f %f','headerlines',2);
   B=B/10;
   spc=(spc-mean(spc))/(max(spc)-mean(spc));
plot(B0,spc0,B,spc);

%calculate Order parameter with C20 using easypin example program

%Easyspin-5.1.4/examples/slowmotion/orderparameter.m




%%


%figure b


clear;
C20 = 3; %%aligned
bincounts=[-110:160]*0;
parfor theta=0:900
k=10000;
   for e=0:180
      for phi=0:180
         D=5;E=0.64;Dpv=diag([-D/3*1+E -D/3*1-E D/3*2]);
         abc=[-e,-theta/10,phi]*pi/180;R=erot(abc);
         rotate=[0,0,0]*pi/180;Q=erot(rotate);
         D=Q.'*(R.'*Dpv*R)*Q;
         k(end+1) =D(3,3)*3/2*10;
      end
   end
   binranges =[-110:160];
bincounts =bincounts + histc(k,binranges)*sin(theta/1800*pi)*exp((3*cos((theta)/1800*pi)-
1)/2*C20);
end

plot(bincounts);
%%
clear;
C20 = 0; %%powder

bincounts=[-110:160]*0;
parfor theta=0:900
k=10000;
   for e=0:180
```

```
        for phi=0:180
            D=5;E=0.64;Dpv=diag([-D/3*1+E -D/3*1-E D/3*2]);
            abc=[-e,-theta/10,phi]*pi/180;R=erot(abc);
            rotate=[0,0,0]*pi/180;Q=erot(rotate);
            D=Q.'*(R.'*Dpv*R)*Q;
            k(end+1) =D(3,3)*3/2*10;
        end
    end
    binranges =[-110:160];
bincounts =bincounts + histc(k,binranges)*sin(theta/1800*pi)*exp((3*cos((theta)/1800*pi)-
1)/2*C20);
end

plot(bincounts);

%%
%figure c

clear, clc, clf

theta = linspace(0,pi/2,1001);

% ordering (pseudo)potential coefficient
C20 = 3;
Y20 = (3*cos(theta).^2-1)/2;

C0=0;

% set up the potential and the probability distribution
kT = boltzm*293;
U = -kT*C20*Y20;
U0 = -kT*C0*Y20;
P = exp(-U/kT).*sin(theta);
P0=exp(-U0/kT).*sin(theta);

% normalize the probability distribution
dtheta = theta(2)-theta(1);
sumP=sum(P);
sumP0=sum(P0);
P = P/sumP/dtheta;
P0 = P0/sumP0/dtheta;

% plotting
subplot(2,1,1)
plot(theta*180/pi,U/echarge,theta*180/pi,U0/echarge);
set(gca,'FontSize',20);
xlabel('theta (deg)');
ylabel('potential energy (eV)');

subplot(2,1,2)
plot(theta*180/pi,P,theta*180/pi,P0);
set(gca,'FontSize',20);
xlabel('theta (deg)');
ylabel('probability density');
```

```
ylim([0 max(P)]);
```

K. EasySpin scripts for the cw-ESR simulation shown in Figure 129

```
%figure b

clear, clc, clf

set(gcf,'DefaultAxesColorOrder',[...
    1 0 0.333;...
    1 0 0;1 0.333 0;1 0.667 0;1 1 0;0.667 1 0;0.333 1 0;...
    0 1 0;0 1 0.333;0 1 0.667;0 1 1;0 0.667 1;0 0.333 1;...
    0 0 1;0.333 0 1 ;0.667 0 1;...
    ]);

C20 = 3;
for mm=0:6:90
m=mm*pi/180;
PP=linspace(0,0,1001);
AA=linspace(0,pi/2,1001);
i=0;
for theta = 0: pi/2/1000: pi/2;
    P=0;
    i=i+1;
for phi = 0: pi/2/1000: pi/2;

Y20 = (3*(cos(theta)*cos(m)-sin(theta)*cos(phi)*sin(m))^2-1)/2;
kT = boltzm*293;
U = -kT*C20*Y20;
P = P+exp(-U/kT);
end
PP(i)=P*sin(theta);
end
PP = PP/sum(PP)/(90/1000)*100;
plot(AA*180/pi,PP,'LineWidth',3);hold all;
end


%%


%figure d



clear, clc;
fid = fopen('waterfall.txt','a+');
for i = 0:90
m=i/180*pi;
C20=3;%use the best C20 to simulate the raw data and plot it
    Sys.g = 2.0023;%fitted from powder spectra
    Sys.S = 3/2;
    Sys.Nucs = '14N';
    Sys.A = 14.65;%fitted from powder spectra
    Sys.lwpp = 0.1047;%fitted from powder spectra
Sys.D=[5 0.64]
    Exp.nPoints=4095;
```

```
    Exp.ModAmp=0.08;
    Exp.Range =  [333.7509  337.2500];
    Exp.mwFreq = 9.401713;
Exp.Temperature = 100;
    Exp.Ordering = @(ph,th) exp(C20*(3*(cos(th)*cos(m)-sin(th).*cos(pi-ph)*sin(m)).^2-
1)/2)+exp(C20*(3*(cos(th)*cos(m)-sin(th).*cos(ph)*sin(m)).^2-1)/2);%Partially axially aligned sample
with the energy profile obeying the distribution model discussed in this work
    [B0,spc0]=pepper(Sys,Exp);
if i==0
fprintf(fid,'%g\t',B0);
fprintf(fid,'\n');
end
fprintf(fid,'%g\t',spc0);
fprintf(fid,'\n');
end
fclose(fid);

%plot “waterfall.txt” with origin
```

L. EasySpin scripts for the cw-ESR simulation shown in Figure 135

```
%figure a
%Initialization
Sy = struct('S',3/2,'Nucs','14N','g',2.00243,'A', 15.36,'D',14.16);
B = 332:338; E = levels(Sy,0,pi,B)/1000; %Based on fitting result
%Plot
subplot(4, 1, 1)
plot(B,E)
xlim([332 338])
ylim([0.455+0.939 0.485+0.939]*10);
subplot(4, 1, 2)
plot(B,E)
xlim([332 338])
ylim([0.455 0.485]*10);
subplot(4, 1, 3)
plot(B,E)
xlim([332 338])
ylim([0.455-0.939 0.485-0.939]*10);
subplot(4, 1, 4)
plot(B,E)
xlim([332 338])
ylim([0.455-0.939*2 0.485-0.939*2]*10);


%%


%figure b


clear, clc;
[B,spc]=textread('N@C60-1-ZnPc.txt','%f %f','headerlines',0);
%this loads the spectrum with file named here
B=B/10; %Unit conversion: G to mT
%Initialization
Sys1.g = 2.00243; %g factor; isotropic
Sys1.S = 3/2; %Spin quantum number
Sys1.Nucs = 'N'; %nucleus
Sys1.A = 15.36; %hyperfine coupling constant; isotropic; Unit: MHz
Sys1.D = [14.16 0]; %zero field splitting parameter; axial; Unit: MHz
Sys1.lwpp = [0.11 0.03]; %positive peak to negative peak distance; Unit: mT
Exp.mwFreq = 9.388970; %Unit: GHz
Exp.Range = [min(B) max(B)]; %Unit: mT
%parameter searching range
Vary1.g=0.0005; %these ranges are changeable according to the fitting result
Vary1.A = 2;
Vary1.D = [2 1];
Vary1.lwpp = [0.04 0.03];
%Fitting
SimOpt.Method = 'perturb' % this is the method used for simulation
FitOpt.Method = 'simplex int'; %this is the method used for fitting
```

```
esfit('pepper',spc,Sys1,Vary1,Exp,SimOpt,FitOpt); %this opens an optimization window
%select “target” “data as is”
%wait for fitting
%Use the best parameter as the initial values and repeat the optimization.
%%plot
[x,y]=pepper(Sys1,Exp);
ratio= (max(spc)-min(spc))/(max(y)-min(y));
offset=0;
plot(x,y*ratio+offset,B,spc);
```

M. EasySpin scripts for the cw-ESR simulation shown in Figure 141

```
clear, clc;
[B,spc]=textread('CuPcCHOinZnPc.dat','%f %f','headerlines',0);%this loads the spectrum with file named here. headliners allows you to input how many lines there are before your data
B=B/10;
Exp.mwFreq = 9.383509; %these are the parameters from the measured spectrum, frequency and field range
Exp.Range = [260 360];
Exp.nPoints = 3000;

Sys2.S=[1/2];
Sys2.g=[2.0405,2.0405,2.1625];
Sys2.Nucs='63Cu, 14N, 14N, 14N, 14N'; %isotope neglected, 65Cu is similar to 63Cu, abundance of 15N is negligible
ACuCu=diag([-86 -86 -643]); %Parameter determined for 63Cu
ALCu=diag([50 50 50]); %weak anisotropy neglected

Sys2.A=[ACuCu;ALCu;ALCu;ALCu;ALCu];
Sys2.lwpp = 0.5;

[x,y]=pepper(Sys2,Exp);
plot(x,y/max(y)+1,B,spc/max(spc));
```

N. EasySpin scripts for the cw-ESR simulation shown in Figure 143

```
%N@C60-1-CuPc
clear, clc;
[B,spc]=textread('CuPcPh1N@C60_100K.txt','%f %f','headerlines',0)
B=B/10;
spc=spc-mean(spc);
Exp.mwFreq =9.385998;
Exp.Range = [min(B) max(B)];
Exp.ModAmp = 0.05;
Exp.nPoints = 2730;
%No aggregation condition
Sys2.S=[3/2 1/2];
Sys2.g=[2.0024 2.0024,2.0024;2.04,2.04,2.16]; %g tensors for N and Cu spins
Sys2.Nucs='N, Cu, N, N, N, N';
ANN=[15.4 15.4 15.4]; %HFC between endohedral N I and S
ANCu=[0 0 0]; %HFC between endohedral N I and Cu S
ACuN=[0 0 0]; %HFC between endohedral N S and Cu I
ACuCu=[-86 -86 -643]; %HFC between Cu S and Cu I
ALCu=[50 50 50]; %HFC between Cu S and ligand N I
ALN=[0 0 0]; %HFC between endohedral N S and ligand N I
Sys2.A=[ANN,ANCu,;ACuN,ACuCu;ALN,ALCu;ALN,ALCu;ALN,ALCu;ALN,ALCu]; %HFC
Sys2.lwpp = [0. 0.13];
D2=14; %ZFS
Dpv2=[-D2/3*1 -D2/3*1 D2/3*2]; %ZFS tensor
ka2=0;
kb2=83;
ky2=38;
Dpa2=[pi/180*ka2 pi/180*kb2 pi/180*ky2]; %ZFS frame Euler angle
R2=erot(Dpa2);
D2=R2*diag(Dpv2)*R2.';
Sys2.D=[D2;[0,0,0;0,0,0;0,0,0]]; %ZFS tensor rotated
jiso2=0*[1,1,1]; %isotropic part of electron spin coupling (=0,according to solution experiment)
i2=5.6; %anisotropic part of electron spin coupling (free space dipolar coupling)
Coupling2=jiso2+i2*[1,1,-2]; %electron spin coupling tensor
ja2=0;
jb2=70;
jy2=0;
Dpa2=[pi/180*ja2 pi/180*jb2 pi/180*jy2]; %spin coupling frame Euler angle
R2=erot(Dpa2);
Sys2.ee=R2*diag(Coupling2)*R2.'; %spin coupling rotated
% aggregation condition, ignore CuPc
Sys3.S=3/2;
Sys3.g=2.0024;
Sys3.Nucs='14N';
Sys3.A=15.7;
Sys3.lwpp = 0.13;
Sys3.D=14;
rms=10000000.0;
R=-1;
for R0=1:10
Sys2.weight=100; %normalized weight
Sys3.weight=R0/2+25; %weight variable
[x,y]=pepper({Sys2,Sys3},Exp);
ratio0= (max(spc)-min(spc))/(max(y)-min(y));
SD=(spc'-y*ratio0).^2;
rms0 = sum(SD);
if rms > rms0
   rms=rms0;
```

```
    yy=y; %best fit
    ratio=ratio0;
    R=R0; %optimal weight 30
end
end

subplot(2,1,1); %spectra compare
plot(x,yy*ratio,B,spc);
subplot(2,1,2); %deviation
plot(B,spc'-y*ratio);


%%
%N@C60-2-CuPc


clear, clc;
[B,spc]=textread('CuPcPh2N@C60_100K.txt','%f %f','headerlines',0);
B=B/10;
spc=spc-mean(spc);
Exp.mwFreq =9.385976;
Exp.Range = [min(B) max(B)];
Exp.ModAmp = 0.05;
Exp.nPoints = 2730;
%No aggregation condition
Sys2.S=[3/2 1/2];
Sys2.g=[2.0024 2.0024,2.0024;2.04,2.04,2.16]; %g tensors for N and Cu spins
Sys2.Nucs='N, Cu, N, N, N, N';
ANN=[15.4 15.4 15.4]; %HFC between endohedral N I and S
ANCu=[0 0 0]; %HFC between endohedral N I and Cu S
ACuN=[0 0 0]; %HFC between endohedral N S and Cu I
ACuCu=[-86 -86 -643]; %HFC between Cu S and Cu I
ALCu=[50 50 50]; %HFC between Cu S and ligand N I
ALN=[0 0 0]; %HFC between endohedral N S and ligand N I
Sys2.A=[ANN,ANCu,;ACuN,ACuCu;ALN,ALCu;ALN,ALCu;ALN,ALCu;ALN,ALCu]; %HFC
Sys2.lwpp = [0. 0.13];
D2=14; %ZFS
Dpv2=[-D2/3*1 -D2/3*1 D2/3*2]; %ZFS tensor
ka2=0;
kb2=21;
ky2=74;
Dpa2=[pi/180*ka2 pi/180*kb2 pi/180*ky2]; %ZFS frame Euler angle
R2=erot(Dpa2);
D2=R2*diag(Dpv2)*R2.';
Sys2.D=[D2;[0,0,0;0,0,0;0,0,0]]; %ZFS tensor rotated
jiso2=0*[1,1,1]; %isotropic part of electron spin coupling (=0,according to solution experiment)
i2=11; %anisotropic part of electron spin coupling (free space dipolar coupling)
Coupling2=jiso2+i2*[1,1,-2]; %electron spin coupling tensor
ja2=0;
jb2=73;
jy2=0;
Dpa2=[pi/180*ja2 pi/180*jb2 pi/180*jy2]; %spin coupling frame Euler angle
R2=erot(Dpa2);
Sys2.ee=R2*diag(Coupling2)*R2.'; %spin coupling rotated
% aggregation condition, ignore CuPc
Sys3.S=3/2;
Sys3.g=2.0024;
Sys3.Nucs='14N';
Sys3.A=15.7;
```

```
Sys3.lwpp = 0.13;
Sys3.D=14;
rms=10000000.0;
R=-1;
for R0=1:10
Sys2.weight=100; %normalized weight
Sys3.weight=R0/2+35; %weight variable
[x,y]=pepper({Sys2,Sys3},Exp);
ratio0= (max(spc)-min(spc))/(max(y)-min(y));
SD=(spc'-y*ratio0).^2;
rms0 = sum(SD);
if rms > rms0
   rms=rms0;
   yy=y; %best fit
   ratio=ratio0;
   R=R0; %optimal weight 37
end
end

subplot(2,1,1); %spectra compare
plot(x,yy*ratio,B,spc);
subplot(2,1,2); %deviation
plot(B,spc'-y*ratio);
```

O. EasySpin scripts for the cw-ESR simulation shown in Figure 145

```
%%E-7
clear, clc;
[B,spc]=textread('CuPcPh1N@C60_E-7.txt','%f %f','headerlines',0);
B=B/10;
spc=spc-mean(spc);
Exp.mwFreq = 9.385931;
Exp.Range = [min(B) max(B)];
Exp.ModAmp = 0.05;
Exp.nPoints = 2730;
%No aggregation condition
Sys2.S=[3/2 1/2];
Sys2.g=[2.0024 2.0024,2.0024;2.04,2.04,2.16]; %g tensors for N and Cu spins
Sys2.Nucs='N, Cu, N, N, N, N';
ANN=[15.4 15.4 15.4]; %HFC between endohedral N I and S
ANCu=[0 0 0]; %HFC between endohedral N I and Cu S
ACuN=[0 0 0]; %HFC between endohedral N S and Cu I
ACuCu=[-86 -86 -643]; %HFC between Cu S and Cu I
ALCu=[50 50 50]; %HFC between Cu S and ligand N I
ALN=[0 0 0]; %HFC between endohedral N S and ligand N I
Sys2.A=[ANN,ANCu,;ACuN,ACuCu;ALN,ALCu;ALN,ALCu;ALN,ALCu;ALN,ALCu]; %HFC
Sys2.lwpp = [0. 0.26];
D2=14; %ZFS
Dpv2=[-D2/3*1 -D2/3*1 D2/3*2]; %ZFS tensor
ka2=0;
kb2=83;
ky2=38;
Dpa2=[pi/180*ka2 pi/180*kb2 pi/180*ky2]; %ZFS frame Euler angle
R2=erot(Dpa2);
D2=R2*diag(Dpv2)*R2.';
Sys2.D=[D2;[0,0,0;0,0,0;0,0,0]]; %ZFS tensor rotated
jiso2=0*[1,1,1]; %isotropic part of electron spin coupling (=0,according to solution experiment)
i2=11; %anisotropic part of electron spin coupling (free space dipolar coupling)
Coupling2=jiso2+i2*[1,1,-2]; %electron spin coupling tensor
ja2=0;
jb2=70;
jy2=0;
Dpa2=[pi/180*ja2 pi/180*jb2 pi/180*jy2]; %spin coupling frame Euler angle
R2=erot(Dpa2);
Sys2.ee=R2*diag(Coupling2)*R2.'; %spin coupling rotated
% aggregation condition, ignore CuPc
Sys3.S=3/2;
Sys3.g=2.0024;
Sys3.Nucs='14N';
Sys3.A=15.7;
Sys3.lwpp = 0.13;
Sys3.D=14;
rms=10000000.0;
R=-1;
for R0=1:10
Sys2.weight=100; %normalized weight
Sys3.weight=R0/2; %weight variable
[x,y]=pepper({Sys2,Sys3},Exp);
ratio0= (max(spc)-min(spc))/(max(y)-min(y));
SD=(spc'-y*ratio0).^2;
rms0 = sum(SD);
if rms > rms0
   rms=rms0;
```

```
    yy=y; %best fit
    ratio=ratio0;
    R=R0; %optimal weight 2.5
end
end

subplot(2,1,1); %spectra compare
plot(x,yy*ratio,B,spc);
subplot(2,1,2); %deviation
plot(B,spc'-y*ratio);
%plot [x,y] using origin

%%E-6
clear, clc;
[B,spc]=textread('CuPcPh1N@C60_E-6.txt','%f %f','headerlines',0);
B=B/10;
spc=spc-mean(spc);
Exp.mwFreq = 9.385945;
Exp.Range = [min(B) max(B)];
Exp.ModAmp = 0.05;
Exp.nPoints = 2730;
%No aggregation condition
Sys2.S=[3/2 1/2];
Sys2.g=[2.0024 2.0024,2.0024;2.04,2.04,2.16]; %g tensors for N and Cu spins
Sys2.Nucs='N, Cu, N, N, N, N';
ANN=[15.4 15.4 15.4]; %HFC between endohedral N I and S
ANCu=[0 0 0]; %HFC between endohedral N I and Cu S
ACuN=[0 0 0]; %HFC between endohedral N S and Cu I
ACuCu=[-86 -86 -643]; %HFC between Cu S and Cu I
ALCu=[50 50 50]; %HFC between Cu S and ligand N I
ALN=[0 0 0]; %HFC between endohedral N S and ligand N I
Sys2.A=[ANN,ANCu,;ACuN,ACuCu;ALN,ALCu;ALN,ALCu;ALN,ALCu;ALN,ALCu]; %HFC
Sys2.lwpp = [0. 0.16];
D2=14; %ZFS
Dpv2=[-D2/3*1 -D2/3*1 D2/3*2]; %ZFS tensor
ka2=0;
kb2=83;
ky2=38;
Dpa2=[pi/180*ka2 pi/180*kb2 pi/180*ky2]; %ZFS frame Euler angle
R2=erot(Dpa2);
D2=R2*diag(Dpv2)*R2.';
Sys2.D=[D2;[0,0,0;0,0,0;0,0,0]]; %ZFS tensor rotated
jiso2=0*[1,1,1]; %isotropic part of electron spin coupling (=0,according to solution experiment)
i2=11; %anisotropic part of electron spin coupling (free space dipolar coupling)
Coupling2=jiso2+i2*[1,1,-2]; %electron spin coupling tensor
ja2=0;
jb2=70;
jy2=0;
Dpa2=[pi/180*ja2 pi/180*jb2 pi/180*jy2]; %spin coupling frame Euler angle
R2=erot(Dpa2);
Sys2.ee=R2*diag(Coupling2)*R2.'; %spin coupling rotated
% aggregation condition, ignore CuPc
Sys3.S=3/2;
Sys3.g=2.0024;
Sys3.Nucs='14N';
Sys3.A=15.7;
Sys3.lwpp = 0.13;
Sys3.D=14;
rms=10000000.0;
```

```
R=-1;
for R0=1:10
Sys2.weight=100; %normalized weight
Sys3.weight=R0/2+10; %weight variable
[x,y]=pepper({Sys2,Sys3},Exp);
ratio0= (max(spc)-min(spc))/(max(y)-min(y));
SD=(spc'-y*ratio0).^2;
rms0 = sum(SD);
if rms > rms0
   rms=rms0;
   yy=y; %best fit
   ratio=ratio0;
   R=R0; %optimal weight 12
end
end

subplot(2,1,1); %spectra compare
plot(x,yy*ratio,B,spc);
subplot(2,1,2); %deviation
plot(B,spc'-y*ratio);
%plot [x,y] using origin

%E-5
clear, clc;
[B,spc]=textread('CuPcPh1N@C60_E-5.txt','%f %f','headerlines',0);
B=B/10;
spc=spc-mean(spc);
Exp.mwFreq = 9.385993;
Exp.Range = [min(B) max(B)];
Exp.ModAmp = 0.05;
Exp.nPoints = 2730;
%No aggregation condition
Sys2.S=[3/2 1/2];
Sys2.g=[2.0024 2.0024,2.0024;2.04,2.04,2.16]; %g tensors for N and Cu spins
Sys2.Nucs='N, Cu, N, N, N, N';
ANN=[15.4 15.4 15.4]; %HFC between endohedral N I and S
ANCu=[0 0 0]; %HFC between endohedral N I and Cu S
ACuN=[0 0 0]; %HFC between endohedral N S and Cu I
ACuCu=[-86 -86 -643]; %HFC between Cu S and Cu I
ALCu=[50 50 50]; %HFC between Cu S and ligand N I
ALN=[0 0 0]; %HFC between endohedral N S and ligand N I
Sys2.A=[ANN,ANCu,;ACuN,ACuCu;ALN,ALCu;ALN,ALCu;ALN,ALCu;ALN,ALCu]; %HFC
Sys2.lwpp = [0. 0.13];
D2=14; %ZFS
Dpv2=[-D2/3*1 -D2/3*1 D2/3*2]; %ZFS tensor
ka2=0;
kb2=83;
ky2=38;
Dpa2=[pi/180*ka2 pi/180*kb2 pi/180*ky2]; %ZFS frame Euler angle
R2=erot(Dpa2);
D2=R2*diag(Dpv2)*R2.';
Sys2.D=[D2;[0,0,0;0,0,0;0,0,0]]; %ZFS tensor rotated
jiso2=0*[1,1,1]; %isotropic part of electron spin coupling (=0,according to solution experiment)
i2=11; %anisotropic part of electron spin coupling (free space dipolar coupling)
Coupling2=jiso2+i2*[1,1,-2]; %electron spin coupling tensor
ja2=0;
jb2=70;
jy2=0;
Dpa2=[pi/180*ja2 pi/180*jb2 pi/180*jy2]; %spin coupling frame Euler angle
```

```
R2=erot(Dpa2);
Sys2.ee=R2*diag(Coupling2)*R2.'; %spin coupling rotated
% aggregation condition, ignore CuPc
Sys3.S=3/2;
Sys3.g=2.0024;
Sys3.Nucs='14N';
Sys3.A=15.7;
Sys3.lwpp = 0.13;
Sys3.D=14;
rms=10000000.0;
R=-1;
for R0=1:10
Sys2.weight=100; %normalized weight
Sys3.weight=R0/2+20; %weight variable
[x,y]=pepper({Sys2,Sys3},Exp);
ratio0= (max(spc)-min(spc))/(max(y)-min(y));
SD=(spc'-y*ratio0).^2;
rms0 = sum(SD);
if rms > rms0
   rms=rms0;
   yy=y; %best fit
   ratio=ratio0;
   R=R0; %optimal weight 24
end
end

subplot(2,1,1); %spectra compare
plot(x,yy*ratio,B,spc);
subplot(2,1,2); %deviation
plot(B,spc'-y*ratio);
%plot [x,y] using origin

%E-4
clear, clc;
[B,spc]=textread('CuPcPh1N@C60_E-4.txt','%f %f','headerlines',0);
B=B/10;
spc=spc-mean(spc);
Exp.mwFreq = 9.385989;
Exp.Range = [min(B) max(B)];
Exp.ModAmp = 0.05;
Exp.nPoints = 2730;
%No aggregation condition
Sys2.S=[3/2 1/2];
Sys2.g=[2.0024 2.0024,2.0024;2.04,2.04,2.16]; %g tensors for N and Cu spins
Sys2.Nucs='N, Cu, N, N, N, N';
ANN=[15.4 15.4 15.4]; %HFC between endohedral N I and S
ANCu=[0 0 0]; %HFC between endohedral N I and Cu S
ACuN=[0 0 0]; %HFC between endohedral N S and Cu I
ACuCu=[-86 -86 -643]; %HFC between Cu S and Cu I
ALCu=[50 50 50]; %HFC between Cu S and ligand N I
ALN=[0 0 0]; %HFC between endohedral N S and ligand N I
Sys2.A=[ANN,ANCu,;ACuN,ACuCu;ALN,ALCu;ALN,ALCu;ALN,ALCu;ALN,ALCu]; %HFC
Sys2.lwpp = [0. 0.13];
D2=14; %ZFS
Dpv2=[-D2/3*1 -D2/3*1 D2/3*2]; %ZFS tensor
ka2=0;
kb2=83;
ky2=38;
Dpa2=[pi/180*ka2 pi/180*kb2 pi/180*ky2]; %ZFS frame Euler angle
```

```
R2=erot(Dpa2);
D2=R2*diag(Dpv2)*R2.';
Sys2.D=[D2;[0,0,0;0,0,0;0,0,0]]; %ZFS tensor rotated
jiso2=0*[1,1,1]; %isotropic part of electron spin coupling (=0,according to solution experiment)
i2=11; %anisotropic part of electron spin coupling (free space dipolar coupling)
Coupling2=jiso2+i2*[1,1,-2]; %electron spin coupling tensor
ja2=0;
jb2=70;
jy2=0;
Dpa2=[pi/180*ja2 pi/180*jb2 pi/180*jy2]; %spin coupling frame Euler angle
R2=erot(Dpa2);
Sys2.ee=R2*diag(Coupling2)*R2.'; %spin coupling rotated
% aggregation condition, ignore CuPc
Sys3.S=3/2;
Sys3.g=2.0024;
Sys3.Nucs='14N';
Sys3.A=15.7;
Sys3.lwpp = 0.13;
Sys3.D=14;
rms=10000000.0;
R=-1;
for R0=1:10
Sys2.weight=100; %normalized weight
Sys3.weight=R0+35; %weight variable
[x,y]=pepper({Sys2,Sys3},Exp);
ratio0= (max(spc)-min(spc))/(max(y)-min(y));
SD=(spc'-y*ratio0).^2;
rms0 = sum(SD);
if rms > rms0
   rms=rms0;
   yy=y; %best fit
   ratio=ratio0;
   R=R0; %optimal weight 40
end
end

subplot(2,1,1); %spectra compare
plot(x,yy*ratio,B,spc);
subplot(2,1,2); %deviation
plot(B,spc'-y*ratio);
%plot [x,y] using origin


%E-3
clear, clc;
[B,spc]=textread('CuPcPh1N@C60_E-3.txt','%f %f','headerlines',0);
B=B/10;
spc=spc-mean(spc);
Exp.mwFreq = 9.385975;
Exp.Range = [min(B) max(B)];
Exp.ModAmp = 0.05;
Exp.nPoints = 2730;
%No aggregation condition
Sys2.S=[3/2 1/2];
Sys2.g=[2.0024 2.0024,2.0024;2.04,2.04,2.16]; %g tensors for N and Cu spins
Sys2.Nucs='N, Cu, N, N, N, N';
ANN=[15.4 15.4 15.4]; %HFC between endohedral N I and S
ANCu=[0 0 0]; %HFC between endohedral N I and Cu S
ACuN=[0 0 0]; %HFC between endohedral N S and Cu I
```

```
ACuCu=[-86 -86 -643]; %HFC between Cu S and Cu I
ALCu=[50 50 50]; %HFC between Cu S and ligand N I
ALN=[0 0 0]; %HFC between endohedral N S and ligand N I
Sys2.A=[ANN,ANCu,;ACuN,ACuCu;ALN,ALCu;ALN,ALCu;ALN,ALCu;ALN,ALCu]; %HFC
Sys2.lwpp = [0. 0.13];
D2=14; %ZFS
Dpv2=[-D2/3*1 -D2/3*1 D2/3*2]; %ZFS tensor
ka2=0;
kb2=83;
ky2=38;
Dpa2=[pi/180*ka2 pi/180*kb2 pi/180*ky2]; %ZFS frame Euler angle
R2=erot(Dpa2);
D2=R2*diag(Dpv2)*R2.';
Sys2.D=[D2;[0,0,0;0,0,0;0,0,0]]; %ZFS tensor rotated
jiso2=0*[1,1,1]; %isotropic part of electron spin coupling (=0,according to solution experiment)
i2=11; %anisotropic part of electron spin coupling (free space dipolar coupling)
Coupling2=jiso2+i2*[1,1,-2]; %electron spin coupling tensor
ja2=0;
jb2=70;
jy2=0;
Dpa2=[pi/180*ja2 pi/180*jb2 pi/180*jy2]; %spin coupling frame Euler angle
R2=erot(Dpa2);
Sys2.ee=R2*diag(Coupling2)*R2.'; %spin coupling rotated
% aggregation condition, ignore CuPc
Sys3.S=3/2;
Sys3.g=2.0024;
Sys3.Nucs='14N';
Sys3.A=15.7;
Sys3.lwpp = 0.13;
Sys3.D=14;
rms=10000000.0;
R=-1;
for R0=1:10
Sys2.weight=100; %normalized weight
Sys3.weight=R0+65; %weight variable
[x,y]=pepper({Sys2,Sys3},Exp);
ratio0= (max(spc)-min(spc))/(max(y)-min(y));
SD=(spc'-y*ratio0).^2;
rms0 = sum(SD);
if rms > rms0
   rms=rms0;
   yy=y; %best fit
   ratio=ratio0;
   R=R0; %optimal weight 70
end
end

subplot(2,1,1); %spectra compare
plot(x,yy*ratio,B,spc);
subplot(2,1,2); %deviation
plot(B,spc'-y*ratio);
%plot [x,y] using origin
```

Appendix C. References

(1) Harneit, W. *Phys. Rev. A* **2002**, *65*, 032322.

(2) Wesenberg, J.; Ardavan, A.; Briggs, G.; et al. *Phys. Rev. Lett.* **2009**, *103*, 070502.

(3) Morton, J. J. L.; Tyryshkin, A. M.; Ardavan, A.; et al. *Nat. Phys.* **2006**, *2*, 40.

(4) Benjamin, S. C.; Ardavan, A. *J. Phys. Condens. Matter* **2006**, *18*, S867.

(5) Harneit, W.; Huebener, K.; Naydenov, B.; et al. *Phys. Status Solidi* **2007**, *244*, 3879.

(6) DiVincenzo, D. *Fortschr. Phys.* **2000**, *48*, 771.

(7) Cirac, J. I.; Zoller, P. *Phys. Rev. Lett.* **1995**, *74*, 4091.

(8) Kielpinski, D.; Monroe, C.; Wineland, D. J. *Nature* **2002**, *417*, 709.

(9) Lekitsch, B.; Weidt, S.; Fowler, A. G.; et al. *Sci. Adv.* **2017**, *3*, e1601540.

(10) Tan, K. Y.; Partanen, M.; Lake, R. E.; et al. *Nat. Commun.* **2017**, *8*, 15189.

(11) Devoret, M. H.; Schoelkopf, R. J. *Science* **2013**, *339*, 1169.

(12) Knill, E. *Nature* **2010**, *463*, 441.

(13) Xu, K.; Xie, T.; Li, Z.; et al. *Phys. Rev. Lett*. **2017**, *118*, 130504

(14) Pingault, B.; Jarausch, D.-D.; Hepp, C.; et al. *Nat. Commun.* **2017**, *8*, 15579.

(15) Kroto, H. W.; Heath, J. R.; O'Brien, S. C.; et al. *Nature* **1985**, *318*, 162.

(16) Raghavachari, K.; Rohlfing, C. M. *J. Phys. Chem.* **1992**, *96*, 2463.

(17) Hirsch, A.; Brettreich, M. Fullerenes; Wiley-VCH Verlag GmbH & Co. KGaA, **2004**.

(18) Bochev, D.; Rouvray, D. H. Chemical topology: Introduction and fundamentals; Gordon and Breach Science Publishers, **1999**.

(19) Liu, S.; Lu, Y.; Kappes, M. M.; et al. *Science* **1991**, *254*, 408.

(20) Yamada, M.; Kurihara, H.; Suzuki, M.; et al. *J. Am. Chem. Soc.* **2015**, *137*, 232.

(21) Lu, X.; Feng, L.; Akasaka, T.; et al. *Chem. Soc. Rev.* **2012**, *41*, 7649.

(22) Wang, T.; Wu, J.; Xu, W.; et al. *Angew. Chemie Int. Ed.* **2010**, *49*, 1786.

(23) Hashikawa, Y.; Murata, M.; Wakamiya, A.; et al. *J. Am. Chem. Soc.* **2016**, *138*, 4096.

(24) Popov, A. A.; Pykhova, A. D.; Ioffe, I. N.; et al. *J. Am. Chem. Soc.* **2014**, *136*, 13536.

(25) Wei, T.; Wang, S.; Lu, X.; et al. *J. Am. Chem. Soc.* **2016**, *138*, 207.

(26) Popov, A. A.; Yang, S.; Dunsch, L. *Chem. Rev.* **2013**, *113*, 5989.

(27) Guilbault, G. G. Practical Fluorescence, 2nd ed.; Marcel Dekker, Inc. **1973**.

(28) Grose, J. E.; Tam, E. S.; Timm, C.; et al. *Nat. Mater.* **2008**, *7*, 884.

(29) Brown, R. M.; Tyryshkin, A. M.; Porfyrakis, K.; et al. *Phys. Rev. Lett.* **2011**, *106*, 110504.

(30) Maroto, E. E.; Mateos, J.; Garcia-Borràs, M.; et al. *J. Am. Chem. Soc.* **2015**, *137*, 1190.

(31) Takata, M.; Umeda, B.; Nishibori, E.; et al. *Nature* **1995**, *377*, 46.

(32) Yamada, M.; Kurihara, H.; Suzuki, M.; et al. *J. Am. Chem. Soc.* **2014**, *136*, 7611.

(33) Stevenson, S.; Lee, H. M.; Olmstead, M. M.; et al. *Chem. - A Eur. J.* **2002**, *8*, 4528.

(34) Wang, C.; Kai, T.; Tomiyama, T.; et al. *Angew. Chemie - Int. Ed.* **2001**, *40*, 397.

(35) Krachmalnicoff, A.; Bounds, R.; Mamone, S.; et al. *Nat. Chem.* **2016**, *8*, 953.

(36) Saunders, M.; Jiménez-Vázquez, H. A.; Cross, R. J.; et al. *Nature* **1994**, *367*, 256.

(37) Morinaka, Y.; Sato, S.; Wakamiya, A.; et al. *Nat. Commun.* **2013**, *4*, 1554.

(38) Murphy, T. A.; Pawlik, T.; Weidinger, A.; et al. *Phys. Rev. Lett.* **1996**, *77*, 1075.

(39) Knapp, C.; Weiden, N.; Kass, H.; et al. *Mol. Phys.* **1998**, *95*, 999.

(40) Parker, D. H.; Wurz, P.; Chatterjee, K.; et al. *J. Am. Chem. Soc.* **1991**, *113*, 7499.

(41) Brown, R. M.; Ito, Y.; Warner, J. H.; et al. *Phys. Rev. B* **2010**, *82*, 033410.

(42) Haddon, R. C. *Science* **1993**, *261*, 1545.

(43) Jakes, P.; Dinse, K. P.; Meyer, C.; et al. *Phys. Chem. Chem. Phys.* **2003**, *5*, 4080.

(44) Kanai, M.; Porfyrakis, K.; Briggs, G. A. D.; et al. *Chem. Commun.* **2004**, *0*, 210.

(45) Mauser, H.; van Eikema Hommes, N. J. R.; Clark, T.; et al. *Angew. Chemie Int. Ed.* **1997**, *36*, 2835.

(46) Plakhutin, B. N.; Breslavskaya, N. N.; Gorelik, E. V.; et al. *J. Mol. Struct. THEOCHEM* **2005**, *727*, 149.

(47) Lu, X.; Chen, Z. *Chem. Rev.* **2005**, *105*, 3643.

(48) Morton, J. J. L.; Tyryshkin, A. M.; Ardavan, A.; et al. *J. Chem. Phys.* **2005**, *122*, 174504.

(49) Morton, J. J. L.; Tyryshkin, A. M.; Ardavan, A.; et al. *J. Chem. Phys.* **2006**, *124*, 014508.

(50) Morton, J. J. L.; Tyryshkin, A. M.; Ardavan, A.; et al. *Phys. Rev. B* **2007**, *76*, 085418.

(51) Weil, J. A.; Bolton, J. R. Electron paramagnetic resonance: elementary theory and practical applications, 2nd ed.; John Wiley & Sons, Inc. **2007**.

(52) Schweiger, A.; Jeschke, G. Principles of Pulse Electron Paramagnetic Resonance; Oxford University Press, **2001**.

(53) Brown, R. M. Coherent transfer between electron and nuclear spin qubits and their decoherence properties, Oxford University, **2011**.

(54) Zadrozny, J. M.; Niklas, J.; Poluektov, O. G.; et al. *ACS Cent. Sci.* **2015**, *1*, 488.

(55) Knapp, C.; Dinse, K. P.; Pietzak, B.; et al. *Chem. Phys. Lett.* **1997**, *272*, 433.

(56) Warner, M.; Din, S.; Tupitsyn, I. S.; et al. *Nature* **2013**, *503*, 504.

(57) Ardavan, A.; Rival, O.; Morton, J. J. L.; et al. *Phys. Rev. Lett.* **2007**, *98*, 057201.

(58) Wedge, C. J.; Timco, G. A.; Spielberg, E. T.; et al. *Phys. Rev. Lett*. **2012**, *108*, 107204.

(59) Tyryshkin, A. M.; Tojo, S.; Morton, J. J. L.; et al. *Nat. Mater*. **2011**, *11*, 143.

(60) Morley, G. W.; Warner, M.; Stoneham, A. M.; et al. *Nat. Mater*. **2010**, *9*, 725.

(61) Takahashi, S.; Hanson, R.; Van Tol, J.; et al. *Phys. Rev. Lett*. **2008**, *101* (4), 047601.

(62) Balasubramanian, G.; Neumann, P.; Twitchen, D.; et al. *Nat. Mater.* **2009**, *8*, 383.

(63) Koehl, W. F.; Buckley, B. B.; Heremans, F. J.; et al. *Nature* **2011**, *479*, 84.

(64) Moore, G. E. *Proc. IEEE* **1965**, *86*, 82.

(65) Beiglbock, W.; Ehlers, J.; Hepp, K.; et al. Theoretical foundations of quantum information processing and communication; Springer, **2010**.

(66) Awschalom, D. D.; Bassett, L. C.; Dzurak, A. S.; et al. *Science* **2013**, *339*, 1174.

(67) Simmons, S.; Brown, R. M.; Riemann, H.; et al. *Nature* **2011**, *470*, 69.

(68) Dolde, F.; Jakobi, I.; Naydenov, B.; et al. *Nat. Phys.* **2013**, 9, 139.

(69) Rivest, R.; Shamir, A.; Adleman, L. *Commun. ACM* **1978**, 21, 120.

(70) Shor, P. W. In Proceedings of 35th Annual Symposium on Foundations of Computer Science (Shafi Goldwasser, ed.), IEEE Computer Society Press; **1994**, 124.

(71) Ferry, D. K. *Science* **2012**, *335*, 45.

(72) Vandersypen, L. M. K.; Steffen, M.; Breyta, G.; et al. *Nature* **2001**, *414*, 883.

(73) Xu, N.; Zhu, J.; Lu, D.; et al. *Phys. Rev. Lett.* **2012**, *108*, 130501.

(74) Warren, W. S.; Gershenfeld, N.; Chuang, I. *Science* **1997**, *277*, 1688.

(75) Moro, F.; Kaminski, D.; Tuna, F.; et al. *Chem. Commun.* **2014**, *50*, 91.

(76) Twamley, J. *Phys. Rev. A* **2003**, *67*, 052318.

(77) Plant, S. R.; Jevric, M.; Morton, J. J. L.; et al. *Chem. Sci.* **2013**, *4*, 2971.

(78) Zhang, J.; Porfyrakis, K.; Morton, J. J. L.; et al. *J. Phys. Chem. C* **2008**, *112*, 2802.

(79) Farrington, B. J.; Jevric, M.; Rance, G. A.; et al. *Angew. Chemie Int. Ed.* **2012**, *51*, 3587.

(80) Smith, B.; Monthioux, M.; Luzzi, D. *Nature* **1998**, *396*, 323.

(81) Simon, F.; Kuzmany, H.; Rauf, H.; et al. *Chem. Phys. Lett.* **2004**, *383*, 362.

(82) Khlobystov, A. N.; Britz, D. A.; Wang, J.; et al. *J. Mater. Chem.* **2004**, *14*, 2852.

(83) Deak, D. S.; Porfyrakis, K.; Castell, M. R. *Chem. Commun*. **2007**, *0*, 2941.

(84) Gimenez-Lopez, M. del C.; Gardener, J. A.; Shaw, A. Q.; et al. *Phys. Chem. Chem. Phys.* **2010**, *12*, 123.

(85) Diaconescu, B.; Yang, T.; Berber, S.; et al. *Phys. Rev. Lett.* **2009**, *102*, 056102.

(86) Deak, D. S.; Silly, F.; Porfyrakis, K.; et al. *J. Am. Chem. Soc.* **2006**, *128*, 13976.

(87) Silly, F.; Shaw, A. Q.; Porfyrakis, K.; et al. *Appl. Phys. Lett.* **2007**, *91*, 253109.

(88) Wei, Y.; Reutt-Robey, J. E. *J. Am. Chem. Soc.* **2011**, *133*, 15232.

(89) Raisanen, M. T.; Slater, A. G.; Champness, N. R.; et al. *Chem. Sci.* **2012**, *3*, 84.

(90) Garelli, M. S.; Kusmartsev, F. V. *Eur. Phys. J. B* **2005**, *48*, 199.

(91) Morton, J. J. L.; Tyryshkin, A. M.; Ardavan, A.; et al. *Phys. Rev. Lett.* **2005**, *95*, 200501.

(92) Suter, D.; Lim, K. *Phys. Rev. A* **2002**, *65*, 052309.

(93) Yang, W. L.; Xu, Z. Y.; Wei, H.; et al. *Phys. Rev. A* **2010**, *81*, 032303.

(94) Meyer, C.; Harneit, W. *Phys. Status Solidi* **2002**, *466*, 462.

(95) Baumann, S.; Paul, W.; Choi, T.; et al. *Science* **2015**, *350*, 417.

(96) Farrington, B. J. A Tale of Two Spins: Electron Spin Centre Assemblies with N@C_{60} for use in QIP, Oxford University, **2013**.

(97) Pietzak, B.; Waiblinger, M.; Murphy, T. A.; et al. *Chem. Phys. Lett.* **1997**, *4*, 259.

(98) Cho, S. C.; Kaneko, T.; Ishida, H.; et al. *J. Appl. Phys.* **2015**, *117*, 123301.

(99) Ito, S.; Shimotani, H.; Takagi, H.; et al. *Fullerenes, Nanotub. Carbon Nanostructures* **2008**, *16*, 206.

(100) Huang, H.; Ata, M.; Ramm, M. *Chem. Commun.* **2002**, *0*, 2076.

(101) Ata, M.; Huang, H.; Akasaka, T. *J. Phys. Chem. B* **2004**, *108*, 4640.

(102) Kaneko, T.; Abe, S.; Ishida, H.; et al. *Phys. Plasmas* **2007**, *14*, 110705.

(103) Miyanaga, S.; Kaneko, T.; Ishida, H.; et al. *Thin Solid Films* **2010**, *518*, 3509.

(104) Cho, S. C.; Kaneko, T.; Ishida, H.; et al. *Appl. Phys. Express* **2012**, *5*, 026202.

(105) Hawkins, J. M.; Lewis, T. A.; Loren, S. D.; et al. *J. Org. Chem.* **1990**, *55*, 6250.

(106) Gasper, M. P.; Armstrong, D. W. J. *Liq. Chromatogr.* **1995**, *18*, 1047.

(107) Liu, X.; Zuo, T.; Dorn, H. C. *J. Phys. Chem. C* **2017**, *121*, 4045.

(108) Plant, S. R.; Porfyrakis, K. *Analyst* **2014**, *139*, 4519.

(109) Wakahara, T.; Matsunaga, Y.; Katayama, A.; et al. *Chem. Commun.* **2003**, *0*, 2940.

(110) Weidinger, A.; Waiblinger, M.; Pietzak, B.; et al. *Appl. Phys. A Mater. Sci. Process.* **1998**, *66*, 287.

(111) Suetsuna, T.; Dragoe, N.; Harneit, W.; et al. *Chem. - A Eur. J.* **2002**, *8*, 5079.

(112) Maggini, M.; Scorrano, G.; Prato, M. *J. Am. Chem. Soc.* **1993**, *115*, 9798.

(113) Kavitha, K.; Venuvanalingam, P. *J. Org. Chem.* **2005**, *70*, 5426.

(114) Zhou, Z.; Magriotis, P. A. *Org. Lett.* **2005**, *7*, 5849.

(115) Schick, G.; Levitus, M.; Kvetko, L.; et al. *J. Am. Chem. Soc.* **1999**, *121*, 3246.

(116) Levitus, M.; Schick, G.; Lunkwitz, R.; et al. *J. Photochem. Photobiol. A Chem.* **1999**, *127*, 13.

(117) D'Souza, F.; Zandler, M. E.; Deviprasad, G. R.; et al. *J. Phys. Chem. A* **2000**, *104*, 6887.

(118) Bagno, A.; Claeson, S.; Maggini, M.; et al. *Chem. - A Eur. J.* **2002**, *8*, 1015.

(119) Belik, P.; Gügel, A.; Spickermann, J.; et al. *Angew. Chemie Int. Ed.* **1993**, *32*, 78.

(120) Krautler, B.; Maynollo, J. *Tetrahedron* **1996**, *52*, 5033.

(121) Diekers, M.; Hirsch, A.; Pyo, S.; et al. *European J. Org. Chem.* **1998**, *1998*, 1111.

(122) Bingel, C. *Chem. Ber.* **1993**, *126*, 1957.

(123) Anderson, H. L.; Faust, R.; Rubin, Y.; et al. *Angew. Chemie Int. Ed.* **1994**, *33*, 1366.

(124) Gao, X.; Ishimura, K.; Nagase, S.; et al. *J. Phys. Chem. A* **2009**, *113*, 3673.

(125) Nierengarten, J.; Gramlich, V. *Angew. Chemie* **1996**, *108*, 2242.

(126) Nierengarten, J. F.; Nicoud, J. F. *Tetrahedron Lett.* **1997**, *38*, 7737.

(127) Chronakis, N.; Hartnagel, U.; Braun, M.; et al. *Chem. Commun.* **2007**, *0*, 607.

(128) Camps, X.; Hirsch, A. *J. Chem. Soc. Perkin Trans. 1* **1997**, *97*, 1595.

(129) Hino, T.; Kinbara, K.; Saigo, K. *Tetrahedron Lett.* **2001**, *42*, 5065.

(130) Wasserthal, L. K.; Kratzer, A.; Hirsch, *A. European J. Org. Chem.* **2013***, 2013*, 2355.

(131) Kessinger, R.; Crassous, J.; Herrmann, A.; et al. *Angew. Chemie Int. Ed.* **1998***, 37*, 1919.

(132) Lamparth, I.; Maichle-Mossmer, C.; Hirsch, A. *Angew. Chemie Int. Ed.* **1995**, *34*, 1607.

(133) Hirsch, A.; Lamparth, I.; Karfunkel, H. R. *Angew. Chemie Int. Ed.* **1994**, *33*, 437.

(134) Reuther, U.; Brandm, T.; Donaubauer, W.; et al. *Chem. - A Eur. J.* **2002***, 8*, 2261.

(135) Thilgen, C.; Herrmann, A.; Diederich, F. *Angew. Chemie Int. Ed.* **1997**, *36*, 2268.

(136) Komatsu, K.; Murata, Y.; Takimoto, N. *J. Org. Chem.* **1994**, *59*, 6101.

(137) Fagan, P. J.; Krusic, P. J.; Evans, D. H. *J. Am. Chem. Soc.* **1992**, *114*, 9697.

(138) Champeil, E.; Crean, C.; Larraya, C.; et al. *Tetrahedron* **2008**, *64*, 10319.

(139) Diederich, F.; Thilgen, C. *Science* **1996**, *271*, 317.

(140) Skiebe, A.; Hirsch, A.; Klos, H.; et al. *Chem. Phys. Lett.* **1994**, *220*, 138.

(141) Hirsch, A. *J. Phys. Chem. Solids* **1997**, *58*, 1729.

(142) Franco, L.; Ceola, S.; Corvaja, C.; et al. *Chem. Phys. Lett.* **2006**, *422*, 100.

(143) Zhang, J.; Morton, J. J. L.; Sambrook, M. R.; et al. *Chem. Phys. Lett.* **2006**, *432*, 523.

(144) Liu, G.; Khlobystov, A. N.; Ardavan, A.; et al. *Chem. Phys. Lett.* **2011**, *508*, 187.

(145) Goedde, B.; Waiblinger, M.; Jakes, P.; et al. *Chem. Phys. Lett.* **2001**, *334*, 12.

(146) Jones, M. A. G.; Britz, D. A.; Morton, J. J. L.; et al. *Phys. Chem. Chem. Phys.* **2006**, *8*, 2083.

(147) Dietel, E.; Hirsch, A.; Pietzak, B. *J. Am. Chem. Soc.* **1999**, *121*, 2432.

(148) Lips, K.; Waiblinger, M.; Pietzak, B.; et al. *Phys. Status Solidi* **2000**, *177*, 81.

(149) Waiblinger, M.; Lips, K.; Harneit, W.; et al. *Phys. Rev. B* **2001**, *64*, 159901.

(150) Hörmann, F.; Hirsch, A.; Porfyrakis, K.; et al. *European J. Org. Chem.* **2011**, *2011*, 117.

(151) Wakahara, T.; Kato, T.; Miyazawa, K.; et al. *Carbon* **2012**, *50*, 1709.

(152) Komatsu, K.; Wang, G. W.; Murata, Y.; et al. *J. Org. Chem.* **1998**, *63*, 9358.

(153) Zhang, J.; Porfyrakis, K.; Sambrook, M. R.; et al. *J. Phys. Chem. B* **2006**, *110*, 16979.

(154) Radford, H. E.; Evenson, K. M. *Phys. Rev.* **1968**, *168*, 70.

(155) Naydenov, B.; Spudat, C.; Harneit, W.; et al. *Chem. Phys. Lett.* **2006**, *424*, 327.

(156) Yang, J.; Feng, P.; Sygula, A.; et al. *Phys. Lett. A* **2012**, *376*, 1748.

(157) Suzuki, A.; Oku, T. In Electronic Properties of Carbon Nanotubes; Marulanda, J. M., Ed.; InTech, **2011**.

(158) Rice, W. D.; Weber, R. T.; Leonard, A. D.; et al. *ACS Nano* **2012**, *6*, 2165.

(159) Watt, A. A. R.; Sambrook, M. R.; Porfyrakis, K.; et al. *Chem. Commun.* **2006**, *0*, 1944.

(160) Komatsu, K.; Wang, G.-W.; Murata, Y.; et al. *Nature* **1997**, *387*, 583.

(161) Lee, K.; Song, H.; Kim, B.; et al. *J. Am. Chem. Soc.* **2002**, *124*, 2872.

(162) Konarev, D. V.; Troyanov, S. I.; Yoshiaki, N.; et al. *Organometallics* **2013***, 32,* 4038.

(163) Timmerman, P.; Anderson, H. L.; Faust, R.; et al. *Tetrahedron* **1996**, *52*, 4925.

(164) Suzuki, T.; Li, Q.; Khemani, K. C.; et al. *J. Am. Chem. Soc.* **1992**, *114*, 7300.

(165) Lucas, A. I. de; Martin, N.; Sfinchez, L.; et al. *Tetrahedron Lett*. **1996**, *37*, 9391.

(166) Liu, S.; Kreher, D.; Delaunay, J.; et al. *Tetrahedron Lett*. **2001**, 42, 3717.

(167) Dresselhaus, G.; Dresselhaus, M. S.; Eklund, P. C. *Phys. Rev. B* **1992**, *45*, 6923.

(168) Pichler, T.; Haluska, M.; Winter, J.; et al. *Fuller. Sci. Technol.* **1996**, *4*, 227.

(169) Bussolotti, F.; Yang, J.; Hiramoto, M.; et al. *Phys. Rev. B* **2015**, *92*, 115102.

(170) Fischer, J. E.; Heiney, P. A.; McGhie, A. R.; et al. *Science* **1991**, *252*, 1288.

(171) David, W. I. F.; Ibberson, R. M.; Dennis, T. J. S.; et al. *Europhys. Lett.* **1992**, *18*, 219.

(172) Kraft, A.; Gsänger, M.; Beuerle, F. *European J. Org. Chem.* **2014**, *2014*, 523.

(173) Crane, J. D.; Hitchcock, P. B.; Kroto, H. W. *J. Chem. Soc., Chem. Commun.* **1992**, 24, 1764.

(174) Maki, S.; Nishibori, E.; Kitamura, Y.; et al. *Cryst. Growth Des*. **2013**, *13*, 3632.

(175) Zhu, Q.; Cox, D.; Fischer, J.; et al. *Nature* **1992**, *355*, 712.

(176) Pekker, S.; Kováts, E.; Oszlányi, G.; et al. *Nat. Mater.* **2005**, *4*, 764.

(177) Hunter, C. A.; Sanders, J. K. M. *J. Am. Chem. Soc.* **1990**, *112*, 5525.

(178) Pekker, S.; Kováts, E.; Oszlányi, G.; et al. *Phys. Status Solidi* **2006**, *243*, 3032.

(179) Bortel, G.; Faigel, G.; Kováts, E.; et al. *Phys. Status Solidi* **2006**, *243*, 2999.

(180) Zólyomi, V.; Koltai, J.; Kürti, J.; et al. *Phys. Rev. B* **2008**, *78*, 115405.

(181) Olmstead, M. M.; de Bettencourt-Dias, A.; Duchamp, J. C.; et al. *J. Am. Chem. Soc.* **2000**, *122*, 12220.

(182) Chen, C.; Zhu, Y.; Fan, Q.; et al. *Tetrahedron Lett.* **2013**, *54*, 4143.

(183) Konarev, D. V.; Khasanov, S. S.; Otsuka, A.; et al. *J. Am. Chem. Soc.* **2002**, *124*, 8520.

(184) Bisoyi, H. K.; Kumar, S. *Chem. Soc. Rev.* **2011**, *40*, 306.

(185) Maeda, K.; Henbest, K. B.; Cintolesi, F.; et al. *Nature* **2008**, *453*, 387.

(186) Lagerwall, J.; Scalia, G.; Haluska, M.; et al. *Adv. Mater.* **2007**, *19*, 359.

(187) Liu, Q.; Yuan, Y.; Smalyukh, I. I. *Nano Lett.* **2014**, *14*, 4071.

(188) Bortolus, M.; Ferrarini, A.; van Tol, J.; et al. *J. Phys. Chem. B* **2006**, *110*, 3220.

(189) Gopee, H.; Cammidge, A. N.; Oganesyan, V. S. *Angew. Chemie Int. Ed.* **2013**, *125*, 9085.

(190) Yankova, T. S.; Chumakova, N. A.; Pomogailo, D. A.; et al. *Liq. Cryst.* **2013**, *40*, 1135.

(191) Polnaszek, C. F.; Freed, J. H. *J. Phys. Chem.* **1977**, *81*, 449.

(192) Jakes, P.; Weiden, N.; Eichel, R. A.; et al. *J. Magn. Reson.* **2002**, *156*, 303.

(193) Meyer, C.; Harneit, W.; Lips, K.; et al. *Phys. Rev. A* **2002**, *65*, 61201.

(194) Pietzak, B.; A. Weidinger; Dinse, K.-P.; et al. Endofullerenes: A New Family of Carbon Clusters; Akasaka, T., Nagase, S., Eds.; Springer, **2002**.

(195) Liu, G.; Gimenez-Lopez, M. del C.; Jevric, M.; et al. *J. Phys. Chem. B* **2013**, *117*, 5925.

(196) Mazzoni, M.; Franco, L.; Ferrarini, A.; et al. *Liq. Cryst.* **2002**, *29*, 203.

(197) Nakazawa, S.; Nishida, S.; Ise, T.; et al. *Angew. Chemie - Int. Ed.* **2012**, *51*, 9860.

(198) Liu, G.; Khlobystov, A. N.; Charalambidis, G.; et al. *J. Am. Chem. Soc.* **2012**, *134*, 1938.

(199) Wu, B.; Wang, T.; Feng, Y.; et al. *Nat. Commun.* **2015**, *6*, 6468.

(200) Ardavan, A.; Bowen, A. M.; Fernandez, A.; et al. *npj Quantum Inf.* **2015**, *1*, 15012.

(201) Kulik, L. V.; Dzuba, S. A.; Grigoryev, I. A.; et al. *Chem. Phys. Lett.* **2001**, *343*, 315.

(202) Boulon, M. E.; Fernandez, A.; Moreno Pineda, E.; et al. *Angew. Chemie - Int. Ed.* **2017**, *56*, 3876.

(203) Hare, J. P.; Kroto, H. W.; Taylor, R. *Chem. Phys. Lett.* **1991**, *177*, 394.

(204) Weiss, H.; Ahlrichs, R.; Häser, M. *J. Chem. Phys.* **1993**, *99*, 1262.

(205) Negri, F.; Orlandi, G.; Zerbetto, F. *J. Chem. Phys*. **1992**, *97*, 6496.

(206) Scientific Instrument Services, Inc. http://www.sisweb.com/mstools/isotope.htm.

(207) Eaton, G. R.; Eaton, S. S.; Barr, D. P.; et al. Quantitative EPR; SpringerWienNewYork, **2010**.

(208) Inakuma, M.; Shinohara, H. *J. Phys. Chem. B* **2000**, *104*, 7595.

(209) Stoll, S.; Schweiger, A. *J. Magn. Reson.* **2006**, *178*, 42.

(210) Harris, R. K.; Becker, E. D.; Menezes, S. M. C. D; et al. *Pure Appl. Chem.* **2001**, *73*, 1795.

(211) ChemDraw http://www.cambridgesoft.com/software/overview.aspx.

(212) Nakaya, M.; Nakayama, T.; Aono, M. *Thin Solid Films* **2004**, *464–465*, 327.

(213) Eckardt, M.; Wieczorek, R.; Harneit, W. *Carbon* **2015**, *95*, 601.

(214) Glueckauf, B. Y. E. *Trans. Faraday Soc.* **1955**, *51*, 34.

(215) Goedde, B.; Jakes, P.; Waiblinger, M.; et al. *Fuller. Sci. Technol.* **2001**, *9*, 329.

(216) Turanov, A. N.; Kremenskaya, I. N. *Russ. Chem. Bull.* **1995**, *44*, 465.

(217) R. S. Ruoff Doris S. Tse, R. M.; Lorents, D. C. *J. Phys. Chem.* **1993**, *97*, 3379.

(218) Bosque, R.; Sales, J. *J. Chem. Inf. Comput. Sci.* **2002**, *42*, 1154.

(219) Sabirov, D. S. *RSC Adv.* **2014**, *4*, 44996.

(220) Liu, G. Functionalization of endohedral fullerenes and their application in Quantum Information Processing, University of Oxford, **2011**.

(221) Prato, M.; Maggini, M. *Acc. Chem. Res.* **1998**, *31*, 519.

(222) Bensasson, R. V.; Bienvenüe, E.; Fabre, C.; et al. *Chem. - A Eur. J.* **1998**, *4*, 270.

(223) Isaacs, L.; Wehrsig, A.; Diederich, F. *Helv. Chim. Acta* **1993**, *76*, 1231.

(224) Arias, F.; Echegoyen, L.; Wilson, S. R.; et al. *J. Am. Chem. Soc.* **1995**, *117*, 1422.

(225) Diederich, F.; Isaacs, L.; Philp, D. *Chem. Soc. Rev.* **1994**, *23*, 243.

(226) Hörmann, F.; Hirsch, *A. Chem. - A Eur. J.* **2013**, *19*, 3188.

(227) Liu, G.; Khlobystov, A. N.; Briggs, G. A. D.; et al. *Chem. Commun.* **2012**, *48*, 5148.

(228) Kukolich, S. G.; Huffman, D. R. *Chem. Phys. Lett.* **1991**, *182*, 263.

(229) Paul, P.; Bolskar, R. D.; Clark, A. M.; et al. *Chem. Commun.* **2000**, *0*, 1229.

(230) Paul, P.; Kim, K.-C.; Sun, D.; et al. *J. Am. Chem. Soc.* **2002**, *124*, 4394.

(231) Chronakis, N.; Hirsch, A. *Chem. Commun.* **2005**, *0*, 3709.

(232) Beulen, M. W. J.; Echegoyen, L.; Rivera, J. A.; et al. *Chem. Commun.* **2000**, *0*, 917.

(233) Louvis, A. da R.; Silva, N. A. A.; Semaan, F. S.; et al. *New J. Chem.* **2016**, *40*, 7643.

(234) Nikawa, H.; Araki, Y.; Slanina, Z.; et al. *Chem. Commun.* **2010**, *46*, 631.

(235) Palewska, K.; Sworakowski*, J. J. Phys. Chem.* **1993**, *97*, 12167.

(236) Djojo, F.; Herzog, A.; Lamparth, I.; et al. *Chem. - A Eur. J.* **1996**, *2*, 1537.

(237) Samal, S.; Geckeler, K. E. *Chem. Commun.* **2000**, *0*, 1101.

(238) Liu, Y.; Zhao, Y. L.; Chen, Y.; et al. *Tetrahedron Lett.* **2005**, *46*, 2507.

(239) Semenov, K. N.; Charykov, N. A.; Keskinov, V. N. *J. Chem. Eng. Data* **2011**, *56*, 230.

(240) Zhang, G.; Liu, Y.; Liang, D.; et al. *Angew. Chemie - Int. Ed.* **2010**, *49*, 5293.

(241) Zhou, S.; Yamamoto, M.; Briggs, G. A. D.; et al. *J. Am. Chem. Soc.* **2016**, *138*, 1313.

(242) Borrill, H. Synthesis of N@C_{60} derivatives for quantum information proessing, Oxford University, **2014**.

(243) Tsuge, O.; Kanemasa, S.; Ohe, M.; et al. *Bull. Chem. Soc. Jpn.* **1987**, *60*, 4079.

(244) Hirsch, A.; Li, Q.; Wudl, F. *Angew. Chemie Int. Ed. Eng.* **1991**, *30*, 1309.

(245) Kanibolotsky, A. L.; Perepichka, I. F.; Skabara, P. *J. Chem. Soc. Rev.* **2010**, *39*, 2695.

(246) Segre, U.; Pasimeni, L.; Ruzzi, M. *Spectrochim. Acta - Part A Mol. Biomol. Spectrosc.* **2000**, *56*, 265.

(247) Franco, L.; Toffoletti, A.; Maggini, M. *Phys. Chem. Chem. Phys.* **2012**, *14*, 14358.

(248) Gennes, P. G. de; Prost, J. The Physics of Liquid Crystals, 2nd ed.; Oxford University Press, **1995**.

(249) Jen, S.; Clark, N. A.; Pershan, P. S.; et al. *J. Chem. Phys.* **1977**, *66*, 4635.

(250) DuPre, D. B.; Chapoy, L. L. *J. Chem. Educ.* **1979**, *56*, 759.

(251) Antharjanam, P. K. S.; Prasad, E. *New J. Chem.* **2010**, *34*, 420.

(252) Filidou, V.; Simmons, S.; Karlen, S. D.; et al. *Nat. Phys.* **2012**, *8*, 596.

(253) Ju, C.; Suter, D.; Du, *J. Phys. Rev. A* **2007**, *75*, 12318.

(254) Ayabe, K.; Sato, K.; Nishida, S.; et al. *Phys. Chem. Chem. Phys.* **2012**, *14*, 9137.

(255) Shultz, D. A.; Fico, R. M.; Bodnar, S. H.; et al. *J. Am. Chem. Soc.* **2003**, *125*, 11761.

(256) Borbat, P. P.; Freed, J. H. *Methods Enzymol.* **2007**, *423*, 52.

(257) Hustedt, E. J.; Stein, R. A.; Sethaphong, L.; et al. *Biophys. J.* **2006**, *90*, 340.

(258) Wagemans, W.; Schellekens, A. J.; Kemper, M.; et al. *Phys. Rev. Lett.* **2011**, *106*, 196802.

(259) Wang, H.; Mauthoor, S.; Din, S.; et al. *ACS Nano* **2010**, *4*, 3921.

(260) Shultz, D. A.; Mussari, C. P.; Ramanathan, K. K.; et al. *Inorg. Chem.* **2006**, *45*, 5752.

(261) Ayabe, K.; Sato, K.; Nishida, S.; et al. *Phys. Chem. Chem. Phys.* **2012**, *14*, 9137.

(262) Banham, J. E.; Baker, C. M.; Ceola, S.; et al. *J. Magn. Reson.* **2008**, *191*, 202.

(263) Finazzo, C.; Calle, C.; Stoll, S.; et al. *Phys. Chem. Chem. Phys.* **2006**, *8*, 1942.

(264) Monahan, A. R.; Brado, J. A.; DeLuca, A. F. *J. Phys. Chem.* **1972**, *76*, 446.

(265) Monahan, A. R.; Brado, J. A.; DeLuca, A. F. *J. Phys. Chem.* **1972**, *76*, 1994.

(266) Serri, M.; Wu, W.; Fleet, L. R.; et al. *Nat. Commun.* **2014**, *5*, 3079.

(267) Heutz, S.; Mitra, C.; Wu, W.; et al. *Adv. Mater.* **2007**, *19*, 3618.

(268) Hajjaj, F.; Tashiro, K.; Nikawa, H.; et al. *J. Am. Chem. Soc.* **2011**, *133*, 9290.

(269) Rajca, A.; Rajca, S. *J. Am. Chem. Soc.* **1996**, *118*, 8121.

(270) D.F.Evans. *J. Chem. Soc.* **1959**, *0*, 2003.

(271) Löliger, J.; Scheffold, R. *J. Chem. Educ.* **1972**, *49*, 646.

(272) Peters, J. C.; Johnson, A. R.; Odom, A. L.; et al. *J. Am. Chem. Soc.* **1996**, *118*, 10175.

(273) Camp, P. J.; Jones, A. C.; Neely, R. K.; et al. *J. Phys. Chem. A* **2002**, *106*, 10725.

(274) Hayashi, H.; Nihashi, W.; Umeyama, T.; et al. *J. Am. Chem. Soc.* **2011**, *133*, 10736.

(275) Guzy, C. M.; Raynor, J. B.; Symons, M. C. R. *J. Chem. Soc.* A **1969**, *0*, 2299.

(276) Greiner, S. P.; Rowlands, D. L.; Kreilick, R. W. *J. Phys. Chem.* **1992**, *96*, 9132.

(277) Warner, M.; Mauthoor, S.; Felton, S.; et al. *ACS Nano* **2012**, *6*, 10808.

(278) Mainali, L. Multifrequency EPR Studies on Copper and Nitroxide Complexes via Bayesian Inference, Density Functional Theory and Lineshape Analysis, The University at Albany, State University of New York, **2009**.